MULTIPHASE FLUID FLOW IN POROUS AND FRACTURED RESERVOIRS

YU-SHU WU
Department of Petroleum Engineering
Colorado School of Mines
Golden, CO, USA

ELSEVIER

Amsterdam • Boston • Heidelberg • London
New York • Oxford • Paris • San Diego
San Francisco • Singapore • Sydney • Tokyo

Gulf Professional Publishing is an imprint of Elsevier

Gulf Professional Publishing is an imprint of Elsevier
225 Wyman Street, Waltham, MA 02451, USA
The Boulevard, Langford Lane, Kidlington, Oxford, OX5 1GB, UK

Notices

Knowledge and best practice in this field are constantly changing. As new research and experience broaden our understanding, changes in research methods, professional practices, or medical treatment may become necessary.

Practitioners and researchers must always rely on their own experience and knowledge in evaluating and using any information, methods, compounds, or experiments described herein. In using such information or methods they should be mindful of their own safety and the safety of others, including parties for whom they have a professional responsibility.

To the fullest extent of the law, neither the Publisher nor the authors, contributors, or editors, assume any liability for any injury and/or damage to persons or property as a matter of products liability, negligence or otherwise, or from any use or operation of any methods, products, instructions, or ideas contained in the material herein.

ISBN: 978-0-12-803848-2

Library of Congress Cataloging-in-Publication Data

A catalog record for this book is available from the Library of Congress

British Library Cataloguing-in-Publication Data

A catalogue record for this book is available from the British Library

DEDICATION

This book is dedicated to my family, teachers, colleagues and students.

PREFACE

This book focuses on the physics of multiphase fluid flow and displacement in porous and fractured media as well as quantitative approaches and analyses for describing such physical processes in reservoirs. The book is intended to complement the existing literature by presenting new advances and updated developments in multiphase fluid flow in porous media. The material of this book is based primarily on (1) a series of peer-reviewed papers, published by me or with co-authors and (2) the course notes that I have used to teach undergraduate and graduate courses on *petroleum reservoir engineering* and *multiphase fluid flow in porous media* at the Colorado School of Mines. The publications that this book is based on are related to the research on the subject of multiphase fluid flows in porous and fractured media, which I have carried out or been involved with since the late 1980s at the University of California, Berkeley, California (CA); HydroGeoLogic, Inc., Reston, Virginia; the Lawrence Berkeley National Laboratory, Berkeley, CA; and the Colorado School of Mines, Golden Colorado.

The book can be used as a textbook or reference for senior undergraduate and graduate students in petroleum engineering, hydrogeology or groundwater hydrology, soil sciences, and other related engineering fields, such as civil and environmental engineering. It can also serve as a reference book for hydrogeologists, petroleum reservoir engineers, and other engineers and scientists working in the area of flow and transport in porous media.

The content of the book is organized to cover fundamentals of multiphase fluid flow in porous media. It discusses the physical processes and principles governing multiphase porous-medium flow using Darcy's law, relative permeability, and capillary-pressure concepts. This book uses the black-oil model as an example of immiscible multiphase fluid flow to discuss flow-governing equations and approaches for their solution to quantity flow and displacement processes in reservoirs. Specifically, this book presents the extensions of the classical Buckley–Leverett fractional flow theory to one-dimensional linear and radial composite systems, to analysis of immiscible displacement of non-Newtonian fluids in porous media, and to non-Darcy displacement using *Forchheimer* and Barree and Conway non-Darcy flow models. In addition, the book reviews the concept, approach, and development for modeling multiphase flow in

fractured porous media and multiphase fluid flow and heat transfer in reservoirs. In an effort to include the new developments, the book also presents mathematical formulations and numerical modeling approaches for multiphase flow coupled with geomechanics and for flow in unconventional petroleum reservoirs.

Yu-Shu Wu
Professor of Petroleum Reservoir Engineering
Department of Petroleum Engineering
Colorado School of Mines
Golden, Colorado, USA
Foundation CMG Chair in Reservoir Modeling

ACKNOWLEDGMENTS

I would like to thank Dr Zhaoqin Huang at the China University of Petroleum (Huadong) for his tremendous help in preparing the manuscript during his postdoctoral research at the Colorado School of Mines (CSM). In addition, he has contributed the MATLAB codes for calculation of most of the analytical solutions for multiphase flow in porous media of the book, which are provided in the appendixes. His MATLAB programs have reproduced the plots from previous publications, and these programs will find more applications in the analysis of multiphase flow in porous media as well as the examination of the numerical simulation results. I could not have completed this book without his support and help.

I would also like to thank my colleague at CSM, Dr. Philip H. Winterfeld, for his thorough technical review of the manuscript and sharing his expertise in reservoir simulation. I am highly indebted to Prof. Jun Yao at the China University of Petroleum (Huadong) for offering and hosting me for a sabbatical leave in the fall of 2014, while I taught several courses related to *multiphase fluid flow in porous media* and had the time to write the majority of the manuscript.

I would like to take this opportunity to thank many of my current and former colleagues and friends in the US and China who have made this book possible. Specifically, I would like to thank the faculty and students of the Petroleum Engineering Department at CSM for their criticisms and suggestions to improve the materials of the book. I am grateful to many of my former colleagues in the Earth Sciences Division of the Lawrence Berkeley National Laboratory, Berkeley, California, and in HydroGeoLogic Inc., Reston, Virginia, for the opportunities of working together on studies of flow and transport in porous media over past decades.

I would like to thank the editorial and production staff of Elsevier for their work and professionalism.

I also acknowledge financial support from Foundation CMG (Computer Modelling Group).

CHAPTER 1

Introduction

1.1 BACKGROUND

Processes of flow and displacement of multiphase fluids though porous media occur in many subsurface systems and have found wide application in many scientific, technical, and engineering fields, such as petroleum engineering, groundwater and vadose zone hydrology, soil sciences, geothermal energy development, subsurface contamination investigation and remediation, and subsurface resource storage or waste disposal. Because of the needs in these areas, tremendous research and development efforts have been devoted to investigating the physics of multiphase flow and transport in porous and fractured media in the past century. As a result of multidisciplinary research efforts, significant progress and scientific advances have been made in the understanding of the dynamics of porous-medium flow of multiple immiscible fluids.

The continual research and development in analyzing flow and transport processes of multiphase fluids in porous media over the past half century have been helped and accelerated by concerted efforts of laboratory experiments on porous-medium samples at various scales, field studies, theoretical analysis, and mathematical modeling. Many quantitative approaches and models have been developed and applied successfully to describe, understand, and predict flow behavior of multiphase fluids in reservoirs. During the same period, our knowledge in understanding porous-medium flow phenomena and our ability to apply those understandings to solving practical problems have been significantly improved using the quantitative modeling approach. Mathematical modeling approaches have matured and become standard practices in subsurface natural resource development, storage system design, contamination investigation, and remediation scheme evaluation. In addition, numerical modeling studies are routinely carried out to investigate physical phenomena for insights as well as to optimize field project design and operation, production, or cleanup, which in many cases may not be possible without the help of a numerical modeling tool.

Multiphase Fluid Flow in Porous and Fractured Reservoirs
ISBN 978-0-12-803848-2
http://dx.doi.org/10.1016/B978-0-12-803848-2.00001-5

1.2 LITERATURE REVIEW, DEVELOPMENT, AND ADVANCE

Humankind may have noticed flow in porous media from the beginning of civilization, when they stood on beach sands facing tides, looked at rain percolating into the ground, or began to grow plants in soils.

The development of the theory of flow through porous media, as a branch of applied science, began with Henry Darcy (1856) who determined experimentally the proportionality of pressure gradient and flux, now known as Darcy's law. Darcy's law was first developed for water in saturated flow, but has since been extended to multiphase and unsaturated flow, and to incorporate other phenomena, such as surface tension, gravity, fracture flow, chemical reaction, and changing fluid properties. Such extension into various coupled processes has been made possible by the use of numerical computation, which in turn depends on powerful computer technology and advances in computational mathematics. Darcy's law and its extensions have been applied to a wide range of activities, including agriculture, environmental management, and most notably, petroleum reservoir engineering.

Darcy's law has been the foundation for studies of flow and transport phenomena through porous media. The empirical Darcy's law can also be derived from the Navier–Stokes equations via a volume averaging method or homogenization theory (e.g., Neuman, 1977; Whitaker, 1986). Even though originally obtained only for describing flow of a single-phase fluid, Darcy's law has been extended and generalized to describe the flow of multiple, immiscible fluids (e.g., Scheidegger, 1974; Hassanizadeh and Gray, 1979a,b). The multiphase extension of Darcy's law has been used exclusively as the basis for quantitative studies of dynamics of multiphase fluid flow in porous and fractured media.

Most significant contributions to understanding multiphase flow in porous media have been made since the 1920s (Willhite, 1986), 1930s (Richards, 1931), and 1940s (Buckley and Leverett, 1942) with the rapid advances in the petroleum industry, groundwater hydrology, and soil sciences. The fundamental understanding of immiscible flow and displacement of Newtonian fluids in porous media was initially contributed by Buckley and Leverett (1942) in their classical study of fractional flow theory. The Buckley–Leverett solution provides insight into immiscible-fluid displacement processes, describing a saturation profile advancing with a sharp front along the flow direction, while capillary pressure and gravity effects are ignored. Effects of gravity and capillary pressure on a linear water

flood have since been included by later studies (e.g., Fayers and Sheldon, 1959; Hovanessian and Fayers, 1961; Codreanu et al., 1966). Some special analytical solutions of immiscible displacement including the effects of capillary pressure were obtained in the literature, such as Yortsos and Fokas (1983), Chen (1988), and McWhorter and Sunada (1990).

Many extensions, generalizations, and improvements to Buckley–Leverett theory have been made to obtain and enhance understandings of complicated flow behavior of multiple phases in porous media. In particular, the Buckley–Leverett fractional flow theory has been generalized and applied by various authors to study Enhanced Oil Recovery (EOR) (Pope, 1980), surfactant flooding (Larson, 1978), polymer flooding (Patton et al., 1971), mechanisms of chemical methods (Larson et al., 1982), and alkaline flooding (DeZabala et al., 1982). An extension to more than two immiscible phases using "coherence theory" was described by Helfferich (1981).

More recently, studies have extended the Buckley–Leverett solution to flow in a composite, one-dimensional heterogeneous, composite-reservoir system (Wu et al., 1993), to non-Newtonian fluid flow (Wu, 1990; Wu et al., 1991, 1992; Wu and Pruess, 1996, 1998), and to non-Darcy displacement of immiscible fluids in porous media (Wu, 2001, 2002a,b; Wu et al., 2011a,b).

Most fundamentals of the physics of flow of multiphase fluids in porous media have been understood by laboratory experiments, theoretical analysis, mathematical modeling, and field studies (Collins, 1961; Bear, 1972; Scheidegger, 1974). Analysis of porous medium flow processes relies traditionally on Darcy's law-based approaches, and application of such analysis has provided quantitative methodologies and modeling tools for many related scientific and engineering disciplines. Among them, one of the best beneficiaries of the theory and advances developed in flow through porous media is perhaps petroleum reservoir engineering, in which calculation of oil, gas, and water flow and production, and assessment of primary and secondary oil recovery and reservoir dynamics, are all based on the physics of multiphase flow in reservoirs (Craft et al., 1959; Dake, 1983; Prats, 1985; Willhite, 1986; Honarpour et al., 1986; Ahmed and McKinney, 2011). Recent development of EOR applications, multiphase flow under chemical flooding, supplementary fluid injection, or thermal recovery is also modeled using various modifications of Darcy's law and multiphase flow concepts (Prats, 1985; Lake, 1989; Sorbie, 1990; Green and Willhite, 1998).

One of the main reasons for the significant scientific advance and related technical development has been development and application of mathematical modeling methodology. Numerical simulation of multiphase subsurface flow and transport phenomena may be one of the most important developments in the earth sciences during the second half of the twentieth century. Due to its generality and effectiveness in handling multiphase flow and transport problems in porous and fractured media, the numerical simulation technique has evolved to become the major tool used by scientists and engineers in studies of flow and transport processes in a porous medium. The continual development of numerical approaches has been motivated by a variety of needs in many industries and earth sciences from developing subsurface natural resources to addressing environmental concerns. Since the late 1950s, significant progress has been made in developing and applying numerical simulation techniques in petroleum engineering (e.g., Peaceman, 1977; Aziz and Settari, 1979; Thomas, 1981; Coats, 1987; Mattax and Dalton, 1990; Ertekin et al., 2001; Fanchi, 2005), in groundwater literature (e.g., Huyakorn and Pinder, 1983; Istok, 1989; Zheng and Bennett, 2002), and more recently in computational science (e.g., Chen et al., 2006; Chen, 2007). It should be mentioned that the advances in numerical simulation have benefited significantly from rapidly advancing modern computer technology, hardware, and computational algorithms.

Numerical modeling approaches currently used for simulating coupled multiphase flow and transport processes are generally based on methodologies developed for petroleum and geothermal reservoir simulation and groundwater modeling. They involve solving fully coupled formulations describing these processes using finite-difference or finite-element schemes with a volume-averaging approach. Earlier researches on modeling multiphase flow in porous media were primarily motivated during the development of petroleum reservoirs (Douglas et al., 1959; Peaceman and Rachford, 1962; Coats et al., 1967) and geothermal reservoirs (Mercer et al., 1974; Thomas and Pierson, 1978; Pruess, 1990, 1991). During the same decades, problems involving unsaturated and two-phase flow and transport in aquifers and subsurface soils were increasingly recognized and investigated in groundwater hydrology and soil science. Many numerical approaches were developed in parallel and applied to modeling flow and transport phenomena in the vadose zone (e.g., Narasimhan and Witherspoon, 1976; Cooley, 1983; Huyakorn et al., 1984; Morel-Seytoux and Billica, 1985; Celia et al., 1990; Wu and Pruess, 2000; Looney and Falta, 2000).

In a parallel development, soil and groundwater contamination by Non-Aqueous Phase Liquids (NAPL), such as contamination from oil and gasoline leakage or other organic chemicals, has received increasing attention. The subsurface environmental concern has motivated significant research activities in developing and applying multiphase flow and transport models for assessing NAPL contamination and associated cleanup operations. As a result, many numerical models and computational algorithms have been developed and improved upon for solving multiphase fluid flow and organic chemical transport problems through porous and fractured media in the subsurface (Abriola and Pinder, 1985; Faust, 1985; Forsyth, 1988, 1991, 1994; Forsyth and Shao, 1991; Kaluarachchi and Parker, 1989; Falta et al., 1992a,b; Huyakorn et al., 1994).

Recent development in several frontiers of energy and natural resources and subsurface storage has revitalized the interest in and further driven the research of flow and transport processes of multiphase fluids in complicated reservoir systems. The last few decades have witnessed wide, diverse interests in theory and application of multiphase fluid flow in porous media. These newly, rapidly developing and emerging fields include the following:

CO_2 geosequestration in subsurface formations: To address the increasing concerns regarding greenhouse gas emission and its impact on global climate, CO_2 geologic sequestration, i.e., injecting large amounts of CO_2 into deep subsurface formations for long-term storage, is considered to be a viable approach for near-term implementation. Carbon dioxide can be sequestered in deep saline aquifers as well as in depleted oil and gas reservoirs, and coal beds that are either uneconomical or producing coal bed methane. The mechanisms of CO_2 storage (Metz et al., 2005) include *structural trapping* (trapping CO_2 as a mobile "gas", i.e., a supercritical fluid, in formations); *residual gas trapping* (trapping CO_2 as an immobile "gas"); *solubility trapping* (trapping of CO_2 as a soluble component in brine); and *mineral trapping* (conversion of CO_2 into carbonate minerals: calcite, dolomite, siderite, etc.). These mechanisms are controlled by physical and chemical processes of CO_2 storage, flow, and transport in reservoirs. To evaluate the integrity and proper design of a CO_2 geologic storage system and to assess the risk associated with a given subsurface system, mathematical models and simulations have been used as the main approach to study and predict the performance of a CO_2 storage system, because of the large space and time scales (Pruess and Garcia, 2002; Oldenburg and Lewicki, 2006; Pruess and Spycher, 2007; Benson and Cole, 2008; Al-Khoury and Bundschuh, 2014; Winterfeld and Wu, 2014).

Unconventional petroleum resources: Large reserves of unconventional petroleum resources, oil and gas from tight sand and shale formations, have recently become recoverable as a result of improved horizontal drilling and hydraulic fracturing technologies (EIA, 2011). US oil production increased from 5 MMBD (million barrels per day) in 2004 to 8 MMBD in 2014. However, understanding and technology needed for effective development of unconventional petroleum reservoirs are still behind the industry needs; oil and gas recovery rates from those unconventional resources remain very low. For example, there are no effective secondary or EOR approaches available for handling these low-permeability reservoirs.

Unconventional petroleum reservoir formations are characterized by extremely low permeability and small pore size. Compared with conventional reservoirs, oil and gas flow in ultra-low-permeability unconventional reservoirs is subject to more nonlinear, coupled physical processes, including nonlinear adsorption/desorption, non-Darcy flow (at both high and low flow rates), strong rock–fluid interaction, and rock deformation within nanopores or microfractures, coexisting with complex flow geometry and multiscaled heterogeneity. Therefore, quantifying the flow in unconventional oil and gas reservoirs has been a significant challenge and motivated significant efforts in developing basic understanding, quantitative methods, mathematical models, and modeling tools and their application (Lee and Hopkins, 1994; Moridis and Freeman, 2014; Wu et al., 2014; Yu and Sepehrnoori, 2014).

Gas hydrates: Natural gas hydrates, long considered a nuisance for blocking transmission pipelines, jeopardizing the foundations of deep-water platforms and pipelines, and causing other damages in deep-water oil and gas production (Sloan and Koh, 2007), may be an important potential energy source in the future of the world. Vast reserves of natural gas hydrates are globally distributed in the permafrost and under the ocean floors (Rutqvist et al., 2009; NETL, 2011). The potential to produce significant amounts of natural gas from gas hydrate formations has recently attracted increased international attention and feasibility tests and studies of long-term gas production from gas hydrates have been reported (Collet et al., 2012) as a potential energy source. However, there are tremendous scientific and technological challenges and significant uncertainties facing commercial hydrate-gas production currently or in the near future (Moridis, 2011; Moridis et al., 2013). Producing natural gas from methane hydrate requires the understanding of physics behind the response of

naturally occurring gas hydrates to depressurization-induced or thermal-, chemical-, or mechanical-stimulated dissociation processes of gas hydrates into producible free gas.

There has been a concerted international effort to determine the technical viability and economic feasibility of natural gas production from gas hydrate deposits with some progress made in this area, but much remains to be understood or dealt with. There is the need to develop economical methods for safely extracting the methane, while minimizing environmental impacts. On the other hand, physics-based mathematical models and numerical simulation associated with gas hydrate movement and production in reservoirs play a critical role in the effort to assess the production potential of hydrates (Moridis et al., 2013).

Enhanced geothermal system (EGS): Abundant and clean geothermal energy from enhanced (or engineered) geothermal systems (EGS) is among the best options as sustainable energy resources of the future. The EGS concept has been receiving worldwide attention and under intensive studies in the last decade. In comparison, hydrothermal reservoir resources, the 'low-hanging fruit' of geothermal energy, are very limited in the world, whereas EGS represents an "infinite" potential to supply the world with all its energy needs. The EGS is an engineered approach of mining subsurface heat by a humanmade reservoir system. Creating an enhanced geothermal reservoir system requires that water (or other fluid) be injected deep into the reservoirs through fractures, heated by contact with the hot rock, and then produced through production wells for electricity generation or other usage (Tester et al., 2006). Even with the significant progress made through laboratory and modeling studies as well as field demonstrations, geothermal energy from EGS reservoirs cannot at present compete with other traditional forms of energy, such as oil and gas, as the primary energy resource. There are significant needs for future research, development, and investment before geothermal energy becomes viable to serve as the primary energy resource.

Heat mining or recovery from fractured EGS reservoirs is subject to many physical and chemical processes with a heated foreign fluid flow and interactions with reservoir rock in high-temperature geological formations, involving heat transfer, multiphase flow, rock deformation, and chemical reactions. These thermal–hydrological–mechanical–chemical (THMC) processes must be understood and managed before a sound engineering design and successful field operation can be achieved, in which numerical modeling will play a critical role (Hu et al., 2013; Wu et al., 2015).

In summary, our understanding of multiphase fluid flow and displacement processes in porous media has been enhanced significantly in the past few decades. As application examples, many physics-based mathematical models and associated numerical modeling methods have been developed and used as standard techniques in subsurface investigations from developing energy and other natural resources and characterizing contamination sites to engineering design of subsurface storage systems. In the past few years, the quantitative modeling approaches have been used even to help laboratory experiments for testing design and data and result analysis.

1.3 PURPOSE AND SCOPE

The objectives of this book are to discuss the physics and principles governing multiphase fluid flow in porous and fractured media; to review mathematical models, quantitative approaches, and constitutive correlations for describing multiphase flow and displacement in porous media; and to discuss and present analytical solutions and mathematical formulations for evaluation of multiphase flow and displacement processes in porous and fractured media. This book complements the existing literature by presenting new advances, current developments, and updated quantitative approaches. Specifically, a significant portion of its content is based on the work and research of the author and his colleagues in the past few decades. In addition, the appendices present a series of computational programs for calculating the analytical solutions presented in the book, making it very convenient for the readers to use the solutions in their own studies to analyze laboratory experiments or to verify numerical modeling results for field applications.

The remaining chapters of the book are organized as follows: Chapter 2 presents the fundamentals of multiphase fluid flow in porous media with basic science and engineering concepts. It discusses physical processes and principles for governing multiphase porous medium flow and introduces Darcy's law, relative permeability, and capillary pressure concepts. Chapter 3 describes flow-governing equations and mathematical models for multiphase flow in porous media, using the black-oil model as an example. It also discusses constitutive relations and solution conditions as well as how to solve these equations. Chapter 4 discusses a unified numerical model and formulation for solving multiphase flow and displacement in porous and fractured media.

Chapters 5 through 8 focus on analytical approaches and recent developments in discussing and extending the classic Buckley–Leverett theory to a composite reservoir and non-Newtonian fluid and non-Darcy displacement of immiscible multiphase fluids in reservoirs. Chapter 5 discusses the classical Buckley–Leverett solution and Welge approach. Chapter 6 presents the extensions of the Buckley–Leverett fractional flow theory to one-dimensional linear and radial composite systems. Chapter 7 presents the analysis of immiscible displacement of non-Newtonian fluids in porous media using the Buckley–Leverett approach, whereas Chapter 8 describes non-Darcy immiscible displacement using the *Forchheimer* and Barree and Conway non-Darcy flow models.

Chapter 9 discusses the concept, approach, and development in modeling multiphase flow in fractured porous media. Chapter 10 deals with multiphase fluid and heat flow in reservoirs. Chapter 11 discusses multiphase flow coupled with geomechanics in porous and fractured media, a new area for multiphase porous-medium flow. Lastly, Chapter 12 introduces recent developments in multiphase fluid flow in unconventional petroleum reservoirs.

Finally, in the Appendixes, codes and computational programs are provided for calculating the analytical solutions presented in Chapters 5 through 8.

REFERENCES

Abriola, L.M., Pinder, G.F., 1985. A multiphase approach to the modeling of porous media contamination by organic compounds: 1. Equation development. Water Resources Research 21 (1), 11–18.

Ahmed, T., McKinney, P., 2011. Advanced Reservoir Engineering. Gulf Professional Publishing.

Al-Khoury, R., Bundschuh, J., 2014. Computational Models for CO_2 Geo-sequestration & Compressed Air Energy Storage. CRC Press.

Aziz, K., Settari, A., 1979. Petroleum Reservoir Simulation. Applied Science Publishers, London.

Bear, J., 1972. Dynamics of Fluids in Porous Media. American Elsevier, New York.

Benson, S.M., Cole, D.R., 2008. CO_2 sequestration in deep sedimentary formations. Elements 4 (5), 325–331.

Buckley, S.E., Leverett, M.C., 1942. Mechanism of fluid displacement in sands. Transactions of the AIME 146 (01), 107–116.

Celia, M.A., Bouloutas, E.T., Zarba, R.L., 1990. A general mass-conservative numerical solution for the unsaturated flow equation. Water Resources Research 26 (7), 1483–1496.

Chen, Z., 2007. Reservoir simulation: mathematical techniques in oil recovery. Society for Industrial and Applied Mathematics. CBMS-NSF regional conference series in applied mathematics, vol. 77.

Chen, Z., Huan, G., Ma, Y., 2006. Computational methods for multiphase flows in porous media. SIAM Series on Computational Science & Engineering, vol. 2.

Chen, Z.-X., 1988. Some invariant solutions to two-phase fluid displacement problems including capillary effect (includes associated papers 18744 and 19037). SPE Reservoir Engineering 3 (02), 691–700.

Coats, K.H., 1987. Reservoir simulation. In: Bradley, H.B. (Ed.), Petroleum Engineering Handbook. Society of Petroleum Engineers, Richardson, Texas, pp. 1–20.

Coats, K.H., Nielsen, R.L., Terhune, M.H., Weber, A.G., 1967. Simulation of three-dimensional two-phase flow in oil and gas reservoirs. Society of Petroleum Engineers Journal 7 (04), 377–388.

Codreanu, D., Hauer, R., Vernescu, A., 1966. Displacement of oil by water in heterogeneous rocks and evaluation of heterogeneity in reservoir engineering calculations. Revue de L'Institut Français Du Pétrole 21 (1), 57–80.

Collett, T.S., Lee, M.W., Zyrianova, M.V., Mrozewski, S.A., Guerin, G., Cook, A.E., Goldberg, D.S., 2012. Gulf of Mexico gas hydrate joint industry project Leg II logging-while-drilling data acquisition and analysis. Marine and Petroleum Geology 34 (1), 41–61.

Collins, R.E., 1961. Flow of Fluids through Porous Materials. PennWell Publishing Company, Tulsa, OK.

Cooley, R.L., 1983. Some new procedures for numerical solution of variably saturated flow problems. Water Resources Research 19 (5), 1271–1285.

Craft, B.C., Hawkins, M.F., Terry, R.E., 1959. Applied Petroleum Reservoir Engineering. Prentice-Hall Englewood Cliffs, NJ.

Dake, L.P., 1983. Fundamentals of Reservoir Engineering. Elsevier.

Darcy, H., 1856. Les fontaines publiques de la ville de Dijon. Dalmont, Paris.

DeZabala, E.F., Vislocky, J.M., Rubin, E., Radke, C.J., 1982. A chemical theory for linear alkaline flooding. Society of Petroleum Engineers Journal 22 (02), 245–258.

Douglas, J.J., Peaceman, D.W., Rachford, J.H.H., 1959. A method for calculating multi-dimensional immiscible displacement. Transactions of the AIME 216, 297–308.

EIA, U. S, 2011. International Energy Outlook 2011. Washington, DC.

Ertekin, T., Abou-Kassem, J.H., King, G.R., 2001. Basic Applied Reservoir Simulation. Society of Petroleum Engineers, Richardson, TX.

Falta, R.W., Pruess, K., Javandel, I., Witherspoon, P.A., 1992a. Numerical modeling of steam injection for the removal of nonaqueous phase liquids from the subsurface: 1. Numerical formulation. Water Resources Research 28 (2), 433–449.

Falta, R.W., Pruess, K., Javandel, I., Witherspoon, P.A., 1992b. Numerical modeling of steam injection for the removal of nonaqueous phase liquids from the subsurface: 2. Code validation and application. Water Resources Research 28 (2), 451–465.

Fanchi, J.R., 2005. Principles of Applied Reservoir Simulation. Gulf Professional Publishing.

Faust, C.R., 1985. Transport of immiscible fluids within and below the unsaturated zone: a numerical model. Water Resources Research 21 (4), 587–596.

Fayers, F.J., Sheldon, J.W., 1959. The effect of capillary pressure and gravity on two-phase fluid flow in a porous medium. Petroleum Transactions, AIME 216, 147–155.

Forsyth, P.A., 1988. Simulation of nonaqueous phase groundwater contamination. Advances in Water Resources 11 (2), 74–83.

Forsyth, P.A., 1991. A control volume finite element approach to NAPL groundwater contamination. SIAM Journal on Scientific and Statistical Computing 12 (5), 1029–1057.

Forsyth, P.A., 1994. Three-dimensional modelling of steam flush for DNAPL site remediation. International Journal for Numerical Methods in Fluids 19 (12), 1055–1081.

Forsyth, P.A., Shao, B.Y., 1991. Numerical simulation of gas venting for NAPL site remediation. Advances in Water Resources 14 (6), 354–367.
Green, D.W., Willhite, G.P., 1998. Enhanced oil recovery. In: Henry, L. (Ed.), Doherty Memorial Fund of AIME. Society of Petroleum Engineers, Richardson, Tex.
Hassanizadeh, M., Gray, W.G., 1979a. General conservation equations for multi-phase systems: 1. Averaging procedure. Advances in Water Resources 2, 131–144.
Hassanizadeh, M., Gray, W.G., 1979b. General conservation equations for multi-phase systems: 2. Mass, momenta, energy, and entropy equations. Advances in Water Resources 2, 191–203.
Helfferich, F.G., 1981. Theory of multicomponent multiphase displacement in porous media. Society of Petroleum Engineers Journal 21 (01), 51–62.
Honarpour, M.M., Koederitz, F., Herbert, A., 1986. Relative Permeability of Petroleum Reservoirs. CRC Press Inc., Boca Raton, FL.
Hovanessian, S.A., Fayers, F.J., 1961. Linear water flood with gravity and capillary effects. Society of Petroleum Engineers Journal 1 (01), 32–36.
Hu, L., Winterfeld, P.H., Fakcharoenphol, P., Wu, Y.-S., 2013. A novel fully-coupled flow and geomechanics model in enhanced geothermal reservoirs. Journal of Petroleum Science and Engineering 107, 1–11.
Huyakorn, P.S., Panday, S., Wu, Y.S., 1994. A three-dimensional multiphase flow model for assessing NAPL contamination in porous and fractured media, 1. Formulation. Journal of Contaminant Hydrology 16 (2), 109–130.
Huyakorn, P.S., Pinder, G.F., 1983. Computational Methods in Subsurface Flow. Academic Press.
Huyakorn, P.S., Thomas, S.D., Thompson, B.M., 1984. Techniques for making finite elements competitve in modeling flow in variably saturated porous Media. Water Resources Research 20 (8), 1099–1115.
Istok, J., 1989. Groundwater Modeling by the Finite Element Method. American Geophysical Union.
Kaluarachchi, J.J., Parker, J.C., 1989. An efficient finite element method for modeling multiphase flow. Water Resources Research 25 (1), 43–54.
Lake, L.W., 1989. Enhanced Oil Recovery. Prentice Hall Inc., Old Tappan, NJ.
Larson, R.G., 1978. Analysis of the physical mechanisms in surfactant flooding. Society of Petroleum Engineers Journal 18 (01), 42–58.
Larson, R.G., Davis, H.T., Scriven, L.E., 1982. Elementary mechanisms of oil recovery by chemical methods. Journal of Petroleum Technology 34 (02), 243–258.
Lee, W.J., Hopkins, C.W., 1994. Characterization of tight reservoirs. Journal of Petroleum Technology 46 (11), 956–964.
Looney, B.B., Falta, R.W., 2000. Vadose Zone Science and Technology Solutions. Battelle Press Columbus, Ohio.
Mattax, C.C., Dalton, R.L., 1990. Reservoir simulation. Journal of Petroleum Technology 42 (6), 692–695.
McWhorter, D.B., Sunada, D.K., 1990. Exact integral solutions for two-phase flow. Water Resources Research 26 (3), 399–413.
Mercer Jr., J.W., Faust, C., Pinder, G.F., 1974. Geothermal reservoir simulation. In: Research for the Development of Geothermal Energy Resources, vol. 1. Princeton University, Princeton, New Jersey, pp. 256–267.
Metz, B., Davidson, O., De Coninck, H., Loos, M., Meyer, L., 2005. Carbon Dioxide Capture and Storage. IPCC Geneva, Switzerland.
Morel-Seytoux, H.J., Billica, J.A., 1985. A two-phase numerical model for prediction of infiltration: applications to a semi-infinite soil column. Water Resources Research 21 (4), 607–615.

Moridis, G.J., 2011. Challenges, uncertainties and issues facing gas production from gas hydrate deposits.
Moridis, G.J., Collett, T.S., Boswell, R., Hancock, S., Rutqvist, J., Santamarina, C., Kowalsky, M., 2013. Gas hydrates as a potential energy source: state of knowledge and challenges. In: Advanced Biofuels and Bioproducts. Springer, pp. 977–1033.
Moridis, G.J., Freeman, C.M., 2014. The RealGas and RealGasH_2O options of the TOUGH+ code for the simulation of coupled fluid and heat flow in tight/shale gas systems. Computers & Geosciences 65, 56–71.
Narasimhan, T.N., Witherspoon, P.A., 1976. An integrated finite difference method for analyzing fluid flow in porous media. Water Resources Research 12 (1), 57–64.
NETL, 2011. Energy resource potential of methane hydrate, an introduction to the science and energy potential of a unique resource.
Neuman, S.P., 1977. Theoretical derivation of Darcy's law. Acta Mechanica 25 (3–4), 153–170.
Oldenburg, C.M., Lewicki, J.L., 2006. On leakage and seepage of CO_2 from geologic storage sites into surface water. Environmental Geology 50 (5), 691–705.
Patton, J.T., Coats, K.H., Colegrove, G.T., 1971. Prediction of polymer flood performance. Society of Petroleum Engineers Journal 11 (01), 72–84.
Peaceman, D.W., 1977. Fundamentals of Numerical Reservoir Simulation. Elsevier Scientific Publishing Co., New York, NY.
Peaceman, D.W., Rachford, J.H.H., 1962. Numerical calculation of multidimensional miscible displacement. Society of Petroleum Engineers Journal 2 (04), 327–339.
Pope, G.A., 1980. The application of fractional flow theory to enhanced oil recovery. Society of Petroleum Engineers Journal 20 (03), 191–205.
Prats, M., 1985. Thermal recovery. HL Doherty Memorial Fund of AIME: Society of Petroleum Engineers, New York.
Pruess, K., 1990. Modeling of geothermal reservoirs: fundamental processes, computer simulation and field applications. Geothermics 19 (1), 3–15.
Pruess, K., 1991. TOUGH2: a general-purpose numerical simulator for multiphase fluid and heat flow.
Pruess, K., Garcia, J., 2002. Multiphase flow dynamics during CO_2 disposal into saline aquifers. Environmental Geology 42 (2–3), 282–295.
Pruess, K., Spycher, N., 2007. ECO2N–A fluid property module for the TOUGH2 code for studies of CO_2 storage in saline aquifers. Energy Conversion and Management 48 (6), 1761–1767.
Richards, L.A., 1931. Capillary conduction of liquids through porous mediums. Journal of Applied Physics 1, 318–333.
Rutqvist, J., Moridis, G.J., Grover, T., Collett, T., 2009. Geomechanical response of permafrost-associated hydrate deposits to depressurization-induced gas production. Journal of Petroleum Science and Engineering 67 (1), 1–12.
Scheidegger, A.E., 1974. The Physics of Flow through Porous Media. University of Toronto Press.
Sloan Jr., E.D., Koh, C., 2007. Clathrate Hydrates of Natural Gases. CRC press.
Sorbie, K.S., 1990. Polymers in Improved Oil Recovery. CRC Press Inc., Boca Raton, FL (USA).
Tester, J.W., Anderson, B.J., Batchelor, A.S., Blackwell, D.D., DiPippo, R., Drake, E.M., Nichols, K., 2006. The Future of Geothermal Energy, vol. 358.
Thomas, G.W., 1981. Principles of Hydrocarbon Reservoir Simulation. IHRDC, Boston, MA.
Thomas, L.K., Pierson, R.G., 1978. Three-dimensional geothermal reservoir simulation. Society of Petroleum Engineers Journal 18 (02), 151–161.

Whitaker, S., 1986. Flow in porous media I: a theoretical derivation of Darcy's law. Transport in Porous Media 1 (1), 3–25.
Willhite, G.P., 1986. Waterflooding. Society of Petroleum Engineers, Richardson, TX.
Winterfeld, P.H., Wu, Y.-S., 2014. Simulation of CO_2 sequestration in brine aquifers with geomechanical coupling. In: Al-Khoury, R., Bundschuh, J. (Eds.), Computational Models for CO_2 Geo-sequestration & Compressed Air Energy Storage. CRC Press, pp. 275–304.
Wu, Y.-S., 1990. Theoretical Studies of Non-newtonian and Newtonian Fluid Flow through Porous Media. Lawrence Berkeley Laboratory, Berkeley, CA.
Wu, Y.-S., 2001. Non-Darcy displacement of immiscible fluids in porous media. Water Resources Research 37 (12), 2943–2950.
Wu, Y.-S., 2002a. An approximate analytical solution for non-Darcy flow toward a well in fractured media. Water Resources Research 38 (3), 5-1–5-7.
Wu, Y.-S., 2002b. Numerical simulation of single-phase and multiphase non-Darcy flow in porous and fractured reservoirs. Transport in Porous Media 49 (2), 209–240.
Wu, Y.-S., Lai, B., Miskimins, J.L., 2011a. Simulation of non-Darcy porous media flow according to the Barree and Conway model. The Journal of Computational Multiphase Flows 3 (2), 107–122.
Wu, Y.-S., Lai, B., Miskimins, J.L., Fakcharoenphol, P., Di, Y., 2011b. Analysis of multiphase non-Darcy flow in porous media. Transport in Porous Media 88 (2), 205–223.
Wu, Y.-S., Li, J., Ding, D., Wang, C., Di, Y., 2014. A generalized framework model for the simulation of gas production in unconventional Gas reservoirs. SPE Journal 19 (05), 845–857.
Wu, Y.-S., Pruess, K., 1996. Flow of non-Newtonian fluids in porous media. Advances in Porous Media 3, 87–184.
Wu, Y.-S., Pruess, K., 1998. A numerical method for simulating non-Newtonian fluid flow and displacement in porous media. Advances in Water Resources 21 (5), 351–362.
Wu, Y.-S., Pruess, K., 2000. Numerical simulation of non-isothermal multiphase tracer transport in heterogeneous fractured porous media. Advances in Water Resources 23 (7), 699–723.
Wu, Y.-S., Pruess, K., Chen, Z.-X., 1993. Buckley-Leverett flow in composite porous media. SPE Advanced Technology Series 1 (02), 36–42.
Wu, Y.-S., Pruess, K., Witherspoon, P.A., 1991. Displacement of a Newtonian fluid by a non-Newtonian fluid in a porous medium. Transport in Porous Media 6 (2), 115–142.
Wu, Y.-S., Pruess, K., Witherspoon, P.A., 1992. Flow and displacement in Bingham non-Newtonian fluids in porous media. SPE Reservoir Engineering 7 (3), 369–376.
Wu, Y.-S., Xiong, Y., Kazemi, H., 2015. Coupled Thermo-hydrological processes in enhanced geothermal systems. In: Poate, J., Illangasekare, T., Kazemi, H., Kee, R. (Eds.), Pore Scale Phenomena Frontiers in Energy and Environment, vol. 10. World Scientific, pp. 279–298. http://doi.org/doi:10.1142/9789814623063_0015.
Yortsos, Y.C., Fokas, A.S., 1983. An analytical solution for linear waterflood including the effects of capillary pressure. Society of Petroleum Engineers Journal 23 (01), 115–124.
Yu, W., Sepehrnoori, K., 2014. Simulation of gas desorption and geomechanics effects for unconventional gas reservoirs. Fuel 116, 455–464.
Zheng, C., Bennett, G.D., 2002. Applied Contaminant Transport Modeling. Wiley-Interscience, New York.

CHAPTER 2

Multiphase Fluids in Porous Media

2.1 INTRODUCTION

The physical processes associated with flow and transport of multiphase fluids in porous media are governed by the same fundamental conservation laws as those used in any branch of the sciences and engineering. Conservation of mass, momentum, and energy governs the behavior of multiphase fluid flow, chemical transport, and heat transfer through porous and fractured media. These physical laws in porous media are well known at the pore level; however, in practice for a particular study of laboratory or field application, one may be interested only in global behavior or volume averaging of the porous medium system. Because of the complexity of pore geometries and the heterogeneity of a porous medium system, the macroscopic behavior is not easily deduced from that on the pore level or micro scale. For example, any attempts to directly apply the Navier–Stokes equation to flow problems through a lot of pores in an actual reservoir porous-medium system will face tremendous difficulties. These include poorly defined or unknown pore geometries or flow boundaries, complex dynamic phenomena of physical and chemical interactions between pores and fluids or between fluids and solids, and too many unknowns or equations, with too many undefined parameters or correlations, which cannot be solved at present for field-scale applications.

The macroscopic continuum approach is most commonly used in studies of flow and displacement processes in reservoirs from laboratory to field scale. For practical application, almost all theories on flow phenomena occurring in porous media lead to macroscopic laws applicable to a finite volume or a subdomain of the system under investigation, the dimensions of which are large compared with those of pores. Consequently, these laws lead to equations in which the porous medium and fluid system are treated as if they were continuous and characterized by the local values of a number of thermodynamic variables and rock and fluid parameters, defined for all points with appropriate averaging or *representative elementary volume* (REV)

Multiphase Fluid Flow in Porous and Fractured Reservoirs
ISBN 978-0-12-803848-2
http://dx.doi.org/10.1016/B978-0-12-803848-2.00002-7

(Bear, 1972). Then, flow equations, derived from combining conservation of mass, energy, and momentum and based on the REV concept, are used to describe flow processes in reservoirs.

2.2 BASIC SCIENCE AND ENGINEERING CONCEPTS, FLUIDS AND POROUS MEDIA

There are two basic goals for analysis of multiphase fluid flow in reservoirs: one is determination of *in situ* mass distribution spatially at a given time and the other is calculation of flow or movement of fluids in reservoirs. To determine mass distribution and calculate movement or "flow" of fluids in a porous-medium system of rock, we need to introduce a number of physical concepts, such as those describing fluid and rock properties. There are a number of excellent books in the literature to define and discuss these rock and fluid properties (e.g., Bear, 1972; Scheidegger, 1974; McCain, 1990; Dullien, 1991).

Determination of spatial mass distribution or local mass balance is a volumetric and static concept. To estimate how much water, oil, or gas is in place, in addition to geological data and geophysical logs, we need to introduce many physical parameters of reservoir rock, such as effective porosity, fluid density, fluid saturation, and their residual values, fluid-phase pressure, fluid and rock compressibility, solution gas–oil ratio, etc. These fluid and rock properties and parameters are not only necessary to estimate mass distribution in a reservoir system, but also provide the bases for mass balance calculation, needed for deriving flow-governing equations of multiphase fluids in reservoirs.

Flow and movement of fluids in porous media is a dynamic process and is driven by energy that is stored within reservoirs or supplied by injection. The key question for reservoir engineers and hydrologists to answer is how much fluid, water, oil, or gas can be produced under given geological and operational conditions. Or, how can the performance of the reservoir be optimized for maintaining long-term productivity or higher recovery rate? The flow and displacement in reservoirs is controlled by conservation laws of mass, energy, and momentum. To calculate flow in porous media, we need to introduce and determine many fluid flow and rock properties, such absolute permeability, fluid viscosity, interface tension (IFT), wettability, relative permeability, and capillary pressure concepts, etc. We also need to know the driving forces or flow mechanisms, i.e., the main energy driving fluid to flow from

reservoir to well, such as pressure and potential gradient, potential energy, or capillary force.

Continuum approaches of fluid mechanics and thermodynamics have been traditionally used for flow analysis in porous and fractured media. Reservoir rock of interest is a porous medium, containing pores (voids) and skeleton (solids). For any engineering application of flow in porous media, we are interested in only the porous medium that has interconnected pores that fluids are able to flow through. The skeletal portion of a porous medium is called the "matrix" and is normally solid and impermeable to fluids. The pores of porous media are typically filled with one or several fluids (e.g., water, oil, or gas). Because the fluids in porous media are not spatially "continuous" *per se*, the REV or volumetric averaging concept has to be used in practice, together with a local thermodynamic equilibrium assumption, to define rock and fluid parameters (e.g., porosity, tortuosity, specific surface area, etc.), and thermodynamic state variables (pressure, temperature, density, concentration, etc.). Then, we treat both fluids and solids as though they were continuous in space all the time. Using continuum concepts, therefore, we are able to define the parameters and state variables needed for mass conservation and flow calculation. As a result, quantitative approaches and tools, developed in fluid dynamics or thermodynamics, are directly applied in analysis of flow through porous media.

The continuum approaches, even though widely applied, have certain limitations. Past investigations of displacement of a more viscous fluid by less viscous fluid, such as a crude oil displaced by gas, and water seepage in thick unsaturated zones of fractured rocks, have indicated that flow and transport processes in such an environment may occur in non-volume-averaged fashion and proceed, in part, by means of localized preferential pathways (Pruess, 1999). Conventional continuum concepts and modeling approaches may not adequately capture the physics of multiphase flow displacement along those preferential flow pathways if the spatial variability is not properly represented by constraints of the computational requirements.

2.3 PHYSICAL PROCESSES AND FLOW-DRIVING MECHANISMS

For a fluid to be able to flow toward a well in a reservoir, there must be some energy in the reservoir to impel it. Flow-driving forces or mechanisms control fluid flow behavior and performance of reservoirs. Taking a

petroleum reservoir as an example, primary recovery is naturally occurring flow toward wells, but this will not persist without enough energy either stored within the reservoir or supplied from outside. To maintain long-term productivity of oil or gas, a secondary recovery method, such as waterflooding and gas injection, is most commonly used to supply energy to reservoirs. In addition, tertiary oil recovery (or Enhanced Oil Recovery, EOR) has been routinely used to inject chemicals or thermal energy into petroleum reservoirs to enhance production or performance of the reservoir.

A *primary recovery* stage of petroleum reservoirs is the production time period when flow to wells relies on the natural energy of the reservoir or before a secondary or tertiary recovery approach is implemented. During this stage, the overall performance of reservoirs is controlled by the nature of the energy, i.e., driving mechanism(s), available for mobilizing the oil to the wellbore. There are a number of driving mechanisms that provide the natural energy necessary for oil to flow into wells (Craft et al., 1959; Willhite, 1986; Ahmed and McKinney, 2011):

Rock and liquid expansion drive: This usually is the main production mechanism for groundwater flow to a well from a confined aquifer and for initial oil production from an "undersaturated" oil reservoir, i.e., current reservoir oil pressure is higher than its bubble point pressure. Then, the reservoir is saturated only with liquid of oil and/or water. As these liquids are withdrawn from wells and the reservoir pressure declines near the well, the rock and fluids will expand according to their individual compressibilities. The reservoir rock compressibility is contributed by the expansion of the individual rock grains within reservoir and formation compaction due to the rock mass overlying the productive formations. Compaction occurs when the reservoir formation is "compacted" as a result of the increase in the net overburden stress for rock solids, as the reservoir pore pressure is reduced due to fluid withdrawal. The degree of consolidation of bulk rock and a decrease of fluid pressure within the pore spaces tend to reduce the pore volume of the reservoir formation through the reduction of the porosity. As the expansion of the fluids and reduction in the pore volume occur with decreasing reservoir pressure, the oil and water will be forced out of the pore space to the wellbore at low pressure.

Because liquids and rocks are only slightly compressible, the reservoir will experience a rapid pressure decline to maintain a given production rate. The oil reservoir under this driving mechanism is characterized by a constant gas–oil ratio, equal to the gas solubility at the bubble-point pressure.

For conventional petroleum reservoirs, this driving mechanism is considered an inefficient driving force and may result in the recovery of only a small percentage of the total original oil-in-place (OOIP).

Depletion- or solution-gas drive: This driving mechanism consists mainly of solution-gas drive and associated gas displacement. A depletion-type petroleum reservoir is not in contact with a large body of permeable water-bearing formation or aquifer. The main energy source for driving flow in this case is from gas released from the oil phase and the subsequent expansion of the solution gas. As reservoir pressure declines with continuous oil production and falls below the bubble-point pressure, gas bubbles are liberated within the microscopic pores and the reservoir becomes "*saturated*." These bubbles expand and force the crude oil out of the pore space. Once the gas saturation, with pressure lowering, exceeds the critical gas saturation, free gas forms flow channels at least locally and begins to flow toward wells and the gas–oil ratio of produced fluids increases. A depletion drive reservoir is characterized by rapid and continuous reservoir pressure decline and gas–oil ratio that increases to a maximum and then declines (Ahmed and McKinney, 2011). Oil production by depletion drive is usually not efficient, because gas is much more mobile than oil and flows much faster than oil, bypassing oil and leading to a rapid depletion of the reservoir energy.

Gascap drive: A gas cap, if exists, can provide additional flow-driving force from the top of a reservoir. A gas cap could be naturally occurring, secondarily formed by release of solution gas, or generated by gas (e.g., nitrogen) injection for pressure maintenance. Due to the ability of the gas cap to expand, according to its size or total energy stored, a gas-cap drive reservoir is characteristic of pressure falling slowly and continuously. Pressure tends to be maintained at a higher level than in a depletion drive reservoir. The natural energy stored in the gas cap, available to produce the oil, comes from the expansion of the gas-cap gas and expansion of the solution gas as it is liberated in oil zones. Oil recovery by gas-cap expansion is actually a two-phase displacing mechanism, which is aided by gravity when denser oil, displaced by lighter gas, flows downward and can yield considerably larger recovery efficiency than depletion-drive reservoirs.

Water drive: Most petroleum reservoirs are partly or completely surrounded by aquifers or located above a bottom water zone. These edge water, bottom water zones or aquifers may be large compared to the hydrocarbon reservoir volume. The surrounding aquifers can supply

sufficient water influx or energy to producing reservoirs. Regardless of the source of water, the water drive is the result of water moving into the pore spaces originally occupied by oil in the oil zone, replacing the oil and driving it to the producing wells. Reservoir dynamics with strong edge or bottom water drive is characterized by reservoir pressure remaining high, produced gas–oil ratio remaining low, water production starting early and water cut increasing rapidly as well as high oil recovery (Ahmed and McKinney, 2011).

Gravity-drainage drive: Gravity drainage occurs in petroleum reservoirs as a result of differences in densities of the reservoir fluids, gas, oil, and water. The fluids in petroleum reservoirs have all been subjected to the forces of gravity, i.e., free gas on top, oil underlying the gas, and water underlying the oil, as initially distributed according to vertical gravity and capillary equilibrium condition. Gravity drive is probably present to some degree in hydrocarbon production from all petroleum reservoirs and always associated with multiphase flow in reservoirs. It is an important mechanism for production from thick, naturally fractured, carbonate reservoirs that are water wet. The favored conditions for gravity drive to work are higher permeability, thick formations, or formation layers with larger angle of inclination. Well design and completion should take advantage of the gravity-drive mechanism.

One example of gravity-drainage drive is application of Steam-Assisted Gravity Drainage (SAGD), which is widely used in thermal recovery of heavy oil by steam injection. The SAGD concept uses a pair of horizontal wells drilled into a heavy oil reservoir with the injector on top and producer on the bottom, with the top injector a few meters above the producing wellbore. Steam is continuously injected into the upper wellbore to heat the viscous oil to reduce its viscosity, then the heated oil drains into the lower wellbore for production.

Combination drive: Many reservoirs are subject not only to one drive mechanism, as discussed above, but to a combination of these mechanisms during their primary recovery stage. The most common type of drive encountered, therefore, is a combination of depletion drive and a weak water drive or depletion drive with a small gas cap and a weak water drive. Oil recovery from combination-drive reservoirs is usually greater than recovery from depletion-drive reservoirs, but less than recovery from strong water-drive or large gas cap-drive reservoirs.

Because of limited natural energy within a given petroleum reservoir, oil recovery relying on the primary recovery mechanisms is in general low,

and the majority of the oil is left within reservoirs if the primary recovery method is used alone. Therefore, the secondary recovery approaches are to inject water or gas into reservoirs to displace fluids produced and supply energy. Waterflooding, proposed and developed more than half a century ago (Willhite, 1986), has been the most commonly applied improved oil recovery (IOR) approach, and is still widely used today in oil fields around the world. Waterflooding is efficient to displace oil and is economical to implement for most conventional reservoirs. Efforts to improve the performance of waterflooding in oil recovery have motivated generations of scientists, reservoir engineers, and geologists to carry out laboratory, theoretical, and field studies for understanding multiphase flow processes in porous media.

Tertiary oil recovery or EOR is the injection of materials not naturally present into reservoirs to supply energy and to improve displacement efficiency. The injected materials include chemicals, thermal energy, and CO_2. Injected fluids and injection processes supplement the natural energy present in the reservoir to drive or displace oil to production wells more efficiently. Injected fluids interact with the reservoir rock/oil system to create conditions favorable for oil mobilization and recovery. The interactions of injected fluids or energy with reservoir fluids are attributable to physical and chemical mechanisms that enhance flow of oil to wells. In both secondary and EOR processes, the main flow drive mechanisms are forcing displacement of reservoir fluids by injected fluids.

2.4 MULTIPHASE POROUS MEDIUM FLOW, DARCY'S LAW AND ITS EXTENSIONS

This section discusses Darcy's law for immiscible flow of multiphase Newtonian fluids as well as its extensions to non-Newtonian fluid displacement and multiphase non-Darcy flow.

Darcy's law describes flow in porous media driven by pressure gradient and potential energy. This empirical or phenomenological relation has been the foundation for studies of flow and transport phenomena through porous and fractured reservoirs. Even though originally derived only for flow of a single-phase fluid, Darcy's law has been extended to describe the flow of multiple, immiscible fluids (e.g., Collins, 1961; Scheidegger, 1974). The generalized Darcy's law for the simultaneous flow of immiscible

Newtonian fluids in a multiphase, isothermal or nonisothermal porous-medium system is given as

$$\boldsymbol{v}_\beta = -\frac{\boldsymbol{k}\, k_{r\beta}}{\mu_\beta}\left(\nabla P_\beta - \rho_\beta g \nabla z\right) \tag{2.1}$$

in which $\boldsymbol{v}_\beta$ is a vector of the Darcy velocity or volumetric flow rate per unit area of fluid phase β, with β being fluid phase index (β = o for oil; g for gas; and w for water); P_β, μ_β, and ρ_β are pressure, viscosity, and density of fluid phase β, respectively; z is the vertical coordinate, positive direction downward; $\boldsymbol{k}$ is absolute or intrinsic permeability, a tensor, in general, for flow through anisotropic media; $k_{r\beta}$ is the relative permeability to fluid phase β; and g is the gravitational constant. The Nomenclature at the end of this book lists all the variables and parameters of the book in the International System of Units (SI) units, if not specifically defined.

In the literature, in particular, for numerical simulation of multiphase flow, Darcy's law is conveniently written using the depth from a datum level, e.g., the ground surface elevation (Peaceman, 1977) as

$$\boldsymbol{v}_\beta = -\frac{\boldsymbol{k}\, k_{r\beta}}{\mu_\beta}\left(\nabla P_\beta - \rho_\beta g \nabla D\right) \tag{2.2}$$

in which D is the depth from a datum or reference level.

Another form of Darcy's law is in terms of fluid potential of each fluid phase of compressible fluids,

$$\boldsymbol{v}_\beta = -\frac{\boldsymbol{k}\, k_{r\beta}}{\mu_\beta}\nabla \Phi_\beta \tag{2.3}$$

in which Hubberts' fluid potential is defined (Hubbert, 1956; Ertekin et al., 2001) as

$$\Phi_\beta^{\mathrm{h}} = \int_{P_r}^{P_\beta} \frac{1}{\rho_\beta g}\,\mathrm{d}P - z \tag{2.4}$$

In practice, the definition of a fluid potential of Eqn (2.4) is not commonly used directly. Instead, we prefer to use a better definition in terms of potential gradient,

$$\nabla \Phi_\beta = \rho_\beta g \nabla \Phi_\beta^{\mathrm{h}} = \rho_\beta g \nabla \left(\int_{P_r}^{P_\beta} \frac{1}{\rho_\beta g}\,\mathrm{d}P - D \right) = \nabla P_\beta - \rho_\beta g \nabla D \tag{2.5}$$

in association with Darcy's law for flow calculation. Here z is replaced by D. Eqn (2.5) simplify indicates that $\nabla \Phi_\beta$ is related to Hubberts' fluid potential gradient $\nabla \Phi_\beta^{\mathrm{h}}$.

Extension to non-Newtonian fluid flow and displacement: The multiphase flow Darcy's law has been extended and used to describe immiscible flow and displacement of non-Newtonian fluids in reservoirs (e.g., Wu, 1990),

$$\boldsymbol{v}_{\mathrm{nn}} = -\frac{\boldsymbol{k}\, k_{\mathrm{rnn}}}{\mu_{\mathrm{nn}}}(\nabla P_{\mathrm{nn}} - \rho_{\mathrm{nn}} g \nabla D) \tag{2.6}$$

in which subscript nn denotes non-Newtonian fluid phase; and an apparent viscosity of a non-Newtonian fluid is defined as

$$\mu_{\mathrm{nn}} = \mu_{\mathrm{nn}}(\nabla \Phi_{\mathrm{nn}}, S_{\mathrm{nn}}) \tag{2.7}$$

in which S_{nn} is saturation of the non-Newtonian fluid in reservoirs. It can be shown (e.g., Wu and Pruess, 1996) that the apparent viscosity of non-Newtonian fluids, as defined by Eqn (2.7), covers all commonly used non-Newtonian fluids, such as power-law and Bingham fluids, in EOR operations or heavy oil reservoirs.

Extension to non-Darcy flow and displacement: Darcy's law, Eqn (2.1) or (2.2), describes a linear relationship between volumetric flow rate per unit area (Darcy velocity) and pressure or potential gradient. Any deviation from this linear relation may be defined as non-Darcy flow. At both very high and very low flow rates, this linear relationship may be broken. In analyzing flow through porous media in the literature, non-Darcy flow normally means high flow velocity. For very high flow velocities in porous media, inertial effects can become significant and can no longer be ignored. If we add an inertial term to the Darcy's equation, we will obtain the *Forchheimer* equation, widely used for account for non-Darcy flow of high flow rate in porous media. If we extend the *Forchheimer* to multiphase displacement, we have (Wu, 2001, 2002),

$$-\nabla \Phi_\beta = \frac{\mu_\beta}{\boldsymbol{k}\, k_{r\beta}} \boldsymbol{v}_\beta + \beta_\beta \rho_\beta \boldsymbol{v}_\beta |\boldsymbol{v}_\beta| \tag{2.8}$$

in which β_β is the effective non-Darcy flow coefficient with a unit m^{-1} for fluid phase β under multiphase flow conditions.

In addition to the *Forchheimer* equation, the Barree and Conway model has recently been proposed and used in the petroleum industry (Barree and Conway, 2004, 2007). Recent studies (Lai et al., 2012) indicate that the *Forchheimer* equation could not accurately predict fluid flow behavior at very high flow velocity in porous media, as observed in the laboratory, whereas the Barree and Conway model is able to match the experimental data with the entire range of flow rates.

The Barree and Conway model for multiphase flows is (Wu et al., 2011a,b):

$$-\nabla \Phi_\beta = \frac{\mu_\beta \boldsymbol{v}_\beta}{k_{\mathrm{d}} k_{r\beta}\left(k_{\mathrm{mr}} + \frac{(1-k_{\mathrm{mr}})\mu_\beta S_\beta \tau}{\mu_\beta S_\beta \tau + \rho_\beta |\boldsymbol{v}_\beta|}\right)} \tag{2.9}$$

in which, k_d is absolute (or Darcy) permeability, constant at low flow velocity; $k_{mr} = k_{min}/k_d$, is the ratio of minimum permeability (k_{min}) to k_d; k_{min} is a constant or minimum permeability at high flow velocity; and τ is the inverse of the characteristic length (m^{-1}). In this model, the non-Darcy flow behavior is characterized by the two parameters, k_{min} and τ, according to Barree and Conway (2004, 2007).

Extensions to EOR and other applications: Darcy's law, Eqn (2.1) or (2.2), has been used in almost all the EOR operations and other multiphase flow conditions in reservoirs:

- For compositional models, fluid viscosity and density, relative permeability, and capillary pressure are handled also as functions of chemical composition/concentration, interfacial tension (IFT), etc.
- For thermal recovery, fluid and rock properties are treated also as functions of temperature and fluid composition.
- For coupling with geomechanics, porosity, absolute permeability, and capillary pressure are dependent also on effective stress in formation.

2.5 CONCEPTS OF WETTABILITY, CAPILLARY PRESSURE, AND RELATIVE PERMEABILITY

Darcy's law, Eqn (2.1), relates flow rates of Newtonian fluids to flow properties and flow potential gradients in a multiphase porous-medium system. This relationship depends only on the instantaneous, local state of the system; flow is driven by pressure, gravity, and viscous forces, with effects of fluid phase interference included in capillary forces and relative permeability. To use Darcy's law for calculation of multiphase fluid flow in reservoirs, capillary pressure and relative permeability and related wettability concepts must be introduced.

Wettability: When multiple immiscible fluids exist within pores of porous media under reservoir conditions, one liquid (water or oil) preferentially wets the solid surface. Wettability is the ability, resulting from intermolecular interactions, of a liquid to maintain contact with a solid surface when the two are brought together in the presence of other immiscible fluids. The degree of wetting (wettability) is determined by a force balance between adhesive and cohesive forces, estimated in terms of contact angles. Therefore, wettability is determined by rock minerals, fluid composition, and saturation history. Wettability has significant impact on fluid saturation distribution as well as oil recovery in reservoirs. Note that under natural conditions, natural gas is always a nonwetting phase.

Two processes closely related to multiphase flow and displacement are imbibition and drainage. *Imbibition* is a fluid flow process in which the saturation of the wetting phase increases and the nonwetting phase saturation decreases, i.e., using a wetting fluid to displace a nonwetting fluid. In contrast, *drainage* is the process of a wetting phase fluid being displaced by a nonwetting phase.

Capillary pressure: If two or more immiscible fluids occupy pore space, in general the pressure in one phase will be different from that in the other phases, with greater pressure in the less-wetting or nonwetting phase. Capillary pressure is defined as this difference across the interface between two immiscible fluids. Therefore, in a three-phase immiscible fluid system there are two capillary pressures, because two interfaces exist. The capillary force in porous media depends primarily on wettability, interfacial tension, and pore size and is closely related to how fluid is locally distributed in pores. In practice, for a given fluid and formation system, fluid and rock properties, such as minerals and fluid compositions, can be assumed to be constant; then the capillary pressure is treated as a function only of fluid saturation. The capillary pressure is one of the most important factors in multiphase flow in porous media. It determines the fluid distribution in reservoirs (such as the initial conditions), oil recovery during imbibition or drainage processes, and is needed for calculation of all fluid phase pressures using Darcy's law.

Relative permeability: When Darcy's law is generalized and extended from single-phase flow to multiphase flow, the actual permeability of a porous medium is replaced by the effective permeability to the phase of interest. Relative permeability, the ratio of the effective permeability of the phase of interest to the absolute permeability, is a dimensionless measure of the conductance of a porous medium for the fluid phase, when the medium is saturated with more than one fluid. The porous medium can have a distinct and measurable conductance to each phase present and flowing in the medium.

Relative permeability for multiphase flow through porous media generally depends strongly on fluid saturation, wettability, pore size distribution, and saturation history (or hysteresis). It also depends weakly on fluid and rock properties, and flow rate. In reservoir simulation and flow modeling studies, however, relative permeability is in general handled as a function only of fluid saturation, as long as all other factors, for a given fluid and porous-medium system, will not change much during the period of production or study.

To evaluate multiphase fluid flow in porous media using the multiphase extension of Darcy's law, capillary pressure and relative permeability must be predetermined using site-specific fluid and rock samples. In applications, field-specific data of capillary pressure and relative permeability can be supplied with a table lookup or in functional forms (Brooks and Corey, 1964; Mualem, 1976; van Genuchten, 1980; Honarpour et al., 1986).

REFERENCES

Ahmed, T., McKinney, P., 2011. Advanced Reservoir Engineering. Gulf Professional Publishing.

Barree, R.D., Conway, M., 2004. Beyond beta factors: a complete model for Darcy Forchheimer and trans-Forchheimer flow in porous media. In: SPE Annual Technical Conference and Exhibition. Houston, Texas. http://dx.doi.org/10.2118/89325-MS.

Barree, R.D., Conway, M., 2007. Multiphase non-Darcy flow in proppant packs. In: SPE Annual Technical Conference and Exhibition. Anaheim, California, U.S.A. http://dx.doi.org/10.2118/109561-MS.

Bear, J., 1972. Dynamics of Fluids in Porous Media. American Elsevier, New York.

Brooks, R.H., Corey, A.T., March 1964. Hydraulic Properties of Porous Media. Hydrology Papers. Colorado State University.

Collins, R.E., 1961. Flow of Fluids through Porous Materials. PennWell Publishing Company, Tulsa, OK.

Craft, B.C., Hawkins, M.F., Terry, R.E., 1959. Applied Petroleum Reservoir Engineering. Prentice-Hall Englewood Cliffs, NJ.

Dullien, F.A.L., 1991. Porous Media: Fluid Transport and Pore Structure. Academic Press.

Ertekin, T., Abou-Kassem, J.H., King, G.R., 2001. Basic Applied Reservoir Simulation. Society of Petroleum Engineers, Richardson, TX.

van Genuchten, M.T., 1980. A closed-form equation for predicting the hydraulic conductivity of unsaturated soils. Soil Science Society of America Journal 44 (5), 892–898.

Honarpour, M.M., Koederitz, F., Herbert, A., 1986. Relative Permeability of Petroleum Reservoirs. CRC Press Inc, Boca Raton, FL.

Hubbert, M.K., 1956. Darcy's law and the field equations of the flow of underground fluids. Petroleum Transcations, AIME 207, 222–239.

Lai, B., Miskimins, J.L., Wu, Y.-S., 2012. Non-Darcy porous-media flow according to the Barree and Conway model: laboratory and numerical-modeling studies. SPE Journal 17 (01), 70–79.

McCain, W.D., 1990. The Properties of Petroleum Fluids. PennWell Publishing Company, Tulsa, OK.

Mualem, Y., 1976. A new model for predicting the hydraulic conductivity of unsaturated porous media. Water Resources Research 12 (3), 513–522.

Peaceman, D.W., 1977. Fundamentals of Numerical Reservoir Simulation. Elsevier Scientific Publishing Co, New York, NY.

Pruess, K., 1999. A mechanistic model for water seepage through thick unsaturated zones in fractured rocks of low matrix permeability. Water Resources Research 35 (4), 1039–1051.

Scheidegger, A.E., 1974. The Physics of Flow through Porous Media. University of Toronto Press.

Willhite, G.P., 1986. Waterflooding. Society of Petroleum Engineers, Richardson, TX.

Wu, Y.-S., 1990. Theoretical Studies of Non-Newtonian and Newtonian Fluid Flow through Porous Media. Lawrence Berkeley Laboratory, Berkeley, CA.
Wu, Y.-S., 2001. Non-Darcy displacement of immiscible fluids in porous media. Water Resources Research 37 (12), 2943–2950.
Wu, Y.-S., 2002. Numerical simulation of single-phase and multiphase non-Darcy flow in porous and fractured reservoirs. Transport in Porous Media 49 (2), 209–240.
Wu, Y.-S., Lai, B., Miskimins, J.L., 2011a. Simulation of non-Darcy porous media flow according to the Barree and Conway model. The Journal of Computational Multiphase Flows 3 (2), 107–122.
Wu, Y.-S., Lai, B., Miskimins, J.L., Fakcharoenphol, P., Di, Y., 2011b. Analysis of multiphase non-Darcy flow in porous media. Transport in Porous Media 88 (2), 205–223.
Wu, Y.-S., Pruess, K., 1996. Flow of non-Newtonian fluids in porous media. Advances in Porous Media 3, 87–184.

CHAPTER 3

Flow-Governing Equations and Mathematical Models

3.1 INTRODUCTION

To model flow processes occurring in porous media, one needs mathematical models or governing flow equations to describe the physical processes quantitatively. In this chapter, we discuss such mathematical models and governing flow equations. We present a set of general governing equations using the black-oil model as an example for immiscible multiphase fluid flow in porous media. Many other types of flow equations, including unsaturated flow in a gas–water, two-phase liquid–gas, or two-phase water–oil system, can be directly derived from the general black-oil governing equations.

A multiphase system consists of several fluid phases, such as oil (or Non-Aqueous Phase Liquid, NAPL), gas, and water, and each fluid in turn may consist of a number of mass components. To derive a set of generalized governing equations for multiphase fluid flow, we assume that these processes can be described using a continuum approach with a representative elementary volume (REV) concept within a porous or fractured medium (Bear, 1972). Then, Darcy's law and its extensions can be applied to describe flow of multiphase immiscible fluids. In addition, a condition of local thermodynamic equilibrium is assumed, so that temperatures, phase pressures, densities, and fluid viscosities are the same locally at each REV of the porous medium at a given time. A combination of mass conservation principles with the flow constitutive laws of Section 2.4 gives rise to a set of governing equations described in subsequent Sections 3.2 and 3.3.

3.2 THE LAW OF MASS CONSERVATION

Instead of a cubic element (cube) method, as used in most textbooks (e.g., Willhite, 1986), let us use a control-volume or integrated approach (Narasimhan and Witherspoon, 1976; Wu, 1990; Pruess et al., 1999) to derive mass conservation equations of each fluid in the porous or fractured continuum.

Multiphase Fluid Flow in Porous and Fractured Reservoirs
ISBN 978-0-12-803848-2
http://dx.doi.org/10.1016/B978-0-12-803848-2.00003-9

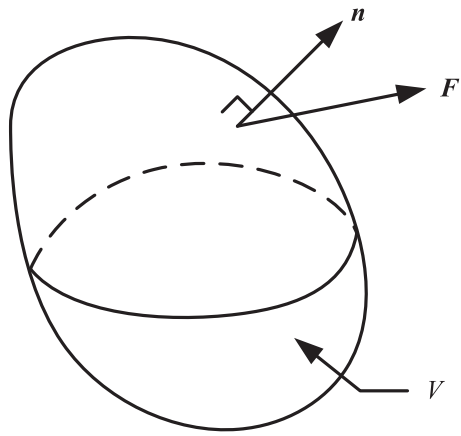

Figure 3.1 An arbitrary control-volume (*V*) of formation within a reservoir flow domain with surface *S*.

As shown in Figure 3.1, consider an arbitrary control-volume (V) in a porous medium in a reservoir flow system, bounded by surface (S). The black-oil multiphase system is assumed to be isothermal and composed of three-phases: oil, gas, and water, and there are three mass (i.e., pseudo-mass) components, oil, gas, and water. Two of the three mass components, oil and water, are assumed to remain with their associate phases. However, the gas is dissolved in the crude oil phase in an undersaturated condition and exists in both oil and gaseous phases in a saturated condition. In an isothermal system containing three mass components, three mass balance equations are needed to fully describe the flow system.

The law of conservation of mass for each fluid states that the sum of the net fluxes crossing the boundary plus the generation rate of the mass of the fluid must be equal to the rate of the mass accumulated in an arbitrary volume (V) for the fluid, over a time period of Δt as follows:

$$\boxed{\begin{array}{c}\text{change in fluid}\\ \text{mass in volume } V\end{array}} = \boxed{\begin{array}{c}\text{net fluid inflow}\\ \text{across surface of } V\end{array}} + \boxed{\begin{array}{c}\text{net gain of fluid from}\\ \text{sinks and sources}\end{array}} \tag{3.1}$$

In an integral form, mathematically, Eqn (3.1) becomes:

$$\Delta\left(\iiint_V \left(\phi S_\beta \rho_\beta\right) \mathrm{d}V\right) = \left(-\oiint_s \boldsymbol{F}_\beta \cdot \boldsymbol{n}\, \mathrm{d}s + \iiint_V q_\beta \mathrm{d}V\right)\Delta t \tag{3.2}$$

in which ϕ is the effective porosity (the porosity of porous media that contributes to fluid flow through the rock) of the porous medium; S_β is the saturation of fluid β; ρ_β is the density of fluid β; $\boldsymbol{F}_\beta$ is mass flux vector for fluid β; $\boldsymbol{n}$ is the unit vector, normal to surface S; and q_β is mass source/sink term for fluid β.

The left-hand side of Eqn (3.2) is the change of fluid mass in volume V over the time period of Δt, and the right-hand side is net mass fluxes across the boundary as well as mass generation term over the same time period. If we divide both sides of Eqn (3.2) by Δt and take the limit, we have the following integral form of mass balance equations for the three fluids:

$$\frac{\partial}{\partial t}\left(\iiint_V \left(\phi S_\beta \rho_\beta\right) \mathrm{d}V\right) = -\oiint_s \boldsymbol{F}_\beta \cdot \boldsymbol{n}\, \mathrm{d}s + \iiint_V q_\beta \mathrm{d}V \tag{3.3}$$

3.3 GOVERNING EQUATIONS OF MULTIPHASE NEWTONIAN FLUID FLOW

The mass conservation Eqn (3.3), can be changed from an integral form to a partial differential equation (PDE). Upon applying the Gauss theorem to Eqn (3.3), the surface integral on the right side of Eqn (3.3) can be transformed into a volume integral,

$$\frac{\partial}{\partial t}\left(\iiint_V \left(\phi S_\beta \rho_\beta\right) \mathrm{d}V\right) = \iiint_V \left(-\nabla \cdot \boldsymbol{F}_\beta + q_\beta\right) \mathrm{d}V \tag{3.4}$$

Because Eqn (3.4) is valid for any arbitrary region in the flow system, it follows that

$$\frac{\partial}{\partial t}\left(\phi S_\beta \rho_\beta\right) = -\nabla \cdot \boldsymbol{F}_\beta + q_\beta \tag{3.5}$$

This is a PDE form of the flow-governing equations for mass conservation of fluids. If the three-phases in a black-oil model are Newtonian fluids, then the mass fluxes, $\boldsymbol{F}_\beta$, in Eqn (3.5) can be defined using Darcy's law, Eqn (2.2),

$$\boldsymbol{F}_\beta = \rho_\beta \boldsymbol{v}_\beta = -\frac{\boldsymbol{k}\, k_{r\beta}}{\mu_\beta} \rho_\beta \left(\nabla P_\beta - \rho_\beta g \nabla D\right) \tag{3.6}$$

However, this equation is applicable only to mass flow of water or oil phase, because gas is moved also by the oil phase in a back-oil model. Let us write the flow-governing equations for all three fluids:

For oil flow,

$$\frac{\partial}{\partial t}(\phi S_o \overline{\rho}_o) = \nabla\cdot\left[\frac{\boldsymbol{k}\, k_{ro}}{\mu_o}\overline{\rho}_o(\nabla P_o - \rho_o g \nabla D)\right] + q_o \tag{3.7}$$

For gas flow,

$$\begin{aligned}\frac{\partial}{\partial t}\left[\phi\left(S_o\overline{\rho}_{dg} + S_g\rho_g\right)\right] = \nabla\cdot\Bigg[&\frac{\boldsymbol{k}\, k_{ro}}{\mu_o}\overline{\rho}_{dg}(\nabla P_o - \rho_o g\nabla D)\\ &+ \frac{\boldsymbol{k}\, k_{r\beta}}{\mu_\beta}\rho_g\left(\nabla P_g - \rho_g g\nabla D\right)\Bigg] + q_g\end{aligned} \tag{3.8}$$

For water flow,

$$\frac{\partial}{\partial t}(\phi S_w \rho_w) = \nabla\cdot\left[\frac{\boldsymbol{k}\, k_{rw}}{\mu_w}\rho_w(\nabla P_w - \rho_w g\nabla D)\right] + q_w \tag{3.9}$$

in which $\overline{\rho}_o$ is the density of oil, excluding dissolved gas, at reservoir conditions; and $\overline{\rho}_{dg}$ is the density of dissolved gas (dg), defined in Eqn (3.54), in oil phase at reservoir conditions.

3.4 CONSTITUTIVE RELATIONS

The governing Eqns (3.7)–(3.9) of mass conservation for the three-phase fluids need to be supplemented with constitutive equations, which express all the parameters as functions of a set of primary thermodynamic variables of interest. These constitutive correlations have to be obtained and provided before multiphase flow equations in porous media can be solved. The following relationships will be used to complete the statement of describing multiple phase flow of Newtonian fluids through porous media (Wu, 1998; Bodvarsson et al., 2000).

3.4.1 Saturation Constraint

In addition to the three governing Eqns (3.7)–(3.9) there are two supplementary equations given by

$$S_o + S_g + S_w = 1 \tag{3.10}$$

or for multiphase flow systems in general

$$\sum_\beta S_\beta = 1 \tag{3.11}$$

3.4.2 Capillary Pressure and Relative Permeability Functions

Capillary pressure and relative permeability are by far the most important functions or constitutive relations for multiphase flow through porous media. The functions of capillary pressure and relative permeability are generally determined from laboratory and field studies for a given site in a tabulated form. There are certain limitations for the capillary and relative permeability functions, discussed in this chapter, which should be noted. For example, effects of hysteresis of the medium are not explicitly included, and effects of heat transfer, non-Newtonian fluids, or non-Darcy displacement are ignored.

Compared to two-phase flow, there are fewer experimental or theoretical studies and data sets available in the literature on the constitutive relations needed for modeling three-phase flow in porous media. In particular, we have very limited knowledge of characteristics of capillary pressure and relative permeability functions in a three-active-phase fluid flow system. This is despite significant efforts in this area over the past half century, and continuing, mainly by those in petroleum reservoir engineering.

A commonly used approach to estimate capillary pressure and relative permeability for three-phase flow is to use several sets of functions measured from separated two-phase systems. This is because two-phase flow measurements can be made in the laboratory much more easily than three-phase measurements.

Under isothermal, two- or three-phase flow conditions, there are many parametric models, closed-form functions, and commonly used approximations in the literature to estimate capillary pressure and relative permeability functions from hydrology, soil sciences, and petroleum reservoir engineering. We present several of the most frequently used relations of capillary pressure and relative permeability functions in the following.

3.4.2.1 Capillary Pressure Functions

The capillary pressures are needed to relate pressures between the phases in a multiphase immiscible fluid flow system. Note that the capillary pressure function for a two-phase flow system is much easier than three-phase flow systems to define or determine experimentally. In the following, we discuss relationships and models for two-phase and three-phase systems separately.

Capillary pressure in two-phase flow systems: Three common two-phase systems are oil–water, gas–oil, and gas–water conditions in

reservoirs. In all the two-phase flow systems, capillary pressure functions are well defined in the following equations.

For a gas–water system (note that gas is the non-wetting phase):

$$P_{\mathrm{cgw}}(S_{\mathrm{w}}) = P_{\mathrm{g}} - P_{\mathrm{w}} \tag{3.12}$$

For a gas–oil system (note that oil is the wetting phase):

$$P_{\mathrm{cgo}}(S_{\mathrm{o}}) = P_{\mathrm{g}} - P_{\mathrm{o}} \tag{3.13}$$

For an oil–water system (note that water is here assumed to be the wetting phase):

$$P_{\mathrm{cow}}(S_{\mathrm{w}}) = P_{\mathrm{o}} - P_{\mathrm{w}} \tag{3.14}$$

in which P_{cgw} is the gas–water capillary pressure; P_{cgo} is the gas–oil capillary pressure; and P_{cow} is the oil–water capillary pressure.

If laboratory-determined capillary pressure curves are available, these data should be directly used for flow calculation. However, in many field simulation studies, capillary pressure data may not be readily available, such as for fractured media. In this case, the following two models with closed-forms may be convenient to use: the first recommended capillary function is the van Genuchten model (Mualem, 1976; van Genuchten, 1980), which is the most-used capillary pressure function for a gas–water flow system of porous media, in particular, in the communities of the groundwater and soil sciences. Here we use it for a gas–liquid system,

$$P_{\mathrm{cgL}} = \frac{\rho_{\mathrm{L}}\, g}{\alpha_{\mathrm{vG}}}\left[\left(\overline{S}_{\mathrm{L}}\right)^{-\frac{1}{\gamma}} - 1\right]^{\frac{1}{\beta}} \tag{3.15}$$

in which subscript L is the phase index for the liquid phase, water or oil; α_{vG} is the parameter α (m^{-1}) of van Genuchten function (1980); and the effective or normalized liquid (water or oil) saturation defined as

$$\overline{S}_{\mathrm{L}} = \frac{S_{\mathrm{L}} - S_{\mathrm{Lr}}}{1 - S_{\mathrm{Lr}}} \tag{3.16}$$

in which γ and β are parameters of the van Genuchten functions (van Genuchten, 1980) with $\gamma = 1 - 1/\beta$; and S_{Lr} is the irreducible liquid saturation. Shown in Figure 3.2 is a typical curve of capillary pressure as described by the van Genuchten model.

The other popular closed-formed capillary pressure function is the Brooks–Corey model (Brooks and Corey, 1964),

$$P_{\mathrm{c}} = P_{\mathrm{d}}\left(\overline{S}_{\mathrm{w}}\right)^{-\frac{1}{\lambda}} \tag{3.17}$$

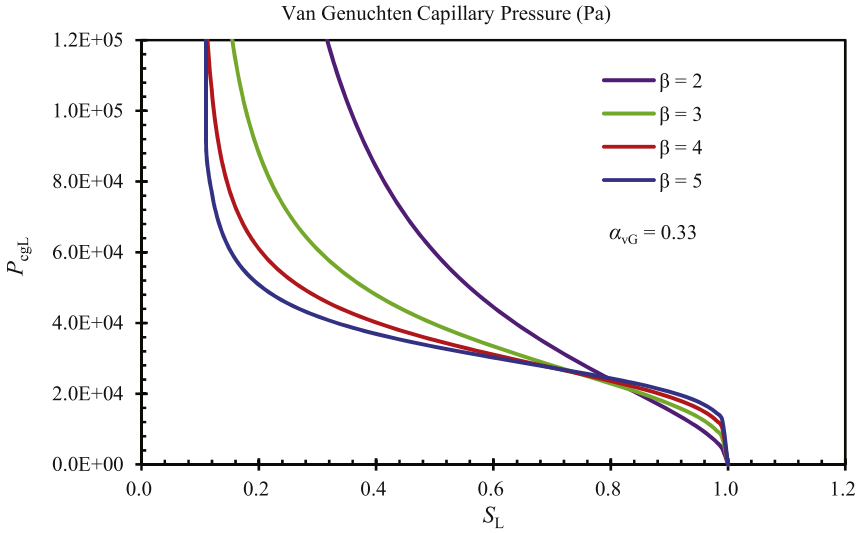

Figure 3.2 Capillary pressures curves with the van Genuchten model.

in which P_c is the capillary pressure between the two-phases; P_d is the entry pressure of the porous medium; and λ is related to the pore-size distribution (normal values of 0.3 to 3.0). A material with a uniform grain size has a large λ value and a material that is highly nonuniform has a small value of λ (Corey, 1994). Figure 3.3 presents a typical curve of capillary pressure with the Brooks and Corey function.

Capillary pressure in three-phase flow systems: When dealing with a three-phase flow system of oil, gas, and water, water- and gas-phase pressures are related by

$$P_w = P_g - P_{cgw}(S_w, S_g) \tag{3.18}$$

in which P_{cgw} is the gas–water capillary pressure in a three-phase system, which is generally assumed to be a function of water and gas saturation. The oil phase pressure may be related to the gas phase pressure by

$$P_o = P_g - P_{cgo}(S_w, S_o) \tag{3.19}$$

in which P_{cgo} is the gas–oil capillary pressure in a three-phase system, which is a function of two saturations of water and oil phases, respectively. For rock materials in a reservoir formation, the wettability order is (1) aqueous phase, (2) oil phase, and (3) gas phase. Then water and gas phases are separated by oil phase and the gas–water capillary pressure is stronger than the

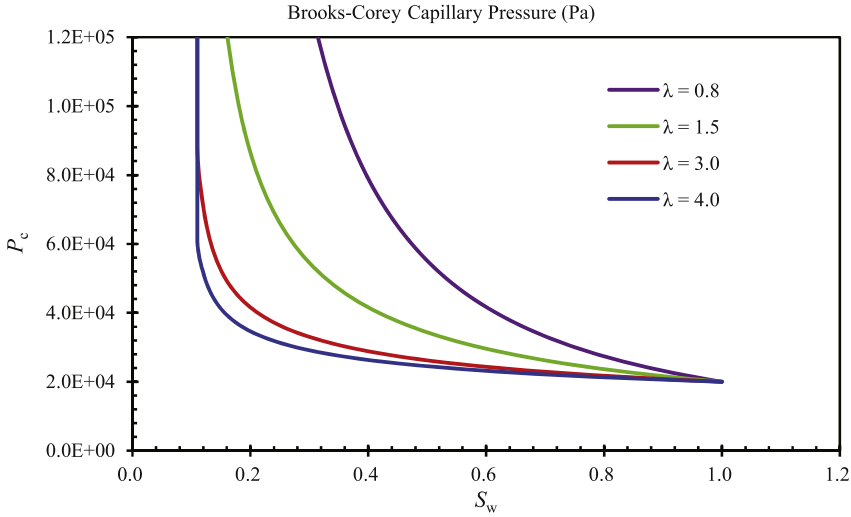

Figure 3.3 Capillary pressures curves with the Brooks–Corey model ($P_d = 2.0 \times 10^4$ Pa).

gas–oil capillary pressure. The oil–water capillary pressure, P_{cow}, in a three-phase system, is defined as

$$P_{cow} = P_{cgw} - P_{cgo} = P_o - P_w \tag{3.20}$$

Let us consider how to derive capillary pressures using two sets of capillary pressure functions measured from separated two-phase systems. We assume that the order of wettability of the three-phases is water–oil–gas, i.e., water as wetting phase, gas as non-wetting, and oil as the intermediate phase. Capillary pressures between oil and water or between gas and oil in a three-phase system are often approximated by

$$P_{cow} = P_{cow}^{ow}(S_w) \tag{3.21}$$

and

$$P_{cgo} = P_{cgo}^{go}(S_g) \tag{3.22}$$

in which P_{cow}^{ow} is the capillary pressure between oil (or NAPL) and water in the oil–water two-phase system (with subscript of ow denoting the two-phase system); and P_{cgo}^{go} denotes the capillary pressure between gas and oil phases in the gas–oil two-phase system. Then the capillary pressure, P_{cgw}, between nonwetting and wetting phases in the three-phase system is given,

$$P_{cgw}(S_w, S_g) = P_{cgo}^{go}(S_g) + P_{cow}^{ow}(S_w) \tag{3.23}$$

For many applications, the only capillary pressure curves available may be those measured in two-phase system experiments, such as a gas–water, oil–water, or gas–oil two-phase system, respectively. In this case, we can use Eqns (3.21)–(3.23) to estimate three-phase capillary pressures using the two-phase measurements.

In the practice of petroleum reservoir simulation, capillary pressure functions are generally supplied through table lookup from laboratory determination. Alternatively, one functional form of capillary pressures from Parker et al. (1987) is included with modification for use. In this approach, modified three-phase capillary functions are defined:

$$P_{\mathrm{cow}} = \frac{\rho_{\mathrm{w}} g}{\alpha_{\mathrm{ow}}}\left[\left(\overline{S}_{\mathrm{w}}\right)^{-\frac{1}{\gamma}} - 1\right]^{\frac{1}{\beta}} \tag{3.24}$$

$$P_{\mathrm{cgo}} = \frac{\rho_{\mathrm{w}} g}{\alpha_{\mathrm{go}}}\left[\left(1 - \overline{S}_{\mathrm{g}}\right)^{-\frac{1}{\gamma}} - 1\right]^{\frac{1}{\beta}} \tag{3.25}$$

and

$$P_{\mathrm{cgw}} = \frac{\rho_{\mathrm{w}} g}{\alpha_{\mathrm{gw}}}\left[\left(1 - \overline{S}_{\mathrm{g}}\right)^{-\frac{1}{\gamma}} - 1\right]^{\frac{1}{\beta}} \tag{3.26}$$

These three-phase capillary functions are the extension of the van Genuchten function two-phase model (van Genuchten, 1980) with the same definitions of basic parameters, except for

$$\alpha_{\mathrm{ow}} = \alpha_{\mathrm{vG}} \frac{\sigma_{\mathrm{gw}}}{\sigma_{\mathrm{ow}}} \tag{3.27}$$

$$\alpha_{\mathrm{go}} = \alpha_{\mathrm{vG}} \frac{\sigma_{\mathrm{gw}}}{\sigma_{\mathrm{go}}} \tag{3.28}$$

$$\overline{S}_{\mathrm{g}} = \frac{S_{\mathrm{g}}}{1 - S_{\mathrm{wr}} - S_{\mathrm{or}}} \tag{3.29}$$

in which σ_{gw} ($=\alpha_{\mathrm{vG}}$), σ_{ow}, and σ_{go} are interfacial tensions between gas and water, oil and water, and gas and oil, respectively; and S_{or} is residual oil saturation.

3.4.2.2 Relative Permeability Functions

The relative permeabilities to a flowing fluid phase, β, in a three-phase system are normally treated to be functions of fluid saturations only:

$$k_{\mathrm{r}\beta} = k_{\mathrm{r}\beta}(S_{\mathrm{w}}, S_{\mathrm{g}}) \tag{3.30}$$

Similarly as for capillary pressure, the relative permeability functions are generally determined from laboratory and field studies for a given site in a tabulated form for most reservoir simulation studies. We discuss several commonly used relations for relative permeability functions as follows.

Relative permeability in two-phase flow systems: Relative permeabilities in a two-phase flow system, e.g., with a water phase, are generally assumed to be only functions of water saturation. One of the two commonly used forms of two-phase relative permeability is the Brooks–Corey function (Brooks and Corey, 1964; Honarpour et al., 1986), given by

$$k_{\mathrm{rw}}(S_{\mathrm{w}}) = \left(\overline{S}_{\mathrm{w}}\right)^{2+\varphi} \tag{3.31}$$

and

$$k_{\mathrm{rg}}(S_{\mathrm{w}}) = \left(1 - \overline{S}_{\mathrm{w}}\right)^{2}\left[1 - \left(\overline{S}_{\mathrm{w}}\right)^{\varphi}\right] \tag{3.32}$$

in which $\varphi = 1 + 2/\lambda$, and λ is referred to as the Brooks–Corey pore-size distribution index.

The other popular relative permeability model is that of Mualem (1976) and van Genuchten (1980), given by

$$k_{\mathrm{rw}} = \left(\overline{S}_{\mathrm{w}}\right)^{1/2}\left\{1 - \left[1 - \left(\overline{S}_{\mathrm{w}}\right)^{\frac{1}{\gamma}}\right]^{\gamma}\right\}^{2} \tag{3.33}$$

for estimating the relative permeability to the wetting, water phase. Note that the model parameter, γ, used here is the same as in the capillary pressure function of Eqn (3.15). The relative permeability to the nonwetting, gas phase, may be described (Parker et al., 1987) by

$$k_{\mathrm{rg}} = \left(\overline{S}_{\mathrm{g}}\right)^{1/2}\left[1 - \left(\overline{S}_{\mathrm{w}}\right)^{\frac{1}{\gamma}}\right]^{2\gamma} \tag{3.34}$$

in which the effective gas saturation is defined as

$$\overline{S}_{\mathrm{g}} = \frac{S_{\mathrm{g}}}{1 - S_{\mathrm{wr}}} \tag{3.35}$$

which is normalized to a maximum mobile water saturation.

Relative permeability in three-phase flow systems: Compared to studies of two-phase fluid flow, there are few experimental data sets or functions are available in the literature, in particular, for three-phase relative permeability of multiphase flow in porous media. A commonly used approach for handling relative permeabilities is the simplified Stone II function (Stone, 1970) for three-phase flow. When water is the wetting

phase and gas is the nonwetting phase, the relative permeability to each phase is then described as

$$k_{rw} = k_{rw}(S_w) \tag{3.36}$$

for the water phase,

$$k_{ro} = k_{ro}(S_w, S_g) \tag{3.37}$$

for the oil phase, and

$$k_{rg} = k_{rg}(S_g) \tag{3.38}$$

for the gas phase.

When no three-phase relative permeability data are available, relative permeability to oil, the intermediate wetting phase, is often determined using the Stone method II (Aziz and Settari, 1979),

$$k_{ro} = k_{ro}^{*wo}\left[\left(\frac{k_{ro}^{ow}}{k_{ro}^{*ow}} + k_{rw}\right)\left(\frac{k_{ro}^{og}}{k_{ro}^{*ow}} + k_{rg}\right) - (k_{rw} + k_{rg})\right] \tag{3.39}$$

in which k_{ro}^{*ow} is the relative permeability value to oil at residual water saturation in the water–oil (ow), two-phase system; k_{ro}^{ow} is the relative permeability to oil in the water–oil, two-phase system; and k_{ro}^{og} is the relative permeability to oil in the oil–gas (og), two-phase system. With Eqns (3.36), (3.38), and (3.39), the Stone II function, we can evaluate three-phase relative permeability using two sets of two-phase flow relative permeabilities, determined from water–oil and oil–gas systems, respectively.

In addition, two functional forms of three-phase relative permeability can be used as alternatives. First, the Brooks–Corey type of functions (Honarpour et al., 1986) may be extended into three-phase flow as

$$k_{rw} = \left(\overline{S}_w\right)^{2+\varphi} \tag{3.40}$$

$$k_{ro} = \left(\overline{S}_o - \overline{S}_{or}\right)^2\left[\left(\overline{S}_L\right)^{\varphi} - \left(\overline{S}_w\right)^{\varphi}\right] \tag{3.41}$$

and

$$k_{rg} = \left[\overline{S}_g\right]^2\left[1 - \left(\overline{S}_L\right)^{\varphi}\right] \tag{3.42}$$

in which $\overline{S}_w$ is defined in Eqn (3.16) and

$$\overline{S}_o = \frac{S_o}{1 - S_{wr}} \tag{3.43}$$

$$\overline{S}_{or} = \frac{S_{or}}{1 - S_{wr}} \tag{3.44}$$

$$\overline{S}_g = \frac{S_g - S_{gr}}{1 - S_{wr}} \tag{3.45}$$

and

$$\overline{S}_L = \overline{S}_w + \overline{S}_o \tag{3.46}$$

with S_{gr} being the residual gas saturation.

The extended three-phase relative permeability of the van Genuchten model is given by (Kaluarachchi and Parker, 1989),

$$k_{rw} = \left(\overline{S}_w\right)^{\frac{1}{2}}\left\{1 - \left[1 - \left(\overline{S}_w\right)^{\frac{1}{\gamma}}\right]^{\gamma}\right\}^2 \tag{3.47}$$

$$k_{ro} = \left(\overline{S}_o - \overline{S}_{or}\right)^{\frac{1}{2}}\left\{\left[1 - \left(\overline{S}_w\right)^{\frac{1}{\gamma}}\right]^{\gamma} - \left[1 - \left(\overline{S}_L\right)^{\frac{1}{\gamma}}\right]^{\gamma}\right\}^2 \tag{3.48}$$

and

$$k_{rg} = \left(\overline{S}_g\right)^{\frac{1}{2}}\left[1 - \left(\overline{S}_L\right)^{\frac{1}{\gamma}}\right]^{2\gamma} \tag{3.49}$$

When using these models or functions for capillary pressure or relative permeability, discussed previously, to estimate capillary pressures or relative permeabilities for simulation of two-phase or three-phase flow, it should be kept in mind that these empirical functions have limitations and are not necessarily applicable to a particular type of rock or formation under study. In addition, model parameters determined from curve fitting of laboratory or field data may not cover the entire ranges of flow conditions for modeling studies. For ranges outside observation data, the models can provide only approximations or extrapolations on capillary pressure or relative permeability curves. For example, at the end near the residual water saturation, the van Genuchten model will predict infinitely high capillary pressures, which may not be physically meaningful. Site-specific studies and experimentally determined capillary pressure and relative permeability relations are recommended to use, even in table lookup forms. The closed-form relations discussed in this section should be used only as alternatives, when there are no experimentally determined functions available.

3.4.3 Fluid and Rock Properties

Density: The densities of oil, gas and water under reservoir conditions can be treated as functions of formation volume factors in general as, for oil,

$$\rho_o = \frac{1}{B_o}\left[\left(\rho_o\right)_{STC} + R_s\left(\rho_g\right)_{STC}\right] = \overline{\rho}_o + \overline{\rho}_{dg} \tag{3.50}$$

for water

$$\rho_{\mathrm{w}} = \frac{(\rho_{\mathrm{w}})_{\mathrm{STC}}}{B_{\mathrm{w}}} \tag{3.51}$$

and for gas

$$\rho_{\mathrm{g}} = \frac{(\rho_{\mathrm{g}})_{\mathrm{STC}}}{B_{\mathrm{g}}} \tag{3.52}$$

in which B_β is formation volume factor for phase β; $(\rho_\beta)_{\mathrm{STC}}$ is density of phase β at standard conditions (or storage tank conditions); R_{s} is solution gas–oil ratio. Note that

$$\overline{\rho}_{\mathrm{o}} = \frac{(\rho_{\mathrm{o}})_{\mathrm{STC}}}{B_{\mathrm{o}}} \tag{3.53}$$

and

$$\overline{\rho}_{\mathrm{dg}} = \frac{R_{\mathrm{s}}(\rho_{\mathrm{g}})_{\mathrm{STC}}}{B_{\mathrm{o}}} \tag{3.54}$$

The formation volume factors for oil, water, and gas are defined as

$$B_{\mathrm{o}} = \frac{(V_{\mathrm{o}} + V_{\mathrm{dg}})_{\mathrm{RC}}}{(V_{\mathrm{o}})_{\mathrm{STC}}} \tag{3.55}$$

$$B_{\mathrm{w}} = \frac{(V_{\mathrm{w}})_{\mathrm{RC}}}{(V_{\mathrm{w}})_{\mathrm{STC}}} \tag{3.56}$$

and

$$B_{\mathrm{g}} = \frac{(V_{\mathrm{g}})_{\mathrm{RC}}}{(V_{\mathrm{g}})_{\mathrm{STC}}} \tag{3.57}$$

The solution gas–oil ratio is defined as

$$R_{\mathrm{s}} = \left(\frac{V_{\mathrm{dg}}}{V_{\mathrm{o}}}\right)_{\mathrm{STC}} \tag{3.58}$$

in which $(V_\beta)_{\mathrm{RC}}$ is the volume of a given mass of phase β (o for oil, g for gas, w for water, and dg for dissolved gas) at reservoir conditions; $(V_\beta)_{\mathrm{STC}}$ is the volume occupied by the same amount of mass of phase β at standard (surface) conditions.

In general, formation volume factors and solution gas–oil ratios are functions of reservoir and bubble-point pressures for an isothermal,

three-phase oil reservoir. The correlations are determined from laboratory PVT experiments and field studies:

$$B_o = B_o(P_o, P_b) \tag{3.59}$$

$$B_g = B_g(P_g) \tag{3.60}$$

$$B_w = \frac{B_w^0}{1 + C_w(P_w - P^0)} \tag{3.61}$$

and

$$R_s = R_s(P_o, P_b) \tag{3.62}$$

in which P_b is the bubble-point pressure of the reservoir; B_w^0 is the formation volume factor of water at reference pressure, P^0; and C_w is compressibility of water phase.

The above relationships among reservoir pressures, bubble-points, and oil formation volume factors, and solution gas–oil ratios are needed in simulation studies, and these data should be determined by PVT data analyses for given reservoir fluids and rock formation.

Fluid Viscosities: Gas is normally treated as a Newtonian fluid, whereas oil and water can be either Newtonian or non-Newtonian. The fluid viscosity for a Newtonian fluid is described as a function of fluid pressure and temperature,

$$\mu_\beta = \mu_\beta(P_\beta, T) \tag{3.63}$$

For non-Newtonian fluid (oil and/or water), the apparent viscosity may be expressed as a function of saturation and flow potential gradient as in Eqn (2.7) (Wu, 1990).

Porosity of Formation: The effective porosity of rock is treated as a function of pressure, P, and reservoir temperature, T, as

$$\phi = \phi^0[1 + C_r(P - P^0) - C_T(T - T^0)] \tag{3.64}$$

in which ϕ^0 is the effective porosity of formation at reference pressure, P^0, and reference temperature, T^0; C_r is rock compressibility; and C_T is thermal expansion coefficient of formation rock.

3.5 INITIAL AND BOUNDARY CONDITIONS

The initial and boundary conditions of a reservoir model or flow system must be specified before the flow-governing equations can be solved. The initial state or initial condition of a multiphase system is generally specified by assigning a complete set of primary thermodynamic variables, such as

fluid pressure and saturation, within the model domain. Initial conditions are commonly estimated according to capillary–gravity equilibrium conditions in a multiphase system of the reservoir under study.

First-type, or Dirichlet, boundary conditions denote constant or time-dependent phase pressure and saturation conditions. Flux-type or Neumann boundary conditions refer recharge/injection or discharge/pumping rates specified at wells or along the boundary, which can be in contact with aquifers. For modeling multiphase fluid flow in reservoirs, specification of boundary conditions is by no means an easy task. In most cases, boundary conditions are a combination of different types and physical constraints for different phases and flow conditions. The problem becomes more complicated when handling multilayered production or injection wells. In general, boundary conditions for multiphase flow models consist more of physical constraints rather than conforming to their traditional concepts of boundary conditions in the solution of partial differential equations (Wu et al., 1996; Wu, 2000).

3.6 SOLUTION APPROACHES

The physical laws governing flow in porous media are represented mathematically on the continuum REV concept or macroscopic level by a set of integral or partial differential equations. These governing equations (e.g., Eqn (3.4) or (3.5)) are intrinsically nonlinear if multiphase flow is involved. Solving these nonlinear governing flow equations with complex boundary geometry and initial conditions has been a scientific challenge in reservoir simulation and many other disciplinary areas of science and engineering. Significant progress has been made due to research efforts in computational mathematics, petroleum and geothermal reservoir engineering, groundwater hydrology, and soil sciences. In general, solution methodologies developed and applied so far consist of three major approaches: (1) analytical solutions; (2) numerical methods; and (3) alternative approaches. Applicability, advantages, and limitations of these approaches are discussed in this section. We will use both analytical solution and numerical modeling approaches in solving multiphase flow problems in this book.

3.6.1 Analytical Solutions

The analytical approach has been the traditional method for solving governing equations of flow through porous media. In this method, exact mathematical solutions are obtained and used to describe physical problems of interest. Historically, analytical solutions have made important contributions

to understanding flow behavior of fluids through porous media (Muskat, 1938; Carslaw and Jaeger, 1959). Despite significant progress in numerical simulation techniques of modeling fluid flow in porous media since the late 1950s, analytical solutions, when available, provide direct or explicit insights into the physics of flow phenomena occurring in porous media, especially when dealing with the effects of various parameters with a given problem. In addition, analytical solutions of transient fluid flow provide the theoretical basis for well and laboratory testing analyses. Even in numerical studies of subsurface fluid flow problems, analytical solutions are always needed to examine and verify numerical schemes or simulation results. However, analytical approaches are mostly restricted to single-phase flow in porous media. Traditionally, many of those solutions for single-phase fluid flow were borrowed from the heat transfer literature (e.g., Carslaw and Jaeger, 1959), because the governing equations for heat conduction in solids and for incompressible single-phase fluid flow in porous media are mathematically analogous. The most commonly used analytical methods for porous-medium transient fluid flow are (1) separation of variables; (2) the integral transformation, including Laplace transformation and Fourier transformation; and finite transformation; (3) Green's function; and (4) similarity transformation.

Analytical solutions, however, have limited applicability to analyzing multiphase flow in reservoirs. This is primarily because of the inherent nonlinearity in flow-governing equations or in boundary conditions for multiphase porous-medium flow problems. Moreover, they are generally unable to account for heterogeneity of the formation. Under very special circumstances with many idealizations and simplifications, analytical solutions may be possible for a two- or even three-phase flow problem. One such example is the Buckley–Leverett solution for noncapillary, two-phase displacement in a one-dimensional, homogeneous system (Buckley and Leverett, 1942), which can also be extended to flow in a composite, one-dimensional heterogeneous system (Wu et al., 1993). Several forms of analytical solutions with capillary effects are also obtained (Chen, 1988; McWhorter and Sunada, 1990). The extension of the Buckley–Leverett solution has been made to non-Newtonian displacement (Wu, 1990; Wu et al., 1991, 1992). More recent studies have extended the Buckley–Leverett theory to immiscible non-Darcy flow and displacement (Wu, 2001; Wu et al., 2011). In the following chapters, we will discuss these new developments and extensions of the Buckley–Leverett theory.

In general, though, problems involving multiphase flow processes in a multidimensional reservoir domain are analytically intractable. Recourse to numerical solutions is necessary if (1) the flow domain has a complicated geometry, (2) the problem is nonlinear either in the governing equation and/or in the boundary conditions, and (3) the porous medium is heterogeneous or anisotropic.

3.6.2 Numerical Methods

Numerical methods have been the most used approaches for modeling multiphase flow in porous media, because the numerical methodology is able to handle the nonlinear nature of the governing equations for multiphase flow as well as complicated flow condition in reservoirs, which cannot be handled by other approaches in general. Significant progress has been made in development and application of numerical approaches in reservoir simulation (Peaceman, 1977; Thomas and Pierson, 1978; Aziz and Settari, 1979; Ertekin et al., 2001; Fanchi, 2005; Chen et al., 2006; Chen, 2007), and in groundwater literature (Huyakorn and Pinder, 1983; Istok, 1989; Helmig, 1997; Zheng and Bennett, 2002). The technical advances in numerical simulations have provided powerful quantitative tools for engineers, hydrologists, and scientists in studies of subsurface multiphase flow.

There are different kinds of numerical approaches developed and used in the literature for solving flow and transport equations in porous media. When applied to multiphase flow in reservoirs, perhaps the most commonly used numerical techniques are the finite or integrated finite difference and the finite-element approaches. In addition, other numerical methods, such as the method of characteristics and boundary element method, have also found certain applications.

3.6.3 Alternative Modeling Methods

In addition to commonly used analytical and numerical solutions, discussed above, many alternative modeling approaches have been developed and used to study multiphase flow and transport problems. Among these alternatives, streamline simulation (Datta-Gupta and King, 2007), stochastic methods (Gelhar, 1993; Zhang, 2001), and pore-scale models (Blunt, 2001) have received significant attention and found many applications, because of their capability and promising potentials in characterizing flow and transport behavior in reservoirs.

REFERENCES

Aziz, K., Settari, A., 1979. Petroleum Reservoir Simulation. Applied Science Publishers, London.

Bear, J., 1972. Dynamics of Fluids in Porous Media. American Elsevier, New York.

Blunt, M.J., 2001. Flow in porous media—pore-network models and multiphase flow. Current Opinion in Colloid & Interface Science 6 (3), 197–207.

Bodvarsson, G.S., Finsterlie, S., Liu, H.H., Oldenburg, C.M., Pruess, K., Sonnenthal, E., Wu, Y.-S., 2000. Flow and transport modeling of the vadose zone. In: Looney, B.B., Falta, R.W. (Eds.), Vadose Zone Science and Technology Solutions. Battelle Press Columbus, Ohio, pp. 591–827.

Brooks, R.H., Corey, A.T., March 1964. Hydraulic Properties of Porous Media. Hydrology Papers. Colorado State University.

Buckley, S.E., Leverett, M.C., 1942. Mechanism of fluid displacement in sands. Transactions of the AIME 146 (01), 107–116.

Carslaw, H.S., Jaeger, J.C., 1959. Heat in Solids. Clarendon Press, Oxford.

Chen, Z., 2007. Reservoir simulation: mathematical techniques in oil recovery. Society for Industrial and Applied Mathematics. CBMS-NSF regional conference series in applied mathematics, vol. 77.

Chen, Z., Huan, G., Ma, Y., 2006. Computational methods for multiphase flows in porous media. Series: Computational Science & Engineering, vol. 2. Siam.

Chen, Z.-X., 1988. Some invariant solutions to two-phase fluid displacement problems including capillary effect (includes associated papers 18744 and 19037). SPE Reservoir Engineering 3 (02), 691–700.

Corey, A.T., 1994. Mechanics of Immiscible Fluids in Porous Media. Water Resources Publication.

Datta-Gupta, A., King, M.J., 2007. Streamline Simulation: Theory and Practice. Society of Petroleum Engineers, Richardson, TX.

Ertekin, T., Abou-Kassem, J.H., King, G.R., 2001. Basic Applied Reservoir Simulation. Society of Petroleum Engineers, Richardson, TX.

Fanchi, J.R., 2005. Principles of Applied Reservoir Simulation. Gulf Professional Publishing.

Gelhar, L.W., 1993. Stochastic Subsurface Hydrology. Prentice-Hall, New Jersey.

van Genuchten, M.T., 1980. A closed-form equation for predicting the hydraulic conductivity of unsaturated soils. Soil Science Society of America Journal 44 (5), 892–898.

Helmig, R., 1997. Multiphase Flow and Transport Processes in the Subsurface: A Contribution to the Modeling of Hydrosystems. Springer-Verlag.

Honarpour, M.M., Koederitz, F., Herbert, A., 1986. Relative Permeability of Petroleum Reservoirs. CRC Press Inc, Boca Raton, FL.

Huyakorn, P.S., Pinder, G.F., 1983. Computational Methods in Subsurface Flow. Academic Press.

Istok, J., 1989. Groundwater Modeling by the Finite Element Method. American Geophysical Union.

Kaluarachchi, J.J., Parker, J.C., 1989. An efficient finite element method for modeling multiphase flow. Water Resources Research 25 (1), 43–54.

McWhorter, D.B., Sunada, D.K., 1990. Exact integral solutions for two-phase flow. Water Resources Research 26 (3), 399–413.

Mualem, Y., 1976. A new model for predicting the hydraulic conductivity of unsaturated porous media. Water Resources Research 12 (3), 513–522.

Muskat, M., 1938. The flow of homogeneous fluids through porous media. Soil Science 46 (2), 169.

Narasimhan, T.N., Witherspoon, P.A., 1976. An integrated finite difference method for analyzing fluid flow in porous media. Water Resources Research 12 (1), 57–64.
Parker, J.C., Lenhard, R.J., Kuppusamy, T., 1987. A parametric model for constitutive properties governing multiphase flow in porous media. Water Resources Research 23 (4), 618–624.
Peaceman, D.W., 1977. Fundamentals of Numerical Reservoir Simulation. Elsevier Scientific Publishing Co, New York, NY.
Pruess, K., Oldenburg, C.M., Moridis, G.J., 1999. TOUGH2 User's Guide Version 2.
Stone, H.L., 1970. Probability model for estimating three-phase relative permeability. Journal of Petroleum Technology 22 (02), 214–218.
Thomas, L.K., Pierson, R.G., 1978. Three-dimensional geothermal reservoir simulation. Society of Petroleum Engineers Journal 18 (02), 151–161.
Willhite, G.P., 1986. Waterflooding. Society of Petroleum Engineers, Richardson, TX.
Wu, Y.-S., 1990. Theoretical Studies of Non-Newtonian and Newtonian Fluid Flow through Porous Media. Lawrence Berkeley Laboratory, Berkeley, CA.
Wu, Y.-S., 1998. MSFLOW: Multiphase Subsurface Flow Model of Oil, Gas and Water in Porous and Fractured Media with Water Shut-off Capability. DOCUMENTATION and User's Guide, Walnut Creek, CA.
Wu, Y.-S., 2000. A virtual node method for handling well bore boundary conditions in modeling multiphase flow in porous and fractured media. Water Resources Research 36 (3), 807–814.
Wu, Y.-S., 2001. Non-Darcy displacement of immiscible fluids in porous media. Water Resources Research 37 (12), 2943–2950.
Wu, Y.-S., Forsyth, P.A., Jiang, H., 1996. A consistent approach for applying numerical boundary conditions for multiphase subsurface flow. Journal of Contaminant Hydrology 23 (3), 157–184.
Wu, Y.-S., Lai, B., Miskimins, J.L., Fakcharoenphol, P., Di, Y., 2011. Analysis of multiphase non-Darcy flow in porous media. Transport in Porous Media 88 (2), 205–223.
Wu, Y.-S., Pruess, K., Chen, Z.-X., 1993. Buckley-Leverett flow in composite porous media. SPE Advanced Technology Series 1 (02), 36–42.
Wu, Y.-S., Pruess, K., Witherspoon, P.A., 1991. Displacement of a Newtonian fluid by a non-Newtonian fluid in a porous medium. Transport in Porous Media 6 (2), 115–142.
Wu, Y.-S., Pruess, K., Witherspoon, P.A., 1992. Flow and displacement in Bingham non-Newtonian fluids in porous media. SPE Reservoir Engineering 7 (3), 369–376.
Zhang, D., 2001. Stochastic Methods for Flow in Porous Media: Coping with Uncertainties. Academic Press.
Zheng, C., Bennett, G.D., 2002. Applied Contaminant Transport Modeling. Wiley-Interscience, New York.

CHAPTER 4

Numerical Model and Formulation

4.1 INTRODUCTION

The methodology of using numerical approaches to simulate multiphase flow consists in general of the following three steps: (1) spatial discretization of mass and/or energy conservation equations, (2) time discretization using a backward, first-order, finite-difference scheme; and (3) iterative approaches to solve the resulting nonlinear, discrete algebraic equations. Among various numerical techniques for reservoir simulation studies is a mass- and energy-conserving discretization scheme, which is based on finite or integrated finite difference, or finite-element methods. This mass- and energy-conservative formulation is the most commonly used approach in application and is discussed in this chapter.

First, we present a generalized, generic numerical formulation that can be used for simulating various types of multiphase fluid flow processes in porous and fractured media. Then, we discuss solution techniques for solving linearized algebraic equations, treatment of initial and boundary conditions, and verification and application of numerical models and results.

4.2 GENERALIZED NUMERICAL DISCRETIZATION

The mass conservation equations, Eqns (3.7)–(3.9), for a black-oil model are discretized in space using a control-volume concept. The control-volume approach provides a general spatial discretization scheme that can represent a one-, two-, or three-dimensional domain using a set of discrete grid blocks. Each grid block has a certain control volume for a proper averaging or interpolation of fluid and rock properties or thermodynamic variables. The control volume concept includes the conventional finite-difference scheme (Peaceman, 1977; Aziz and Settari, 1979), an integrated finite difference method (Figure 4.1) (Narasimhan and Witherspoon, 1976; Pruess, 1991), a control-volume finite element (Forsyth, 1991; Forsyth et al., 1995), and Galerkin finite-element methods (Huyakorn et al., 1994; Chen et al., 2006).

Multiphase Fluid Flow in Porous and Fractured Reservoirs
ISBN 978-0-12-803848-2
http://dx.doi.org/10.1016/B978-0-12-803848-2.00004-0

These are the most widely used schemes for discretization of multiphase flow equations. Time discretization is carried out using a backward, first-order, fully implicit finite-difference scheme.

The spatial and temporal discretization and numerical formulation, discussed below, follow the numerical models implemented in the Multiphase Subsurface FLOW (MSFLOW) simulator (Wu, 1998, 2004), which is based on the "integrated finite difference" method (Narasimhan and Witherspoon, 1976; Pruess, 1991). The mass-balance equations for oil, gas, and water are expressed in a set of discrete integrated finite-difference equations. These discrete nonlinear equations are then solved fully implicitly to provide stability and large time-step sizes to speed up simulation time. Thermodynamic properties of fluids and rock are represented by averages over explicitly defined finite subdomains or grid blocks, whereas fluxes of mass across surface segments between connected grid blocks are evaluated by finite-difference approximations. The discretized, nonlinear, finite-difference mass-balance equations are then solved simultaneously, using the Newton iteration procedure (normally called Newton–Raphson iteration in reservoir simulation). Note that there is no distinction made in this book between the terms *block, grid block, element*, or *node* in the following. They all mean the same, a finite, discretized rock domain with a certain volume.

The continuum Eqns (3.4) or (3.5) is discretized in space using the integrated finite-difference scheme (Figure 4.1). The discrete nonlinear equations for mass of oil, gas, and water at grid block or node i can be written in a general form:

$$\left(A_i^{\beta,n+1} - A_i^{\beta,n}\right)\frac{V_i}{\Delta t} = \sum_{j\in\eta_i} flow_{ij}^{\beta,n+1} + Q_i^{\beta,n+1} \quad (i = 1, 2, 3, \ldots, N) \qquad (4.1)$$

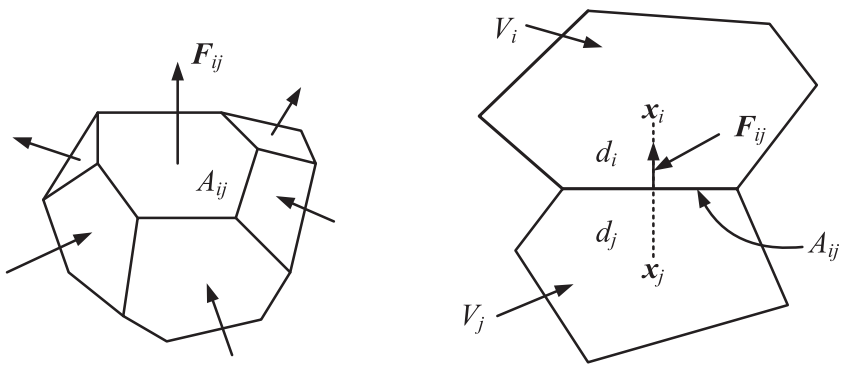

Figure 4.1 Space discretization, connection, and flow-term evaluation in the integrated finite-difference method *(Modified from Pruess et al., 1999)*.

in which A_i^{β} is the mass accumulation term at node i; the "flow" term, $flow_{ij}^{\beta}$, is the mass flux between two neighboring nodes i and j; and Q_i^{β}, the mass sink/source term at node i for fluid β, respectively, defined below.

For oil flow,

$$A_i^{\mathrm{o}} = \left(\phi S_{\mathrm{o}} \overline{\rho}_{\mathrm{o}}\right)_i \tag{4.2}$$

$$flow_{ij}^{\mathrm{o}} = \left(\overline{\rho}_{\mathrm{o}} \lambda_{\mathrm{o}}\right)_{ij+1/2}^{n+1} \gamma_{ij} \left(\Phi_{\mathrm{o}j}^{n+1} - \Phi_{\mathrm{o}i}^{n+1}\right) \tag{4.3}$$

For gas flow,

$$A_i^{\mathrm{g}} = \left(\phi S_{\mathrm{o}} \overline{\rho}_{\mathrm{dg}} + \phi S_{\mathrm{g}} \rho_{\mathrm{g}}\right)_i \tag{4.4}$$

$$flow_{ij}^{\mathrm{g}} = \left(\overline{\rho}_{\mathrm{dg}} \lambda_{\mathrm{o}}\right)_{ij+1/2}^{n+1} \gamma_{ij} \left(\Phi_{\mathrm{o}j}^{n+1} - \Phi_{\mathrm{o}i}^{n+1}\right) + \left(\rho_{\mathrm{g}} \lambda_{\mathrm{g}}\right)_{ij+1/2}^{n+1} \gamma_{ij} \left(\Phi_{\mathrm{g}j}^{n+1} - \Phi_{\mathrm{g}i}^{n+1}\right) \tag{4.5}$$

and for water flow,

$$A_i^{\mathrm{w}} = \left(\phi S_{\mathrm{w}} \rho_{\mathrm{w}}\right)_i \tag{4.6}$$

$$flow_{ij}^{\mathrm{w}} = \left(\rho_{\mathrm{w}} \lambda_{\mathrm{w}}\right)_{ij+1/2}^{n+1} \gamma_{ij} \left(\Phi_{\mathrm{w}j}^{n+1} - \Phi_{\mathrm{w}i}^{n+1}\right) \tag{4.7}$$

In the Eqns (4.2)–(4.7) previously, n denotes the previous time-step level; $n+1$ is for the current time-step level to be solved; V_i is the volume of element i; Δt is time-step size; η_i is the set of neighboring elements or nodes (j) of element i, to which element i is directly connected; N is the total number of grid blocks of the grid; subscript $ij{+}1/2$ denotes a proper averaging at the interface between two elements i and j (Figure 4.1), with the mobility of phase β defined as

$$\lambda_{\beta} = \frac{k_{\mathrm{r}\beta}}{\mu_{\beta}} \tag{4.8}$$

the transmissivity of flow terms is defined as

$$\gamma_{ij} = \frac{A_{ij} k_{ij+1/2}}{d_i + d_j} \tag{4.9}$$

and

$$\Phi_{\beta i}^{n+1} = P_{\beta i}^{n+1} - \rho_{\beta, ij+1/2}^{n+1} \, g D_i \tag{4.10}$$

in which A_{ij} is the common interface area between connected elements i and j (Figure 4.1); d_i is the distance from the center of element i to

the interface between elements i and j (Figure 4.1); d_j is the distance from the center of element j perpendicular to the interface between elements i and j (Figure 4.1); $k_{ij+1/2}$ is the averaged absolute permeability along the connection between elements i and j; D_i is the depth to the center of element i to a reference datum level; and the sink/source term for element i, Q_i^β, is defined as

$$Q_i^{\beta,n+1} = q_{\beta i}^{n+1} \, V_i \tag{4.11}$$

Here, the sink/source term, $q_{\beta i}$, is defined as the mass exchange rate per unit volume of rocks at grid block i, (kg/sm^3). It is normally used to treat boundary conditions, such as production or injection through wells.

In evaluating properties for the flow term, the upstream weighting scheme is normally used for averaging relative permeability of the mobility term, Eqn (4.8), and the harmonic weighting is used for absolute permeability in Eqn (4.9). In addition, the definition of the transmissivity, Eqn (4.9), can be easily modified or extended to include some other spatial discretization schemes, such as the control volume finite-element method (Forsyth, 1991; Forsyth et al., 1995).

Note that Eqn (4.1) presents a precise form of the mass-balance equation for each fluid mass at grid block i in a discrete form. It states that the rate of change in mass accumulation at any node during a time step is exactly balanced by the net sum of inflow/outflow of mass and sink/source terms for that node. As long as all flow terms have mass flow from node i to node j equal to and opposite to that of node j to node i for the fluid, no mass will be lost or created in the formulation during the numerical solution. Therefore, the discretization in Eqn (4.1) is called conservative. In addition, Eqn (4.1) has the same form regardless of the dimensionality of the flow system, i.e., it applies to one-, two-, or three-dimensional flow as well as chemical transport and heat-transfer analyses (Wu, 2004).

4.3 NUMERICAL SOLUTION SCHEME

We can write Eqn (4.1) in residual form,

$$R_i^{\beta,n+1} = \left(A_i^{\beta,n+1} - A_i^{\beta,n}\right)\frac{V_i}{\Delta t} - \sum_{j\in\eta_i} flow_{ij}^{\beta,n+1} - Q_i^{\beta,n+1} = 0 \qquad (i = 1, 2, 3, \ldots, N) \tag{4.12}$$

Substitution of Eqns (4.2)–(4.7) into Eqn (4.12) leads to three discretized, nonlinear, algebraic mass-balance equations for oil, gas, and water flow in residual forms, respectively, as follows:

$$R_i^{o,n+1} = \left[(\phi S_o \overline{\rho}_o)_i^{n+1} - (\phi S_o \overline{\rho}_o)_i^n\right] \frac{V_i}{\Delta t} - \sum_{j\in\eta_i} (\overline{\rho}_o\ \lambda_o)_{ij+1/2}^{n+1} \gamma_{ij} \left(\Phi_{oj}^{n+1} - \Phi_{oi}^{n+1}\right) - Q_i^{o,n+1} = 0 \tag{4.13}$$

$$R_i^{g,n+1} = \left[\left(\phi S_o \overline{\rho}_{dg} + \phi S_g \rho_g\right)_i^{n+1} - \left(\phi S_o \overline{\rho}_{dg} + \phi S_g \rho_g\right)_i^n\right] \frac{V_i}{\Delta t} - \sum_{j\in\eta_i} \left(\overline{\rho}_{dg} \lambda_o\right)_{ij+1/2}^{n+1} \gamma_{ij} \left(\Phi_{oj}^{n+1} - \Phi_{oi}^{n+1}\right) - \sum_{j\in\eta_i} \left(\rho_g \lambda_g\right)_{ij+1/2}^{n+1} \gamma_{ij} \left(\Phi_{gj}^{n+1} - \Phi_{gi}^{n+1}\right) - Q_i^{g,n+1} = 0 \tag{4.14}$$

and

$$R_i^{w,n+1} = \left[(\phi S_w \rho_w)_i^{n+1} - (\phi S_w \rho_w)_i^n\right] \frac{V_i}{\Delta t} - \sum_{j\in\eta_i} (\rho_w \lambda_w)_{ij+1/2}^{n+1} \gamma_{ij} \left(\Phi_{wj}^{n+1} - \Phi_{wi}^{n+1}\right) - Q_i^{w,n+1} = 0 \tag{4.15}$$

for $i = 1, 2, 3, \ldots, N$.

The Newton iteration is used to solve Eqns (4.13)–(4.15) for a three-phase flow system, represented by $3 \times N$ coupled nonlinear algebraic equations, which include, for each element, three mass-balance equations of oil, gas, and water components. Three primary variables (x_1, x_2, x_3) are selected for each element, which are oil pressure, oil saturation, and saturation pressure (or gas saturation), as shown in Table 4.1. The selection of primary variables in the numerical solution is based on an automatic variable switching scheme, which is used to handle the transition of free gas appearing and disappearing during simulation studies of oil production with oil, gas, and water three-phase flow conditions (Wu and Forsyth, 2001).

Table 4.1 Choice of the primary variables

Primary variable	Physical variable
$x_1 = P_o$	Oil pressure
$x_2 = S_o$	Oil saturation
$x_3 = P_s$ or	Saturation pressure or
$x_3 = S_g$	Gas saturation

As indicated by Table 4.1, the first two of the three primary variables are fixed as oil pressure and oil saturation, and the third variable depends on the phase condition at a node. If there is no free gas, a node is said to be undersaturated or above the bubble point, and saturation pressure, P_s, is used as the third primary variable. When free gas is present, a node is said to be saturated or below the bubble point, and gas saturation, S_g, is used as the third primary variable. This variable switching scheme, as implemented in the MSFLOW simulator (Wu, 1998), is very rigorous and efficient in handling variable bubble-point problems, which are often encountered in reservoir simulations (Thomas et al., 1976). Numerical experiment has shown that choice of different primary variables makes a difference in numerical performance during iteration solution of solving a three-phase, nonlinear flow problem (Wu and Forsyth, 2001). The best combination of primary variables is to select the mixed formulation of pressures and saturations, as shown in Table 4.1, for handling phase transitions under different capillary/phase conditions.

In terms of the residual for element i and equation β, and the primary variables, the Newtonian scheme gives rise to

$$R_i^{\beta,n+1}(x_{k,p+1}) = R_i^{\beta,n+1}(x_{k,p}) + \sum_k \frac{\partial R_i^{\beta,n+1}(x_{k,p})}{\partial x_k}(x_{k,p+1} - x_{k,p}) = 0 \tag{4.16}$$

in which index $k = 1$, 2, and 3 for primary variable 1, 2, and 3 (See Table 4.1), respectively; p is Newton iteration level. Equation (4.16) can be written as

$$\sum_k \frac{\partial R_i^{\beta,n+1}(x_{k,p})}{\partial x_k}(\delta x_{k,p+1}) = -R_i^{\beta,n+1}(x_{k,p}) \quad \text{for } k = 1,\ 2 \text{ and } 3 \tag{4.17}$$

for $i = 1, 2, 3, \ldots, N$ and with an increment of primary variables over the iteration,

$$x_{k,p+1} = x_{k,p} + \delta x_{k,p+1} \tag{4.18}$$

The iteration process continues until the residuals $R_i^{\beta,n+1}$ or other convergence criteria over an iteration are reduced below preset convergence tolerances.

Equation (4.17) represents a set of $3 \times N$ linear equations for $3 \times N$ unknowns of vector, $\delta x_{k,p+1}$. A numerical method is normally used to construct the Jacobian matrix for Eqn (4.17) using numerical

differentiation, as outlined by Forsyth et al. (1995). The linear system of Eqn (4.17) in general has a nonsymmetric Jacobian matrix for three-phase flow problems and is commonly solved using an iterative method.

4.4 TREATMENT OF INITIAL AND BOUNDARY CONDITIONS

Treatment of reservoir boundary conditions as well as wells is perhaps the most difficult part in formulating and coding a multiphase numerical simulator. This is primarily because of the nature of the partial differential equations (PDEs) governing multiphase subsurface flow. In general, these flow-governing PDEs can be of parabolic-type, hyperbolic-type, elliptic-type, or mixed one, and the equation type may vary dynamically in the model domain during simulation, depending on transient flow, steady-state flow, and existing flowing-phase condition. Maximum changes in primary variables and mass fluxes will occur at boundary or well nodes with small volume. Therefore, these boundary nodes are in general nearly singular mathematically or the most difficult to converge computationally during a simulation.

In addition, multiphase interactions along a model boundary make the description of boundary conditions for multiphase flow quite different from single-phase flow. For example, a phase-pressure specification at boundaries must be consistent with other phase pressures at the same boundary location, which are correlated by capillary-pressure functions of the local rock. In many cases, there may be only one or two phases present at described boundaries, and extreme caution should be taken to describe the pressure conditions for the nonexisting phases to avoid an artificial injection or pumping, which could falsely occur for nonexisting phases at boundaries. It is always helpful to know in advance whether a boundary node is an inflow or outflow node for a given phase, but in many situations this is impossible. In that case, it is most important to maintain the physical consistency in describing inflow or outflow at a boundary element; for example, by treating boundary conditions as part of the solution.

Strictly speaking, boundary condition in modeling multiphase flow is a constraint rather than rigorous "boundary condition," as used and defined in mathematical terms for solving partial differential equations. A generalized methodology for boundary condition treatment in multiphase flow simulation has been discussed in the literature (e.g., Thomas, 1981; Wu et al., 1996) and it is based on a general, physically consistent approach. In this method, any type of boundary condition is treated as a physical sink or

source term, i.e., the boundary node either gains or loses mass over a time step. This source/sink method is applicable to all kinds of boundary conditions encountered in practice for simulating multiphase flow in reservoirs.

Also, it should be mentioned that in reservoir simulation, any nodes or grid blocks can be treated as boundary nodes, whether they are located along or inside the model domain boundary. For nodes along model boundaries, if no boundary conditions are specified to them, they are treated implicitly as closed or no-flow boundaries in the formulation.

4.4.1 First-Type Boundary Conditions

In modeling multiphase phase flow in reservoirs, first-type boundary conditions denote constant (or time-varying) phase pressure and saturation conditions. This type of boundary condition can be treated using the big-volume method, in which a constant pressure/saturation node is specified with a huge volume and keeping all the other geometric properties of the mesh unchanged for a control-volume type of discretization. This is normally done in a TOUGH2 simulation (Pruess, 1991; Pruess et al., 1999). However, caution should be taken on (1) phase conditions when specifying the "initial condition" for the big-volume boundary node, and (2) distinguishing upstream/injection or downstream/production nodes. Once specified, primary variables will be fixed at the big-volume boundary nodes at all the times, and the code handles these boundary nodes exactly the same way as all other nodes. Inflow into and outflow from these big-volume boundary nodes are also evaluated by Darcy's law or the flow-term calculation. Keep in mind that the bottom line in applying the big-volume approach is to maintain the inflow and outflow to be consistent with the physical process of interest.

4.4.2 Flux-Type Boundary Conditions

Flux-type boundary conditions are treated as sink/source terms, depending on pumping (production) or injection condition, which can be directly added into the mass-balance Eqns (4.13)–(4.15). This treatment of flux-type boundary conditions is especially useful for a situation in which flux distribution along the boundary is known, such as dealing with natural water influx. This method may also be used for an injection or pumping well that is connected only a single grid block of a single-grid-layered reservoir without concerning injection or pumping pressures to be

estimated. However, it cannot apply to a well penetrating a multilayered formation in general.

4.4.3 Well Treatment

The boundary condition along a multiple-layer penetrating wellbore is very complicated to handle and it belongs to more general mixed-type boundaries with either production/injection rate or bottom-hole pressure specified. In general, multilayered well boundary conditions are the part of the solution. A general procedure of handling such boundary conditions, the "virtual node" method, is discussed in Wu et al. (1996) and Wu (2000). This method handles a wellbore as a single or several computational nodes screened and connected to many neighboring nodes of formations for a multilayered well. Therefore, it can rigorously couple reservoir flow with wellbore flow (Wu, 2000). In this approach, a wellbore can be vertical, inclined, or horizontal, and a borehole node is treated in the same way as any other nonwell node, and pumping/injection conditions are accounted for using sink or source terms to the wellbore node, depending on whether they are flux specified or pressure specified. In general, the mass-balance Eqns (4.13)–(4.15) are still applicable to well nodes, except that the transmissivity between well and formation nodes is not evaluated by Eqn (4.9), but using productivity or injectivity, based on different well flow models (e.g., Peaceman, 1978, 1983, 1993, 1995; Fung et al., 1992; Lee and Milliken, 1993).

4.5 MODEL VERIFICATION AND VALIDATION

To assure that the physical phenomena are represented correctly in mathematical models, verification and validation of numerical formulations and model results are among the most important steps in development of numerical models and solutions for modeling multiphase flow in porous media. This is also necessary to verify correctness of formulation and programing as well as accuracy of numerical model solutions. In this effort of investigation, model verification and validation have been traditionally carried out by (1) comparison with analytical solutions under simplified conditions; (2) benchmark against model results from other existing reservoir simulators for each computational module under the same or simpler flow and geological conditions; (3) use of the numerical model to analyze and match laboratory test data and results; and (4) use of the numerical model for analysis of field data.

REFERENCES

Aziz, K., Settari, A., 1979. Petroleum Reservoir Simulation. Applied Science Publishers, London.

Chen, Z., Huan, G., Ma, Y., 2006. Computational methods for multiphase flows in porous media. Siam.

Forsyth, P.A., 1991. A control volume finite element approach to NAPL groundwater contamination. SIAM Journal on Scientific and Statistical Computing 12 (5), 1029–1057.

Forsyth, P.A., Wu, Y.S., Pruess, K., 1995. Robust numerical methods for saturated-unsaturated flow with dry initial conditions in heterogeneous media. Advances in Water Resources 18 (1), 25–38.

Fung, L.-K., Hiebert, A.D., Nghiem, L.X., 1992. Reservoir simulation with a control-volume finite-element method. SPE Reservoir Engineering 7 (03), 349–357.

Huyakorn, P.S., Panday, S., Wu, Y.S., 1994. A three-dimensional multiphase flow model for assessing NAPL contamination in porous and fractured media, 1. Formulation. Journal of Contaminant Hydrology 16 (2), 109–130.

Lee, S.H., Milliken, W.J., 1993. The productivity index of an inclined well in finite-difference reservoir simulation. In: SPE Symposium on Reservoir Simulation, New Orleans, Louisiana. http://doi.org/10.2118/25247-MS.

Narasimhan, T.N., Witherspoon, P.A., 1976. An integrated finite difference method for analyzing fluid flow in porous media. Water Resources Research 12 (1), 57–64.

Peaceman, D.W., 1977. Fundamentals of Numerical Reservoir Simulation. Elsevier Scientific Publishing Co., New York, NY.

Peaceman, D.W., 1978. Interpretation of well-block pressures in numerical reservoir simulation (includes associated paper 6988). Society of Petroleum Engineers Journal 18 (03), 183–194.

Peaceman, D.W., 1983. Interpretation of well-block pressures in numerical reservoir simulation with nonsquare grid blocks and anisotropic permeability. Society of Petroleum Engineers Journal 23 (03), 531–543.

Peaceman, D.W., 1993. Representation of a horizontal well in numerical reservoir simulation. SPE Advanced Technology Series 1 (01), 7–16.

Peaceman, D.W., 1995. A new method for representing multiple wells with arbitrary rates in numerical reservoir simulation. In: Symposium on Reservoir Simulation, pp. 257–272.

Pruess, K., 1991. TOUGH2: A General-Purpose Numerical Simulator for Multiphase Fluid and Heat Flow.

Pruess, K., Oldenburg, C.M., Moridis, G.J., 1999. TOUGH2 User's Guide Version 2.

Thomas, G.W., 1981. Principles of Hydrocarbon Reservoir Simulation. IHRDC, Boston, MA.

Thomas, L.K., Lumpkin, W.B., Reheis, G.M., 1976. Reservoir simulation of variable bubble-point problems. Society of Petroleum Engineers Journal 16 (01), 10–16.

Wu, Y.-S., 1998. MSFLOW: Multiphase Subsurface Flow Model of Oil, Gas and Water in Porous and Fractured Media with Water Shut-off Capability. Documentation and User's Guide. Walnut Creek, California.

Wu, Y.-S., 2000. A virtual node method for handling well bore boundary conditions in modeling multiphase flow in porous and fractured media. Water Resources Research 36 (3), 807–814.

Wu, Y.-S., 2004. A unified numerical framework model for simulating flow, transport, and heat transfer in porous and fractured media. Developments in Water Science 55, 645–658.

Wu, Y.-S., Forsyth, P.A., 2001. On the selection of primary variables in numerical formulation for modeling multiphase flow in porous media. Journal of Contaminant Hydrology 48 (3), 277–304.

Wu, Y.-S., Forsyth, P.A., Jiang, H., 1996. A consistent approach for applying numerical boundary conditions for multiphase subsurface flow. Journal of Contaminant Hydrology 23 (3), 157–184.

CHAPTER 5

Two-Phase Immiscible Displacement

5.1 INTRODUCTION

Immiscible flow and displacement of multiple-phase fluids in porous media are of fundamental importance to many problems relating to underground natural resource recovery and storage projects, or waste disposal and contamination transport evaluation. Immiscible flow of multiple-phase fluids through porous media, as compared with single-phase flow, is much more complicated and is still not well understood in many areas due to the complex interactions of different fluid phases in porous media.

Many contributions to this subject have been made since the 1940s. A fundamental understanding of immiscible displacement of Newtonian fluids in porous media was contributed by Buckley and Leverett (1942) in their classic study of fractional-flow theory. The Buckley–Leverett solution gives a saturation profile with a sharp front along the flow direction, but ignores capillary pressure and gravity effects. As time progresses, the saturation becomes a multiple-valued function of the distance coordinate, x, which can be overcome by material balance consideration. When the initial saturation in the flow system is uniform, a simple graphic approach developed by Welge (1952) can be used to determine the sharp saturation front without difficulty. Sheldon and Cardwell (1959) solved the Buckley–Leverett problem with the method of characteristics. Effects of gravity and capillary pressure on a linear waterflood were included by Fayers and Sheldon (1959), and Hovanessian and Fayers (1961), by numerical models. Codreanu et al. (1966) presented a treatment of non-capillary immiscible displacement in heterogeneous media. Some special analytical solutions of immiscible displacement including the effects of capillary pressure were obtained in the Russian and Chinese literature in the 1960s, such as Chen (1988), and more recent developments have been contributed to Buckley–Leverett theory by Yortsos and Fokas (1983) and McWhorter and Sunada (1990).

The purpose of this chapter is to describe the process of two-phase immiscible displacement in porous media. The first portion of the

Multiphase Fluid Flow in Porous and Fractured Reservoirs
ISBN 978-0-12-803848-2
http://dx.doi.org/10.1016/B978-0-12-803848-2.00005-2

chapter is devoted to immiscible two-phase flow and begins with a brief description of governing equations and constitutive relations. Then, the subject is introduced to describe frontal-advance equation of two-phase immiscible displacement. After introducing several basic assumptions, the Buckley–Leverett theory and solutions and Welge's approach for determining average saturations are discussed. The chapter concludes with discussion of applications of the Buckley–Leverett solution, including calculation of oil recovery and pressure profiles.

5.2 TWO-PHASE FLOW GOVERNING EQUATIONS

In petroleum engineering and groundwater hydrogeology, we are often interested in the simultaneous flow of two or more fluid phases within a reservoir. In this section, we consider two-phase flow in which the two fluids are immiscible. One phase (e.g., water) wets the porous medium more than the other (e.g., oil), and is called the wetting phase, and the other phase is termed the nonwetting phase. Assuming that there is no mass transfer between phases in the immiscible fluid flow, the mass is conserved within the water and oil phase (denoted by subscripts w and o):

$$-\nabla\cdot\left(\rho_\beta \boldsymbol{v}_\beta\right)+q_\beta=\frac{\partial\left(\rho_\beta S_\beta\phi\right)}{\partial t},\quad \beta=\mathrm{w},\ \mathrm{o} \tag{5.1}$$

in which q_β is the sink/source term; and Darcy velocity $\boldsymbol{v}_\beta$ for fluid β is given by:

$$\boldsymbol{v}_\beta=-\frac{kk_{r\beta}}{\mu_\beta}\left(\nabla P_\beta-\rho_\beta \boldsymbol{g}\right),\quad \beta=\mathrm{w},\ \mathrm{o} \tag{5.2}$$

in which $\boldsymbol{g}$ is the gravity acceleration vector.

These equations, when solved for flow in a particular geometry, can give pressure and saturation distributions as well as phase-flow velocities at any point (x, y, z) and time in the porous media. To describe the displacement in a simple and clear way, we assume that flow is one-dimensional along the x-direction and described by

$$-\frac{\partial}{\partial x}\left(\rho_{\mathrm{o}} v_{\mathrm{ox}}\right)=\frac{\partial}{\partial t}\left(\rho_{\mathrm{o}} S_{\mathrm{o}}\phi\right) \tag{5.3}$$

and

$$-\frac{\partial}{\partial x}\left(\rho_{\mathrm{w}} v_{\mathrm{wx}}\right)=\frac{\partial}{\partial t}\left(\rho_{\mathrm{w}} S_{\mathrm{w}}\phi\right) \tag{5.4}$$

Here, the sink/source term q_β is neglected and the subscript x will be dropped, because all discussions apply to the x-direction in the rest of this chapter. Equations (5.3) and (5.4) may also be written in terms of volumetric flow rates q_o and q_w by multiplying both sides of the equations by a constant, cross-sectional area (A) available for flow. Thus

$$-\frac{\partial}{\partial x}(\rho_o q_o) = A\frac{\partial}{\partial t}(\rho_o S_o \phi) \tag{5.5}$$

and

$$-\frac{\partial}{\partial x}(\rho_w q_w) = A\frac{\partial}{\partial t}(\rho_w S_w \phi) \tag{5.6}$$

In this chapter, we assume that oil displacement takes place under the so-called diffuse-flow condition or stable displacement. This means that fluid saturations at any point in the linear displacement path are uniformly distributed with respect to thickness or cross-sectional area of the one-dimensional flow domain. The sole reason for making this assumption is that it permits the displacement to be described mathematically in one dimension. This is the simplest possible model of immiscible displacement processes in reservoirs. The one-dimensional description follows the fact that because the water saturation is uniformly distributed in the plane normal to the flow direction then, so too, are the relative permeabilities to oil and water, which are themselves functions of the water saturation at any point. Then, the simultaneous flow of oil and water can be modeled using thickness- or area-averaged relative permeabilities along the one-dimensional flow domain. Throughout the chapter, displacement will be considered exclusively in a linear prototype reservoir model, as shown in Figure 5.1.

Consider oil displacement in a tilted linear reservoir block, as shown in Figure 5.1, which has a uniform cross-sectional area, A. Applying Darcy's

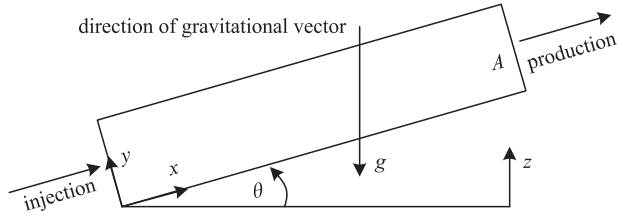

Figure 5.1 Linear prototype reservoir model with cross-sectional area *A*.

law (Eqn (5.2)), for one-dimensional linear flow, equations for the simultaneous flow of oil and water are

$$q_o = -A\frac{kk_{ro}}{\mu_o}\left(\frac{\partial P_o}{\partial x} + \rho_o g \sin\theta\right) \tag{5.7}$$

and

$$q_w = -A\frac{kk_{rw}}{\mu_w}\left(\frac{\partial P_w}{\partial x} + \rho_w g \sin\theta\right) \tag{5.8}$$

The pressures in the two phases are related by the capillary pressure, $P_c = P_o - P_w$. Various aspects of capillary pressure and its effects are discussed in Chapters 2 and 3.

5.3 FRACTIONAL FLOW EQUATION

To introduce the fractional-flow concept, the flow or displacement system is assumed to be incompressible, i.e., oil, water, and formation are all incompressible, and thus ρ_o and ρ_w are constant. Porosity is also assumed constant, which means the solid matrix is rigid. So Eqns (5.5) and (5.6) become

$$-\frac{\partial q_o}{\partial x} = A\phi\frac{\partial S_o}{\partial t} \tag{5.9}$$

and

$$-\frac{\partial q_w}{\partial x} = A\phi\frac{\partial S_w}{\partial t} \tag{5.10}$$

The sum of the above two equations is

$$-\frac{\partial}{\partial x}(q_o + q_w) = A\phi\frac{\partial}{\partial t}(S_o + S_w) \tag{5.11}$$

Because $S_o + S_w = 1$, then

$$\frac{\partial}{\partial x}(q_o + q_w) = 0 \tag{5.12}$$

It means that the total volumetric flow rate $q_t = q_o + q_w =$ constant, or is independent of the distance of x at any time.

Note that the assumption of incompressibility of fluids and rock is necessary to derive the Buckley and Leverett solution using the fractional-flow concept (Buckley and Leverett, 1942; Willhite, 1986). In practice, this

assumption also provides a good approximation for many applications, such as for water and oil displacement at both laboratory and field scale, because of the small compressibility of the liquids and reservoir rock. Even for gas and liquid displacement, the incompressibility assumption or the Buckley–Leverett theory has been routinely applied in petroleum reservoir engineering, as demonstrated by Buckley and Leverett themselves in their original work (Buckley and Leverett, 1942). One of the reasons the Buckley–Leverett theory is applicable to highly compressible-gas displacement is the small pressure drop expected in a gas-flowing zone, allowing gas pressure to be approximated as constant. This is because of the low viscosity of gas phase, leading to a small pressure drop over a flow domain. In addition, displacement processes of reservoir flooding are most controlled by constant rate injection/production in maintaining the pressure at a constant level, which makes fluid and rock compressibility have a small impact on displacement of fluids.

The fractional flow of a fluid phase, f, is defined as the volumetric flux fraction of the phase that is flowing at position x and time t (Willhite, 1986). For flow of oil and water phases, fractional flow to oil is

$$f_o = \frac{q_o}{q_t} = \frac{q_o}{q_o + q_w} \tag{5.13}$$

and to water,

$$f_w = \frac{q_w}{q_t} = \frac{q_w}{q_o + q_w} \tag{5.14}$$

It is obvious that the definition of the fractional flow leads to

$$f_o + f_w = 1.0 \tag{5.15}$$

Substituting the fractional flow into Eqns (5.7) and (5.8), we obtain

$$(1 - f_w)q_t = -A\frac{kk_{ro}}{\mu_o}\left(\frac{\partial P_o}{\partial x} + \rho_o g \sin\theta\right) \tag{5.16}$$

and

$$f_w q_t = -A\frac{kk_{rw}}{\mu_w}\left(\frac{\partial P_w}{\partial x} + \rho_w g \sin\theta\right) \tag{5.17}$$

Rearranging Eqns (5.16) and (5.17),

$$-(1 - f_w)\frac{q_t}{A}\frac{\mu_o}{kk_{ro}} = \frac{\partial P_o}{\partial x} + \rho_o g \sin\theta \tag{5.18}$$

and

$$-f_w \frac{q_t}{A} \frac{\mu_w}{k k_{rw}} = \frac{\partial P_w}{\partial x} + \rho_w g \sin\theta \tag{5.19}$$

By abstracting the above two equations and rearranging, we can solve the fractional flow of water phase as follows

$$f_w = \frac{1 + \frac{A k k_{ro}}{q_t \mu_o}\left(\frac{\partial P_c}{\partial x} - \Delta\rho g \sin\theta\right)}{1 + \frac{k_{ro}}{k_{rw}} \cdot \frac{\mu_w}{\mu_o}} \tag{5.20}$$

in which

$$\frac{\partial P_c}{\partial x} = \frac{\partial}{\partial x}(P_o - P_w)$$

is the capillary-pressure gradient along the direction of flow; and $\Delta\rho = \rho_w - \rho_o$.

Equation (5.20) is the fractional-flow equation of water for the displacement of oil by water in a one-dimensional reservoir. It is worthwhile considering the influence of the various terms or factors in this expression. According to the convention adopted in this text,θ is the angle measured from the horizontal to the line indicating the direction of flow (Figure 5.1). Therefore, the gravity term $\Delta\rho g \sin\theta$ will be positive for oil displacement in the upslope-dipping direction ($0 < \theta < \pi$), as shown in Figure 5.1, and negative for displacement downslope dipping ($\pi < \theta < 2\pi$). As a result, provided all the other terms in Eqn (5.20) are the same, the fractional flow of water for displacement upslope dipping is lower than that for displacement downslope dipping because in the former case gravity tends to suppress the flow of water. The effect of the capillary-pressure gradient term is less obvious, but can be qualitatively understood by expressing the gradient as

$$\frac{\partial P_c}{\partial x} = \frac{dP_c}{dS_w} \cdot \frac{\partial S_w}{\partial x} \tag{5.21}$$

The first term on the right-hand side in Eqn (5.21) is the slope of the capillary-pressure curve, Figure 5.2(a), which is always negative. The second term is the slope of the water-saturation profile in the direction of flow, a typical profile being shown in Figure 5.2(b). From this it can be seen that the second term $\partial S_w/\partial x$ is also negative. Therefore $\partial P_c/\partial x$ is always positive and consequently the presence of the capillary-pressure gradient term tends to increase the fractional flow of water. Quantitatively, it is difficult to determine the capillary-pressure gradient, even though the

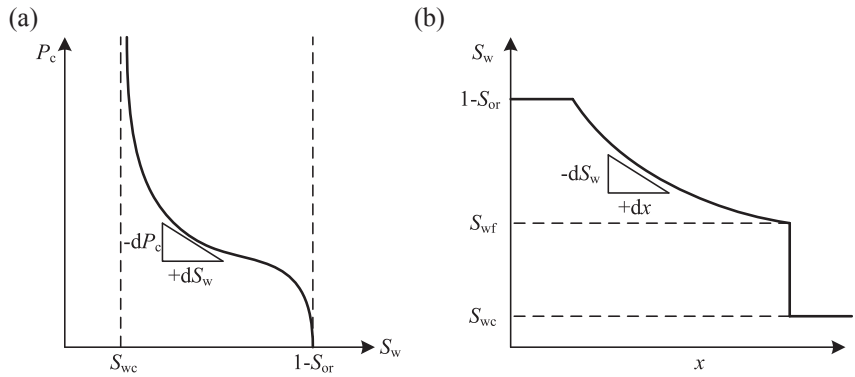

Figure 5.2 (a) Capillary-pressure function and (b) water-saturation distribution as a function of distance in the displacement path.

capillary-pressure curve may be available, but the water-saturation profile, Figure 5.2(b), is unknown and needs to be solved.

As shown in Figure 5.2(b), there is a distinct flood front or shock front of saturation, at which point there is a discontinuity in the water saturation that increases abruptly from connate water S_{wc} to S_{wf}, the flood sharp-front saturation. Steep saturation changes or large gradients may be present near the advancing front of the invading water region. It is at this shock front at which $\partial P_c/\partial x$ is at maximum. However, we can consider that there is a gradual increase in saturation from S_{wf} to the maximum $1 - S_{or}$ behind the flood front. In this region, it is normally considered that the product of $\partial S_w/\partial x$ and $\partial P_c/\partial S_w$ are small and therefore the capillary-pressure gradient can be neglected in the fractional-flow equation.

When flow is in a horizontal reservoir, i.e., $\theta = 0$, the gravity term is absent. Then the fractional-flow equation of water phase is reduced to the following,

$$f_w = \frac{1}{1 + \frac{k_{ro}}{k_{rw}} \cdot \frac{\mu_w}{\mu_o}} \tag{5.22}$$

Thus, for a given pair of water and oil viscosities, fractional flow is strictly a function of the water saturation through the saturation dependence of relative permeabilities. Figure 5.3 shows a typical water fractional-flow curve with saturation limits S_{wc} and $1 - S_{or}$, between which the fractional flow increases from zero to unity. Equation (5.22) shows that the shape of this curve is also impacted by the viscosity ratio of water to oil.

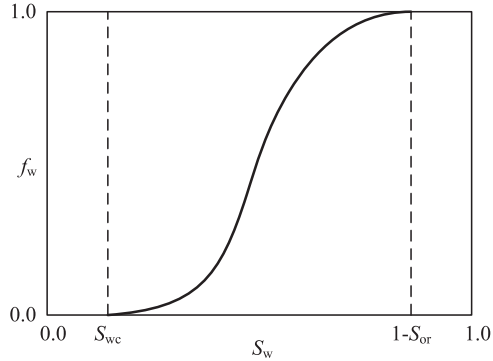

Figure 5.3 Typical fractional-flow curve as a function of water saturation.

The dependence of fractional flow on water saturation alone is important, because it allows us to develop a simple method to calculate the water fraction of the total flow at any point and any time in the reservoir, assuming the water saturation at that point is known. Precisely how to determine when a given water-saturation plane reaches a particular distance in the linear system requires the application of the displacement theory presented in the following section.

5.4 BUCKLEY–LEVERETT SOLUTION AND WELGE'S APPROACH

5.4.1 Buckley–Leverett Solution

In 1942, Buckley and Leverett presented what is recognized as the basic equation and solution for describing immiscible displacement in a one-dimensional, linear reservoir. First, by substituting Eqn (5.14) into Eqn (5.10), we obtain

$$-\frac{\partial f_w}{\partial x} = \frac{A\phi}{q_t}\frac{\partial S_w}{\partial t} \tag{5.23}$$

To solve Eqn (5.23), it is necessary to obtain an equivalent form of Eqn (5.23), which involves only one dependent variable (i.e., either f_w or S_w). In the Buckley–Leverett theory, an expression for $\partial S_w/\partial t$ is obtained following the full differential. Because the water saturation is a function of two dependent variables, x and t, we can obtain

$$dS_w = \left.\frac{\partial S_w}{\partial x}\right|_t dx + \left.\frac{\partial S_w}{\partial t}\right|_x dt \tag{5.24}$$

If we focus on the movement of a plane of a particular or *constant* saturation, S_w, then $dS_w = 0$ in Eqn (5.24), leading to

$$\left.\frac{\partial S_w}{\partial t}\right|_x = -\left.\frac{\partial S_w}{\partial x}\right|_t \cdot \left.\frac{dx}{dt}\right|_{S_w} \tag{5.25}$$

Furthermore, we have

$$\left.\frac{\partial f_w}{\partial x}\right|_t = \left(\frac{\partial f_w}{\partial S_w} \cdot \frac{\partial S_w}{\partial x}\right)_t \tag{5.26}$$

and substituting Eqns (5.25) and (5.26) into Eqn (5.23) yields

$$-\left.\frac{\partial f_w}{\partial S_w}\right|_t \cdot \left.\frac{\partial S_w}{\partial x}\right|_t = -\frac{A\phi}{q_t}\left.\frac{\partial S_w}{\partial x}\right|_t \cdot \left.\frac{dx}{dt}\right|_{S_w} \tag{5.27}$$

Then we can obtain the Buckley–Leverett equation (also called the frontal-advance equation) as follows:

$$\left.\frac{dx}{dt}\right|_{S_w} = \frac{q_t}{A\phi} \cdot \left.\frac{\partial f_w}{\partial S_w}\right|_t \tag{5.28}$$

This equation states that in a linear displacement process, a particular water saturation moves in the porous rock at a velocity that can be evaluated from the derivative of the fractional flow with respect to the water saturation. If the capillary-pressure gradient in Eqn (5.20) or (5.21) can be neglected, then the fractional flow is strictly a function of the water saturation, irrespective of whether the gravity term is included or not and $\partial f_w/\partial S_w = df_w/dS_w$. Hence, we can use the differential of f_w in the Buckley–Leverett equation with respect to water saturation instead. Integrating for the total time since the start of injection yields

$$\int_0^{x_{S_w}} dx_{S_w} = \frac{1}{A\phi} \cdot \left.\frac{df_w}{dS_w}\right|_{S_w} \int_0^t q_t dt \tag{5.29}$$

or

$$x_{S_w} = \frac{W_i}{A\phi} \cdot \left.\frac{df_w}{dS_w}\right|_{S_w} \tag{5.30}$$

in which $W_i = \int_0^t q_{inj}(\tau)d\tau$ is the cumulative water injected; and $q_{inj} = q_t(x = 0,t)$ with q_{inj} being the injection rate at $x = 0$ as a function of time in general. Note that $W_i = 0$, when $t = 0$. Therefore, at a given

time after the start of injection (W_i = constant), the positions of different water-saturation planes can be plotted, using Eqn (5.30), merely by determining the slope of the fractional-flow curve for the particular value of saturation.

However, there is a mathematical difficulty encountered in applying this solution, which can be appreciated by considering the typical fractional-flow curve shown in Figure 5.3 in conjunction with Eqn (5.30). Because there is frequently a point of inflexion in the fractional-flow curve, the plot of df_w/dS_w versus S_w will have a maximum value, as shown in Figure 5.4(a). Using Eqn (5.30) to plot the saturation profile at a particular time will therefore result in multiple values of saturation (see the solid line shown in Figure 5.4(b)). This is physically impossible because it indicates that multiple water saturations can coexist at a given point along the linear reservoir. Buckley and Leverett suggested drawing a saturation shock or sharp front, as indicated by the vertical line in Figure 5.4(b). The position of

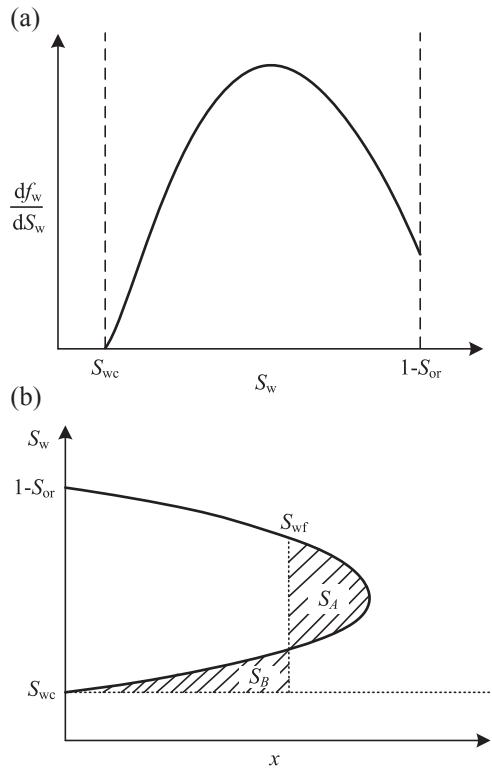

Figure 5.4 (a) Saturation derivative of a typical fractional-flow curve and (b) resulting water-saturation distribution in the displacement path.

the shock is chosen so that the two areas enclosed by the shock and the dashed lines are equal. The dashed line then represents the saturation discontinuity at the shock front.

5.4.2 Welge's Approach

Estimating the position of the shock saturation front in Figure 5.4(b) by balancing the area is satisfactory but cumbersome in application. A more elegant approach that achieves the same result was presented by Welge (1952). The principle of Welge's suggestion is as follows: (1) At any time, traveling velocities of a saturation leaving the injection point must increase with increase in saturation initially from its residual value until the plot of df_w/dS_w versus S_w reaches its maximum value (Figure 5.4(a)); (2) At points at which the fractional-flow curve suggests a decreasing velocity with increasing saturation values, a saturation "shock" or step change is needed or developed.

The velocity of the saturation shock can be obtained from a material balance. Consider a volume element of length Δx as shown in Figure 5.5. At time t, the saturation shock is at position x; at time $t + \Delta t$, the saturation shock advances to $x + \Delta x$. Then the change in water content of the differential volume element from time t to time $t + \Delta t$ can be expressed in terms of the flow in and out of the element.

$$A\phi\Delta x(S_{w-} - S_{w+}) = q_t(f_{w-} - f_{w+})\Delta t \tag{5.31}$$

Here, the subscripts '−' and '+' refer to values behind and ahead the saturation shock, respectively. Then, the velocity of the saturation shock can be quickly obtained as

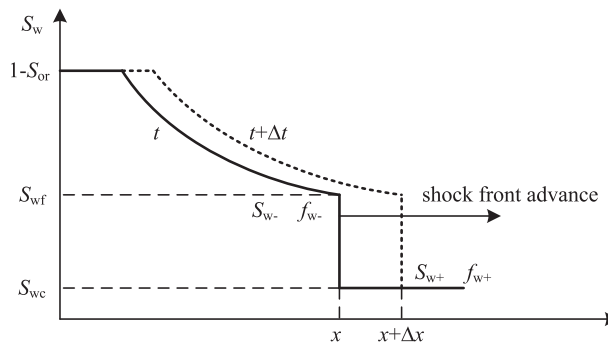

Figure 5.5 Water-saturation profiles for a saturation shock at time t advancing to the right.

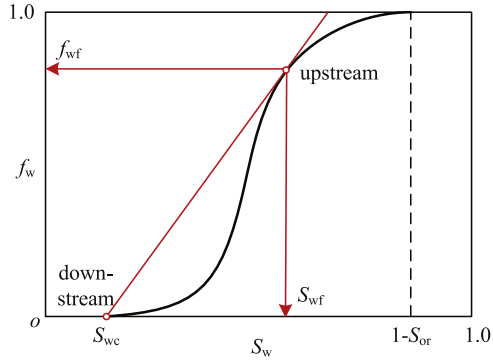

Figure 5.6 Determination of flood shock-front saturation by Welge's approach.

$$v_{shock} = \lim_{\Delta x \to 0} \frac{\Delta x}{\Delta t} = \frac{q_t}{A\phi} \cdot \frac{f_{w-} - f_{w+}}{S_{w-} - S_{w+}} \tag{5.32}$$

Equation (5.32) gives the velocity of the saturation shock whereas Eqn (5.28) describes the velocity of the saturations upstream of the shock. Obviously, the velocity of the shock front and the saturation immediately upstream from the shock must be equal, thus

$$\frac{f_{w-} - f_{w+}}{S_{w-} - S_{w+}} = \left.\frac{df_w}{dS_w}\right|_{S_{wf}} \tag{5.33}$$

Usually, the downstream saturation ahead of the saturation shock is initial water saturation S_{wc}, so f_{w+} equals zero. Equation (5.33) suggests a graphical method for locating the saturation shock. Draw a line that starts at the point defined by the beginning of water injection of $S_w = S_{wc}$. The other end of the line must be tangent to the fractional-flow curve, as depicted in Figure 5.6.

5.4.3 Examples: One-Dimensional Linear Waterflood at Constant Injection Rate

Analytical example 1: A linear waterflood is under consideration for a narrow box reservoir, which is 60 m long with a unit area of cross-section. The reservoir is horizontal, has a porosity of 0.25, and is saturated with oil and water with an initial water saturation of 0.1 at its residual value. It is approximated as a one-dimensional flow system with injection at one end, the inlet of the reservoir, injected by water at a constant rate of 8.64 m^3/day. Viscosities of the oil and water are 5.0 cP and 1.0 cP (1 cP = 10^{-3} Pa·s), respectively. Relative permeability data corresponding to the displacement of oil by water are given by the Eqns (5.34) and (5.35), which are generated

using the exponential expressions (Christiansen, 2008), similar to those suggested by Brooks and Corey (1964):

$$k_{rw} = k_{rw,max}\left(\frac{S_w - S_{wc}}{1 - S_{wc} - S_{or}}\right)^{n_w} \tag{5.34}$$

$$k_{ro} = k_{ro,max}\left(\frac{1 - S_w - S_{or}}{1 - S_{wc} - S_{or}}\right)^{n_o} \tag{5.35}$$

In this example, all the fluid and formation parameters are summarized in Table 5.1 and the corresponding curves of relative permeability are shown in Figure 5.7(a). Neglecting the capillary pressure and gravity terms, the corresponding fractional flow Eqn (5.22) and its derivative are:

$$f_w = \frac{1}{1 + \frac{k_{ro}}{k_{rw}} \cdot \frac{\mu_w}{\mu_o}}$$

$$\frac{df_w}{dS_w} = -\frac{\left(\frac{k_{ro}}{k_{rw}} \cdot \frac{\mu_w}{\mu_o}\right) \cdot \left(\frac{n_w}{S_w - S_{wc}} + \frac{n_o}{1 - S_w - S_{wc}}\right)}{\left(1 + \frac{k_{ro}}{k_{rw}} \cdot \frac{\mu_w}{\mu_o}\right)^2} \tag{5.36}$$

Table 5.1 Fluid and Formation Parameters

Parameters	Value	Unit
Porosity, ϕ	0.25	[-]
Absolute permeability, k	9.869×10^{-12}	[m^2]
Cross-section area, A	1.0	[m^2]
Length of formation, L	100.0	[m]
Injection rate, q_t	1.0×10^{-4}	[m^3/s]
Injection time, t	0.1, 0.4, 0.7, 1.0	[days]
Viscosity of water, μ_w	1.0×10^{-3}	[Pa·s]
Viscosity of oil, μ_o	5.0×10^{-3}	[Pa·s]
Residual water saturation, S_{wc}	0.1	[-]
Residual oil saturation, S_{or}	0.1	[-]
Maximum relative permeability of water, $k_{rw,max}$	0.80	[-]
Maximum relative permeability of oil, $k_{ro,max}$	0.80	[-]
Power index of water relative permeability, n_w	2.0	[-]
Power index of oil relative permeability, n_o	2.0	[-]
Density of water, ρ_w	800	[Kg/m^3]
Density of oil, ρ_o	1000	[Kg/m^3]
Directional angle, θ	0	[rad]

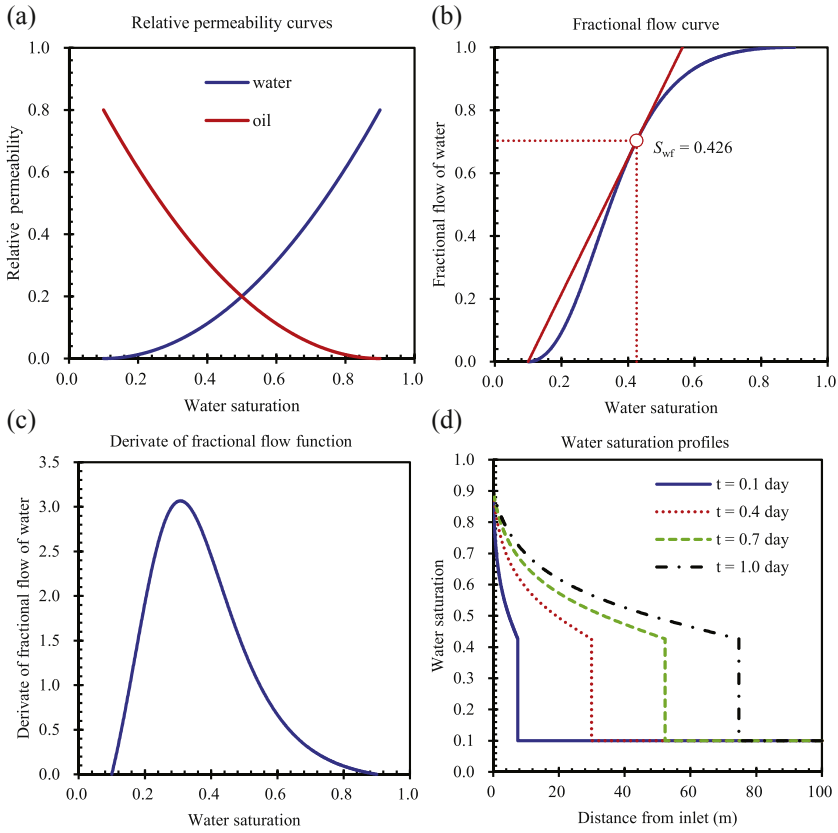

Figure 5.7 One-Dimensional linear waterflood profiles and corresponding curves of relative permeability, fractional flow, its derivatives, and saturation profiles.

The graph of f_w versus water saturation is presented in Figure 5.7(b), and the derivative versus water saturation is plotted in Figure 5.7(c), based on Eqn (5.36). Using Welge's approach, we can obtain the waterflood frontal saturation, S_{wf}, by drawing a tangent in Figure 5.7(b) from $S_{wc} = 0.1$ to the fractional-flow curve. The point of tangency is at $S_w = 0.426$, which is the waterflood frontal saturation, S_{wf}. Sometimes, it is difficult to determine the exact point in which the tangent to the fractional-flow curve intersects the curve, when the fractional-flow curve does not change rapidly with water saturation. Figure 5.7(d) is a plot of water-saturation profiles at different times. Note that the saturation front advances beyond the outlet end ($x = 60$ m) of the one-dimensional flow system at $t = 1.0$ d, as shown

in Figure 5.7(d). This treatment is necessary to calculate the increase in saturation within the physical domain at later times after breakthrough of injected water at the outlet. Mathematically, the saturation profile is assumed to travel continuously even after breakthrough of the saturation shock front at the production end of the finite reservoir, whereas the physical range of saturations is from 0 to 60 m along the x-direction after breakthrough.

Analytical example 2: To study the effect of parameters of relative permeability, we only change the power-law coefficients in Eqns (5.34) and (5.35) which are given by $n_w = 2.50$, $n_o = 2.00$. The corresponding curves are shown in Figure 5.8. The water-saturation profiles (see Figure 5.8(d))

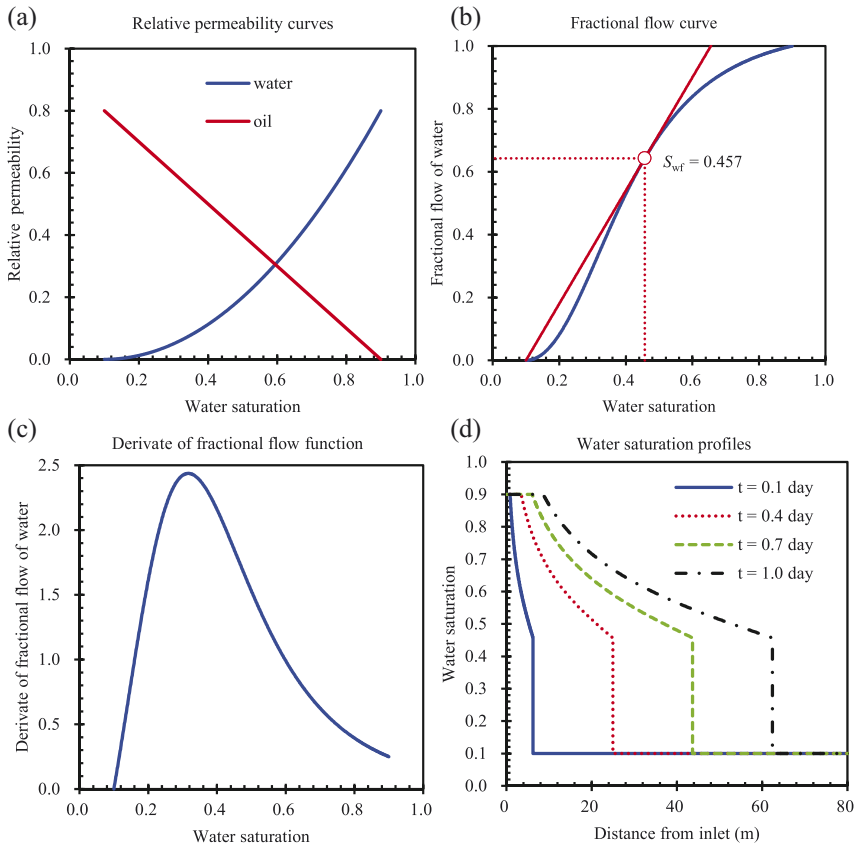

Figure 5.8 One-Dimensional linear waterflood profiles and corresponding curves of relative permeability, fractional flow, and its derivatives.

are a little different from the Figure 5.7(d). The corresponding MATrix LABoratory (MATLAB) program used for this example to calculate the Buckley–Leverett solution with the Welge approach is provided in the Appendix A.1.

5.4.4 Integral Method Based on Mass Balance Principle

Welge's method consists in drawing a tangent to the f_w curve originating at the irreducible water saturation; the point of tangency defines the water saturation at the flood or sharp saturation front. However, it is sometimes difficult to determine the exact point of tangency. This will occur when the fractional-flow curve does not change rapidly with water saturation. To overcome this drawback with the Welge's method, the integral method based on the mass balance principle is suggested as follows.

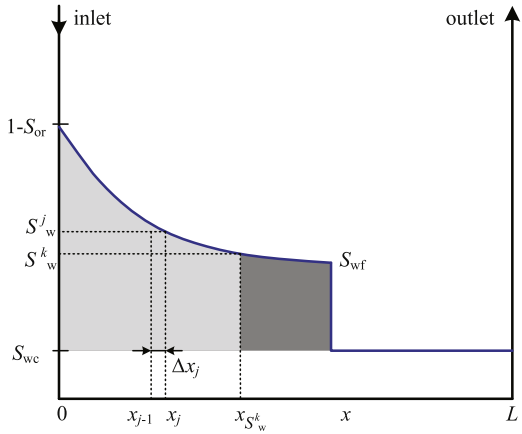

Figure 5.9 Schematic of integral method.

As illustrated in Figure 5.9, the front shock saturation, S_{wf}, should be at a position in which the entire shaded area must equal the total injection volume, $W_i(t) = \int_0^t q_{inj}(\tau)d\tau$. Therefore, there are simply four steps in the integral method to calculate the saturation profile in the domain as follows:

Step 1: first, choose a water saturation S_w^k ($k = 0, 1, 2, \ldots, N$) from its highest value down, in which $1 - S_{or} = S_w^0 > S_w^1 > S_w^2 > S_w^3, \ldots$;

Step 2: calculate the traveling distance $x_{S_w^k}$ of saturation S_w^k from $x = 0$ using Eqn (5.30);

Step 3: calculate the injected fluid volume V (the area with black slant lines) contained from $x = 0$ to $x = x_{S_w^k}$ in the portion of domain with $S_w > S_w^k$ by

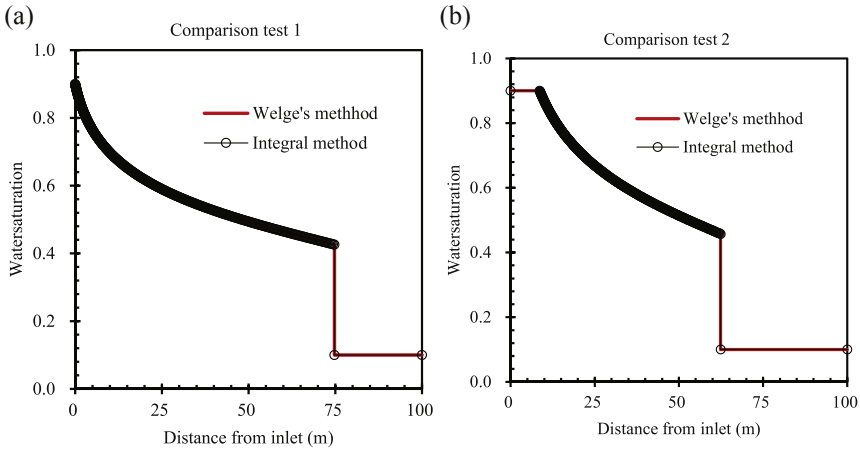

Figure 5.10 Comparison of analytical results between Welge and integral methods.

$$V = A\phi \int_0^{x_{S_w^k}} (S_w - S_{wc})\mathrm{d}x \approx A\phi \sum_{j=1}^{k} \left(S_w^j - S_{wc}\right)\Delta x_j \tag{5.37}$$

in which $\Delta x_j = x_j - x_{j-1}$, and $x_0 = 0$.

Step 4: compare V with $W_i(t)$. If $V < W_i(t)$, the saturation shock front has not yet been reached, and the process is continued with the next saturation value S_w^{k+1} until the integrated volume, V, is equal to or larger the total injected volume. If $V \geq W_i(t)$, stop the calculation, and set $S_{wf} = S_w^k$ and $x_{wf} = x_{S_w^k}$. If $S_w^k - S_w^{k+1}$ is taken to be sufficiently small (e.g., 0.001), the calculation of the sharp front will be accurate.

The above procedure is easy to implement and overcomes the drawback of the Welge's method with the need of plotting or graphic determination. The corresponding MATLAB program of the integral mass-balance method is provided in Appendix A.2. Comparisons between the integral method with Welge's method are given in Figure 5.10 using the two examples as shown, In this comparison, we have used the integral method with $\Delta S_w^k = 0.001$. Figure 5.10 shows that the results of the integral method are almost identical to that of the Welge's method.

5.5 APPLICATION OF BUCKLEY–LEVERETT SOLUTION

5.5.1 Average Water Saturation

In the method of Welge, if we integrate the saturation over the distance from the injection point to the shock saturation or displacement front, we

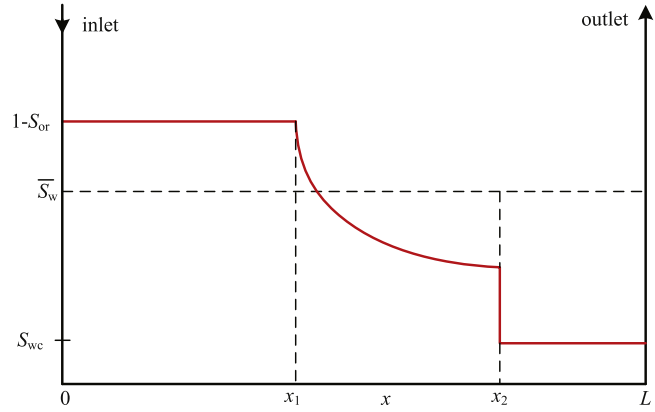

Figure 5.11 Water-saturation profile, prior to breakthrough in the producing well.

can obtain the average water saturation, $\overline{S}_w$, behind the front S_{wf}, as shown in Figure 5.11.

The situation depicted is at a fixed time, before water breakthrough in the producing well or outlet end of a finite reservoir, corresponding to the amount of water injection W_i. At this time, the maximum water saturation, $S_w = 1 - S_{or}$, has moved a distance x_1, its velocity being proportional to the slope of the fractional-flow curve evaluated for the maximum saturation which, as shown in Figure 5.11, is small but finite. The flood-front saturation S_{wf} is located at position x_2 measured from the injection point. Applying the simple material balance principle,

$$W_i = x_2 A\phi\left(\overline{S}_w - S_{wc}\right) \tag{5.38}$$

and using Eqn (5.30), which is applicable up to the flood front at x_2, then

$$\overline{S}_w - S_{wc} = \frac{W_i}{x_2 A\phi} = \frac{1}{\left.\frac{df_w}{dS_w}\right|_{S_{wf}}} \tag{5.39}$$

An expression for the average water saturation behind the saturation sharp front can also be obtained by direct integration of the saturation profile as

$$\overline{S}_w = \frac{1}{x_2}\int_0^{x_2} S_w dx \tag{5.40}$$

Then, integrating by parts,

$$\overline{S}_{\mathrm{w}} = \frac{1}{x_2}\left[(S_{\mathrm{w}}x)\big|_0^{x_2} - \int_{1-S_{\mathrm{or}}}^{S_{\mathrm{wf}}} x\mathrm{d}S_{\mathrm{w}}\right] = S_{\mathrm{wf}} + \frac{1}{x_2}\int_{S_{\mathrm{wf}}}^{1-S_{\mathrm{or}}} x\mathrm{d}S_{\mathrm{w}} \tag{5.41}$$

Next, incorporating Eqn (5.30),

$$\overline{S}_{\mathrm{w}} = S_{\mathrm{wf}} + \frac{1}{x_2}\int_{S_{\mathrm{wf}}}^{1-S_{\mathrm{or}}} \frac{W_i}{A\phi}\cdot\frac{\mathrm{d}f_{\mathrm{w}}}{\mathrm{d}S_{\mathrm{w}}}\Big|_{S_{\mathrm{w}}}\mathrm{d}S_{\mathrm{w}} = S_{\mathrm{wf}} + \frac{W_{\mathrm{i}}}{x_2 A\phi}\int_{S_{\mathrm{wf}}}^{1-S_{\mathrm{or}}} \frac{\mathrm{d}f_{\mathrm{w}}}{\mathrm{d}S_{\mathrm{w}}}\Big|_{S_{\mathrm{w}}}\mathrm{d}S_{\mathrm{w}} \tag{5.42}$$

This leads to

$$\overline{S}_{\mathrm{w}} = S_{\mathrm{wf}} + \frac{W_{\mathrm{i}}}{x_2 A\phi}\left(1 - f_{\mathrm{w}}(S_{\mathrm{wf}})\right) \tag{5.43}$$

And finally, the desired expression is obtained

$$\overline{S}_{\mathrm{w}} = S_{\mathrm{wf}} + \frac{1 - f_{\mathrm{w}}(S_{\mathrm{wf}})}{\left.\frac{\mathrm{d}f_{\mathrm{w}}}{\mathrm{d}S_{\mathrm{w}}}\right|_{S_{\mathrm{wf}}}} \tag{5.44}$$

This equation indicates that the average saturation behind the shock saturation front can be obtained in the following manner graphically:

1. Construct a tangent to the fractional-flow curve at S_{wf};
2. Extrapolate that tangent to intersect $f_{\mathrm{w}} = 1$;
3. The saturation at the intersection of the tangent and the horizontal line: $f_{\mathrm{w}} = 1$ is the average saturation.

This determination of average water saturation from $x = 0$ to the displacement front is illustrated in Figure 5.12.

As noted previously, application of the Buckley–Leverett solution with the Welge's approach depends on the assumption that the effect of the capillary-pressure gradient, $\partial P_{\mathrm{c}}/\partial x$, is small and can be ignored. This assumption is only applicable for a saturation range of $S_{\mathrm{wf}} < S_{\mathrm{w}} < 1 - S_{\mathrm{or}}$ behind the shock displacement saturation. The portion of the fractional-flow curve for saturations smaller than S_{wf} is, therefore, outside physical ranges, and the first real point on the fractional-flow curve to be used has the coordinates $(S_{\mathrm{wf}}, f_{\mathrm{w}}(S_{\mathrm{wf}}))$, corresponding to the shock-front saturation. The simple graphical technique of Welge, discussed here for determination of average water saturation, has much wider application in calculation of oil recovery rate and one example is described in the following section.

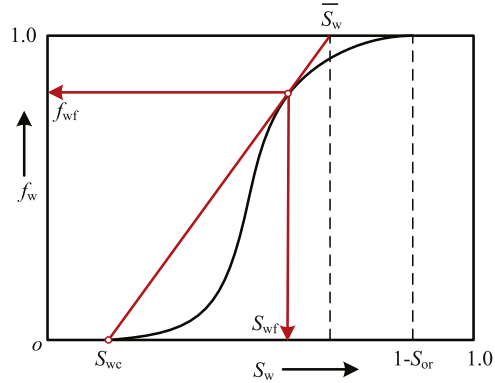

Figure 5.12 Tangent to the fractional-flow curve.

5.5.2 Oil Recovery Calculation

Before water breakthrough (bt) in the producing well or the outlet end, Eqn (5.30) can be applied to determine the positions of traveling planes of constant water saturation, for $S_{wf} < S_w < 1 - S_{or}$, as both the displacement saturation front and the water-saturation profile move through the reservoir. At the time of breakthrough and subsequently, the following equation is used to estimate the increase in the water cut at the producing well. In this case of $x = L$ at the producing end or the length of the one-dimensional, linear reservoir, Eqn (5.30) can be expressed as

$$W_{id} = \frac{W_i}{LA\phi} = \frac{1}{\left.\frac{df_w}{dS_w}\right|_{S_{wp}}} \tag{5.45}$$

in which S_{wp} is the current value of the water saturation in the producing well, $x = L$, as shown in Figure 5.13, and W_{id} the dimensionless number of pore volumes (PV) of water injected (1 PV $= LA\phi$).

Before water breakthrough at the producing well occurs, the oil recovery calculations are trivial. For incompressible displacement the oil volume recovered is simply equal to the volume of water injected, because no water is produced during this production phase. At the time of water breakthrough when the flood-front saturation, $S_{wf} = S_{w,bt}$, reaches the producing well, the water cut in the production well increases suddenly from zero to $f_{w,bt} = f_w(S_{wf})$. This sudden increase in water cut is a phenomenon frequently observed in the waterflooding reservoirs, indicating the existence of a shock displacement front. At this time, Eqn (5.39) can be interpreted in terms of Eqn (5.45) to give

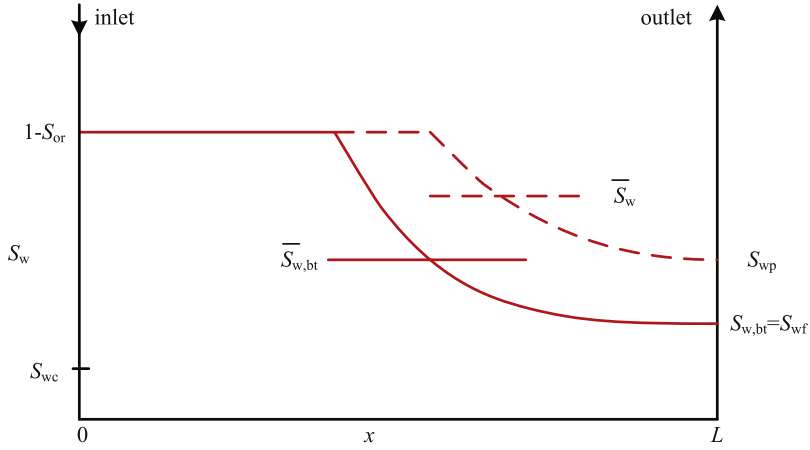

Figure 5.13 Water-saturation distributions at breakthrough and subsequently in a linear waterflood reservoir.

$$W_{id} = q_{id}t_{bt} = \overline{S}_{w,bt} - S_{wc} = \frac{1}{\left.\frac{df_w}{dS_w}\right|_{S_{wf}}} \tag{5.46}$$

in which all volumes are expressed, for convenience, as dimensionless pore volumes (PV). In particular, the dimensionless injection rate (PV/time) is $q_{id} = q_t/(LA\phi)$, which facilitates the calculation of the time when breakthrough occurs as $t_{bt} = W_{id}/q_{id}$.

After water breakthrough, L remains constant in Eqn (5.45), however, S_{wp} and f_{wp}, the water saturation and fractional flow at the producing well, respectively, continuously increase as if the flood front were to move through the semi-infinite, linear one-dimensional reservoir. During this phase, the calculation of the oil recovery is more complex and requires application of the Welge Eqn (5.44), as

$$\overline{S}_w = S_{wp} + (1 - f_w(S_{wp})) \Big/ \left.\frac{df_w}{dS_w}\right|_{S_{wp}} \tag{5.47}$$

which, using Eqn (5.45), can also be expressed as

$$\overline{S}_w = S_{wp} + (1 - f_w(S_{wp}))W_{id} \tag{5.48}$$

Finally, subtracting S_{wc} from both sides of Eqn (5.48) gives the oil recovery equation

$$N_{pd} = \overline{S}_w - S_{wc} = (S_{wp} - S_{wc}) + (1 - f_w(S_{wp}))W_{id}(\text{PV}) \tag{5.49}$$

The application of Eqns (5.46) and (5.49) is described as follows:

1. Calculate and plot the fractional-flow curve using Eqn (5.20) or (5.22), allowing for gravity effects if necessary, but neglecting the capillary-pressure gradient $\partial P_c/\partial x$.
2. Draw the tangent to this curve from the point $S_w = S_{wc}$, $f_w = 0$. As described in the previous section, the point of tangency has the coordinates $S_w = S_{wf} = S_{w,bt}, f_{w,bt} = f_w(S_{wf})$ and the extrapolation of this line to $f_w = 1$ gives the value of the averaged saturation behind the displacement front at breakthrough $\overline{S}_w = \overline{S}_{w,bt}$. Equation (5.46) is then applied to calculate the oil recovery and time when the water breakthrough occurs.
3. Choose S_{wp} as the independent variable, allow its value to increase in increments of, say, 5% above the saturation at breakthrough. Each point on the fractional-flow curve, for $S_{wp} > S_{w,bt}$, has coordinates $S_w = S_{wp}$, $f_{wp} = f_w(S_{wp})$ and, applying Eqn (5.48).

Figure 5.14 demonstrates that the tangent to the fractional-flow curve intersects the line $f_w = 1$ to give the current value of the average water saturation in the reservoir block, $\overline{S}_w$.

For each new value of $S_w = S_{wp}$ the corresponding value of $\overline{S}_w$ is determined graphically and the oil recovery calculated as

$$N_{pd} = \overline{S}_w - S_{wc} \quad \text{(PV)} \tag{5.50}$$

The reciprocal of the slope of the fractional-flow curve, for each value of $S_w = S_{wp}$, gives W_{id}, the number of pore volumes of water injected, Eqn (5.45). This allows a time scale to be attached to the recovery because $W_{id} = q_{id}t$.

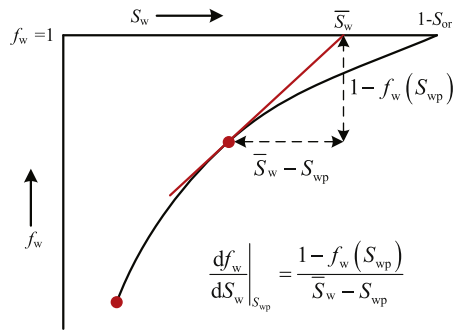

Figure 5.14 Application of the Welge method to determine the oil recovery after water breakthrough.

Alternatively, Eqn (5.49) can be used directly to calculate the oil recovery by determining f_{wp} and W_{id} from the fractional-flow curve for each chosen value of S_{wp}. In addition, for a fixed distance, $x = L$, and time, t, the Buckley–Leverett solution can be used to solve the derivative of fractional flow, leading to the determination of the saturation value, S_{wp}, at the producer. Then repeating the procedure above, we are able to determine the relation of time versus oil recovery as well as time versus water cut at the well. In summary, the Welge technique for calculating displacement performance and oil recovery, as a function of water injected and time, is a very useful method in practice.

5.5.3 Pressure Profile Calculation

The Buckley–Leverett theory can also be used to calculate pressure profiles along the one-dimensional flow system. For a given time, t, we need first to determine a saturation profile $S_w(x)$ using the Buckley–Leverett solution. The pressure profile or distribution along the x-direction is then calculated relative to a pressure at a fixed point. For example, if a pressure at $x = L$ is fixed as P_L at the time, $P(x \leq L)$ is calculated point by point from $x = L - \Delta x$, $x = L - 2\Delta x$, …, to $x = 0$, with or without gravity effect:

At any x,

$$q_o = q_t(1 - f_w(S_w)) = \frac{Akk_{ro}(S_w)}{\mu_o}\left(\frac{\partial P}{\partial x} + \rho_o g \sin\theta\right) \tag{5.51}$$

and at $x = L - \Delta x$,

$$q_t(1 - f_w(S_w(L - \Delta x))) = \frac{Akk_{ro}(S_w(L - \Delta x))}{\mu_o} \times \left(\frac{P(L - \Delta x) - P_L}{\Delta x} + \rho_o g \sin\theta\right) \tag{5.52}$$

At the fixed time, t, $S_w(L - \Delta x)$ is first determined using the Buckley–Leverett solution from its derivative. Here, for each value of df_w/dS_w, there are two corresponding values of S_w. Choose the value with $S_w > S_{wf}$. Once $S_w(L - \Delta x)$ is known, k_{rw} and f_w are known, then we calculate $P(L - \Delta x)$:

$$P(L - \Delta x) = \Delta x\left(\frac{q_t(1 - f_w(S_w(L - \Delta x)))}{\frac{Akk_{ro}(S_w(L - \Delta x))}{\mu_o}} - \rho_o g \sin\theta\right) + P_L \tag{5.53}$$

Next let $P_1 = P(L - \Delta x)$ and find S_w at $L - 2\Delta x$, to calculate one more point of pressure as:

$$P_2 = P(L - 2\Delta x) = \Delta x \left(\frac{q_t(1 - f_w(S_w(L - 2\Delta x)))}{\frac{Akk_{ro}(S_w(L-2\Delta x))}{\mu_o}} - \rho_o g \sin\theta \right) + P_1 \tag{5.54}$$

Repeat this calculation until $x = 0$.

Note that ahead of the sharp saturation front S_{wf}, $f_w = 0$ and k_{ro} is constant, when S_w is at its residual value, and P is a linear function of x. So the pressure distribution from $x = x_{S_{wf}}$ to $x = L$, is a straight line. However, for $x < x_{S_{wf}}$, $P(x)$ is not a linear function of x in the two-phase flow zone, and must be calculated by the scheme above.

The pressure profiles of the two analytical examples (see Section 5.4.3) are shown in Figure 5.15. Here, the pressure at outlet equals atmospheric pressure. Figure 5.15 indicates that the points of pressure profiles are corresponding to the saturation profiles (Figures 5.7(d) and 5.8(d)). Welge (1952) did not discuss the calculation of pressure profile during one-dimensional displacement. The pressure profile is obviously important for any injection operation. For example, the pressure needed in an injection well to accomplish a desired displacement rate should not exceed the fracturing pressure of the formation. In addition, pressure drop measurements are necessary for obtaining relative permeabilities from unsteady-state laboratory displacements. Furthermore, we can use the measured pressure profiles to locate the saturation shock front for unsteady-state laboratory displacement.

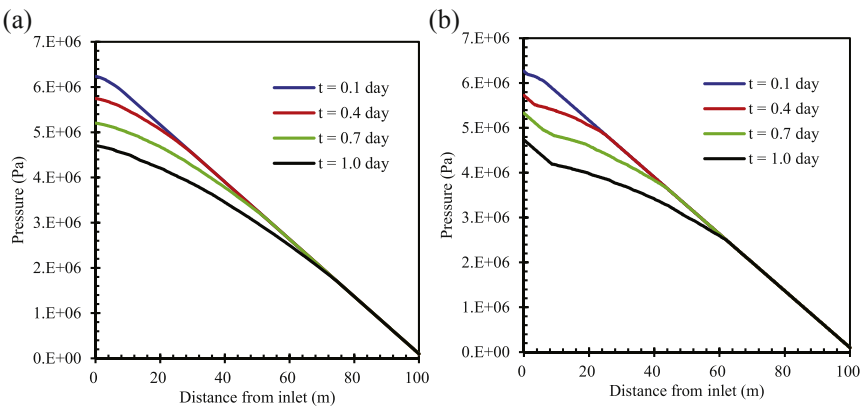

Figure 5.15 Pressure profiles of the two analytical examples in Section 5.4.3 (a) analytical example 1 and (b) analytical example 2.

5.5.4 Verification of Numerical Simulations

In this section, the analytical solutions are used to examine the results of the numerical method implemented in a general purpose, three-phase flow reservoir simulator, the MSFLOW code (Wu, 1998), for modeling multiphase Newtonian flow. To reduce the effects of discretization on numerical simulation results, very fine, uniform mesh spacing ($\Delta x = 0.01$ m) is chosen. A one-dimensional 5-m linear domain is discretized into 500 one-dimensional uniform gridblocks.

The flow description and the parameters for this problem are illustrated in Table 5.2. The comparison between the numerical and analytical solutions is shown in Figure 5.16. Figure 5.16 indicates that the numerical results are in excellent agreement with the analytical solutions of the displacement for the entire sweeping zone. Except at the shock front, the numerical solutions deviate only slightly from the analytical solutions, resulting from a typical "smearing front" phenomenon of numerical

Table 5.2 Fluid and Formation Parameters for Verification

Parameters	Numerical test 1	Numerical test 2	Unit
Porosity, ϕ	0.2	0.15	[-]
Absolute permeability, k	9.869×10^{-14}	9.869×10^{-14}	[m^2]
Cross-section area, A	1.0	1.0	[m^2]
Length of formation, L	5.0	5.0	[m]
Injection rate, q_t	5.0×10^{-6}	5.0×10^{-6}	[m^3/s]
Injection time, t	36,000	36,000	[s]
Viscosity of water, μ_w	1.0×10^{-3}	1.0×10^{-3}	[Pa·s]
Viscosity of oil, μ_o	5.0×10^{-3}	6.0×10^{-3}	[Pa·s]
Residual water saturation, S_{wc}	0.2	0.2	[-]
Residual oil saturation, S_{or}	0.2	0.2	[-]
Maximum relative permeability of water, $k_{rw,max}$	0.75	0.75	[-]
Maximum relative permeability of oil, $k_{ro,max}$	0.75	0.75	[-]
Power index of water relative permeability, n_w	2.0	2.0	[-]
Power index of oil relative permeability, n_o	2.0	1.0	[-]
Density of water, ρ_w	800	800	[Kg/m^3]
Density of oil, ρ_o	1000	1000	[Kg/m^3]
Directional angle, θ	0	0	[rad]

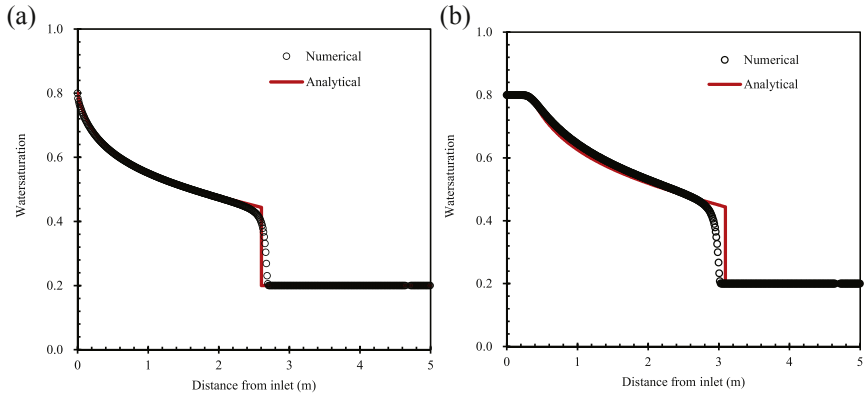

Figure 5.16 Comparison between analytical and numerical solutions after 10 h of injection (a) numerical text 1 and (b) numerical text 2.

dispersion effects when matching the Buckley–Leverett solution using numerical results (Aziz and Settari, 1979). The results from Figure 5.16 provide a very encouraging indication that our numerical model is correct in describing the multiphase immiscible fluid flow in porous media.

REFERENCES

Aziz, K., Settari, A., 1979. Petroleum Reservoir Simulation. Applied Science Publishers, London.

Brooks, R.H., Corey, A.T., March 1964. Hydraulic Properties of Porous Media. Hydrology Papers. Colorado State University.

Buckley, S.E., Leverett, M.C., 1942. Mechanism of fluid displacement in sands. Transactions of the AIME 146 (01), 107–116.

Chen, Z.-X., 1988. Some invariant solutions to two-phase fluid displacement problems including capillary effect (includes associated papers 18744 and 19037). SPE Reservoir Engineering 3 (02), 691–700.

Christiansen, R.L., 2008. Multiphase Flow through Porous Media. KNQ Engineering, Salt Lake City, Utah.

Codreanu, D., Hauer, R., Vernescu, A., 1966. Displacement of oil by water in heterogeneous rocks and evaluation of heterogeneity in reservoir engineering calculations. Revue de L'Institut Fran{ç}ais Du P{é}trole 21 (1), 57–80.

Fayers, F.J., Sheldon, J.W., 1959. The effect of capillary pressure and gravity on two-phase fluid flow in a porous medium. Petroleum Transactions, AIME 216, 147–155.

Hovanessian, S.A., Fayers, F.J., 1961. Linear water flood with gravity and capillary effects. Society of Petroleum Engineers Journal 1 (01), 32–36.

McWhorter, D.B., Sunada, D.K., 1990. Exact integral solutions for two-phase flow. Water Resources Research 26 (3), 399–413.

Sheldon, J.W., Cardwell Jr., W.T., 1959. One-dimensional incompressible noncapillary two-phase fluid flow in a porous medium. Petroleum Transactions, AIME 216, 290–296.

Welge, H.J., 1952. A simplified method for computing oil recovery by gas or water drive. Journal of Petroleum Technology 4 (04), 91–98.

Willhite, G.P., 1986. Waterflooding. Society of Petroleum Engineers, Richardson, TX.
Wu, Y.-S., 1998. MSFLOW: Multiphase Subsurface Flow Model of Oil, Gas and Water in Porous and Fractured Media with Water Shut-off Capability. DOCUMENTATION and User's Guide, Walnut Creek, Califonia.
Yortsos, Y.C., Fokas, A.S., 1983. An analytical solution for linear waterflood including the effects of capillary pressure. Society of Petroleum Engineers Journal 23 (01), 115–124.

CHAPTER 6

Extensions of Buckley–Leverett Theory

6.1 INTRODUCTION

This chapter discusses the extensions of the Buckley–Leverett theory and their applications. As discussed in Chapter 5, the classic Buckley–Leverett theory only considers a homogeneous one-dimensional linear reservoir system. However, many important applications of multiphase fluid flow in permeable media involve one-dimensional radial flow. Especially in petroleum engineering and groundwater hydrology, we are often interested in fluid flowing toward or away from a well, so it is more convenient to use radial (cylindrical) coordinates, rather than Cartesian coordinates for radial flow. Moreover, heterogeneities always exist in reservoir formations and must be taken into account in practical applications. Thus, immiscible multiphase flow processes in composite reservoirs with heterogeneity in rock properties have to be considered and solved.

The purpose of this chapter is to extend the classic Buckley–Leverett theory to radial and composite porous-medium systems. We first discuss immiscible two-phase flow in a one-dimensional radial system from governing and frontal-advance equations of two-phase immiscible displacement in a radial system. Then, a Buckley–Leverett type analytical solution for one-dimensional, two-phase immiscible displacement in a linear composite porous medium is presented. An extension of classical Buckley–Leverett theory to a radial composite system is also discussed. Our treatment considers a composite medium consisting of two domains with uniform initial conditions; extension to an arbitrary number of flow domains, to nonuniform initial saturation distribution, and to one-dimensional horizontal flow in a composite system with nonconstant cross-sectional areas would be straightforward. As applications, these analytical solutions have been used to verify the numerical simulation results.

Multiphase Fluid Flow in Porous and Fractured Reservoirs
ISBN 978-0-12-803848-2
http://dx.doi.org/10.1016/B978-0-12-803848-2.00006-4

6.2 BUCKLEY–LEVERETT FLOW IN A ONE-DIMENSIONAL RADIAL SYSTEM

To derive the proper form of the Buckley–Leverett equation in radial coordinates, consider fluid flowing radially toward (or away from) a vertical well in a radially symmetric manner, as illustrated in Figure 6.1(a).

6.2.1 Buckley–Leverett Equation and Solution

Considering a one-dimensional, horizontal radial flow system, as illustrated in Figure 6.1(b), the mass balance equation for a fluid phase is given by,

$$\rho q|_r - \rho q|_{r+\mathrm{d}r} = 2\pi r h \mathrm{d}r \frac{\partial}{\partial t}(\phi\rho) \tag{6.1}$$

The left-hand side can also be expanded as

$$\rho q|_r - \left(\rho q|_r + \frac{\partial(\rho q)}{\partial r}\mathrm{d}r\right) = 2\pi r h \mathrm{d}r \frac{\partial}{\partial t}(\phi\rho) \tag{6.2}$$

which can be reduced to

$$-\frac{1}{r}\frac{\partial}{\partial r}(\rho q) = 2\pi h \frac{\partial}{\partial t}(\phi\rho) \tag{6.3}$$

and for the consideration of immiscible incompressible two-phase flow (e.g., water and oil):

$$-\frac{1}{r}\frac{\partial q_{\mathrm{w}}}{\partial r} = 2\pi h \phi \frac{\partial S_{\mathrm{w}}}{\partial t} \tag{6.4}$$

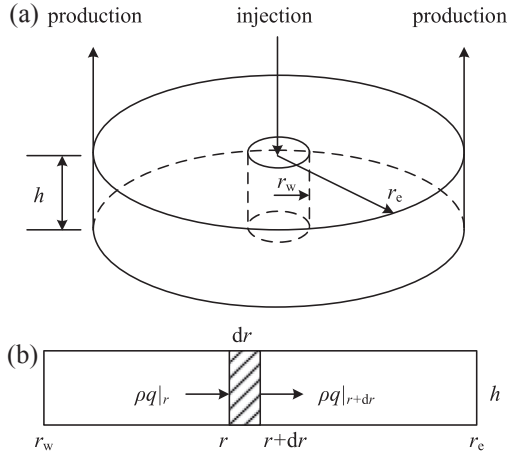

Figure 6.1 Schematic of a radial flow system. (a) Cylindrical flow system from a vertical well; (b) One-dimensional model along *r*-direction.

$$-\frac{1}{r}\frac{\partial q_o}{\partial r} = 2\pi h\phi\frac{\partial S_o}{\partial t} \tag{6.5}$$

If Darcy's law for multiphase flow is used for the radial flow, we have

$$q_o = -2\pi rh\frac{kk_{ro}}{\mu_o}\frac{\partial P_o}{\partial r} \tag{6.6}$$

$$q_w = -2\pi rh\frac{kk_{rw}}{\mu_w}\frac{\partial P_w}{\partial r} \tag{6.7}$$

The sum of the above two equations is

$$-\frac{1}{r}\frac{\partial}{\partial r}(q_o + q_w) = 2\pi h\phi\frac{\partial}{\partial t}(S_o + S_w) \tag{6.8}$$

Considering at the arbitrary radial distance, r, and the condition: $S_o + S_w = 1$,

$$\frac{\partial}{\partial r}(q_o + q_w) = 0 \tag{6.9}$$

This means that the total volumetric flow rate $q_t(r,t) = q_o + q_w =$ constant or independent of r. Similar to the analysis of Section 5.3, we can obtain the corresponding fractional flow equation to water in a radial flow system as

$$f_w = \frac{1 + \frac{2\pi rhkk_{ro}}{q_t\mu_o}\frac{\partial P_c}{\partial r}}{1 + \frac{k_{ro}}{k_{rw}}\cdot\frac{\mu_w}{\mu_o}} \tag{6.10}$$

in which

$$\frac{\partial P_c}{\partial r} = \frac{\partial}{\partial r}(P_o - P_w)$$

is the capillary-pressure gradient in the direction of flow. The Eqn (6.10) is the water fractional-flow equation for the displacement of oil by water in a one-dimension radial system. If we neglect the capillary-pressure gradient along the radii, the fractional-flow equation is reduced to

$$f_w = \frac{1}{1 + \frac{k_{ro}}{k_{rw}}\cdot\frac{\mu_w}{\mu_o}} \tag{6.11}$$

It is the same as Eqn (5.22). It means that the fractional flow in a one-dimensional radial flow system is also a function of only the water

saturation through the saturation dependence of relative permeabilities, when fluid viscosities are treated as constant.

Using the same analysis process as that in Section 5.3, the mass conservation of a one-dimensional flow and displacement in a radial system can be rewritten as follows:

$$-\frac{1}{r}\frac{\partial f_w}{\partial r}q_t = 2\pi h\phi\frac{\partial S_w}{\partial t} \tag{6.12}$$

To develop a solution for Eqn (6.12), it is necessary to obtain an equivalent form of Eqn (6.12) that involves only one dependent variable (i.e., either f_w or S_w). As in the Buckley–Leverett solution in one-dimensional linear flow, an expression for $\partial S_w/\partial t$ is obtained following the total differentiation. Because the water saturation is a function of two dependent variables, r and t, we can obtain

$$dS_w(r,t) = \left.\frac{\partial S_w}{\partial r}\right|_t dr + \left.\frac{\partial S_w}{\partial t}\right|_r dt \tag{6.13}$$

If we focus on the movement of a particular or constant saturation, S_w, then $dS_w = 0$ in Eqn (6.13). We then solve,

$$\left.\frac{\partial S_w}{\partial t}\right|_r = -\left.\frac{\partial S_w}{\partial r}\right|_t \cdot \left.\frac{dr}{dt}\right|_{S_w} \tag{6.14}$$

Furthermore,

$$\left.\frac{\partial f_w}{\partial r}\right|_t = \left(\frac{\partial f_w}{\partial S_w}\cdot\frac{\partial S_w}{\partial r}\right)_t \tag{6.15}$$

and substituting Eqns (6.14) and (6.15) into Eqn (6.12) yields

$$2r\left.\frac{dr}{dt}\right|_{S_w} = \frac{q_t}{\pi h\phi}\cdot\left.\frac{\partial f_w}{\partial S_w}\right|_t \tag{6.16}$$

Here, h is reservoir thickness. Equation (6.16) states that in a one-dimensional displacement process within a radial system, each water saturation moves in the porous rock at a velocity that is proportional to the derivative, $\partial f_w/\partial S_w (= df_w/dS_w)$, of the fractional flow, but inversely proposal to radial distance, r. Integrating Eqn (6.16) over the radial distance as well as the time since the start of injection yields

$$\int_{r_w}^{r_{S_w}} 2r dr = \frac{1}{\pi h\phi}\cdot\left.\frac{df_w}{dS_w}\right|_{S_w}\int_0^t q_t(\tau)d\tau \tag{6.17}$$

or

$$r_{S_w}^2 = r_w^2 + \frac{W_i}{\pi h \phi} \cdot \left.\frac{df_w}{dS_w}\right|_{S_w} \tag{6.18}$$

Here, $W_i = \int_0^t q_t(\tau)d\tau$ is the cumulative water injected, with q_t being the injection rate at $r = r_w$, a function of time in general. At the initial condition, $W_i = 0$ when $t = 0$. And r_{S_w} is the location of tracking the saturation away from the injecting point or wellbore. It should be noted that Eqn (6.18) is different from Eqn (5.30), because of the quadratic term of the radius (r_{S_w} and r_w) instead of a linear term. To complete the mathematical description of the physical problem, the initial and boundary conditions must be specified. A simple system is initially uniformly saturated with both wetting and nonwetting fluids, for which the Welge approach also applies as follows.

6.2.2 Welge's Approach

In this section, we will estimate the position and advance of the shock saturation front using Welge's method, as discussed in Section 5.4.2. The velocity of the saturation shock can be obtained from a material balance. Consider a volume element of length Δr as shown in Figure 6.2. At time t, the saturation shock is at position r; at time $t + \Delta t$, the saturation shock is moved to $r + \Delta r$. Then the change in water content of the differential volume element from time t to time $t + \Delta t$ can be expressed in terms of the flow in and out of the element:

$$2\pi r h \Delta r \phi (S_{w-} - S_{w+}) = q_t (f_{w-} - f_{w+}) \Delta t \tag{6.19}$$

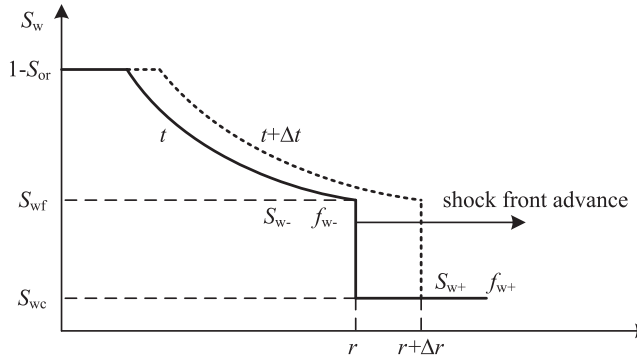

Figure 6.2 The movement for a saturation shock at time t advancing to the right.

Here, the subscripts '−' and '+' refer to values behind and ahead of the saturation shock, respectively. Then, the velocity of the saturation shock can be quickly obtained as:

$$v_{\text{shock}} = \lim_{\Delta r \to 0} \frac{\Delta r}{\Delta t} = \frac{q_t}{2\pi r h \phi} \cdot \frac{f_{w-} - f_{w+}}{S_{w-} - S_{w+}} \tag{6.20}$$

Equation (6.20) describes the velocity of the saturation shock and Eqn (6.16) is for the velocity of the saturations upstream of the shock. Obviously, the traveling velocity of the shock and the saturation immediately upstream from the shock must be the same, thus

$$\frac{f_{w-} - f_{w+}}{S_{w-} - S_{w+}} = \left.\frac{df_w}{dS_w}\right|_{S_{wf}} \tag{6.21}$$

When the downstream saturation ahead the shock is at initial water saturation, S_{wc}, f_{w+} equals zero. Equation (6.21) suggests a graphical method for locating the saturation shock. Draw a line that starts at the point of $S_w = S_{wc}$, defined by the beginning of water injection. The other end of the line must be tangent to the fractional-flow curve, as depicted in Figure 5.6. Note that Eqn (6.21), determining the shock front water saturation in a radial system, is identical to Eqn (5.33) for a linear one-dimensional system.

In the method of Welge, if we integrate the saturation profile over the distance from the injection point ($r = r_w$) to the shock front, we can obtain the average water saturation behind the front, S_{wf}, as shown in Figure 6.3.

The situation depicted is at a fixed time, before water breakthrough in the producing well or outlet end of a finite radial-symmetric reservoir, corresponding to the amount of water injection W_i. At this time, the maximum water saturation, $S_w = 1 - S_{or}$, has moved a distance to r_1 with its velocity being proportional to the slope of the fractional-flow curve, evaluated for the maximum saturation, as shown in Figure 6.3. The flood-front saturation S_{wf} is located at a position of r_2, measured from the injection point. Applying the simple material balance principle,

$$W_i = \pi h \phi \left(r_2^2 - r_w^2\right)\left(\overline{S}_w - S_{wc}\right) \tag{6.22}$$

and using Eqn (6.18), which is applicable up to the flood front at r_2, then

$$\overline{S}_w - S_{wc} = \frac{W_i}{\pi h \phi \left(r_2^2 - r_w^2\right)} = \frac{1}{\left.\frac{df_w}{dS_w}\right|_{S_{wf}}} \tag{6.23}$$

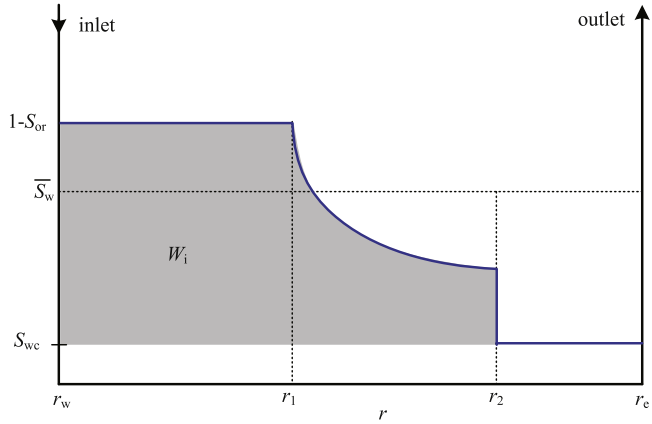

Figure 6.3 Water saturation profile, prior to breakthrough in the outside edge.

An expression for the average water saturation behind the saturation shock front can also be obtained by direct integration of the saturation profile as

$$\overline{S}_w = \frac{1}{\pi h\left(r_2^2 - r_w^2\right)} \int_{r_w}^{r_2} S_w 2\pi r h \mathrm{d}r \tag{6.24}$$

Then, integrating by parts,

$$\begin{aligned} \overline{S}_w &= \frac{1}{r_2^2 - r_w^2}\left[\left(S_w r^2\right)\Big|_{r_w}^{r_2} - \int_{1-S_{or}}^{S_{wf}} r^2 \mathrm{d}S_w\right] \\ &= S_{wf} - \left(1 - S_{or} - S_{wf}\right)\frac{r_w^2}{r_2^2 - r_w^2} + \frac{1}{r_2^2 - r_w^2}\int_{S_{wf}}^{1-S_{or}} r^2 \mathrm{d}S_w \end{aligned} \tag{6.25}$$

Next, incorporating Eqn (6.18) yields

$$\begin{aligned} \overline{S}_w &= S_{wf} + \frac{1}{r_2^2 - r_w^2}\int_{S_{wf}}^{1-S_{or}} \frac{W_i}{\pi h \phi} \cdot \left.\frac{\mathrm{d}f_w}{\mathrm{d}S_w}\right|_{S_w} \mathrm{d}S_w \\ &= S_{wf} + \frac{W_i}{\pi h \phi\left(r_2^2 - r_w^2\right)}\int_{S_{wf}}^{1-S_{or}} \left.\frac{\mathrm{d}f_w}{\mathrm{d}S_w}\right|_{S_w} \mathrm{d}S_w \end{aligned} \tag{6.26}$$

This leads to

$$\overline{S}_w = S_{wf} + \frac{W_i}{\pi h \phi \left(r_2^2 - r_w^2\right)} \left(1 - f_w(S_{wf})\right) \tag{6.27}$$

And finally, the desired expression for the average saturation is obtained as

$$\overline{S}_w = S_{wf} + \frac{1 - f_w(S_{wf})}{\left.\frac{df_w}{dS_w}\right|_{S_{wf}}} \tag{6.28}$$

This equation indicates that the average saturation behind the shock saturation front in a radial flow system can be obtained in the following manner graphically:

1. Construct a tangent to the fractional-flow curve at S_{wf};
2. Extrapolate that tangent to intersect $f_w = 1$; and
3. The saturation at the intersection of the tangent and the horizontal line: $f_w = 1$, is the average saturation behind the shock saturation front.

This determination of average water saturation from $r = r_w$ to the displacement front is illustrated in Figure 5.12. As noted in Section 5.4, the use of either the Buckley–Leverett solution or Welge's approach in a radial flow system depends also on the assumption that the effect of the capillary-pressure gradient, $\partial P_c/\partial r$, is small and can be ignored. This assumption is only used for saturation range of $S_{wf} < S_w < 1 - S_{or}$ behind the shock displacement saturation.

6.2.3 Examples: Linear Waterflood in a One-Dimensional Radial System

Analytical example 1: A one-dimensional waterflood is under consideration for a radial cylindrical reservoir of 100 m radius with unit thickness. The reservoir is horizontal, has a porosity of 0.25, and is at an initial water saturation of 0.1, which is considered immobile. Relative permeability data corresponding to the displacement of oil by water are given by the Eqns (5.34) and (5.35), which are the exponential functions and similar to those suggested by Brooks and Corey (1964). The input parameters used in the example are listed in Table 6.1.

The generated curves of relative permeability are shown in Figure 6.4(a). The fractional-flow function and its derivative are shown in Figure 6.4(b) and (c), respectively. Using the Welge's approach, we can obtain the waterflood frontal saturation, S_{wf}, from a tangent drawn to Figure 6.4(b) from $S_{wc} = 0.15$

Table 6.1 Parameters for immiscible displacement in a radial system

Parameter	Value	Units
Porosity of domains, ϕ	0.25	[-]
Radius of outer boundary, R	100.0	[m]
Radii of injection well, r_w	0.10	[m]
Height of domain, h	1.00	[m]
Injection rate, q_t	2.0×10^{-3}	[m^3/s]
Water-phase viscosity, μ_w	1.0	[mPa·s]
Oil-phase viscosity, μ_o	5.0	[mPa·s]
Permeability of domain, k	9.869×10^{-13}	[m^2]
Initial water-phase saturation, S_{wc}	0.15	[-]
Initial oil-phase saturation, S_{or}	0.15	[-]
Relative permeability parameters, $k_{rw,max}$	0.85	[-]
Relative permeability parameters, $k_{ro,max}$	0.85	[-]
Relative permeability parameters, n_w	2.00	[-]
Relative permeability parameters, n_o	2.00	[-]

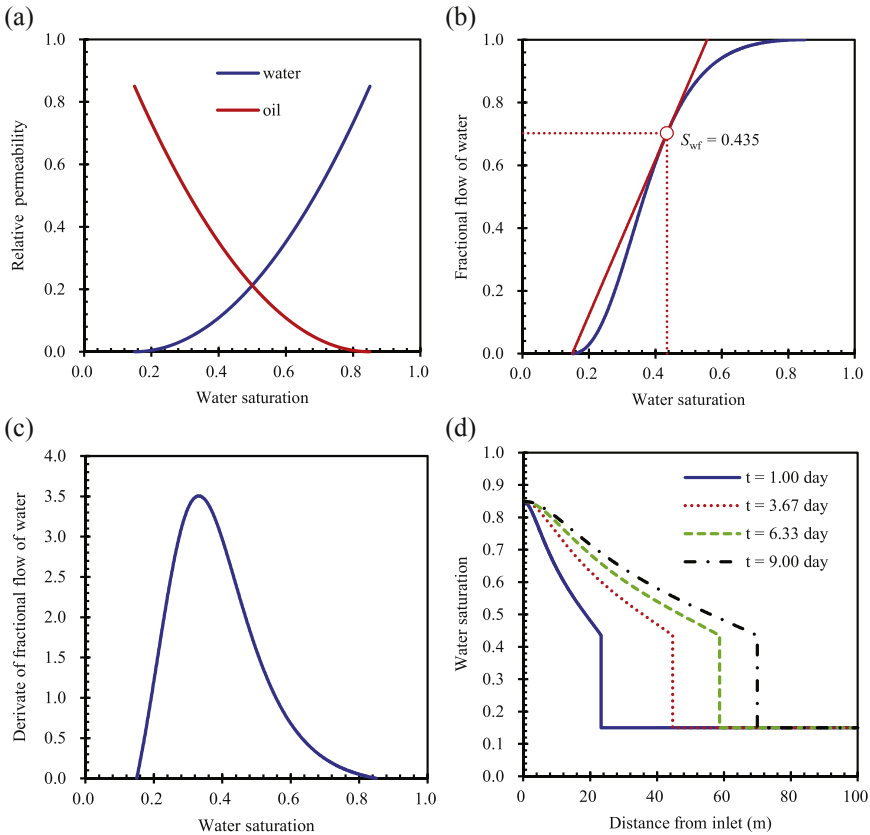

Figure 6.4 One-dimensional radial waterflood profiles and corresponding calculation curves. (a) Relative permeability curves; (b) Fractional flow curve; (c) Derivate of fractional flow function; (d) Water saturation profiles.

intersects the fractional flow curve at $S_w = 0.435$, which is the waterflood frontal saturation, S_{wf}. The water-saturation profiles (see Figure 6.4(d)) are a little different from Figure 5.7(d). As the increase in the displacing front radius, the displacing velocity of water shock-front saturation becomes slower because of the larger displaced fluid volume in a radial system than in a linear reservoir.

Analytical example 2: To study the effect of parameters of relative permeability, we change only the power exponents in Eqns (5.34) and (5.35), which are given by $n_w = 2.0$, $n_o = 1.0$. The corresponding curves are shown in Figure 6.5. The water-saturation profiles (see Figure 6.5(d)) are similar to, but a little different from, Figure 6.4(d). The corresponding MATLAB

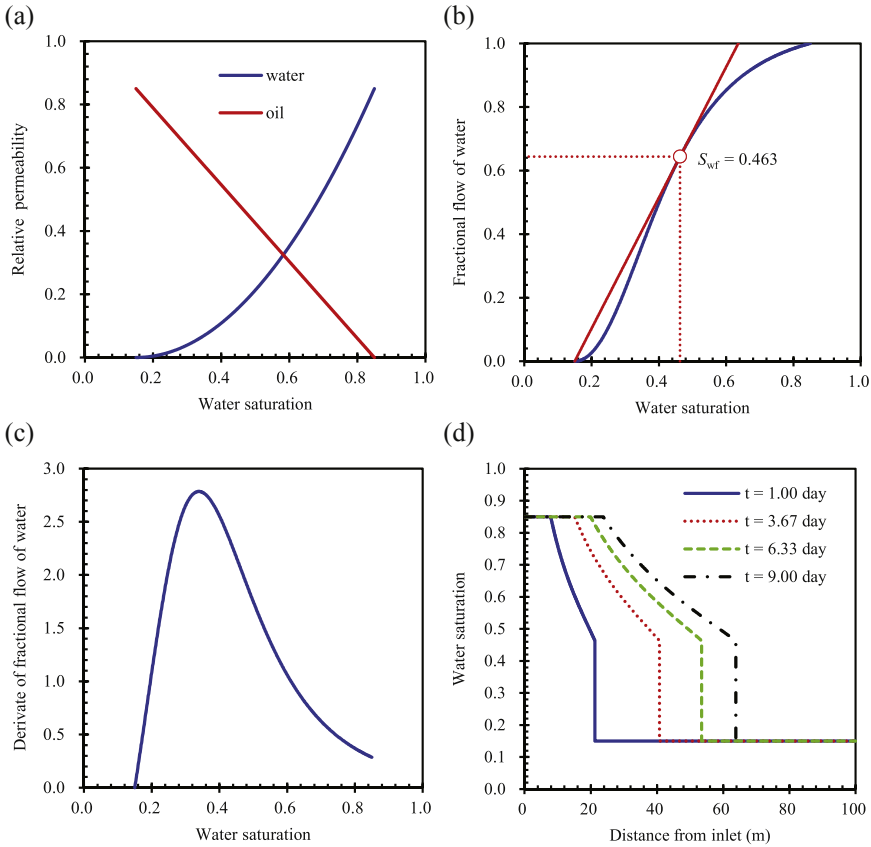

Figure 6.5 One-dimensional radial linear waterflood profiles and corresponding calculation curves. (a) Relative permeability curves; (b) Fractional flow curve; (c) Derivate of fractional flow function; (d) Water saturation profiles.

program used for these two examples to calculate the Buckley–Leverett solution in one-dimensional radial system with the Welge approach is provided in the Appendix B.1.

6.2.4 Integral Method Based on the Mass Balance Principle

As discussed in Section 5.4.4, with the Welge's approach it may be difficult to determine the exact tangential point at which the tangent to the fractional-flow curve intersects the curve, when the fractional-flow curve does not change rapidly with water saturation. In this section, we will extend the integral method based on the mass balance principle to the radial system.

As illustrated in Figure 6.4, the shock-front saturation, S_{wf}, should be at a position at which the shaded area of Figure 6.4 or Figure 6.6 must equal the total injection volume, $W_i(t) = \int_0^t q_{inj}(\tau)d\tau$. Therefore, there are four

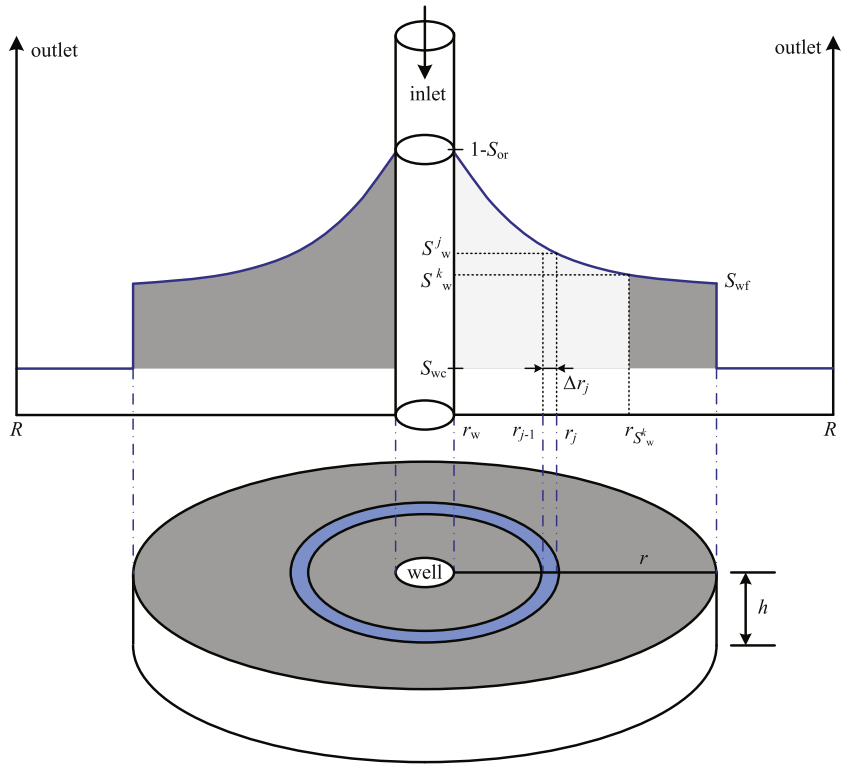

Figure 6.6 Schematic of integral method.

steps in the integral method to calculate the saturation profile in domain as follows (see Figure 6.6):

Step 1: first, choose a water saturation S_w^k ($k = 0, 1, 2, \ldots, N$) from its highest value down, in which $1-S_{or} = S_w^0 > S_w^1 > S_w^2 > S_w^3, \ldots$;

Step 2: calculate the traveling distance $r_{S_w^k}$ of a saturation S_w^k from $r = r_w$ using Eqn (6.18);

Step 3: calculate the injected fluid volume V (the area with black slant lines of Figure 6.6) contained from $r = r_w$ to $r = r_{S_w^k}$ in the portion of domain with $S_w > S_w^k$ by

$$V = h\phi \int_{r_w}^{r_{S_w^k}} (S_w - S_{wc}) 2\pi r dr \approx \pi h\phi \sum_{j=1}^{k} \left(S_w^j - S_{wc}\right)\left(r_j^2 - r_{j-1}^2\right) \qquad (6.29)$$

in which $r_0 = r_w$; and

Step 4: compare V with $W_i(t)$. If $V < W_i(t)$, the saturation shock front has not yet been reached, and the process is continued with the next saturation value S_w^{k+1} until the integrated volume, V, is equal to or larger the total injected volume. If $V \geq W_i(t)$, stop the calculation, and set $S_{wf} = S_w^k$ and $r_{wf} = r_{S_w^k}$. If $S_w^k - S_w^{k+1}$ is taken to be sufficiently small (e.g., 0.001), the calculation of the sharp front will be accurate.

The above procedure is easy to implement, and overcomes the drawback of Welge's method for plotting or graphic determination. The corresponding MATLAB program is provided in Appendix B.2. Comparisons

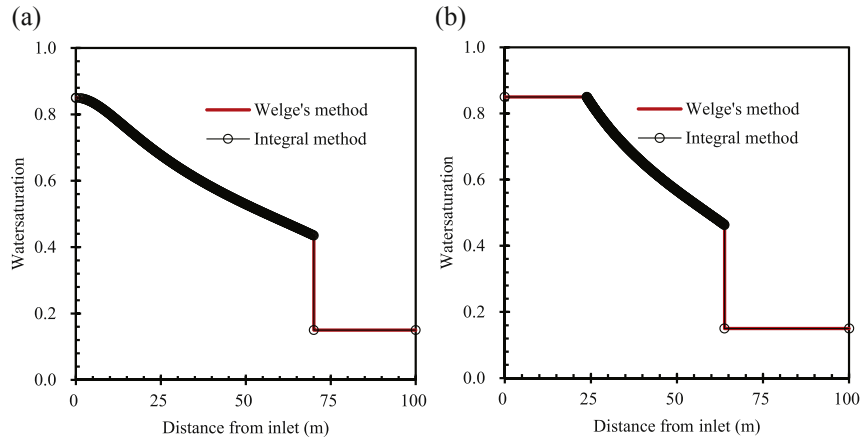

Figure 6.7 Comparison of analytical results between Welge and integral methods ($t = 9$ days). (a) Comparison test 1; (b) Comparison test 2.

between the integral method and Welge's method are given in the two examples in Section 6.2.3. In this section, the integral method with $\Delta S_w^k = 0.001$ is used. Figure 6.7 shows that the results of the integral method are identical to those of Welge's method.

6.3 BUCKLEY–LEVERETT FLOW IN A LINEAR COMPOSITE SYSTEM

This section presents a Buckley–Leverett-type analytical solution for one-dimensional immiscible displacement in a linear composite porous medium. As discussed in Section 5.5, the classical Buckley–Leverett theory is applicable only to flow in a homogeneous, one-dimensional linear porous-medium system. It is here extended to the flow in a one-dimensional heterogeneous, composite porous medium, in which the formation is treated as consisting of a number of flow domains with different rock properties. The analytical solution, obtained under the same conditions for the Buckley–Leverett solution for each flow domain, can be used to determine the complete saturation profile in the composite system at all times. The analytical results indicate that noncapillary immiscible displacement of two fluids in a composite system is characterized by discontinuities in saturation profiles across the interfaces between adjacent flow domains (Wu et al., 1993).

6.3.1 Mathematical Formulation and Solution

Two-phase flow of immiscible fluids is considered in an incompressible composite system, consisting of two flow domains ($j = 1, 2$) with each domain having different rock properties. The mathematical formulation of immiscible multiple-phase flow in porous media, discussed in the literature (e.g., Willhite, 1986) is extended for displacement in a composite reservoir. For the derivation of the analytical solution, the same assumptions as used for the Buckley–Leverett solution are made for each flow domain, namely.

- The two fluids and the porous medium are incompressible,
- The capillary-pressure gradient is negligible,
- The flow is one-dimensional linear,
- The fluid and rock properties are constant within each domain, and additionally,
- The formation properties change in discontinuous fashion at the contact between domains 1 and 2.

The flow system under consideration (See Figure 6.8) is a one-dimensional, linear, composite flow channel with a constant cross-sectional area, A. The

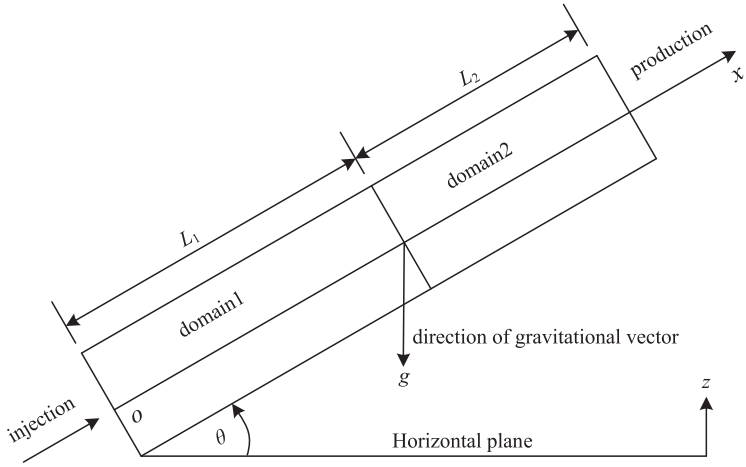

Figure 6.8 Schematic of a two-domain composite porous-medium system.

system is initially saturated uniformly with a mixture of a nonwetting-phase fluid (such as oil) and a wetting-phase fluid (such as water), and at time $t = 0$, injection of the same wetting fluid is started at the inlet ($x = 0$). It is further assumed that gravity segregation is negligible and that stable displacement exists (no viscous fingering). The fractional-flow function for the wetting phase in domain j ($j = 1, 2$) may be written in the following form (Willhite, 1986; Wu et al., 1993):

$$f_{w,j} = \frac{1 + \frac{Ak_j k_{rn,j}}{q_t \mu_n}(\rho_n - \rho_w) g \sin\theta}{1 + \frac{k_{rn,j}}{k_{rw,j}} \cdot \frac{\mu_w}{\mu_n}} \tag{6.30}$$

in which $k_{rn,j}$ and $k_{rw,j}$ are relative permeabilities of domain j ($j = 1, 2$) to nonwetting and wetting phases, respectively, as functions of wetting-phase saturation, S_w.

The partial differential equation for the wetting-phase flow in each domain can be expressed in terms of water saturation and fractional flow as

$$\frac{\partial f_{w,j}}{\partial x} + \frac{A\phi_j}{q_t} \frac{\partial S_w}{\partial t} = 0 \quad \text{for } j = 1, 2 \tag{6.31}$$

in which ϕ_j is the formation porosity in domain j. As shown by Buckley and Leverett (1942), this equation describes propagation of different saturations at different characteristic speeds, given by Willhite (1986), Wu et al. (1993),

$$\left.\frac{dx}{dt}\right|_{S_w} = \frac{q_t}{A\phi_j} \cdot \left.\frac{\partial f_{w,j}}{\partial S_w}\right|_t \quad \text{for } j = 1, 2 \tag{6.32}$$

The interface at $x = L_1$ between domains 1 and 2 is a discontinuity surface for porosity and absolute and relative permeability. This surface is fixed in space, so that the volumetric flow rates for both phases to flow through must be continuous at $x = L_1$ at all times. Thus

$$f_{w,1}\left(S_{w,1}^{-}\right) = f_{w,2}\left(S_{w,2}^{+}\right) \quad \text{at } x = L_1 \tag{6.33}$$

in which $S_{w,1}^{-}$ and $S_{w,2}^{+}$ are saturations of the wetting phase on the interface $L_1^{-} = L_1 - \varepsilon$, $L_1^{+} = L_1 + \varepsilon$ in domains 1 and 2, respectively (ε is an infinitesimally small increment).

The complete saturation solution for immiscible displacement in a composite medium is obtained in this section by solving the frontal advance Eqn (6.32) in both domains, subject to the continuity condition, Eqn (6.33). Because the downstream conditions of the flow system have no effect on the upstream flow, then the saturation distribution in domain 1 at all times is given by the Buckley–Leverett theory. Suppose that at $t = t^*$, the displacement saturation shock front with saturation $S_w = S_{wf,1}$ in domain 1 reaches the interface at $x = L_1$. For $t > t^*$, the injected wetting fluid has entered domain 2. The total volume of the injected fluid remaining in domain 1 at time t can be calculated by mass balance as

$$W_1(t) = A\phi_1 \int_0^{L_1} (S_w(x) - S_{wc,1})\mathrm{d}x \tag{6.34}$$

in which $S_{wc,1}$ is the initial saturation in domain 1.

The volume of injected fluid that has crossed the interface at $x = L_1$ into domain 2 is then given from mass balance considerations as

$$W_2(t) = W(t) - W_1(t) \tag{6.35}$$

in which $W(t) = \int_0^t q_t(\tau)\mathrm{d}\tau$, the total injected fluid volume. Equation (6.35) will be used to find the moving shock saturation front in domain 2. Consider a particular saturation S_w in domain 2, which begins to propagate from the interface $x = L_1$ at $t = t_s$. Multiplying Eqn (6.32) with $\mathrm{d}t$ and integrating from t_s to t, we have

$$x_s = L_1 + \frac{1}{A\phi_2} \int_{t_s}^{t} \left(\frac{\mathrm{d}f_{w,2}}{\mathrm{d}S_w}\right) q_t(\tau)\mathrm{d}\tau \tag{6.36}$$

in which x_s is the traveling distance of saturation S_w at time t from the inlet of domain 1.

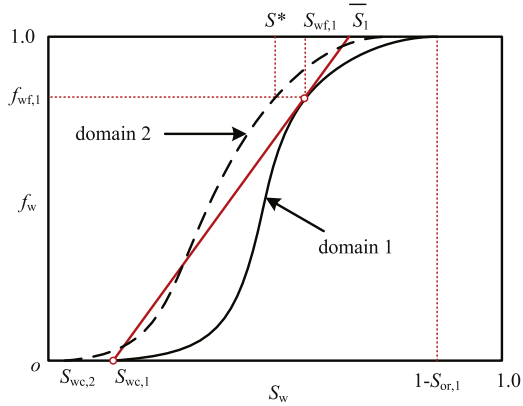

Figure 6.9 Fractional flow curves for the two-domain composite system.

As normally done for evaluation of the Buckley–Leverett solution, we pick a particular value of saturation in domain 2, and then use Eqn (6.36) to calculate its distance of traveling at the given time. The starting time t_s for each saturation $S_w = S^+_{w,2}$ at the interface can be determined by using the continuity condition, Eqn (6.33). Indeed, for each value $S^+_{w,2}$ of saturation at $x = L^+$ in domain 2, there exists a unique corresponding saturation $S^-_{w,1}$ at $x = L^-$ in domain 1 (see Figure 6.9), $S^-_{w,1} = S^-_{w,1}(S^+_{w,2})$, implicitly defined by Eqn (6.33), and there are two possibilities:

1. For $S^-_{w,1} \geq S_{wf,1}$, i.e., for a value of $S^-_{w,1}$ larger than or equal to that of the sharp-front saturation in domain 1, the time t_s for $S_w = S^+_{w,2}(S^-_{w,1})$ to start traveling into domain 2 is equal to the time at which the corresponding saturation $S^-_{w,1}$ reaches the interface of domain 1,

$$\int_0^{t_s} q_t(\tau)\mathrm{d}\tau = \frac{A\phi_1 L_1}{\left.\frac{\mathrm{d}f_{w,1}}{\mathrm{d}S_w}\right|_{S^-_{w,1}}} \tag{6.37}$$

2. For $S^-_{w,1} < S_{wf,1}$, i.e., for values of the corresponding saturation in domain 1 smaller than or equal to that of the sharp-front saturation in domain 1, the actual starting time t_s is the time, t^*, when the sharp front of domain 1 arrives at the interface,

$$t_s = t^* \tag{6.38}$$

As in the Buckley–Leverett solution of Chapter 5, a direct use of Eqn (6.36) to calculate saturation profiles in domain 2 will result in a multivalued

solution at the displacement front. Physically, this corresponds to the development of a moving saturation shock front in domain 2. The location $x_{f,2}$ and saturation $S_{w,2}$ of the shock front can be obtained from the mass-balance constraint,

$$W_2(t) = A\phi_2 \int_{L_1}^{x_{f,2}} (S_w(x,t) - S_{wc,2})\mathrm{d}x \tag{6.39}$$

in which $S_{wc,2}$ is the initial saturation in domain 2. Then, the saturation profile in domain 2 at any injection time t ($t \geq t^*$) is determined by Eqns (6.36) and (6.39), with the starting time given by Eqn (6.37) or (6.38).

6.3.2 Evaluation of Saturation Profiles in Composite Domains

The fundamental displacement behavior of two immiscible fluids in a linear composite system can be discussed using the analytical solution obtained above. For simplicity, let us consider a linear horizontal composite system with a constant cross-sectional area, A. Initially, the system is saturated with a wetting phase and a nonwetting phase, and a wetting fluid is injected at a constant volumetric rate, q_t, at the inlet $x = 0$ from $t = 0$. Then, the Solution (6.36) for the saturation distribution in domain 2 ($x > L_1$) is simplified as

$$x_s = L_1 + \frac{q_t}{A\phi_2}\left(\frac{\mathrm{d}f_{w,2}}{\mathrm{d}S_w}\right)_{S_w}(t - t_s) \tag{6.40}$$

in which the starting time t_s for this saturation at $x = L_1$ in domain 2 is, from Eqn (6.37),

$$t_s = \frac{A\phi_1 L_1}{q_t \frac{\mathrm{d}f_{w,1}}{\mathrm{d}S_w}\Big|_{S_{w,1}^-}} \quad \text{for} \quad S_{w,1} > S_{wf,1} \tag{6.41}$$

Here, $S_{w,1}^- = S_{w,1}^-(S_{w,2}^+)$ is the interface saturation in domain 1, corresponding to $S_{w,2}^+$ in domain 2, according to Eqn (6.33). When $S_{w,1} \leq S_{wf,1}$, we have $t_s = t^*$.

From Eqns (6.34), (6.35), and (6.39), the mass balance for determining the sharp displacement front in domain 2 becomes

$$Q_2(t) = A\phi_2 \int_{L_1}^{x_{f,2}} (S_w(x,t) - S_{wc,2})\mathrm{d}x = tq_t - A\phi_1 L\left(\overline{S}_1 - S_{wc,1}\right) \tag{6.42}$$

in which $\overline{S}_1$, is the average saturation in domain 1, which can be determined by Welge's graphic method. The detailed procedure for calculating saturation profiles is given as following:

1. Determine the sharp-front saturation $S_{wf,1}$ in domain 1 by the Welge method or the integral method, based on the mass-balance principle, as discussed in Section 5.4. Calculate the time t^* at which $S_{wf,1}$ reaches the interface by

$$t^* = \frac{A\phi_1 L_1}{q_t \left.\frac{df_{w,1}}{dS_w}\right|_{S_{wf,1}}} \tag{6.43}$$

2. For a given time t ($t > t^*$), calculate $S^-_{w,1}$ at the interface in domain 1 by

$$tq_t = \frac{A\phi_1 L_1}{\left.\frac{df_{w,1}}{dS_w}\right|_{S^-_{w,1}}} \tag{6.44}$$

   Then solve for $S^+_{w,2}$ in domain 2 by Eqn (6.33). Calculate the average saturation $\overline{S}_1$ in domain 1 by

$$\overline{S}_1 = S^-_{w,1} + \frac{1 - f_{w,1}\left(S^-_{w,1}\right)}{\left.\frac{df_{w,1}}{dS_w}\right|_{S^-_{w,1}}} \tag{6.45}$$

3. Calculate the saturation profile in domain 2 as follows:
   - **i.** choose a saturation $S^k_{w,2}$ ($k = 0, 1, 2, \ldots N$), in which $S^+_{w,2} = S^0_{w,2} > S^1_{w,2} > S^2_{w,2} > S^3_{w,2}, \ldots$;
   - **ii.** calculate the traveling distance $x_{S^k_{w,2}}$ of a saturation $S^k_{w,2}$ from $x = L_1$ by Eqn (6.40);
   - **iii.** calculate the injected-fluid volume V contained from $x = L_1$ to $x = x_{S^k_{w,2}}$ in the portion of domain 2 with $S_{w,2} > S^k_{w,2}$ by

$$V = A\phi_2 \int_{L_1}^{x_{S^k_{w,2}}} (S_{w,2} - S_{wc,2})dx \approx A\phi_2 \sum_{j=1}^{k} \left(S^j_{w,2} - S_{wc,2}\right)\Delta x_j \tag{6.46}$$

     in which $\Delta x_j = x_j - x_{j-1}$, and $x_0 = L_1$.
   - **iv.** compare V with $Q_2(t)$ as given by Eqn (6.42). If $V < Q_2(t)$, the saturation shock front has not been reached yet, and the process is continued with the next saturation value $S^{k+1}_{w,2}$. If $V > Q_2(t)$, stop the calculation, and set $S_{wf,2} = S^k_{w,2}$ and $x_{wf,2} = x_k$.

If $S_{w,2}^{k} - S_{w,2}^{k+1}$ is taken to be sufficiently small, the calculation of the sharp front will be accurate. In this section, we have used $\Delta S_{w,2}^{k} = 0.001$.

The above procedure has been programmed and carried out by computer (Appendix B.3) and also can be easily extended to composite media with an arbitrary number of domains. This is because saturation profiles are solely determined from upstream conditions. Given the time-dependence of saturations at the interface between domains N and $N+1$, our method will yield the saturation distribution in domain $N+1$, which in turn defines the time dependence of saturations at the interface to domain $N+2$, etc.

Note that the saturation profile in domain 2, described by Eqns (6.40)–(6.42), is determined from rock porosity and fractional-flow curves which, for horizontal flow, depend only on relative permeabilities and viscosities of fluids. Thus, we have the important conclusion that, under the approximation or condition of Buckley–Leverett flow, saturation profiles in a horizontal composite medium are dependent only on formation porosities and relative permeabilities, and are completely independent of absolute permeabilities. In heterogeneous geological systems, the relative permeabilities may be quite different in different flow domains, resulting in a diverse variety of possible saturation profiles.

6.3.3 Examples: One-Dimensional Linear Waterflood in a Two-domain Composite System

Analytical example 1: The fluid and rock properties for illustrative examples are given in Table 6.2, in which the Brooks–Corey type relative permeability functions are chosen for oil and water flow in different media (see Table 6.2 and Figure 6.10(a)).

The fractional-flow functions for the two domains are shown in Figure 6.10(b), and the predicted saturation profiles after an injection times of $t = 0.1$, 0.33, 0.55, 0.78, and 1.00 days are given in Figure 6.10(d). In fact, $t = 1$ day is the time when the sharp-front water saturation in domain 1 arrives at the interface between domains 1 and 2.

The distinguishing features of immiscible displacement in a composite porous medium, as shown in Figure 6.11, are that there exists a discontinuity in saturation at or across the interface between the two domains as well as that the derivative $\partial S_w/\partial x$ has a discontinuity at a point $(x^*, S_{w,2}^*)$ in domain 2, at which the value of saturation $S_{w,2}^*$ corresponds to the shock-front saturation $S_{wf,1}$ of domain 1, $f_{w,2}(S_{w,2}^*) = f_{w,1}(S_{wf,1})$.

The wave-traveling behavior of saturation profiles in a two-domain linear composite medium can be represented by characteristics in the (x, t) space, as shown in Figure 6.12 (Wu et al., 1993). Each straight line

Table 6.2 Parameters for immiscible displacement in a composite system

Parameters	Domain 1	Domain 2	Unit
Porosity of domains, ϕ	0.25	0.25	[-]
Permeability, k	9.869×10^{-13}	9.869×10^{-13}	[m^2]
Length of domains, L	$L_1 = 60$	$L_2 = 60$	[m]
Cross-sectional area, A	1.00	1.00	[m^2]
Injection rate, q_t	1.0×10^{-4}	–	[m^3/s]
Water-phase viscosity, μ_w	1.0	1.0	[mPa·s]
Oil-phase viscosity, μ_o	5.0	5.0	[mPa·s]
Initial water-phase saturation, S_{wc}	0.15	0.15	[-]
Residual oil saturation, S_{or}	0.10	0.15	[-]
Relative permeability parameters, $k_{rw,max}$	0.90	0.80	[-]
Relative permeability parameters, $k_{ro,max}$	0.90	0.80	[-]
Relative permeability parameters, n_w	2.50	2.00	[-]
Relative permeability parameters, n_o	1.00	1.50	[-]

represents a constant saturation, and travels at different velocity, which is described by the slope of the straight lines.

Each value of saturations (S_1, S_2, or S_3) in domain 1 corresponds to a unique saturation wave (S_1^*, S_2^*, or S_3^*) across the interface $x = L_1$ if $S_{w,2} \geq S_{w,2}^*$ in domain 2. For saturations in the range $S_{wf,2} \leq S_{w,2} \leq S_{w,2}^*$ (corresponding to the sharp-front saturation of domain 1) in domain 2, the starting times for a saturation to travel from the interface are the same, corresponding to the time when the sharp moving front in domain 1 reaches the interface. For a given time $t = T$ ($T > t^*$), the intersections of characteristic straight lines with the vertical line ($t = T$) on Figure 6.12 give the complete saturation profile, such as given by Figure 6.12 in $S_w - x$ space.

Analytical example 2: If we switch the fractional flow curves for the two domains, the corresponding parameters and water-saturation profiles before injected water arrives at the interface, are shown in Figure 6.13.

The water-saturation profiles of the composite system after time $t = 0.77$ day of injection is shown in Figure 6.14. The mass balance (6.42) is satisfied after the moving saturation front reaches the interface, $x = L_1$, and there is no discontinuity in $\partial S/\partial x$ versus x in domain 2 in this case.

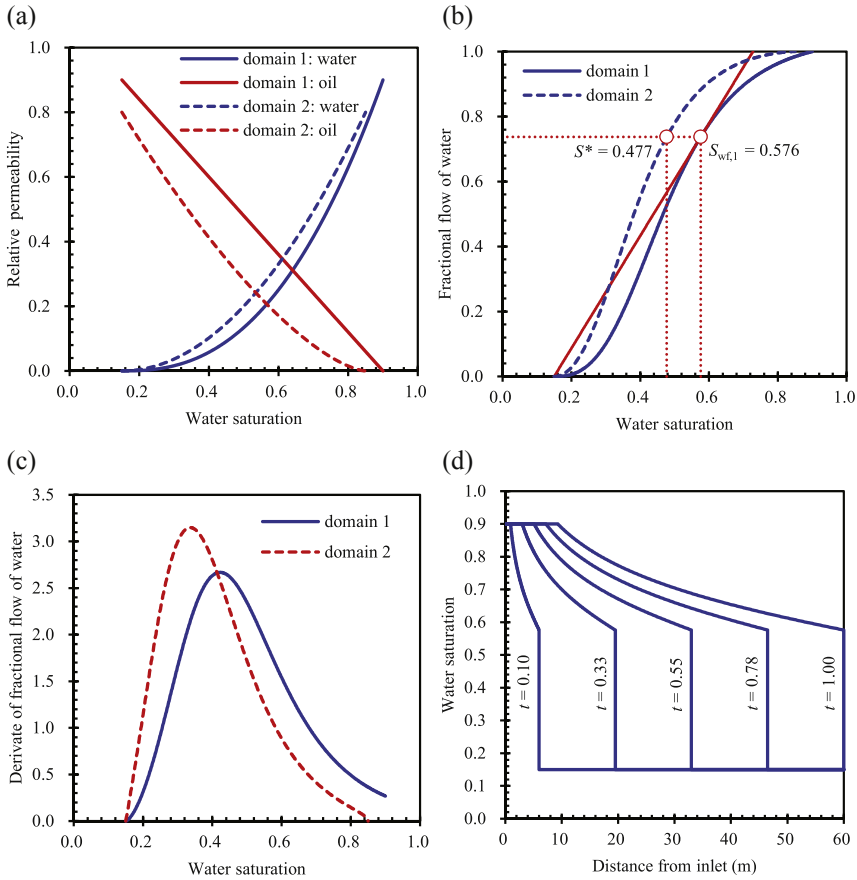

Figure 6.10 Corresponding curves of relative permeability, fractional flow for two-domain composite system, and saturation profiles in domain 1 before injected water reaches at the interface. (a) Relative permeability curves; (b) Fractional flow curve; (c) Derivate of fractional flow function; (d) Water saturation profiles.

The values of the saturation on the interface for both domains are always increasing with time. Equation (6.40) indicates that the traveling distance of a particular saturation S_w from the interface between domains 1 and 2 is proportional to derivatives of the fractional-flow function of domain 2 with respect to saturation. In the above two examples, saturation variations happen to be in a range over which $(df_{w,2}/dS_w)$ decreases as $S^+_{w,2}$ increases, i.e., a higher saturation, later reaching and departing from the interface, has a lower velocity (see Figure 6.13(c)). The physical range for saturations in domain 1 is the range of $f_{w,1} \geq f_{w,1}(S_{wf,1})$ or $S_{w,1} \geq S_{wf,1}$, and for domain

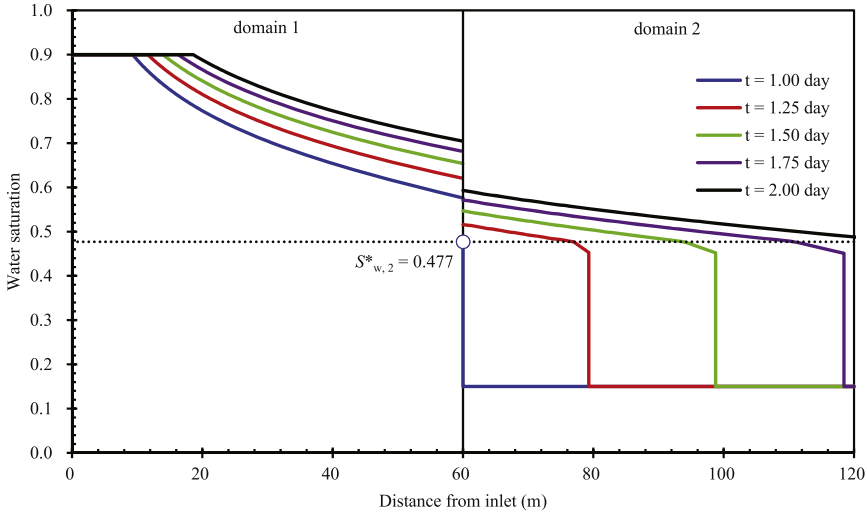

Figure 6.11 Water-saturation profiles in the linear composite system after injected water reaches at the interface between the two domains.

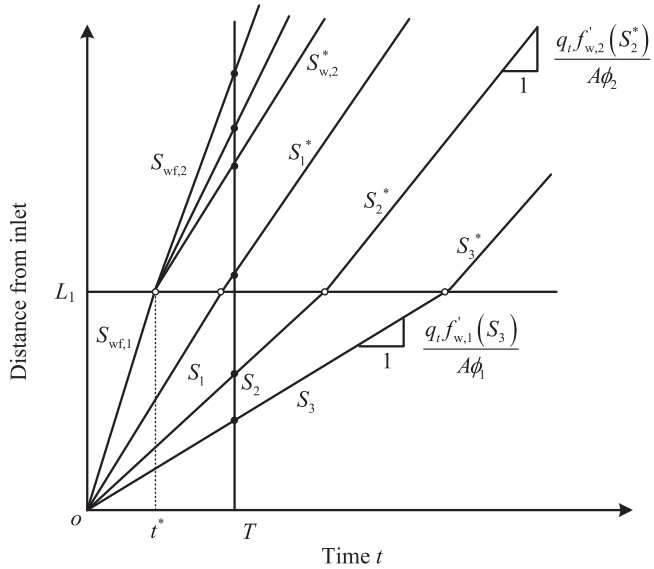

Figure 6.12 Characteristic for Buckley–Leverett flow in a two-domain composite system (Wu et al., 1993).

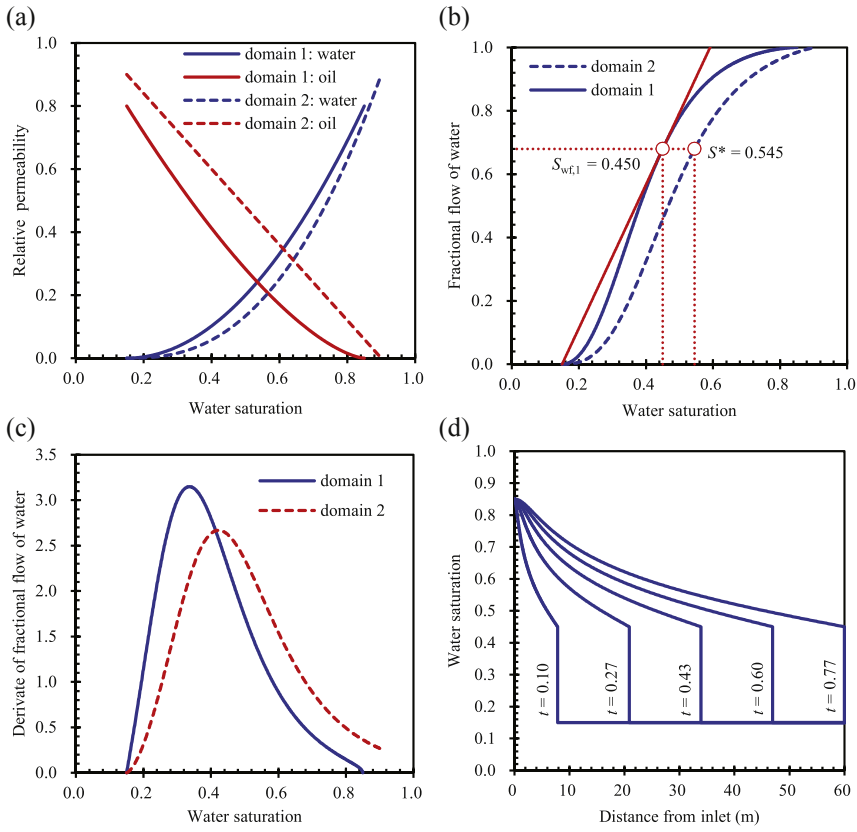

Figure 6.13 Corresponding calculation curves for two-domain composite system and saturation profiles in domain 1 before injected water reaches the interface. (a) Relative permeability curves; (b) Fractional flow curve; (c) Derivate of fractional flow function; (d) Water saturation profiles.

2, the physical range at a given time when $S_w = S^+_{w,2}$ at the interface is given by $S_{wf,2} \leq S_{w,2} \leq S^+_{w,2}$ or $f_{w,2}(S_{wf,2}) \leq f_{w,2} \leq f_{w,2}(S^+_{w,2})$.

Note that relative permeabilities in different regions of a composite medium are generally independent and we may have a situation in which the traveling velocity increases in domain 2 as the saturation increases. The derivatives of the fractional flow with respect to saturation increase as saturation and fractional flow increases in domain 2. The resulting saturation distribution is shown in Figure 6.14. In this case, $S_{wf,2} \geq S^*_{w,2}$, so that there is no discontinuity for $\partial S_w/\partial x$ in domain 2. The saturation profile in domain 2 has a negative curvature because the derivative $df_{w,2}/dS_w$ decreases as $S_{w,2}$ decreases in domain 2.

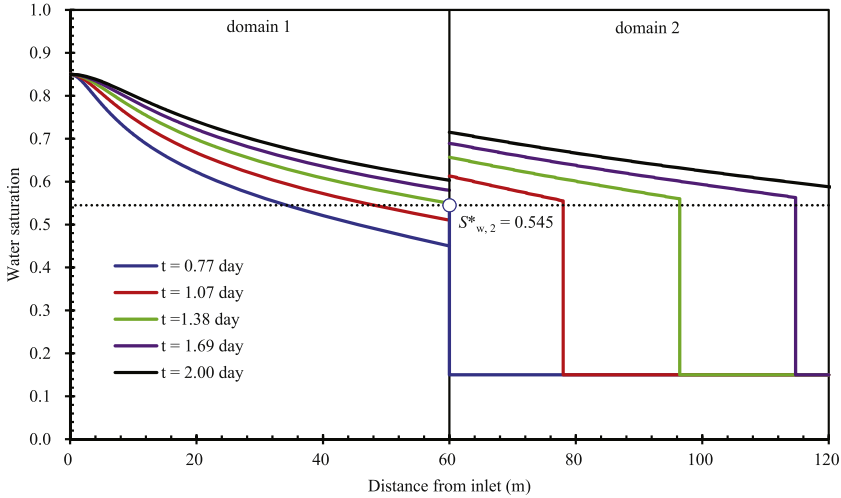

Figure 6.14 Water-saturation profiles in composite system with switched fractional-flow curves.

In this section, a Buckley–Leverett-type analytical solution for one-dimensional two-phase immiscible displacement in a composite porous medium has been developed. Our treatment has considered a composite medium consisting of two domains, each with uniform initial conditions; an extension to an arbitrary number of domains, to nonuniform initial saturation distribution, or to one-dimensional horizontal flow in a composite system with nonconstant cross-sectional areas, such as radial flow of the next section, would be straightforward. Immiscible displacement in composite porous media is found to be characterized by discontinuities in saturation profiles across the interfaces of adjacent flow domains, and by discontinuous saturation derivatives in domain 2. Saturation profiles for horizontal displacement depend only on relative permeability curves, porosities, and ratio of fluid viscosities, and are independent of absolute permeability. The corresponding MATLAB code of this example can be found in the Appendix B.3.

6.4 BUCKLEY–LEVERETT FLOW IN A RADIAL COMPOSITE SYSTEM

In this section, we present Buckley–Leverett solutions as well as a solution procedure for solving the two-phase flow problem in a radial composite porous medium. Radially composite systems usually do not occur naturally, except in some deltaic-origin formations. However, solutions for

such systems have a variety of applications in groundwater hydrogeology and reservoir engineering. Drilling, completion, stimulation, and secondary and/or tertiary oil recovery processes may create radially composite systems. The solution and analysis process of Buckley–Leverett flow in a radial composite system is similar to that of a linear composite system in Section 6.3. Therefore, only a brief description will be elaborated in this section.

6.4.1 Radial Composite Flow Model

A radial composite flow model consists of an inner cylindrical homogeneous region (domain 1) surrounded by an outer region (domain 2) of different rock properties, as illustrated in Figure 6.15. An infinitesimally thin radial discontinuity or interface is assumed to separate the two reservoir regions ($j = 1, 2$) at $r = R_1$. The flow in both regions is one-dimensional, radial, and horizontal. The mathematical formulation of immiscible multiple-phase flow in porous media, discussed in the literature (e.g., Willhite, 1986; Wu et al., 1993), is extended for displacement in a radial composite reservoir.

For the derivation of the analytical solution, the same assumptions as used for the Buckley–Leverett solution are made for each flow domain, as

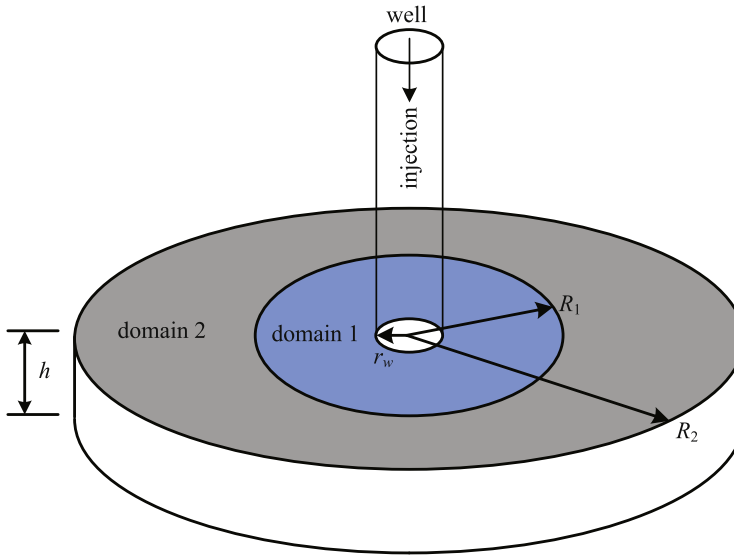

Figure 6.15 Schematic of a radial composite system.

illustrated in Section 6.3.1. The flow system under consideration (See Figure 6.15) is a radial composite flow model with a constant reservoir thickness, h. The system is initially saturated uniformly with a mixture of a nonwetting-phase fluid (such as oil) and a wetting-phase fluid (such as water), and at time $t = 0$, injection of the same wetting fluid starts at the inlet ($r = r_w$). It is further assumed that gravity segregation is negligible and that stable displacement exists (no viscous fingering in the radial direction). The fractional-flow function for the wetting phase in domain j ($j = 1, 2$) may be written in the following form (Willhite, 1986):

$$f_{w,j} = \frac{1}{1 + \frac{k_{rn,j}}{k_{rw,j}} \cdot \frac{\mu_w}{\mu_n}} \tag{6.47}$$

in which $k_{rn,j}$ and $k_{rw,j}$ are relative permeabilities of domain j ($j = 1, 2$) to non-wetting and wetting phases, respectively, as functions of wetting-phase saturation, S_w.

The partial differential equation for the wetting-phase flow in each radial domain can be expressed in terms of saturation and fractional flow as

$$\frac{\partial f_{w,j}}{\partial r} + \frac{2\pi r h \phi_j}{q_t} \frac{\partial S_w}{\partial t} = 0 \quad \text{for } j = 1, 2 \tag{6.48}$$

in which ϕ_j is the formation porosity in domain j. As shown in Section 6.2.1, this equation describes propagation of different saturations at different characteristic speeds, given by

$$2r \frac{dr}{dt}\bigg|_{S_w} = \frac{q_t}{\pi h \phi_j} \cdot \frac{\partial f_{w,j}}{\partial S_w}\bigg|_t \quad \text{for } j = 1, 2 \tag{6.49}$$

The interface at $r = R_1$ between domain 1 and 2 is a discontinuity interface for porosity and absolute and relative permeabilities. This interface is fixed in space, so that the volumetric flow rates for both phases to cross must be continuous at $r = R_1$ at all times. Thus,

$$f_{w,1}\left(S_{w,1}^{-}\right) = f_{w,2}\left(S_{w,2}^{+}\right) \quad \text{at } r = R_1 \tag{6.50}$$

in which $S_{w,1}^{-}$ and $S_{w,2}^{+}$ are saturations of the wetting phase on the interface $R_1^{-} = R_1 - \varepsilon$, $R_1^{+} = R_1 + \varepsilon$ in domains 1 and 2, respectively (ε is an infinitesimally small increment).

The complete saturation solution for immiscible displacement in a radial composite medium is obtained in this section by solving the frontal advance

Eqn (6.49) in both domains, subject to the continuity condition, Eqn (6.50). Because the downstream conditions of the flow system have no effects on the upstream flow, the saturation distribution in domain 1 at all times is described by the Buckley–Leverett theory. Suppose that at $t = t^*$, the displacement shock front with saturation $S_w = S_{wf,1}$ in domain 1 reaches the interface. For $t > t^*$, the injected wetting fluid has entered domain 2. The total volume of the injected fluid remaining in domain 1 at time t can be calculated as

$$W_1(t) = 2\pi h\phi_1 \int_{r_w}^{R_1} (S_w(r) - S_{wc,1}) r dr \tag{6.51}$$

in which $S_{wc,1}$ is the initial water (wetting-phase) saturation in domain 1.

The volume of injected fluid that has crossed the interface $r = R_1$ into domain 2 is then given from mass-balance consideration as

$$W_2(t) = W(t) - W_1(t) \tag{6.52}$$

in which $W(t) = \int_0^t q_t(\tau)d\tau$, the total injected-fluid volume. Equation (6.52) will be used to find the moving shock saturation front in domain 2. Consider a particular saturation S_w in domain 2, which begins to propagate from the interface $r = R_1$ at $t = t_s$. Multiplying Eqn (6.49) with dt and integrating from t_s to t, we have

$$R_S^2 = R_1^2 + \frac{1}{\pi h\phi_2} \int_{t_s}^{t} \left(\frac{df_{w,2}}{dS_w}\right) q_t(\tau)d\tau \tag{6.53}$$

in which R_S is the traveling distance of saturation S_w at time t from the inlet or wellbore.

Similar to the evaluation of the Buckley–Leverett solution in flow through a linear composite reservoir, we pick a value of saturation in domain 2, and then use Eqn (6.52) to calculate its radial location at the given time. The starting time t_s for each saturation $S_w = S_{w,2}^+$ at the interface can be determined by using the continuity condition, Eqn (6.50). Similar to flow in a linear composite reservoir, for each value $S_{w,2}^+$ of saturation at $r = R_1^+$ in domain 2, there exists a unique corresponding saturation $S_{w,1}^-$ at $r = R_1^-$ in domain 1 (see Figure 6.15), $S_{w,1}^- = S_{w,1}^-(S_{w,2}^+)$, implicitly defined by Eqn (6.50), and there are two possibilities:

1. For $S_{w,1}^- > S_{wf,1}$, i.e., for a value of $S_{w,1}^-$ larger than that of the sharp-front saturation in domain 1, the time t_s for $S_w = S_{w,2}^+(S_{w,1}^-)$ to start

traveling into domain 2 from the interface is equal to the time at which the corresponding saturation $S_{w,1}^{-}$ reaches the interface of domain 1,

$$\int_0^{t_s} q_t(\tau)\mathrm{d}\tau = \frac{\pi h\phi_1\left(R_1^2 - r_w^2\right)}{\left.\frac{\mathrm{d}f_{w,1}}{\mathrm{d}S_w}\right|_{S_{w,1}^{-}}} \tag{6.54}$$

2. For $S_{w,1}^{-} < S_{wf,1}$, i.e., for values of the corresponding saturation in domain 1 smaller than or equal to that of the sharp-front saturation of domain 1, the actual starting time t_s is the time when the sharp front arrives at the interface,

$$t_s = t^* \tag{6.55}$$

in which t^* is the time when the sharp saturation front in domain 1 arrives at the interface.

Note that direct use of Eqn (6.49) to calculate saturation profiles in domain 2 will result in a multivalued solution at the displacement front. Physically, this corresponds to the development of a moving saturation shock front in domain 2. The location $R_{f,2}$ and saturation $S_{w,2}$ of the shock saturation front can be obtained from the following mass-balance constraint,

$$W_2(t) = 2\pi h\phi_2 \int_{R_1}^{R_{f,2}} \left(S_w(r,t) - S_{wc,2}\right) r\mathrm{d}r \tag{6.56}$$

in which $S_{wc,2}$ is the initial water saturation in domain 2. Then, the saturation profile in domain 2 at any injection time t ($t \geq t^*$) is determined by Eqns (6.49) and (6.56), with the starting time given by Eqn (6.54) or (6.55).

6.4.2 Evaluation of Saturation Profiles in Radial Composite Domains

The fundamental displacement behavior of two immiscible fluids in a radial composite system can be discussed using the analytical solution obtained previously. Initially, the system is saturated with a mobile nonwetting phase and an immobile wetting phase, and a wetting fluid is injected at a constant

volumetric rate, q_t, at the inlet $r = r_w$ from $t = 0$. Then, the Solution (6.53) for the saturation distribution in domain 2 ($r > R_1$) is simplified as

$$R_S^2 = R_1^2 + \frac{q_t}{\pi h \phi_2}\left(\frac{df_{w,2}}{dS_w}\right)_{S_w}(t - t_s) \tag{6.57}$$

in which the starting time t_s for this saturation at $r = R_1$ in domain 2 is, from Eqn (6.54),

$$t_s = \frac{\pi h \phi_1 \left(R_1^2 - r_w^2\right)}{q_t \frac{df_{w,1}}{dS_w}\Big|_{S_{w,1}^-}} \quad \text{for} \quad S_{w,1} > S_{wf,1} \tag{6.58}$$

Here, $S_{w,1}^- = S_{w,1}^-(S_{w,2}^+)$ is the interface saturation in domain 1, corresponding to $S_{w,2}^+$ in domain 2, according to Eqn (6.50). When $S_{w,1} \le S_{wf,1}$, we have $t_s = t^*$.

From Eqns (6.50)–(6.52), the mass balance for determining the sharp displacement front in domain 2 becomes

$$\begin{aligned} W_2(t) &= 2\pi h \phi_2 \int_{R_1}^{R_{f,2}} (S_w(r,t) - S_{wc,2}) r dr \\ &= t q_t - \pi h \phi_1 \left(R_1^2 - r_w^2\right)\left(\overline{S}_{w,1} - S_{wc,1}\right) \end{aligned} \tag{6.59}$$

in which $\overline{S}_{w,1}$, is the average saturation in domain 1, which can be determined by the Welge's graphic method. The detailed procedure for calculating saturation profiles is given as following:

1. Determine the sharp-front saturation $S_{wf,1}$ in domain 1 by the Welge method or the integral method based on the mass balance principle, as discussed in Section 6.2. Calculate the time t^* at which $S_{wf,1}$ reaches the interface by

$$t^* = \frac{\pi h \phi_1 \left(R_1^2 - r_w^2\right)}{q_t \frac{df_{w,1}}{dS_w}\Big|_{S_{wf,1}}} \tag{6.60}$$

2. For a given time t ($t > t^*$), calculate $S_{w,1}^-$ at the interface in domain 1 by

$$t q_t = \frac{\pi h \phi_1 \left(R_1^2 - r_w^2\right)}{\frac{df_{w,1}}{dS_w}\Big|_{S_{w,1}^-}} \tag{6.61}$$

Then solve for $S^{+}_{w,2}$ in domain 2 by Eqn (6.50). Calculate the average saturation $\overline{S}_1$ in domain 1 using Eqn (6.28), as follows:

$$\overline{S}_{w,1} = S^{-}_{w,1} + \frac{1 - f_{w,1}\left(S^{-}_{w,1}\right)}{\left.\frac{df_{w,1}}{dS_w}\right|_{S^{-}_{w,1}}} \tag{6.62}$$

3. Calculate the saturation profile in domain 2 as follows:
   - **i.** choose a saturation $S^{k}_{w,2}$ ($k = 0, 1, 2, \ldots N$), in which $S^{+}_{w,2} = S^{0}_{w,2} > S^{1}_{w,2} > S^{2}_{w,2} > S^{3}_{w,2}, \ldots$;
   - **ii.** calculate the traveling distance $r_{S^{k}_{w,2}}$ of a saturation $S^{k}_{w,2}$ from $r = R_1$ by Eqn (6.53);
   - **iii.** calculate the injected fluid volume V contained from $r = R_1$ to $r = r_{S^{k}_{w,2}}$ in the portion of domain 2 with $S_{w,2} > S^{k}_{w,2}$ by

$$V = h\phi_2 \int_{R_1}^{r_{S^{k}_{w,2}}} (S_{w,2} - S_{wc,2}) 2\pi r dr \approx \pi h \phi_2 \sum_{j=1}^{k} \left(S^{j}_{w,2} - S_{wc,2}\right)\left(r_j^2 - r_{j-1}^2\right) \tag{6.63}$$

   in which $r_0 = r_w$.
   - **iv.** compare V with $W_2(t)$, as given by Eqn (6.52). If $V < W_2(t)$, the saturation shock front has not been reached yet and the process is continued with the next saturation value $S^{k+1}_{w,2}$. If $V \geq W_2(t)$, stop the calculation, and set $S_{wf,2} = S^{k}_{w,2}$ and $r_{wf,2} = r_k$.

     If $\Delta S^{k}_{w,2} = S^{k}_{w,2} - S^{k+1}_{w,2}$ is taken to be sufficiently small, the estimate of the sharp front will be accurate. In the following example, we have used $\Delta S^{k}_{w,2} = 0.001$.

The above procedure can be easily extended to radial composite media with an arbitrary number of radial domains, because saturation profiles are solely determined from upstream conditions. Given the time dependence of saturations at the interface between domains N and $N + 1$, our method will yield the saturation distribution in domain $N + 1$, which in turn defines the time dependence of saturations at the interface to domain $N + 2$, etc.

6.4.3 Examples: Waterflood in a Radial Composite System

Analytical example 1: The fluid and rock properties for illustrative examples are given in Table 6.3, in which the Brooks–Corey type relative

Table 6.3 Parameters for immiscible displacement in a radial composite system

Parameters	Domain 1	Domain 2	Unit
Porosity of domains, ϕ	0.25	0.25	[-]
Permeability, k	9.869×10^{-13}	9.869×10^{-13}	[m^2]
Radius of domains, R	50	100	[m]
Radius of injection well, r_w	0.10	—	[m]
Reservoir thickness, h	1.00	1.00	[m^2]
Injection rate, q_t	3.0×10^{-3}	—	[m^3/s]
Water-phase viscosity, μ_w	1.0	1.0	[mPa·s]
Oil-phase viscosity, μ_o	5.0	5.0	[mPa·s]
Initial water-phase saturation, S_{wc}	0.15	0.15	[-]
Residual oil saturation, S_{or}	0.10	0.15	[-]
Relative permeability parameters, $k_{rw,max}$	0.90	0.80	[-]
Relative permeability parameters, $k_{ro,max}$	0.90	0.80	[-]
Relative permeability parameters, n_w	2.50	2.00	[-]
Relative permeability parameters, n_o	1.00	1.50	[-]

permeability functions were chosen for oil and water flow in different media (see Table 6.3 and Figure 6.16(a)). The fractional-flow functions for the domains are shown in Figure 6.16(b), and the predicted saturation profile until the injection time of $t = 4.37$ day is given in Figure 6.16(d).

The time, $t = 4.37$ day, is when the sharp-front water saturation in domain 1 arrives at the interface ($r = R_1 = 50$ m) between domains 1 and 2. Similar to flow in a linear composite reservoir, the distinguishing feature of immiscible displacement in a radial composite porous medium, as shown in Figure 6.17, is that there also exists a saturation discontinuity at the interface between the two domains as well as that the derivative $\partial S_w/\partial r$ has a discontinuity at a point $(r^*, S^*_{w,2})$ within domain 2, at which the value of $S^*_{w,2}$ corresponds to the shock-front saturation $S_{wf,1}$ of domain 1, $f_{w,2}(S^*_{w,2}) = f_{w,1}(S_{wf,1})$.

Analytical example 2: If we switch the fractional-flow curves for the two domains, the corresponding relative permeability, fractional flow, and its derivative curves and water-saturation profiles, before injected water arrives at the interface, are shown in Figure 6.18.

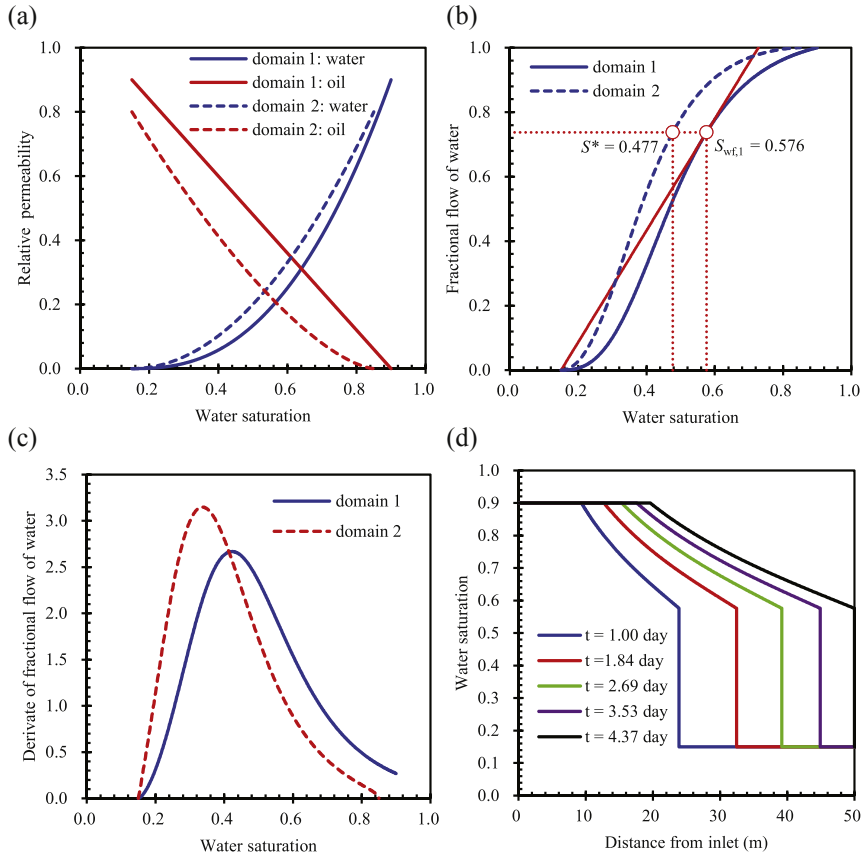

Figure 6.16 Corresponding calculation curves for a radial composite system and saturation profiles in domain 1 before injected water reaches the interface. (a) Relative permeability curves; (b) Fractional flow curve; (c) Derivate of fractional flow function; (d) Water saturation profiles.

The water-saturation profiles of the composite system after time $t = 3.33$ days of injection is shown in Figure 6.19. At this time, the moving sharp saturation front of domain 1 reaches the interface. Note that there is no discontinuity in $\partial S_w/\partial r$ versus r within domain 2 in this case. Although the fluid and rock parameters of the above two examples are same as the Section 6.3.3 for flow through a linear composite reservoir, the water-saturation profiles in a radial composite system are a little different from those in a linear composite system, because of varying or larger reservoir volume per unit length in r in this radial flow case.

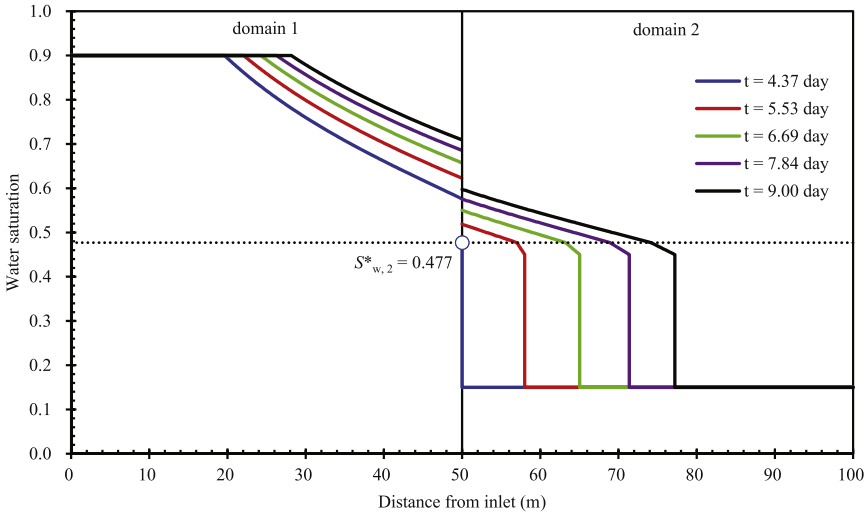

Figure 6.17 Water saturation profiles in the composite system after injected water reaches at the interface between the two domains.

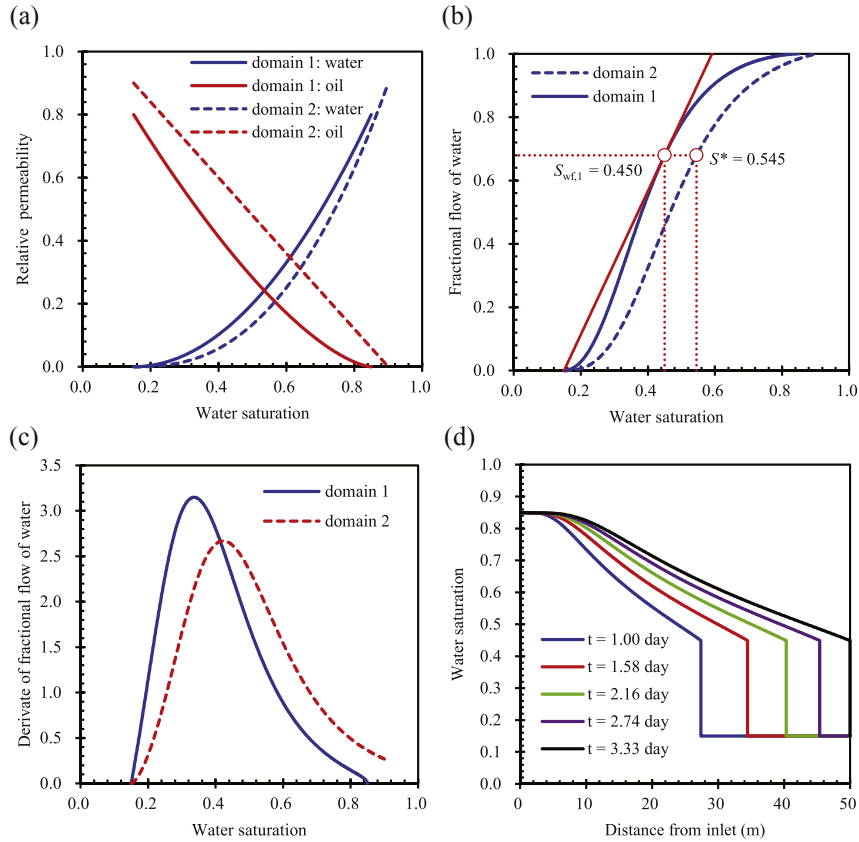

Figure 6.18 Corresponding calculation curves for two-domain composite system and saturation profiles in domain 1 before injected water reaches the interface. (a) Relative permeability curves; (b) Fractional flow curve; (c) Derivate of fractional flow function; (d) Water saturation profiles.

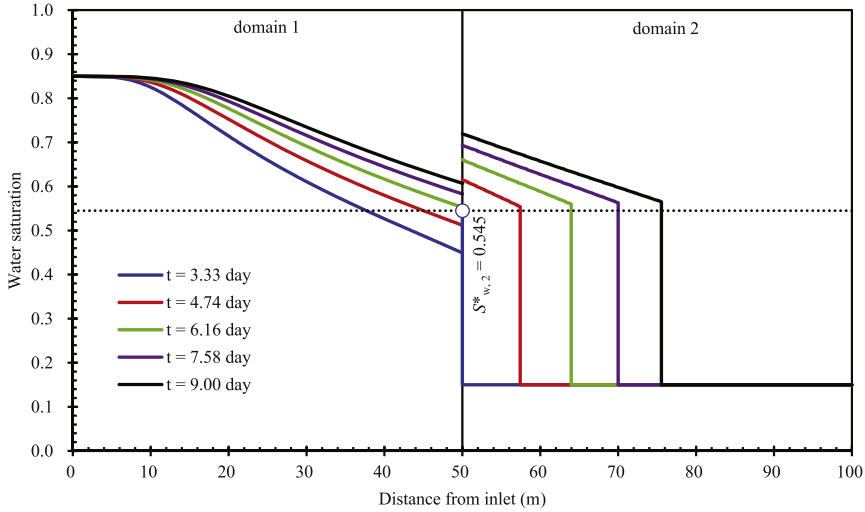

Figure 6.19 Water saturation profiles in composite system with switched fractional-flow curves.

6.5 ANALYSIS AND VERIFICATION OF NUMERICAL SIMULATION

One application of the above extended Buckley–Leverett solutions is to verify results of numerical simulation models. In this case, MSFLOW code (Wu, 1998), a general purpose, three-phase reservoir simulator, is verified with the analytical solutions.

6.5.1 Numerical Simulation in a One-Dimensional Radial System

The flow domain and parameters for this problem are illustrated in Table 6.4. To reduce the effects of discretization on numerical simulation results, very fine, uniform mesh spacing ($\Delta r = 0.0198$ m) is chosen for the radial model domain, $r_w = 0.1\,\text{m} \leq r \leq R_1 = 10\,\text{m}$, which is discretized into 500 uniform grid blocks. The comparison between the numerical and analytical solutions is shown in Figure 6.20. Figure 6.20 indicates that the numerical results are in excellent agreement with the analytical solution of the displacement in the entire sweeping zone of the radial reservoir.

6.5.2 Numerical Simulation in a Linear Composite System

In this problem, flow in a linear composite system is considered. The parameters of fluid and two rocks are listed in Table 6.5. To reduce the

Table 6.4 Fluid and formation parameters for verification in a radial system

Parameters	Values	Unit
Porosity of domains, ϕ	0.25	[-]
Length of domains, R_1	10.0	[m]
Radius of injection well, r_w	0.10	[m]
Height of domain, h	1.00	[m]
Injection rate, q_t	1.0×10^{-4}	[m^3/s]
Water-phase viscosity, μ_w	1.0	[mPa·s]
Oil-phase viscosity, μ_o	5.0	[mPa·s]
Permeability of domains, k	9.869×10^{-14}	[m^2]
Initial water-phase saturation, S_{wc}	0.15	[-]
Residual oil saturation, S_{or}	0.15	[-]
Relative permeability parameters, $k_{rw,max}$	0.75	[-]
Relative permeability parameters, $k_{ro,max}$	0.75	[-]
Relative permeability parameters, n_w	2.00	[-]
Relative permeability parameters, n_o	2.00	[-]

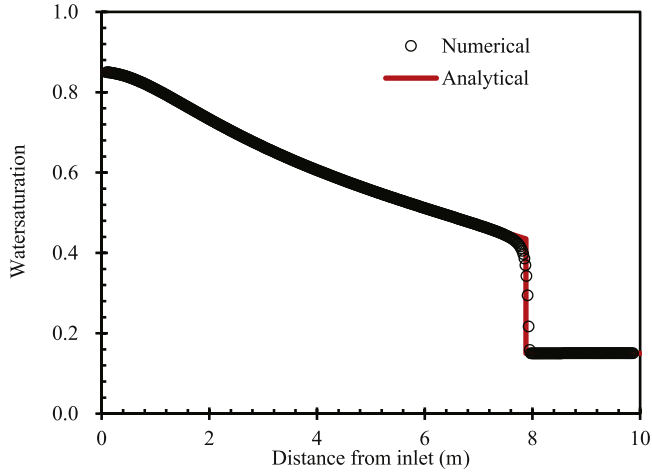

Figure 6.20 Comparison between analytical and numerical solutions after 2.23 days of injection.

effects of discretization on numerical simulation results, very fine, uniform mesh spacing ($\Delta x = 0.02$ m) is chosen, i.e., the model is discretized into 600 uniform grid blocks. The comparison between the numerical and analytical solutions is shown in Figure 6.21, which shows that the numerical results are an excellent match with the analytical solution of the displacement for the two-domain linear composite system.

Table 6.5 Parameters for immiscible displacement in a linear composite system

Parameters	Domain 1	Domain 2	Unit
Porosity of domains, ϕ	0.30	0.30	[-]
Permeability, k	1.0×10^{-13}	1.0×10^{-13}	[m^2]
Length of domains, L_1	6.0	6.0	[m]
Cross-sectional area, A	1.00	1.00	[m^2]
Injection rate, q_t	1.0×10^{-5}	–	[m^3/s]
Water phase viscosity, μ_w	1.0	1.0	[mPa·s]
Oil-phase viscosity, μ_o	5.0	5.0	[mPa·s]
Initial water-phase saturation, S_{wc}	0.20	0.15	[-]
Residual oil saturation, S_{or}	0.20	0.15	[-]
Relative permeability parameters, $k_{rw,max}$	0.80	0.75	[-]
Relative permeability parameters, $k_{ro,max}$	0.80	0.75	[-]
Relative permeability parameters, n_w	1.50	2.50	[-]
Relative permeability parameters, n_o	2.50	1.50	[-]

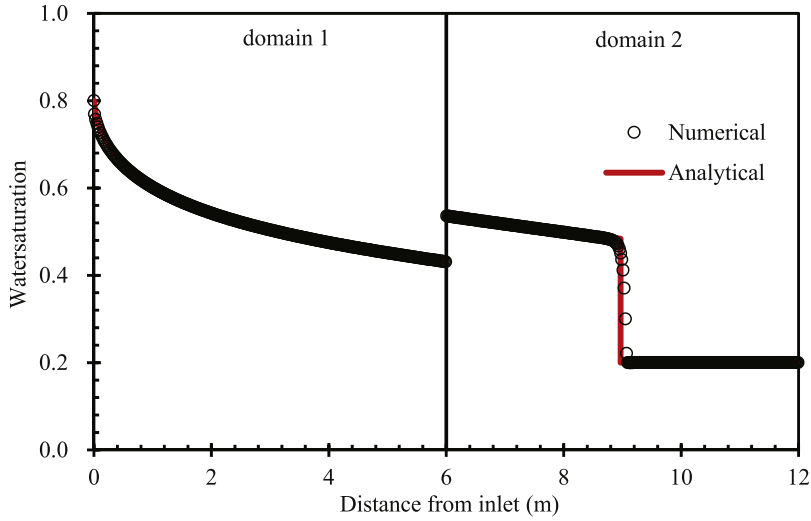

Figure 6.21 Comparison between analytical and numerical solutions after 1.0 day injection.

6.5.3 Numerical Simulation in a Radial Composite System

In this problem, flow in a radial composite system is considered. The parameters of fluid and two rocks are listed in Table 6.6. To reduce the effects of discretization on numerical simulation results, very fine, uniform

Table 6.6 Parameters for immiscible displacement simulation in a radial composite system

Parameters	Domain 1	Domain 2	Unit
Porosity of domains, ϕ	0.30	0.30	[-]
Permeability, k	1.0×10^{-13}	1.0×10^{-13}	[m^2]
Radius of domains, R	4.0	8.0	[m]
Radius of injection well, r_w	0.10	—	[m]
Reservoir thickness, h	1.00	1.00	[m^2]
Injection rate, q_t	2.5×10^{-4}	—	[m^3/s]
Water-phase viscosity, μ_w	1.0	1.0	[mPa·s]
Oil-phase viscosity, μ_o	5.0	5.0	[mPa·s]
Initial water-phase saturation, S_{wc}	0.20	0.20	[-]
Residual oil saturation, S_{or}	0.20	0.20	[-]
Relative permeability parameters, $k_{rw,max}$	0.75	0.80	[-]
Relative permeability parameters, $k_{ro,max}$	0.75	0.80	[-]
Relative permeability parameters, n_w	2.50	1.50	[-]
Relative permeability parameters, n_o	1.50	2.50	[-]

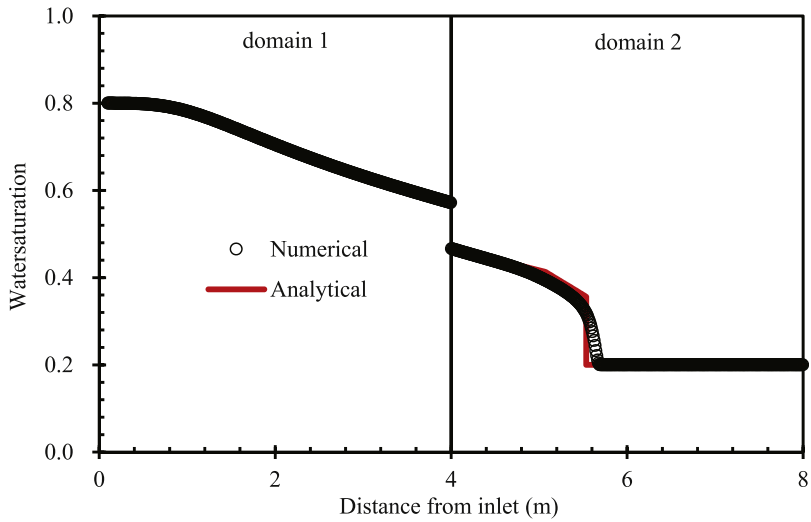

Figure 6.22 Comparison between analytical and numerical solutions after 0.463 day injection.

mesh spacing ($\Delta r = 0.01$ m) is chosen, i.e., the model is discretized into 790 uniform grid blocks. The comparison between the numerical and analytical solutions is shown in Figure 6.22, which also shows that the numerical results are in excellent agreement with the analytical solutions of the displacement for the radial composite sweeping system.

REFERENCES

Brooks, R.H., Corey, A.T., March, 1964. Hydraulic Properties of Porous Media. Hydrology Papers. Colorado State University.

Buckley, S.E., Leverett, M.C., 1942. Mechanism of fluid displacement in sands. Transactions of the AIME 146 (1), 107–116.

Willhite, G.P., 1986. Waterflooding. Society of Petroleum Engineers, Richardson, TX.

Wu, Y.-S., 1998. MSFLOW: Multiphase Subsurface Flow Model of Oil, Gas and Water in Porous and Fractured Media with Water Shut-off Capability, Documentation and User's Guide. Walnut Creek, Califonia.

Wu, Y.-S., Pruess, K., Chen, Z.-X., 1993. Buckley-Leverett flow in composite porous media. SPE Advanced Technology Series 1 (2), 36–42.

CHAPTER 7

Immiscible Displacement of Non-Newtonian Fluids

7.1 INTRODUCTION

Flow and displacement of non-Newtonian fluids through porous media occurs in many subsurface systems and has found applications in underground natural resource recovery and storage projects, as well as environmental remediation schemes. Previous studies on the flow of fluids through porous media were limited for the most part to Newtonian fluids (Muskat and Meres, 1936; Bear, 1972; Scheidegger, 1974). Since the 1950s, studies of non-Newtonian fluid flow through porous media have received a great deal of attention because of its important industrial applications, in petroleum industry, groundwater, and environmental problems (Savins, 1969; Wu, 1990). Considerable progress has been made in our understanding of single-phase porous flow behavior of non-Newtonian fluids through many quantitative and experimental studies in the past few decades (Wu and Pruess, 1996; Sochi, 2010). In comparison, however, the research on multiphase non-Newtonian fluid flow, either laboratory studies or numerical modeling approaches, has been lacking in the literature (Gleasure, 1990; Wu and Pruess, 1998; Yilmaz et al., 2009).

Many studies on the flow of non-Newtonian fluids in porous media have been conducted in chemical engineering, rheology, and petroleum engineering since the early 1960s. Because of the complexity of pore geometries in a porous medium, a macroscopic continuum flux law must be used to obtain meaningful insight into the physics of non-Newtonian flow in reservoirs. Some equivalent or apparent viscosities for non-Newtonian fluids are required in the modified Darcy flow equation. Therefore, many experimental and theoretical investigations have been conducted to determine rheological models or correlations of apparent viscosities with flow properties for a given non-Newtonian fluid as well as a given porous material. The viscosity of a non-Newtonian fluid depends upon the shear rate or the velocity gradient. However, it is practically impossible to determine the distribution of the shear rate in a microscopic

Multiphase Fluid Flow in Porous and Fractured Reservoirs
ISBN 978-0-12-803848-2
http://dx.doi.org/10.1016/B978-0-12-803848-2.00007-6

sense precisely within a porous medium, and the rheological models developed in fluid mechanics for non-Newtonian fluids cannot be applied directly to the flow in porous media. As a result, many laboratory studies were undertaken in an attempt to relate the rheological properties of a non-Newtonian fluid to the pore flow velocity of the fluid or the imposed pressure drop in a real core or in a packed porous medium to derive Darcy-scale relations (Gogarty, 1967; Savins, 1969; Pearson and Tardy, 2002; Sochi, 2010).

The subject of transient flow and displacement of non-Newtonian fluids in porous media is relatively new to many applications, starting from the late 1960s (van Poollen and Jargon, 1969). Pressure transient theory of flow of non-Newtonian, power-law fluids in porous media was developed by Ikoku and Ramey (1978) and Odeh and Yang (1979). Since then, new well-test analysis techniques of non-Newtonian flow have been improved for interpreting pressure data observed during injectivity and fall-off tests in reservoirs. The numerical modeling methods were also used for simulating power-law fluid flow by Gencer and Ikoku (1984) and Vongvuthipornchai and Raghavan (1987a,b). In some recent studies of non-Newtonian fluid flow (Wu, 1990; Wu et al., 1991, 1992), we developed and applied the Buckley–Leverett type of analytical solutions for analysis of multiphase non-Newtonian fluid flow in porous media.

The first portion of this chapter is devoted to discussion of non-Newtonian fluids and rheological models. Then following is a description of the governing equations for immiscible flow of non-Newtonian fluids. A Buckley–Leverett solution for displacement of Newtonian and non-Newtonian fluids is then presented. In the remainder of the chapter, we discuss and analyze displacement of a Newtonian fluid by a power-law non-Newtonian fluid, displacement of a Bingham non-Newtonian fluid by a Newtonian fluid, and immiscible displacement of non-Newtonian fluids in a radial system.

7.2 NON-NEWTONIAN FLUIDS AND RHEOLOGICAL MODELS

A Newtonian fluid is defined as a fluid the viscous stress for which is related to the shear rate (or velocity gradient) by the simpler linear equation,

$$\tau = \pm\mu \frac{\mathrm{d}u}{\mathrm{d}\gamma} \tag{7.1}$$

in which τ is shear stress; μ is called dynamic viscosity of a fluid, the measure of a fluid's ability to resist gradual deformation by shear or tensile stresses, which is a constant of proportionality for a Newtonian fluid; u is the velocity; du/dy is the strain or shear rate or velocity gradient perpendicular to the direction of shearing.

The viscosity μ of non-Newtonian fluids is no longer constant, but dependent on shear rate or velocity gradient. For flow through porous media, apparent viscosity functions for a non-Newtonian fluid in porous media depend on the pore velocity or the potential gradient in a complex way (Savins, 1969). The rheological correlations for different non-Newtonian fluids are quite different. Therefore, it is impossible to develop a general mathematical model or numerical scheme that can be universally applied to all non-Newtonian fluids. Instead, special treatment for a particular fluid of interest has to be worked out. Typical relationships of shear stress and shear rate for commonly encountered non-Newtonian fluids in porous media are shown in Figure 7.1. Some of the most often used or encountered non-Newtonian fluids in petroleum reservoirs, such as the power-law and Bingham plastic fluids, will be discussed in this chapter.

7.2.1 Power-Law Fluid

The power-law model is the most widely used in describing the rheological property of shear-thinning non-Newtonian fluids, such as polymer and

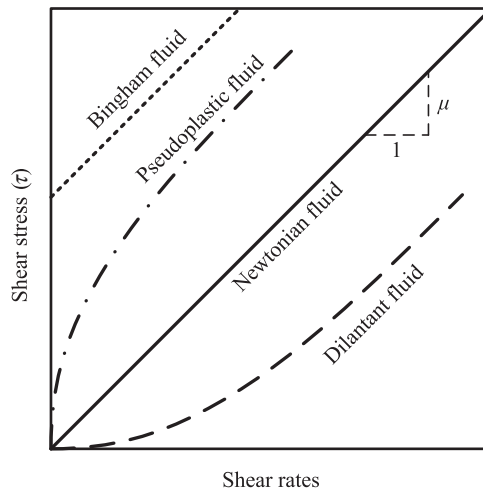

Figure 7.1 Typical shear stress and shear rate relationships for non-Newtonian fluids.

foam solutions, in porous-medium flow. Its multiphase extension (Wu et al., 1991)

$$\mu_{nn} = \mu_{eff}\left(\frac{kk_{rnn}}{\mu_{eff}}(|\nabla\Phi_{nn}|)\right)^{\frac{n-1}{n}} \tag{7.2}$$

in which k is the absolute permeability; k_{rnn} is the relative permeability of non-Newtonian fluid; subscript nn denotes a non-Newtonian fluid; n is the power-law index; $\nabla\Phi$ is flow potential gradient; and μ_{eff} is defined as

$$\mu_{eff} = \frac{H}{12}\left(9+\frac{3}{n}\right)^{n}\left[150kk_{rnn}\phi(S_{nn}-S_{nn,ir})\right]^{\frac{1-n}{2}} \tag{7.3}$$

in which H is a consistence parameter; S_{nn} is the non-Newtonian, power-law fluid saturation; and $S_{nn,ir}$ is irreducible saturation of the non-Newtonian phase. The two power-law parameters, n and H, are normally obtained from laboratory measurement and experimental data fitting.

The power index, n, ranges between 0 and 1 for a shear-thinning fluid, and the viscosity from Eqn (7.2) becomes infinite as the flow potential gradient tends to zero for a shear-thinning fluid. Therefore, direct use of Eqn (7.2) in the calculation will cause numerical difficulties in numerical simulation. Instead, a linear interpolation scheme is used when the potential gradient is very small. As shown in Figure 7.2, the viscosity for a small value of potential gradient is calculated by (Wu and Pruess, 1998)

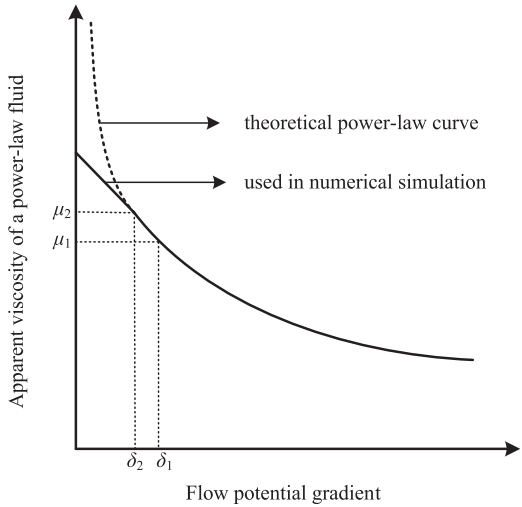

Figure 7.2 Schematic of linear interpolation of viscosities of power-law fluids with small flow potential gradient fluids.

$$\mu_{\text{nn}} = \mu_1 + \frac{\mu_1 - \mu_2}{\delta_1 - \delta_2}(|\nabla\Phi| - \delta_1) \tag{7.4}$$

for $|\nabla\Phi| \leq \delta_1$, in which the two interpolation parameters are δ_1, ($\sim$10 Pa/m) and δ_2 ($\delta_1 - \delta_2 = 10^{-7}$ Pa/m); and the values for μ_1 and μ_2 may be taken as (see Figure 7.2),

$$\mu_j = \mu_{\text{eff}}\left(\frac{k}{\mu_{\text{eff}}}\delta_j\right)^{\frac{n-1}{n}} \quad j = 1,\ 2 \tag{7.5}$$

7.2.2 Bingham Fluid

Instead of introducing an apparent viscosity for Bingham fluids, the following effective potential gradient approach has been proven more efficient numerically (Wu and Pruess, 1998). Using the effective potential gradient as illustrated by Figure 7.3, Darcy's law of Bingham flow (Wu et al., 1992) is described by

$$\boldsymbol{v} = -\frac{kk_{\text{rnn}}}{\mu_{\text{B}}}\nabla\Phi_{\text{e}} \tag{7.6}$$

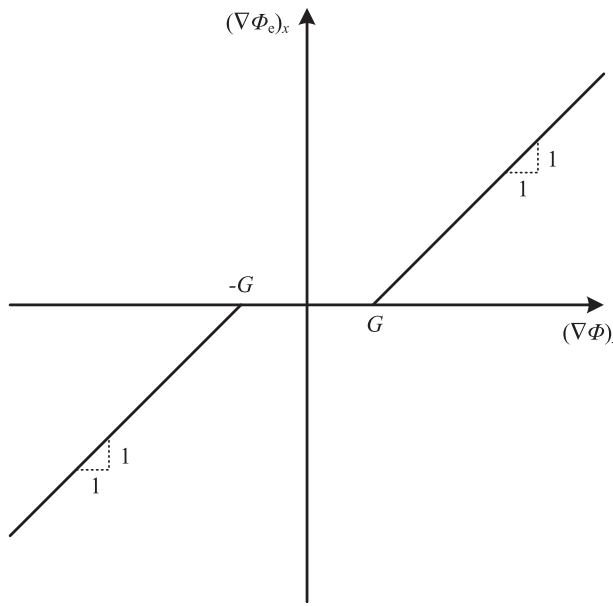

Figure 7.3 Effective potential gradient for Bingham fluids, dashed linear extension for numerical calculation of derivative fluids.

in which μ_B is the Bingham plastic viscosity coefficient and $\nabla\Phi_e$ is the effective potential gradient the scalar component for which in the x-direction, flow direction, is defined as

$$\begin{cases} (\nabla\Phi_e)_x = (\nabla\Phi)_x + G & \text{if } (\nabla\Phi)_x < -G \\ (\nabla\Phi_e)_x = 0 & \text{if } -G \le (\nabla\Phi)_x \le +G \\ (\nabla\Phi_e)_x = (\nabla\Phi)_x - G & \text{if } (\nabla\Phi)_x > +G \end{cases} \tag{7.7}$$

in which G (>0) is the minimum potential or threshold gradient of Bingham fluid flow.

7.3 FLOW GOVERNING EQUATIONS OF IMMISCIBLE FLOW OF NON-NEWTONIAN FLUIDS

The two-phase flow of non-Newtonian and Newtonian fluids is considered in a homogeneous and isotropic porous medium. There is no mass transfer between the non-Newtonian (nn) and Newtonian (ne) phases, and dispersion and adsorption on rock are also ignored. Then, the governing equations are given by

$$-\nabla\cdot(\rho_{ne}\boldsymbol{v}_{ne}) = \frac{\partial}{\partial t}(\rho_{ne}S_{ne}\phi) \tag{7.8}$$

for the Newtonian fluid, and

$$-\nabla\cdot(\rho_{nn}\boldsymbol{v}_{nn}) = \frac{\partial}{\partial t}(\rho_{nn}S_{nn}\phi) \tag{7.9}$$

for the non-Newtonian fluid. The Darcy velocities for the Newtonian and the non-Newtonian phase are described by a multiphase extension of Darcy's law as

$$\boldsymbol{v}_{ne} = -\frac{kk_{rne}}{\mu_{ne}}(\nabla P_{ne} - \rho_{ne}\boldsymbol{g}) \tag{7.10}$$

and

$$\boldsymbol{v}_{nn} = -\frac{kk_{rnn}}{\mu_{nn}}(\nabla P_{nn} - \rho_{nn}\boldsymbol{g}) \tag{7.11}$$

The pressures in the two phases are related by means of the capillary pressure,

$$P_c(S_{nn}) = P_{ne} - P_{nn} \tag{7.12}$$

The relative permeabilities, k_{rne}, k_{rnn}, and the capillary pressure P_c are assumed to be functions of saturation only. Also, from the definition of saturation, we have,

$$S_{ne} + S_{nn} = 1 \tag{7.13}$$

7.4 BUCKLEY–LEVERETT SOLUTION FOR DISPLACEMENT OF NEWTONIAN AND NON-NEWTONIAN FLUIDS

7.4.1 Buckley–Leverett Solution

For the derivation of the Buckley–Leverett analytical solution, the following assumptions similar to those used in the Buckley–Leverett solution are made (Wu et al., 1991).

- the two fluids and the porous medium are incompressible,
- the capillary-pressure gradient is negligible,
- the apparent viscosity of non-Newtonian fluids is a function of the flow potential and saturation as

$$\mu_{nn} = \mu_{nn}(S_{nn}, \nabla\Phi_{nn}) \tag{7.14}$$

in which $\nabla\Phi_{nn}$ is the flow potential gradient, a vector. Its component in the x coordinate is

$$\frac{\partial\Phi_{nn}}{\partial x} = \frac{\partial P}{\partial x} + \rho_{nn}\, g \sin\theta \tag{7.15}$$

By definition, the viscosity of a non-Newtonian fluid is a function of the shear rate. For flow through porous media, it has been shown that the shear rate depends only on the pore velocity for a given porous material (Gogarty, 1967). The pore velocity is determined by the local potential gradient and by the local saturation within the two-phase fluids. We assume that the apparent viscosity of the non-Newtonian fluid is described by Eqn (7.14) or Eqn (2.7) for multiple-phase flow, which should be determined by experiment for the non-Newtonian fluid and the porous medium of interest.

The flow system considered is a semi-infinite linear reservoir, shown in Figure 7.4. It is further assumed that gravity segregation is negligible and that stable displacement exists near the displacement front. Then, Eqns (7.8) and (7.9) become

$$-\frac{\partial v_{ne}}{\partial x} = \phi\frac{\partial S_{ne}}{\partial t} \tag{7.16}$$

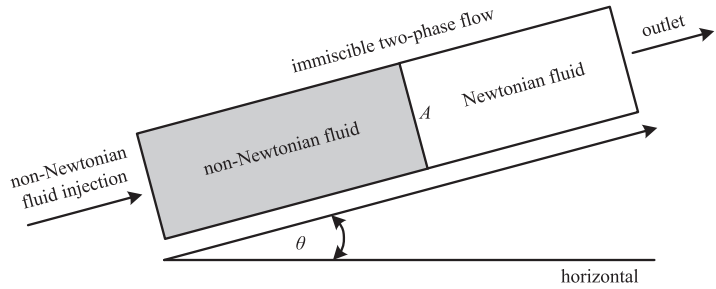

Figure 7.4 Schematic of displacement of a Newtonian fluid by a non-Newtonian fluid.

and

$$-\frac{\partial v_{\mathrm{nn}}}{\partial x} = \phi \frac{\partial S_{\mathrm{nn}}}{\partial t} \tag{7.17}$$

For the Newtonian phase, the flow rate is

$$v_{\mathrm{ne}} = -\frac{k k_{\mathrm{rne}}}{\mu_{\mathrm{ne}}} \left(\frac{\partial P}{\partial x} + \rho_{\mathrm{ne}}\, g \sin\theta \right) \tag{7.18}$$

and for the non-Newtonian phase, it is

$$v_{\mathrm{nn}} = -\frac{k k_{\mathrm{rnn}}}{\mu_{\mathrm{nn}}} \left(\frac{\partial P}{\partial x} + \rho_{\mathrm{nn}}\, g \sin\theta \right) \tag{7.19}$$

In analytical analysis and numerical simulation, we relate the flow velocity to the pressure gradient as is normally done in multiple-phase extension of Darcy flow, with all of the nonlinearities combined into an equivalent non-Newtonian viscosity (Wu et al., 1991). Thus, we write:

$$v_{\mathrm{nn}} = -\frac{k k_{\mathrm{rnn}}}{\mu_{\mathrm{nn}}} \frac{\partial \Phi_{\mathrm{nn}}}{\partial x} \tag{7.20}$$

This requires that the volumetric flux be equal to Eqn (7.20) for a power-law fluid flow, leading to:

$$\mu_{\mathrm{nn}}(S_{\mathrm{nn}}, \nabla\Phi_{\mathrm{nn}}) = \mu_{\mathrm{eff}} \left(\frac{k k_{\mathrm{rnn}}}{\mu_{\mathrm{eff}}} (|\nabla\Phi_{\mathrm{nn}}|) \right)^{1-\frac{1}{n}} \tag{7.21}$$

To complete the mathematical description, the initial and boundary conditions must be specified. Initially, a Newtonian fluid is at its maximum saturation in the system. Thus,

$$S_{\mathrm{ne}}(x, 0) = 1 - S_{\mathrm{nn,ir}} \tag{7.22}$$

in which $S_{nn,ir}$ is the initial immobile non-Newtonian fluid saturation. For practical field problems before injection of a non-Newtonian fluid, $S_{nn,ir}$ is usually zero before non-Newtonian fluid is injected, which can be treated as a special case. In this problem, we are concerned with continuously injecting a non-Newtonian fluid from the inlet $x = 0$, at a known rate, $q_t(t)$, which can be a function of injection time, t.

The boundary conditions at $x = 0$ are

$$v_{nn}(0, t) = v(t) = \frac{q_t}{A} \tag{7.23}$$

$$v_{ne}(0, t) = 0 \tag{7.24}$$

in which A is the cross-sectional area for flow. Finally, in a semi-infinite system, the following conditions must be imposed at $x \to \infty$

$$S_{ne} \to 1 - S_{nn,ir} \tag{7.25}$$

The governing Eqns (7.16) and (7.17), with the boundary and initial conditions of Eqns (7.22)–(7.25), can be solved to obtain the following solution using the fractional-flow concept (Wu et al., 1991),

$$f_{nn} = \frac{v_{nn}}{v_{nn} + v_{ne}} \tag{7.26}$$

and

$$\left.\frac{dx}{dt}\right|_{S_{nn}} = \left.\frac{q_t}{\phi A}\frac{\partial f_{nn}}{\partial S_{nn}}\right|_t \tag{7.27}$$

This is the frontal advance equation for the non-Newtonian displacement and it has the same form as the Buckley–Leverett equation. The difference, however, is the dependence of the fractional flow f_{nn} for the non-Newtonian displacement on saturation not only through the relative permeability, but also through the non-Newtonian phase viscosity, which is a function of both potential gradient and saturation. For a given time, a given injection rate, and given fluid and rock properties, the potential gradient can be shown to be a function of saturation only. Equation (7.27) shows that a particular non-Newtonian fluid saturation profile propagates through the porous medium at a constant velocity for a given time and injection rate.

As in the Buckley–Leverett theory, the saturation for a vanishing capillary-pressure gradient will, in general, become a triple-valued function of distance near the displacement front. Equation (7.27) will then fail to

describe the velocity of the shock saturation front, because $\partial f_{nn}/\partial S_{nn}$ does not exist on the front. Consideration of material balance across the shock front (Sheldon and Cardwell, 1959) provides the velocity of the front,

$$\left.\frac{dx}{dt}\right|_{S_{nn,f}} = \frac{q_t}{\phi A}\left.\frac{\partial f_{nn}}{\partial S_{nn}}\right|_{S_{nn,f}} = \frac{q_t}{\phi A}\left(\frac{f_{nn-} - f_{nn+}}{S_{nn-} - S_{nn+}}\right)_{S_{nn,f}} \tag{7.28}$$

in which $S_{nn,f}$ is the front saturation of the displacing non-Newtonian phase. The superscripts '+' and '−' refer to values ahead of and behind the shock, respectively.

The location x_{Snn} of any saturation S_{nn} traveling from the inlet can be determined by integrating Eqn (7.27) with respect to time, which yields

$$x_{S_{nn}} = \frac{W_i(t)}{A\phi}\left.\frac{\partial f_{nn}}{\partial S_{nn}}\right|_{S_{nn}} \tag{7.29}$$

in which $W_i(t)$ is the cumulative volume of injected fluid

$$W_i(t) = \int_0^t q_t(\tau)d\tau \tag{7.30}$$

A direct use of Eqn (7.29), given x and t, will result in a multiple-valued saturation distribution, which can be handled by a mass-balance calculation, as in the Buckley–Leverett solution, discussed in Section 5.4.

7.4.2 Graphical Evaluation Method

The fractional flow of the displacing non-Newtonian phase is a function of its saturation only, after taking into account the following constraint condition:

$$\frac{q_t}{A} + k\left[\frac{k_{rne}(S_{nn})}{\mu_{ne}} + \frac{k_{rnn}(S_{nn})}{\mu_{nn}}\right]\frac{\partial P}{\partial x} + k\left[\frac{\rho_{ne}k_{rne}(S_{nn})}{\mu_{ne}} + \frac{\rho_{nn}k_{rnn}(S_{nn})}{\mu_{nn}}\right]g\sin\theta = 0 \tag{7.31}$$

The Welge (1952) graphic method can be shown to be applicable to evaluation of non-Newtonian fluid displacement by an integration of the mass balance of injection into the system and incorporation of Eqn (7.29). The only additional constraint is the need to take into account the contribution of a velocity-dependent apparent viscosity of non-Newtonian fluids on the fractional-flow curve.

As discussed in Section 5.4, at the moving saturation front, we have

$$\left.\frac{df_{nn}}{dS_{nn}}\right|_{S_{nn,f}} = \left(\frac{f_{nn-} - f_{nn+}}{S_{nn-} - S_{nn+}}\right)_{S_{nn,f}} = \frac{f_{nn}|_{S_{nn,f}} - f_{nn}|_{S_{nn,ir}}}{S_{nn,f} - S_{nn,ir}} \tag{7.32}$$

and the average saturation in the displaced zone is given by

$$\left.\frac{df_{nn}}{dS_{nn}}\right|_{S_{nn,f}} = \frac{1}{\overline{S}_{nn} - S_{nn,ir}} \tag{7.33}$$

in which $\overline{S}_{nn}$ is the average saturation of the non-Newtonian phase in the swept zone. To satisfy Eqns (7.32) and (7.33), a simple geometric construction can be used (see Figure 7.5).

On a curve of fractional flow f_{nn} versus saturation S_{nn} (Figure 7.5), draw the tangent to the fractional-flow curve, from the point $(S_{nn} = S_{nn,ir},\ f_{nn} = 0)$. The point of tangency has coordinates $(S_{nn} = S_{nn,f},\ f_{nn} = f_{nn}|_{Snn,f})$, and the extrapolated tangent must intercept the line $f_{nn} = 1$ at the point $(S_{nn} = \overline{S}_{nn}, f_{nn} = 1)$. Therefore, the graphic method of Welge can also be applied if the fractional-flow curves are provided for the non-Newtonian displacement process. The only difference is in the determination of the non-Newtonian fractional-flow curve, because we have to include the effects of the apparent viscosity of

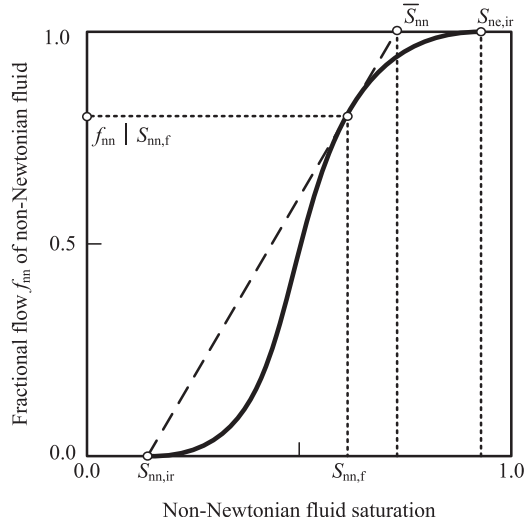

Figure 7.5 Method of determining shock front and average displacing non-Newtonian phase saturations from fractional-flow curve.

non-Newtonian fluids, which are also a function of saturation under the Buckley–Leverett flow condition.

Given relative permeability data and the rheological model μ_{nn}, the general procedure for evaluating the flow behavior of non-Newtonian one-dimensional linear displacement is as follows:

1. Solve pressure gradients $(-\partial P/\partial x)$ from Eqn (7.31) for different injection rates and plot the relationship between pressure gradient and saturation corresponding to the injection rate, as shown in Figure 7.6.
2. Calculate the fractional flow, f_{nn}, by the fractional function, Eqn (7.26) or (7.34), using the pressure gradients, from Figure 7.6, to calculate the corresponding potential gradients, then, use Eqn (7.21) or (7.35) to compute the non-Newtonian phase viscosity. An example of fractional-flow curves is shown in Figure 7.7

$$f_{nn} = \frac{1}{1 + \frac{k_{rne}}{\mu_{ne}} \frac{\mu_{nn}}{k_{rnn}}} + \frac{\frac{k k_{rne}}{\mu_{ne} q_t(t)} (\rho_{ne} - \rho_{nn}) g \sin\theta}{1 + \frac{k_{rne}}{\mu_{ne}} \frac{\mu_{nn}}{k_{rnn}}} \tag{7.34}$$

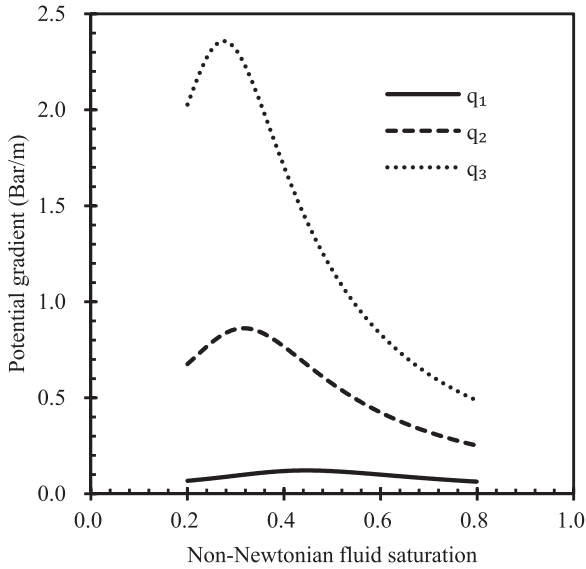

Figure 7.6 Pressure gradients versus non-Newtonian phase saturation for different injection rates.

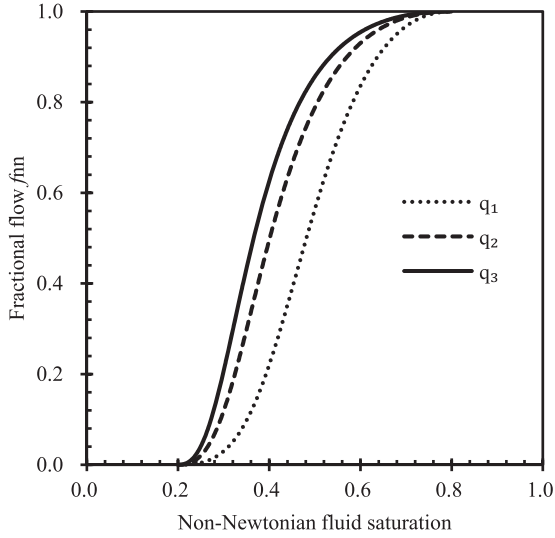

Figure 7.7 Fractional-flow curves of non-Newtonian fluids for different injection rates.

and

$$\mu_{nn}\left(S_{nn}, \frac{\partial \Phi}{\partial x}\right) = \mu_{eff}\left[\frac{k k_{rnn}(S_{nn})}{\mu_{eff}}\left(-\frac{\partial \Phi}{\partial x}\right)\right]^{1-\frac{1}{n}} \tag{7.35}$$

3. Calculate the derivatives of fractional flow, $\partial f_{nn}/\partial S_{nn}$, numerically, with respect to saturation from Figure 7.6. These are shown in Figure 7.8.
4. Determine the shock-front saturation from Figure 7.7, as illustrated in Figure 7.5.
5. Calculate the saturation profile for $S_{nn,f} < S_{nn} < 1 - S_{ne,ir}$ from $x = 0$ to $x = x_{Snn,f}$ according to Eqn (7.29) for a given injection rate and using the corresponding derivatives of fractional-flow curves from Figure 7.8. This profile is shown in Figure 7.9.
6. Determine the average saturation in the swept zone from Figure 7.7, as illustrated in Figure 7.5. This can be used to calculate the cumulative Newtonian fluid displaced, N_p,

$$N_p = A\phi x_{S_{nn,f}}\left(\overline{S}_{nn} - S_{nn,ir}\right) \tag{7.36}$$

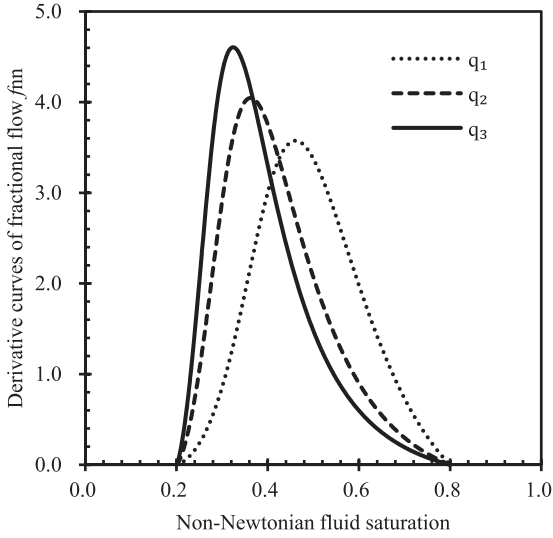

Figure 7.8 Derivatives of fractional flow with respect to non-Newtonian phase saturation for different injection rates.

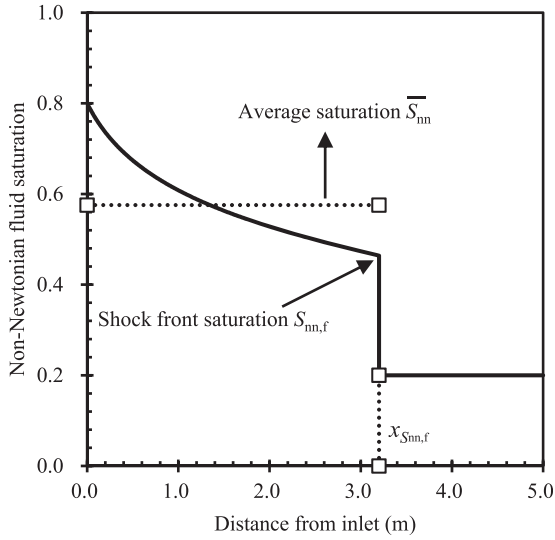

Figure 7.9 Saturation distributions of non-Newtonian fluids in the system at a given injection time.

7.5 DISPLACEMENT OF A NEWTONIAN FLUID BY A POWER-LAW NON-NEWTONIAN FLUID

For a given operating condition, non-Newtonian fluid displacement in porous media is controlled not only by relative permeability effects, as in the case of Newtonian fluid displacement, but also by the non-Newtonian fluid rheological properties. Some fundamental behavior of power-law non-Newtonian fluid displacement will be discussed in this section by using results from the analytical solution. The solution evaluation procedure, as discussed above, is computer programmed for the analysis (Appendix C.1).

For horizontal displacement of Newtonian fluids in porous media, based on the Buckley–Leverett solution, the injection rate has no effect on displacement efficiency or sweep efficiency. When a non-Newtonian fluid is involved, however, changes in the injection rate will result in changes in the pore velocity, which will in turn affect the viscosity of the non-Newtonian phase and fractional-flow curves, impacting displacement efficiency. The effect of injection rates for non-Newtonian fluid displacement can be revealed by the analytical solution.

Here, the example of interest is a one-dimensional linear flow problem of incompressible two-phase fluids in a one-dimensional, semi-infinite, horizontal homogeneous and isotropic porous medium with a unit cross-sectional area. A constant injection rate of a power-law fluid is maintained at the inlet ($x = 0$) from time $t = 0$. The properties of rock and fluids used are given in Table 7.1. The aqueous phase is treated as a displacing, power-law fluid and oil is treated as a displaced, Newtonian fluid for the problem. The relative permeability curve is shown in Figure 7.10, which is described in Section 5.4.3. Capillary effects are assumed to be negligible.

7.5.1 Effects of Injection Rate

Figure 7.11 gives non-Newtonian viscosity versus saturation curves for three different injection rates in a semi-infinite linear horizontal system. Considering the constraint condition, Eqn (7.31), the viscosity of non-Newtonian fluids depends only on the non-Newtonian phase saturation. The resulting saturation profiles corresponding to the injection rates are shown in Figure 7.12. The horizontal lines are the average saturations in the swept zone, which reflect the sweep efficiency. Because the only varying parameter in this calculation is the injection rate, the saturation distributions in Figure 7.12 indicate that injection rate has a significant effect on displacement. For a displacement process with this type of a shear-thinning fluid, the lower the injection rate, the higher the displacement efficiency becomes, because of higher viscosity of the displacing fluid.

Table 7.1 Fluid and rock parameters

Parameters	Value	Unit
Porosity, ϕ	0.20	[-]
Absolute permeability, k	9.869×10^{-13}	[m^2]
Cross-section area, A	1.0	[m^2]
Length of formation, L	10.0	[m]
Injection rate, q_t	1.0×10^{-5}	[m^3/s]
Injection time, t	10.0	[h]
Viscosity of Newtonian fluid, μ_{ne}	5.0×10^{-3}	[Pa·s]
Power-index, n	0.5	[-]
Consistency of power-law fluid, H	0.01	[Pa·s^n]
Residual Newtonian fluid saturation, $S_{ne,ir}$	0.20	[-]
Residual non-Newtonian fluid saturation, $S_{nn,ir}$	0.00	[-]
Maximum relative permeability, $k_{rne,max}$	0.75	[-]
Maximum relative permeability, $k_{rnn,max}$	0.75	[-]
Power index of relative permeability, n_{ne}	2.0	[-]
Power index of relative permeability, n_{nn}	2.0	[-]
Density of Newtonian fluid, ρ_{ne}	1000	[kg/m^3]
Density of non-Newtonian fluid, ρ_{nn}	800	[kg/m^3]
Directional angle, θ	0	[rad]

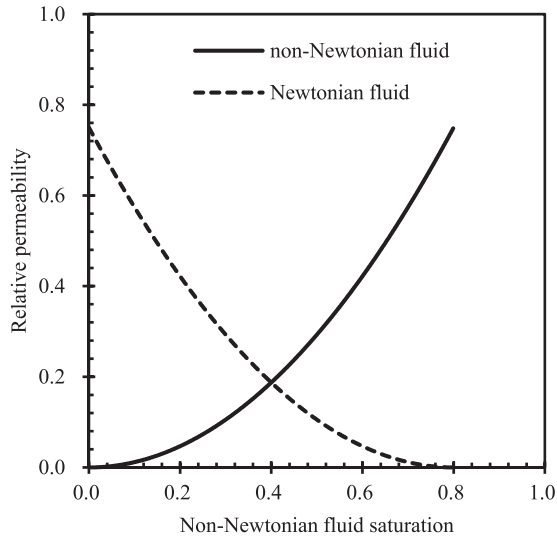

Figure 7.10 Relative permeability curves used in Section 7.5.

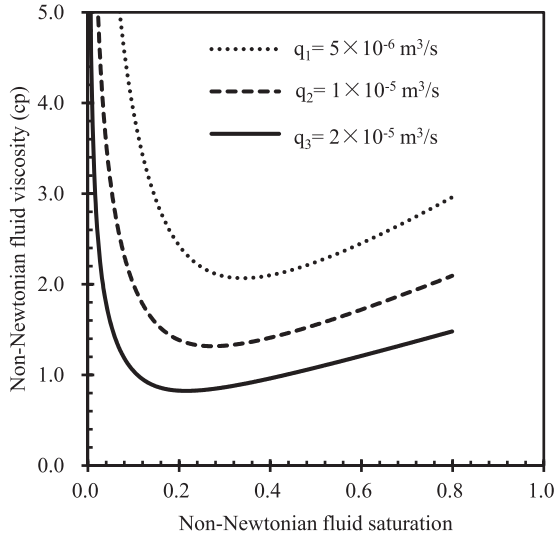

Figure 7.11 Non-Newtonian fluid apparent viscosities versus non-Newtonian fluid saturation for different injection rates.

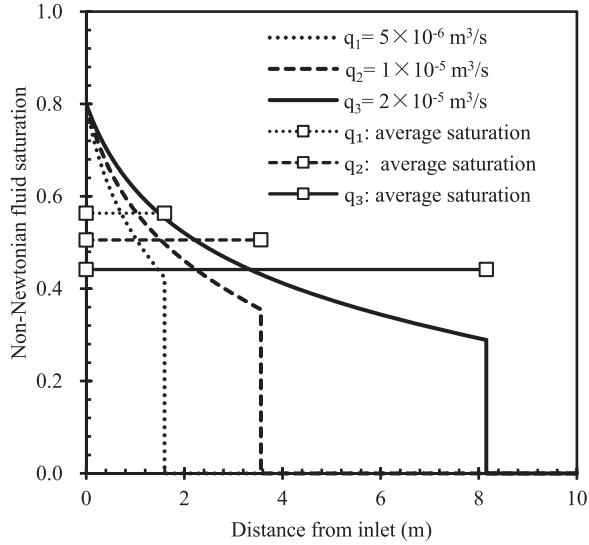

Figure 7.12 Non-Newtonian fluid saturation profiles for different injection rates after 10-h injection.

7.5.2 Effects of Power-Law Index, *n*

There are two parameters that characterize the flow behavior of a power-law fluid, which are exponential index, n, and consistency coefficient, H. For a pseudoplastic fluid, $0 < n < 1$ if $n = 1$, the fluid becomes Newtonian. The effect of the power-law index, n, on linear horizontal displacement can be quite significant. Figure 7.13(a) shows that pressure gradients are changed tremendously as a function of saturation for different values of n. The apparent viscosities of several non-Newtonian fluids are given in Figure 7.13(b), and the resulting fractional-flow curves are shown in Figure 7.13(c). Saturation profiles after a 10-h injection period in the system are plotted in Figure 7.13(d). Note the significant differences also in sweep

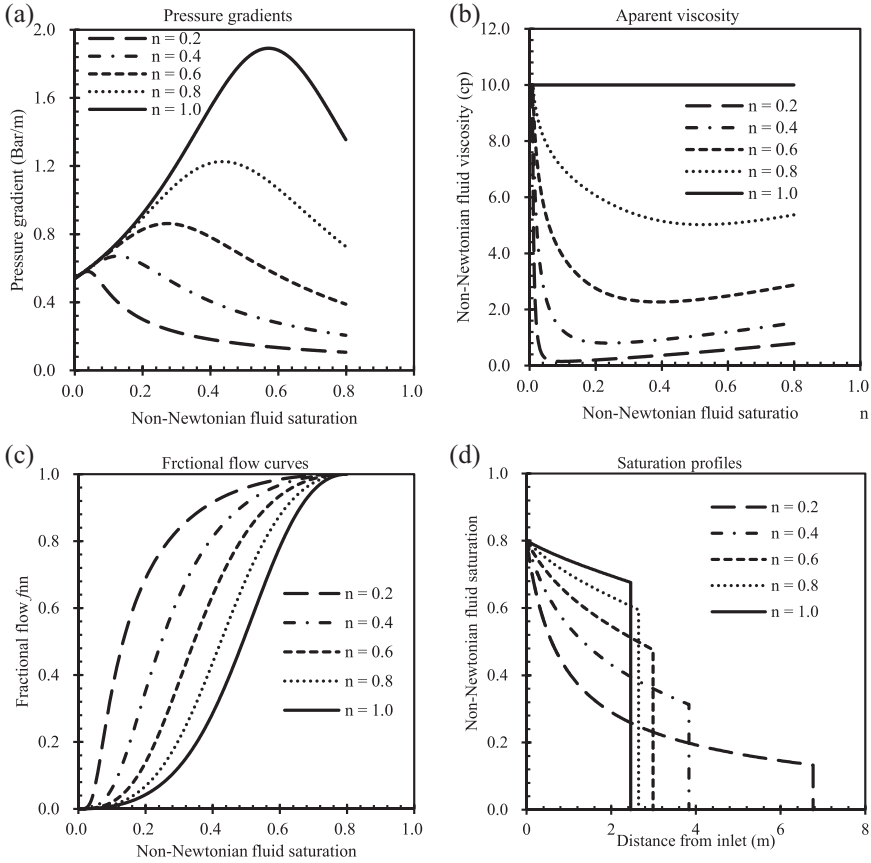

Figure 7.13 (a) Effects of the power-law index on pressure gradients; (b) non-Newtonian fluid viscosities; (c) fractional-flow curves; and (d) and non-Newtonian fluid saturation profiles.

efficiency. Here, the fluid and rock properties are summarized in Table 7.1, except the viscosity of Newtonian fluid, $\mu_{ne} = 4.0$ cp.

Because the power-law index, n, is usually determined from an experiment or from well-testing analysis, some errors cannot be avoided in determined values of n. These results in Figure 7.13 show how difficult it will be to use a numerical code to match experimental data from non-Newtonian displacement investigations in the laboratory, because of the extreme sensitivity of the core saturation distribution to n. The sensitivity of the displacement behavior to the power index, n, suggests that in determining the index n, it may be helpful to match experimental saturation profiles using the analytical solution.

7.5.3 Effects of Gravity

It is expected that gravity may have more significant effects on non-Newtonian displacement than on Newtonian displacement, because it influences mobility by affecting the non-Newtonian phase viscosity, in addition to the effect on the potential gradient as in Newtonian displacement. This can be demonstrated by the following example. A power-law

Table 7.2 Fluid and rock parameters

Parameters	Value	Unit
Porosity, ϕ	0.20	[-]
Absolute permeability, k	9.869×10^{-13}	[m^2]
Cross-section area, A	1.0	[m^2]
Length of formation, L	1.0	[m]
Injection rate, q_t	1.0×10^{-5}	[m^3/s]
Injection time, t	1.5	[h]
Viscosity of Newtonian fluid, μ_{ne}	1.0×10^{-3}	[Pa·s]
Power-index, n	0.4	[-]
Consistency of power-law fluid, H	1.5×10^{-3}	[$Pa \cdot s^n$]
Residual Newtonian fluid saturation, $S_{ne,ir}$	0.20	[-]
Residual non-Newtonian fluid saturation, $S_{nn,ir}$	0.00	[-]
Maximum relative permeability, $k_{rnn,max}$	0.75	[-]
Maximum relative permeability, $k_{rne,max}$	0.75	[-]
Power index of relative permeability, n_{ne}	2.0	[-]
Power index of relative permeability, n_{nn}	2.0	[-]
Density of Newtonian fluid, ρ_{ne}	1000	[kg/m^3]
Density of non-Newtonian fluid, ρ_{nn}	200	[kg/m^3]
Directional angle, θ	$\pi/2$, 0, $-\pi/2$	[rad]

non-Newtonian fluid is injected upward ($\theta = \pi/2$), horizontally ($\theta = 0$), and downward ($\theta = -\pi/2$), to displace a heavier *in situ* Newtonian fluid (see Table 7.2).

The fractional-flow curves are given in Figure 7.14(a). Because counter-flow may occur physically at very low or very high displacing-phase saturations under gravity effects, we will have the situations theoretically that $f_{nn} > 1$ for upward flow and $f_{nn} < 0$ for downward flow. The final saturation distributions in Figure 7.14(b) show the significance of effects of the gravity on non-Newtonian displacement in porous media. Injection of a lighter now-Newtonian fluid (such as foam in this case) from the top of the flow system has much better displacement efficiency than that injected from the bottom because of the effect of the gravity.

7.5.4 Verification for Numerical Simulations

A numerical reservoir simulator of MSFLOW (Wu, 1998, 2004) has implemented several commonly used rheological models, e.g., Eqn (7.2), for modeling multiple-phase flow of non-Newtonian and Newtonian fluids in porous media under a wide range of operating conditions. We have programmed an apparent non-Newtonian viscosity, given by Eqn (7.4), into the simulator for modeling a power-law fluid flow. The validity of the numerical formulation and results from this code has been tested for immiscible displacement of a Newtonian fluid by a power-law, non-Newtonian fluid by comparison with the Buckley–Leverett type solution obtained above.

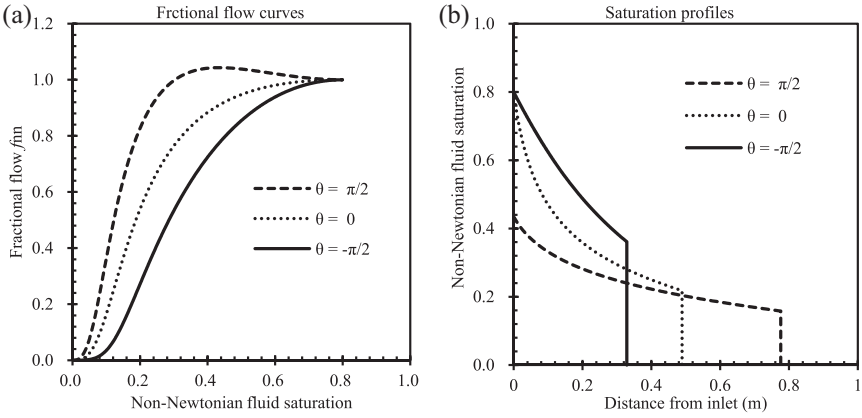

Figure 7.14 Effects of gravity on fractional-flow curves and displacement efficiency.

The properties of rock and fluids used are given in Table 7.3 for the two numerical tests. The aqueous phase was treated as a displacing, power-law fluid and oil was treated as the displaced, Newtonian fluid for the problem. To reduce effects of grid discretization in a finite system of the numerical model, very fine mesh spacing ($\Delta x = 0.01$ m) is chosen. A one-dimensional 5-m linear domain is discretized into 500 one-dimensional uniform grid blocks.

A comparison of the saturation profiles from the numerical and analytical calculations after 10 h of non-Newtonian fluid injection into the system for the two testing cases is given in Figure 7.15. This shows that the

Table 7.3 Fluid and rock parameters

Parameters	Numerical test 1	Numerical test 2	Unit
Porosity, ϕ	0.30	0.20	[-]
Absolute permeability, k	9.869×10^{-13}	9.869×10^{-13}	[m^2]
Cross-section area, A	1.0	1.0	[m^2]
Length of formation, L	5.0	5.0	[m]
Injection rate, q_t	1.0×10^{-5}	1.0×10^{-4}	[m^3/s]
Injection time, t	10.0	10.0	[h]
Viscosity of Newtonian fluid, μ_{ne}	5.0×10^{-3}	6.0×10^{-3}	[Pa·s]
Power-index, n	0.5	0.6	[-]
Consistency of power-law fluid, H	1.0×10^{-2}	1.0×10^{-2}	[Pa·s^n]
Residual Newtonian fluid saturation, $S_{ne,ir}$	0.20	0.15	[-]
Residual non-Newtonian fluid saturation, $S_{nn,ir}$	0.20	0.15	[-]
Maximum relative permeability, $k_{rnn,max}$	0.75	0.85	[-]
Maximum relative permeability, $k_{rne,max}$	0.75	0.85	[-]
Power index of relative permeability, n_{ne}	2.0	3.0	[-]
Power index of relative permeability, n_{nn}	2.0	3.0	[-]
Density of Newtonian fluid, ρ_{ne}	1000	1000	[kg/m^3]
Density of non-Newtonian fluid, ρ_{nn}	800	800	[kg/m^3]
Directional angle, θ	0	0	[rad]

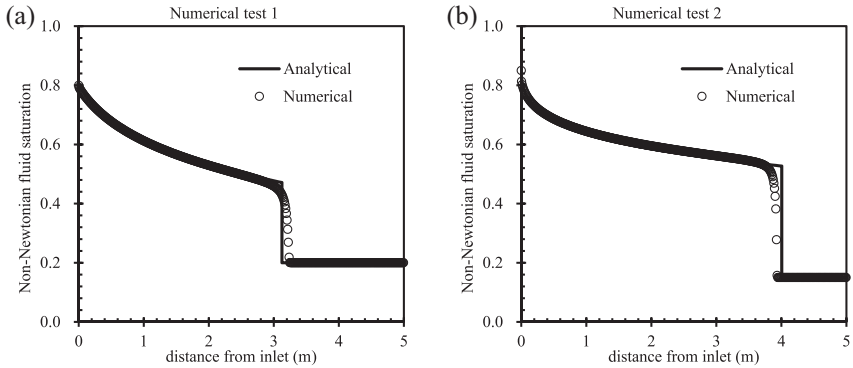

Figure 7.15 Comparison of saturation profiles calculated from analytical and numerical solutions after 10-h injection.

numerical results are in excellent agreement with the analytical prediction. Only at the shock advancing saturation front does the numerical solution deviate somewhat from the analytical solution, which is a typical 'smearing front' effect from numerical dispersion there (Aziz and Settari, 1979). Considering the complexity introduced when non-Newtonian fluids are involved in a multiple-phase flow problem, Figure 7.15 provides a very encouraging indication that the numerical model is correct in describing the multiple-phase immiscible displacement of non-Newtonian and Newtonian fluid flow in porous media.

7.6 DISPLACEMENT OF A BINGHAM NON-NEWTONIAN FLUID BY A NEWTONIAN FLUID

In an effort to obtain some insights into the physics behind two-phase immiscible displacement with Bingham, non-Newtonian fluids, we use the Buckley–Leverett analytical solution, Eqn (7.27), to study the displacement of a Bingham non-Newtonian fluid by a Newtonian fluid. One possible application of this study is the production of heavy oil by waterflooding. Note that because of the one-dimensional approximation in our analysis, we cannot address issues of viscous or gravitational instabilities.

The analytical solution, Eqn (7.27), obtained for immiscible non-Newtonian fluid displacement is in the same form as the Buckley–Leverett frontal-advance equation. The crucial difference is in the fractional-flow function, which now depends, not only on relative permeability data, but also, through apparent or effective or apparent viscosities, on the rheological

properties of the non-Newtonian fluid. This feature introduces strong rate dependence into the displacement process. Here, we are dealing with two fluids, water as the displacing Newtonian fluid and oil as the displaced Bingham non-Newtonian fluid. The fractional-flow function of the displacing Newtonian fluid is (Willhite, 1986; Wu et al., 1992)

$$f_{ne} = \frac{1}{1 + \frac{k_{rnn}(S_{ne})}{k_{rne}(S_{ne})}\frac{\mu_{ne}}{\mu_{nn}}} + \frac{\frac{Akk_{rnn}(S_{ne})}{\mu_{nn}q_t(t)}(\rho_{nn} - \rho_{ne})g\sin\theta}{1 + \frac{k_{rnn}(S_{ne})}{k_{rne}(S_{ne})}\frac{\mu_{ne}}{\mu_{nn}}} \tag{7.37}$$

in which μ_{nn} is the apparent viscosity of the Bingham non-Newtonian fluid of oil as a function of saturation and flow potential gradient

$$\mu_{nn} = \mu_{nn}(\nabla\Phi_{nn}, S_{ne}) \tag{7.38}$$

Similarly to power-law fluid displacement, Eqns (7.37) and (7.38) indicate that the fractional flow of the displacing Newtonian phase, f_{ne}, is generally a function of both saturation and potential gradient. Under the same simplifications made in the Buckley–Leverett solution (i.e., incompressible one-dimensional linear flow and uniform fluid and formation properties), the potential gradient is also related uniquely to saturation as in Eqn (7.31) (Wu et al., 1991, 1992). Therefore, the fractional-flow function in Eqn (7.37) ends up being a function of saturation only, and the Welge graphic method can be applied for evaluation of Bingham non-Newtonian fluid displacement in this case (Wu et al., 1992).

The rheological model for the apparent viscosity of a Bingham plastic fluid is follows:

$$\mu_{nn} = \begin{cases} \dfrac{\mu_B}{1 - \frac{G}{|\partial\Phi/\partial x|}}, & |\partial\Phi/\partial x| > G \\ \infty \quad , & |\partial\Phi/\partial x| \le G \end{cases} \tag{7.39}$$

For a particular saturation of the Newtonian phase, S_{ne}, the corresponding flow potential gradient for the non-Newtonian phase can be derived by introducing Eqn (7.39) into Eqn (7.31) as follows:

$$-\left.\frac{\partial\Phi}{\partial x}\right|_{S_{ne}} = -\rho_{nn}g\sin\theta + \frac{\frac{q_t}{Ak} + \frac{k_{rnn}}{\mu_B}G + \left(\frac{k_{rne}}{\mu_{ne}}\rho_{ne} + \frac{k_{rnn}}{\mu_B}\rho_{nn}\right)g\sin\theta}{\frac{k_{rne}}{\mu_{ne}} + \frac{k_{rnn}}{\mu_B}} \tag{7.40}$$

The apparent viscosity for the Bingham fluid is determined by introducing Eqn (7.40) into Eqn (7.39).

7.6.1 Effects of Minimum Pressure Gradient and Bingham Plastic Coefficients

This analysis concerns a scenario of heavy-oil displacement by waterflooding. Initially, the system is assumed to be saturated with only a Bingham fluid or heavy oil, and a Newtonian fluid (water) is injected at a constant volumetric rate at the inlet, $x = 0$, starting from $t = 0$. The fluid and formation parameters are listed in Table 7.4. The relative permeabilities are given as functions of saturation of the displacing Newtonian fluid, which is described in Section 5.4.3, and capillary effects are assumed to be negligible. The solution evaluation procedure, as discussed above, is computer programmed for the analysis (Appendix C.2).

A basic feature of the displacement process of a Bingham fluid in porous media is the existence of an ultimate or maximum displacement saturation, S_{max}, for the displacing Newtonian phase (see Figure 7.16). The maximum-displacement saturation occurs at the point of the fractional-flow curve in which $f_{ne} = 1.0$. For this particular displacement system, initially saturated with only the Bingham fluid, the displacing saturation cannot exceed the maximum value $S_{ne,max}$.

Table 7.4 Fluid and rock parameters

Parameters	Value	Unit
Porosity, ϕ	0.20	[-]
Absolute permeability, k	9.869×10^{-13}	[m^2]
Cross-section area, A	1.0	[m^2]
Length of formation, L	10.0	[m]
Injection rate, q_t	2.0×10^{-6}	[m^3/s]
Injection time, t	10.0	[h]
Viscosity of Newtonian fluid, μ_{ne}	1.0×10^{-3}	[Pa·s]
Bingham plastic coefficient, μ_B	4.0×10^{-3}	[Pa·s]
Residual Newtonian fluid saturation, $S_{ne,ir}$	0.00	[-]
Residual Bingham fluid saturation, $S_{nn,ir}$	0.20	[-]
Maximum relative permeability, $k_{rne,max}$	0.75	[-]
Maximum relative permeability, $k_{rnn,max}$	0.75	[-]
Power index of relative permeability, n_{ne}	2.0	[-]
Power index of relative permeability, n_{nn}	2.0	[-]
Density of Newtonian fluid, ρ_{ne}	1000	[kg/m^3]
Density of non-Newtonian fluid, ρ_{nn}	800	[kg/m^3]
Directional angle, θ	0	[rad]

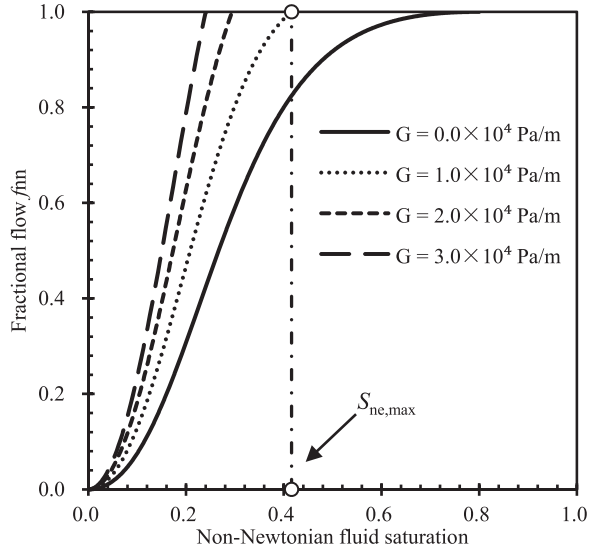

Figure 7.16 Fractional-flow curves for a Bingham fluid displaced by a Newtonian fluid for different minimum pressure gradient.

The resulting saturation distributions after 10-h water injection are given in Figure 7.17 for different minimum potential gradient, G. It is obvious that the sweep efficiency decreases rapidly as G increases. In contrast, for Newtonian displacement, the ultimate saturation of the displacing fluid is equal to the total mobile saturation of the displacing fluid, as shown by the curve for $G = 0$ in Figure 7.17.

Physically, the phenomenon of the ultimate displacement saturation occurs as the flow potential gradient approaches the minimum threshold pressure gradient, G, at which the apparent viscosity is infinite. Then the only flowing phase is the displacing Newtonian fluid. Consequently, once the maximum saturation is reached for a flow system, no further improvement of sweep efficiency can be obtained no matter how long the displacement process continues, as shown in Figure 7.17. The flow condition in reservoirs is more complicated than in this linear 1-D semi-infinite system. Because oil wells usually are drilled according to certain patterns, some regions always exist with low potential gradients between production and injection wells. The presence of the ultimate displacement saturation for a Bingham fluid indicates that no oil can be driven out of these regions. Therefore, the ultimate displacement saturation phenomenon will contribute to the low oil recovery as observed in heavy-oil reservoirs developed by waterflooding, in addition to effects from the high oil viscosity.

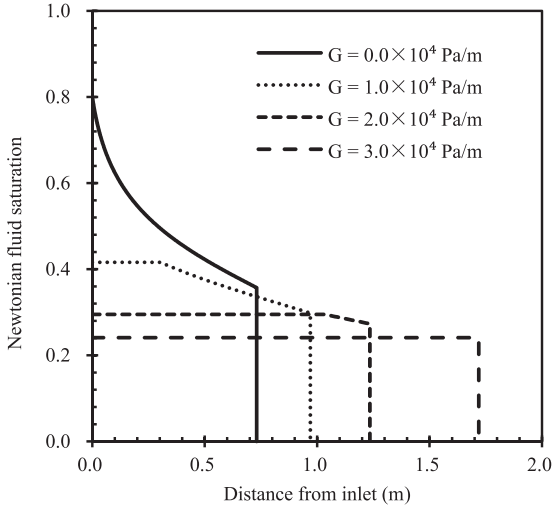

Figure 7.17 Newtonian phase saturation distribution for different values of the minimum pressure gradient of a Bingham fluid.

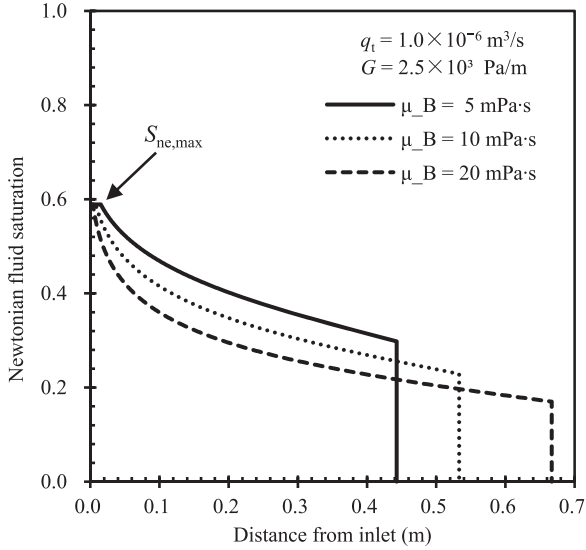

Figure 7.18 Newtonian fluid saturation distributions for different Bingham coefficient μ_B.

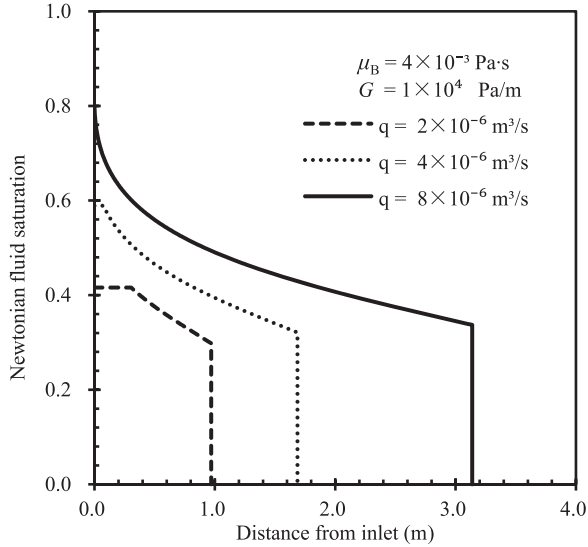

Figure 7.19 Newtonian phase saturation distribution for different injection rates of a Newtonian fluid displacing a Bingham fluid.

Figure 7.18 shows the effects of the other rheological parameter, the Bingham plastic coefficient, μ_B. Note that the ultimate displacement saturations change also with μ_B. The average saturations in the swept zones, however, are quite different for different values of μ_B. The ultimate displacement saturation, however, is essentially determined by G, not by μ_B. Changes in μ_B have insignificant effect on the ultimate displacement saturation, because the flow potential gradient in Eqn (7.39) hardly varies with μ_B as $\partial P/\partial x \rightarrow G$.

7.6.2 Effects of Injection Rate

In this analysis, a Bingham fluid in a horizontal porous medium is also displaced by water, a Newtonian fluid. If the water injection rate at the inlet is increased, the pressure gradient in the system will increase and the apparent viscosity for the displaced Bingham fluid will be reduced. Therefore, a better sweep efficiency will result. Figure 7.19 presents the saturation profiles after 10 h of injection at the different rates. Note that both the sweep efficiency and the ultimate displacement saturation can be increased greatly by increasing the injection rate (see Table 7.5).

Table 7.5 Fluid and rock parameters

Parameters	Value	Unit
Porosity, ϕ	0.20	[-]
Absolute permeability, k	9.869×10^{-13}	[m^2]
Cross-section area, A	1.0	[m^2]
Length of formation, L	1.0	[m]
Injection rate, q_t	1.0×10^{-6}	[m^3/s]
Injection time, t	10.0	[h]
Viscosity of Newtonian fluid, μ_{ne}	1.0×10^{-3}	[Pa·s]
Bingham plastic coefficient, μ_B	1.0×10^{-2}	[Pa·s]
Minimum threshold pressure gradient, G	5.0×10^{3}	[Pa/m]
Residual Newtonian fluid saturation, $S_{ne,ir}$	0.00	[-]
Residual Bingham fluid saturation, $S_{nn,ir}$	0.20	[-]
Maximum relative permeability, $k_{rne,max}$	0.75	[-]
Maximum relative permeability, $k_{rnn,max}$	0.75	[-]
Power index of relative permeability, n_{ne}	2.0	[-]
Power index of relative permeability, n_{nn}	2.0	[-]
Density of Newtonian fluid, ρ_{ne}	1000	[kg/m^3]
Density of non-Newtonian fluid, ρ_{nn}	850	[kg/m^3]
Directional angle, θ	$\pi/2$, 0, $-\pi/2$	[rad]

7.6.3 Effects of Gravity

The effects of gravity on Bingham-fluid displacement by a Newtonian fluid can be examined by considering the following example. A heavier Newtonian fluid with $\rho_{ne} = 1000$ kg/m is used to displace a Bingham fluid with $\rho_{nn} = 850$ kg/m^3. The flow directions are upward ($\theta = \pi/2$), horizontal ($\theta = 0$), and downward ($\theta = -\pi/2$). The fluid and rock properties are listed in Table 7.4. Even though displacement flow directions in oil reservoirs are mostly horizontal, upward or downward flow may occur because of the inhomogeneity of layered formations or may occur in laboratory displacement tests. Figure 7.20 shows the saturation distributions after 10 h of displacement. The difference in density of the two fluids is small, so the influence of gravity on displacement efficiency near the front is not very significant. However, gravity does change the ultimate displacement saturation. The best displacement performance is obtained by upward flow. Because gravity resists the upward flow of the heavier displacing phase, the flow potential gradient must be larger to maintain the same flow rate. Consequently, the apparent viscosity of the Bingham fluid is decreased for upward flow, resulting in better sweep efficiency.

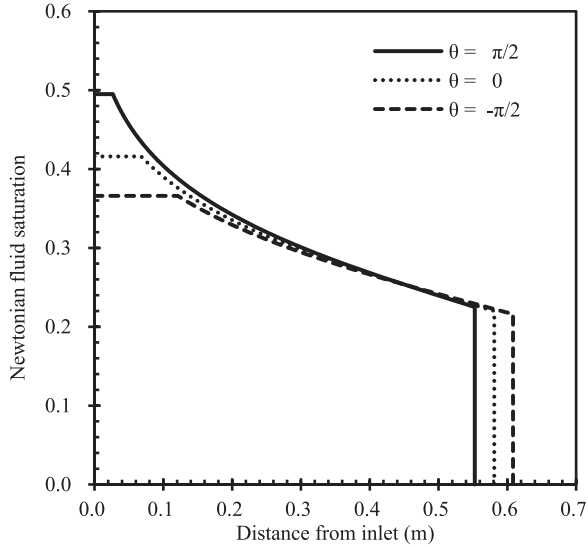

Figure 7.20 Newtonian phase saturation distribution for Bingham fluid displacement by a Newtonian fluid with gravity effects.

In summary, the fundamental feature of immiscible displacement involving a Bingham plastic fluid is that there exists an ultimate displacement saturation that is essentially determined by the minimum pressure gradient, G, of a Bingham, non-Newtonian fluid. This saturation can be considerably larger than residual saturations from relative permeability effects. Once the saturation approaches the ultimate saturation in the formation, no further displacement can be obtained, regardless of how long the displacement lasts for a given operating condition. A simple way to gain a better sweep efficiency is to increase injection rates, thereby reducing the apparent viscosity of the displaced Bingham fluid. A better displacement also can be obtained by using gravity to increase the flow potential gradient in the flow direction for a given flow rate.

7.6.4 Verification for Numerical Simulations

This section is to provide an example for numerical model verification by checking of numerical modeling results against the analytical solution. The problem is one-dimensional immiscible displacement, in which a Bingham liquid is displaced by a Newtonian fluid. It is similar to the case of heavy-oil production by waterflooding in the petroleum industry. The problem description is similar to the power-law fluid displacement

problem and we also use the analytical solution for Bingham fluid flow to examine the numerical simulation results. The one-dimensional rock column is initially saturated with a Bingham fluid only, and then a Newtonian liquid, water, is injected at the inlet as a displacing agent to drive the *in situ* Bingham liquid.

The properties of rock and fluids are given in Table 7.6. The numerical simulations are carried out by MSFLOW and a comparison of the saturation profiles at the time of one day from the numerical and analytical solutions of water injection is shown in Figure 7.21. To reduce effects of grid

Table 7.6 Fluid and rock parameters for numerical tests

Parameters	Numerical test 1	Numerical test 2	Unit
Porosity, ϕ	0.20	0.20	[-]
Absolute permeability, k	9.869×10^{-13}	9.869×10^{-13}	[m^2]
Cross-section area, A	1.0	1.0	[m^2]
Length of formation, L	4.0	4.0	[m]
Injection rate, q_t	2.0×10^{-6}	2.0×10^{-6}	[m^3/s]
Injection time, t	1.0	1.0	[day]
Viscosity of Newtonian fluid, μ_{ne}	1.0×10^{-3}	1.0×10^{-3}	[Pa·s]
Bingham plastic coefficient, μ_B	4.0×10^{-3}	5.0×10^{-3}	[Pa·s]
Minimum threshold pressure gradient, G	1.0×10^{4}	5.0×10^{3}	[Pa/m]
Residual Newtonian fluid saturation, $S_{ne,ir}$	0.00	0.00	[-]
Residual Bingham fluid saturation, $S_{nn,ir}$	0.20	0.20	[-]
Maximum relative permeability, $k_{rne,max}$	1.0	0.75	[-]
Maximum relative permeability, $k_{rnn,max}$	1.0	0.75	[-]
Power index of relative permeability, n_{ne}	2.0	2.0	[-]
Power index of relative permeability, n_{nn}	2.0	2.0	[-]
Density of Newtonian fluid, ρ_{ne}	1000	1000	[kg/m^3]
Density of non-Newtonian fluid, ρ_{nn}	900	900	[kg/m^3]
Directional angle, θ	0	0	[rad]

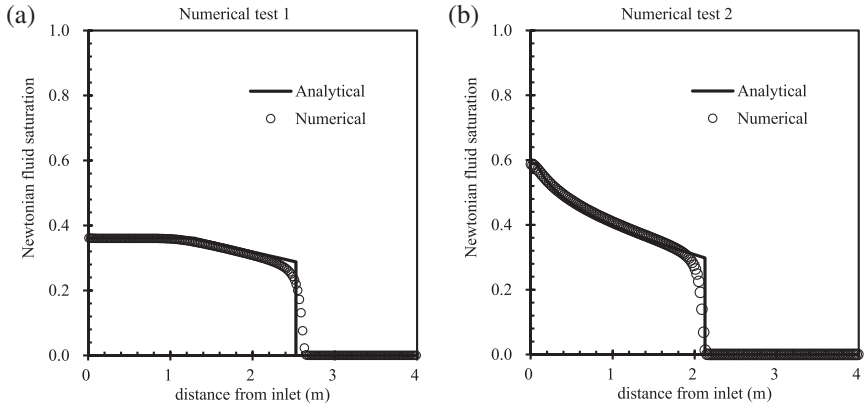

Figure 7.21 Comparison of the water saturation profiles from the numerical and analytical solutions at $t = 1$ day of Bingham fluid displacement.

discretization in a finite system of the numerical model, very fine mesh spacing ($\Delta x = 0.02$ m) is chosen. A one-dimensional 4-m linear domain is discretized into 200 one-dimensional uniform grid blocks. Figure 7.21 indicates that the numerical results are in good agreement with the analytical solution, although some small smearing at the sharp saturation front exists. Note that the flat saturation on the top of curves of Figure 7.21, called as "ultimate displacement saturation," is also captured by the numerical solution.

7.7 IMMISCIBLE DISPLACEMENT OF NON-NEWTONIAN FLUIDS IN A RADIAL SYSTEM

Similar to the solution for displacement of Newtonian fluids in a radial reservoir in Section 6.2, this section discusses radial flow of immiscible non-Newtonian fluids. Among the two fluids, one or both could be non-Newtonian fluids. The radial flow domain is homogeneous, isothermal, isotropic, and horizontal, as shown in Figure 6.1.

7.7.1 Buckley–Leverett Solution and Evaluation Procedure

The flow-governing equation for fluid β in a one-dimensional radial system is given by the mass-conservation equation,

$$-\frac{1}{r}\frac{\partial}{\partial r}\left(\rho_\beta q_\beta\right) = 2\pi h \frac{\partial}{\partial t}\left(\phi S_\beta \rho_\beta\right) \tag{7.41}$$

in which β is fluid index ($\beta = \text{nn}$ for non-Newtonian fluid and $\beta = \text{ne}$ for Newtonian fluid; ρ_β is the density of fluid β; S_β is the saturation of fluid β; and the volumetric flow rate is defined as

$$v_\beta = \frac{q_\beta}{2\pi rh} = -\frac{kk_{r\beta}}{\mu_\beta}\frac{\partial P_\beta}{\partial r} \tag{7.42}$$

in which v_β is the volumetric (or Darcy flow) velocity of fluid β. If fluid β is a non-Newtonian fluid, its apparent viscosity of a non-Newtonian fluid is defined in Eqn (7.14) as

$$\mu_{\text{nn}} = \mu_{\text{nn}}\left(S_{\text{nn}}, \frac{\partial P_{\text{nn}}}{\partial r}\right) \tag{7.43}$$

Similar to analysis of Section 6.2, we can obtain the fractional-flow equation for fluid β under the Buckley–Leverett radial-flow condition,

$$f_\beta = \frac{v_\beta}{v_{\text{nn}} + v_{\text{ne}}} = \frac{v_\beta}{v_{\text{t}}} \tag{7.44}$$

in which $v_{\text{t}}(r, t) = v_{\text{nn}} + v_{\text{ne}}$, a total volumetric flow rate at any radial distance r and time t. From the definition, we have $f_{\text{nn}} + f_{\text{ne}} = 1$.

It can be shown that the fractional flow, f_β, is a function of saturation only for non-Newtonian fluid flow, because the pressure gradient is determined uniquely or correlated with saturation by the constraint condition:

$$\frac{q_{\text{t}}(r,t)}{2\pi rh} + \frac{kk_{\text{rnn}}}{\mu_{\text{nn}}}\frac{\partial P_{\text{nn}}}{\partial r} + \frac{kk_{\text{rne}}}{\mu_{\text{ne}}}\frac{\partial P_{\text{ne}}}{\partial r} = 0 \tag{7.45}$$

If we neglect the capillary-pressure gradient along the radii, the constraint equation is reduced to

$$\frac{q_{\text{t}}(r,t)}{2\pi rh} + \frac{kk_{\text{rnn}}}{\mu_{\text{nn}}}\frac{\partial P}{\partial r} + \frac{kk_{\text{rne}}}{\mu_{\text{ne}}}\frac{\partial P}{\partial r} = 0 \tag{7.46}$$

Considering an incompressible-flow process, as discussed in Section 6.2, it means that the total volumetric flow rate $q_{\text{t}}(r, t) = q_{\text{nn}} + q_{\text{ne}} = \text{constant}$ or independent of r. This leads to

$$\frac{q_{\text{t}}(r_{\text{w}},t)}{2\pi r_{\text{w}}h} + \frac{kk_{\text{rnn}}}{\mu_{\text{nn}}}\frac{\partial P}{\partial r} + \frac{kk_{\text{rne}}}{\mu_{\text{ne}}}\frac{\partial P}{\partial r} = 0 \tag{7.47}$$

in which r_{w} is wellbore radius.

As discussed in Section 6.2, the mass conservation of a one-dimensional flow and displacement in a radial-flow system for Newtonian and non-Newtonian fluids can be rewritten as follows (Fakcharoenphol and Wu, 2010):

$$\frac{\partial r_{S_\beta}^2}{\partial t} = \frac{q_t}{\phi \pi h}\left(\frac{\partial f_\beta}{\partial S_\beta}\right)_{S_\beta} \tag{7.48}$$

Integrating Eqn (7.48) yields

$$r_{S_\beta}^2 = r_w^2 + \frac{W_i}{\pi h \phi}\cdot\left.\frac{\mathrm{d}f_\beta}{\mathrm{d}S_\beta}\right|_{S_\beta} \tag{7.49}$$

in which $W_i = \int_0^t q_t(\tau)\mathrm{d}\tau$ is the cumulative injected fluid at the well.

7.7.2 A Newtonian Fluid Displaced by a Power-Law Non-Newtonian Fluid

The power-law model is used in describing the rheological property of shear-thinning fluids, such as polymer and foam solutions, in porous-medium flow. Its multiphase extension in a radial system is

$$\mu_{nn} = \mu_{eff}\left(\frac{k k_{rnn}}{\mu_{eff}}\left(\left|\frac{\partial P}{\partial r}\right|\right)\right)^{\frac{n-1}{n}} \tag{7.50}$$

A displacement of a Newtonian fluid by a power-law non-Newtonian fluid is under consideration in a radial-disk reservoir with a radius of 8 m and unit thickness. The reservoir is horizontal and has a porosity of 0.25 with the initial water saturation of 0.2, which is considered immobile. Relative permeability data corresponding to the displacement of oil by water are given by the Eqns (5.34) and (5.35). The input parameters in the example are listed in Table 7.7.

The corresponding curve of pressure gradient is shown in Figure 7.22(a). The fractional-flow function and its derivative are shown in Figure 7.22(b). Figure 7.22(c) presents the apparent viscosity change versus non-Newtonian fluid saturation. Using the Welge's approach or integral method, we can obtain the waterflood frontal saturation, $S_{nn,f}$. The non-Newtonian fluid saturation profiles are shown in Figure 7.22(d), similarly to the case of the one-dimensional linear system, as discussed in the Section 7.5. However, with the advance of the displacing-front radius, the moving velocity of water shock-front saturation becomes smaller and smaller with the increase in r, because of the larger displaced-fluid volume as r increases

Table 7.7 Parameters for a Power-law non-Newtonian fluid displacement in a radial system

Parameters	Value	Unit
Porosity, ϕ	0.20	[-]
Absolute permeability, k	9.869×10^{-13}	[m^2]
Radius of outer boundary, R	8.0	[m]
Radius of injection well, r_w	0.1	[m]
Thickness of reservoir, h	1.0	[m]
Injection rate, q_t	1.0×10^{-4}	[m^3/s]
Injection time, t	1.0	[day]
Viscosity of Newtonian fluid, μ_{ne}	4.0×10^{-3}	[Pa·s]
Power-index, n	0.6	[-]
Consistency of power-law fluid, H	0.01	[Pa·s^n]
Residual Newtonian fluid saturation, $S_{ne,ir}$	0.20	[-]
Residual non-Newtonian fluid saturation, $S_{nn,ir}$	0.20	[-]
Maximum relative permeability, $k_{rne,max}$	0.75	[-]
Maximum relative permeability, $k_{rnn,max}$	0.75	[-]
Power index of relative permeability, n_{ne}	2.0	[-]
Power index of relative permeability, n_{nn}	2.0	[-]
Density of Newtonian fluid, ρ_{ne}	1000	[kg/m^3]
Density of non-Newtonian fluid, ρ_{nn}	800	[kg/m^3]

in a radial system. This leads to larger viscosity of the displacing phase and better displacement efficiency.

7.7.3 A Bingham Non-Newtonian Fluid Displaced by a Newtonian Fluid

The rheological model for the apparent viscosity of a Bingham plastic fluid in a radial system is as follows:

$$\mu_{nn} = \begin{cases} \dfrac{\mu_B}{1 - \frac{G}{|\partial P/\partial r|}}, & |\partial P/\partial r| > G \\ \infty \quad , & |\partial P/\partial r| \le G \end{cases} \tag{7.51}$$

For a particular saturation of the Newtonian phase, S_{ne}, the corresponding flow potential gradient for the non-Newtonian phase can be derived by introducing Eqn (7.51) into Eqn (7.47) as follows:

$$-\left.\frac{\partial \Phi}{\partial r}\right|_{S_{ne}} = \frac{\frac{q_t}{2\pi r_w hk} + \frac{k_{rnn}}{\mu_B} G}{\frac{k_{rne}}{\mu_{ne}} + \frac{k_{rnn}}{\mu_B}} \tag{7.52}$$

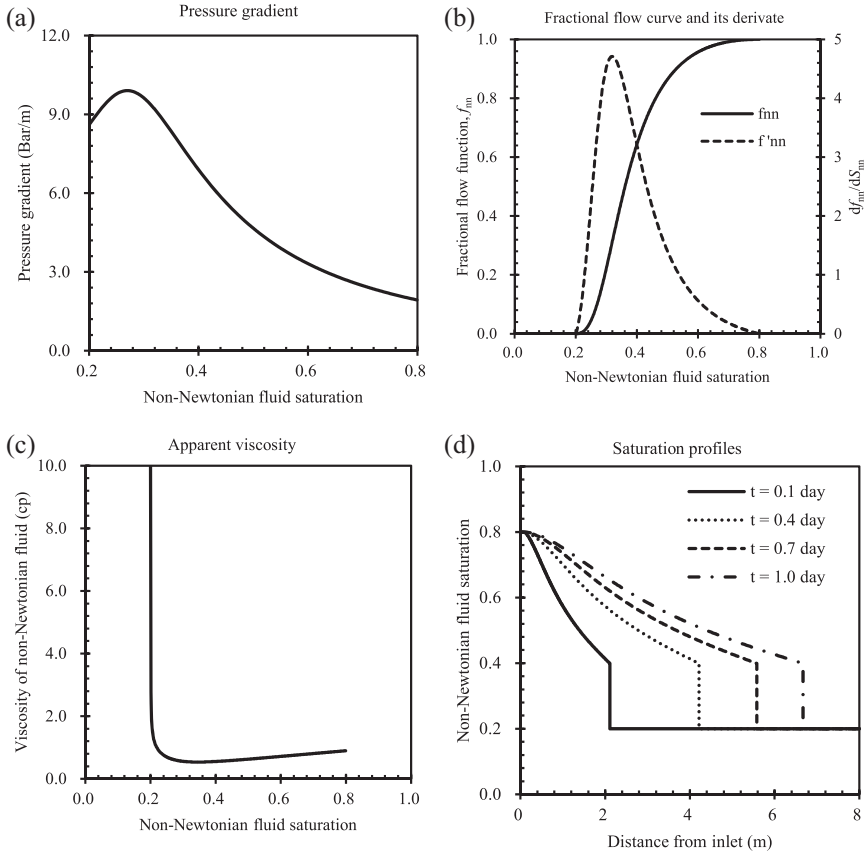

Figure 7.22 The corresponding results of displacement by a power-law non-Newtonian fluid.

The apparent viscosity for the Bingham fluid is determined by introducing Eqn (7.52) into Eqn (7.51).

Displacement of a Bingham fluid by a Newtonian fluid is under consideration for a radial cylindrical reservoir of an 8-m radius and unit thickness. Relative permeability data corresponding to the displacement of oil by water are given also by the Eqns (5.34) and (5.35). The detailed parameters in the example are listed in Table 7.8.

The pressure-gradient curve is plotted in Figure 7.23(a). As discussed in Section 7.6.1, a basic feature of displacement process of a Bingham fluid in porous media is the existence of an ultimate or maximum displacement saturation, S_{max}, for the displacing Newtonian phase (see Figure 7.23(b)). The maximum displacement saturation occurs at the

Table 7.8 Parameters for a Power-law non-Newtonian fluid displacement in a radial system

Parameters	Value	Unit
Porosity, ϕ	0.20	[-]
Absolute permeability, k	9.869×10^{-12}	[m^2]
Radius of outer boundary, R	8.0	[m]
Radius of injection well, r_w	0.1	[m]
Thickness of reservoir, h	1.0	[m]
Injection rate, q_t	1.0×10^{-4}	[m^3/s]
Injection time, t	10.0	[day]
Viscosity of Newtonian fluid, μ_{ne}	1.0×10^{-3}	[Pa·s]
Bingham plastic coefficient, μ_B	5.0×10^{-3}	[Pa·s]
Minimum threshold pressure gradient, G	5.0×10^{3}	[Pa/m]
Residual Newtonian fluid saturation, $S_{ne,ir}$	0.00	[-]
Residual non-Newtonian fluid saturation, $S_{nn,ir}$	0.20	[-]
Maximum relative permeability, $k_{rne,max}$	0.75	[-]
Maximum relative permeability, $k_{rnn,max}$	0.75	[-]
Power index of relative permeability, n_{ne}	2.0	[-]
Power index of relative permeability, n_{nn}	2.0	[-]
Density of Newtonian fluid, ρ_{ne}	1000	[kg/m^3]
Density of non-Newtonian fluid, ρ_{nn}	800	[kg/m^3]

point of the fractional-flow curve at which $f_{ne} = 1.0$. For this particular displacement system, initially saturated with only the Bingham fluid, the displacing saturation cannot exceed the maximum value $S_{ne,max}$. The resulting saturation distributions during 10-day water injection are given in Figure 7.24.

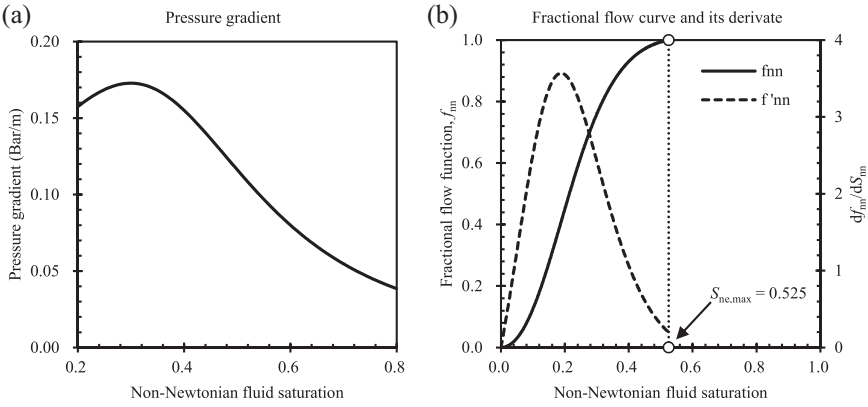

Figure 7.23 Pressure gradient and fractional-flow function curves.

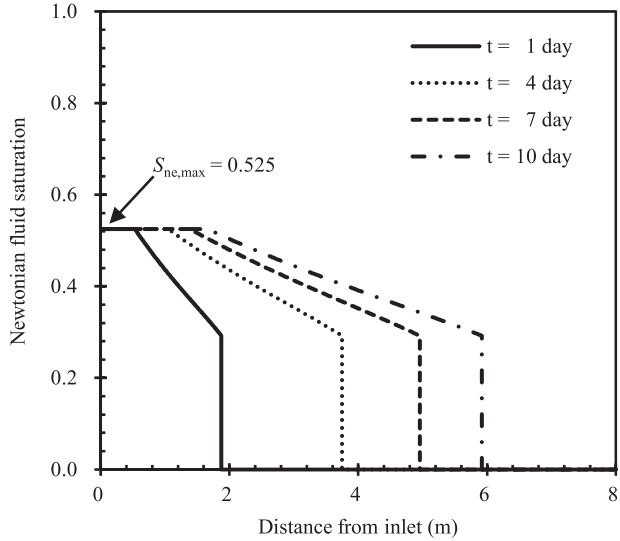

Figure 7.24 Newtonian fluid-saturation profiles at different time.

7.7.4 Verification for Numerical Simulations

This is to provide two examples for numerical model verification by checking of numerical modeling results against the analytical solution for power-law (test 1) and Bingham (test 2) fluid displacement in a radial system.

The flow domain and parameters for this problem are illustrated in Table 7.9. To reduce the effects of discretization on numerical

Table 7.9 Parameters for numerical simulations in a radial system

Parameters	Numerical test 1	Numerical test 2	Unit
Porosity, ϕ	0.30	0.20	[-]
Absolute permeability, k	9.869×10^{-13}	9.869×10^{-13}	[m^2]
Radius of outer boundary, R	8.0	8.0	[m]
Radius of injection well, r_w	0.1	0.1	[m]
Thickness of reservoir, h	1.0	1.0	[m]
Injection rate, q_t	4.0×10^{-4}	2.5×10^{-4}	[m^3/s]
Injection time, t	0.289	0.463	[day]
Viscosity of Newtonian fluid, μ_{ne}	2.0×10^{-3}	1.0×10^{-3}	[Pa·s]
Power-index, n	0.8	-	[-]
Consistency of power-law fluid, H	0.01	-	[Pa·s^n]

Continued

Table 7.9 Parameters for numerical simulations in a radial system—cont'd

Parameters	Numerical test 1	Numerical test 2	Unit
Bingham plastic coefficient, μ_B	-	5.0×10^{-3}	[Pa·s]
Minimum threshold pressure gradient, G	-	1.0×10^{4}	[Pa/m]
Residual Newtonian fluid saturation, $S_{ne,ir}$	0.20	0.00	[-]
Residual non-Newtonian fluid saturation, $S_{nn,ir}$	0.20	0.20	[-]
Maximum relative permeability, $k_{rne,max}$	0.75	0.75	[-]
Maximum relative permeability, $k_{rnn,max}$	0.75	0.75	[-]
Power index of relative permeability, n_{ne}	2.0	2.0	[-]
Power index of relative permeability, n_{nn}	2.0	2.0	[-]
Density of Newtonian fluid, ρ_{ne}	1000	1000	[kg/m^3]
Density of non-Newtonian fluid, ρ_{nn}	800	800	[kg/m^3]

simulation results, very fine, uniform mesh spacing ($\Delta r = 0.01$ m) is chosen. The outside radius of the radial model is 8 m, and the model is discretized into 500 uniform grid blocks. The comparison between the numerical and analytical solutions is shown in Figure 7.25. Figure 7.25

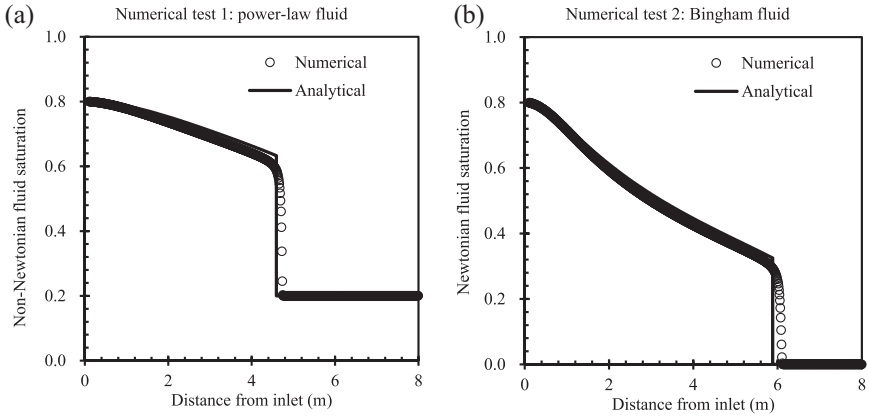

Figure 7.25 Comparison of saturation profiles calculated from analytical and numerical solutions.

indicates that the numerical results are in excellent agreement with the analytical solutions of the displacement for the entire sweeping zone in both cases.

REFERENCES

Aziz, K., Settari, A., 1979. Petroleum Reservoir Simulation. Applied Science Publishers, London.

Bear, J., 1972. Dynamics of Fluids in Porous Media. American Elsevier, New York.

Fakcharoenphol, P., Wu, Y., 2010. Displacement of non-Newtonian fluids in linear and radial composite porous media. In: The 3rd International Conference on Porous Media and Its Applications in Science and Engineering (pp. 1–9). Montecatini, Italy.

Gencer, C.S., Ikoku, C.U., 1984. Well test analysis for two-phase flow of non-Newtonian power-law and Newtonian fluids. Journal of Energy Resources Technology 106 (2), 295–305.

Gleasure, R.W., 1990. An experimental study of non-Newtonian polymer rheology effects on oil recovery and injectivity. SPE Reservoir Engineering 5 (4), 481–486.

Gogarty, W.B., 1967. Rheological properties of pseudoplastic fluids in porous media. Society of Petroleum Engineers Journal 7 (2), 149–160.

Ikoku, C.U., Ramey Jr., H.J., 1978. Transient Flow of Non-Newtonian Power-law Fluids in Porous Media.

Muskat, M., Meres, M.W., 1936. The flow of heterogeneous fluids through porous media. Journal of Applied Physics 7 (9), 346–363.

Odeh, A.S., Yang, H.T., 1979. Flow of non-Newtonian power-law fluids through porous media. Society of Petroleum Engineers Journal 19 (3), 155–163.

Pearson, J.R.A., Tardy, P.M.J., 2002. Models for flow of non-Newtonian and complex fluids through porous media. Journal of Non-Newtonian Fluid Mechanics 102 (2), 447–473.

van Poollen, H.K., Jargon, J.R., 1969. Steady-state and unsteady-state flow of non-Newtonian fluids through porous Media. Society of Petroleum Engineers Journal 9 (1), 80–88.

Savins, J.G., 1969. Non-Newtonian flow through porous media. Industrial & Engineering Chemistry 61 (10), 18–47.

Scheidegger, A.E., 1974. The Physics of Flow through Porous Media. University of Toronto Press.

Sheldon, J.W., Cardwell Jr., W.T., 1959. One-dimensional incompressible noncapillary two-phase fluid flow in a porous medium. Petroleum Transactions, AIME 216, 290–296.

Sochi, T., 2010. Flow of non-Newtonian fluids in porous media. Journal of Polymer Science Part B: Polymer Physics 48 (23), 2437–2767.

Vongvuthipornchai, S., Raghavan, R., 1987a. Pressure falloff behavior in vertically fractured wells: non-Newtonian power-law fluids. SPE Formation Evaluation 2 (4), 573–589.

Vongvuthipornchai, S., Raghavan, R., 1987b. Well test analysis of data dominated by storage and skin: non-Newtonian power-law fluids. SPE Formation Evaluation 2 (4), 618–628.

Welge, H.J., 1952. A simplified method for computing oil recovery by gas or water drive. Journal of Petroleum Technology 4 (4), 91–98.

Willhite, G.P., 1986. Waterflooding. Society of Petroleum Engineers, Richardson, TX.

Wu, Y.-S., 1990. Theoretical Studies of Non-Newtonian and Newtonian Fluid Flow through Porous Media. Lawrence Berkeley Laboratory, Berkeley, CA.

Wu, Y.-S., 1998. MSFLOW: Multiphase Subsurface Flow Model of Oil, Gas and Water in Porous and Fractured Media with Water Shut-off Capability. Documentation and User's Guide, Walnut Creek, Califonia.

Wu, Y.-S., 2004. A unified numerical framework model for simulating flow, transport, and heat transfer in porous and fractured media. Developments in Water Science 55, 645–658.

Wu, Y.-S., Pruess, K., 1996. Flow of non-Newtonian fluids in porous media. Advances in Porous Media 3, 87–184.

Wu, Y.-S., Pruess, K., 1998. A numerical method for simulating non-Newtonian fluid flow and displacement in porous media. Advances in Water Resources 21 (5), 351–362.

Wu, Y.-S., Pruess, K., Witherspoon, P.A., 1991. Displacement of a Newtonian fluid by a non-Newtonian fluid in a porous medium. Transport in Porous Media 6 (2), 115–142.

Wu, Y.-S., Pruess, K., Witherspoon, P.A., 1992. Flow and displacement in Bingham non-Newtonian fluids in porous media. SPE Reservoir Engineering 7 (3), 369–376.

Yilmaz, N., Bakhtiyarov, A.S., Ibragimov, R.N., 2009. Experimental investigation of Newtonian and non-Newtonian fluid flows in porous media. Mechanics Research Communications 36 (5), 638–641.

CHAPTER 8

Non-Darcy Flow of Immiscible Fluids

8.1 INTRODUCTION

Darcy's Law has been used exclusively in calculation of both single-phase and multiphase fluid flow in reservoirs. However, it has been observed that high-velocity, non-Darcy flow occurs also in many oil and gas reservoirs and subsurface systems, in particular, for flow in the formation near high-rate oil or gas production, groundwater pumping, and liquid-waste injection wells. Theoretically, any deviation from a linear relation between flow rate and pressure or potential gradient may be defined as non-Darcy flow. In this chapter, our focus is only on the non-Darcy flow behavior caused by high flow velocities or inertial effect. Effects of non-Darcy or high-velocity regimes on flow in porous media have been noticed and investigated for decades (e.g., Tek et al., 1962; Ramey, 1965; Scheidegger, 1974; Katz and Lee, 1990; Cooper et al., 1999; Wu, 2001). The majority of the studies on non-Darcy flow in porous media has been carried out mostly on single-phase flow in petroleum reservoir engineering (e.g., Tek et al., 1962; Swift and Kiel, 1962; Firoozabadi and Katz, 1979; Lee et al., 1987). Several investigations have been conducted for non-Darcy flow in naturally fractured reservoirs (e.g., Skjetne and Auriault, 1999; Wu, 2002a) and for non-Darcy flow into highly permeable fractured wells (e.g., Holditch and Morse, 1976; Guppy et al., 1981, 1982; Hagoort, 2004; Friedel and Voigt, 2006). In an effort to calculate non-Darcy flow, many studies in laboratory and field have concentrated on finding and validating correlations of non-Darcy flow coefficients with the *Forchheimer* model (e.g., Liu et al., 1995; Narayanaswamy et al., 1999; Macini et al., 2011). More recently, additional efforts on modeling non-Darcy flow in porous and fractured media have been reported (e.g., Wu, 2002b; Al-Otaibi and Wu, 2010, 2011).

Recent advances in development of tight oil and tight or shale gas from unconventional petroleum reservoirs in the past decade have revitalized the interest in non-Darcy flow in porous and fractured reservoirs. This is

Multiphase Fluid Flow in Porous and Fractured Reservoirs
ISBN 978-0-12-803848-2
http://dx.doi.org/10.1016/B978-0-12-803848-2.00008-8

because the technology of developing oil and gas from unconventional, low-permeability reservoir formations depends on multistage hydraulic fractures along long horizontal wellbores. These hydraulic fractures are supported open in formation near wells by sands or proppants to supply high-permeability channels and large effective wellbore formation-contacting areas to significantly reduce flow resistance to wells from reservoirs. Due to the high contrast in permeability of hydraulic fractures and reservoirs, non-Darcy flow often occurs in the fractures near wells (e.g., Hagoort, 2004; Friedel and Voigt, 2006; Nashawi, 2006; Wu et al., 2014). The non-Darcy flow to wellbore along the hydraulic fractures could have a large impact on productivity of a fractured well (Miskimins et al., 2005).

In studies of non-Darcy flow through porous media, the *Forchheimer* Equation (1901) has been mostly used to describe such nonlinear flow behavior. However, the *Forchheimer* equation was originally proposed for single-phase fluid non-Darcy flow only. Similar to Darcy's law, the Forchheimer non-Darcy flow model has been extended to multiphase flow conditions in the literature and application (Evans et al., 1987; Evans and Evans, 1988; Liu et al., 1995; Wu, 2001, 2002b). In one recent development of characterizing non-Darcy flow in porous media, Barree and Conway (2004) have proposed a new, single-phase non-Darcy flow model to overcome the limitations of the Forchheimer equation at very high-flow rates through proppant packs. Later on, they have extended the new model to multiphase non-Darcy flow conditions (Barree and Conway, 2007, 2009). Several researchers (Lopez-Hernandez, 2007; Lai et al., 2012) have shown that the Barree and Conway model is able to describe the entire range of nonlinear relationships between flow rate and potential gradient from low- to high-flow rates through porous media, including those in transitional zones in their laboratory studies and analyses. However, modeling studies by Al-Otaibi and Wu (2010, 2011) in field scale simulation for well testing analysis indicate that the difference in modeling results from the two models, the Forchheimer equation and the Barree and Conway model, is small under single-phase flow conditions. In fact, the two models give all the same results when using an equivalent parameter of a non-Darcy flow coefficient with the Forchheimer equation for the simulation.

This chapter summarizes studies of modeling multiphase non-Darcy flow in reservoirs according to both Forchheimer and Barree and Conway models. The objective of this chapter is to present a mathematical method for quantitative analysis of multiphase non-Darcy flow through porous and fractured rocks using both numerical and analytical approaches. In this

chapter, we discuss a mathematical and numerical model by incorporating the *Forchheimer* equation and the Barree and Conway model into general numerical formulation, as discussed in Chapter 4, for modeling multiphase non-Darcy flow in porous and fractured media. Furthermore, we present a series of Buckley and Leverett-type analytical solutions for one-dimensional non-Darcy displacement of immiscible fluids in a linear and radial, and composite system according to both the *Forchheimer* equation and the Barree and Conway model. For application of the analytical solutions, a practical procedure is presented for calculating phase-saturation profiles for non-Darcy immiscible displacement. The analytical solutions and the resulting procedure of its evaluation can be regarded as an extension of the Buckley–Leverett theory to non-Darcy displacement. As an application example, we use the analytical solutions to obtain some insight into one-dimensional non-Darcy displacement of two immiscible fluids according to the Forchheimer as well as the Barree and Conway model.

8.2 NON-DARCY FLOW MODELS

Darcy's law, stating a linear relationship between volumetric flow rate per unit cross-sectional area (or Darcy velocity) and pressure (or potential) gradient, has been the fundamental principle in analyzing flow processes in porous media. Any flow deviated from this linear relation can be defined as non-Darcy flow. In this chapter, we are interested primarily in the non-Darcy flow caused by high-flow velocities through porous media. For describing high-velocity non-Darcy flow, the *Forchheimer* equation (Forchheimer, 1901) has been the most widely used model in the literature from laboratory, theoretical to field studies. In recent years, the Barree and Conway non-Darcy flow model (Barree and Conway, 2004, 2007) have received attention for its capability to handle extremely high-flow velocity through proppant packs or propped hydraulic fractures. We will discuss both non-Darcy flow models and their solutions.

8.2.1 *Forchheimer* Equation

Darcy's law correlates the pressure gradient to the fluid superficial velocity (or Darcy velocity) for a one-dimensional single-phase fluid horizontal flow as follows:

$$-\frac{\partial P}{\partial L}=\frac{\mu v}{k} \tag{8.1}$$

in which L is the flow direction of one-dimensional fluid flow. Any deviations from this linear relation, Eqn (8.1), may be defined as non-Darcy flow. Because we are concerned only with the non-Darcy flow caused by high fluid flow velocities in this chapter, Darcy's law needs to be modified to include such high-flow velocity, nonlinear behavior. Forchheimer (1901) added an additional quadratic flow term, as in Eqn (8.2), and even a cubic term, Eqn (8.3), to correct Darcy's linear form in an attempt to correct Darcy's law to represent the microscopic inertial effect. This Eqn (8.2), is generally known as *Forchheimer* equation (Scheidegger, 1974):

$$-\frac{\partial P}{\partial L}=\frac{\mu v}{k}+\beta\rho v^2 \tag{8.2}$$

and in cubic form,

$$-\frac{\partial P}{\partial L}=\frac{\mu v}{k}+\beta\rho v^2+\gamma\rho v^3 \tag{8.3}$$

in which β is the non-Darcy flow coefficient, an intrinsic property of porous media [m^{-1}]; and γ is another non-Darcy flow coefficient of the cubic term [$s\cdot m^{-1}$]. In the literature and application, the *Forchheimer* equation, Eqn (8.2), is the most-used model for depicting non-Darcy flow in porous media. In addition, this quadratic equation for non-Darcy flow can be derived theoretically using a volume-average approach (Whitaker, 1996).

In general, Eqn (8.2) can be extended for multidimensional flow by replacing pressure gradient by flow potential gradient in a vector form. Volumetric flow rate (namely Darcy velocity for Darcy flow) for non-Darcy flow of each fluid in a multiphase flow system may be described using the multiphase extension of the *Forchheimer* equation, Eqn (8.2),

$$-\nabla\Phi_\beta=\frac{\mu_\beta}{kk_{r\beta}}\boldsymbol{v}_\beta+\beta_\beta\rho_\beta\boldsymbol{v}_\beta|\boldsymbol{v}_\beta| \tag{8.4}$$

This is the extended *Forchheimer* equation of Eqn (8.2) to multidimensional, immiscible multiphase non-Darcy flow in porous media (Wu, 2001).

The linear term, the first term $(\mu_\beta/kk_{r\beta})\boldsymbol{v}_\beta$ on the right-hand side of Eqn (8.4), represents viscous flow; it is dominant at low-flow rates or Darcy flow regime. The additional pressure drop or energy assumption resulting from non-Darcy, inertia or high-flow velocity effect is described by the second term $(\beta_\beta\rho_\beta)\boldsymbol{v}_\beta|\boldsymbol{v}_\beta|$ on the right-hand side of Eqn (8.4) for the extra friction or inertial effects. Equation (8.4) indicates that the non-Darcy flow equation

reduces to the multiphase Darcy's law if the non-Darcy term $(\beta_\beta \rho_\beta)\boldsymbol{v}_\beta|\boldsymbol{v}_\beta|$ can be ignored. When compared with the first term, $(\mu_\beta/kk_{r\beta})\boldsymbol{v}_\beta$, at low-flow velocity, Eqn (8.4) becomes Darcy's law. For high velocities, however, the second term becomes dominant and must be included. Therefore, Darcy flow can generally be considered as a special case of non-Darcy flow, as described by Eqn (8.4).

According to the *Forchheimer* equation, Eqn (8.2) or (8.4), high velocity non-Darcy flow is characterized by the non-Darcy flow coefficient, β, an intrinsic rock property, in addition to the permeability. Similar to intrinsic permeability to Darcy flow, Forchheimer-β is the most important property of characterizing non-Darcy flow in porous media, when described using the *Forchheimer* equation. There have been many studies and correlations in the literature to estimate the non-Darcy flow coefficient (e.g., Evans and Evans, 1988; Katz and Lee, 1990; Liu et al., 1995; Narayanaswamy et al., 1999; Macini et al., 2011). In general, permeability, porosity, and tortuosity are the three major parameters used in the non-Darcy flow coefficient correlations. Under single-phase flow conditions the coefficient, β_β, is traditionally called a turbulence coefficient or an inertial resistance coefficient. In the literature, there are a number of correlations for the single-phase non-Darcy flow coefficient, which have been extended for analyzing experimental multiphase non-Darcy flow (Evans and Evans, 1988).

In this chapter, we select one of those published relations for use in the demonstration examples of calculation of non-Dracy flow. The selected expression is based on experimental study of single-phase flow, β is described as follows (Evans and Evans, 1988; Katz and Lee, 1990),

$$\beta = \frac{C_\beta}{k^{5/4}\phi^{3/4}} \tag{8.5}$$

in which C_β is a non-Darcy flow constant with a unit of $[m^{3/2}]$, when converted to International System of Units (SI) units. A recent study indicates that the β-coefficient may be also correlated to tortuosity or the representative length of tortuous flow paths in pore structure of a porous medium.

Most empirical correlations, e.g., Eqn (8.5), for estimating the non-Darcy flow coefficient, β, are originally determined experimentally for single-phase flow. Recent work has extended the single-phase non-Darcy flow correlations, such as Eqn (8.5), to incorporate the multiphase effect in terms of the saturation and effective permeability correction. These studies

show that non-Darcy flow coefficients may be dependent on relative permeability functions as well as fluid saturations under multiphase-flow conditions as an effective non-Darcy flow coefficient as (Wu, 2001),

$$\beta_\beta = \frac{C_\beta}{(k k_{r\beta})^{5/4}[\phi(S_\beta - S_{\beta r})]^{3/4}} \tag{8.6}$$

in which $S_{\beta r}$ is residual saturation of fluid, β.

The correlation, Eqn (8.5) or (8.6), for the non-Darcy flow coefficient, indicates that the β-coefficient or non-Darcy flow effect becomes larger with lower permeability, lower effective porosity, or lower fluid content. Moreover, it must be true that the β-coefficient will increase with the length of tortuous flow paths or larger tortuosity in pores of porous media, because of the large inertia effect.

8.2.2 Barree and Conway Model

Barree and Conway (2004, 2007, 2009) present both single-phase and multiphase fluid non-Darcy flow models in porous media in their recent work. We discuss the two models in this section.

Single-phase flow model: Barree and Conway (2004), based on experimental results and field observations, propose a new, physical-based model for describing non-Darcy flow in porous media for single-phase fluid flow, which does not rely on the assumption of a constant permeability or a constant Forchheimer-β factor. The Barree and Conway model suggests using a concept of an apparent permeability (k_{app}) to describe Darcy (linear) and non-Darcy (nonlinear) flow in porous media (Barree and Conway, 2004). The general form of this equation is given by,

$$k_{app} = k_{min} + \frac{(k_d - k_{min})}{(1 + N_{Re})^E} \tag{8.7}$$

in which k_{min} is the minimum-permeability plateau; k_d is constant or Darcy's permeability; and E is an exponential constant; and N_{Re} is the Reynolds number, defined as

$$N_{Re} = \frac{\rho v}{\mu \tau} \tag{8.8}$$

in which ρ is the fluid density; v is the velocity of fluid; μ is the fluid viscosity; and τ is the inverse of characteristic length, which is constant for a rock system and is related to the mean particle size of sands for flow through proppant packs (Barree and Conway, 2004). In laboratory analysis, Lai et al. (2012) find that the value of the exponential E is approximated as 1.0.

Using Eqn (8.8) in Eqn (8.7), setting $E = 1$, and polling out k_d, Eqn (8.7) becomes,

$$k_{app} = k_d\left(k_{mr} + \frac{1 - k_{mr}}{1 + \frac{\rho v}{\mu\tau}}\right) \tag{8.9}$$

in which

$$k_{mr} = \frac{k_{min}}{k_d} \tag{8.10}$$

Then the complete nonlinear flow model for single-phase non-Darcy 1-D flow following the Barree and Conway model (Barree and Conway, 2004; Al-Otaibi and Wu, 2010) is given by

$$-\frac{\partial P}{\partial L} = \frac{\mu v}{k_d\left(k_{mr} + \frac{(1-k_{mr})\mu\tau}{\mu\tau + \rho v}\right)} \tag{8.11}$$

The 1-D Barree and Conway model can be extended to multidimensional single-phase fluid flow as follows,

$$-\nabla\Phi = \frac{\mu \boldsymbol{v}}{k_d\left(k_{mr} + \frac{(1-k_{mr})\mu\tau}{\mu\tau + \rho|\boldsymbol{v}|}\right)} \tag{8.12}$$

Multiphase flow model: To extend their model to multiphase non-Darcy flow, Barree and Conway (2007, 2009) presents a one-dimensional flow equation for gas-phase pressure gradient, correlated multiphase flow rate,

$$-\left(\frac{\partial P}{\partial L}\right)_g = \left(\frac{\mu v}{k_{g\_eff}}\right)_g \tag{8.13}$$

in which the effective permeability of gas phase, k_{g_eff}, can be written as:

$$k_{g\_eff} = k_d k_{rg} k_{mr} + \frac{(1 - k_{mr})k_d k_{rg}}{\left(1 + \frac{\rho_g v_g}{\mu_g S_g \tau}\right)} \tag{8.14}$$

Substituting Eqn (8.14) into Eqn (8.13), we have the one-dimensional form of the Barree and Conway non-Darcy flow equation, pressure gradient as a function of flow velocity as

$$-\left(\frac{\partial P}{\partial L}\right)_g = \frac{\mu_g v_g}{k_d k_{rg} k_{mr} + \frac{(1-k_{mr})k_d k_{rg}}{\left(1 + \frac{\rho_g v_g}{\mu_g S_g \tau}\right)}} \tag{8.15}$$

If we replace pressure gradient by potential gradient, extend one-dimensional velocity in Eqn (8.15) for gas flow to a multidimensional vector as well as to water flow in a multiphase flow system, we have a general form of Eqn (8.16) of correlating flow potential gradient and flow rate for multiphase non-Darcy flow with the Barree and Conway model (Wu et al., 2011a,b),

$$-\nabla\Phi_\beta = \frac{\mu_\beta v_\beta}{k_d k_{r\beta}\left(k_{mr} + \frac{(1-k_{mr})\mu_\beta\tau}{\mu_\beta\tau + \rho_\beta|v_\beta|}\right)} \tag{8.16}$$

Recent laboratory studies and analyses (Lopez-Hernandez, 2007; Lai, 2010; Lai et al., 2012) have shown that the Barree-Conway model provides a single equation to describe the entire range of flow velocities versus pressure or potential gradient from low-flow rate, Darcy to high-flow rate, non-Darcy flow regimes, including those in transitional zones, using their experimental data. At low-flow rates, the Barree-Conway model collapses into Darcy's law with a constant permeability, k_d, and it converges to the *Forchheimer* equation for the intermediate-flow rate. The Barree–Conway model provides a plateau at high rates, i.e., there may exist a constant permeability (or minimum permeability).

As indicated in Figure 8.1, the experimental data (Lopez-Hernandez, 2007; Lai, 2010; Lai et al., 2012) show that the Barree and Conway non-Darcy flow model is able to fit all the testing data. In Figure 8.1, one point or symbol of the curve represents one steady-state flow-testing result using gas nitrogen flow though proppant packs. The test data covers flow rates from less than 707.2 m^3/D to more than 283,168 m^3/D. As it can be seen in Figure 8.1, all the experimental data seem to collapse onto one curve, which matches closely the theoretical prediction by the Barree and Conway model (shown as a dashed line). One data plateau is clearly observed ($\eta = 1.0$) or the apparent permeability becomes Darcy permeability at low Reynolds number or low-flow rate. Note that the transition zones with the increase in Reynolds number are captured. At the other end of high Reynolds numbers, the curve appears to reach another plateau or the minimum-permeability phenomenon.

8.3 FLOW-GOVERNING EQUATIONS

Here, we use a three-phase model for study of non-Darcy flow in reservoirs (Wu, 2002b). A multiphase system in a porous or fractured reservoir is

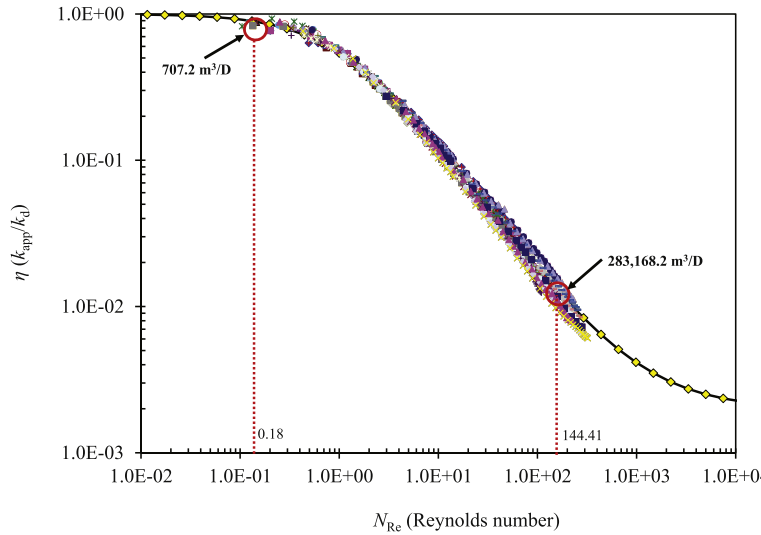

Figure 8.1 Dimensionless plot of η ($=k_{app}/k_d$) versus N_{Re} with all tests using nitrogen flow through proppant packs and the Barree and Conway model *(Modified using the data from Lai, 2010).*

assumed to be composed of three phases: oil, gas (or air), and water. For simplicity, the three fluid components, water, oil, and gas, are assumed to be present only in their associated phases, a simplified black-oil model by ignoring solution gas in oil. Each phase flows in response to pressure, gravitational, and capillary forces according to the multiphase extension of the *Forchheimer* equation and the Barree-Conway model for non-Darcy flow. In an isothermal system containing three mass components, three mass-balance equations are needed to fully describe the system, as described in an arbitrary flow region of a porous or fractured domain.

For flow of phase β($\beta = $ o for oil or NAPL, $\beta = $ g for gas, and $\beta = $ w for water),

$$\frac{\partial}{\partial t}\left(\phi S_\beta \rho_\beta\right) = -\nabla\cdot\left(\rho_\beta \boldsymbol{v}_\beta\right) + q_\beta \tag{8.17}$$

To incorporate non-Darcy flow behavior, volumetric flow velocity $\boldsymbol{v}_\beta$ is described using non-Darcy flow models. In this study, two non-Darcy flow equations are of interest. First, the Forchheimer non-Darcy flow equation is described in Eqn (8.4). Second, the Barree and Conway model is described in Eqn (8.16).

With incorporation of the *Forchheimer* Eqn (8.4) or the Barree–Conway model Eqn (8.16), the governing mass-balance equation for three phases, Eqn (8.17), also needs to be supplemented with constitutive equations, such as capillary pressure and relative permeability functions. The following relationships will be used to complete the description of multiphase non-Darcy flow through porous media,

$$S_w + S_o + S_g = 1 \tag{8.18}$$

Capillary pressure: The capillary pressures relate pressures between the phases and are assumed to be functions of fluid saturation only under non-Darcy flow condition, similar to those discussed in Section 3.4.2.1 for three-phase Darcy flow. Within a three-phase flow system of gas, water, and oil, water- and gas-phase pressures are related by aqueous- and oil-phase pressures by

$$P_w = P_o - P_{cow}(S_w, S_o) \tag{8.19}$$

in which P_{cow} is the oil–water capillary pressure in a three-phase system, which is assumed to be a function of water and oil saturation. The oil-phase pressure is related to the gas-phase pressure by

$$P_o = P_g - P_{cgo}(S_o, S_g) \tag{8.20}$$

in which P_{cgo} is the gas–oil capillary pressure in a three-phase system, which is a function of two saturations of oil and gas phases, respectively. For rock materials of reservoir formation, the wettability order is (1) aqueous phase, (2) oil phase, and (3) gas phase. Then the gas–water capillary pressure is usually stronger than the gas–oil or oil–water capillary pressure. The gas–water capillary pressure, P_{cgw}, in a three-phase system, is defined as

$$P_{cgw} = P_{cow} + P_{cgo} = P_g - P_w \tag{8.21}$$

Relative permeability: We assumed relative permeability under multiphase non-Darcy flow to be functions of fluid saturations only. This assumption has been shown to be valid in recent laboratory experiments of measuring relative permeability for non-Darcy flow (Lai, 2010; Lai and Miskimins, 2010). The relative permeability to the water phase is taken to be described by

$$k_{rw} = k_{rw}(S_w) \tag{8.22}$$

to the oil phase by

$$k_{rn} = k_{rn}(S_w, S_g) \tag{8.23}$$

and to the gas phase by

$$k_{rg} = k_{rg}(S_g) \tag{8.24}$$

The densities of water, oil, and gas, as well as the viscosities of fluids can be treated as functions of fluid pressures in general, as normally done with multiphase-flow simulation in reservoirs, discussed in Section 3.4.3.

8.4 BUCKLEY–LEVERETT SOLUTION FOR NON-DARCY DISPLACEMENT ACCORDING TO FORCHHEIMER EQUATION

This section discusses a Buckley–Leverett type analytical solution describing the displacement mechanism of non-Darcy two-phase flow in porous media according to the Forchheimer equation. For the derivation of the analytical solution, we assume the following Buckley–Leverett flow conditions (Wu et al., 1991; Wu, 2001):

- Both two-phase fluids and the porous medium are incompressible;
- Capillary-pressure gradient is negligible;
- Gravity segregation effect is negligible (i.e., stable displacement exists near the displacement front); and
- One-dimensional flow and displacement is along the x-coordinate of a semi-infinite linear flow system with a constant cross-sectional area (A).

8.4.1 Analytical Solution

As we discussed in Chapter 5, among these assumptions for the Buckley–Leverett flow, incompressibility of both fluids and formation is critical to deriving the Buckley–Leverett solution. This assumption provides a good approximation to displacement processes of two liquids (e.g., oil and water) through porous media, because of the small compressibility of the two liquids. For gas and liquid displacement, however, this assumption may pose certain limitations to the resulting solution, when large pressure gradients build up in a flow system, such as in the case of non-Darcy gas–water flow near a well in a low-permeability formation. In many cases, however, this assumption may still provide acceptable approximations, because the viscosity of gas (air) phase in normal condition is about two orders of magnitude lower than the liquid one. This tends to prevent high pressure gradients from building up, as in the case of the Buckley–Leverett solution, which was also originally derived for oil and gas displacement.

Under Buckley–Leverett flow condition of two incompressible fluids in a one-dimensional, incompressible system, Eqn (8.17) can then be changed to read as follows:

$$-\frac{\partial v_\beta}{\partial x} = \phi \frac{\partial S_\beta}{\partial t} \tag{8.25}$$

in which v_β is the Darcy velocity component or volumetric flow rate (m/s) per unit area of formation for fluid β. For the one-dimensional flow, v_β can be determined from Eqn (8.4), the multiphase-flow *Forchheimer* equation (Wu, 2001),

$$v_\beta = \frac{1}{2k\rho_\beta\beta_\beta}\left\{-\frac{\mu_\beta}{k_{r\beta}} + \sqrt{\left(\frac{\mu_\beta}{k_{r\beta}}\right)^2 - 4k^2\rho_\beta\beta_\beta\left(\frac{\partial P}{\partial x} + \rho_\beta g \sin\theta\right)}\right\} \tag{8.26}$$

in which $\partial P/\partial x$ is a component of the pressure gradient along the x coordinate or flow direction, the same for the two fluids (because there is no difference in capillary gradients of the two phases); g is the gravitational acceleration constant; and θ is the angle between the horizontal plane and the flow direction (the x coordinate). Note that we treat the fluids as one wetting and one nonwetting phase in the following analysis.

To complete the mathematical description of the physical problem, the initial and boundary conditions must be specified. For simplicity in derivation, the system is initially assumed to be uniformly saturated with both wetting ($\beta = \mathrm{w}$) and nonwetting ($\beta = \mathrm{n}$) fluids. The wetting phase is at its residual saturation, and a nonwetting fluid, such as oil or gas, is at its maximum saturation in the system as follows:

$$S_\mathrm{n}(x, t = 0) = 1 - S_\mathrm{wr} \tag{8.27}$$

in which S_wr is the initial, residual wetting-phase saturation. The wetting fluid, such as water, is continuously being injected at a known rate $q_\mathrm{t}(t)$, generally a function of injection time t. Therefore, the boundary conditions at the inlet ($x = 0$) are

$$v_\mathrm{w}(x = 0, t) = \frac{q_\mathrm{t}(t)}{A} \tag{8.28}$$

$$v_\mathrm{n}(x = 0, t) = 0 \tag{8.29}$$

The fractional flow of a fluid phase is defined the same as that in Darcy displacement, i.e., a volume fraction of the phase flowing at a location x and time t to the total volume of the flowing phases (Willhite, 1986; Wu, 2001). The fractional flow can be written as

$$f_\beta = \frac{v_\beta}{v_w + v_n} = \frac{v_\beta}{v_t(t)} \tag{8.30}$$

in which the total flow is

$$v_t(t) = v_w + v_n \tag{8.31}$$

From volume balance due to incompressibility of the system, we have

$$f_w + f_n = 1 \tag{8.32}$$

When the *Forchheimer* Eqn (8.26) is substituted into Eqn (8.30) for one-dimensional non-Darcy flow, the fractional-flow function for the wetting phase may be written in the following form:

$$f_w = \frac{1}{1 + \frac{\rho_w \beta_w}{\rho_n \beta_n} \left(\frac{-\frac{\mu_n}{k_{rn}} + \sqrt{\left(\frac{\mu_n}{k_{rn}}\right)^2 - 4k^2 \rho_n \beta_n \left(\frac{\partial P}{\partial x} + \rho_n g \sin\theta\right)}}{-\frac{\mu_w}{k_{rw}} + \sqrt{\left(\frac{\mu_w}{k_{rw}}\right)^2 - 4k^2 \rho_w \beta_w \left(\frac{\partial P}{\partial x} + \rho_w g \sin\theta\right)}} \right)} \tag{8.33}$$

In general, relative permeability functions and effective non-Darcy flow coefficients are functions of saturation, Eqn (8.33) indicates that the fractional flow, f_w, of the wetting phase is a function of both saturation and pressure gradient. However, for a given injection rate at a time and for given fluid and rock properties of a porous material, the pressure gradient at a given time can be shown by the following to be a function of saturation only under the Buckley–Leverett flow condition:

$$\frac{q_t(t)}{A} - \frac{1}{2k\rho_w\beta_w}\left(-\frac{\mu_w}{k_{rw}} + \sqrt{\left(\frac{\mu_w}{k_{rw}}\right)^2 - 4k^2\rho_w\beta_w\left(\frac{\partial P}{\partial x} + \rho_w g \sin\theta\right)}\right) - \frac{1}{2k\rho_n\beta_n}\left(-\frac{\mu_n}{k_{rn}} + \sqrt{\left(\frac{\mu_n}{k_{rn}}\right)^2 - 4k^2\rho_n\beta_n\left(\frac{\partial P}{\partial x} + \rho_n g \sin\theta\right)}\right) = 0 \tag{8.34}$$

Equation (8.34) shows that the pressure gradient and the saturation are interdependent for this particular displacement system of Buckley–Leverett flow. Similar to non-Newtonian fluid displacement discussed in Chapter 7, Eqn (8.34) implicitly defines the pressure gradient in the system as a function of saturation or vice versa.

The governing Eqn (8.25), subject to the boundary and initial conditions described in Eqns (8.27)–(8.29), can be solved as follows (Wu, 2001),

$$\left(\frac{\mathrm{d}x}{\mathrm{d}t}\right)_{S_w} = \frac{q_t(t)}{\phi A}\left(\frac{\partial f_w}{\partial S_w}\right)_t \tag{8.35}$$

This is the frontal-advance equation for the non-Darcy displacement of two immiscible fluids with the same form as the Buckley–Leverett equation. However, the dependence of the fractional flow f_w for the non-Darcy displacement on saturation is different. The fractional flow f_w is related to saturation not only through the relative permeability functions but also through the non-Darcy flow relation, the effective non-Darcy flow coefficient.

Equation (8.35) shows that for a given time and a given injection rate, a particular wetting-fluid saturation profile propagates through the porous medium at a constant velocity. As in the Buckley–Leverett theory, the saturation for a vanishing capillary-pressure gradient will, in general, become a triple-valued function of distance near the displacement front. Equation (8.35) will then fail to describe the velocity of the shock saturation front because $\partial f_w/\partial S_w$ does not exist on the front because of the discontinuity in S_w at that point. Consideration of material balance across the shock front provides the velocity of the front, as discussed in Section 5.4.2:

$$\left(\frac{\mathrm{d}x}{\mathrm{d}t}\right)_{S_{wf}} = \frac{q_t(t)}{\phi A}\left(\frac{f_w^+ - f_w^-}{S_w^+ - S_w^-}\right)_t \tag{8.36}$$

in which S_{wf} is the displacement-front saturation of the displacing wetting phase. The plus and minus superscripts refer to values immediately ahead of and behind the front, respectively.

The location x_{S_w} of any saturation S_w traveling from the inlet at time t can be determined by integrating Eqn (8.35) with respect to time, which yields

$$x_{S_w} = \frac{1}{\phi A}\int_0^t q_t(\tau)\left(\frac{\partial f_w}{\partial S_w}\right)_{S_w} \mathrm{d}\tau \tag{8.37}$$

This shows that for a general, time-varying injection rate $q_t(t)$, the derivative $\partial f_w/\partial S_w$ of fractional flow with respect to saturation within the integral may also be a time-dependent function (see Eqns (8.33) and (8.34) for how to calculate fractional flow, f_w). Therefore, the solution Eqn (8.37) for non-Darcy displacement differs from the Buckley–Leverett solution. However, if a constant injection rate, q_t, is proposed, then Eqn (8.37) becomes

$$x_{S_w} = \frac{tq_t}{\phi A}\left(\frac{\partial f_w}{\partial S_w}\right)_{S_w} \tag{8.38}$$

in which q_t is the constant injection rate and tq_t is the cumulative volume of the injected fluid at time t. The solution Eqn (8.38) is the same in form as the Buckley–Leverett solution with the same constant injection rate.

Direct use of Eqn (8.38), given x and t, will result in a multiple-valued saturation distribution, which can be handled by a mass-balance calculation, as in the Buckley–Leverett solution. An alternative graphic method of Welge (1952) can be shown (Wu et al., 1991; Wu, 2001) to apply to calculating the above solution in this case. What is different is that the contribution of the pressure gradient dependence on the non-Darcy flow coefficient should be taken into account when calculating the solution in this case. Therefore, the wetting-phase saturation at the displacement saturation front may be determined by

$$\left(\frac{\partial f_w}{\partial S_w}\right)_{S_{wf}} = \frac{(f_w)_{S_{wf}} - (f_w)_{S_{wr}}}{S_{wf} - S_{wr}} \tag{8.39}$$

The average saturation in the displaced zone is given by

$$\left(\frac{\partial f_w}{\partial S_w}\right)_{S_{wf}} = \frac{1}{\overline{S}_w - S_{wr}} \tag{8.40}$$

in which $\overline{S}_w$ is the average saturation of the wetting phase in the swept zone behind the sharp displacement front. Then, the complete saturation profile can be determined using Eqn (8.38) for a given non-Darcy displacement problem with constant injection rate using Welge's approach.

8.4.2 Effects of Forchheimer Non-Darcy Coefficient

The analytical solution presented above is used to give us some insight into non-Darcy flow and displacement phenomena. The physical flow model is a one-dimensional linear porous medium, which is at first saturated uniformly with a nonwetting fluid ($S_n = 0.8$) and a wetting fluid ($S_w = S_{wr} = 0.2$). A constant volumetric injection rate of the wetting fluid is imposed at the inlet ($x = 0$), starting from $t = 0$. The relative permeability curves used for all the calculations here are shown in Figure 8.2(a). The properties of the rock and fluids used are listed in Table 8.1. The solution, Eqn (8.38), is used to obtain the saturation profiles, with the sharp-front saturation determined by Eqn (8.36). The solution evaluation procedure, as discussed above, is computer programmed for the analysis (Appendix D.1).

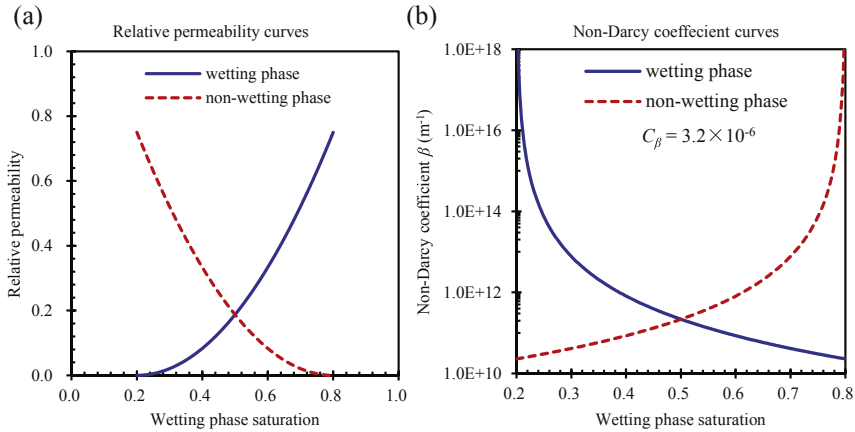

Figure 8.2 (a) Relative permeability curves and (b) non-Darcy flow coefficients as a function of displacing phase saturation.

Table 8.1 Parameters for the non-Darcy displacement examples with Forchheimer equation

Parameters	Value	Unit
Porosity, ϕ	0.30	[-]
Absolute permeability, k	9.869×10^{-13}	[m^2]
Cross-section area, A	1.0	[m^2]
Length of formation, L	5.0	[m]
Injection rate, q_t	1.0×10^{-4}	[m^3/s]
Injection time, t	10.0	[h]
Viscosity of wetting fluid, μ_w	1.0×10^{-3}	[Pa·s]
Viscosity of nonwetting fluid, μ_n	5.0×10^{-3}	[Pa·s]
Residual wetting fluid saturation, S_{wr}	0.2	[-]
Residual nonwetting fluid saturation, S_{nr}	0.2	[-]
Maximum relative permeability, $k_{rw,max}$	0.75	[-]
Maximum relative permeability, $k_{rn,max}$	0.75	[-]
Power index of relative permeability, n_w	2.0	[-]
Power index of relative permeability, n_n	2.0	[-]
Forchheimer non-Darcy flow constant, C_β	3.2×10^{-6}	[m$^{3/2}$]
Density of wetting fluid, ρ_w	1000	[kg/m^3]
Density of nonwetting fluid, ρ_n	800	[kg/m^3]
Directional angle, θ	0	[rad]

Equation (8.6) is incorporated into the calculation of the fractional flow to solve pressure gradients and then the fractional-flow curve corresponding to saturations under different flow conditions. For a given operating condition of constant injection rate, the solution Eqn (8.38)

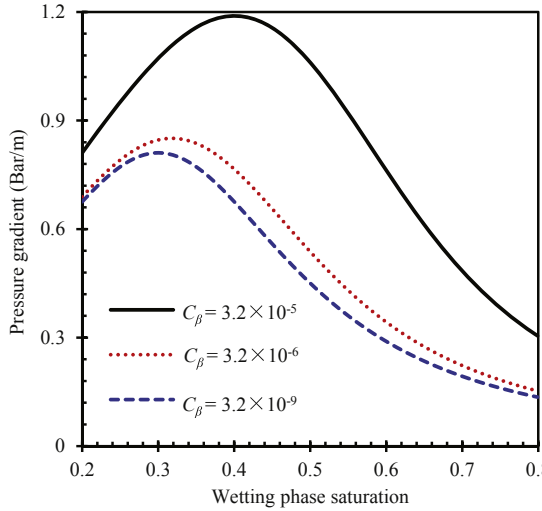

Figure 8.3 Pressure gradients versus wetting-phase saturation for different non-Darcy flow constants.

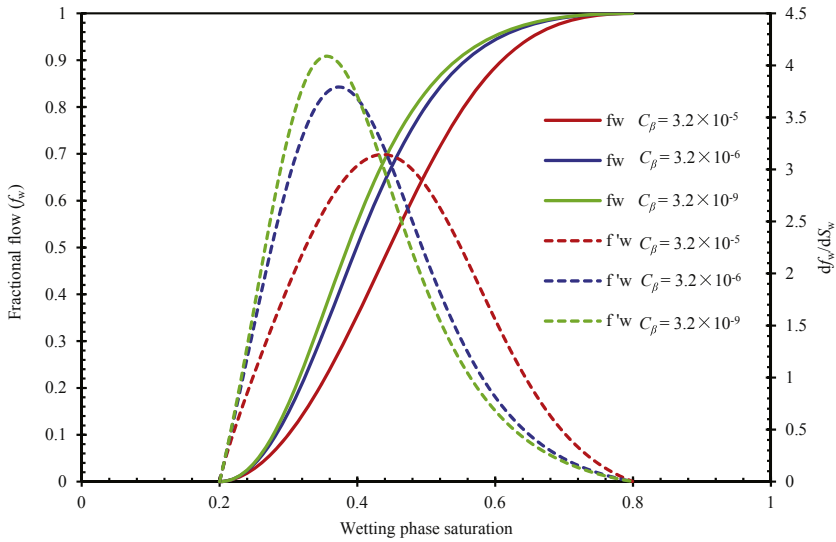

Figure 8.4 Fractional-flow curves and their derivatives with respect to wetting-phase saturation for different non-Darcy flow constants ($q_t = 10^{-5}$ m^3/s).

shows that non-Darcy fluid displacement, according to the *Forchheimer* equation, in a porous medium is characterized not only by relative permeability data, as in Buckley–Leverett displacement, but also by non-Darcy flow coefficients of the two fluids. Using the results from the

analytical solution, some fundamental aspects of non-Darcy fluid displacement will be established.

Figure 8.2(b) shows the relationship of non-Darcy flow coefficient versus saturation, as described by Eqn (8.6), with the relative permeability functions of Figure 8.2(a). The large (or infinite) values of non-Darcy flow coefficients at both ends of the wetting-phase saturation of Figure 8.2(b) are a result of one phase becoming nearly immobile. This is equivalent to that when approaching the two ends; decrease in effective permeability and porosity to the disappearing phase causes an increase in non-Darcy flow coefficients. Physically, for any flow to occur under near residual saturation or near zero effective permeability condition, the corresponding non-Darcy flow coefficient must tend toward infinity.

Figure 8.3, determined using Eqn (8.34) for the flow system, shows that pressure gradients change significantly as a function of saturation for different non-Darcy flow constants. At both high and low values for the wetting-phase saturation the pressure gradients become relatively smaller, because the total flow resistance decreases as the flow is close to the single-phase flow condition. In addition, Figure 8.3 shows that as the non-Darcy flow constant increases, the pressure gradient increases at the same saturation value under the same injection rate, and this is due to a larger non-Darcy flow term or a large second, inertial term on the right-hand side of Eqn (8.4). The resulting fractional-flow curves and their derivatives with the three non-Darcy flow constants are shown in Figure 8.4. Note that fractional-flow curves change also with the non-Darcy flow constants, because of the change in pressure gradient for different non-Darcy flow constants under the same saturation.

Saturation profiles of displacement after a 10-h injection period are plotted in Figure 8.5. In terms of higher sweeping efficiency or shorter displacement front travel distance, a larger non-Darcy flow constant or coefficient gives lower wetting phase flow rates. This results in a better displacement efficiency: more nonwetting phase is displaced from the swept zone. On the other hand, the displacement becomes the Buckley–Leverett process as the non-Darcy constant C_β becomes small or tends to zero.

8.4.3 Effects of Injection Rates

Effect of injection rates on non-Darcy displacement is shown in Figure 8.6, in which a constant non-Darcy flow constant, $C_\beta = 3.2 \times 10^{-6}\ \mathrm{m}^{3/2}$, is used with all three injection rates. Figure 8.6 indicates that non-Darcy displacement may be very sensitive to injection or flow rates. This rate-dependent displacement behavior is entirely different from a Buckley–Leverett or Darcy displacement, because for the latter displacement efficiency is independent of

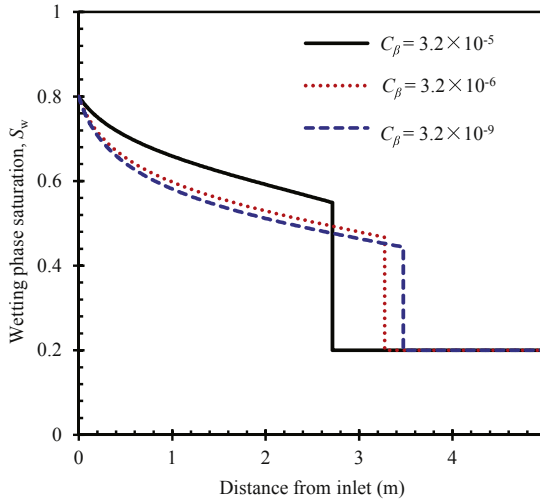

Figure 8.5 Saturation profiles of the non-Darcy displacement for different non-Darcy flow constants after 10 h of injection ($q_t = 10^{-5}$ m^3/s).

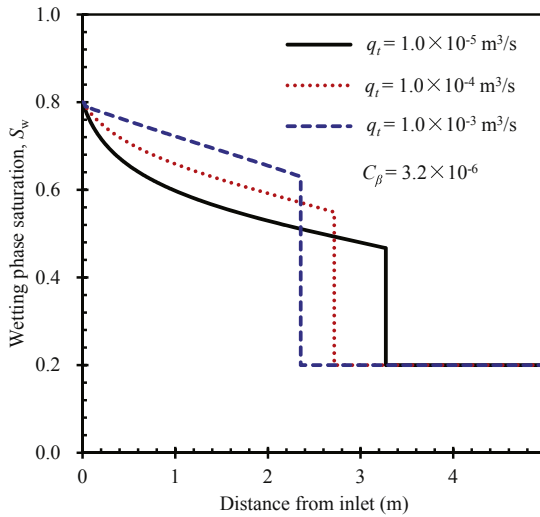

Figure 8.6 Saturation profiles of the non-Darcy displacement for different injection rates after injection of 0.36 m^3 of water.

injection or flow rates for horizontal flow. Under non-Darcy flow condition, Figure 8.6 shows that for the same volume of water injected with the three injection rates, saturation profiles in the system are very different. Larger injection rates display better sweeping efficiency overall. This is because higher injection rates create larger flow resistance to the displacing phase, because of

the non-Darcy effect, and as a result this will lower flow velocity of the displacing phase, relative to that of the displaced phase, resulting in a better displacement performance.

This section presents a Buckley–Leverett analytical solution for non-Darcy displacement of two immiscible fluids through porous media using an extended *Forchheimer* equation. The analytical solution is used to obtain some insight into the physics of displacement involving non-Darcy flow when the effects of non-Darcy flow coefficients in porous media are included using the *Forchheimer* equation. The analysis reveals that non-Darcy displacement is a more complicated process than the Darcy displacement described by the Buckley–Leverett solution. Multiphase non-Darcy flow and displacement are controlled not only by relative permeability curves, such as in Darcy displacement, but also by non-Darcy flow relations and parameters as well as injection or flow rates.

8.5 BUCKLEY–LEVERETT SOLUTION FOR NON-DARCY DISPLACEMENT ACCORDING TO BARREE AND CONWAY MODEL

This section presents a Buckley–Leverett-type analytical solution for the displacement of non-Darcy, two-phase immiscible flow in porous media according to the Barree and Conway model (Wu et al., 2011b). The derivation of the analytical solution is very similar to that used in Section 8.4.1 for the analytical solution of non-Darcy flow with the *Forchheimer* equation.

8.5.1 Analytical Solution

Basically, we use the same assumptions under solution conditions for Buckley–Leverett flow as those in Section 8.4.1 with the *Forchheimer* equation. Then, the flow-governing Eqn (8.25) remains the same, but the flow velocity is now described by Eqn (8.16), i.e., the velocity term in Eqn (8.26) is replaced by

$$v_\beta = -\frac{1}{2\mu_\beta\rho_\beta}\left(\mu_\beta^2 S_\beta \tau + \left(\frac{\partial P}{\partial x} + \rho_\beta g \sin\theta\right) k_{\mathrm{d}} k_{\mathrm{r}\beta} k_{\mathrm{mr}} \rho_\beta\right) + \frac{1}{2\mu_\beta\rho_\beta}\sqrt{\left(\mu_\beta^2 S_\beta \tau + \left(\frac{\partial P}{\partial x} + \rho_\beta g \sin\theta\right) k_{\mathrm{d}} k_{\mathrm{r}\beta} k_{\mathrm{mr}} \rho_\beta\right)^2 - 4\rho_\beta k_{\mathrm{d}} k_{\mathrm{r}\beta} \mu_\beta^2 S_\beta \tau \left(\frac{\partial P}{\partial x} + \rho_\beta g \sin\theta\right)} \tag{8.41}$$

Then the fractional-flow function for the wetting phase may be written in the following form:

$$f_w = \frac{v_w}{v_w + v_n} \tag{8.42}$$

in which the flux v_w and v_n for wetting and nonwetting phases are defined in Eqn (8.41) for non-Darcy flow according the Barree and Conway model. To evaluate the fractional-flow curve using Eqn (8.42), we need to substitute Eqn (8.41) into Eqn (8.42) for both the wetting and nonwetting phases. It appears that the fractional flow f_w of the wetting phase is a function of both saturation and pressure gradient. However, the pressure gradient at a given time can be shown to be constrained by the following to be a function of saturation only under the Buckley–Leverett flow condition (Wu et al., 2011b):

$$\begin{aligned}
&\frac{q_t(t)}{A} + \frac{1}{2\mu_w\rho_w}\left[\mu_w^2 S_w\tau + \left(\frac{\partial P}{\partial x} + \rho_w g\sin\theta\right)kk_{rw}k_{mr}\rho_w\right] \\
&-\frac{1}{2\mu_w\rho_w}\sqrt{\left(\mu_w^2 S_w\tau + \left(\frac{\partial P}{\partial x} + \rho_w g\sin\theta\right)kk_{rw}k_{mr}\rho_w\right)^2 - 4\rho_w kk_{rw}\mu_w^2 S_w\tau\left(\frac{\partial P}{\partial x} + \rho_w g\sin\theta\right)} \\
&+\frac{1}{2\mu_n\rho_n}\left[\mu_n^2 S_n\tau + \left(\frac{\partial P}{\partial x} + \rho_n g\sin\theta\right)kk_{rn}k_{mr}\rho_n\right] \\
&-\frac{1}{2\mu_n\rho_n}\sqrt{\left(\mu_n^2 S_n\tau + \left(\frac{\partial P}{\partial x} + \rho_n g\sin\theta\right)kk_{rn}k_{mr}\rho_n\right)^2 - 4\rho_n kk_{rn}\mu_n^2 S_n\tau\left(\frac{\partial P}{\partial x} + \rho_n g\sin\theta\right)} = 0
\end{aligned} \tag{8.43}$$

Equation (8.43) shows that the pressure gradient and the saturation are interdependent for this particular displacement system of Buckley–Leverett non-Darcy flow. Therefore, Eqn (8.43) implicitly defines the pressure gradient in the system as a function of saturation.

Using the definition of the velocity by Eqn (8.41) and the constraining condition Eqn (8.43) to correlate saturation and pressure gradient in the fractional flow Eqn (8.42), the Buckley–Leverett-type analytical solution with the Barree and Conway model is in the same form as Eqn (8.37) or (8.38) for non-Darcy displacement with the *Forchheimer* equation in Section 8.4.1. However, the difference is the dependence of the fractional flow, f_w, which is now evaluated instead using the Barree and Conway model, Eqn (8.41). We can also show that all the procedures for calculation of the analytical solution Section 8.4.1 are applicable in this case. The solution evaluation procedure is computer programmed for the analysis (Appendix D2).

8.5.2 Effects of Injection Rates

In this section, we use the analytical solution presented in Section 8.5.1 to obtain some insight into non-Darcy flow and displacement phenomena according the Barree and Conway model. The physical flow system is the same as in Section 8.4.2, i.e., a one-dimensional linear porous medium, initially saturated uniformly with a nonwetting fluid ($S_n = 0.8$) and a wetting fluid ($S_w = S_{wr} = 0.2$). A constant volumetric injection rate of the wetting fluid is imposed at the inlet ($x = 0$), starting from $t = 0$. The relative permeability curves for all the calculations here are also shown in Figure 8.7. The properties of the rock and fluids used are listed in Table 8.2.

For a given displacement system with constant injection rate, the solution, Eqn (8.38), shows that non-Darcy fluid displacement in a porous medium is characterized not only by relative permeability data, as in Buckley–Leverett displacement, but also by non-Darcy flow parameters of the Barree and Conway model of the two fluids, as introduced in Eqn (8.42) for the definition of the fractional flow. Using the results from the analytical solution, some fundamental aspects of non-Darcy fluid displacement are established. Figure 8.8, determined using Eqns (8.41)–(8.43) for the flow system, shows that both fractional flow and its

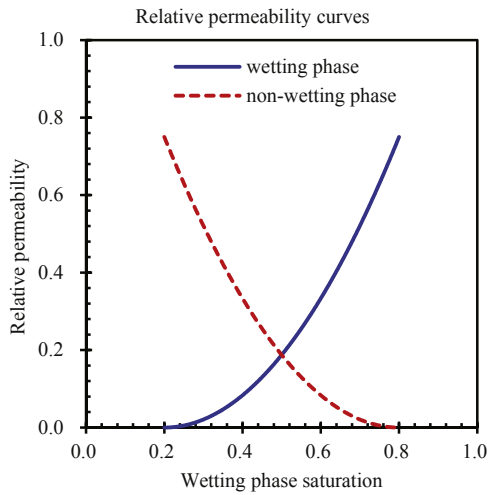

Figure 8.7 Relative permeability curves.

Table 8.2 Parameters for the non-Darcy displacement example with Barree and Conway model

Parameters	Value	Unit
Porosity, ϕ	0.30	[-]
Darcy permeability, k_d	9.869×10^{-12}	[m^2]
Minimum permeability fraction, k_{mr}	0.01	[-]
Inverse of characteristic length, τ	1×10^{3}	[m^{-1}]
Cross-section area, A	1.0	[m^2]
Length of formation, L	5.0	[m]
Injection rate, q_t	1×10^{-4}, 1×10^{-3}, 1×10^{-2}	[m^3/s]
Injection wetting-fluid volume, W_i	0.36	[m^3]
Viscosity of wetting fluid, μ_w	1.0×10^{-3}	[Pa·s]
Viscosity of nonwetting fluid, μ_n	5.0×10^{-3}	[Pa·s]
Residual wetting-fluid saturation, S_{wr}	0.2	[-]
Residual nonwetting-fluid saturation, S_{nr}	0.2	[-]
Maximum relative permeability, $k_{rw,max}$	0.75	[-]
Maximum relative permeability, $k_{rn,max}$	0.75	[-]
Power index of relative permeability, n_w	2.0	[-]
Power index of relative permeability, n_n	2.0	[-]
Density of wetting fluid, ρ_w	1000	[kg/m^3]
Density of nonwetting fluid, ρ_n	800	[kg/m^3]
Directional angle, θ	0	[rad]

derivative curves change significantly with a change in injection rates for the horizontal displacement system, which is entirely different from Darcy displacement behavior.

Saturation profiles after 0.36 m^3 injection for the three injection rates are shown in Figure 8.9, indicating very different displacement efficiency or larger average saturation of the displacing wetting phase within the flooded zones. Similar to the results with the *Forchheimer* non-Darcy flow, the higher the injection rate, the better the displacement efficiency, because of the large flow resistance to the displacing phase due to the non-Darcy flow effect.

8.5.3 Effects of Barree-Conway Non-Darcy Coefficients

Figures 8.10–8.13 present results for sensitivity of two non-Darcy flow characteristic parameters: k_{mr} and τ, of the Barree–Conway model. The corresponding parameters of fluid and rock are summarized in Table 8.2. The

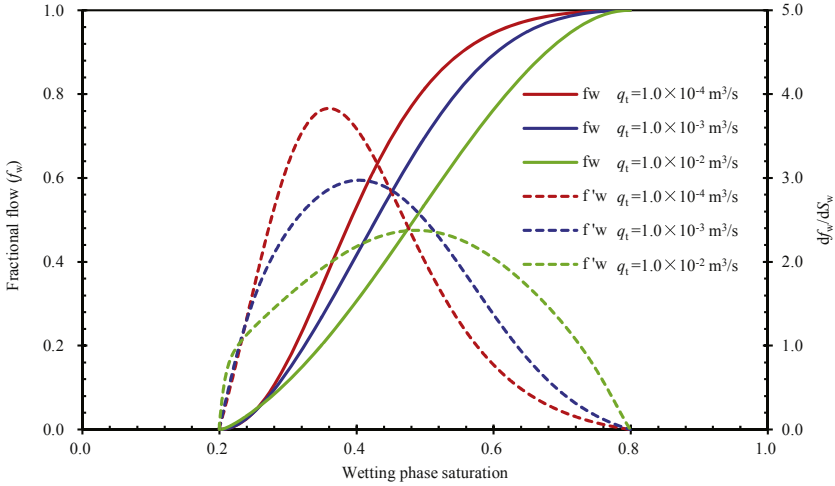

Figure 8.8 Fractional flow and their derivative curves with respect to wetting-phase saturation with different injection rates.

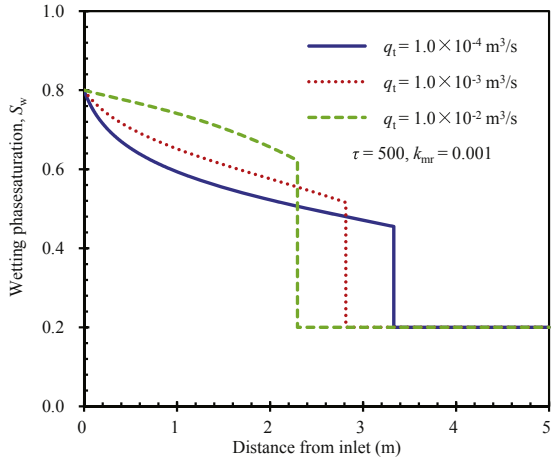

Figure 8.9 Displacement saturation distribution of the non-Darcy displacement system with different injection rates.

resulting fractional flow and its derivative curves are shown in Figures 8.10 and 8.12. As shown in the two figures, fractional-flow curves change also with the non-Darcy model parameters under the same saturation. Pressure gradients and saturation profiles of non-Darcy displacement with varying k_{mr} and τ are

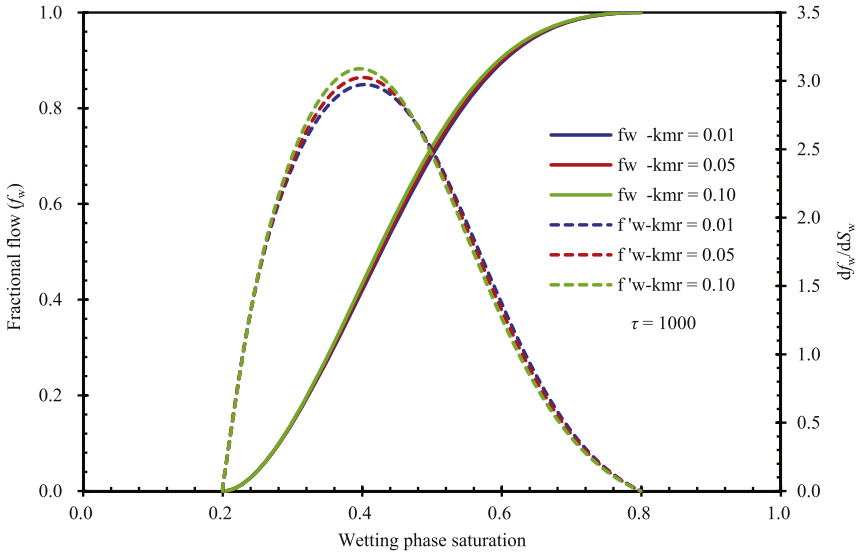

Figure 8.10 Fractional flow and its derivative curves with respect to wetting-phase saturation with different minimum-permeability ratios.

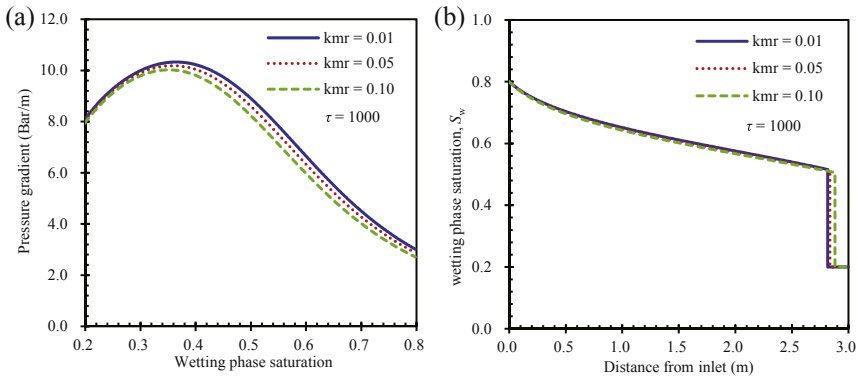

Figure 8.11 Pressure gradient (left) and displacement saturation distributions (right) of the non-Darcy displacement system with different minimum permeability ratios.

plotted in Figure 8.11 and 8.13, showing typical behavior of non-Darcy displacement according to the Barree–Conway model with different model parameters.

For the minimum-permeability ratio, k_{mr}, the ratio value ranges physically from 0 to 1. According to Eqns (8.9) and (8.10), if the permeability ratio approaches 1, the Barree and Conway equation turns into Darcy's law.

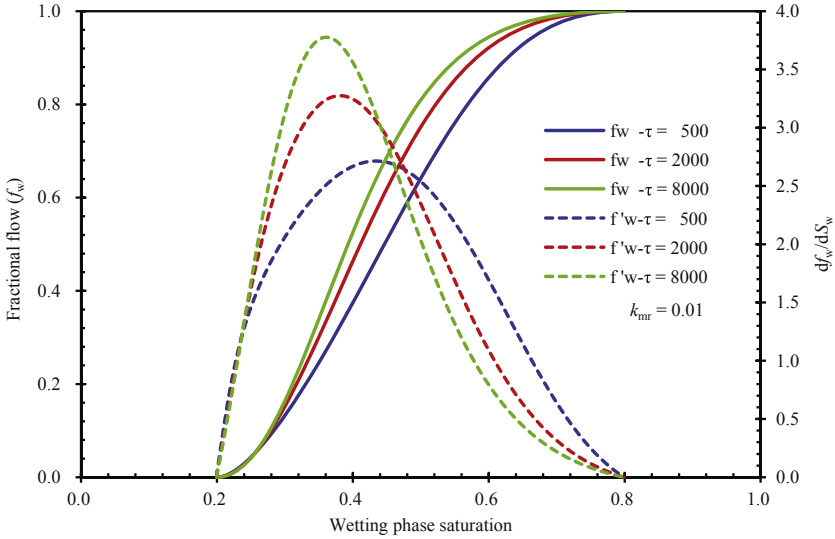

Figure 8.12 Fractional flow and their derivative curves with respect to wetting-phase saturation with different inverses of characteristic lengths.

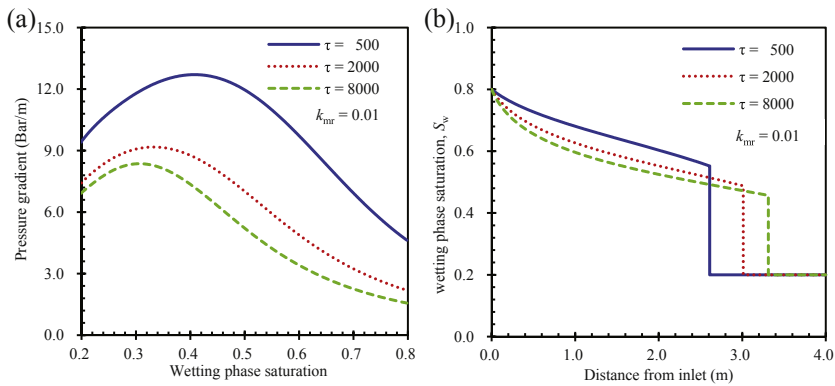

Figure 8.13 Displacement saturation distribution of the non-Darcy displacement system with different inverses of characteristic lengths.

The smaller the minimum-permeability ratio or the smaller the minimum permeability, the stronger is the non-Darcy effect, as shown in Figure 8.11. If the inverse of characteristic length, τ, goes to infinity, the model can be also reduced to the standard Darcy's equation, e.g., the higher the inverse of characteristic length, the less is the non-Darcy effect. This effect can be seen in

Figure 8.13. Higher inverse of characteristic length or lower non-Darcy effect increases the shock-front traveling speed or lower average saturation of the displacing phase. Figures 8.10–8.13 also indicate that the Barree–Conway model results are more sensitive to the parameter τ than to k_{mr}, from the parameters selected.

8.5.4 Comparison with Forchheimer Equation

In an effort to evaluate and compare the two non-Darcy flow models, i.e., *Forchheimer* and Barree–Conway models. Equivalent parameters are derived in the literature between the two models (Al-Otaibi and Wu, 2011; Wu et al., 2011b). They show that the equivalent *Forchheimer* non-Darcy parameters can be calculated from Barree and Conway input parameters with some approximation. From Eqns (8.4) and (8.16), we can solve non-Darcy parameter β_β in term of Barree–Conway input parameters:

$$\beta_\beta = \frac{\mu_\beta(1-k_{mr})}{k_d k_{r\beta}\left(k_{mr}\rho_\beta|v_\beta| + \mu_\beta S_\beta \tau\right)} \tag{8.44}$$

We can calculate the non-Darcy constant in Eqn (8.6), when it is selected for use, as

$$C_\beta(S_\beta) = \frac{\mu_\beta(1-k_{mr})(k_d k_{r\beta})^{\frac{5}{4}}(\phi(S_\beta - S_{\beta r}))^{\frac{3}{4}}}{k_d k_{r\beta}\left(k_{mr}\rho_\beta|v_\beta| + \mu_\beta S_\beta \tau\right)} \tag{8.45}$$

Equation (8.45) indicates that the Forchheimer non-Darcy parameter, C_β, is a function of fluid saturation. As discussed in Section 8.2.1, however, this parameter is generally a constant in Forchheimer Eqn (8.4). Thus, we will calculate the non-Darcy constant, C_β, for both wetting phase and nonwetting phase by

$$C_\beta = \frac{\mu_\beta(1-k_{mr})(k_d k_{r\beta,max})^{\frac{5}{4}}(\phi(S_{\beta,max} - S_{\beta r}))^{\frac{3}{4}}}{k_d k_{r\beta,max}\left(k_{mr}\rho_\beta|v_\beta| + \mu_\beta S_{\beta,max} \tau\right)} \tag{8.46}$$

In application, it is more convenient to use a constant velocity, such as constant injection rate, to approximate the phase velocity, $v_\beta(x, t)$, a function of x coordinate and time to be solved, in Eqn (8.46), instead of the exact solution of substituting Eqn (8.45) into Eqn (8.4). Such an approximation is shown to provide excellently accurate results in single-phase non-Darcy flow (Al-Otaibi and Wu, 2011). For multiphase displacement, Figure 8.14 shows

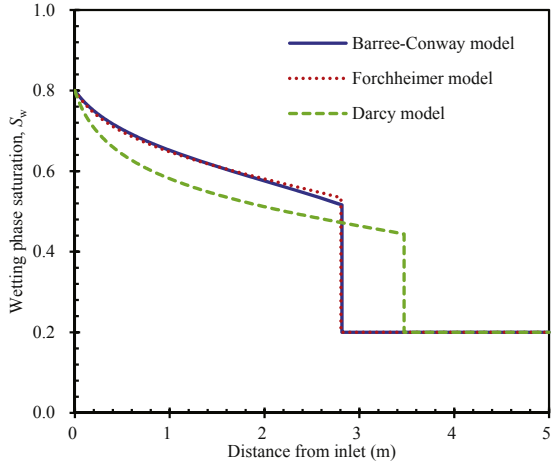

Figure 8.14 Comparison of the results from Darcy, non-Darcy *Forchheimer* and Barree–Conway models.

a comparison of results from Darcy, non-Darcy Forchheimer, and Barree and Conway models. The fluid and rock parameters are listed in Table 8.3. Note that to compare the results from the two models, equivalent non-Darcy flow parameters are used for the two models.

Table 8.3 Parameters for the comparison between with Barree and Conway model

Parameters	Value	Unit
Porosity, ϕ	0.30	[-]
Darcy permeability, k_d	9.869×10^{-12}	[m^2]
Minimum permeability fraction, k_{mr}	0.01	[-]
Inverse of characteristic length, τ	5.0×10^{2}	[m^{-1}]
Cross-section area, A	1.0	[m^2]
Length of formation, L	5.0	[m]
Injection rate, q_t	5×10^{-4}	[m^3/s]
Injection time, t	0.2	[h]
Equivalent non-Darcy flow constant, C_w	8.357×10^{-6}	[$m^{3/2}$]
Equivalent non-Darcy flow constant, C_n	8.444×10^{-6}	[$m^{3/2}$]
Viscosity of wetting fluid, μ_w	1.0×10^{-3}	[Pa·s]
Viscosity of nonwetting fluid, μ_n	5.0×10^{-3}	[Pa·s]
Residual wetting fluid saturation, S_{wr}	0.2	[-]
Residual nonwetting fluid saturation, S_{nr}	0.2	[-]
Maximum relative permeability, $k_{rw,max}$	0.75	[-]
Maximum relative permeability, $k_{rn,max}$	0.75	[-]
Power index of relative permeability, n_w	2.0	[-]
Power index of relative permeability, n_n	2.0	[-]
Density of wetting fluid, ρ_w	1000	[kg/m^3]
Density of nonwetting fluid, ρ_n	800	[kg/m^3]
Directional angle, θ	0	[rad]

As shown in Figure 8.14, the two non-Darcy models, when using the equivalent non-Darcy flow parameters with constant velocity approximation in Eqn (8.46), present very similar flow behavior in which non-Darcy effect decreases the frontal velocity. The slight discrepancy between the two non-Darcy model results is due to the constant velocity approximation and appears to be minimal. However, the difference between the non-Darcy and Darcy displacement seems large in this case in Figure 8.14.

8.6 NON-DARCY DISPLACEMENT IN A ONE-DIMENSIONAL RADIAL SYSTEM

Similar to the derivation in Chapter 6.2 for Buckley–Leverett radial displacement and in Section 7.7 for immiscible displacement of non-Newtonian fluids in a radial system, we can obtain the Buckley–Leverett type analytical solutions for immiscible non-Darcy radial flow according to *Forchheimer* and Barree and Conway models.

8.6.1 Analytical Solution for Non-Darcy Displacement

The assumptions or conditions used to derive the analytical solutions for non-Darcy radial flow are the same as discussed in Section 8.4.1, except we are dealing with horizontal radial flow in this case. Let us consider that the radial flow system consists of two fluids (see Figure 6.1), one as the wetting phase ($\beta = \mathrm{w}$) and the other as the nonwetting phase ($\beta = \mathrm{n}$), then the *Forchheimer* equation of phase β in a radial system can be written as

$$-\frac{\partial P}{\partial r} = \frac{\mu_\beta}{k k_{\mathrm{r}\beta}}\left(\frac{q_\beta}{2\pi r h}\right) + \beta_\beta \rho_\beta \left(\frac{q_\beta}{2\pi r h}\right)\left|\frac{q_\beta}{2\pi r h}\right| \tag{8.47}$$

Then, the volumetric flow rate of phase β at a radial distance and time (r, t) is given by

$$q_\beta = \frac{\pi r h}{k \rho_\beta \beta_\beta}\left(-\frac{\mu_\beta}{k_{\mathrm{r}\beta}} + \sqrt{\left(\frac{\mu_\beta}{k_{\mathrm{r}\beta}}\right)^2 - 4k^2 \rho_\beta \beta_\beta \left(\frac{\partial P}{\partial r}\right)}\right) \tag{8.48}$$

For non-Darcy flow with the Barree and Conway model, we also can obtain the following volumetric flow rate of phase β at a radial system:

$$-\frac{\partial P}{\partial r} = \frac{\mu_\beta\left(\frac{q_\beta}{2\pi r h}\right)}{k_{\mathrm{d}} k_{\mathrm{r}\beta}\left(k_{\mathrm{mr}} + \frac{(1-k_{\mathrm{mr}})\mu_\beta \tau}{\mu_\beta \tau + \rho_\beta \left|\frac{q_\beta}{2\pi r h}\right|}\right)} \tag{8.49}$$

and

$$q_\beta = -\frac{\pi rh}{\mu_\beta \rho_\beta}\left(\mu_\beta^2 S_\beta \tau + \frac{\partial P}{\partial r} k_d k_{r\beta} k_{mr} \rho_\beta\right) + \frac{\pi rh}{\mu_\beta \rho_\beta}\sqrt{\left(\mu_\beta^2 S_\beta \tau + \frac{\partial P}{\partial r} k_d k_{r\beta} k_{mr} \rho_\beta\right)^2 - 4\frac{\partial P}{\partial r}\rho_\beta k_d k_{r\beta} \mu_\beta^2 S_\beta \tau} \tag{8.50}$$

The fractional flow, f_w, for the wetting phase is defined as

$$f_w = \frac{q_w}{q_w + q_n} \tag{8.51}$$

in which h is formation thickness; q_w and q_n are functions of radial distance r and time t, defined in Eqns (8.48) and (8.50), respectively, for using the *Forchheimer* and Barree and Conway models.

It can be shown that the fractional flow, f_w, is a function of saturation only for non-Darcy radial flow, because for a constant injection or production rate, q_t, at the well, the pressure gradient is determined uniquely by the following constraint condition, as discussed in Section 7.7.

$$\frac{q_t}{\pi r_w h} + \frac{1}{k\rho_w \beta_w}\left(\frac{\mu_w}{k_{rw}} - \sqrt{\left(\frac{\mu_w}{k_{rw}}\right)^2 - 4k^2 \rho_w \beta_w \frac{\partial P}{\partial r}}\right) + \frac{1}{k\rho_n \beta_n}\left(\frac{\mu_n}{k_{rn}} - \sqrt{\left(\frac{\mu_n}{k_{rn}}\right)^2 - 4k^2 \rho_n \beta_n \frac{\partial P}{\partial r}}\right) = 0 \tag{8.52}$$

for non-Darcy flow with the *Forchheimer* equation; or,

$$\frac{q_t}{\pi r_w h} + \frac{1}{\mu_n \rho_n}\left[\left(\mu_n^2 S_n \tau + \frac{\partial P}{\partial r} k_d k_{rn} k_{mr} \rho_n\right) - \sqrt{\left(\mu_n^2 S_n \tau + \frac{\partial P}{\partial r} k_d k_{rn} k_{mr} \rho_n\right)^2 - 4\frac{\partial P}{\partial r}\rho_n k_d k_{rn} \mu_n^2 S_n \tau}\right] + \frac{1}{\mu_w \rho_w}\left[\left(\mu_w^2 S_w \tau + \frac{\partial P}{\partial r} k_d k_{rw} k_{mr} \rho_w\right) - \sqrt{\left(\mu_w^2 S_w \tau + \frac{\partial P}{\partial r} k_d k_{rw} k_{mr} \rho_w\right)^2 - 4\frac{\partial P}{\partial r}\rho_w k_d k_{rw} \mu_w^2 S_w \tau}\right] = 0 \tag{8.53}$$

for non-Darcy flow with the Barree and Conway model.

With the definition of the fractional flow, f_w, in Eqn (8.51) and using the same assumptions of the Buckley–Leverett theory, we can obtain the Buckley–Leverett type equation, frontal advance equation, in a radial system as discussed in Section 6.2.1,

$$\frac{\partial r_{S_w}^2}{\partial t} = \frac{q_t}{\phi \pi h}\left(\frac{\partial f_w}{\partial S_w}\right)_{S_w} \tag{8.54}$$

Integrating Eqn (8.54) yields

$$r_{S_w}^2 = r_w^2 + \frac{q_t t}{\pi h \phi} \cdot \left.\frac{\partial f_w}{\partial S_w}\right|_{S_w} \tag{8.55}$$

in which r_w is wellbore radius. Equation (8.55) describes a constant saturation, S_w, traveling to r_{S_w} at time of t.

8.6.2 Evaluation and Application of the Solution

With given relative permeability curves, fluid and rock properties, and non-Darcy flow model parameters of the non-Darcy flow model, selected one from the *Forchheimer* equation and the Barree and Conway model, a general procedure for evaluating the flow and displacement behavior of non-Darcy flow using the Buckley–Leverett type analytical solution, Eqn (8.55), is as follows:

1. Pick a value of the injection phase, saturation, e.g., S_w, solve pressure gradients $\frac{\partial P}{\partial r}$, using Eqn (8.52) or (8.53), according to the selection of the *Forchheimer* equation or the Barree and Conway model, for different injection rates to obtain and plot the relationship between pressure gradient and saturation corresponding to the injection rate.
2. Calculate the fractional flow, f_w, by the fractional function, Eqn (8.51), i.e., using a saturation and its corresponding pressure gradients determined in Step (1).
3. Calculate the derivatives of fractional flow, $\partial f_w / \partial S_w$, with respect to saturation.
4. Determine the shock-front saturation, S_{wf}, location by Welge graphic method or integral method based on mass-balance principle.
5. Calculate the saturation profile for $S_{wf} < S_w < 1 - S_{wr}$ from $r = r_w$ to $r = r_{S_{wf}}$ according to Eqn (8.55) for a given injection rate.

Applying the above solution and evalution procedure, two analytical examples are presented. One is based on the *Forchheimer* equation, and the other proceeds according to the Barree–Conway model. The fluid and rock parameters are summarized in Table 8.4.

Table 8.4 Parameters for the examples in the radial system

Parameters	Forchheimer	Barree–Conway	Unit
Porosity, ϕ	0.20	0.30	[-]
Darcy permeability, k_d	9.869×10^{-12}	9.869×10^{-12}	[m^2]
Minimum permeability fraction, k_{mr}	-	0.01	[-]
Inverse of characteristic length, τ	-	5.0×10^{2}	[m^{-1}]
Radius of outer boundary, R	6.0	6.0	[m]
Radius of injection well, r_w	0.1	0.1	[m]
Thickness of reservoir, h	1.0	1.0	[m]
Injection rate, q_t	1×10^{-4}	1×10^{-4}	[m^3/s]
Injection time, t	1.0	1.0	[day]
Equivalent non-Darcy flow constant, C_w	3.2×10^{-6}	-	[$m^{3/2}$]
Equivalent non-Darcy flow constant, C_n	3.2×10^{-6}	-	[$m^{3/2}$]
Viscosity of wetting fluid, μ_w	1.0×10^{-3}	1.0×10^{-3}	[Pa·s]
Viscosity of nonwetting fluid, μ_n	5.0×10^{-3}	5.0×10^{-3}	[Pa·s]
Residual wetting-fluid saturation, S_{wr}	0.2	0.2	[-]
Residual nonwetting-fluid saturation, S_{nr}	0.2	0.2	[-]
Maximum relative permeability, $k_{rw,max}$	0.75	0.75	[-]
Maximum relative permeability, $k_{rn,max}$	0.75	0.75	[-]
Power index of relative permeability, n_w	2.0	2.0	[-]
Power index of relative permeability, n_n	2.0	2.0	[-]
Density of wetting fluid, ρ_w	1000	1000	[kg/m^3]
Density of nonwetting fluid, ρ_n	800	800	[kg/m^3]
Directional angle, θ	0	0	[rad]

Figures 8.15 and 8.16 show the corresponding curves of pressure gradient and wetting- or injected-phase saturations. As the displacing front radius increases, the displacing velocity of water shock-front saturation becomes slower and slower, because of the larger fluid volume to be displaced in a radial reservoir. As discussed in Sections 8.4 and 8.5, we also can

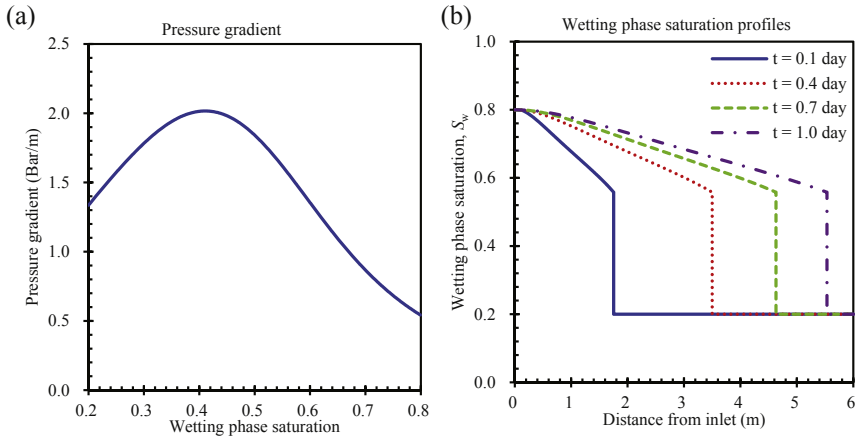

Figure 8.15 Pressure gradient and wetting-phase saturation profiles in a radial system according to the *Forchheimer* equation.

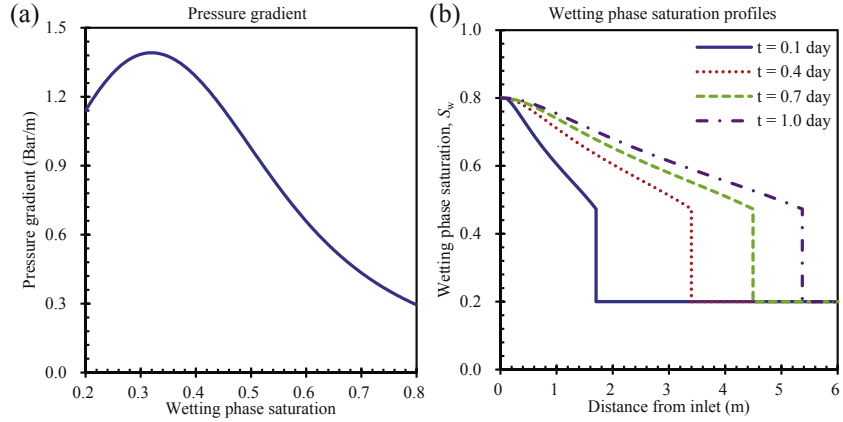

Figure 8.16 Pressure gradient and wetting-phase saturation profiles in a radial system according to the Barree–Conway model.

analyze the sensitivities of the non-Darcy parameters and injection rates in a radial flow case using the analytical solutions.

8.7 NUMERICAL MODEL, SOLUTION AND VERIFICATION

8.7.1 Numerical Formulation and Solution

Equations (8.17) and (8.4) or (8.16), for implementation of the *Forchheimer* equation and the Barree–Conway model, respectively, for multiphase non-Darcy flow of gas, oil, and water in porous media, are highly nonlinear and

in general need to be solved numerically. In this chapter, we use the general numerical framework model, which is discussed in Chapter 4 and is also applicable to non-Darcy flow, to derive a numerical formulation and its solution scheme for solving the non-Darcy flow equations. As discussed in chapter 4, the numerical formulation and solution procedure consists of three steps: (1) spatial discretization of the mass-conservation equation using a control volume or integrated finite difference approach; (2) fully implicit time discretization; and (3) Newton iterative approaches to solve the resulting nonlinear, discrete algebraic equations. The discrete nonlinear equations for water, oil, and gas flow at node i are written, similar to Eqn (4.1), as follows (Wu, 2002b; Wu et al., 2011a)

$$\left[\left(\phi S_\beta \rho_\beta\right)_i^{n+1} - \left(\phi S_\beta \rho_\beta\right)_i^{n}\right] \frac{V_i}{\Delta t} = \sum_{j \in \eta_i} flow_{ij}^{\beta,n+1} + Q_i^{\beta,n+1}, \quad \beta = \mathrm{w}, \mathrm{o}, \mathrm{g} \tag{8.56}$$

in which symbols and notations are the same as used for Eqn (4.1) and the sink/source term, $Q_i^{\beta,n+1}$ is evaluated using Eqn (4.11). However, the mass-flow term is defined differently with non-Darcy flow. For evaluation of flow between two neighboring grid blocks (i,j), the mass-flow term, "$flow_{ij}^{\beta}$", can be directly evaluated, for non-Darcy flow modeled using the *Forchheimer* equation and the Barree–Conway model, as follows.

For the non-Darcy flow described by the *Forchheimer* equation, the mass-flow term is evaluated as (Wu, 2002b)

$$flow_{ij}^{\beta} = \frac{A_{ij}}{2\left(k\beta_\beta\right)_{ij+1/2}} \left[-\frac{1}{\lambda_\beta} + \sqrt{\left(\frac{1}{\lambda_\beta}\right)^2 - \overline{\gamma}_{ij}\left(\Phi_{\beta j} - \Phi_{\beta i}\right)} \right] \tag{8.57}$$

In Eqn (8.57), we also use the same definitions for symbols and notations as in Eqns (4.3), (4.5), and (4.7)–(4.10); i.e., subscript $ij + 1/2$ denotes a proper averaging of properties at the interface between the two grid blocks; and A_{ij} is the common interface area between connected grid blocks i and j (as illustrated in Figure 4.1). The mobility, λ_β, of phase β is defined and calculated using Eqn (4.8); and the flow potential term, $\Phi_{\beta i}$, is evaluated using Eqn (8.4). The transmissivity of flow terms is defined (if the integrated finite difference scheme is used) as

$$\overline{\gamma}_{ij} = \frac{4\left(k^2 \rho_\beta \beta_\beta\right)_{ij+1/2}}{d_i + d_j} \tag{8.58}$$

in which d_i is the distance from the center of grid block i to the interface between elements i and j (Figure 4.1).

In the numerical model formulation, absolute permeability, relative permeability, and the effective non-Darcy flow coefficient, β_β, are all considered as flow properties of the porous media and need to be averaged between connected elements in calculating the mass-flow terms. In general, weighting approaches used are that absolute permeability is harmonically weighted along the connection between grid blocks i and j, relative permeability and effective non-Darcy flow coefficients are both upstream weighted.

For the non-Darcy flow described by the *Barree and Conway* model and the mass-flow term is evaluated as (Wu et al., 2011b):

$$flow_{ij}^{\beta} = \frac{A_{ij}}{2\rho_\beta \mu_\beta}\left\{ -\left(\mu_\beta^2 S_\beta \tau + \delta\Phi_{\beta,ij} k_{\mathrm{d}} k_{\mathrm{r}\beta} k_{\mathrm{rm}} \rho_\beta\right) + \sqrt{\left(\mu_\beta^2 S_\beta \tau + \delta\Phi_{\beta,ij} k_{\mathrm{d}} k_{\mathrm{r}\beta} k_{\mathrm{rm}} \rho_\beta\right)^2 - 4\mu_\beta \rho_\beta \delta\Phi_{\beta,ij} k_{\mathrm{d}} k_{\mathrm{r}\beta} \mu_\beta S_\beta \tau}\right\} \tag{8.59}$$

in which the discrete flow potential 'gradient,' $\delta\Phi_{\beta,ij}$, between two grid blocks, i and j, is defined in an integrated finite difference as

$$\delta\Phi_{\beta,ij} = \frac{\left(P_{\beta,i} - \rho_{\beta,ij+1/2}\ g\ D_i\right) - \left(P_{\beta,j} - \rho_{\beta,ij+1/2}\ g\ D_j\right)}{d_i + d_j} \tag{8.60}$$

Note that Eqn (8.56), with flow terms evaluated by Eqn (8.57) for non-Darcy flow according to the *Forchheimer* equation or by Eqn (8.59) according to the Barree and Conway model, has the same form regardless of the dimensionality of the model flow domain, i.e., it applies to one-, two-, or three-dimensional analyses of multiphase non-Darcy flow through porous and fractured media.

Newton iterations are used to solve Eqn (8.56), which is written in a residual form,

$$R_i^{\beta,n+1} = \left\{\left(\phi S_\beta \rho_\beta\right)_i^{n+1} - \left(\phi S_\beta \rho_\beta\right)_i^{n}\right\}\frac{V_i}{\Delta t} - \sum_{j\in\eta_i}\left(flow_{ij}^{\beta}\right)^{n+1} - Q_i^{\beta,n+1} = 0, \quad i = 1, 2, \ldots, N \tag{8.61}$$

in which N is the total number of grid blocks in the grid. For a three-phase flow system, $3 \times N$ coupled nonlinear equations must be solved, including three equations at each grid block for the three mass-balance equations of

water, oil, and gas, respectively. The three primary variables selected for each grid block are gas pressure, gas saturation, and oil saturation, respectively. In terms of the residual for element i and equation β, and the primary variables, the Newtonian scheme gives rise to

$$\sum_m \frac{\partial R_i^{\beta,n+1}(x_{m,p})}{\partial x_m}(\delta x_{m,p+1}) = -R_i^{\beta,n+1}(x_{m,p}), \quad m = 1,2,3 \tag{8.62}$$

in which x_m is the primary variable m with $m = 1, 2,$ and 3, respectively, at node i and all its direct neighbors; p is the iteration level; and $i = 1, 2, 3, \ldots, N$, the nodal index. The primary variables are updated after each iteration:

$$x_{m,p+1} = x_{m,p} + \delta x_{m,p+1} \tag{8.63}$$

The iteration process continues until the residuals $R_i^{\beta,n+1}$ or other convergence criteria over an iteration are reduced below preset convergence tolerances. A numerical method is used to construct the Jacobian matrix for Eqn (8.62), as outlined by Forsyth et al. (1995).

8.7.2 Comparison with Analytical Solutions

In this section, the analytical solutions are used to examine the validity of the numerical formulation, discussed in Section 8.7.1, which is implemented in a general-purpose, three-phase reservoir simulator, the MSFLOW code (Wu, 1998), for modeling multiphase non-Darcy flow and displacement processes with the *Forchheimer* equation or the Barree and Conway model.

To reduce the effects of discretization on numerical simulation results, very fine, uniform mesh spacing ($\Delta x = 0.01$ m) is chosen. A one-dimensional 5-m linear domain is discretized into 500 one-dimensional uniform grid blocks. For Forchheimer non-Darcy flow, the fluid and rock parameters used for this problem are identical to those in Section 8.4.2, as illustrated in Table 8.5. In the numerical simulation, the non-Darcy flow coefficient, Eqn (8.6), is treated as a flow property and is estimated using a full upstream weighting scheme as that for the relative permeability function. For Barree–Conway non-Darcy flow, the fluid and rock parameters are also summarized in Table 8.4.

The comparison between the analytical and numerical solutions is shown in Figure 8.17. The figures indicate that the numerical results are in excellent agreement with the analytical prediction of the non-Darcy displacement for the entire wetting-phase sweeping zone. Similar to modeling the

Table 8.5 Fluid and rock parameters for comparison between analytical and numerical results

Parameters	Forchheimer	Barree–Conway	Unit
Porosity, ϕ	0.30	0.30	[-]
Darcy permeability, k_d	9.869×10^{-13}	9.869×10^{-13}	[m^2]
Minimum permeability fraction, k_{mr}	-	0.01	[-]
Inverse of characteristic length, τ	-	5.0×10^{2}	[m^{-1}]
Length of formation, L	5.0	5.0	[m]
Cross-section area, A	1.0	1.0	[m]
Injection rate, q_t	1×10^{-5}	1×10^{-5}	[m^3/s]
Injection time, t	10.0	10.0	[day]
Equivalent non-Darcy flow constant, C_w	3.2×10^{-6}	-	[$m^{3/2}$]
Equivalent non-Darcy flow constant, C_n	3.2×10^{-6}	-	[$m^{3/2}$]
Viscosity of wetting fluid, μ_w	1.0×10^{-3}	1.0×10^{-3}	[Pa·s]
Viscosity of nonwetting fluid, μ_n	5.0×10^{-3}	5.0×10^{-3}	[Pa·s]
Residual wetting-fluid saturation, S_{wr}	0.2	0.2	[-]
Residual nonwetting-fluid saturation, S_{nr}	0.2	0.2	[-]
Maximum relative permeability, $k_{rw,max}$	0.75	0.75	[-]
Maximum relative permeability, $k_{rn,max}$	0.75	0.75	[-]
Power index of relative permeability, n_w	2.0	2.0	[-]
Power index of relative permeability, n_n	2.0	2.0	[-]
Density of wetting fluid, ρ_w	1000	1000	[kg/m^3]
Density of nonwetting fluid, ρ_n	800	800	[kg/m^3]
Directional angle, θ	0	0	[rad]

displacement of non-Newtonian fluids, at the shock, advancing saturation front, the numerical solution deviates only slightly from the analytical solution, resulting from a typical "smearing front" phenomenon of numerical dispersion effects when matching the Buckley–Leverett type solution using numerical simulation (Aziz and Settari, 1979).

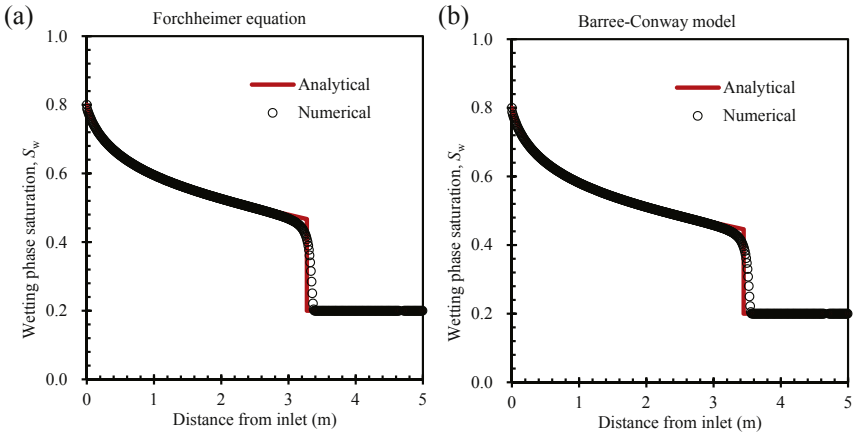

Figure 8.17 Comparison between analytical and numerical solutions of non-Darcy models.

REFERENCES

Al-Otaibi, A.M., Wu, Y.-S., 2010. Transient behavior and analysis of non-Darcy flow in porous and fractured reservoirs according to the Barree and Conway model. In: SPE Western Regional Meeting. Anaheim, California, USA. http://doi.org/10.2118/133533-MS.

Al-Otaibi, A., Wu, Y.-S., 2011. An alternative approach to modeling non-Darcy flow for pressure transient analysis in porous and fractured reservoirs. In: SPE/DGS Saudi Arabia Section Technical Symposium and Exhibition. Al-Khobar, Saudi Arabia. http://doi.org/10.2118/149123-MS.

Aziz, K., Settari, A., 1979. Petroleum Reservoir Simulation. Applied Science Publishers, London.

Barree, R.D., Conway, M.W., 2004. Beyond beta factors: a complete model for Darcy Forchheimer and trans-Forchheimer flow in porous media. In: SPE Annual Technical Conference and Exhibition. Houston, Texas. http://doi.org/10.2118/89325-MS.

Barree, R.D., Conway, M., 2007. Multiphase non-Darcy flow in proppant packs. In: SPE Annual Technical Conference and Exhibition. Anaheim, California, USA. http://doi.org/10.2118/109561-MS.

Barree, R.D., Conway, M., 2009. Multiphase non-Darcy flow in proppant packs. SPE Production & Operations 24 (2), 257–268.

Cooper, J.W., Wang, X., Mohanty, K.K., 1999. Non-Darcy-flow studies in anisotropic porous media. SPE Journal 4 (4), 334–341.

Evans, R.D., Hudson, C.S., Greenlee, J.E., 1987. The effect of an immobile liquid saturation on the non-Darcy flow coefficient in porous media. SPE Production Engineering 2 (4), 331–338.

Evans, E.V., Evans, R.D., 1988. Influence of an immobile or mobile saturation on non-Darcy compressible flow of real gases in propped fractures. Journal of Petroleum Technology 40 (10), 1343–1351.

Firoozabadi, A., Katz, D.L., 1979. An analysis of high-velocity gas flow through porous media. Journal of Petroleum Technology 31 (2), 211–216.

Forchheimer, P., 1901. Wasserbewegung durch boden. Zeitschrift des Vereines Deutscher Ingenieure, 45, 1782–1788.

Forsyth, P.A., Wu, Y.S., Pruess, K., 1995. Robust numerical methods for saturated-unsaturated flow with dry initial conditions in heterogeneous media. Advances in Water Resources 18 (1), 25–38.
Friedel, T., Voigt, H.-D., 2006. Investigation of non-Darcy flow in tight-gas reservoirs with fractured wells. Journal of Petroleum Science and Engineering 54 (3), 112–128.
Guppy, K.H., Cinco-Ley, H., Ramey Jr., H.J., 1981. Effect of non-Darcy flow on the constant-pressure production of fractured wells. Society of Petroleum Engineers Journal 21 (3), 390–400.
Guppy, K.H., Cinco-Ley, H., Ramey Jr., H.J., 1982. Non-Darcy flow in wells with finite-conductivity vertical fractures. Society of Petroleum Engineers Journal 22 (5), 681–698.
Hagoort, J., 2004. Non-Darcy flow near hydraulically fractured wells. SPE Journal 9 (2), 180–185.
Holditch, S.A., Morse, R.A., 1976. The effects of non-Darcy flow on the behavior of hydraulically fractured gas wells. Journal of Petroleum Technology 28 (10), 1169–1179.
Katz, D.L.V., Lee, R.L., 1990. Natural Gas Engineering: Production and Storage. McGraw-Hill, New York.
Lai, B., 2010. Experimental Measurements and Numerical Modeling of High Velocity Multiphase Non-Darcy Flow Effects in Porous Media. Colorado School of Mines.
Lai, B., Miskimins, J.L., 2010. A new technique for accurately measuring two-phase relative permeability under non-Darcy flow conditions. In: SPE Annual Technical Conference and Exhibition. Florence, Italy. Society of Petroleum Engineers. http://doi.org/10.2118/134501-MS.
Lai, B., Miskimins, J.L., Wu, Y.-S., 2012. Non-darcy porous-media flow according to the Barree and Conway model: laboratory and numerical-modeling studies. SPE Journal 17 (1), 70–79.
Lee, R.L., Logan, R.W., Tek, M.R., 1987. Effect of turbulence on transient flow of real gas through porous media. SPE Formation Evaluation 2 (1), 108–120.
Liu, X., Civan, F., Evans, R.D., 1995. Correlation of the non-Darcy flow coefficient. Journal of Canadian Petroleum Technology 34 (10), 50–54.
Lopez-Hernandez, H.D., 2007. Experimental Analysis and Macroscopic and Pore-level Flow Simulations to Compare Non-Darcy Flow Models in Porous Media. Colorado School of Mines.
Macini, P., Mesini, E., Viola, R., 2011. Laboratory measurements of non-Darcy flow coefficients in natural and artificial unconsolidated porous media. Journal of Petroleum Science and Engineering 77 (3), 365–374.
Miskimins, J.L., Lopez, H.D.J., Barree, R.D., 2005. Non-Darcy flow in hydraulic fractures: does it really matter?. In: SPE Annual Technical Conference and Exhibition. Dallas, Texas http://doi.org/10.2118/96389-MS.
Narayanaswamy, G., Sharma, M.M., Pope, G.A., 1999. Effect of heterogeneity on the non-Darcy flow coefficient. SPE Reservoir Evaluation and Engineering 2 (3), 296–302.
Nashawi, I.S., 2006. Constant-pressure well test analysis of finite-conductivity hydraulically fractured gas wells influenced by non-Darcy flow effects. Journal of Petroleum Science and Engineering 53 (3), 225–238.
Ramey, J.H.J., 1965. Non-Darcy flow and wellbore storage effects in pressure build-up and drawdown of gas wells. Journal of Petroleum Technology 17 (2), 223–233.
Scheidegger, A.E., 1974. The Physics of Flow through Porous Media. University of Toronto Press.
Skjetne, E., Auriault, J.L., 1999. New insights on steady, non-linear flow in porous media. European Journal of Mechanics-B/Fluids 18 (1), 131–145.
Swift, G.W., Kiel, O.G., 1962. The prediction of gas-well performance including the effect of non-Darcy flow. Journal of Petroleum Technology 14 (7), 791–798.

Tek, M.R., Coats, K.H., Katz, D.L., 1962. The effect of turbulence on flow of natural gas through porous reservoirs. Journal of Petroleum Technology 14 (7), 799–806.
Welge, H.J., 1952. A simplified method for computing oil recovery by gas or water drive. Journal of Petroleum Technology 4 (4), 91–98.
Whitaker, S., 1996. The Forchheimer equation: a theoretical development. Transport in Porous Media 25 (1), 27–61.
Willhite, G.P., 1986. Waterflooding. Society of Petroleum Engineers, Richardson, TX.
Wu, Y.-S., 1998. MSFLOW: Multiphase Subsurface Flow Model of Oil, Gas and Water in Porous and Fractured Media with Water Shut-off Capability. DOCUMENTATION and User's Guide, Walnut Creek, Califonia.
Wu, Y.-S., 2001. Non-Darcy displacement of immiscible fluids in porous media. Water Resources Research 37 (12), 2943–2950.
Wu, Y.-S., 2002a. An approximate analytical solution for non-Darcy flow toward a well in fractured media. Water Resources Research 38 (3), 5-1–5–7.
Wu, Y.-S., 2002b. Numerical simulation of single-phase and multiphase non-Darcy flow in porous and fractured reservoirs. Transport in Porous Media 49 (2), 209–240.
Wu, Y.-S., Lai, B., Miskimins, J.L., 2011a. Simulation of non-Darcy porous Media flow according to the Barree and Conway model. Journal of Computational Multiphase Flows 3 (2), 107–122.
Wu, Y.-S., Lai, B., Miskimins, J.L., Fakcharoenphol, P., Di, Y., 2011b. Analysis of multiphase non-Darcy flow in porous media. Transport in Porous Media 88 (2), 205–223.
Wu, Y.-S., Li, J., Ding, D., Wang, C., Di, Y., 2014. A generalized framework model for the simulation of gas production in unconventional Gas reservoirs. SPE Journal 19 (5), 845–857.
Wu, Y.-S., Pruess, K., Witherspoon, P.A., 1991. Displacement of a Newtonian fluid by a non-Newtonian fluid in a porous medium. Transport in Porous Media 6 (2), 115–142.

CHAPTER 9

Multiphase Flow in Fractured Porous Media

9.1 INTRODUCTION

Naturally fractured reservoirs exist throughout the world and represent significant amounts of oil and gas reserves, water, and other natural resources on Earth. In the past half-century, the study of fluid flow and transport processes in fractured porous media has received great attention and has been one of the most active areas in investigating multiphase flow in subsurface reservoirs. This is because of its importance to underground natural-resource recovery, waste storage and disposal, environmental remediation, CO_2 geosequestration, and many other subsurface applications. There has been an increasing interest in fracture flow in recent years, because of the need to characterize flow through hydraulically fractured reservoirs with low permeability in the petroleum industry.

Since the 1960s, significant progress has been made toward understanding and modeling flow and transport processes in fractured rock (Barenblatt et al., 1960; Warren and Root, 1963; Kazemi, 1969; Pruess and Narasimhan, 1985; Wu and Pruess, 1988; Kazemi et al., 1992). Despite these advances, modeling the coupled processes of multiphase fluid flow, heat transfer, and chemical migration in a fractured porous medium remains a conceptual and mathematical challenge. The challenge arises primarily from (1) the inherent heterogeneity and uncertainties associated with characterization of a fracture–matrix system for any field-scale problem; (2) the difficulties in conceptualizing, understanding, and describing flow and transport processes in such a complicated formation system; and (3) the limitations from measurements of field fracture properties to computational intensity for incorporation of realistic three-dimensional (3-D) field fractures in mathematical models.

Research efforts, driven by the increasing need to develop petroleum and geothermal energy as well as other natural underground resources in subsurface and to resolve concerns of subsurface contamination, have developed many numerical modeling approaches and techniques (Warren

Multiphase Fluid Flow in Porous and Fractured Reservoirs
ISBN 978-0-12-803848-2
http://dx.doi.org/10.1016/B978-0-12-803848-2.00009-X

and Root, 1963; Kazemi, 1969; Pruess and Narasimhan, 1985; Wu and Pruess, 1988; Berkowitz, 2002; Neuman, 2005). Mathematical modeling approaches developed in the past few decades in general rely on continuum approaches and involve developing conceptual fracture models, incorporating the geometrical information of a given fracture–matrix system, setting up mass- and energy-conservation equations for fracture–matrix domains, and then solving discrete nonlinear algebraic equations, which couple multiphase fluid flow with other physical processes and are solved numerically. The key issue for simulating flow in fractured rock, however, is how to handle fracture–matrix interaction under different conditions involving multiple-phase flow. This is because the fracture–matrix interaction distinguishes the flow through *fractured* porous media from that through homogeneous or heterogeneous *single-porosity* porous media.

To model fracture–matrix interaction for multiphase fluid flow in fractured porous media, investigators have developed and applied many different conceptual models and various modeling approaches (Kazemi, 1969; Pruess and Narasimhan, 1985; Wu and Pruess, 1988; Neuman, 2005). In modeling multiphase flow, chemical transport, and heat transfer in fractured porous media, the most critical issue is how to handle interporosity "flow" or interaction of mass and thermal energy at fracture–matrix interfaces under multiphase flow and isothermal or nonisothermal conditions. Commonly used mathematical methods for dealing with fracture–matrix interaction include: (1) an explicit discrete-fracture and matrix model (e.g., Snow, 1965, 1969; Gong et al., 2008; Li and Lee, 2008; Moinfar et al., 2012, 2014; Huang et al., 2014); (2) the dual-continuum method, including double- and multi-porosity, dual-permeability, or the more general "Multiple INteraction Continua" (MINC) method (Warren and Root, 1963; Kazemi, 1969; Pruess and Narasimhan, 1985; Wu and Pruess, 1988; Wu et al., 2004a); and (3) the effective-continuum method (ECM) (Wu et al., 1999; Wu, 2000).

In this chapter, we discuss the physical process of multiphase flow in fractured porous media as well as commonly used physical concepts for fracture–matrix interaction in fractured reservoirs and their implementation into mathematical models. Then, we present a unified numerical approach for modeling multiphase flow processes in fractured rock, which is applicable to both discrete-fracture and multicontinuum modeling methods. Note that the numerical modeling scheme for fractured reservoir simulation in this chapter follows the general framework numerical model, discussed in Chapter 4.

In an effort to accurately quantify fracture–matrix flow, we discuss a general mathematical framework model and numerical approach for dealing with fracture–matrix interactions, which is applicable to both continuum and discrete-fracture conceptualization. The main objective of this chapter is to show that it is possible to formulate a uniform, generalized mathematical model as well as design a unified numerical scheme that can be used to simulate any types of multiphase fluid flow in fractured reservoirs, based on different fracture–matrix conceptual models. We demonstrate that with this unified approach, modeling a particular process of porous-medium or fractured-media flow and transport, becomes simply a matter of defining a set of state variables, along with describing their interrelations or mutual effects, once a fractured-medium system is properly discretized into a structured or unstructured grid using the multicontinuum approach.

In numerical modeling of fracture–matrix interaction, the most important is how to accurately calculate mass flux at the fracture–matrix interface, in which a mobility weighting scheme is critical. In conventional simulation practice, especially in petroleum reservoir simulation, the fully upstream weighting scheme (or simply *upstream weighting* or *upwinding*) is routinely used (e.g., Aziz and Settari, 1979). As a result, the fracture relative permeability may be conveniently selected in estimating such mobility when local flow is toward the matrix from fractures. However, this scheme is physically incorrect, because of the inherent anisotropy of the fracture–matrix medium at this scale. The fracture relative permeability functions are properties for evaluating multiphase fluid flow along fractures, determined independently from matrix flow, for example, by laboratory studies (e.g., Persoff and Pruess, 1995). In general, fracture–matrix flow or interaction occurs along the direction perpendicular to fracture planes, which is controlled mainly by matrix flow properties. Therefore, using fracture relative permeability in this case to determine fracture-to-matrix flow is physically incorrect and may lead to nonphysical solutions or significant numerical errors. To provide a better solution to the problem, we present a physically based upstream weighting scheme for determining relative permeability functions or mobility terms that can be generally applicable to calculating multiphase flow between fractures and the rock matrix using a dual-continuum concept and discrete-fracture modeling approach (Wu et al., 2004b).

The main objective of this chapter is to provide a generalized methodology, from conceptualization and mathematical formulation to numerical modeling approaches, for quantifying the physical process of

multiphase flow in fractured porous media. As application examples of our general numerical formulation, we demonstrate the application of the methodology to multicontinuum conceptual models of fractured reservoirs and analysis of pressure transients and laboratory testing results.

9.2 PHYSICAL AND CONCEPTUAL MODELS

Fractures, naturally occurring or human-made (hydraulic) ones, in rock are any separations or openings in a geologic formation that separate the rock apart. The main objective of characterizing fractures in reservoirs is to understand the behavior of flow and transport through this fractured rock and to quantity the effect of fracture–matrix interaction on the flow. In term of its influence on flow in fractured porous media, a fracture may be defined as a narrow, high-permeability, and heterogeneous 3-D zone or a special porous-medium sheet surrounded by low-permeability, but permeable rock matrix. As observed in the field, the aperture of fractures is always small and is supported by fillings or contacts, because of the huge *in situ* stress acting on the rock matrix in deep reservoir formations. In the case of hydraulic fractures, they need to be supported by proppants or sands to remain open to conduct flow of fluids.

A distinguishing feature of fractures is their high permeability or connectivity for fluids to flow through. Natural fractures, if existing and well connected in formations, such as in carbonate reservoirs, will provide fast-flow channels to carry the majority of fluid flow from injection wells to production wells or from a far-field reservoir to a well. Another feature of fractures is that fractures have a small pore volume or small total fracture porosity as a secondary porosity in comparison with the primary porosity within the surrounding porous rock matrix. This is because of their small fracture aperture as well as their relatively sparse distribution within a formation. Therefore, fractures in general have a small capacity for storing fluids. Physically, fractures should be better characterized as part of the heterogeneity of the formation instead of a separate medium in terms of their impact on flow and transport of fluids in reservoirs.

Estimates of *in situ* fracture properties have been a challenge to characterization of fractured reservoirs. This is because fracture properties, such as aperture, porosity, or permeability, cannot be measured directly as is normally done in general for matrix rock cores in the laboratory. We have to rely on observations from outcrops, boreholes, or underground tunnels, or use geological and geophysical tools to provide some indirect

measurements or qualitative data. On the other hand, a number of field-testing technologies, such as transient pressure tests, underground tracer tests, and production data analysis, are proven very effective in detecting natural fractures and estimating their properties in reservoirs (e.g., Wu et al., 2006a, 2007a).

If fractures are conceptualized as a special porous medium, then it is natural to use Darcy's law to quantify the flow through the fractures in reservoirs. This is what has been done in the literature and in field application for analyzing flow in fractured porous media; i.e., Darcy's law has also been applied to quantify flow within fractures. Similar to describing flow in a porous medium using Darcy's law, we need all Darcy's law-related properties and correlations, such as porosity, permeability, capillary pressure, and relative permeability for calculation of multiphase fluid flow within a fracture medium. Note that there is more complexity for fracture flow in fractured porous media than flow in purely porous media, because for the latter Darcy's law is sufficient to describe the flow process with those model properties. However, fracture flow cannot be determined alone by Darcy's law for describing flow along fractures; it depends also on fracture–matrix interaction, and is impacted by the flow inside the matrix as well as the spatial distribution and geometry of the fractures and the matrix in the formation. Because of the unknown nature of *in situ* fractures, from geometric properties to spatial distributions, a number of simple or simplified conceptual models and scenarios, such as *discrete fracture*, *double-porosity*, *dual-permeability*, and *multi-continuum*, etc., have been proposed, developed, and used to approximate or characterize complicated flow behavior in fractured porous-media systems, for which calculation of fracture flow with fracture–matrix interaction can be made. In this section, we are summarizing the commonly used conceptual models for simulation of fracture flow in fractured reservoirs.

Discrete-fracture model: The explicit or discrete-fracture modeling approach includes every fracture in the model domain of formation and describes the flow explicitly through every fracture with fracture–matrix interaction. The discrete-fracture model is, in principle, a rigorous method as opposed to other conceptual fracture-modeling approaches. However, application of this method in field-scale modeling studies is in general demanding in both data requirements and computational intensity, because the number of fractures is normally too large to include in a field simulation. Furthermore, this approach requires a detailed knowledge of the fracture and matrix geometric properties and their spatial distributions,

which are rarely known at a given field site for natural fractures. This explicit modeling approach becomes more difficult and demanding when modeling multiphase flow and thermal processes in a complicated fracture–matrix system of actual reservoirs, which requires additional multiphase flow properties and correlations for both fracture and matrix systems in the entire reservoir domain. For these reasons, the explicit-fracture modeling approach has not found wide application in field-scale studies until a few years ago (Gong et al., 2008; Li and Lee, 2008; Moinfar et al., 2012, 2014; Huang et al., 2014). Recently, the discrete-fracture model has become very popular and found wide application to handling hydraulic fractures in combination with single- or dual-continuum approaches in unconventional reservoirs (e.g., Wu et al., 2014).

Dual-continuum model: The dual-continuum method (e.g., Barenblatt et al., 1960; Warren and Root, 1963; Kazemi, 1969; Pruess and Narasimhan, 1985) is conceptually simpler and computationally much less demanding than the discrete-fracture approach. The dual-continuum model is able to handle fracture–matrix interaction more easily than the discrete-fracture model, because it represents the fracture continuum with the representative elementary volume (REV) concept that could include many fractures or fracture networks locally. For these reasons, the dual-continuum approach has been developed and used as the main approach for modeling fluid flow, heat transfer, and chemical transport through fractured reservoirs (Kazemi et al., 1976; Gilman and Kazemi, 1982; Pruess and Narasimhan, 1985; Wu and Pruess, 1988; Wu et al., 1999, 2007a). However, it should be mentioned that the applicability of such dual-continuum approaches is in general dependent upon (1) relatively uniform distribution of denser fractures or fracture networks and (2) knowledge of fracture and matrix properties. Because of its computational efficiency and its ability to match many types of laboratory- or field-observed data simultaneously (e.g., Kazemi and Merrill, 1979; Wu et al., 1999, 2002, 2004b), the dual-continuum model, such as double-porosity and dual-permeability, has been the most widely used modeling approach in fractured-reservoir simulation in petroleum and geothermal engineering as well as groundwater hydrogeology. In addition, it has been implemented in most commercially available reservoir simulators.

Dual-continuum approaches, as discussed in this book as well as in the literature, include the classical double-porosity model (Warren and Root, 1963; Kazemi, 1969), the dual-permeability concept (Pruess, 1991; Pruess et al., 1999), the more rigorous dual-continuum generalization of the MINC (Pruess and Narasimhan, 1985; Narasimhan and Pruess, 1988), and

the multicontinuum model (Wu and Pruess, 1988) for modeling flow in fractured porous media. The dual-continuum approach treats fracture and matrix both as continua distributed within reservoir domains of interest. Transient flow in both fractures and matrix system is described by Darcy's law; however, the fracture–matrix interaction is generally simplified or approximated using a pseudosteady-state flow condition, under which analytical solutions are available and used for calculation of flow within the matrix system, such as the matrix system is handled as a sink/source term.

Among the dual-continuum conceptual models, the *double-porosity model* has been the most popular and most applied since it was first proposed by Warren and Root (1963). Schematic illustration for the double-porosity concept is shown in Figure 9.1. In this double-porosity model, the flow domain of a naturally fractured reservoir is composed of matrix blocks with low permeability, embedded in a network of interconnected fractures. Global flow and transport in the formation occur only through the fracture system, conceptualized as an effective continuum. This model treats matrix blocks as spatially distributed sinks or sources to the fracture system without accounting for global matrix–matrix flow and the fracture–matrix flow at fracture–matrix interfaces is calculated based on the analytical solution of pseudosteady-state flow within the matrix system with a simple geometry of matrix blocks (Warren and Root, 1963).

In an attempt to incorporate additional interaction for global flow along matrix–matrix connection, the *dual-permeability* model has been developed and implemented into a numerical scheme of nonisothermal multiphase

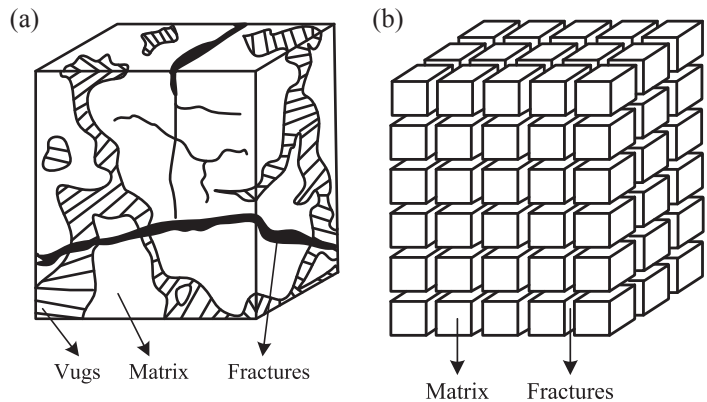

Figure 9.1 Schematic of conceptual double-porosity model of fractured reservoirs. (a) Actual reservoir. (b) Reservoir model *(Modified from Warrant and Root (1963))*.

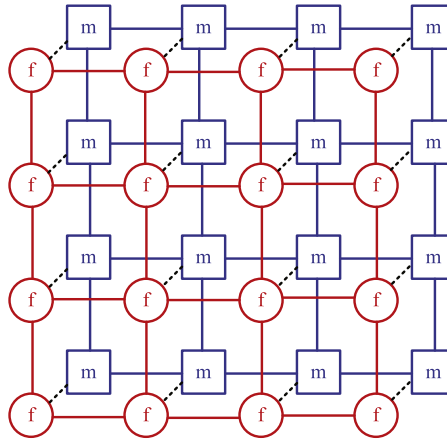

Figure 9.2 Flow connections in the "dual-permeability" model. Global flow occurs along both fracture (f) and matrix (m) systems in addition to local fracture–matrix (F–M) interporosity flow.

fluid and heat flow in fractured rock (Pruess, 1991; Pruess et al., 1999). This type of dual-continuum model considers global flow occurring not only between fractures but also between matrix–matrix connections, as shown in Figure 9.2 for the concept of a dual-permeability model. In this numerical modeling approach, fractures and the matrix are each represented by separate grid blocks that are also connected to each other locally. The same pseudosteady-state flow assumption as that in the double-porosity concept (Warren and Root, 1963) is also used to handle fracture–matrix interflow for this dual-permeability conceptual model.

MINC conceptual model: As a generalization of the dual-continuum model, the Multiple INteraction Continua (MINC) concept (Pruess and Narasimhan, 1985; Wu and Pruess, 1988) is more rigorous to handle transient "flow" between fractures and the matrix. The MINC method takes into account gradients of pressures or capillary forces, temperatures, and concentrations by further subdividing individual matrix blocks near fractures and within the matrix. The MINC concept, as shown in Figure 9.3, treats interporosity flow in a fully transient way by computing the gradients, which drive interporosity flow from the matrix–fracture interface into or from the matrix block. The MINC concept is based on the notion that changes in fluid pressures, temperatures, mass component concentrations, etc. in fractured reservoirs will propagate rapidly through the fracture system, whereas "flow" into or out of the tight matrix blocks is

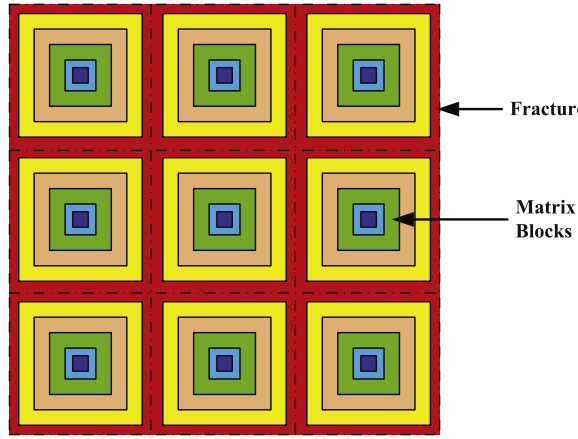

Figure 9.3 Subgridding in the concept of "Multiple INteraction Continua" (MINC) *(Modified from Pruess and Narasimhan (1985))*.

only a slow process. Therefore, changes in matrix thermodynamic conditions will be mainly controlled locally by the nearest distance from the surrounding fractures. Fluid and heat flow from the fractures into the matrix blocks or from the matrix blocks into the fractures can then be modeled by means of one-dimensional or multi-dimensional strings of nested grid blocks.

The MINC method takes into full account transient fracture–matrix interaction, which is calculated rigorously using gradients in pressure, capillary force, temperature, and concentration within the matrix. Therefore, it provides a better approximation for modeling *transient* fracture–matrix interactions than the pseudosteady-state flow assumption, which is needed and used in the double-porosity or dual-permeability model. It has been shown that MINC is particularly needed to replace the double-porosity model when the transient flow period may last very long because matrix permeability is low or matrix block size is large (Wu and Pruess, 1988). The MINC method is applicable and has been used for numerical simulation of heat, and compositional and multiphase fluid flow in multidimensional fractured porous media. The method permits treatment of multiphase fluids with large and variable compressibility and allows for phase transitions with latent heat effects as well as for coupling between fluid and heat flow. By dividing the matrix into subdomains, as shown in Figure 9.3, the transient interaction between matrix and fractures is treated in a more realistic way. The numerical implementation of the MINC

method is accomplished easily by means of an integrated finite difference formulation (Pruess, 1983, 1991).

In a waterflooding fractured petroleum reservoir, imbibition displacement of oil by water in relatively tight matrix blocks is a basic oil-recovery mechanism, because most of the oil in place is present within the low-permeability matrix system, and flows into the fracture system under viscous, gravity, and capillary forces during oil production. Similar to the limitation to a double-porosity model, the assumption that global flow occurs only through the fractures breaks down for multiphase system with strong capillary effects. Depending on overall phase composition and rock minerals, the wetting phase(s) will preferentially occupy the small pores in the rock matrix, whereas the nonwetting phase(s) will tend to reside in the largest pores, i.e., in fractures or vugs. If the phases tend to be highly segregated between primary and secondary porosity, then global flow of the wetting phase will take place through the primary porosity, crossing fractures at asperity contacts. Furthermore, if there are large density differences between segregated phases, interporosity flow will be subject to strong gravity effects. Such conditions can arise in gas/oil drainage, in water imbibition in large matrix blocks, and in vapor-dominated geothermal reservoirs, in which the fractures contain only steam whereas mobile liquid water is present in the matrix blocks. Global matrix–matrix flow and gravity effects in interporosity flow can be described by first discretizing matrix blocks into horizontal layers and then applying nested subregions within each layer (e.g., Gilman and Kazemi, 1988), instead of one-dimensional (1-D) approximation of a "spherical" flow from the inner of matrix blocks to surrounding fractures, as shown in Figure 9.3.

The MINC method covers the double-porosity approximation as a special case. It can be implemented simply by defining only one matrix continuum or block in MINC gridding and using an appropriate nodal distance for matrix–fracture flow, as shown in Figure 9.4(b) (Wu and Pruess, 1988), for a matrix cube. Figure 9.4(a) is a traditional MINC discretization within a matrix block, whereas Figure 9.4(c) is more detailed 3-D discretization, which can be considered as a generalized MINC concept, used to describe effects of matrix rock heterogeneity or gravity segregation in surrounding fractures (Gilman and Kazemi, 1988).

Triple-continuum conceptual model: In a dual-continuum concept, such as the Warren and Root's double-porosity model, fracture and matrix systems are both locally considered uniform and homogeneous. In actual fractured reservoirs, there may exist significant heterogeneity in

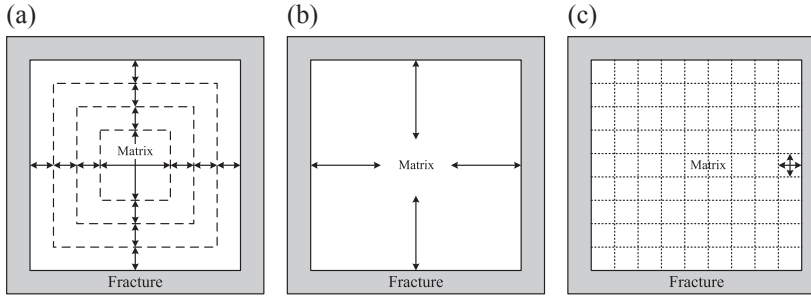

Figure 9.4 Schematic of discretization of matrix blocks: (a) MINC, (b) double-porosity, (c) explicit discretization *(Modified from Wu and Pruess (1988))*.

fractures or within rock matrix. To investigate the effect of heterogeneity in fractures or in rock matrix on flow through fractured porous media, the double-porosity concept of Warren and Root has been extended in the literature. In particular, a number of triple-continuum models have been developed for heterogeneous rock matrix effect (e.g., Closmann, 1975; Wu and Ge, 1983; Abdassah and Ershaghis, 1986; Bai et al., 1993; Liu et al., 2003), for small fracture effect (Wu et al., 2004a), and for fractured vuggy reservoirs (Wu et al., 2007b, 2011; Wu and Qin, 2009). In general, these multicontinuum models have focused on handling different level and scaled heterogeneity of rock matrix or fractures, e.g., subdividing the rock matrix or fractures into two or more subdomains or continua with different properties for single-phase and multiphase flow in such fractured reservoirs.

One example of high heterogeneity in multiscale fractures is the observation of the fracture data, collected from more than decade-long field characterization and study of the fractured unsaturated formation of the Yucca Mountain for a potential repository of high-level radioactive waste for the US during the 1900s and 2000s (e.g., Wu et al., 2000). Analysis of a large amount of fracture data collected from the Yucca Mountain site reveals that many "small" fractures exist in the unsaturated tuffs of the formation (Wu et al., 2004a). Although the majority of these small fractures may not contribute much to global flow and transport through the system, they may provide additional connection areas for interflow between well-connected, large-scale fractures and surrounding matrix blocks, which ultimately affects fracture–matrix interactions. In addition, these small fractures may offer a buffer zone for interaction between well-connected large fracture and the matrix, because of their high storage capacity compared to that of a few large fractures.

To capture effects of small-scale fractures in fractured reservoirs, the fracture–matrix system is conceptualized as a *triple-continuum model*, consisting of a single porous-medium rock matrix and two types of fractures: (1) "large" *globally connected* fractures and (2) "small" fractures that are *locally connected* to the large fractures and the rock matrix (Wu et al., 2004a). Figure 9.5 illustrates the triple-continuum concept, as compared to an effective-continuum model (ECM), double-porosity, and dual-permeability concepts. The triple-continuum method (Figure 9.5(d)) extends the dual-permeability concept by adding one more connection (via small fractures) between the large fractures and the matrix blocks. Note that fractures not directly connected with large fractures (i.e., fractures that are isolated within the matrix) are not considered part of the small fracture continuum in this model. Instead, these isolated fractures are treated as part of the matrix continuum.

Figure 9.6 illustrates the triple-continuum conceptualization for a fracture–matrix system in which the small-fracture–matrix connections occur in only one dimension (shown horizontally). A second set of small-fracture–matrix connections can also be added to occur in two dimensions (i.e., horizontally and vertically, Figure 9.7). In a similar manner, a third set of fractures can be added to extend the system of small-fracture–matrix

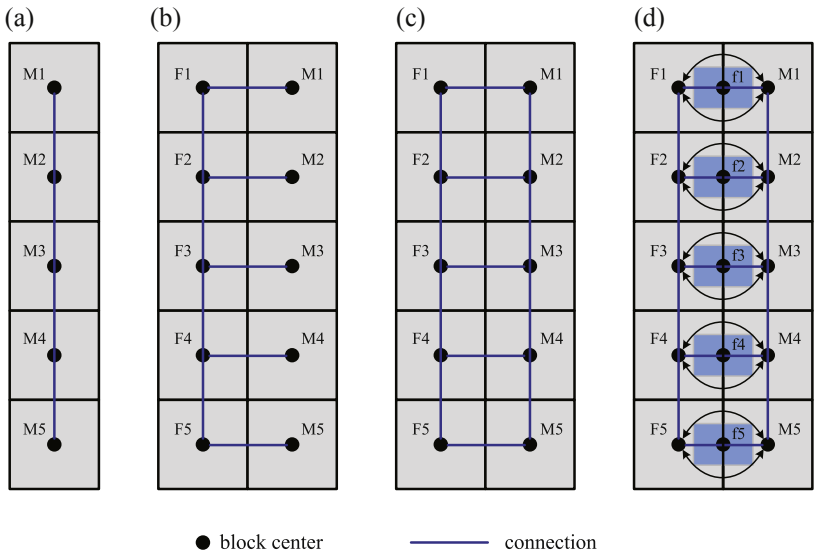

Figure 9.5 Schematic of different conceptualizations for handling fracture–matrix interactions: (a) effective-continuum model (ECM); (b) double-porosity model; (c) dual-permeability model; and (d) triple-continuum model. M, matrix; F, large-fractures; f, small-fractures *(Modified from Wu et al., (2004a))*.

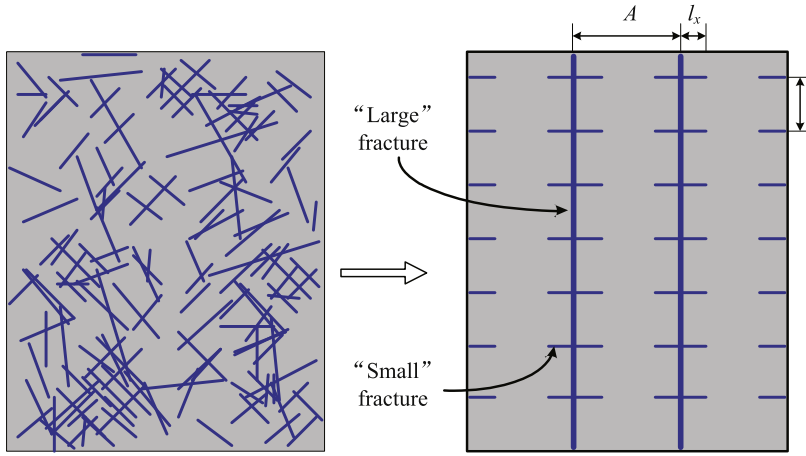

Figure 9.6 Basic conceptualization for triple-continuum approximation of one-dimensional large-fracture, small-fracture, and rock matrix systems.

interactions to occur in three dimensions. Note that the triple-continuum model is not limited to the orthogonal idealization of the fracture systems illustrated in Figures 9.6 and 9.7. Irregular and stochastic distributions of small and large fractures can be handled using a similar approach to the MINC methodology (Pruess, 1983), as long as the actual distributions and patterns of fractures are known.

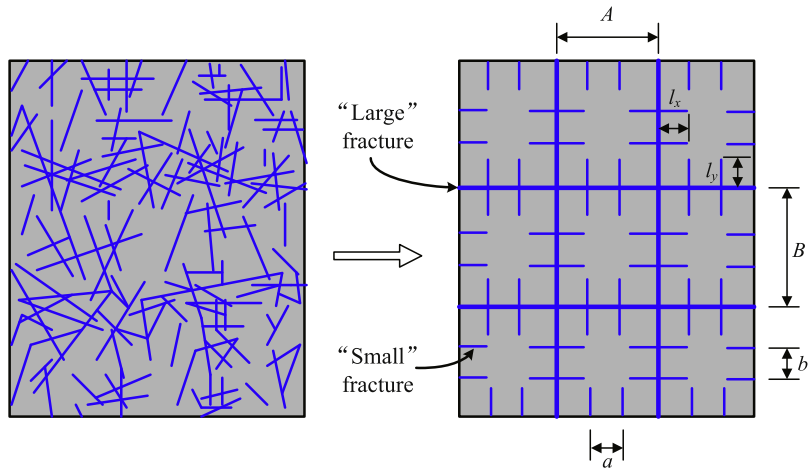

Figure 9.7 Basic conceptualization for triple-continuum approximation of two-dimensional large-fracture, small-fracture, and rock matrix systems.

In principle, the proposed triple-continuum, small-fracture model, similar to the dual-continuum approach, uses an "effective" porous medium to approximate the two types of fractures and the rock matrix, and considers the three continua spatially occupying the entire reservoir volume. Similar to other continuum approaches, the triple-continuum model relies on the assumption that approximate thermodynamic equilibrium exists (locally) within each of the three continua at all times at a given location. Based on the local equilibrium assumption, we can define thermodynamic variables, such as pressures, concentrations, and temperatures, for each continuum.

Studies of flow through fractured porous media have focused primarily on naturally fractured reservoirs without taking into consideration of large cavities or vugs. Recently, characterizing vuggy fractured rock has also received attention, because a number of fractured vuggy petroleum reservoirs and a large number of Karst aquifers have been found and developed worldwide that can significantly contribute to natural resource reserves and production. In addition to relying on the traditional dual-continuum models, investigators (Liu et al., 2003; Camacho-Velazquez et al., 2005; Wu et al., 2011) present several updated triple-continuum models for single-phase flow in a fracture–matrix system that includes cavities or vugs within the rock matrix as an additional porous portion of the matrix.

As observed from the field, a typical fractured vuggy reservoir consists of large and well-connected fractures and lower-permeable rock matrix as well as a large number of varying-sized cavities or vugs. Those vugs and cavities are irregular in shape and very different in size from millimeter to meters in diameter. Many of small-sized cavities appear to be isolated from fractures. Similar to the conventional double-porosity concept, large fractures, or the fracture continuum, are conceptualized to serve as main pathways for global flow, whereas vuggy and matrix continua, mainly providing storage space as sinks or sources, are locally connected to each other, as well as directly or indirectly interacting with globally connecting fractures. Note that vugs and cavities directly connected with globally connected fractures are considered part of the fracture continuum. Specifically, as shown in Figures 9.8–9.10, we conceptualize the fracture–vug–matrix system as consisting of (1) "large" fractures (or fractures), globally connected on the model scale of flow to a well; (2) various-sized vugs or cavities, which are locally connected to fractures either through "small" fractures or across rock matrix; and (3) rock matrix, which may contain a number of cavities, locally connected to large fractures and/or to vugs.

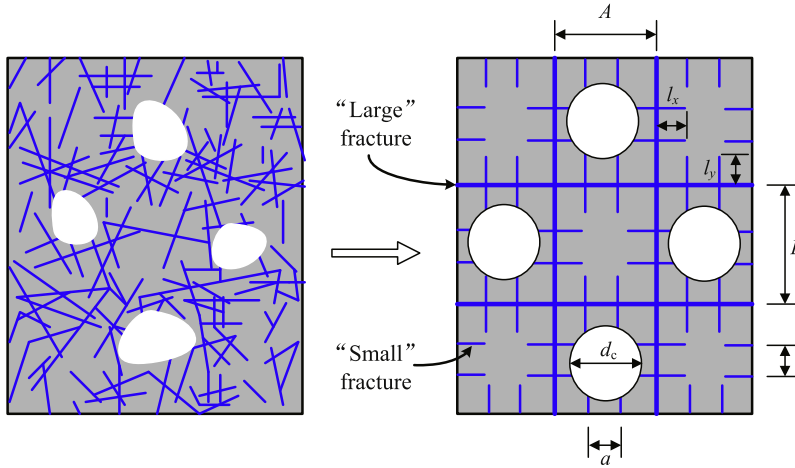

Figure 9.8 Conceptualization #1 of fractured vuggy rock as a triple-continuum system with vugs indirectly connected to fractures through small fractures.

In principle, the fracture–vug–matrix, triple-continuum model (Wu et al., 2011) can be considered to be a natural extension of the generalized multicontinuum approach, discussed previously. In this approach, an "effective" porous medium is used to approximate the fracture, vugs, and rock matrix continua, respectively, by considering the three continua to occupy the entire reservoir space and the three continua are interacting with each other. Similarly, this triple-continuum conceptual model assumes that approximate thermodynamic equilibrium exists locally within each of

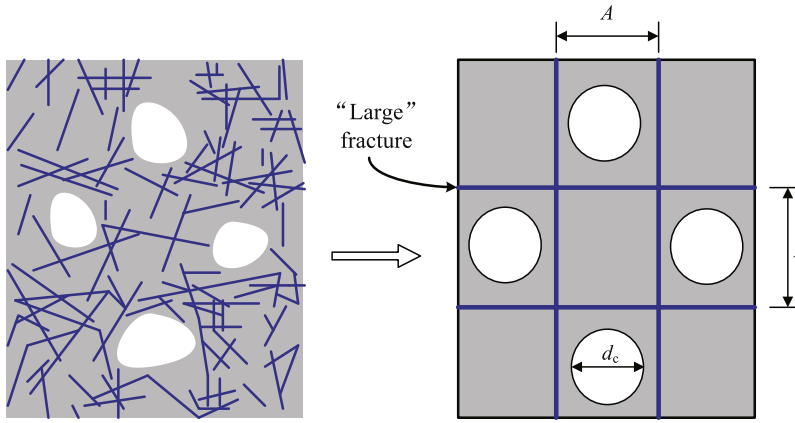

Figure 9.9 Conceptualization #2 of fractured vuggy rock as a triple-continuum system with vugs isolated from or indirectly connected to fractures through rock matrix.

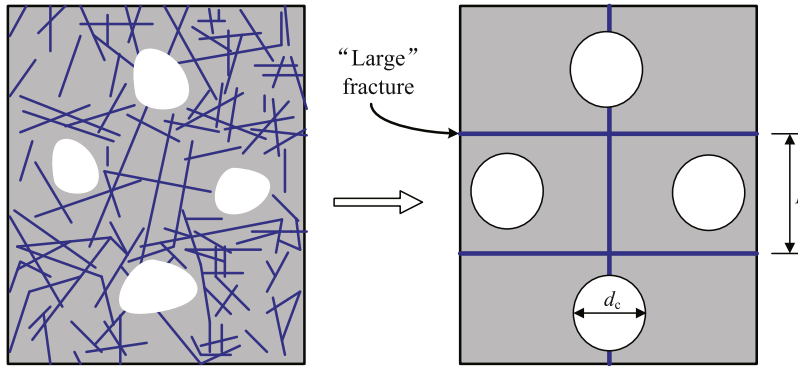

Figure 9.10 Conceptualization #3 of fractured vuggy rock as a triple-continuum system with partial vugs isolated from fractures.

the three continua at all times. In addition, the flow of fluids within vugs is assumed to be simultaneously completed, because of the small flow resistance when compared with that in fracture or in matrix systems. Note that the triple-continuum model is also not limited to the orthogonal idealization of the fracture system or uniform size or distribution of vugs or cavities, as those illustrated in Figures 9.8–9.10. Irregular and stochastic distributions of fractures and cavities can be handled numerically, as long as the actual distributions of fractures and vugs are known (Pruess, 1983).

Effective continuum model (ECM): As an alternative modeling method to the dual- or multiple-continuum models of the above, the effective continuum method (ECM) represents fractures and rock matrix as a single effective continuum. The ECM has long been used for modeling fracture–matrix flow, because of its simple data requirements and computational efficiency. This approach may be applicable to modeling multiphase, nonisothermal flow, and solute transport in fractured porous media under near-thermodynamic-equilibrium conditions (Wu et al., 1999; Wu, 2000). When rapid flow and transport processes occur in subsurface fractured reservoirs, however, thermodynamic equilibrium conditions cannot hold in general, then this approach may be no longer applicable. Therefore, the instantaneous thermodynamic equilibrium assumption for fracture–matrix systems will limit the application of the ECM approach for general multiphase flow, transport, and heat transfer processes. However, if the contrast in permeability between fractures and the matrix is not very large or a highly fractured reservoir with small matrix blocks, the ECM is expected to provide a good approximation.

9.3 GENERALIZED FLOW MATHEMATICAL MODEL

Based on the concept of dual- and multiple-continua for handling flow through fractured porous media, the physical processes associated with flow and transport in fractured porous media are treated separately within *each continuum*, fracture#1, fracture#2, …, matrix#1, matrix#2, …, or vug#1, vug#2, …, etc. The flow within each continuum is governed by the same fundamental conservation laws of mass, momentum, and energy, i.e., multiphase flow processes in fractured rock are described separately or individually for each continuum. This multi-continuum conceptualization results in a set of partial differential equations for flow in each continuum, which are in the same form as that for flow in a single-continuum porous medium.

In this section, the multiphase flow system, assumed in an isothermal, fractured porous formation, consists of three phases: oil (or Non-Aqueous Phase Liquid (NAPL)), gas (air), and water. Although each of the three phases contains a number of components, they are treated here as a single "pseudo-component" with average properties of the fluids. In addition, the three fluid components (oil, gas, and water) are assumed present only in their associated phases. Each phase flows in response to its pressure gradients, gravitational, and capillary forces, according to the multiphase extension of Darcy's law, a non-Darcy law, or other flow relations.

Flow governing equation: In an isothermal system containing three mass components, three mass-balance equations are needed to describe flow and transport in the fracture and matrix blocks. For flow of phase β ($\beta = \mathrm{o}$ for oil, $\beta = \mathrm{g}$ for gas, $\beta = \mathrm{w}$ for water) within each continuum (fractures, small fractures, matrix#1, matrix#2, or vugs, etc.), the conservation law leads to:

$$\frac{\partial}{\partial t}\left(\phi S_\beta \rho_\beta\right) = -\nabla\cdot\left(\rho_\beta \boldsymbol{v}_\beta\right) + q_\beta, \quad \beta = \mathrm{o}, \mathrm{g} \text{ or } \mathrm{w} \tag{9.1}$$

In Eqn (9.1), we use the same notations and symbols as those used and defined in other chapters of this book in governing flow equations. Please note, however, that the variables and parameters in Eqn (9.1) are medium or continuum specific, i.e., the equation represents two sets of flow equations and two sets of fluid and rock properties, one for fractures and one for matrix, if a dual-continuum conceptual model is applied. In general, the number of multiple continua is equal to the number of sets of the flow-governing PDE's, as described by Eqn (9.1), to solve with the

multicontinuum concept. In addition, the flow velocity, $\boldsymbol{v}_\beta$, of phase β is determined by Darcy's law, non-Darcy law, or other flow relations of interest, and different flow laws can be used for describing the flow in different continua.

It should be mentioned that Eqn (9.1) is equally applicable to the discrete-fracture model as well. In that case, Eqn (9.1) is used to determine flow along discrete fractures as well as within the rock matrix surrounding the fractures.

Continuity condition: the flow behavior cannot be determined by using the flow-governing Eqn (9.1) alone in a fractured reservoir with the multicontinuum approach. In addition to initial and boundary conditions that need to be specified, the continuity condition must be satisfied at interfaces between different continua or media (e.g., fracture–matrix, fracture–fracture, fracture–vug, vug–matrix, etc.) in terms of pressure, temperature, concentration, and mass/heat fluxes. Specifically, in an isothermal multiphase flow system, phase pressure and capillary pressure must be the same at the interface of different media, and the mass flux at the interface out of a continuum must be equal to that flowing into the other continuum across the same interface boundary.

Constitutive relations: The governing flow equation of mass balance for three-phase fluids, Eqn (9.1), needs to be supplemented with the same number of sets of constitutive relations and properties as the number of continua (e.g., two sets of constitutive relations and fluid and rock properties for a double-porosity model, one for fracture and the other for matrix). The constitutive relations, as discussed in Chapters 2 and 3, include relative permeability and capillary-pressure functions as well as other PVT data.

9.4 NUMERICAL FORMULATION AND SOLUTION

9.4.1 Discrete Equations and Numerical Solution

Equation (4.1), a general discrete equation for multiphase flow in porous media discretized with the integrated finite difference or control volume scheme, as discussed in Section 4.2, is applicable to multiphase flow in a single-porosity medium as well as in fractured porous media, if fracture and matrix continua are properly represented in a numerical grid of the fractured formation of interest. As discussed in this section, this generalized discrete numerical formulation, Eqn (4.1), is able to model multiphase flow in fractured reservoirs with various conceptual fracture models, such as discrete-

fracture, dual-continuum, and multicontinuum modeling approaches. Let us define the mass accumulation term of Eqn (4.1) explicitly and write the nonlinear algebraic equation for multiphase flow through a multidimensional fractured porous-medium system in a residual form,

$$R_i^{\beta,n+1} = \left[\left(\phi S_\beta \rho_\beta\right)_i^{n+1} - \left(\phi S_\beta \rho_\beta\right)_i^{n}\right]\frac{V_i}{\Delta t} - \sum_{j\in\eta_i} flow_{ij}^{\beta,n+1} - Q_i^{\beta,n+1} = 0, \quad i = 1, 2, \ldots, N \tag{9.2}$$

in which symbols and notations used are the same as those used for Eqn (4.12) and N is the total number of grid blocks combining all fracture and matrix elements or grid blocks.

Note that there is an important difference in Eqns (4.1) and (9.2), when they are used for modeling flow in a single porous medium or in a fractured porous medium, even though the discretized equation is applicable to both. For flow in single-continuum porous media, the grid block volume, V_i, is the bulk formation volume, V_B, of the subdivided formation domain for grid block i in gridding. For flow in fractured or multicontinuum media, however, V_i represents the volume of the continuum (e.g., fracture or matrix individually) only and a summation *locally* over all the continuum subvolumes is equal to the bulk volume, V_B, which is called a primary mesh in discretizing fractured reservoirs using the integrated finite difference approach (Pruess, 1983; Pruess et al., 1999).

In modeling flow in fractured reservoirs using Eqn (9.2), the key is how the mass-flow term, "$flow_{ij}^{\beta}$" for various connections between continua or along or within the same medium. There are three types of "flow" to be determined: (1) flow within the fracture continuum along fracture–fracture connection; (2) flow within the matrix block along matrix–matrix connection; and (3) flow between fracture and matrix systems across fracture–matrix interface. For the first two types, i.e., flow within fractures or inside the matrix, the flow calculation is carried out in the same way as if the flow were in a single-continuum medium, though flow calculation in the matrix is often much simplified to one-dimensional flow in a dual-continuum or MINC conceptual model. The flow between the fracture and the matrix systems, called the fracture–matrix interaction, is what distinguishes the flow in fractured porous media from that in single-continuum porous media. The treatment of fracture–matrix flow, i.e., implementation of the continuity condition at the interfaces in various fracture conceptual models, is discussed in Section 9.4.2 as follows.

For evaluation of flow between two neighboring grid blocks (i, j) within the same continuum (i.e., fracture or rock matrix), the mass-flow term, "$flow_{ij}^{\beta}$", can be directly evaluated, respectively, using Darcy flow or non-Darcy flow modeled using the *Forchheimer* equation or the Barree–Conway model with appropriate weighting scheme implemented as follows.

For the Darcy flow along fractures or within the matrix block,

$$flow_{ij}^{\beta} = \gamma_{ij}\left(\rho_{\beta}\lambda_{\beta}\right)_{ij+1/2}\left(\Phi_{\beta j} - \Phi_{\beta i}\right) \tag{9.3}$$

in which symbols, notations, superscripts, and subscripts, such as phase mobility, λ_{β}, transmissivity, γ_{ij}, and flow term, $\Phi_{\beta j}$, for the medium of interest are defined and evaluated in the same way as those in Eqn (4.7).

For the *Forchheimer* non-Darcy flow, the mass-flow term between two directly connecting grid blocks (i, j) within the same continuum is evaluated flow (Wu, 2002), as discussed in Section 8.7:

$$flow_{ij}^{\beta} = \frac{A_{ij}}{2\left(k\beta_{\beta}\right)_{ij+1/2}}\left[-\frac{1}{\lambda_{\beta}} + \sqrt{\left(\frac{1}{\lambda_{\beta}}\right)^2 - \overline{\gamma}_{ij}\left(\Phi_{\beta j} - \Phi_{\beta i}\right)}\right] \tag{9.4}$$

in which the same definitions for symbols and notations as those in Eqn (8.57) are used, and, in particular, the transmissivity, $\overline{\gamma}_{ij}$, of non-Darcy flow terms is defined in Eqn (8.58).

For the non-Darcy flow according to the *Barree and Conway* model, the mass-flow term within the same continuum is evaluated by Eqn (8.59):

$$\begin{aligned} flow_{ij}^{\beta} = \frac{A_{ij}}{2\rho_{\beta}\mu_{\beta}}\Bigg\{ &-\left(\mu_{\beta}^2 S_{\beta}\tau + \nabla\Phi_{\beta,ij}k_d k_{r\beta}k_{rm}\rho_{\beta}\right) \\ &+\sqrt{\left(\mu_{\beta}^2 S_{\beta}\tau + \nabla\Phi_{\beta,ij}k_d k_{r\beta}k_{rm}\rho_{\beta}\right)^2 - 4\mu_{\beta}\rho_{\beta}\nabla\Phi_{\beta,ij}k_d k_{r\beta}\mu_{\beta}S_{\beta}\tau}\Bigg\} \end{aligned} \tag{9.5}$$

in which the discrete flow potential gradient, $\nabla\Phi_{\beta,ij}$, is defined in Eqn (8.60).

Equation (9.2) represents a coupled, nonlinear algebraic equation system with a total of $3 \times N$ equations or unknowns for three-phase flow within a fracture porous-medium reservoir and are solved with the Newton scheme, as discussed in Section 4.3.

9.4.2 Treatment of Fracture–Matrix Interaction

The dynamics of multiphase fluid flow in fractured reservoirs depends on simultaneous flow within fracture and matrix continua, coupled with the

interaction at fracture–matrix interfaces of the two media. The method used for handling multiphase flow through fractured rock generally follows the dual-continuum methodology (Warren and Root, 1963; Kazemi, 1969; Pruess and Narasimhan, 1985; Wu and Pruess, 1988). This dual-continuum method treats fracture and matrix interporosity flow and interaction using a multicontinuum numerical modeling approach, including the double- or multiporosity method, the dual-permeability method, and the more general MINC method. It can be shown that the same multicontinuum concept of handling fracture–matrix interporosity flow is also applicable to multiphase flow though a discrete fracture network.

The discretized multiphase flow formulation, Eqn (9.2), is applicable to flow in multicontinuum media of fractured reservoirs as long as the mass-flow term is properly defined and evaluated for (1) flow along fractures; (2) flow within rock matrix; and (3) inter-porosity flow at fracture–matrix interfaces. In Section 9.4.1, we have discussed how multiphase flow along fractures and inside matrix blocks is calculated under the dual-continuum concept. In this section, we present a general methodology for how to determine fracture-matrix interaction using different conceptual fracture models. Because both fracture and rock matrix are porous media, the flow between fractures and the matrix may be evaluated using Darcy's law, which is similar to modeling flow across multi-layered beds of formations. Therefore, we use a Darcy's law based model, Eqn (9.3), instead of a shape factor or transfer function approach, to compute fracture-matrix flow as

$$flow^{\beta}_{\mathrm{fm}} = \gamma_{\mathrm{fm}}\left(\rho_{\beta}\lambda_{\beta}\right)_{\mathrm{fm}+1/2}\left(\Phi_{\beta\mathrm{m}} - \Phi_{\beta\mathrm{f}}\right) \tag{9.6}$$

in which the mass-flow term, $flow^{\beta}_{\mathrm{fm}}$, is for the flow between two neighboring, connected grid blocks: one fracture element ($i = \mathrm{f}$) and one matrix element ($j = \mathrm{m}$), respectively. Note that the transmissivity and mobility terms in Eqn (9.6) must be defined in a physically meaningful manner,

$$\gamma_{\mathrm{fm}} = \frac{A_{\mathrm{fm}}k_{\mathrm{m}}}{l_{\mathrm{fm}}} \tag{9.7}$$

in which A_{fm} is the total interfacial area between fractures and the matrix within the bulk volume containing elements f and m; k_{m} is the matrix absolute permeability along the fracture-matrix connection; and l_{fm} is a *characteristic distance* for calculation of the flow crossing fracture–matrix interfaces, which can be determined for idealized 1-D, 2-D, and 3-D rectangular matrix

blocks or normal fracture sets, when using the double-porosity model (Warren and Root, 1963). The mobility term to phase β is defined as

$$\lambda_{\beta,\mathrm{fm}+1/2} = \left(\frac{k_{\mathrm{r}\beta}}{\mu_\beta}\right)_{\mathrm{fm}+1/2} \tag{9.8}$$

Before the mass transfer can be accurately calculated at the fracture–matrix interface, we need to discuss a physically based weighting scheme for estimating the correct mobility at the fracture–matrix interface in Eqn (9.6) (Wu et al., 2004b).

Mobility weighting scheme: The appropriate spatial weighting scheme for averaging flow properties, such as the mobility of Eqn (9.8), for simulation of flow in a heterogeneous formation has been investigated from the beginning of reservoir simulation and groundwater-modeling literature (Peaceman, 1977; Huyakorn and Pinder, 1983). Single-point or fully upstream weighting has been the exclusive approach for averaging mobility or relative permeability in calculating the flux term, using a discrete Darcy's law for multiphase flow in heterogeneous petroleum reservoirs (Aziz and Settari, 1979). The reasons behind the application of the conventional upstream weighting scheme for relative permeability are based on several physical arguments, such as the need for upstream weighting to initialize imbibition of a wetting fluid into completely dry rock. In addition, the upstream weighting approach is found necessary to avoid incorrect solutions in immiscible displacement (hyperbolic) problems (Aziz and Settari, 1979). Several theoretical studies (Forsyth et al., 1995; Forsyth and Kropinski, 1997) have shown that the upstream weighting scheme, if used with the control-volume discretization of the Richards' equation, will guarantee that converged numerical solutions are physically correct, whereas other weighting schemes, such as central weighting, may converge to an incorrect, nonphysical solution.

To determine flow along fracture–matrix connections (i.e., flow across fracture–matrix interfaces in the direction perpendicular to fracture planes) is different from fracture–fracture or matrix–matrix flow, as shown in Figure 9.11, because of the high contrast in fracture and matrix flow properties. The conventional upstream weighting scheme may no longer be applicable. This is because fracture-relative permeability functions are fracture flow properties describing flow along fractures, determined independently from matrix flow. Conversely, fracture–matrix flow or interaction normally occurs along the directions perpendicular to fractures and is

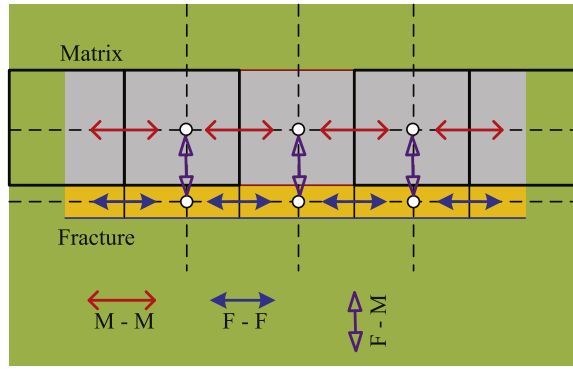

Figure 9.11 Schematic of fracture–matrix interaction with fracture–fracture (F–F) flow; matrix–matrix (M–M); and fracture–matrix (F–M) flow in fractured reservoirs.

largely controlled by matrix properties, i.e., by high flow resistance near the matrix surface within the matrix block. For treatment of fracture–matrix flow, we use a modified upstream weighting scheme to select appropriate mobility for fracture–matrix interaction (Wu et al., 2004b). This physically based mobility weighting scheme is based on the principle that the capillary pressure is continuous at the fracture–matrix interface and the assumption that there is instantaneous local equilibrium in pressure for each phase between fractures and the matrix surface or fracture boundary. This assumption should hold true for most subsurface fractured reservoirs, because fracture aperture is normally very small and fracture lateral boundaries are defined by matrix surfaces. Any dynamic changes in fractures, such as capillary pressures, could be instantaneously equilibrated locally with that at contacted matrix surfaces. As a result, the matrix relative permeability at the matrix surface can be readily determined as a function of fracture (or matrix) capillary pressure or the saturation at matrix surfaces corresponding to that fracture capillary pressure. Therefore, the scheme, when the upstream direction for fracture–matrix flow is at the fracture, uses the matrix relative permeability function (instead of the fracture relative permeability function, as in the conventional upstream weighting scheme) as a function of matrix surface saturation to calculate the mobility. Physically, this is equivalent to evaluating flow from fracture to matrix through the fracture–matrix interface by flow from the matrix surface into inside the matrix with the effective matrix permeability at that interface, obviously a more physically reasonable, upstream weighting approach.

The weighting scheme under discussion is still dependent on the upstream fracture condition and therefore does not lose the advantages of upstream schemes. In addition, in case fracture–matrix flow is from matrix to fractures, such as in a situation of drainage or flow between globally connected fractures and along global or local matrix–matrix (e.g., MINC) connections, as shown in Figure 9.11, the conventional upstream weighting scheme should still be used. We may call this hybrid mobility-averaging scheme *physically based upstream weighting* to determine mobility terms for fracture–matrix flow. Mathematically, the mobility-weighting scheme requires the appropriate selection of relative permeability for fracture–matrix flow, used for calculating the mobility term in Eqn (9.8) as

$$(k_{r\beta})_{fm+1/2} = k_{r\beta,m}\left(S^*_{\beta,m}\right) \quad \text{for} \quad \Phi_{\beta f} \geq \Phi_{\beta m} \tag{9.9}$$

and

$$(k_{r\beta})_{fm+1/2} = k_{r\beta,m}(S_{\beta,m}) \quad \text{for} \quad \Phi_{\beta f} < \Phi_{\beta m} \tag{9.10}$$

in which $(k_{r\beta})_{fm+1/2}$ is the physically upstream relative permeability for estimating fracture–matrix flow of phase β; $k_{r\beta,m}$ is relative permeability of phase β in the matrix, a function of matrix saturation ($S_{\beta,m}$); and $S^*_{\beta,m}$ is matrix saturation of phase β on the matrix surface, determined from inverting the matrix capillary-pressure function by setting matrix capillary pressure equal to fracture capillary pressure at the time.

Within the context of the dual-continuum concept, the proposed weighting approach can be applied to different fracture-modeling conceptual models, such as double-porosity, dual-permeability, MINC, and discrete-fracture model grids, to calculate flow at the fracture–matrix interface.

***Characteristic distance* for fracture-matrix flow**: The characteristic distance or nodal length, l_{fm}, in Eqn (9.7) needs some special attention to determine. Physically, the characteristic distance represents the average "traveling" distance from fracture to matrix or from matrix to fracture to calculate potential gradient for occurrence of flow between fracture and matrix. The method for determination of a characteristic distance is different for different fracture conceptual models. For discrete-fracture or MINC modeling approaches, the characteristic distance is simply half the width of a grid cell around fractures. For the use of double-porosity, dual-permeability, and triple-continuum models, however, the *characteristic distance* is mostly calculated based on analytical solutions of pseudosteady-state flow of a single-phase fluid within the matrix system in a simplified geometry, which is then equivalent to Darcy's law using

a volume-averaged pressure from the pseudosteady-state solutions, as derived originally by Warren and Root (1963).

In handling fracture-matrix interaction with *double-porosity* or *dual-permeability* models, the matrix is represented by a single grid block, as shown in Figures 9.4 and 9.5. The fracture–matrix interporosity flow is in general calculated by Eqn (9.6) with the transmissivity defined in Eqn (9.7). The mobility is determined in Eqn (9.8) with a proper upstream weighting of relative permeability. Table 9.1 lists the characteristic distance used for double-porosity and dual-permeability models, which is derived using *characteristic dimension of heterogeneous region* of Warren and Root (1963). Note that these characteristic distances, listed in Table 9.1, for evaluating fracture–matrix flow is valid only for single-phase flow under pseudosteady-state condition. In fractured reservoir simulation, however, they have been extended for use in transient flow (e.g., Kazemi, 1969) as well as in multiphase flow simulation with satisfactory results in many applications as long as the pseudosteady state provides a good approximation (e.g., Wu and Pruess, 1988).

For the triple-continuum model with small fractures, as shown in Figures 9.6 and 9.7, Eqn (9.3) or (9.6) is still applicable for calculation of mass-flow terms between large fractures (F) and matrix (M); between large fracture and small fractures (f); and between small fractures and matrix. The *characteristic distance* in calculation of the transmissivity for flow among the triple continua with small fractures is given in Table 9.2 (Wu et al., 2004a). In this triple-continuum model with small fracture effect, the fracture–matrix interactions between large fractures and matrix and between small fractures and matrix are handled using the same pseudo-steady state flow assumption within the fracture-matrix system. The flow between the two fracture systems is using a midpoint finite difference approximation.

For another type of triple-continuum model, i.e., for flow through fractured vuggy reservoirs, the three conceptual models are shown in Figures 9.8–9.10. Table 9.3 (Wu et al., 2011) summarizes several models for estimating characteristic distances in calculating interporosity flow among

Table 9.1 Characteristic distances[a] for evaluating transmissivity of fracture–matrix flow in double-porosity and dual-permeability models

Fracture sets	1-D	2-D	3-D
Characteristic f-m distances (m)	$l_{\text{fm}} = \frac{a}{6}$	$l_{\text{fm}} = \frac{ab}{4(a+b)}$	$l_{\text{fm}} = \frac{3abc}{10(ab+bc+ca)}$

[a]Note in Table 9.1, a, b, and c are dimensions of matrix blocks or fracture spacings along x, y, and z directions, respectively, for normal sets of fractures.

Table 9.2 Characteristic distances[a] for evaluating transmissivity of fracture-matrix flow between two fractures and matrix system in the triple-continuum model of Figures 9.6 and 9.7

Fracture sets	1-D	2-D	3-D
Dimensions of matrix blocks (m)	A	A, B	A, B, C
Characteristic F−M distances (m)	$l_{\mathrm{FM}} = \frac{A}{6}$	$l_{\mathrm{FM}} = \frac{AB}{4(A+B)}$	$l_{\mathrm{FM}} = \frac{3ABC}{10(AB+BC+CA)}$
Characteristic F−f distances (m)	$l_{\mathrm{Ff}} = \frac{l_x}{2}$	$l_{\mathrm{Ff}} = \frac{l_x+l_y}{4}$	$l_{\mathrm{Ff}} = \frac{l_x+l_y+l_z}{6}$
Characteristic f−M distances (m)	$l_{\mathrm{fM}} = \frac{a}{6}$	$l_{\mathrm{fM}} = \frac{ab}{4(a+b)}$	$l_{\mathrm{fM}} = \frac{3abc}{10(ab+bc+ca)}$

[a]Note in Table 9.2, as shown in Figures 9.6 and 9.7, A, B, and C are dimensions of matrix blocks or large-fracture spacings along x, y, and z directions, respectively; dimensions a, b, and c are fracture spacings of small fractures along x, y, and z directions, respectively; and l_x, l_y, and l_z are lengths of small fractures from large fractures along x, y, and z directions, respectively. Subscript F represents large fracture; f for small fracture; and M for matrix systems, respectively.

Table 9.3 Characteristic distances[a] for evaluating transmissivity of flow terms between fractures, vugs, and matrix systems of the fracture–vug–matrix, triple-continuum model

Fracture sets	1-D	2-D	3-D
Dimensions of matrix blocks (m)	A	A, B	A, B, C
Characteristic F−M distances (m)	$l_{\mathrm{FM}} = \frac{A}{6}$	$l_{\mathrm{FM}} = \frac{AB}{4(A+B)}$	$l_{\mathrm{FM}} = \frac{3ABC}{10(AB+BC+CA)}$
Characteristic F−V distances (m)	$l_{\mathrm{FV}} = \frac{l_x}{2}$	$l_{\mathrm{FV}} = \frac{l_x+l_y}{4}$	$l_{\mathrm{FV}} = \frac{l_x+l_y+l_z}{6}$
Characteristic V−M distances[b] (m)	$l_{\mathrm{VM}} = \frac{a}{6}$	$l_{\mathrm{VM}} = \frac{ab}{4(a+b)}$	$l_{\mathrm{VM}} = \frac{3abc}{10(ab+bc+ca)}$
Characteristic V−M distances[c] (m)	$l_{\mathrm{VM}} = \frac{A-d_c}{2}$	$l_{\mathrm{VM}} = \frac{A+B-2d_c}{4}$	$l_{VM} = \frac{A+B+C-3d_c}{6}$

[a]Note in Table 9.3, as shown in Figures 9.8–9.10, A, B, and C are dimensions of matrix blocks along x, y, and z directions, respectively; dimensions a, b, and c are fracture spacings of small fractures along x, y, and z directions, respectively; and l_x, l_y, and l_z are lengths of small fractures from large fractures along x, y, and z directions, respectively.
[b]Characteristic V–M distances are estimated for the case (Figure 9.8), i.e., vuggy-matrix connections are dominated by small fractures, in which dimensions a, b, and c are fracture spacings of small fractures along x, y, and z directions, respectively.
[c]Characteristic V–M distances are used for the case (Figures 9.9 and 9.10), i.e., vugs are isolated from fractures.

large fractures (F), small fractures (f), vugs (V), and the matrix (M), in which cases we have regular one-, two-, or three-dimensional large-fracture networks, each with uniformly distributed small fractures connecting vugs or isolating vugs from fractures (Figures 9.8–9.10). The formulation in Table 9.3 relies on the same pseudosteady-state flow assumption of Warren and Root (1963) to derive characteristic distances for the flow between large fracture–matrix (F–M) through small fractures and vug (f–V) connections. Another condition for using the formulation in Table 9.3 is that fractures, vug, and matrix are all represented by only one grid block. In addition, the flow distance between large fractures and vugs, when connected through small fractures, is taken to be half the length of the small fractures within a matrix block (Figure 9.8). Furthermore, the interface areas between vugs and the matrix should include the contribution of small fractures for the case of Figure 9.8. Interface areas between large fractures and the matrix and between large fractures and vugs through connecting small fractures should be treated using the geometry and distribution of the large fractures alone. This treatment implicitly defines the permeabilities of the two types of fractures in a continuum sense, such that bulk connection areas are needed to calculate Darcy flow between the two fracture continua.

9.5 APPLICATION EXAMPLES

In this section, we present several application examples to demonstrate the use of the generalized numerical formulation of this chapter for modeling flow through fractured reservoirs. Note that the general numerical formulations and solution approaches, as discussed in Section 9.4, are developed for simulation of multiphase fluid flow in fractured porous media. However, they are equally applicable to modeling single-phase flow. In practice of numerical model development and application, multiphase flow simulators or formulations are often benchmarked or verified against simpler analytical solutions for single-phase flow and multiphase flow, if they are available, as well as against laboratory experimental results, as it is demonstrated in this section.

The four example problems in this section for demonstrating the applicability of the numerical approach are:

1. To compare numerical simulation results with an analytical solution for transient liquid flow in triple-continuum media with small fracture effect.

2. To investigate transient flow behavior and contribution of vug parameters in triple-continuum, fractured vuggy reservoirs.
3. To compare with the analytical solution for imbibition into a single matrix block.
4. To compare with laboratory experimental results of oil and water displacement in a fractured core.

9.5.1 Comparison with Analytical Solution of Small-Fracture, Triple-continuum Media

The application problem concerns typical transient flow toward a well that fully penetrates a radially infinite, horizontal, and uniformly fractured reservoir (Wu et al., 2004a). In the numerical model, a radially finite reservoir ($r_e = 10{,}000$ m) with 20 m thickness, as illustrated by Figure 9.12, is used and discretized into a one-dimensional (primary) grid for the radial flow problem.

The distance r_e (10,000 m) is subdivided into 2100 intervals following a logarithmic scale. A triple-continuum mesh is then generated from the primary grid, in which the one-dimensional, horizontal large-fracture plate network is assumed to separate uniform disk-shaped matrix blocks. Fracture and matrix parameters are given in Table 9.4. Note that the values of these parameters in Table 9.4 are selected within the typical range of a triple-continuum model (i.e., $k_F >> k_f >> k_M$ and $\phi_M >> \phi_f >> \phi_F$). The

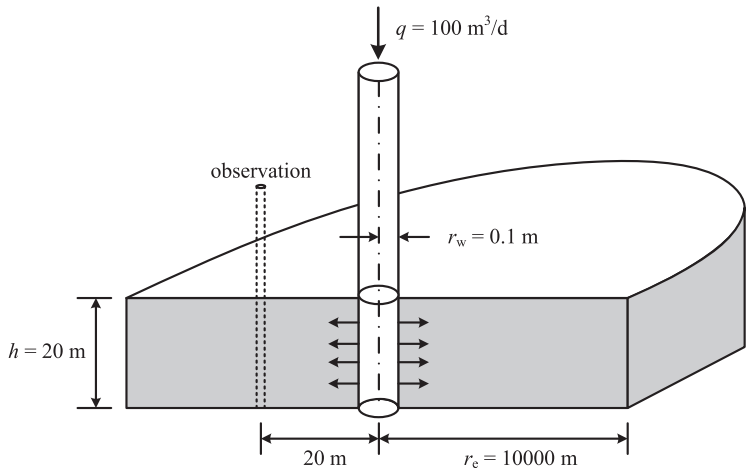

Figure 9.12 Schematic illustration of a fully penetrating injection well in a radial, uniform, and horizontal formation used for well flow analyses.

Table 9.4 Parameters used in the single-phase flow problem through the triple-continuum, fractured reservoir with small-fracture effect

Parameter	Value	Unit
Matrix porosity, ϕ_M	0.263	[-]
Large-fracture porosity, ϕ_F	0.001	[-]
Small-fracture porosity, ϕ_f	0.01	[-]
Large-fracture spacing, A	5	[m]
Small-fracture spacing, a	1.6	[m]
F characteristic length, l_x	3.472	[m]
F–M/F–f areas per unit volume rock, A_{FM}, A_{Ff}	0.61	[m^2/m^3]
Reference water density, ρ_w	1000	[kg/m^3]
Water-phase viscosity, μ_w	0.001	[Pa·s]
Matrix permeability, k_M	1.572×10^{-16}	[m^2]
Large-fracture permeability, k_F	1.383×10^{-13}	[m^2]
Small-fracture permeability, k_f	1.383×10^{-14}	[m^2]
Water production rate, q_t	100	[m^3/day]
Total compressibility of three media, $C_F = C_M = C_f$	1.0×10^{-9}	[1/Pa]
Well radius, r_w	0.1	[m]
Formation thickness, h	20	[m]

properties of large fractures and matrix correspond to those of the Yucca Mountain fractured formation (Wu et al., 2000, 2004a).

For this example problem, Figure 9.13 presents a comparison of numerical-modeling results (circles) of a triple-continuum simulation with an analytical solution (Wu et al., 2004a; solid-line) using the input parameter values (Table 9.4) in terms of dimensionless pressure and dimensionless time. Excellent agreement exists between the two solutions, except for very small differences at very early times with the dimensionless time <10 (here, a dimensionless time of 50 corresponds to 1 s).

The analytical solution, which is long-time asymptotic and similar to the Warren–Root solution, may not be valid for dimensionless time <100. In addition, the analytical solution may also introduce some errors at early times because it relies on the pseudosteady-state assumption for inter-continuum flow, which is not satisfied during the early rapid transient flow. Furthermore, the analytical solution ignores the effect of global matrix–matrix flow, which is included in the numerical solution. Therefore, the numerical solution may be considered more accurate for early time behavior (Figure 9.13).

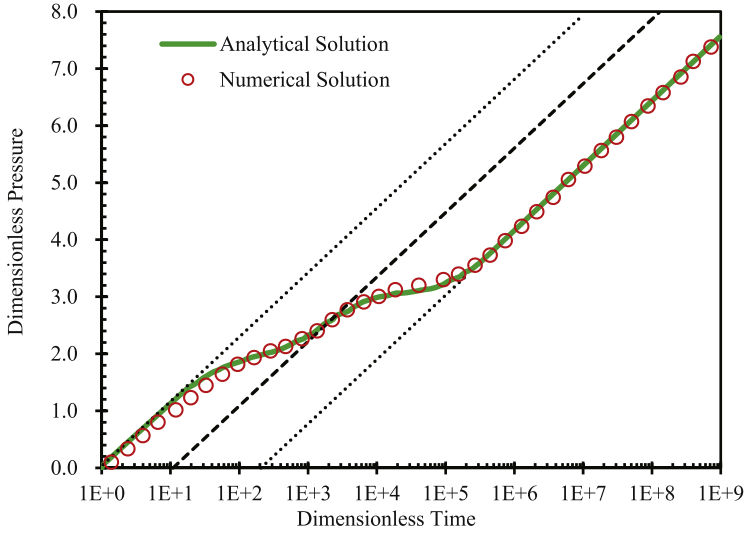

Figure 9.13 Typical behavior curve of flow through a small-fracture, triple-continuum medium, showing three parallel semi-log straight lines from effects of three continua.

9.5.2 Transient Flow Behavior in Triple-Continuum, Fractured Vuggy Reservoirs

In this problem, the conceptual models, as shown in Figures 9.8 and 9.9 (Conceptualization #1 and Conceptualization #2 respectively), are used to investigate behavior of transient flow in a triple-continuum, vuggy fractured reservoir. An infinite radial reservoir of 10 m thick is represented by a 1-D (primary) radial grid of 1101 grids. Single-phase flow simulation is used to generate sets of pressure transient data for the reservoir. Base-case fracture, vug, and matrix parameters are also given in Table 9.5.

Comparison of simulation results between Conceptualizations #1 and #2 are shown in Figure 9.14. It is clear from the figure that fracture and vug connection (F–V) plays a major role in the behavior. Conceptualization #1 that has F–V connection generates triple-porosity behavior (i.e., triple parallel lines on a semi-log scale), whereas simulation results from Conceptualization #2 that does not have F–V direct connection yields double-porosity results (i.e., a two parallel-line curve). In Conceptualization #1, the start of fluid flow in the vug continuum takes place before that in the matrix continuum, because the vug has higher permeability, contributed by the small fractures. In contrast, the beginning of fluid flow in the vug of Conceptualization #2 cannot be clearly identified, because it is dominated by flow in the matrix as the vug does not directly connect to

Table 9.5 Parameters used in the single-phase flow problem in the triple-continuum, fractured vuggy reservoir

Parameter	Value	Unit
Matrix porosity, ϕ_M	0.200	[-]
Fracture porosity, ϕ_F	0.001	[-]
Vug porosity, ϕ_V	0.01	[-]
Fracture spacing, A	1.0	[m]
Vug spacing, a	0.2	[m]
F characteristic length, l_x	0.4	[m]
F−M areas per unit volume rock, A_{FM}	6.2	[m^2/m^3]
F−V areas per unit volume rock, A_{FV}	0.356	[m^2/m^3]
Reference water density, ρ_w	1000	[kg/m^3]
Water-phase viscosity, μ_w	0.001	[Pa·s]
Matrix permeability, k_M	1.0×10^{-16}	[m^2]
Fracture permeability, k_F	1.0×10^{-12}	[m^2]
Vug permeability, k_V	1.0×10^{-13}	[m^2]
Water production rate, q_t	864	[m^3/day]
Total compressibility of three media, $C_F = C_M = C_f$	1.0×10^{-10}	[1/Pa]
Well radius, r_w	0.1	[m]
Formation thickness, h	10	[m]

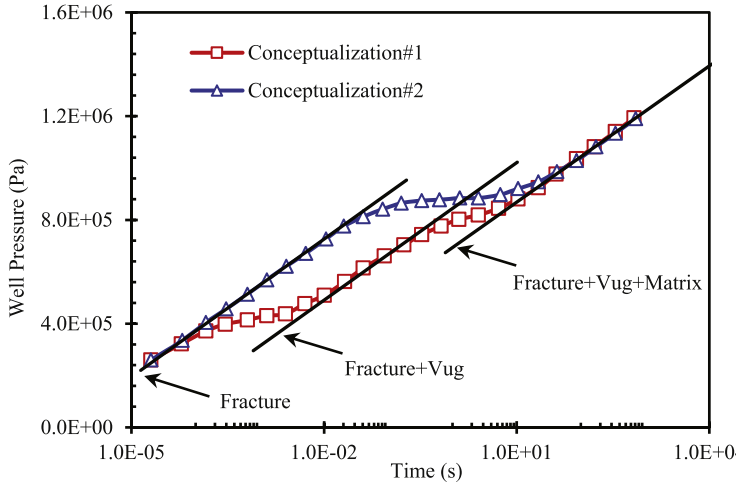

Figure 9.14 Comparison between Conceptualization #1 and Conceptualization #2 for base-case fracture, vug, and matrix parameters.

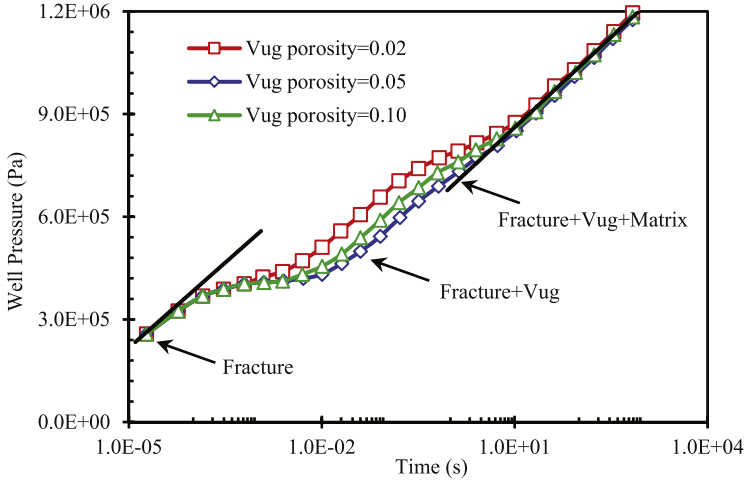

Figure 9.15 Effect of vug porosity on transient flow for Conceptualization #1.

the fracture and has to flow through matrix. As a result, the vug is acting like an additional storage term or a source to the matrix.

Figures 9.15 and 9.16 show the results of effects of vug porosity. It can be seen from Figure 9.15 that vug porosity controls the appearance of the intermediate range of interporosity flow in Conceptualization #1's simulation results. In contrast, vug porosity does not affect flow behavior in Conceptualization #2 as shown in Figure 9.16. This observed effect is caused by F–V connectivity through small fractures in Conceptualization #1 and change in the vug's rock properties directly influences flow between F–V continua. In comparison with Conceptualization #1, the flow in the vug in Conceptualization #2 is controlled by matrix properties; as such, change in the vug porosity does not significantly affect the flow behavior.

Figure 9.17 illustrates the sensitivity or the effects of vug or small-fracture permeability on flow behavior from Conceptualization #1. Vug permeability in Conceptualization #1 controls flow or interaction between large fractures and vugs. The larger is the vug permeability, the sooner the flow from vugs takes place.

Figures 9.18 and 9.19 show results of sensitivity or effects of matrix permeability on flow behavior based on Conceptualization #1 and Conceptualization #2, respectively. Both figures indicate large effects of change in matrix permeability. It is observed that matrix permeability controls the transition time from fracture-dominated to matrix-dominated flow. The larger is the matrix permeability, the shorter is the flow transition.

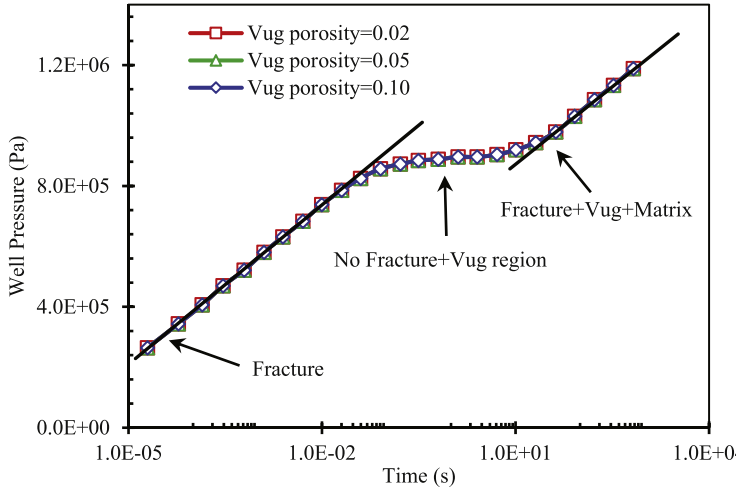

Figure 9.16 Effect of vug porosity on transient flow for Conceptualization #2.

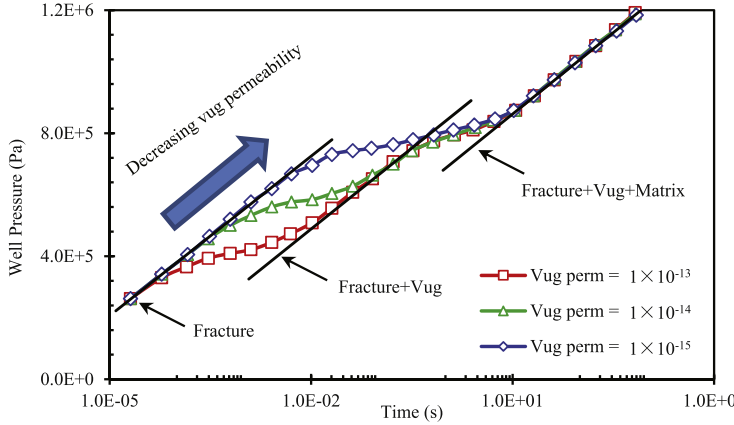

Figure 9.17 Effect of vug or small-fracture permeability on transient flow for Conceptualization #1.

9.5.3 Comparison with Analytical Solution for Imbibition into a Single Matrix Block

This sample problem is used to demonstrate the importance of correct weighting of relative permeability or mobility in modeling multiphase flow at the fracture–matrix interface. We use an analytical solution, which is derived for water imbibition into an unsaturated cubic matrix block with the Richards' equation (Wu and Pan, 2003), to examine numerical simulation results with the upstream mobility-weighting scheme. We select a

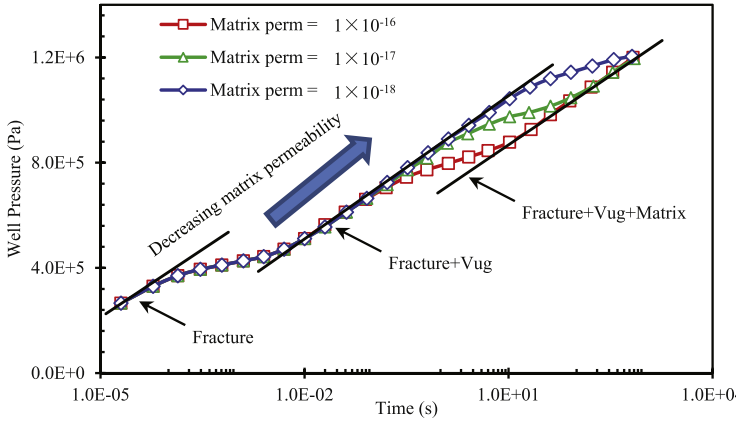

Figure 9.18 Effect of matrix permeability on transient flow for Conceptualization #1.

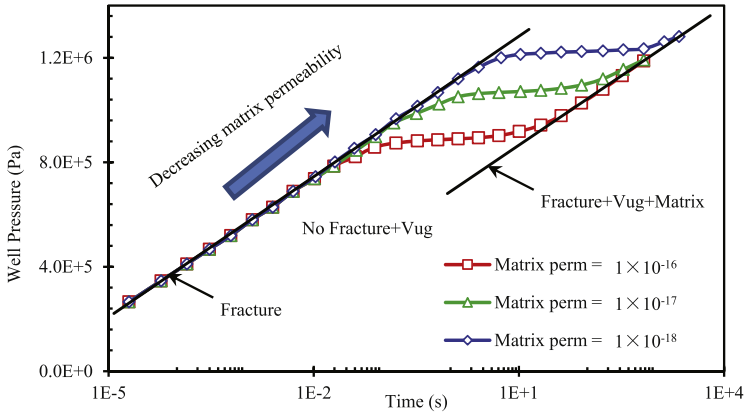

Figure 9.19 Effect of matrix permeability on transient flow for Conceptualization #2.

1-D "spherical" flow analytical solution in this study, and the analytical solution requires the following special forms of relative permeability k_{rw} and capillary pressure P_c for water and air two-phase flow,

$$k_{rw}(S_w) = C_k\left(\overline{S}_w\right)^{\alpha^*} \tag{9.11}$$

and

$$P_c(S_w) \equiv P_g - P_w = C_p\left(\overline{S}_w\right)^{-\beta^*} \tag{9.12}$$

in which P_g is a constant air (or gas) pressure; C_k and C_p (Pa) are coefficients, and α^* and β^* are exponential coefficients of relative permeability and capillary-pressure functions, respectively, and they are correlated with

$\alpha^* = \beta^* + 1$ for the analytical solution; and $\overline{S}_w$ is the normalized water saturation,

$$\overline{S}_w = \frac{S_w - S_{wr}}{1 - S_{wr}} \tag{9.13}$$

with S_{wr} being the residual water saturation.

To examine the mobility weighting scheme, Eqns (9.9) and (9.10), at the fracture–matrix interface for imbibition into a matrix block, numerical simulations are performed with incorporation of the same relative permeability and capillary-pressure functions, Eqns (9.11) and (9.12), as required by the analytical solution (Wu and Pan, 2003; Wu et al., 2004b). The example problem deals with transient water imbibition into a $1 \times 1 \times 1$ m, low initial water-saturation matrix cube, which is surrounded by a uniform fracture network of three orthogonal sets with constant liquid saturation. The imbibition starts at $t = 0$, owing to nonequilibrium in capillarity between the fracture and matrix systems, imposed as the boundary condition to the matrix surface.

For comparison, the imbibition process is modeled by both the analytical and numerical solutions. In the analytical solution, the continuity condition in capillary pressure is imposed on the matrix surface, i.e., the matrix block surface is subject to a constant saturation condition. The

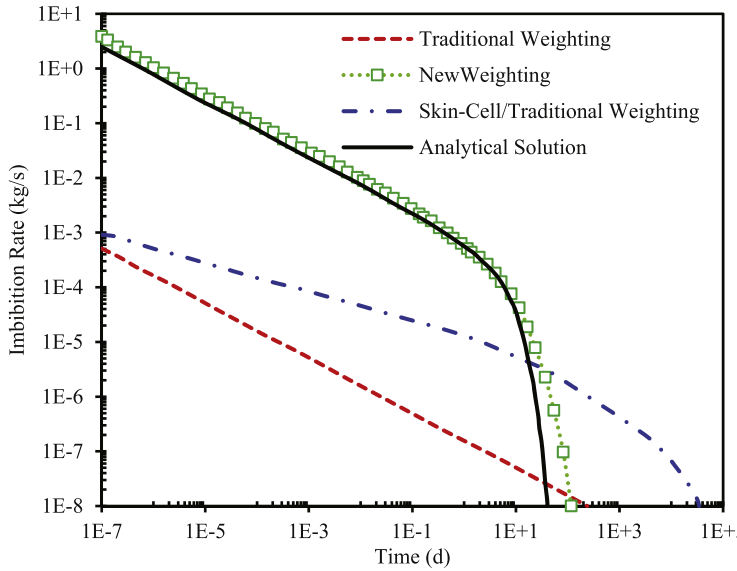

Figure 9.20 Comparison of calculated water imbibing rates from analytical and numerical solutions into a cubic matrix block.

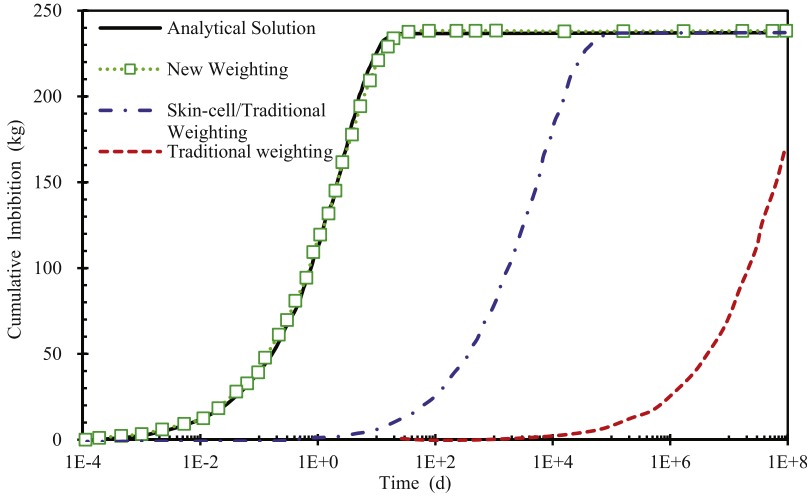

Figure 9.21 Comparison of calculated cumulative water mass imbibition from analytical and numerical solutions into a cubic matrix block.

numerical model uses one double-porosity grid (Figure 9.4(b)) and one MINC grid (Figure 9.4(a)). The MINC grid subdivides the matrix cube into two elements only, and the first matrix element on the matrix outer surface is a tiny-volume, skin-layer cell, with a volumetric fraction set at 0.0001 of the original matrix volume for comparison of modeling results with the analytical and double-porosity model solutions.

The fracture–matrix parameters, including the coefficients of fracture–matrix relative permeability and capillary-pressure functions, used for the example are listed in Table 9.6. Note that in the numerical model, *fracture* relative permeability and capillary-pressure functions are also needed, for which van Genuchten relations (1980) are selected. One the other hand, the analytical solution needs the parameters and correlations for the matrix only, defined in Eqns (9.11) and (9.12). The initial fracture water saturation is 0.012, which corresponds to $S_w = 0.99$ on the matrix surface by capillary equilibrium. It should be mentioned that, in this work, we are concerned mainly with multiphase mass exchange at fracture–matrix interfaces, not with detailed spatial distributions of saturation within fractures or the matrix. Specifically, we compare the results in terms of mass flux (or imbibition rate) and cumulative mass exchange (or imbibition) between the fracture and matrix systems, as shown in Figure 9.20.

Figure 9.20 presents the results of transient imbibition rates on the matrix surface, calculated from the analytical solution and numerical

Table 9.6 Parameters for the comparison problem of imbibing into a single-matrix block

Parameter	Value	Unit
Effective matrix porosity, ϕ_M	0.30	[-]
Absolute matrix permeability, k_M	1.0×10^{-15}	[m^2]
Initial water density, ρ_w	1000	[Kg/m^3]
Water viscosity, μ_w	1.0×10^{-3}	[Pa·s]
Residual matrix saturation, $S_{wr,M}$	0.2	[-]
Initial matrix saturation, S_{Mi}	0.2	[-]
Coefficient of matrix relative permeability, C_k	1.0	[-]
Exponent of matrix relative permeability, α^*	2.0	[-]
Coefficient of matrix capillary pressure, $C_{p,M}$	1.0×10^4	[Pa]
Exponent of matrix capillary pressure, β^*	1.0	[-]
Initial fracture saturation, S_{Fi}	0.012	[-]
Residual fracture saturation, S_{Fr}	0.01	[-]
van Genuchten constant, γ	0.611	[-]
van Genuchten constant, α_{vG}	1.0×10^{-3}	[1/Pa]

simulations using traditional upstream weighting, the new, physical upstream weighting from Eqns (9.9) and (9.10), and skin cell with traditional upstream weighting schemes. Comparison of the three numerical model results with the analytical solution in Figure 9.20 clearly indicates that numerical results with the new weighting scheme agree the best with the analytical solution during the entire transient imbibing period. The simulation results with the skin-layer cell in this case do not match the analytical result very well. In contrast, the simulation using the traditional upstream weighting scheme presents the worst comparison, with more than three orders of magnitude lower than the results of the analytical solution during the entire transient imbibition period. This is because the upstream fracture relative permeability, selected by the traditional approach, significantly underestimated the mobility term for fracture–matrix flow. In terms of cumulative imbibition, similarly, Figure 9.21 also shows that the proposed weighting approach matches the analytical results very well, whereas adding a skin layer in matrix discretization provides an intermediate result and the traditional weighting scheme gives the worst prediction.

9.5.4 Comparison with Laboratory Experiment of Oil–Water Displacement in a Fractured Core

Kazemi and Merrill (1979) presented a series of laboratory experimental results of water imbibition into fractured matrix cores to displace oil.

The laboratory tests were conducted on three sets of artificial fractured cores using cylindrical and rectangular blocks, with one fracture along the long axis for each set. The cylindrical and rectangular matrix blocks were actually cut from Berea Sandstone. The laboratory model we consider here consists of a fractured core with two brick-type matrix blocks. Each matrix block has a brick shape with dimension of width, height, and length (50.8 × 50.8 × 101.6 mm's) as shown in Figure 9.22. The fracture formed between the two matrix cores has an aperture of 0.30 mm. The experimental data used in this study was from Test 38423 (Kazemi and Merrill, 1979) as an example. In the experiment, flow channels were left open only at the inlet and outlet ends of the fracture (i.e., for water injection and for oil and water flow out), and side fracture and matrix surfaces were sealed. Initially, the fracture and matrix system was fully saturated uniformly with oil (diesel), and then water was injected with a constant rate at the inlet (Figure 9.22) to displace the oil.

Basic model experimental and modeling parameters are listed in Table 9.7. The relative permeability and capillary pressure curves used in this case are shown in Figures 9.23 and 9.24, respectively. Note that relative permeability curves for both fracture and matrix, shown in Figure 9.23, were estimated using the equations given in Kazemi and Merrill (1979), and the matrix capillary pressure curve was taken from the capillary-pressure

Table 9.7 Parameters used in the comparison with laboratory testing results (Kazemi and Merrill, 1979)

Parameter	Value	Unit
Fracture aperture, b	0.0003	[m]
Fracture porosity, ϕ_F	1.0	[-]
Matrix porosity, ϕ_M	0.21	[-]
Absolute fracture permeability, k_F	1×10^{-11}	[m^2]
Absolute matrix permeability, k_M	4.23×10^{-13}	[m^2]
Water density, ρ_w	1000	[Kg/m^3]
Water viscosity, μ_w	1×10^{-3}	[Pa·s]
Oil (diesel) density, ρ_w	828	[Kg/m^3]
Oil (diesel) viscosity, μ_w	4.6×10^{-3}	[Pa·s]
Residual fracture water saturation, $S_{wr,F}$	0.10	[-]
Residual matrix water saturation, $S_{wr,M}$	0.20	[-]
Residual fracture oil saturation, $S_{or,F}$	0.0001	[-]
Initial fracture water saturation, $S_{wi,F}$	0.00	[-]
Initial matrix water saturation, $S_{wi,M}$	0.00	[-]
Water injection rate, q_t	2.568×10^{-5}	[m^3/day]

curve on the Berea core of Figure 12 in Kazemi and Merrill (1979). However, several important parameters were not provided in Kazemi and Merrill (1979), including residual water saturation, residual oil saturation, and fracture capillary-pressure curves. Actual values used for these missing parameters were determined in this work by model calibration (Wu et al., 2004b), with the final estimates given in Table 9.7 and Figures 9.23 and 9.24.

Here, this test is analyzed using a double-porosity approach (equivalent to the explicit-fracture model in this case) to examine the numerical scheme for handling fracture–matrix interaction under multiphase flow conditions. The fracture–matrix set of Figure 9.22 is treated as a 2-D system along the longitudinal (x) direction (from inlet to outlet). Because of the symmetry, only half of the 2-D model domain (one matrix block and half the fracture) is discretized into a double-porosity model grid, using a 1-D parallel fracture concept, with one (actually half) fracture element corresponding to one matrix element in the transverse direction (perpendicular to the fracture plane). Along the x direction, a uniform linear grid of 10 elements is generated for both the fracture and the matrix block, with a uniform grid spacing of $\Delta x = 10.16$ mm.

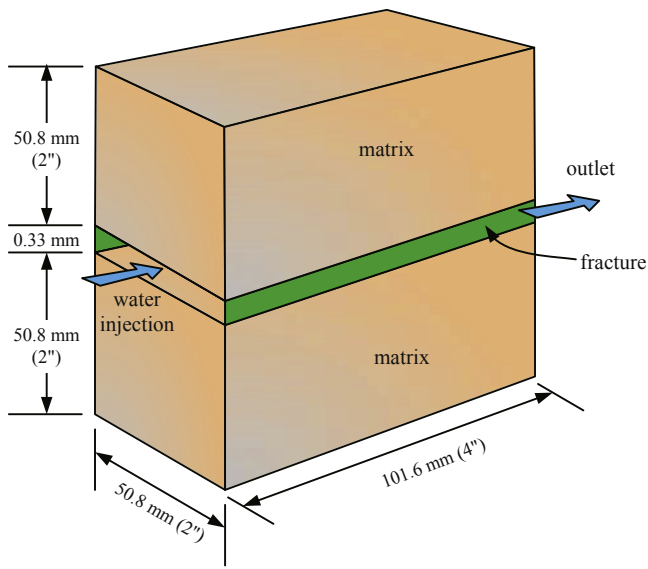

Figure 9.22 Schematic of fractured cores used in the experimental studies *(Modified from Kazemi and Merrill (1979) and Wu et al. (2004b))*.

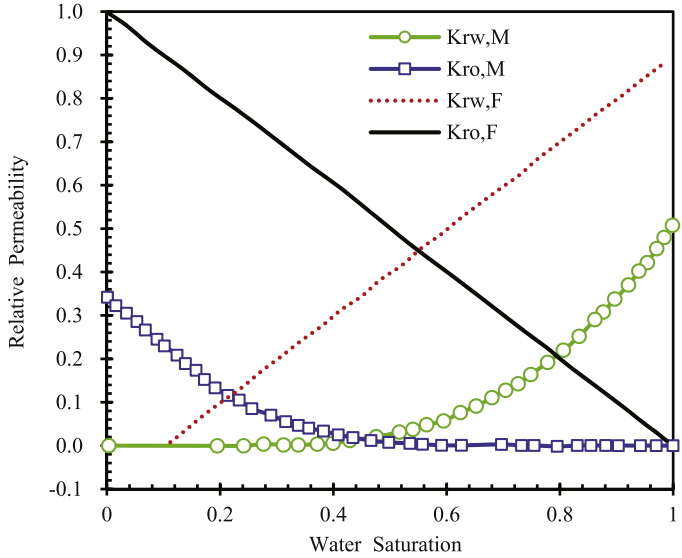

Figure 9.23 Relative permeability curves for fractures and matrix used in matching laboratory experiment results.

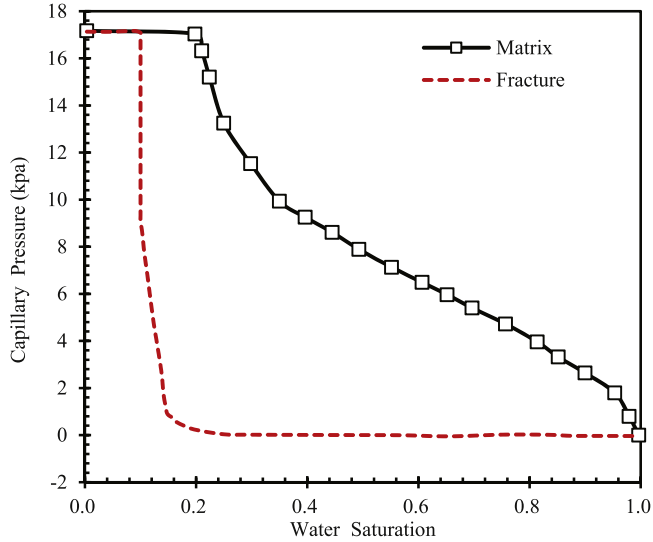

Figure 9.24 Capillary pressure curves for fractures and matrix used in matching laboratory experiment results.

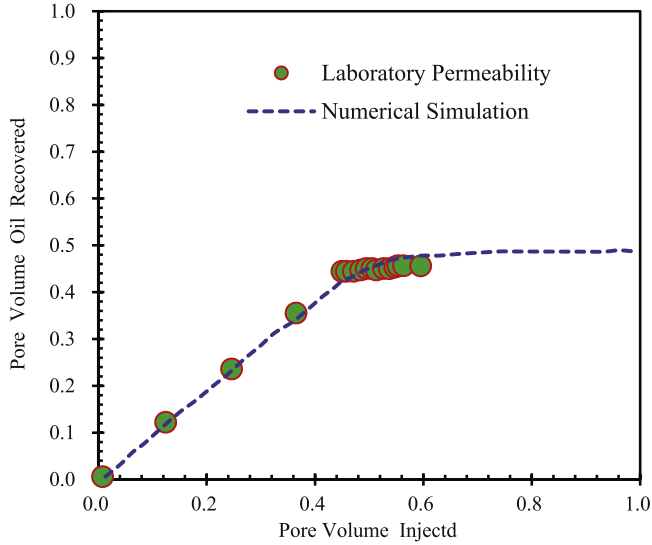

Figure 9.25 Comparison of simulation results with experimental data *(From Kazemi and Merrill (1979))*.

The simulation results using the new physical upstream weighting scheme are compared with the laboratory experimental data in Figure 9.25. Figure 9.25 shows excellent agreement between measured and simulated volumetric fractional oil recovery versus pore volume of water injected. This result indicates that the proposed new upstream mobility-weighting scheme is able to capture the main factors that control fracture–matrix interaction during the oil–water displacement for this test problem.

9.6 SUMMARY AND CONCLUDING REMARKS

In this chapter, we discuss a generalized methodology, from conceptual models and mathematical formulations to numerical modeling approaches, for modeling multiphase flow in fractured porous media. Specifically, a unified, generalized numerical formulation has been presented for simulation of multiphase fluid flow processes through fractured porous media. We explore the possibility by proposing a generalized framework as well as a mathematical formulation for modeling all known flow phenomena in fractured porous media.

As demonstrated in this chapter, the proposed unified numerical modeling approach, based on a general multiple-continuum concept, is suitable for modeling any type of fractured reservoir, including the

double-porosity, triple-, and other multiple-continuum conceptual models, as well as the discrete-fracture modeling approach. In addition, a new, physically based upstream weighting scheme is discussed to calculate multiphase flow between fractures and the matrix, using the continuity condition of capillary forces at the fracture–matrix interface. The numerical implementation of the unified formulation for fractured reservoir simulation is based on a control-volume spatial discretization, using an unstructured grid, and the time discretized with a fully implicit finite-difference method. The final discrete linear or nonlinear equations are handled fully implicitly, using Newton iteration. The proposed general modeling methodology is demonstrated for its application in special cases in which analytical solutions and laboratory experimental data are available.

REFERENCES

Abdassah, D., Ershaghi, I., 1986. Triple-porosity systems for representing naturally fractured reservoirs. SPE Formation Evaluation 1 (2), 113–127.

Aziz, K., Settari, A., 1979. Petroleum Reservoir Simulation. Applied Science Publishers, London.

Bai, M., Elsworth, D., Roegiers, J.-C., 1993. Multiporosity/multipermeability approach to the simulation of naturally fractured reservoirs. Water Resources Research 29 (6), 1621–1633.

Barenblatt, G.I., Zheltov, I.P., Kochina, I.N., 1960. Basic concepts in the theory of seepage of homogeneous liquids in fissured rocks. Journal of Applied Mathematics and Mechanics 24 (5), 1286–1303.

Berkowitz, B., 2002. Characterizing flow and transport in fractured geological media: a review. Advances in Water Resources 25 (8), 861–884.

Camacho-Velazquez, R., Vasquez-Cruz, M.A., Castrejon-Aivar, R., Arana-Ortiz, V., 2005. Pressure transient and decline curve behaviors in naturally fractured vuggy carbonate reservoirs. SPE Reservoir Evaluation & Engineering 8 (2), 95–112.

Clossman, P.J., 1975. An aquifer model for fissured reservoirs. Society of Petroleum Engineers Journal 15 (5), 385–398.

Forsyth, P.A., Kropinski, M.C., 1997. Monotonicity considerations for saturated–unsaturated subsurface flow. SIAM Journal on Scientific Computing 18 (5), 1328–1354.

Forsyth, P.A., Wu, Y.S., Pruess, K., 1995. Robust numerical methods for saturated-unsaturated flow with dry initial conditions in heterogeneous media. Advances in Water Resources 18 (1), 25–38.

Gilman, J.R., Kazemi, H., 1982. Improvements in simulation of naturally fractured reservoirs, paper SPE-10511. In: Sixth SPE-Symposium on Reservoir Simulation, New Orleans, LA.

Gilman, J.R., Kazemi, H., 1988. Improved calculations for viscous and gravity displacement in matrix blocks in dual-porosity simulators (includes associated papers 17851, 17921, 18017, 18018, 18939, 19038, 19361 and 20174). Journal of Petroleum Technology 40 (1), 60–70.

Gong, B., Karimi-Fard, M., Durlofsky, L.J., 2008. Upscaling discrete fracture characterizations to dual-porosity dual-permeability models for efficient simulation of flow with Strong gravitational effects. SPE Journal 13 (1), 58–67.

van Genuchten, M.T., 1980. A closed-form equation for predicting the hydraulic conductivity of unsaturated soils. Soil Science Society of America Journal 44 (5), 892–898.
Huang, Z., Yan, X., Yao, J., 2014. A two-phase flow simulation of discrete-fractured media using mimetic finite difference method. Communications in Computational Physics 16 (3), 799–816.
Huyakorn, P.S., Pinder, G.F., 1983. Computational Methods in Subsurface Flow. Academic Press.
Kazemi, H., 1969. Pressure transient analysis of naturally fractured reservoirs with uniform fracture distribution. Society of Petroleum Engineers Journal 9 (4), 451–462.
Kazemi, H., Gilman, J.R., Eisharkawy, A.M., 1992. Analytical and numerical solution of oil recovery from fractured reservoirs with empirical transfer functions. SPE Reservoir Engineering 7 (2), 219–227.
Kazemi, H., Merrill Jr., L.S., Porterfield, K.L., Zeman, P.R., 1976. Numerical simulation of water-oil flow in naturally fractured reservoirs. Society of Petroleum Engineers Journal 16 (6), 317–326.
Kazemi, H., Merrill, L.S., 1979. Numerical simulation of water imbibition in fractured cores. Society of Petroleum Engineers Journal 19 (3), 175–182.
Li, L., Lee, S.H., 2008. Efficient field-scale simulation of black oil in a naturally fractured reservoir through discrete fracture networks and homogenized media. SPE Reservoir Evaluation & Engineering 11 (4), 750–758.
Liu, J., Bodvarsson, G.S., Wu, Y.-S., 2003. Analysis of flow behavior in fractured lithophysal reservoirs. Journal of Contaminant Hydrology 62, 189–211.
Moinfar, A., Varavei, A., Sepehrnoori, K., Johns, R.T., 2012. Development of a novel and computationally-efficient discrete-fracture model to study IOR processes in naturally fractured reservoirs. In: SPE Improved Oil Recovery Symposium.
Moinfar, A., Varavei, A., Sepehrnoori, K., Johns, R.T., 2014. Development of an efficient embedded discrete fracture model for 3D compositional reservoir simulation in fractured reservoirs. SPE Journal 19 (2), 289–303.
Narasimhan, T.N., Pruess, K., 1988. MINC: an approach for analyzing transport in strongly heterogeneous systems. In: Custodio, E., Gurgui, A., Ferreira, J.P.L. (Eds.), Groundwater Flow and Quality Modelling, vol. 224. Springer, Netherlands, pp. 375–391. http://dx.doi.org/10.1007/978-94-009-2889-3_21.
Neuman, S.P., 2005. Trends, prospects and challenges in quantifying flow and transport through fractured rocks. Hydrogeology Journal 13 (1), 124–147.
Peaceman, D.W., 1977. Fundamentals of Numerical Reservoir Simulation. Elsevier Scientific Publishing Co., New York, NY.
Persoff, P., Pruess, K., 1995. Two-phase flow visualization and relative permeability measurement in natural rough-walled rock fractures. Water Resources Research 31 (5), 1175–1186.
Pruess, K., 1983. GMINC: A Mesh Generator for Flow Simulations in Fractured Reservoirs: Lawrence Berkeley Laboratory Report LBL-15227. Berkeley, California.
Pruess, K., 1991. TOUGH2: A General-Purpose Numerical Simulator for Multiphase Fluid and Heat Flow.
Pruess, K., Narasimhan, N.T., 1985. A practical method for modeling fluid and heat flow in fractured porous media. Society of Petroleum Engineers Journal 25 (1), 14–26.
Pruess, K., Oldenburg, C.M., Moridis, G.J., 1999. TOUGH2 User's Guide Version 2.
Snow, D.T., 1965. A Parallel Plate Model of Fractured Permeable Media. University of California, Berkeley.
Snow, D.T., 1969. Anisotropie permeability of fractured media. Water Resources Research 5 (6), 1273–1289.
Warren, J.E., Root, P.J., 1963. The behavior of naturally fractured reservoirs. Society of Petroleum Engineers Journal 3 (3), 245–255.

Wu, Y.-S., 2000. On the effective continuum method for modeling multiphase flow, multicomponent transport, and heat transfer in fractured rock. In: Faybishenko, B., And, P.A.W., Benson, S.M. (Eds.), Dynamics of Fluids in Fractured Rock. Wiley Online Library, Washington, DC, pp. 299–312. http://dx.doi.org/10.1029/GM122p0299.

Wu, Y.-S., 2002. Numerical simulation of single-phase and multiphase non-Darcy flow in porous and fractured reservoirs. Transport in Porous Media 49 (2), 209–240.

Wu, Y.-S., Di, Y., Kang, Z., Fakcharoenphol, P., 2011. A multiple-continuum model for simulating single-phase and multiphase flow in naturally fractured vuggy reservoirs. Journal of Petroleum Science and Engineering 78 (1), 13–22.

Wu, Y.-S., Lu, G., Zhang, K., Pan, L., Bodvarsson, G.S., 2007a. Analyzing unsaturated flow patterns in fractured rock using an integrated modeling approach. Hydrogeology Journal 15, 553–572.

Wu, Y.-S., Ehlig-Economides, C., Qin, G., Kang, Z., Zhang, W., Ajayi, B., Tao, Q., 2007b. A Triple-continuum Pressure-transient Model for a Naturally Fractured Vuggy Reservoir. Society of Petroleum Engineers, Anaheim, California, U.S.A. http://dx.doi.org/10.2118/110044-MS.

Wu, Y.-S., Ge, J.-L., 1983. The transient flow in naturally fractured reservoirs with three-porosity systems. Acta Mechanica Sinica 14 (1), 81–84.

Wu, Y.-S., Haukwa, C., Bodvarsson, G.S., 1999. A site-scale model for fluid and heat flow in the unsaturated zone of Yucca Mountain, Nevada. Journal of Contaminant Hydrology 38 (1), 185–215.

Wu, Y.-S., Li, J., Ding, D., Wang, C., Di, Y., 2014. A generalized framework model for the simulation of gas production in unconventional gas reservoirs. SPE Journal 19 (5), 845–857.

Wu, Y.-S., Liu, H.H., Bodvarsson, G.S., 2004a. A triple-continuum approach for modeling flow and transport processes in fractured rock. Journal of Contaminant Hydrology 73 (1), 145–179.

Wu, Y.-S., Liu, J., Xu, T., Haukwa, C., Zhang, W., Liu, H.H., Ahlers, C.F., 2000. UZ Flow Models and Submodels. Report MDL-NBS-HS-000006. Lawrence Berkeley National Laboratory. CRWMS M&O.

Wu, Y.-S., Pan, L., 2003. Special relative permeability functions with analytical solutions for transient flow into unsaturated rock matrix. Water Resources Research 39 (4).

Wu, Y.-S., Pan, L., Pruess, K., 2004b. A physically based approach for modeling multiphase fracture–matrix interaction in fractured porous media. Advances in Water Resources 27 (9), 875–887.

Wu, Y.S., Pan, L., Zhang, W., Bodvarsson, G.S., 2002. Characterization of flow and transport processes within the unsaturated zone of yucca mountain. Journal of Contaminant Hydrology 54, 215–247.

Wu, Y.-S., Pruess, K., 1988. A multiple-porosity method for simulation of naturally fractured petroleum reservoirs. SPE Reservoir Engineering 3 (1), 327–336.

Wu, Y.-S., Qin, G., 2009. A generalized numerical approach for modeling multiphase flow and transport in fractured porous media. Communications Computational Physics 6 (1), 85–108.

Wu, Y.-S., Zhang, K., Liu, H.-H., 2006a. Estimating large-scale fracture permeability of unsaturated rock using barometric pressure data. Vadose Zone Journal 5, 1129–1142, 13.

CHAPTER 10

Multiphase Fluid and Heat Flow in Porous Media

10.1 INTRODUCTION

This book is primarily dealing with the isothermal flow condition for multiphase fluids through porous media, which is a simplification or approximation to the physical processes of general flow and transport in actual reservoirs. Multiphase fluid flow and heat transfer or non-isothermal flow in porous media occur in many reservoir systems and subsurface engineering applications. For example, geothermal energy represents a clean, abundant, and sustainable energy source for mankind. Production of geothermal energy from subsurface hydrothermal reservoirs and enhanced (or engineered) geothermal systems (EGS) is a typical scenario of multiphase fluid and heat flow in the rock of formations, because thermal energy is carried out from reservoirs and produced through wells in the form of fluids (e.g., water and steam) (Grant et al., 1984; Grant, 2013). Therefore, there has been a need to understand and model fluid and heat flow in geothermal reservoirs to effectively develop such energy sources (Pruess, 2002; Wu et al., 2015).

In the petroleum industry, thermal recovery methods are among the most widely used Enhanced Oil Recovery (EOR) techniques for effective development of heavy oil and bitumen in the world (Prats, 1985; Butler and Mokrys, 1991). In the past half century, thermal EOR methods have produced more crude oil than any other EOR approaches, in particular, in northern and southern America. The thermal recovery approaches mainly include steam flooding, hot water injection, and *in situ* combustion. Mechanisms of thermally stimulated recovery consists of reduction of heavy oil viscosity, expansion of reservoir oil, other fluids, and rock, crude-oil distillation, and gas and hot-water drive (Prats, 1985). Fluid flow in thermally stimulated reservoirs is controlled by the thermodynamics of multiphase fluid flow, coupled with heat transfer in reservoirs.

In addition, nonisothermal flow in porous media has received significant interest in investigation and application of subsurface Non-Aqueous Phase

Multiphase Fluid Flow in Porous and Fractured Reservoirs
ISBN 978-0-12-803848-2
http://dx.doi.org/10.1016/B978-0-12-803848-2.00010-6

Liquid (NAPL) contamination and thermal cleanup approaches (Falta et al., 1992a,b; Forsyth, 1994; Panday et al., 1995; Pruess and Battistelli, 2002). Furthermore, subsurface storage for high-level nuclear wastes and CO_2 geosequestration also involve multiphase fluid flow and heat transfer coupling processes (Wu et al., 2006; Winterfeld and Wu, 2014). Modeling fluid and heat flow processes is critical to application and improvement of such thermal technology in subsurface systems.

10.2 PHYSICS FOR MULTIPHASE FLUID AND HEAT FLOW IN POROUS MEDIA

The physical processes of multiphase flow associated with heat transfer in rock are governed by the same physical laws of mass and energy conservation. Fluid flow and heat transfer in porous media are coupled physically and dynamically, i.e., they have strong mutual impact on each other. This is simply because fluid flow carries convective heat flow, whereas heat flow and temperature variation will in turn alter fluid-flow properties, such as fluid viscosity and density, and rock properties, directly impacting viscous and gravity forces or flow behavior. In reservoirs, the two coupled processes of fluid flow and heat transfer are further complicated by other interactions between multiphase fluids, multi-components, and associated changes in fluid phases, internal energy, and enthalpy. Therefore, the two processes of fluid and heat flow have to be physically modeled in a fully coupled fashion or simultaneously in modeling studies. If a gas phase exists or evolves, pressure and temperature are correlated by the gas law, indicating a very strong coupling of fluid flow and heat transfer.

To accurately account for strong interactions between fluid flow and heat transfer in porous media, a compositional modeling approach has been in general use for simulation of coupled fluid and heat flow, instead of a black-oil type multiphase flow model (e.g., Panday et al., 1995; Bodvarsson et al., 2001; Pruess and Battistelli, 2002). This is because a compositional model is able to correctly describe the thermodynamics governing mass and heat transfer among multiple phases during the fluid and heat flow in reservoirs.

10.2.1 Advective and Dispersive Mass Transport

Multiphase flow in a compositional model is described by the movement of dissolved mass components within each fluid in a multiphase porous-medium system, which is governed by advective, diffusive, and dispersive processes. It may be also subject to other processes, such as mass exchange

or partitioning between phases, adsorption, radioactive decay, dissolution, precipitation, and other chemical reactions. However, many of these processes may not occur simultaneously or can be ignored in a site-specific field reservoir simulation using a compositional model. The advective transport of a component is carried by flow of a fluid, and diffusive and dispersive flux is contributed by molecular diffusion and mechanical dispersion. The combined effects of molecular diffusion and mechanical dispersion are called hydrodynamic dispersion and are often described using a modified Fick's law for transport through a single-phase porous medium (Scheidegger, 1961; Bear, 1972).

In analogy to the extension of Darcy's law from single-phase flow to multiphase flow, Fick's law of diffusion has been generalized to describe the transport of components in multiphase, miscible or immiscible fluid systems (e.g., Corapcioglu and Baehr, 1987; Sleep and Sykes, 1989; Wu and Pruess, 2000). The generalized Fick's law, including hydrodynamic dispersion effects in a multiphase system, is used in this section to evaluate dispersive flux of mass transport. Then, the total mass flux of advection and dispersion in a fluid is written as

$$\boldsymbol{F}_\beta^k = \rho_\beta X_\beta^k \boldsymbol{v}_\beta - \boldsymbol{D}_\beta^k \nabla\left(\rho_\beta X_\beta^k\right) \tag{10.1}$$

in which superscript k is an index for mass components; $\boldsymbol{F}_\beta^k$ is the total mass flux vector of component k within fluid β; ρ_β is the density (or mole density) of fluid β; X_β^k is the mass (or mole) fraction of component k in fluid β; and $\boldsymbol{D}_\beta^k$ is the hydrodynamic dispersion tensor, accounting for both molecular diffusion and mechanical dispersion for component k in phase β. Here, we extend the general dispersion model (Scheidegger, 1961) to include multiphase fluid effects as (Wu and Pruess, 2000),

$$\boldsymbol{D}_\beta^k = \alpha_{\mathrm{T}}^\beta |\boldsymbol{v}_\beta| \delta_{ij} + \left(\alpha_{\mathrm{L}}^\beta - \alpha_{\mathrm{T}}^\beta\right) \frac{\boldsymbol{v}_\beta \boldsymbol{v}_\beta}{|\boldsymbol{v}_\beta|} + \phi S_\beta \tau d_\beta^k \delta_{ij} \tag{10.2}$$

in which $\alpha_{\mathrm{T}}^\beta$ and $\alpha_{\mathrm{L}}^\beta$ are transverse and longitudinal dispersivities, respectively, in fluid β of porous media; τ is tortuosity of the porous medium; d_β^k is the molecular diffusion coefficient of component k within fluid β; and δ_{ij} is the Kronecker delta function ($\delta_{ij} = 1$ for $i = j$, and $\delta_{ij} = 0$ for $i \neq j$) with i and j being coordinate indexes.

The hydrodynamic dispersion tensor (10.2) describes the combined effects of hydrodynamic dispersion to be controlled by mechanical dispersion (the first two terms on the right-hand side of Eqn (10.2)) and molecular diffusion (the last term on the right-hand side of Eqn (10.2)). The

mechanical dispersion within a fluid phase is assumed proportional to the magnitude of the velocity of the fluid and consists of longitudinal dispersion along the direction of the flow and transverse dispersion perpendicular to the flow direction.

10.2.2 Convective and Conductive Heat Transfer

Heat transfer in porous media is in general a result of both convective and conductive processes. These processes are complicated by interactions between multiphase fluids, multi-components, and associated changes in phases, internal energy and enthalpy. Heat convection is contributed by thermal energy carried mainly by bulk flow of all fluids as well as by dispersive mass fluxes. On the other hand, heat conduction is driven by temperature gradients and may follow Fourier's law. Then the overall heat flux vector in reservoirs may be described as

$$\boldsymbol{F}^{\mathrm{T}} = \sum_{\beta}\left(h_{\beta}\rho_{\beta}\boldsymbol{v}_{\beta}\right) - \sum_{\beta}\sum_{k}\left(h_{\beta}^{k}\boldsymbol{D}_{\beta}^{k}\cdot\nabla\left(\rho_{\beta}X_{\beta}^{k}\right)\right) - \left(K_{\mathrm{T}}\nabla T\right) \qquad (10.3)$$

in which $\boldsymbol{F}^{\mathrm{T}}$ is the combined heat flux vector, including both advective, diffusive, and conductive heat flow in a multiphase, multicomponent system; h_{β} and h_{β}^{k} are specific enthalpies of fluid-phase β and of component k in fluid β, respectively; K_{T} is the overall thermal conductivity, which is a function of fluid saturations; and T is temperature.

As shown in Eqn (10.3), the total heat flow in a multiphase, multicomponent system is determined by heat convection of fluid flow, mass diffusion, and dispersion, the first two terms on the right-hand side of the equation, as well as heat conduction, the last term on the right-hand side. In practice, heat flow associated with diffusive fluxes is generally neglected in reservoir simulation.

10.3 CONCEPTUAL AND MATHEMATICAL MODEL

In this section, we present a set of generalized governing equations for multiphase fluid flow, multicomponent transport, and heat transfer in porous and fractured media. The objective is to include physical processes of porous media as commonly occurring in petroleum reservoirs. This will provide a framework for discussion, simplification, extension, and application in practice to cover more specific scenarios of flow and transport in reservoirs.

Before we derive the mass- and energy-conservation equations, we need to discuss several assumptions and simplifications used in the literature as well

as in this chapter. First, we will ignore some minor effects of potential and kinetic energy in the total energy balance in heat flow equations. We also ignore adsorption, radioactive decay, solid dissolution and precipitation, and other chemical reactions, i.e., no chemical reactions to take place other than interphase mass transfer by partitioning in mass transport equations.

A multiphase system consists of several fluid phases, such as oil, gas, and water, and each fluid in turn consists of a number of mass components. To derive a set of generalized governing equations for multiphase fluid flow, multicomponent transport, and heat transfer, we assume that these processes can be described using a continuum approach within a representative elementary volume (REV) in a porous or fractured medium (Bear, 1972). In addition, the condition of local chemical and thermal equilibrium is assumed, so that temperatures, phase pressures, densities, viscosities, enthalpies, internal energies, and component concentrations or mass fractions are the same locally within each REV of the porous medium at any time.

A combination of mass- and energy-conservation principles of the flow and transport constitutive laws with the mass transport, Eqn (10.1), and heat transfer, Eqn (10.3), gives rise to a set of governing equations subsequently described. The mass-conservation equations of each component k in the porous continuum can be written as follows:

For mass transport,

$$\frac{\partial}{\partial t}\left[\phi\sum_{\beta}\left(\rho_{\beta}S_{\beta}X_{\beta}^{k}\right)\right]=-\sum_{\beta}\nabla\cdot\left(\rho_{\beta}X_{\beta}^{k}\boldsymbol{v}_{\beta}\right)+\sum_{\beta}\nabla\cdot\left(\boldsymbol{D}_{\beta}^{k}\cdot\nabla\left(\rho_{\beta}X_{\beta}^{k}\right)\right)+q^{k} \tag{10.4}$$

and the energy-conservation equation is

$$\frac{\partial}{\partial t}\left[\sum_{\beta}\left(\phi\rho_{\beta}S_{\beta}U_{\beta}\right)+(1-\phi)\rho_{\mathrm{s}}U_{\mathrm{s}}\right]=-\sum_{\beta}\nabla\cdot\left(h_{\beta}\rho_{\beta}\boldsymbol{v}_{\beta}\right)+\sum_{\beta}\sum_{k}\nabla\cdot\left(h_{\beta}^{k}\boldsymbol{D}_{\beta}^{k}\cdot\nabla\left(\rho_{\beta}X_{\beta}^{k}\right)\right)+\nabla\cdot\left(K_{\mathrm{T}}\nabla T\right)+q^{\mathrm{E}} \tag{10.5}$$

in which subscript k is the index for the components, $k = 1, 2, 3,\ldots, N_c$, with N_c being the total number of mass components; ρ_{s} is the density of rock solids; q^{k} and q^{E} are external source/sink terms or fracture–matrix exchange terms for mass component k and energy; and U_{β} andU_{s} are the internal energies of fluid β and rock solids, respectively.

In Eqns (10.4) and (10.5), the volumetric flow velocity, $\boldsymbol{v}_\beta$, of each fluid phase can be determined by Darcy's law, non-Darcy flow, or non-Newtonian fluid flow, when their processes are involved for a particular application. Equations (10.4) and (10.5) are a generalized system of equations for transport of mass components by advection and dispersion processes, coupled with heat transfer by convection and conduction mechanisms.

10.4 PHYSICAL CONSTRAINTS AND CONSTITUTIVE CORRELATIONS

To complete the mathematical description of multiphase fluid flow and heat transfer in porous media, the governing Eqns (10.4) and (10.5), which are the general mass and energy balance equations, need to be supplemented with a number of constitutive equations. These constitutive correlations express interrelations and constraints of physical processes, variables, and parameters, and allow the evaluation of secondary variables and parameters as functions of a set of primary unknowns or variables, selected to make numerically discretized governing equations solvable.

Table 10.1 lists a commonly used set of constitutive relationships for describing multiphase flow, multicomponent mass transport, and heat transfer through porous media (Wu and Qin, 2009). Many of these correlations for estimating properties and interrelationships are determined by experimental studies. Concepts, constitutive functions, and correlations as well as fluid and rock properties, discussed in Section 3.4 for isothermal flow, may still be applicable, but need to add the dependencies on component, temperature, and phase behavior

Compared to constitutive correlations used for the black-oil model in an isothermal reservoir system, fluid properties and constitutive correlations for a compositional model with multiphase fluid and heat flow, as discussed above, are much more complicated and difficult to determine or evaluate. Among them are description and evaluation of phase behavior and equilibrium partitioning of mass components among the phases. The most common approaches used for calculating phase equilibria for gas and liquid hydrocarbon mixtures are based on (1) the K-value approach, (2) *equations of state* (EOS), and (3) a variety of empirical tables from experiments (McCain, 1990; Pruess and Battistelli, 2002; Chen et al., 2006). Note that the Table 10.1 lists an equilibrium K-value approach only. The *equation of state* method is based on the chemical potential (called Gibbs molar free energy) in which the equilibrium gas equals to the chemical potential of the

Table 10.1 Constitutive Relationships and Functional Dependence of Multiphase Fluid and Heat Flow in Porous Media

Definition	Function	Description
Fluid saturation	$\sum_{\beta} S_{\beta} = 1$	Constraint on summation of total fluid saturation.
Mass fraction	$\sum_{k} X_{\beta}^{k} = 1$	Constraint on mass fractions within phase β.
Capillary pressure	$P_{c\beta} = P_{c\beta}(S_{\beta}, T)$	In a multiphase system, the capillary pressure relates pressures between the phases and is defined as functions of fluid saturation and temperature.
Relative permeability	$k_{r\beta} = k_{r\beta}(S_{\beta}, T)$	The relative permeability of a fluid phase in a multiphase system is normally assumed to be functions of fluid saturation and temperature.
Fluid density	$\rho_{\beta} = \rho_{\beta}(P, T, X_{\beta}^{k})$	Density of a fluid phase is treated as a function of pressure and temperature, as well as mass compositions ($k = 1, 2, 3,\ldots, N_c$).
Fluid viscosity	$\mu_{\beta} = \mu_{\beta}(P, T, X_{\beta}^{k})$	The functional dependence or empirical expressions of viscosity of a fluid is treated as a function of pressure, temperature, and composition.
Henry's law	$P_{g}^{k} = K_{H}^{k}\omega_{w}^{k}$	P_{g}^{k} is Partial pressure of component k in gas phase; K_{H}^{k} is Henry's constant for component k; and ω_{w}^{k} is the mole fraction of component k in the water phase.
Equilibrium partitioning	$\omega_{\alpha}^{k} = K_{\alpha:\beta}^{k}\omega_{\beta}^{k}$	ω_{α}^{k} and ω_{β}^{k} are the mole fraction of component k in phase α and β, respectively; and $K_{\alpha:\beta}^{k}$ is the equilibrium partitioning coefficient of component k between phases α and β.
Partitioning coefficient	$K_{\alpha:\beta}^{k} = K_{\alpha:\beta}^{k}(P_{\beta}, T, X_{\beta}^{k})$	Depends on chemical properties of the component and is a function of temperature, pressure and composition
Specific enthalpy of liquid	$h_{\beta} = U_{\beta} + \frac{P_{\beta}}{\rho_{\beta}}$	Internal energy, U_{β}, of liquid phase β is a function of pressure and temperature.
Specific enthalpies of gas	$h_{g}^{k} = U_{g}^{k} + \frac{P_{g}^{k}}{C_{g}^{k}}$	U_{g}^{k} the Specific internal energy of component k in the gas phase; C_{g}^{k} concentration of component k in gas phase (kg/m^3).
Thermal conductivity	$K_{T} = K_{T}(S_{\beta})$	The thermal conductivity of the porous medium is treated as a function of fluid saturation.

equilibrium liquid to calculate gas–liquid equilibria of the compositional system under the condition of thermodynamic equilibrium.

In compositional modeling practice, fluid properties of gas, aqueous (water) and oil phases, and thermal parameters are often evaluated using published data sets, table lookups, or functionally formed correlations in the literature with coefficients to be determined from specific field data (Reid et al., 1987; Pruess and Battistelli, 2002). In addition, the actual number of hydrocarbon components in reservoirs is in general too large to model if all the components are included. This is because of the intensity of computational and data requirements. Common practice is to introduce the *pseudo-components* concept for approximating crude oil using a few lumped components (or pseudo-components) (e.g., Chen et al., 2006).

10.5 NUMERICAL FORMULATION, SOLUTION, AND APPLICATION

The methodology for solving the governing equations, Eqns (10.4) and (10.5), of multiphase fluid and heat flow in porous media is the same numerical approach as those discussed in Chapter 4. It should be mentioned that the governing equations for compositional modeling coupled with heat transfer are highly nonlinear and much more difficult to solve than isothermal multiphase flow equations, such as the black-oil model. In reality, a numerical approach is the only choice for solution of multiphase fluid and heat flow problems to deal with the complicated thermodynamics and phase changes involved.

10.5.1 Discrete Equations

The component mass and energy balance equations, Eqns (10.4) and (10.5), are discretized in space using a control-volume concept. Time discretization is carried out using a backward, first-order, fully implicit finite-difference scheme. The discrete nonlinear equations for mass components of oil, gas, and water, and heat at grid block or node i can be written in the same form, as Eqn (4.1), in terms of component, k,

$$\left(A_i^{k,n+1} - A_i^{k,n}\right)\frac{V_i}{\Delta t} = \sum_{j\in\eta_i} flow_{ij}^{k,n+1} + Q_i^{k,n+1}, \quad k = 1, 2, 3, \ldots, N_c + 1$$
$$\text{and} \quad i = 1, 2, 3, \ldots, N \tag{10.6}$$

in which superscript k serves also as an equation index for all mass components with $k = 1, 2, 3, \ldots, N_c$ and $k = N_c + 1$ denotes the energy equation;

A_i^k, $flow_{ij}^k$, and Q_i^k are the accumulation terms, the "flow" term between nodes i and j, and the sink/source term at node i for component k or thermal energy, respectively, to be defined subsequently. Note that Eqn (10.6) has the same form regardless of the dimensionality of the system, i.e., it applies to one-, two-, or three-dimensional multi-phase flow, mass transport, and heat-transfer analyses in porous or fractured reservoirs.

The accumulation terms for mass components or thermal energy are evaluated in the following. For mass components,

$$A_i^k = \left[\phi \sum_\beta \left(\rho_\beta S_\beta X_\beta^k\right)\right]_i, \quad k = 1, 2, 3, \ldots, N_c \tag{10.7}$$

For thermal energy,

$$A_i^{N_c+1} = \left[\sum_\beta \left(\phi \rho_\beta S_\beta U_\beta\right) + (1-\phi)\rho_s U_s\right]_i \tag{10.8}$$

The "flow" terms, $flow_{ij}^k$, in Eqn (10.6) are generic and include mass fluxes by advective and dispersive processes, as described by Eqn (10.1), as well as heat transfer, described by Eqn (10.3). For mass-component transport, the flow term or the net mass flux by advection and hydrodynamic dispersion of a component along the connection of nodes i and j, is determined by (Wu and Pruess, 2000)

$$flow_{ij}^k = F_{\mathrm{A},ij}^k + F_{\mathrm{D},ij}^k, \quad k = 1, 2, 3, \ldots, N_c \tag{10.9}$$

in which $F_{\mathrm{A},ij}^k$ and $F_{\mathrm{D},ij}^k$ are the net mass fluxes by advection and hydrodynamic dispersion along the connection, respectively, with

$$F_{A,ij}^k = A_{ij} \sum_\beta \left(X_\beta^k\right)_{ij+1/2} F_{\beta,ij} \tag{10.10}$$

and

$$F_{\mathrm{D},ij}^k = -\boldsymbol{n}_{ij} \cdot A_{ij} \sum_\beta \mathbf{D}_\beta^k \cdot \nabla\left(\rho_\beta X_\beta^k\right) \tag{10.11}$$

in which $\boldsymbol{n}_{ij}$ is the unit vector along the connection of the two grid blocks i and j. When Darcy law is applied with an integrated finite difference approach, the phase mass-flow term, $F_{\beta,ij}$, in Eqn (10.10) is evaluated as

$$F_{\beta,ij} = \left(\frac{\rho_\beta k_{r\beta}}{\mu_\beta}\right)_{ij+1/2} \gamma_{ij}\left(\Phi_{\beta j} - \Phi_{\beta i}\right) \tag{10.12}$$

The total heat flux along the connection of nodes i and j, including advective and conductive terms, may be evaluated, when using a finite-difference scheme, by

$$flow_{ij}^{N_c+1} = A_{ij} \sum_{\beta} \left[(h_\beta)_{ij+1/2} F_{\beta,ij} \right] + (K_T)_{ij+1/2} \left(\frac{T_j - T_i}{d_i + d_j} \right) \tag{10.13}$$

In evaluating the "flow" terms in the Eqns (10.10) and (10.13), subscript $ij + 1/2$ is used to denote a proper averaging or weighting of fluid flow, component transport, or heat-transfer properties at the interface or along the connection between two grid blocks or nodes i and j. The convention for the signs of flow terms is that flow from node j into node i is defined as "+" (positive) in calculating the flow terms.

The mass or energy sink/source in Eqn (10.6) at node i, Q_i^k, is defined as the mass or energy exchange rate per unit volume of rock. It is normally used to treat boundary conditions, such as production and injection through wells.

Note that we present explicit, discrete expressions for estimating all the flow terms above, except for dispersive fluxes in Eqn (10.11). This is because of the numerical difficulties introduced in handling the hydrodynamic tensor of dispersion, which is treated very differently with different numerical approaches, such as finite difference or finite element. In most formulations for solute transport, the off-diagonal terms and contributions of the dispersion tensor are ignored, and dispersive transport is considered only along the principal directions. However, a general procedure for using the integrated finite difference to incorporate a full dispersion tensor is presented by Wu and Pruess (2000).

Note that Eqn (10.6), similar to Eqn (4.1), presents an exact form of the balance equation for each mass component and thermal energy in a discrete form. It states that the rate of change in mass or energy accumulation at a node over a time step is exactly balanced by inflow/outflow of mass and energy, and also by sink/source terms, when existing for the node. As long as all flow terms have flow from node i to node j equal to and opposite to that of node j to node i for fluids, components, and heat, no mass or energy will be lost or created in the formulation during the solution. Therefore, the numerical discretization in Eqn (10.16) is conservative.

10.5.2 Numerical Solution Scheme

There are a number of numerical solution techniques that have been developed and used in the literature over the past few decades to solve the

nonlinear, discrete equations of reservoir simulations (e.g., Chen et al., 2006). When handling multiphase flow, multicomponent transport, and heat transfer in a multiphase flow system, the predominant approach is to use a fully implicit scheme with Newton iteration. This scheme is the best, because of its ability to handle the extremely high nonlinearity inherent in those discrete equations and many other numerical schemes with different level of explicitness that often fail to converge in practice. In this section, we discuss a general procedure, similar to Section 4.3, to solve the discrete nonlinear Eqn (10.6) fully implicitly, using a Newton iteration method.

Let us write the discrete nonlinear Eqn (10.6) in a residual form as

$$R_i^{k,n+1} = \left(A_i^{k,n+1} - A_i^{k,n}\right)\frac{V_i}{\Delta t} - \sum_{j\in\eta_i} flow_{ij}^{k,n+1} - Q_i^{k,n+1} = 0, \qquad k = 1, 2, 3, \ldots, N_c + 1 \text{ and } i = 1, 2, 3, \ldots, N \tag{10.14}$$

Equation (10.14) defines a set of $(N_c + 1) \times N$ coupled nonlinear algebraic equations that need to be solved for every balance equation of mass components and heat, respectively. In general, $(N_c + 1)$ primary variables per node are needed to use the Newton iteration for the associated $(N_c + 1)$ equations per node. The primary variables are usually selected among fluid pressures, fluid saturations, mass (mole) fractions of components in fluids, and temperatures. In many applications, however, primary variables cannot be fixed and must be allowed to vary dynamically to deal with some phase appearance and disappearance (Forsyth, 1994; Pruess and Battistelli, 2002; Chen et al., 2006). The rest of the dependent variables, such as relative permeability, capillary pressures, viscosity and densities, partitioning coefficients, specific enthalpies, thermal conductivities, dispersion tensor, as well as nonselected pressures, saturations, or mass (mole) fractions, are treated as secondary variables, which are calculated from the selected primary variables.

In terms of the primary variables, the residual equation, Eqn (10.6), at a node i and for equation β, is regarded as a function of the primary variables at not only node i, but also at all its direct neighboring nodes j. The Newton iteration scheme gives rise,

$$\sum_m \frac{\partial R_i^{k,n+1}(x_{m,p})}{\partial x_m}(\delta x_{m,p+1}) = -R_i^{k,n+1}(x_{m,p}) \tag{10.15}$$

in which x_m is the primary variable m with $m = 1, 2, 3, \ldots, N_c + 1$, respectively, at node i and all its direct neighbors; p is the iteration level; and $i = 1,$

2, 3,…, N. The primary variables in Eqn (10.15) need to be updated after each iteration:

$$x_{m,p+1} = x_{m,p} + \delta x_{m,p+1} \tag{10.16}$$

The Newton iteration process continues until the residuals $R_n^{k,\,n+1}$ or changes in the primary variables $\delta x_{m,p+1}$ over one iteration are reduced below preset convergence tolerances. Numerical methods are generally used to construct the Jacobian matrix for Eqn (10.15), as outlined in Forsyth et al. (1995). At each Newton iteration, Eqn (10.15) represents a system of $(N_c + 1) \times N$ linearized algebraic equations with sparse matrixes, which are solved by a linear equation solver.

10.5.3 Summary

Physical processes associated with energy and natural source production and storage as well as environmental assessment and remediation in subsurface systems are inherently non-isothermal, involving multiphase fluid flow and heat transfer. This chapter discusses physical processes and conceptual models and presents generalized governing equations for multiphase fluid flow, multicomponent transport, and heat transfer in porous and fractured media. This provides a framework mathematical model for simplification, extension, and application in practice to cover more general or specific scenarios of fluid and heat flow and chemical transport in reservoirs. In addition, this chapter presents a general numerical model formulation and its solution scheme for simulation of multiphase fluid and heat flow in reservoirs. As we continue to explore deeper earth for seeking out solutions of energy, natural resources, and environment, analysis of multiphase fluid and heat flow in subsurface formations will find wider applications in these related fields and along the new frontiers.

REFERENCES

Bear, J., 1972. Dynamics of Fluids in Porous Media. American Elsevier, New York.

Bodvarsson, G.S., Liu, H.H., Ahlers, C.F., Wu, Y.-S., Sonnenthal, E., 2001. Parameterization and upscaling in modeling flow and transport in the unsaturated zone of Yucca Mountain. In: National Research Council (Ed.), Conceptual Models of Flow and Transport in the Fractured Vadose Zone. National Academy Press, Washington, DC, pp. 335–366.

Butler, R.M., Mokrys, I.J., 1991. A new process (VAPEX) for recovering heavy oils using hot water and hydrocarbon vapour. Journal of Canadian Petroleum Technology 30 (1), 97–106.

Chen, Z., Huan, G., Ma, Y., 2006. Computational Methods for Multiphase Flows in Porous Media. Siam.

Corapcioglu, M.Y., Baehr, A.L., 1987. A compositional multiphase model for groundwater contamination by petroleum products: 1. Theoretical considerations. Water Resources Research 23 (1), 191–200.

Falta, R.W., Pruess, K., Javandel, I., Witherspoon, P.A., 1992a. Numerical modeling of steam injection for the removal of nonaqueous phase liquids from the subsurface: 1. Numerical formulation. Water Resources Research 28 (2), 433–449.

Falta, R.W., Pruess, K., Javandel, I., Witherspoon, P.A., 1992b. Numerical modeling of steam injection for the removal of nonaqueous phase liquids from the subsurface: 2. Code validation and application. Water Resources Research 28 (2), 451–465.

Forsyth, P.A., 1994. Three-dimensional modelling of steam flush for DNAPL site remediation. International Journal for Numerical Methods in Fluids 19 (12), 1055–1081.

Forsyth, P.A., Wu, Y.S., Pruess, K., 1995. Robust numerical methods for saturated-unsaturated flow with dry initial conditions in heterogeneous media. Advances in Water Resources 18 (1), 25–38.

Grant, M., 2013. Geothermal Reservoir Engineering. Elsevier.

Grant, M.A., Truesdell, A.H., Mañón M, A., 1984. Production induced boiling and cold water entry in the Cerro Prieto geothermal reservoir indicated by chemical and physical measurements. Geothermics 13 (1), 117–140.

McCain, W.D., 1990. The Properties of Petroleum Fluids. PennWell Publishing Company, Tulsa, OK.

Panday, S., Forsyth, P.A., Falta, R.W., Wu, Y., Huyakorn, P.S., 1995. Considerations for robust compositional simulations of subsurface nonaqueous phase liquid contamination and remediation. Water Resources Research 31 (5), 1273–1289.

Prats, M., 1985. Thermal Recovery. HL Doherty Memorial Fund of AIME: Society of Petroleum Engineers, New York.

Pruess, K., 2002. Mathematical modeling of fluid flow and heat transfer in geothermal systems – an introduction in five lectures. Lawrence Berkeley National Laboratory Report LBNL-51295, Berkeley, CA.

Pruess, K., Battistelli, A., 2002. TMVOC, a Numerical Simulator for Three-phase Non-isothermal Flows of Multicomponent Hydrocarbon Mixtures in Saturated-unsaturated Heterogeneous Media.

Reid, R.C., Prausnitz, J.M., Poling, B.E., 1987. The Properties of Gases and Liquids. McGraw Hill Book Co., New York, NY.

Scheidegger, A.E., 1961. General theory of dispersion in porous media. Journal of Geophysical Research 66 (10), 3273–3278.

Sleep, B.E., Sykes, J.F., 1989. Modeling the transport of volatile organics in variably saturated media. Water Resources Research 25 (1), 81–92.

Winterfeld, P.H., Wu, Y.-S., 2014. Simulation of CO_2 sequestration in brine aquifers with geomechanical coupling. In: Al-Khoury, R., Bundschuh, J. (Eds.), Computational Models for CO_2 Geo-sequestration & Compressed Air Energy Storage. CRC Press, pp. 275–304.

Wu, Y.-S., Mukhopadhyay, S., Zhang, K., Bodvarsson, G.S., 2006. A mountain-scale thermal–hydrologic model for simulating fluid flow and heat transfer in unsaturated fractured rock. Journal of Contaminant Hydrology 86 (1), 128–159.

Wu, Y.-S., Pruess, K., 2000. Numerical simulation of non-isothermal multiphase tracer transport in heterogeneous fractured porous media. Advances in Water Resources 23 (7), 699–723.

Wu, Y.-S., Qin, G., 2009. A generalized numerical approach for modeling multiphase flow and transport in fractured porous media. Communications in Computational Physics 6 (1), 85–108.

Wu, Y.-S., Xiong, Y., Kazemi, H., 2015. Coupled thermo-hydrological processes in enhanced geothermal systems. In: Poate, J., Illangasekare, T., Kazemi, H., Kee, R. (Eds.), Pore Scale Phenomena Frontiers in Energy and Environment, vol. 10. World Scientific, pp. 279–298. http://dx.doi.org/:10.1142/9789814623063_0015.

CHAPTER 11

Multiphase Fluid and Heat Flow Coupled with Geomechanics

11.1 INTRODUCTION

It has been noticed that physical or chemical disturbances of *in situ* conditions in permeable reservoir formations—resulting from oil and gas production, cold-fluid injection, CO_2 sequestration, or geofluid withdrawal, etc., in subsurface reservoirs—cause rock deformation. The fluid-flow- or pressure- or temperature-variation-induced rock deformation, in turn, could have profound effects on poroelastic, fluid flow, and transport properties in a low-permeability reservoir, in particular, on fracture conductivity or permeability, impacting fluid flow and mass transport at various spatial scales. For example, permeability for pre-existing fractures may be enhanced or reduced significantly by deformation of rock matrix in response to changes in stress fields, pore pressure, or temperature. In general, the permeability of porous and fractured media is dependent on pore pressure or the stress field within a formation. In most studies of fluid flow and heat transfer in porous or fractured media, however, it has been assumed that the influence of rock deformation on permeability and other rock properties is negligible, i.e., only fluid density and effective porosity are treated as functions of pressure. This assumption may be reasonable for slightly compressible fluid flow in high-permeability reservoirs, such as sandstone formations, under normal ranges of production and injection conditions. In such cases, the pore compressibility of the sandstone is usually very small and pressure disturbance is not very large compared with the original *in situ* conditions. Nevertheless, even for flow in fractured media or operational conditions with high-pressure injection or production, the same assumption of constant permeability has often been taken for granted in calculation of flow in such reservoirs.

Application of rock mechanics in subsurface systems has been until recently mostly limited to analysis of wellbore integrity and underground tunnel instability or safety design of building foundation. The influence of geomechanics or rock deformation on rock properties in reservoirs has not

Multiphase Fluid Flow in Porous and Fractured Reservoirs
ISBN 978-0-12-803848-2
http://dx.doi.org/10.1016/B978-0-12-803848-2.00011-8

been taken into account in most reservoir characterization, such that the effect of geomechanics on permeability has been ignored in practice. During the last decade, however, the effect of geomechanics on flow through low-permeability rock has received a lot of attention. This is because of the important roles played by geomechanics for flow in low-permeability, stress-sensitive formations in conventional and unconventional petroleum reservoirs and geothermal energy resources as well as carbon dioxide (CO_2) storage formations and other subsurface waste disposal sites. In these engineering practices, the effect of rock deformation on fluid mobility and storability in permeable porous and fractured rock may no longer be negligible if one wants to avoid faulty model predictions.

The development of oil and gas from unconventional tight and shale reservoirs has been one of the most active areas of energy supply worldwide in the last decade. This is because of large reserves of unconventional resources discovered as well as technical advances in developing them. As a result of improved horizontal drilling and hydraulic fracturing technologies, significant progress has been made toward commercial oil and gas production from such unconventional reservoirs. However, understandings and technologies needed for effective development of unconventional reservoirs are far behind the industry needs, e.g., oil and gas recovery rates from those unconventional resources remain very low. Compared with conventional reservoirs, oil and gas flow in ultra-low-permeability unconventional reservoirs is subject to more nonlinear, coupled physical processes, including strong effect of geomechanics on permeability of tight or shale formations with variously scaled natural and hydraulic fractures (Cipolla, 2009; Wang et al., 2009; Fakcharoenphol et al., 2013; Wu et al., 2014). Figure 11.1 shows that gas permeability in the shale formations of the US is confining pressure (or total stress) dependent and decreases significantly with an increase in effective stress (Soeder, 1988; Wang et al., 2009).

On the other hand, most geothermal reservoirs are situated in igneous and metamorphic rocks that have low matrix permeability. Thermal energy recovery from geothermal reservoirs depends on natural or human-made fractures to provide permeable fluid-flow paths from or to unfractured tight rock matrix. Geothermal reservoirs include not only the more easily developed hydrothermal resources; but also the earth's deeper thermal energy, such as hot dry rock. The quality of a specific geothermal resource would depend on its geothermal gradient, reservoir rock properties of permeability and porosity, fluid saturation, and recharge capability

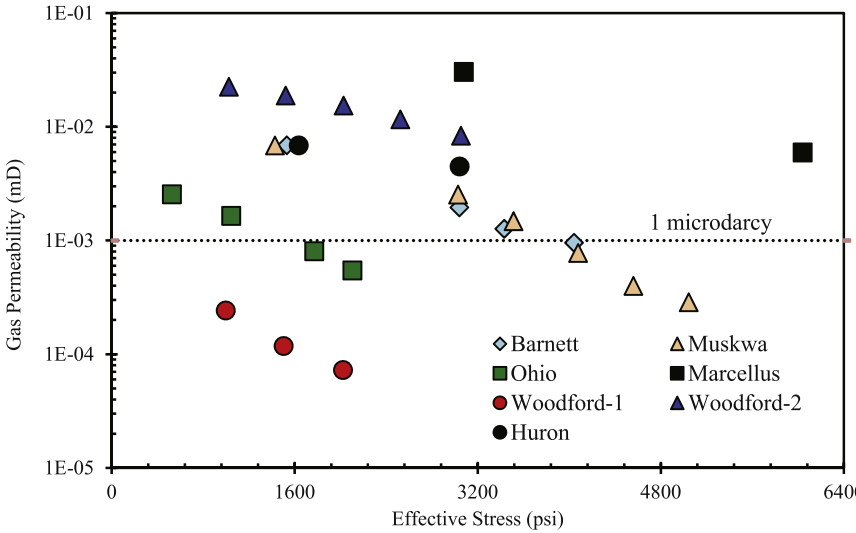

Figure 11.1 Effect of confining pressure on gas permeability in gas shales *(Modified from Soeder, 1988 and Wang et al., 2009).*

(Tester et al., 2006). The coexistence of substantial amounts of heat, fluids, and permeability in geothermal reservoirs is not commonplace in the earth; thus high-grade geothermal resources are limited. An alternative to dependence on naturally occurring hydrothermal reservoirs involves human intervention to create engineered reservoirs in hot rocks for extracting an economical amount of heat, known as "Enhanced (or Engineered) Geothermal Systems (EGS)." The high potential of EGS resources has recently been drawing worldwide attention and intensive research efforts, particularly in the US. Even with research efforts and progresses made in studies of EGS reservoirs, there are needs for more research, development, and investment before EGS geothermal energy becomes viable to serve as the primary energy resource, because of the technical difficulties and high cost currently associated with development of thermal energy from EGS reservoirs.

To mine heat from an EGS reservoir, water or other fluid is injected through wells and fractures into the reservoirs. After the injected fluid is heated by contact with the *in situ* hot rock, it is then produced through production wells for use as energy. Heat mining from a fractured EGS reservoir is subject to many physical and chemical processes, whereas heated foreign-fluid flow and interaction with reservoir rock occurs in high-temperature geological formations, involving heat transfer, multiphase

flow, and rock deformation. Under the external stimulus, the contrast in rates of thermodynamic change between high-permeability fractures and tight matrix rock causes large thermodynamic variations between the two media of fractures and matrix. Changes in stress and strain due to external disturbances in temperature cause deformation in the rock framework. This deformation, in turn, alters hydraulic properties, such as fracture aperture, porosity, and permeability, and affects fluid and heat flow. Thus, to simulate these complex fluid-flow and heat-transfer processes in an EGS system, it is important to include the effect of stress–strain changes on hydraulic properties, especially for fractured rock. These thermal–hydrological–mechanical (THM) processes need to be understood and handled before a sound engineering design and successful field operation can be achieved. Geomechanical processes under EGS reservoir conditions may be prevalent in EGS applications, because cold-water injection and steam or hot-fluid extraction have strong thermoporoelastic effects on fluid flow and heat transfer in EGS reservoirs (Hu et al., 2013; Fakcharoenphol et al., 2013; Wu et al., 2015).

Another example of geomechanical effects occurs in CO_2 sequestration reservoirs. To address the increasing concerns regarding greenhouse gas emission and its impact on global climate, CO_2 geologic sequestration is considered among the most promising, viable approaches for near-term implementation. Carbon dioxide can be sequestered in several types of geological media including deep saline aquifers, depleted oil and gas reservoirs, and coal beds. To achieve significant reduction of atmospheric emissions, large amounts of CO_2 need to be injected into geologic storage reservoirs, leading to buildup of pressure and significant changes in formation stress. Physically, CO_2 leakage from a storage formation will occur when the reservoir pressure is high enough to cause mechanical failure in sealing caprock creating fracturing, reactivating fractures or faults. To predict potential CO_2 leakage pathways and quantify leakage rates in storage geological formations, the effect of geomechanics and rock deformation must be included in the model formulation (Winterfeld and Wu, 2014).

Thermal–hydrological–mechanical (THM) processes arise in porous media that often contain fractures, because of the sensitivity of fracture aperture to stress variation. Coupled physical or chemical processes in reservoirs are common in nature. Pore pressure, temperature, stress, and strain fields in geological media directly or indirectly influence each other. Fluid-saturated porous and fractured rocks can be deformed as a result of

change in internal pore pressure, change in temperature, and change in external load or stress (Rutqvist and Stephansson, 2003). For example, an increased internal pore pressure reduces the effective compressive stress acting on rock body, leading the whole rock and it's internal pore space to expand. On the other hand, an elevated temperature causes solid-rock expansion, reduces the pore space, and increases the compressive stress. In addition to these direct interactions, hydraulic and mechanical properties of rocks are altered during the coupled processes impacting fluid flow and heat transfer (see Figure 11.2).

Modeling approaches for simulation of coupled flow and geomechanics in reservoirs may be classified into several categories: (i) decoupled or explicit coupling, (ii) sequential coupling, and (iii) fully coupled methods (Settari and Walters, 2001; Dean et al., 2006). In a decoupled or explicitly coupled method, the stress in formation is predetermined, estimated as a function of spatial coordinates and pressure, or calculated a few times independently with flow simulation. The effective stress is treated only as a function of pressure and spatial coordinates, decoupled from the stress calculation, to be used to evaluate rock and flow properties in flow simulation. The second, sequentially coupled, approach is an iterative coupling scheme that solves the fluid flow and the geomechanical equations independently and sequentially. Sequential coupling or information exchange between the two solutions of flow and displacement can be simply carried out using a reservoir simulator for multiphase flow and a geomechanical simulator for displacement at the end of each time step or

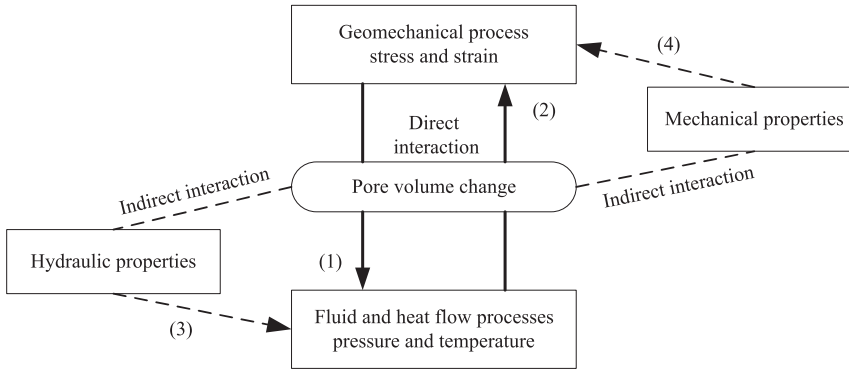

Figure 11.2 Flow–geomechanical couplings in geological media. (1) and (2) are direct couplings through pressure–temperature pore and volume interactions, whereas (3) and (4) are indirect couplings through changes in material properties *(Modified from Fakcharoenphol et al., 2013).*

even at a nonlinear iteration level. Therefore, this sequential iterative approach has been the most used scheme in coupled geomechanics and reservoir flow modeling (e.g., Fung et al., 1994; Rutqvist et al., 2002). However, the primary problem with this sequential method is that conservation of mass and energy may not be achieved during the iteration for fluid and heat flow, and geomechanical simulation, because modified rock properties such as porosity and rock volume need geomechanical calculation before inclusion in the flow simulation of the next time step. In comparison, the fully coupled method is an internally consistent, most rigorous, and numerically stable approach, because the fluid flow and geomechanical equations are solved simultaneously on the same discretized grid at the nonlinear iteration level (e.g., Hu et al., 2013; Winterfeld and Wu, 2014).

The objective of this chapter is to present a new fully coupled multiphase, heat-flow, and geomechanical model, based on the generalized version of Hooke's law, mean stress, and volumetric strain. In this chapter, we discuss the mathematical and numerical model for fluid and heat flow coupled with geomechanics, which describes fully coupled THM processes of multiphase fluid flow, heat transfer, and rock deformation in porous and fractured reservoirs. The geomechanical equations relating stresses and displacements are combined to yield an equation in terms of mean stress as a function of pore pressure and temperature as well as an equation for volumetric strain. The multiphase-fluid and heat-flow formulation is based on the general multiphase compositional fluid and heat-flow model. The coupling of fluid and heat flow with geomechanics is based on the theory of poroelasticity using the effective stress concept (difference between mean stress and pore pressure), first introduced by Terzaghi (1936) during his studies of the mechanics of saturated soils and later on was further refined by Biot (1941) and others. Then, the mutual impacts of fluid flow, heat transfer, and rock deformation are described by correlating rock and fluid properties, such as porosity, permeability, and capillary pressure, to effective stress and temperature in a fully coupled manner.

In the numerical formulation and solution, the compositional fluid-flow, heat-transfer, and geomechanical equations of mean stress are discretized using the same control-volume, integrated finite difference grid for both fluid heat flow and rock deformation as discussed in Chapter 4. The resulting discrete nonlinear equations are solved simultaneously and implicitly by Newton iteration. At the end, we will give a few examples of model verification and application for THM modeling exercises.

11.2 MATHEMATICAL MODEL FOR FLUID AND HEAT FLOW WITH GEOMECHANICAL COUPLING

The governing equations for multiphase fluid flow, multicomponent transport, and heat transfer in THM processes of porous and fractured media are also considered to be based on the same fundamental laws of mass and energy conservation as those discussed for fluid and heat flow in Chapter 10. In addition, these fluid and heat flow-governing equations use similar constitutive correlations and are subject to similar assumptions and simplifications. In this chapter, however, the geomechanical effect is added to the coupled process modeling formulation for its influence on fluid and heat flow in reservoirs. The geomechanical equations relating force balance, stress, and displacement are combined to yield an equation in terms of mean stress as a function of pore pressure and temperature as well as an equation for volumetric strain. In this chapter, we present two types of geomechanical equations, one for a single-porosity porous-medium reservoir and one for multiporosity media of fractured reservoirs, for modeling THM processes in both porous and fractured reservoirs.

11.2.1 Equations for Multiphase Flow and Heat Transfer

A multiphase system consists of multiple fluid phases, such as oil, gas, and water, and each fluid in turn consists of a number of mass components. If we ignore the effects of molecular diffusion and mechanical dispersion on mass transport and heat transfer, mass- and energy-conservation principles of the flow and transport constitutive laws, as discussed in Chapter 10, give rise to a set of governing equations for mass conservation of each component k in the porous continuum:

$$\frac{\partial}{\partial t}\left[\phi \sum_{\beta}\left(\rho_{\beta} S_{\beta} X_{\beta}^{k}\right)\right] = -\sum_{\beta} \nabla \cdot \left(\rho_{\beta} X_{\beta}^{k} \boldsymbol{v}_{\beta}\right) + q^{k} \tag{11.1}$$

and for heat transfer in the system:

$$\begin{aligned} &\frac{\partial}{\partial t}\left[\sum_{\beta}\left(\phi \rho_{\beta} S_{\beta} U_{\beta}\right) + (1-\phi)\rho_{\mathrm{s}} U_{\mathrm{s}}\right] \\ &\quad = -\sum_{\beta} \nabla \cdot \left(h_{\beta} \rho_{\beta} \boldsymbol{v}_{\beta}\right) + \nabla \cdot \left(K_{\mathrm{T}} \nabla T\right) + q^{\mathrm{E}} \end{aligned} \tag{11.2}$$

in which the notations and symbols used are the same as those in Chapter 10, i.e., subscript k is the index for the components, $k = 1, 2, 3, \ldots, N_{\mathrm{c}}$, with N_{c} being the total number of mass components; ρ_{s} is the density of rock

solids; q^k and q^E are external source/sink terms or fracture–matrix exchange terms for mass component k and energy, respectively; and U_β and U_s are the internal energies of fluid β and rock solids,. In Eqns (11.1) and (11.2), the volumetric flow velocity, $\boldsymbol{v}_\beta$, of each fluid phase can be determined by Darcy's law or another non-Darcy flow law of interest.

11.2.2 Geomechanical Equations for Single-Porosity Media

The geomechanical equations for THM processes in a single-porosity reservoir are based on an extended version of the classical theory of elasticity (Winterfeld and Wu, 2014). In the theory of elasticity, the stress–strain ($\boldsymbol{\sigma}-\boldsymbol{\varepsilon}$) behavior of an isothermal elastic material is described by Hooke's law:

$$\boldsymbol{\sigma} = 2G\boldsymbol{\varepsilon} + \lambda \mathrm{tr}(\boldsymbol{\varepsilon})\boldsymbol{I} \tag{11.3}$$

in which $\boldsymbol{\sigma}$ is the tensor of stress; $\boldsymbol{\varepsilon}$ is the tensor of strain; G is shear modulus; λ is the Lamé parameter; and $\boldsymbol{I}$ is the identity matrix of size 3×3. For isothermal fluid-filled porous rock, the stress–strain behavior is also dependent on pore pressure and the poroelastic version of Hooke's law is:

$$\boldsymbol{\sigma} - \alpha P\boldsymbol{I} = 2G\boldsymbol{\varepsilon} + \lambda \mathrm{tr}(\boldsymbol{\varepsilon})\boldsymbol{I} \tag{11.4}$$

in which α is Biot's coefficient (Biot and Willis, 1957). For an elastic material that is subject to changes in both temperature and stress, the theory of thermoelasticity assumes that the resulting strain is the sum of the thermal strain and the stress-caused strain. This theory is mathematically analogous to poroelastic theory (Norris, 1992), and Hooke's law for thermoelastic media has the form:

$$\boldsymbol{\sigma} - 3\beta_T K(T - T_{\mathrm{ref}})\boldsymbol{I} = 2G\boldsymbol{\varepsilon} + \lambda \mathrm{tr}(\boldsymbol{\varepsilon})\boldsymbol{I} \tag{11.5}$$

in which β_T is linear thermal expansion coefficient for a thermally unstrained state; K is bulk modulus; and T_{ref} is reference temperature. For a thermoporoelastic medium, a porous medium subject to changes in both temperature and stress (McTigue, 1986), the pore-pressure and temperature terms both appear in the generalized Hooke's law as:

$$\boldsymbol{\sigma} - \alpha P\boldsymbol{I} - 3\beta_T K(T - T_{\mathrm{ref}})\boldsymbol{I} = 2G\boldsymbol{\varepsilon} + \lambda \mathrm{tr}(\boldsymbol{\varepsilon})\boldsymbol{I} \tag{11.6}$$

Two other fundamental relations in the theory of linear elasticity (Jaeger et al., 2009) are the relation between the strain tensor, $\boldsymbol{\varepsilon}$, and the displacement vector, $\boldsymbol{u}$, as

$$\boldsymbol{\varepsilon} = \frac{1}{2}\left[\nabla \boldsymbol{u} + (\nabla \boldsymbol{u})^T\right] \tag{11.7}$$

and the static equilibrium equation:

$$\nabla\cdot\boldsymbol{\sigma} + \boldsymbol{F}_{\mathrm{b}} = 0 \tag{11.8}$$

in which $\boldsymbol{F}_{\mathrm{b}}$ is the body force. We combine Eqns (11.5)–(11.7) to obtain the thermoporoelastic Navier equation:

$$\nabla(\alpha P + 3\beta_{\mathrm{T}} KT) + (\lambda + G)\nabla(\nabla\cdot\boldsymbol{u}) + G\nabla^2\boldsymbol{u} + \boldsymbol{F}_{\mathrm{b}} = 0 \tag{11.9}$$

Taking the divergence of Eqn (11.9) yields:

$$\nabla^2(\alpha P + 3\beta_{\mathrm{T}} KT) + (\lambda + 2G)\nabla^2(\nabla\cdot\boldsymbol{u}) + \nabla\cdot\boldsymbol{F}_{\mathrm{b}} = 0 \tag{11.10}$$

The divergence of the displacement vector, $\nabla\cdot\boldsymbol{u}$, is the sum of the normal strain components, the volumetric strain:

$$\nabla\cdot\boldsymbol{u} = \frac{\partial u_x}{\partial x} + \frac{\partial u_y}{\partial y} + \frac{\partial u_z}{\partial z} = \varepsilon_{xx} + \varepsilon_{yy} + \varepsilon_{zz} = \varepsilon_{\mathrm{v}} \tag{11.11}$$

in which ε_{v} is volumetric strain or invariant of the symmetric tensor of strain.

The trace of the stress tensor, $\boldsymbol{\sigma}$, is an invariant, having the same value in any coordinate system. We obtain the following by taking the trace of Eqn (11.6), Hooke's law for a thermoporoelastic medium:

$$\sigma_{xx} + \sigma_{yy} + \sigma_{zz} - 3[\alpha P + 3\beta_{\mathrm{T}} K(T - T_{\mathrm{ref}})] = (3\lambda + 2G)(\varepsilon_{xx} + \varepsilon_{yy} + \varepsilon_{zz}) \tag{11.12}$$

Defining mean stress as the average of the normal stress components $[\sigma_m = (\sigma_{xx} + \sigma_{yy} + \sigma_{zz})/3]$ and using the relationship between bulk modulus, shear modulus, and Lamé parameter:

$$K = \frac{(3\lambda + 2G)}{3} \tag{11.13}$$

yields the following equation relating volumetric strain, mean stress, pore pressure, and temperature:

$$K\varepsilon_{\mathrm{v}} = \sigma_{\mathrm{m}} - [\alpha P + 3\beta_{\mathrm{T}} K(T - T_{\mathrm{ref}})] \tag{11.14}$$

Finally, combining Eqns (11.10), (11.11), and (11.14), and using the relationship between Poisson's ratio, υ, shear modulus, and Lamé parameter:

$$\frac{\lambda}{G} = \frac{2\upsilon}{(1 - 2\upsilon)} \tag{11.15}$$

yield an equation relating mean stress, pore pressure, temperature, and body force:

$$\nabla\cdot\left[\frac{3(1-\upsilon)}{1+\upsilon}\nabla\sigma_{\mathrm{m}}+\boldsymbol{F}_{\mathrm{b}}-\frac{2(1-2\upsilon)}{1+\upsilon}\nabla(\alpha P+3\beta_{\mathrm{T}}KT)\right]=0 \qquad (11.16)$$

Equations (11.14) and (11.16) are the governing single-porosity-medium geomechanical equations with mean stress and volumetric strain as the geomechanical variables associated with these governing equations. Equation (11.16) is a statement of momentum conservation in terms of mean stress, pressure, and temperature. Equation (11.14) is a property relation, relating volumetric strain to mean stress and several other parameters in analog to the Hooke's law.

11.2.3 Geomechanical Equations for Multiple-Porosity or Fractured Media

Fractured formations respond to geomechanics or rock deformation very differently from nonfractured rock because of the discontinuity in rock mass. Naturally fractured reservoirs are in general more sensitive to changes in stress or geomechanical behavior when fracture aperture or permeability is strongly influenced by rock deformation in fractured rock (Bagheri and Settari, 2008). Bai et al. (1993) present a generalization of Hooke's law for a single-porosity medium (Eqn (11.4)) to a multiporosity, fractured one, a common example of which is the double-porosity medium consisting of a network of fractures and rock matrix (Winterfeld and Wu, 2014):

$$\boldsymbol{\sigma}-\sum_{l}\alpha_l P_l\boldsymbol{I}=2G\boldsymbol{\varepsilon}+\lambda\mathrm{tr}(\boldsymbol{\varepsilon})\boldsymbol{I} \qquad (11.17)$$

in which subscript l refers to a multiporosity continuum, such as fracture or matrix medium. Expressions for the generalized Biot's coefficients, α_l, for a double-porosity medium have been presented by Wilson and Aifantis (1982):

$$\alpha_1=1-\frac{K}{K_*} \qquad (11.18)$$

and

$$\alpha_2=\frac{K}{K_*}\left(1-\frac{K_*}{K_{\mathrm{s}}}\right) \qquad (11.19)$$

in which K_{s} is the solid modulus; K_* is the modulus of the porous medium without the fractures; subscript 1 refers to the fractures; and subscript 2 refers to the matrix. We obtain Hooke's law for a thermo-multiporoelastic

medium by including the temperature term from Eqn (11.6) in Eqn (11.17) for each multiporosity continuum, because temperature varies between multiporosity continua:

$$\boldsymbol{\sigma} - \sum_l [\alpha_l P_l \boldsymbol{I} + 3\beta_T K \omega_l (T_l - T_{ref}) \boldsymbol{I}] = 2G\boldsymbol{\varepsilon} + \lambda \mathrm{tr}(\boldsymbol{\varepsilon})\boldsymbol{I} \tag{11.20}$$

in which ω_l is the multiporosity continuum volume fraction under the Multiple INteraction Continua (MINC) concept of gridding. We combine Eqns (11.20), (11.7), and (11.8) to obtain the thermo-multiporoelastic Navier equation:

$$\nabla \left[\sum_l (\alpha_l P_l + 3\beta_T K \omega_l T_l) \right] + (\lambda + G)\nabla(\nabla \cdot \boldsymbol{u}) + G\nabla^2 \boldsymbol{u} + \boldsymbol{F}_b = 0 \tag{11.21}$$

Taking the divergence of Eqn (11.21) and following the same steps as for the single-porosity-medium derivation results in an equation analogous to Eqn (11.14) relating volumetric strain, mean stress, pore pressures, and temperatures:

$$K\varepsilon_v = \sigma_m - \sum_l [\alpha_l P_l + 3\beta_T K \omega_l (T_l - T_{ref})] \tag{11.22}$$

and an equation analogous to Eqn (11.16) relating mean stress, pore pressures, temperatures, and body force for governing multiple-porosity-medium geomechanics is given as:

$$\nabla \cdot \left\{ \frac{3(1-\upsilon)}{1+\upsilon} \nabla \sigma_m + \boldsymbol{F}_b - \frac{2(1-2\upsilon)}{1+\upsilon} \nabla \left[\sum_l (\alpha_l P_l + 3\beta_T K \omega_l T_l) \right] \right\} = 0 \tag{11.23}$$

11.3 ROCK PROPERTY CORRELATIONS FOR GEOMECHANICAL COUPLING

Rock properties play a key role in coupling THM processes, and the coupled effects of fluid, heat flow, and rock deformation are described through the following correlations. These rock properties and their correlations must be defined and predetermined for a THM process to be simulated. We discuss the dependence of permeability and porosity on effective stress and other quantities in this section. Effective stress was

initially defined as the difference between average stress and pore pressure by Terzhagi (1936) and was generalized by Biot and Willis (1957) as:

$$\sigma' = \sigma_m - \alpha P \tag{11.24}$$

in which α is the Biot's or effective stress coefficient. Correlations have been developed for porosity as a function of effective stress and other quantities and permeability as a function of either porosity or effective stress, which need to be developed for a specific set of conditions.

We use an expression for porosity as an example to start with its modified definition to include rock deformation effect. Porosity is the ratio of pore volume to bulk volume of rock, and because pore volume plus solid volume equals bulk rock volume, porosity can be written as:

$$\phi = 1 - \frac{V_s}{V} \tag{11.25}$$

in which V is bulk volume of rock and V_s solid volume. Gutierrez et al. (2001) presented expressions for solid volume change with pressure and effective stress. These expressions can be integrated to yield an expression for solid volume:

$$V_s(P, \sigma') = V_{s,r}\left[1 - \frac{1-\phi_r}{K_s}(P - P_r) - \frac{1}{K_s}\left(\sigma' - \sigma'_r\right)\right] \tag{11.26}$$

in which subscript r refers to reference condition. To relate bulk volume (V) to volumetric strain (ε_v), when combined with Eqns (11.25) and (11.26), we have porosity as a function of pressure, temperature, and effective stress relative to a reference condition (r):

$$\phi = 1 - (1-\phi_r)(1-\varepsilon_{v,r})\frac{1 - \frac{1-\phi_r}{K_s}(P - P_r) - \frac{1}{K_s}\left(\sigma' - \sigma'_r\right)}{1 - \varepsilon_v} \tag{11.27}$$

An example of reference conditions for Eqn (11.27) is the initial conditions for a simulation, in which volumetric strain, porosity, mean stress, and pressure are specified. Rutqvist et al. (2002) presented the following function for porosity, obtained from laboratory experiments on sedimentary rock (Davies and Davies, 2001):

$$\phi = \phi_1 + (\phi_0 - \phi_1)\exp(-a\sigma') \tag{11.28}$$

in which ϕ_0 is zero effective stress porosity; ϕ_1 is high effective stress porosity; and the exponent a is a parameter. They also presented an associated function for permeability in terms of porosity:

$$k = k_0 \exp\left(c\left(\frac{\phi}{\phi_0} - 1\right)\right) \tag{11.29}$$

McKee et al. (1988) derived a relationship between porosity and effective stress from hydrostatic poroelasticity theory by assuming incompressible rock grains:

$$\phi = \frac{\phi_0 \exp\left(-c_p\left(\sigma' - \sigma'_0\right)\right)}{1 - \phi_0\left[1 - \exp\left(-c_p(\sigma' - \sigma'_0)\right)\right]} \tag{11.30}$$

in which c_p is average pore compressibility. They also related permeability and porosity using the Carman–Kozeny equation (Bear, 1972):

$$k = \frac{d_m^2}{180}\frac{\phi^3}{(1-\phi)^2} \tag{11.31}$$

These relationships fit laboratory and field data for granite, sandstone, clay, and coal. Ostensen (1986) studied the relationship between effective stress and permeability for tight gas sands and approximated permeability as:

$$k^n = D \ln \frac{\sigma'_0}{\sigma'} \tag{11.32}$$

in which exponential n is 0.5; D is a parameter; and σ'_0 is effective stress for zero permeability, obtained by extrapolating measured square root permeability versus effective stress on a semi-log plot. Verma and Pruess (1988) presented a power law expression relating permeability to porosity:

$$\frac{k - k_c}{k_0 - k_c} = \left(\frac{\phi - \phi_c}{\phi_0 - \phi_c}\right)^n \tag{11.33}$$

in which k_c and ϕ_c are asymptotic values of permeability and porosity, respectively; and exponent n is a parameter.

A theory of hydrostatic poroelasticity (Jaeger et al., 2009) that accounts for the coupling of rock deformation with fluid flow yields the following expression for porosity changes as a function of effective stress:

$$\mathrm{d}\phi = -\left(\frac{1-\phi}{K} - C_r\right)\mathrm{d}\sigma' \tag{11.34}$$

in which C_r is rock grain compressibility.

In addition, capillary pressure also changes with pore size under multiphase fluid flow rock deformation condition. To incorporate the effect of rock deformation on capillary pressure, permeability and porosity are used to scale capillary pressure according to the relation by Leverett (1941):

$$P_c = P_{c0}\sqrt{\left(\frac{\phi}{k}\right)\left(\frac{k}{\phi}\right)_0} \tag{11.35}$$

in which subscript 0 refers to a reference or zero rock-deformation condition. Here, we use the Leverett *J*-function to include effect of changes in porosity or pore size and permeability due to rock deformation on capillary forces in pores and fractures.

11.4 NUMERICAL FORMULATION AND SOLUTION

In this section, we describe a general numerical formulation for solving multiphase fluid and heat flow, coupled with geomechanical equations. Specifically, the mass and energy conservation equations (Eqns (11.1) and (11.2)), the geomechanical equations (Eqns (11.14) and (11.16)) for a single-porosity-medium reservoir or (Eqns (11.22) and (11.23)) for a multiple-porosity, fractured reservoir are discretized in space using the same control-volume concept or integrated finite difference grid as discussed in Chapters 4 and 10. Time discretization is also carried out using a backward, first-order, fully implicit finite-difference scheme. The resulting discrete nonlinear algebraic equation systems for multiphase fluid flow, heat transfer, and momentum balance of mean stress are solved simultaneously. Therefore, the numerical formulation is applicable for handling THM processes in one-, two-, or three-dimensional porous and fractured-medium reservoirs.

Note that there is an important difference between the space discretization scheme of the integrated finite difference used for geomechanical coupling of this chapter and nonrock deformation problems, as discussed in Chapters 4 and 10, as well as those in Pruess et al. (1999). The difference, because of rock deformation, is that mesh geometric properties of discretization, such as volume of grid blocks, interface areas between grid blocks, and distances from grid blocks' centers to their interfaces, are no longer constant. In a THM simulation, those geometrical properties of meshes from spatial discretization are in general functions of stress and need to be treated as part of the solution.

11.4.1 Numerical Formulation for Modeling THM Processes in Single-Porosity Reservoirs

The conservation equations of mass- and energy-balance equations, Eqns (11.1) and (11.2), describe fluid and heat flow in general multiphase, multicomponent systems. Fluid advection is described with a multiphase extension of Darcy's law; in addition, we ignore diffusive mass transport in any phase. Heat flow occurs by conduction and convection, the latter including sensible as well as latent heat effects. The description of

thermodynamic conditions is based on the assumption of local equilibrium of all phases and solids. Fluid and formation parameters can be arbitrary, but defined, functions of the thermodynamic variables. We extend this formulation to include geomechanical effects. In addition to the mass- and energy-balance equations, we need also to solve a momentum balance equation for mean stress, derived in the previous section (Eqns (11.16) and (11.23)) in single-porosity porous and fractured media, respectively. We add mean stress to the primary thermodynamic variables and add volumetric strain to the calculated variables and properties.

The component mass- and energy-balance equations, Eqns (11.1) and (11.2), are discretized in space using in the integrated finite difference concept, as shown in Figure 4.1. Time discretization is carried out using a backward, first-order, fully implicit finite-difference scheme. The discrete nonlinear equations for mass components of fluids and heat at grid block or node i can be written in a similar form to Eqn (4.1) or (10.6),

$$\left[\left(V_i A_i^k\right)^{n+1} - \left(V_i A_i^k\right)^n\right] \frac{1}{\Delta t} = \sum_{j \in \eta_i} flow_{ij}^{k,n+1} + Q_i^{k,n+1}, \quad k = 1, 2, 3, \ldots, N_c \text{ and } i = 1, 2, 3, \ldots, N \tag{11.36}$$

in which superscript $k = 1, 2, 3, \ldots, N_c$ for all the mass components and $k = N_c + 1$ denoting the heat equation; V_i is volume of grid block i; A_i^k, $flow_{ij}^k$, and Q_i^k are also the accumulation term, the "flow" term between nodes i and j, and the sink/source term at node i for component k or thermal energy, respectively; and N is the total number of grid blocks in the grid. Though Eqn (11.36) is similar to Eqn (4.1) or (10.6), there are important differences and a number of the terms need to be redefined, because of the dependence of gridding geometric properties on stress or rock deformation, as discussed below.

Strictly speaking, Eqn (11.36), derived from the integrated finite difference scheme, applies to fixed grid block geometry only. Because volumetric strain is a variable in our geomechanical formulation, grid block volume as well as grid block distances and areas between them are no longer fixed in space. To handle these deformation-dependent variables or quantities, we introduce volumetric strain dependence into the volumes, areas, and distances that arise when the discrete Eqn (11.36) is solved. These dependencies are based on the definition of volumetric strain (Winterfeld and Wu, 2014):

$$V_i(\varepsilon_{v,i}) = V_{i,0}(1 - \varepsilon_{v,i}) \tag{11.37}$$

in which $V_{i,0}$ is the volume of grid block i at zero strain; and $\varepsilon_{v,i}$ is the average volumetric strain at grid block i. Changes in volumetric strain also cause changes in grid block connection areas as well as distances between them. We account for these by first defining analogs of Eqn (11.37) for areas and distances (A_{ij} and d_i) in terms of average area and distance strain (ε_A and ε_d):

$$A_{ij}\left(\varepsilon_{A,ij+1/2}\right) = A_{ij,0}\left(1 - \varepsilon_{A,ij+1/2}\right) \tag{11.38}$$

and

$$d_i(\varepsilon_{d,i}) = d_{i,0}(1 - \varepsilon_{d,i}) \tag{11.39}$$

in which $\varepsilon_{A,ij+1/2}$ is the average of area strains $\varepsilon_{A,i}$ and $\varepsilon_{A,j}$. Using Eqn (11.37) to evaluate the accumulative term in Eqn (11.36) yields: for mass component,

$$\left(V_i A_i^k\right) = V_{i,0}(1 - \varepsilon_{v,i})A_i^k = V_{i,0}(1 - \varepsilon_{v,i})\left[\phi \sum_\beta \left(\rho_\beta S_\beta X_\beta^k\right)\right]_i \tag{11.40}$$

and for thermal energy,

$$\begin{aligned}\left(V_i A_i^{N_c+1}\right) &= V_{i,0}(1 - \varepsilon_{v,i})A_i^{N_c+1} \\ &= V_{i,0}(1 - \varepsilon_{v,i})\left[\phi \sum_\beta \left(\rho_\beta S_\beta U_\beta\right) + (1 - \phi)\rho_s U_s\right]_i\end{aligned} \tag{11.41}$$

To evaluate connection areas and distances between two adjacent grid blocks, we relate area and distance strains to volumetric strain. Because our geomechanical formulation is in terms of volumetric strain only, we assume either isotropic or uniaxial volumetric strain. For isotropic volumetric strain, area strain and volumetric strain are related by:

$$(1 - \varepsilon_v) = (1 - \varepsilon_A)^{\frac{3}{2}} \tag{11.42}$$

and because strains are small:

$$\varepsilon_A \approx \frac{2\varepsilon_v}{3} \tag{11.43}$$

Distance strain and volumetric strain are related by:

$$(1 - \varepsilon_v) = (1 - \varepsilon_d)^3 \tag{11.44}$$

and because strains are small:

$$\varepsilon_{\mathrm{d}} \approx \frac{\varepsilon_{\mathrm{v}}}{3} \tag{11.45}$$

For uniaxial volumetric strain, distance strain in the strain direction would be equal to volumetric strain, and distance strain in other directions would be zero; area strain in the strain direction would be zero, and area strain in the other directions would be equal to volumetric strain.

The mass-flow term, $flow_{ij}^{k}$, in Eqn (11.36) is evaluated as

$$flow_{ij}^{k} = A_{ij} \sum_{\beta} \left(X_{\beta}^{k}\right)_{ij+1/2} F_{\beta,ij}, \quad k = 1, 2, 3, \ldots, N_{\mathrm{c}} \tag{11.46}$$

in which the phase mass flux

$$F_{\beta,ij} = \left(\frac{\rho_{\beta} k_{\mathrm{r}\beta}}{\mu_{\beta}}\right)_{ij+1/2} \frac{k_{ij+1/2}}{d_i + d_j} \left(\Phi_{\beta j} - \Phi_{\beta i}\right) \tag{11.47}$$

The total heat flux along the connection of grid blocks i and j, including advective and conductive heat transfer terms, may be evaluated by

$$flow_{ij}^{N_{\mathrm{c}}+1} = A_{ij} \left\{ \sum_{\beta} \left[\left(h_{\beta}\right)_{ij+1/2} F_{\beta,ij} \right] + \left(K_{\mathrm{T}}\right)_{ij+1/2} \left(\frac{T_j - T_i}{d_i + d_j} \right) \right\} \tag{11.48}$$

Let us substitute Eqn (11.43) into Eqn (11.38) and Eqn (11.45) into Eqn (11.39) to correlate connection areas and distances between grid blocks to volumetric strain, then mass flow and heat flow terms are written as:

$$flow_{ij}^{k} = A_{ij,0} \left(1 - \frac{2\varepsilon_{\mathrm{v},ij+1/2}}{3}\right) \sum_{\beta} \left(X_{\beta}^{k}\right)_{ij+1/2} F_{\beta,ij} \tag{11.49}$$

and

$$flow_{ij}^{N_{\mathrm{c}}+1} = A_{ij,0} \left(1 - \frac{2\varepsilon_{\mathrm{v},ij+1/2}}{3}\right) \times \left\{ \sum_{\beta} \left[\left(h_{\beta}\right)_{ij+1/2} F_{\beta,ij} \right] + \frac{\left(K_{\mathrm{T}}\right)_{ij+1/2} \left(T_j - T_i\right)}{d_{i,0}\left(1 - \frac{\varepsilon_{\mathrm{v},i}}{3}\right) + d_{j,0}\left(1 - \frac{\varepsilon_{\mathrm{v},j}}{3}\right)} \right\} \tag{11.50}$$

in which the phase mass-flow term is given by

$$F_{\beta,ij} = \left(\frac{\rho_{\beta} k_{\mathrm{r}\beta}}{\mu_{\beta}}\right)_{ij+1/2} \frac{k_{ij+1/2}}{d_{i,0}\left(1 - \frac{\varepsilon_{\mathrm{v},i}}{3}\right) + d_{j,0}\left(1 - \frac{\varepsilon_{\mathrm{v},j}}{3}\right)} \left(\Phi_{\beta j} - \Phi_{\beta i}\right) \tag{11.51}$$

Equations (11.40), (11.41), and (11.49)–(11.51) are used in Eqn (11.36) in a residual form,

$$R_i^{k,n+1} = \left\{ \left[V_{i,0}(1-\varepsilon_{\mathrm{v},i}) A_i^k \right]^{n+1} - \left[V_{i,0}(1-\varepsilon_{\mathrm{v},i}) A_i^k \right]^n \right\} \frac{1}{\Delta t} - \sum_{j\in\eta_i} flow_{ij}^{k,n+1} - Q_i^{k,n+1} = 0 \tag{11.52}$$

Evaluating the relation between mean stress and volumetric strain for gridlock volumetric strain in terms of grid block mean stress, pore pressure, and temperature in a single-porosity medium:

$$K\varepsilon_{\mathrm{v},i} = \sigma_{\mathrm{m},i} - [\alpha P_i + 3\beta_{\mathrm{T}} K(T_i - T_{\mathrm{ref}})] \tag{11.53}$$

Applying the integrated finite difference method to Eqn (11.16), leads to a discrete equation that is a sum of momentum fluxes, which are contributed by the body force, and the mean stress, pressure, and temperature difference terms over grid block surface segments, in a residual form,

$$R_i^{\sigma,n+1} = \sum_{j\in\eta_i} \left[F_{\sigma,ij} + (\boldsymbol{F}_{\mathrm{b}} \cdot \boldsymbol{n})_{ij+1/2} - F_{\mathrm{PT},ij} \right] A_{ij,0} \left(1 - \frac{2\varepsilon_{\mathrm{v},ij}}{3} \right) = 0 \tag{11.54}$$

in which

$$F_{\sigma,ij} = \left[\frac{3(1-\upsilon)}{(1+\upsilon)} \right]_{ij+1/2} \frac{\sigma_{\mathrm{m},j} - \sigma_{\mathrm{m},i}}{d_{i,0}\left(1 - \frac{\varepsilon_{\mathrm{v},i}}{3}\right) + d_{j,0}\left(1 - \frac{\varepsilon_{\mathrm{v},j}}{3}\right)} \tag{11.55}$$

and

$$F_{\mathrm{PT},ij} = \left[\frac{2(1-2\upsilon)}{(1+\upsilon)} \right]_{ij+1/2} \left[\frac{\alpha_i (P_j - P_i) + (3\beta_{\mathrm{T}} K)_{ij+1/2} (T_j - T_i)}{d_{i,0}\left(1 - \frac{\varepsilon_{\mathrm{v},i}}{3}\right) + d_{j,0}\left(1 - \frac{\varepsilon_{\mathrm{v},j}}{3}\right)} \right] \tag{11.56}$$

If a simulation domain is discretized into a total of N grid blocks with N_{c} mass components, N_{c} mass conservation equations, one energy conservation equation, and one momentum balance equation are associated with each grid block. Therefore, there is a total of $N \times (2 + N_{\mathrm{c}})$ equations to be fully solved implicitly for the entire simulation domain in a single-porosity-medium reservoir.

11.4.2 Numerical Formulation for Modeling THM Processes in Multiple-Porosity Reservoirs

The mass, energy, and momentum balance equations in multiple-porosity reservoirs are discretized in space using the same integrated finite difference method (Winterfeld and Wu, 2014). Equation (11.52) for solving mass

and energy conservation is applicable to both single-porosity porous and multiporosity fractured media. To be consistent with geomechanical equations, however, we use a different subscript notation system in this section for the numerical formulation in modeling THM in a fractured reservoir. For a multiple-porosity, fractured-medium system, the reservoir simulation domain is subdivided first into N primary grid blocks with unstrained volume $V_{i,0}$ ($i = 1, 2, 3, \ldots, N$) using the MINC concept. Then, each primary grid block i, with unstrained volume, $V_{i,0}$, is subdivided into the total number (N_ϕ) of (one) fracture and (several) porous continua. Unstrained volume, $V_{i,0}$, is equal to the summation of $V_{i,0,l}$, unstrained volumes of MINC cells, over all l, or $V_{i,0} = \sum_l V_{i,0,l}$ with l is an index varying from with $l = 1$ to N_ϕ. When using the double-porosity, $N_\phi = 2$ and $l = 1$ and 2; or with the MINC concept, $N_\phi > 2$, as it is normally done in the TOUGH technology (Pruess et al., 1999). Note that $V_{i,0,l}$ is normally denoted as a fracture cell or subgrid block with $l = 1$ at each primary grid block i.

The mass and energy conservation equations are integrated over each fracture or porous continuum volume of a subgridded cell of MINC and the resulting set of these equations in residual form in Eqn (11.52) is rewritten as:

$$R_{i,l}^{k,n+1} = \left\{ \left[V_{i,0,l}(1-\varepsilon_{\mathrm{v},i}) A_{i,l}^{k} \right]^{n+1} - \left[V_{i,0,l}(1-\varepsilon_{\mathrm{v},i}) A_{i,l}^{k} \right]^{n} \right\} \frac{1}{\Delta t} - \sum_{j \in \eta_{i,l}} flow_{ij,l}^{k,n+1} - Q_{i,l}^{k,n+1} = 0, \qquad (11.57)$$

$$i = 1, 2, 3, \ldots, N; \quad l = 1, 2, 3, \ldots, N_\phi$$

in which the subscripts i and l (i,l) appearing together refer to one grid block for local fracture or porous continuum l, belonging to primary grid block i and with unstrained volume $V_{i,0,l}$, before MINC gridding; subscript j indexes a grid block neighboring to grid block (i,l); $\eta_{i,l}$ is a set of grid blocks containing all the neighbors of grid block (i,l).

The mass and energy accumulation terms of grid block (i,l) in Eqn (11.57) are evaluated using Eqns (11.40) and (11.41); and mass and energy flow terms $\left(flow_{ij,l}^{k,n+1}\right)$ are still evaluated using Eqns (11.49) and (11.50) for global-flow connections, respectively. However, for local interaction between fracture–matrix or matrix–matrix connections within primary grid block i, $\left(flow_{ij,l}^{k,n+1}\right)$ should be evaluated using the general dual-continuum approach (Wu and Qin, 2009) with stress-dependent characteristic distances and interface areas with a double-porosity or MINC model.

The multiple-porosity geomechanical equations are integrated over each primary grid block volume. When this is applied to Eqn (11.22), we obtain the following:

$$K\varepsilon_{\mathrm{v},i} = \sigma_{\mathrm{m},i} - \sum_{l}[\alpha_l P_{i,l} + 3\beta_{\mathrm{T}} K\omega_{i,l}(T_{i,l} - T_{ref})] \tag{11.58}$$

When this is applied to Eqn (11.23), we obtain the following:

$$R_i^{\sigma,n+1} = \sum_{j\in\eta_i}\left[F_{\sigma,ij} + (\boldsymbol{F}_{\mathrm{b}}\cdot\boldsymbol{n})_{ij+1/2} - F_{\mathrm{PT},ij,l}\right]A_{ij,0}(1-\varepsilon_{\mathrm{A},ij}) = 0 \tag{11.59}$$

in which $F_{\sigma,ij}$ is defined in Eqn (11.55); and $F_{\mathrm{PT},ij,l}$ is defined as

$$F_{\mathrm{PT},ij,l} = \left[\frac{2(1-2\upsilon)}{(1+\upsilon)}\right]_{ij+1/2}\sum_{l}\left[\frac{\alpha_l(P_{j,l}-P_{i,l}) + (3\beta_{\mathrm{T}}K\omega_l)_{ij+1/2}(T_{j,l}-T_{i,l})}{d_{i,0}\left(1-\frac{\varepsilon_{\mathrm{v},i}}{3}\right) + d_{j,0}\left(1-\frac{\varepsilon_{\mathrm{v},j}}{3}\right)}\right] \tag{11.60}$$

Consider a simulation domain discretized into a total of N primary grid blocks with N_{c} mass components. When using the MINC approach with N_ϕ multi-porous continua (e.g., $N_\phi = 2$ for double-porosity model) in each primary grid block, N_{c} mass conservation equations and one energy conservation equation are associated with each subdivided porous continuum, and one momentum equation is associated with each primary grid block. Therefore, there is a total of $N \times (1 + N_\phi \times (1 + N_{\mathrm{c}}))$ equations to be solved for the entire simulation domain of the fractured reservoir.

11.4.3 Treatment of Geomechanical Boundary Conditions

The momentum conservation equation, Eqn (11.16), is the divergence of a momentum flux. Applying the integrated finite difference method to Eqn (11.16) yields an integral of momentum flux over the grid-block surface, which is approximated as a discrete sum over surface-averaged segments. Grid-block surface segments are common to another grid block or border the surroundings. The Eqn (11.54) summation term applies to surface segments that are common to another grid block. For grid-block surface segments that border the surroundings, we modify that term by applying the geomechanical boundary conditions.

There are four terms that compose the momentum flux in Eqn (11.16) or (11.54): mean stress-, body force-, pressure-, and temperature-difference terms. The body-force term contains the dot product of the body force, which points in the direction of the gravitational vector, with the vector

pointing between grid blocks i and j, as shown in Figure 4.1. We neglect this term for surface segments bordering the surroundings by assuming the vector pointing between grid block i and the surroundings is orthogonal to the gravitational vector. Surface segments bordering the surroundings generally have no fluid flowing through them (fluid loss to the surroundings is generally represented as a constant pressure sink), so there would be no pore-pressure communication between a grid block and the surroundings. Consequently, we neglect the pressure difference term as well. Finally, we assume the temperature and mean stress of the surroundings are the grid block's initial values.

We apply the above boundary conditions to the Eqn (11.54) summation term and obtain the form for a surface segment bordering the surroundings:

$$\left\{\left[\frac{3(1-\upsilon)}{(1+\upsilon)}\right]_i \frac{\sigma_{\mathrm{m},i}-\sigma^0_{\mathrm{m},i}}{2d_{i,0}(1-\varepsilon_{\mathrm{d},i})} - \left[\frac{2(1-2\upsilon)}{(1+\upsilon)}\right]_i \times \left[\frac{(3\beta_{\mathrm{T}}K)_{ij+1/2}\left(T_i-T_i^0\right)}{2d_{i,0}(1-\varepsilon_{\mathrm{d},i})}\right]\right\} A_{ij,0}(1-\varepsilon_{\mathrm{A},i}) \tag{11.61}$$

in which superscript 0 refers to grid block initial value and $d_{j,0}$ is replaced by $d_{i,0}$.

11.4.4 Numerical Solution Scheme

The resulting set of nonlinear of discretized algebraic equations in residual form for conservation equations of mass and energy is given by Eqn (11.52) and for the momentum balance is given in Eqn (11.54) in a single-porosity reservoir. For multiple-porosity-reservoir discretization, the equation system is given by Eqns (11.57) and (11.59), respectively, for mass and energy conservation and momentum balance. These equations are expressed in vector form as:

$$\boldsymbol{R}(\boldsymbol{x}^{n+1}) = 0 \tag{11.62}$$

in which $\boldsymbol{x}^{n+1}$ is the primary variable vector at time level $n+1$. The vector of equations, Eqn (11.62), is solved by the Newton method. Equation (11.62) defines a total of $(N_{\mathrm{c}}+2)\times N$ coupled nonlinear algebraic equations for a single-porosity-medium reservoir and a total of $N\times(1+N_\phi\times(1+N_{\mathrm{c}}))$ equations for a multiple-porosity, fractured reservoir, which need to be solved for modeling THM processes, respectively. In general, primary variables per grid block are needed to select in the Newton iteration, which are equal to

the number of equations to be solved per grid block. The primary variables are usually selected among fluid pressures, fluid saturations, mass (mole) fractions of components in fluids, temperatures, and mean stress (Winterfeld and Wu, 2014).

The Newton method is used to solve systems of nonlinear equations of Eqn (11.62), which, at a grid block i is regarded as a function of the primary variables not only at grid block i, but also at all its direct neighboring grid blocks j. Denoting iteration number by subscript p, the following system of equations result from applying the Newton method to Eqn (11.63):

$$\sum_m \frac{\partial R_i^{k,n+1}(x_{m,p})}{\partial x_m}(\delta x_{m,p+1}) = -R_i^{k,n+1}(x_{m,p}) \tag{11.63}$$

in which x_m is the primary variable m at grid block i ($i = 1, 2, 3, \ldots, N_c + 2$ for a single-porosity-medium reservoir; and $i = 1, 2, 3, \ldots, 1 + N_\phi \times (1 + N_c)$ for a multiporosity reservoir) and all its direct neighbors; p is the iteration level; and $i = 1, 2, 3, \ldots, N$. The primary variables in Eqn (11.64) need to be updated after each iteration:

$$x_{m,p+1} = x_{m,p} + \delta x_{m,p+1} \tag{11.64}$$

The Newton iteration process continues until the residuals $R_i^{k,n+1}$ or changes in the primary variables $\delta x_{m,p+1}$ over one iteration are reduced below preset convergence tolerances.

11.5 SIMULATION EXAMPLES

We present three simulation samples to provide model verification and simulation examples (Winterfeld and Wu, 2014). The first two are dealing with flow in a single-porosity medium with one-dimensional consolidation and two-dimensional simulation of the Mandel–Cryer effect, which are compared to analytical solutions. The third example is another one-dimensional consolidation of a double-porosity medium and is also is compared to the analytical solution.

11.5.1 One-Dimensional Consolidation

In the one-dimensional consolidation problem (Jaeger et al., 2009), a z-directional stress is applied to the top of a fluid-filled porous-rock column, instantaneously inducing a uniaxial deformation and a pore-pressure increase. Afterwards, the fluid is allowed to drain out of the column top and

Table 11.1 Input parameters for one-dimensional consolidation problem

Parameters	Value	Unit
Initial porosity, ϕ	0.09	[-]
Permeability, k	10^{-13}	[m^2]
Bulk Modulus, K	3.33	[GPa]
Poisson's ratio, υ	0.25	[-]
Applied load, F_L	3.0	[MPa]
Relaxation pressure, P_{rx}	0.1	[MPa]
Fluid compressibility, C_f	4.0×10^{-10}	[1/Pa]
Fluid viscosity, μ_f	4.7×10^{-4}	[Pa·s]
Length, L	1000	[m]
Number of grid blocks, N	1000	[-]

the induced pore pressure dissipates. An analytical solution to this problem is used (Winterfeld and Wu, 2014).

We adapt this problem to our flow and stress formulations. Starting from an initial unstressed state of the system in which pore pressure and mean stress both equal P_i, the pore pressure P induced by an applied mean stress is given by

$$P = B(\sigma_m - P_i) + P_i \tag{11.65}$$

in which B is the Skempton coefficient. For uniaxial strain, mean stress, z-direction stress, and pore pressure are related by:

$$\sigma_m = \frac{(1+\upsilon)}{3(1-\upsilon)}(\sigma_{zz} - \alpha P) + \alpha P \tag{11.66}$$

For a constant z-directional stress, the induced pore pressure and mean stress are obtained by solving Eqns (11.65) and (11.66). Our simulation is initialized with those results. Fluid leaves the top grid block via a constant-pressure fluid sink that is set to the unstressed pore pressure P_i. The top grid block mean stress is obtained from Eqn (11.66) using P_i and the constant z-directional stress. Finally, porosity varies according to Eqn (11.34). Our input parameters are listed in Table 11.1.

We run the simulation for 10^6 s with 10^2 s time steps. Comparisons of pore pressure from simulation and analytical solution are shown in Figure 11.3, with excellent agreement.

11.5.2 Mandel–Cryer Effect

A constant compressive force is applied to the top and bottom of a fluid-filled poroelastic material, inducing an instantaneous uniform pore-pressure

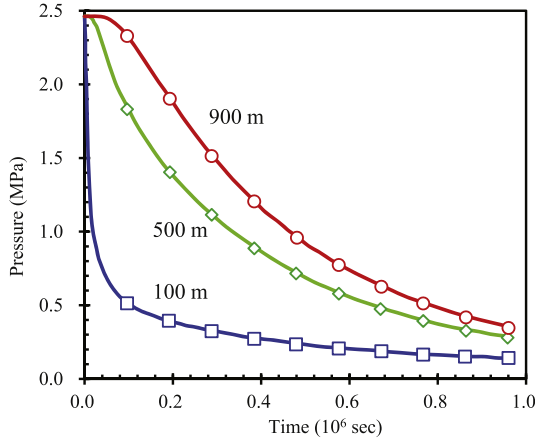

Figure 11.3 Simulated pressure (markers) and analytical (solid lines) versus time at 100, 500, and 900 m for one-dimensional consolidation problem.

increase and compression. Afterwards, the material is allowed to drain laterally. Because the pore pressure near the edges must decrease due to drainage, the material there becomes less stiff and there is a load transfer to the center, resulting in a further increase in center pore pressure that reaches a maximum and then declines. This pore-pressure behavior is called the Mandel–Cryer effect (Mandel, 1953; Cryer, 1963), and Abousleiman et al. (1996) present an analytical solution to which we compare our simulated results.

We simulate this problem in two steps. The first step is the application of force that induces the pore-pressure increase. We start from an unstrained state in which pore pressure and mean stress are both equal ($\sigma_{\mathrm{m},0} = P_0$) and impose a greater mean stress ($\sigma_{\mathrm{m},1}$) at the top and bottom. These greater stresses compress the system and produce a pore-pressure increase from pressure P_0 to pressure P_1. In the analytical solution, uniaxial stress is assumed, so mean stress and z-direction stress are related by:

$$\sigma_{\mathrm{m}} = \frac{\sigma_{zz}}{3} \tag{11.67}$$

We next simulate fluid drainage. The system is initially at the previous equilibrated state, mean stress $\sigma_{\mathrm{m},1}$ and pore pressure P_1, and we impose the initial pore pressure on the lateral boundaries to allow the system to drain. We simulate the Mandel–Cryer effect for a 1000 m square domain that is subdivided into a uniform 200 × 200 grid. The initial pore pressure and mean stress are 0.1 MPa, the applied mean stress is 5.0 MPa, the equilibrium

Table 11.2 Rock Properties for Mandel–Cryer effect simulation

Parameters	Value	Unit
Porosity, ϕ	0.094	[-]
Permeability, k	10^{-13}	[m^2]
Young's Modulus, E	5.0	[GPa]
Poisson's ratio, υ	0.25	[-]
Biot's coefficient, α	1.0	[MPa]

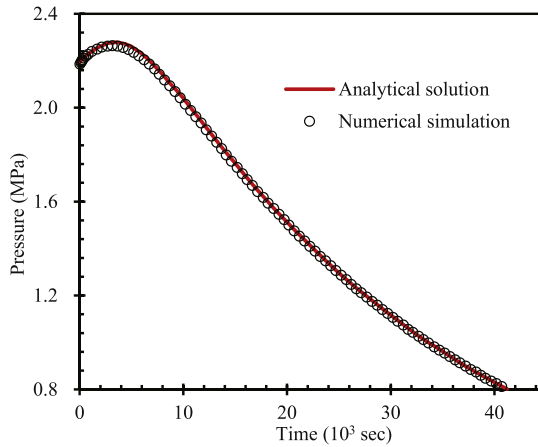

Figure 11.4 Comparison of Mandel–Cryer effect analytical solution to simulation for pore pressure located at the system center.

pore pressure is 2.18 MPa, and rock properties are shown in Table 11.2. The system drains for 50,000 s.

We compare pressure at the middle of the system with the analytical solution, shown in Figure 11.4. The simulated results exhibit the pore-pressure maximum characteristic of the Mandel–Cryer effect and lie extremely close to the analytical solution. The analytical solution and numerical simulation result do differ in that the simulator allows pore pressure to vary in two dimensions whereas, in the analytical solution, pressure varies only laterally.

11.5.3 One-Dimensional Consolidation of Double-Porosity, Fractured Medium

In this one-dimensional consolidation problem, a z-directional stress is applied to the top of a fluid-filled double-porosity (fracture and matrix) porous-rock column, instantaneously inducing a deformation and a pore-pressure increase.

The fluid then is allowed to drain out of the column top and the pore-pressure increase dissipates. An analytical solution to this problem was presented by Wilson and Aifantis (1982). In their analysis, strain is uniaxial and z-direction stress is constant throughout the process.

We simulate this problem in two steps. The first step is the load application to produce the pore-pressure increase. We start from an unstrained state in which pore pressures (fracture and matrix) and mean stress are both equal ($\sigma_{m,0} = P_{1,0} = P_{2,0}$) and impose a greater mean stress at the column top ($\sigma_{m,1}$) that induces a pore-pressure increase ($P_{l,1}$) in the column after the system equilibrates. For uniaxial deformation in an isothermal double-porosity system, mean stress, z-direction stress, and pore pressures are related by:

$$\sigma_m = \frac{(1+\upsilon)}{3(1-\upsilon)}\left(\sigma_{zz} - \sum_l \alpha_l P_l\right) + \sum_l \alpha_l P_l \tag{11.68}$$

Using this equation, we calculate the constant z-direction stress ($\sigma_{m,0}$) from the imposed mean stress ($\sigma_{m,1}$) and the equilibrated pore pressures ($P_{l,1}$).

The second step is simulation of fluid drainage. The column is initially at the above equilibrated state. We set the pore pressures at the column top to the initial pore pressures ($P_{l,0}$). Because z-direction stress is constant, the mean stress at the column top must set as well, calculated from Eqn (11.68) using $\sigma_{m,0}$ and $P_{l,0}$. Fluid then drains out of the column top as the pore pressures return to the initial values, $P_{l,0}$. Our simulated column is 400 m long with rock properties shown in Table 11.3. The column is subdivided into 400 grid blocks, each of which contains two porous continua, fracture and matrix.

Initial pore pressures and mean stress are 5.0 MPa and the imposed mean stress is 8.0 MPa. The resulting equilibrium pore pressures are 6.2 MPa and

Table 11.3 Rock properties for one-dimensional consolidation of double-porosity column

Parameters	Fracture	Matrix	Unit
Porosity, ϕ	0.004	0.20	[-]
Permeability, k	8.9×10^{-13}	8.9×10^{-17}	[m^2]
Young's modulus, E	8.0	8.0	[GPa]
Poisson's ratio, υ	0.20	0.20	[-]
Biot's coefficient, α	0.1	0.9	[Mpa]
Volume fraction	0.5	0.5	[-]

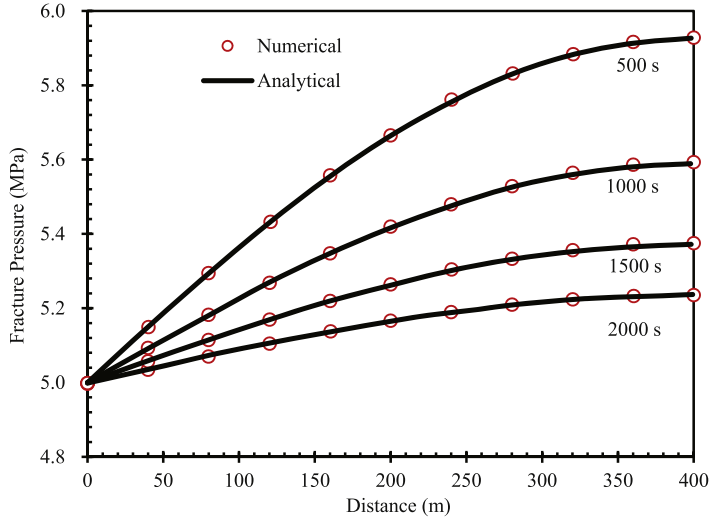

Figure 11.5 Comparison of fracture pressure analytical solution (solid lines) to simulation (points) for one-dimensional consolidation of double-porosity column.

the calculated z-direction stress is 9.8 MPa. We run the drainage portion of the simulation for 4000 s with 1-s time steps. Comparison of simulated fracture pressure with the analytical solution is shown in Figure 11.5, with excellent agreement.

11.6 SUMMARY AND CONCLUSIONS

In this chapter, we present a geomechanical momentum conservation equation in terms of mean stress, pressure, and temperature, and the equation is derived from the fundamental equations describing rock deformation of thermal, porous, and fractured elastic media. We implement the geomechanical equation alongside the mass and energy conservation equations into numerical formulation for modeling THM processes in porous and fractured-medium reservoirs. In addition, rock properties, namely permeability and porosity, are included as functions of effective stress and other variables that are obtained from the literature for simulation of coupled geomechanical effects.

We present three simulation examples to provide model verification problems with the model formulation and numerical implementation. The examples include one-dimensional and two-dimensional consolidations in a single-porosity porous medium and a double-porosity medium, for which

analytical solutions exist. We obtain a good match with the analytical solutions for all three simulation problems.

REFERENCES

Abousleiman, Y., Cheng, A.-D., Cui, L., Detournay, E., Roegiers, J.-C., 1996. Mandel's problem revisited. Geotechnique 46 (2), 187–195.

Bagheri, M.A., Settari, A., 2008. Modeling of geomechanics in naturally fractured reservoirs. SPE Reservoir Evaluation & Engineering 11 (1), 108–118.

Bai, M., Elsworth, D., Roegiers, J.-C., 1993. Multiporosity/multipermeability approach to the simulation of naturally fractured reservoirs. Water Resources Research 29 (6), 1621–1633.

Bear, J., 1972. Dynamics of Fluids in Porous Media. American Elsevier, New York.

Biot, M.A., 1941. General theory of three-dimensional consolidation. Journal of Applied Physics 12 (2), 155–164.

Biot, M.A., Willis, G.D., 1957. The elastic coefficients of the theory of consolidation. Journal of Applied Mechanics 24, 594–601.

Cipolla, C.L., 2009. Modeling production and evaluating fracture performance in unconventional gas reservoirs. Journal of Petroleum Technology 61 (9), 84–90.

Cryer, C.W., 1963. A comparison of the three-dimensional consolidation theories of Biot and Terzaghi. The Quarterly Journal of Mechanics and Applied Mathematics 16 (4), 401–412.

Davies, J.P., Davies, D.K., 2001. Stress-dependent permeability: characterization and modeling. SPE Journal 6 (2), 224–235.

Dean, R.H., Gai, X., Stone, C.M., Minkoff, S.E., 2006. A comparison of techniques for coupling porous flow and geomechanics. SPE Journal 11 (1), 132–140.

Fakcharoenphol, P., Charoenwongsa, S., Kazemi, H., Wu, Y.-S., 2013. The effect of water-induced stress to enhance hydrocarbon recovery in shale reservoirs. SPE Journal 18 (5), 897–909.

Fung, L.S.K., Buchanan, L., Wan, R.G., 1994. Couplled geomechanical-thermal simulation for deforming heavy-oil reservoirs. Journal of Canadian Petroleum Technology 33 (4).

Gutierrez, M., Lewis, R.W., Masters, I., 2001. Petroleum reservoir simulation coupling fluid flow and geomechanics. SPE Reservoir Evaluation & Engineering 4 (3), 164–172.

Hu, L., Winterfeld, P.H., Fakcharoenphol, P., Wu, Y.-S., 2013. A novel fully-coupled flow and geomechanics model in enhanced geothermal reservoirs. Journal of Petroleum Science and Engineering 107, 1–11.

Jaeger, J.C., Cook, N.G.W., Zimmerman, R., 2009. Fundamentals of Rock Mechanics. John Wiley & Sons.

Leverett, M.C., 1941. Capillary behavior in porous solids. Transactions of the AIME 142 (1), 152–169.

Mandel, J., 1953. Consolidation Des SolsÉtude Mathématique. Geotechnique 3 (7), 287–299.

McKee, C.R., Bumb, A.C., Koenig, R.A., 1988. Stress-dependent permeability and porosity of coal and other geologic formations. SPE Formation Evaluation 3 (1), 81–91.

McTigue, D.F., 1986. Thermoelastic response of fluid-saturated porous rock. Journal of Geophysical Research: Solid Earth (1978–2012) 91 (B9), 9533–9542.

Norris, A., 1992. On the correspondence between poroelasticity and thermoelasticity. Journal of Applied Physics 71 (3), 1138–1141.

Ostensen, R.W., 1986. The effect of stress-dependent permeability on gas production and well testing. SPE Formation Evaluation 1 (3), 227–235.

Pruess, K., Oldenburg, C.M., Moridis, G.J., 1999. TOUGH2 User's Guide Version 2.
Rutqvist, J., Stephansson, O., 2003. The role of hydromechanical coupling in fractured rock engineering. Hydrogeology Journal 11 (1), 7–40.
Rutqvist, J., Wu, Y.-S., Tsang, C.-F., Bodvarsson, G., 2002. A modeling approach for analysis of coupled multiphase fluid flow, heat transfer, and deformation in fractured porous rock. International Journal of Rock Mechanics and Mining Sciences 39 (4), 429–442.
Settari, A., Walters, D.A., 2001. Advances in coupled geomechanical and reservoir modeling with applications to reservoir compaction. SPE Journal 6 (3), 334–342.
Soeder, D.J., 1988. Porosity and permeability of eastern Devonian gas shale. SPE Formation Evaluation 3 (1), 116–124.
Terzaghi, von K., 1936. The shearing resistance of saturated soils and the angle between the planes of shear. In: Proceedings of the 1st international conference on soil mechanics and foundation engineering, vol. 1, pp. 54–56.
Tester, J.W., Anderson, B.J., Batchelor, A.S., Blackwell, D.D., DiPippo, R., Drake, E.M., Nichols, K., 2006. The Future of Geothermal Energy, vol. 358.
Verma, A., Pruess, K., 1988. Thermohydrological conditions and silica redistribution near high-level nuclear wastes emplaced in saturated geological formations. Journal of Geophysical Research: Solid Earth (1978–2012) 93 (B2), 1159–1173.
Wang, F.P., Reed, R.M., Jackson, J.A., Jackson, K.G., 2009. Pore networks and fluid flow in gas shales. In: SPE Annual Technical Conference and Exhibition. New Orleans, Louisiana, USA. http://doi.org/10.2118/124253-MS.
Wilson, R.K., Aifantis, E.C., 1982. On the theory of consolidation with double porosity. International Journal of Engineering Science 20 (9), 1009–1035.
Winterfeld, P.H., Wu, Y.-S., 2014. Simulation of CO_2 sequestration in brine aquifers with geomechanical coupling. In: Al-Khoury, R., Bundschuh, J. (Eds.), Computational Models for CO_2 Geo-sequestration & Compressed Air Energy Storage. CRC Press, pp. 275–304.
Wu, Y.-S., Li, J., Ding, D., Wang, C., Di, Y., 2014. A generalized framework model for the simulation of gas production in unconventional gas reservoirs. SPE Journal 19 (5), 845–857.
Wu, Y.-S., Qin, G., 2009. A generalized numerical approach for modeling multiphase flow and transport in fractured porous media. Communications in Computational Physics 6 (1), 85–108.
Wu, Y.-S., Xiong, Y., Kazemi, H., 2015. Coupled thermo-hydrological processes in enhanced geothermal systems. In: Poate, J., Illangasekare, T., Kazemi, H., Kee, R. (Eds.), Pore Scale Phenomena Frontiers in Energy and Environment, vol. 10. World Scientific, pp. 279–298. http://doi.org/doi:10.1142/9789814623063_0015.

CHAPTER 12

Multiphase Flow in Unconventional Petroleum Reservoirs

12.1 INTRODUCTION

Multiphase flow in unconventional petroleum reservoirs of tight sands and shale formations is a new area in studies of flow through porous media. This new emerging field, however, has received a lot of attention in the last decade, because of the needs and successes in developing oil and gas from such unconventional, low-permeability formations. Even though significant progress has been made in the effort to economically produce oil and gas from unconventional reservoirs, the physics of multiphase flow and transport processes have not been well understood. In particular, knowledge and technology needed for effective development of unconventional petroleum reservoirs are currently very limited and far behind the needs of the industry. Oil and gas production from unconventional reservoirs relies only on engineering approaches of long horizontal wells and multistage hydraulic fractures to increase effective contact areas between wellbore and formation or reduce flow resistance from reservoir to well. As a result, hydrocarbon recovery rates from those unconventional resources remain very low. There are no effective improved oil and gas recovery technologies, such as secondary or tertiary oil recovery methodologies that have been developed for enhancing oil or gas recovery from these low-permeability reservoirs.

Compared with the flow in conventional reservoirs, multiphase flow in low-permeability unconventional reservoirs is a more complex process and subject to more nonlinear physical processes. These include adsorption or desorption of hydrocarbon molecules on rock solids, non-Darcy flow, strong rock–fluid interaction, intermolecular forces, and effects of rock geomechanics within nanopores or micro- and natural fractures on rock and flow properties. In addition, gas and oil storage and flow in such extremely low-permeability formations are further complicated by *in situ* flow conditions and many coexisting processes, such as complex flow

Multiphase Fluid Flow in Porous and Fractured Reservoirs
ISBN 978-0-12-803848-2
http://dx.doi.org/10.1016/B978-0-12-803848-2.00012-X

geometry and severe heterogeneity on any scales, Knudsen diffusion or Klinkenberg effect (Klinkenberg, 1941), and strong interactions between fluid (gas, oil, and water) molecules and solid materials within tiny pores, as well as micro- and macrofractures of shale and tight formations. Currently, there are few fundamental understandings on the relationships of these complicated processes and flow-driving mechanisms in such reservoirs. Therefore, how to quantify the flow in unconventional oil and gas reservoirs has been a scientific challenge and has become the main research effort for investigating the flow in unconventional reservoirs in developing basic understanding, quantitative methods, and mathematical models (e.g., Akkutlu and Fathi, 2012; Moridis and Freeman, 2014; Wu et al., 2014; Yu and Sepehrnoori, 2014; Sun et al., 2015).

As a typical formation of unconventional reservoirs, shales contain fine-grained, organic-rich sedimentary rocks. Unlike conventional oil or gas formation rock, shales are both source and storing rock for natural gas and oil. They consist of extremely small pores and are impermeable to gas or oil flow if there are no natural or hydraulic fractures. Although there is currently no universally accepted definition of an unconventional petroleum reservoir, such as tight sands or shale gas formations, a common consensus is that unconventional reservoirs are those with extra-low permeability, on the order of tens and hundreds of nanodarcies to microdarcies, and these reservoirs cannot be produced economically or commercially in general without applying massive stimulation technology. Figure 12.1 (Holditch, 2006; Kelkar and Atiq, 2010) shows the famous resource triangle for unconventional reservoirs, to illustrate the difference between conventional and unconventional natural gas resources for their basic characteristics.

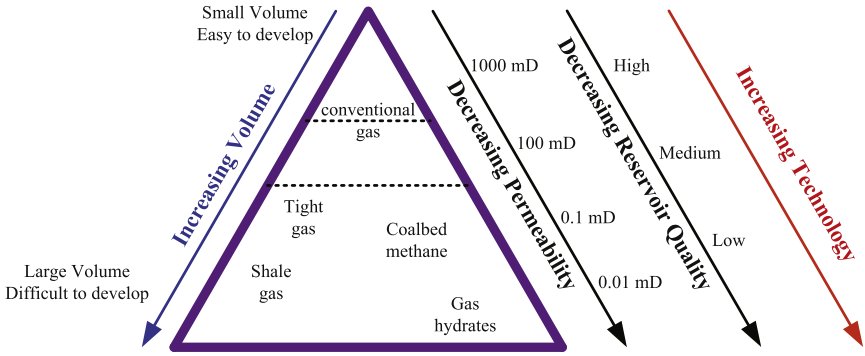

Figure 12.1 The concept of the resource triangle applies to hydrocarbon-producing basins in the world *(Modified from Holditch (2006) and Kelkar and Atiq (2010))*.

Figure 12.1 also presents an understandable definition of unconventional gas reservoirs. In addition, one distinguishing feature for unconventional shale gas and oil reservoirs, as compared with conventional ones mentioned previously, is that, for shale gas, the formation acts as its own source (due to thermal or biological alteration of *in situ* organic content), reservoir, and seal (due to the low permeability) (Burns et al., 2012).

To describe multiphase fluid-flow behavior in low-permeability, highly heterogeneous porous or (natural or humanmade) fractured, stress-sensitive unconventional reservoirs, flow mechanisms must be first understood and impacts of all the key relevant physical processes must be quantified before a suitable mathematical model can be developed. Currently, the physics behind flow and transport processes in unconventional reservoirs is poorly understood. As a result, there are no effective modeling approaches or few reservoir simulators available for engineers to use in developing unconventional tight or shale reservoirs (MIT, 2011). The common practice in field application is using Darcy's law-based commercial reservoir simulators for scope calculations and predictions with many overly simplified assumptions. Therefore, there is a need to develop physics-based mathematical models as well as associated modeling tools for assisting petroleum engineers in developing unconventional oil and gas resources.

Flow behavior in tight and shale petroleum reservoirs is characterized by multiphase (oil and brine, gas and liquid, and gas, oil, and brine) flow in extremely low-permeability, highly heterogeneous porous-fractured, and stress-sensitive rock. Because of low permeability and geological complexity in such tight or shale rock, the traditional Darcy's law-based simulators will not be applicable or realistic to handle nonlinearity of such flow in unconventional reservoirs. For example, the traditional double-porosity model may not be suitable for handling fracture–matrix interaction of gas flow in these reservoirs, due to the long-lasting transient flow nature of fracture–matrix interaction from the extremely low-permeability rock. This is because of the large time scale to reach pseudosteady flow condition between fractures and the matrix. In addition to the need for general capability of modeling multiple-scale heterogeneous porous or fractured formations, the physical processes of gas adsorption onto, desorption from solid grains or organic matter, as well as diffusion into flow streams, are in general not described rigorously in existing commercial petroleum reservoir simulators.

In this chapter, we discuss a mathematical model in an effort to simulate both oil and gas flow and their production processes in tight and shale oil

and gas reservoirs. To describe oil or gas flow behavior in low-permeability, highly heterogeneous porous or fractured, and stress-sensitive unconventional reservoirs, a mathematical model is presented to incorporate many key relevant physical processes, i.e., nonlinear and non-Darcy flow, Klinkenberg effect, and coupled fluid flow and rock deformation, as well as sorption phenomena. The proposed numerical modeling approach is suitable for modeling various types of tight and shale oil and gas reservoirs, including discrete-, hybrid-, double-, and other multiple-continuum conceptual models for simulation of multiscaled fractures and matrix systems and flow domains. The mathematical models and numerical modeling approaches can be used and further improved upon for quantitative studies of unconventional reservoir dynamics and performance, fractures and their effects on oil or gas production, well and stimulation design, and optimal production schedules in the field.

12.2 COUPLED PROCESSES FOR MULTIPHASE FLOW IN UNCONVENTIONAL RESERVOIRS

Flow dynamics in unconventional reservoirs is characterized by highly nonlinear behavior of multiphase flow in extremely low-permeability rock, coupled by many coexisting physical processes, e.g., rock deformation or geomechanical impact, the Klinkenberg or gas-slippage effect, adsorption and desorption, and non-Darcy flow at high- or low-flow rates. This is because the flow occurs in unconventional reservoir rock with small pore size, extremely low permeability, and low porosity. Because of this complicated flow behavior, strong interaction between fluid and rock as well as multiscaled heterogeneity, the traditional Darcy law- and Representative Elementary Volume (REV)-based model may not be generally applicable for describing flow phenomena in unconventional reservoirs. Studies point out that nonlaminar/non-Darcy-flow concept of high velocity and low velocity may turn out to be important in tight oil or shale gas production. Several key factors and physical processes for multiphase fluid flow in unconventional reservoir porous media are discussed in this section.

12.2.1 Geomechanical Effect

Geomechanics or rock deformation plays a critical role in multiphase flow during gas or oil production from unconventional reservoirs, because of the large variation in reservoir pressure during production and its impact on pore geometry. The scope spans from well stability, hydraulic fracturing

design, to reservoir flow management. In conventional oil and gas reservoirs, the effect of geomechanics or rock deformation on permeability is generally small and has been mostly ignored in practice. However, in unconventional shale formations with nanosize pores or nanosize microfractures, such a geomechanical effect can be relatively large and may have a significant impact on both fracture and matrix permeability, which has to be considered in general in the analysis of production performance. Wang et al. (2009) showed that permeability in the Marcellus Shale is pressure dependent and decreases significantly with an increase in confining pressure (or total stress).

To incorporate the effects of geomechanics on flow in porous media, effective porosity, permeability, and capillary pressure, as well as other rock and fluid properties, as discussed in Chapter 11, are assumed to correlate with the mean effective stress (σ_m), defined as

$$\sigma'_m = \sigma_m(x, y, z, p) - \alpha p \tag{12.1}$$

in which α is the Biot constant, and

$$\sigma_m(x, y, z, p) = \frac{\sigma_x(x, y, z, p) + \sigma_y(x, y, z, p) + \sigma_z(x, y, z, p)}{3} \tag{12.2}$$

in which σ_x, σ_y, and σ_z are normal stress in x, y, and z-directions, respectively. With the definition of the mean effective stress in Eqn (12.1), the effective porosity of formation (fractures or porous media) is defined as a function of mean effective stress to include rock deformation,

$$\phi = \phi\left(\sigma'_m\right) \tag{12.3}$$

Similarly, the intrinsic permeability is related to the effective stress, i.e.,

$$k = k\left(\sigma'_m\right) \tag{12.4}$$

Several correlations have been used in Chapter 11 for porosity as a function of effective stress and permeability as a function of porosity.

Capillary pressure is another function related to stress as well as fluid saturation, if rock-pore geometry is altered due to rock deformation. Capillary pressure may be determined by the well-known Young–Laplace equation,

$$P_c = \frac{2\sigma \cos\theta}{r} \tag{12.5}$$

in which σ is the Inter-Facial Tension (IFT); r is the pore or pore-throat size; and θ is the contact angle. Because it is difficult to build the direct

relationship between pore size and effective stress for varying pore size in porous media, the Leverett *J*-function approach (Leverett, 1941) may be used to obtain the capillary pressure, based on measured capillary-pressure curves at reference condition, to correlate with saturation, and stress-dependent permeability and porosity,

$$P_c\left(S,\sigma'_m\right)=\frac{J(S)\sigma\cos\theta}{\sqrt{\frac{k(\sigma'_m)}{\phi(\sigma'_m)}}} \tag{12.6}$$

in which S is the saturation of the wetting phase; ϕ and k are effective porosity and permeability, defined by Eqns (12.3) and (12.4), respectively. $J(S)$ is the Leverett *J*-function, which is a dimensionless number used to correlate capillary-pressure data for the reservoir rocks with the same lithology.

12.2.2 Klinkenberg Effect

The Klinkenberg effect on gas flow and transport in porous media has been observed and is handled using the gas apparent permeability of pressure dependence. This phenomenon is also known and related to slip flow (or Knudsen diffusion). The Klinkenberg effect on gas flow is described in the following expression for apparent permeability (Klinkenberg, 1941),

$$k_g=k_\infty\left(1+\frac{b}{P_g}\right) \tag{12.7}$$

in which k_∞ is constant, absolute gas-phase permeability under very large gas-phase pressure (when the Klinkenberg effect is minimized); and b is the Klinkenberg b-factor and could be pressure or temperature dependent, accounting for gas-slippage effect for gas flow through unconventional reservoirs.

Klinkenberg effect has been practically ignored in conventional gas reservoir studies, except in some cases when analyzing pressure responses or flow near gas production wells at very low pressure. This is because of larger pore size and relatively high pressure existing in those conventional gas reservoirs. In shale gas reservoirs, however, the formation is characterized by extremely low permeability and very small-size pores. As summarized by Wang et al. (2009), the permeability of deep organic-lean mud rocks ranges from smaller than tens of nanodarcies, whereas permeability values in organic-rich gas shale range from subnanodarcies to tens of microdarcies. Thus, the Klinkenberg or slippage effect is expected to be significant,

because the nanosize pore size approaches or even becomes smaller than the mean free path of gas molecules in such formations, leading to significant molecular collisions with the pore walls. Gas permeability is then enhanced by 'slip flow'. It has been shown (Wang et al., 2009) that gas permeability in the Marcellus Shale increases from 19.6 μD at 1000 psi to 54 μD at 80 psi, because of the strong slippage effect.

Studies on gas-slippage dynamic theory include gas travel under the influence of a concentration field (random molecular flow) and a pressure field (macroscopic flow) (e.g., Ertekin et al., 1986). According to this theory, the Klinkenberg factor, b, is not a constant, but pressure dependent. In a separate study, apparent gas permeability is proposed as a function of gas pressure to modify Darcy's law for a given pore size of mud-rock systems (Javadpour, 2009). This study also finds out that the apparent permeability is much higher than Darcy permeability, which may explain the unusually high gas productivity from such strata. Javadpour (2009) concludes that the Klinkenberg effect or Knudsen diffusion is an important gas-transport process in mud-rock systems with temperature and gas molar mass having minimal effects.

12.2.3 Gas Adsorption and Desorption

Natural gas in shale formations is present both as a free-gas phase in pores and as an adsorbed-gas phase on solids. The adsorbed gas represents significant quantities of total gas reserves (20–80%) as well as gas production and ultimate recovery rates, which has to be included in model formulation or modeling analysis. Studies have found that methane molecules are adsorbed mainly to the carbon-rich components, i.e., kerogen, correlated with total organic content (TOC) (EIA, 2011; Mengal and Wattenbarger, 2011; Silin and Kneafsey, 2012). As the formation pressure decreases with continuous gas production from reservoirs, more adsorbed gas is released from solid to free-gas phase, contributing to the flow or production.

The amount of adsorbed gas in a given shale gas formation is described mostly using the Langmuir's isotherm (e.g., Moridis et al., 2010; EIA, 2011; Mengal and Wattenbarger, 2011; Silin and Kneafsey, 2012; Wu et al., 2014). As shown in Figure 12.2 is a typical adsorption curve that follows the Langmuir's isotherm used for US shale gas reservoirs (EIA, 2011). To incorporate the mass term due to gas adsorption or desorption in the mass conservation equation of gas flow, the mass of adsorbed gas in formation

volume is generally correlated to gas pressure according to the Langmuir's isotherm (Langmuir, 1918). To calculate the amount of adsorbed gas, the gas content and the sorption isotherm need to be determined in the laboratory using core samples. Gas content is the amount of total gas adsorbed on the surface of reservoir rock, whereas the sorption isotherm is the capacity of the reservoir rock to hold adsorbed gas with respect to pressure at constant temperature. Then, it is used to define the relationship of pressure and gas storage capacity of the reservoir rock as

$$m_g = \rho_R \rho_g V_E \tag{12.8}$$

in which m_g is absorbed gas mass in unit formation volume; ρ_R is rock bulk density; ρ_g is gas density at standard condition; V_E is the adsorption isotherm function or gas content in standard cubic foot (scf)/ton of field unit (or standard gas volume adsorbed per unit rock mass). If the adsorbed gas terms can be represented by the Langmuir isotherm (Langmuir, 1918), the dependency of adsorbed-gas volume on pressure at constant temperature is given as

$$V_E = V_L \frac{P}{P + P_L} \tag{12.9}$$

in which V_L is the Langmuir's volume in scf/ton; P is reservoir gas pressure; and P_L is Langmuir's pressure, the pressure at which 50% of the gas is desorbed. In general, Langmuir's volume, V_L, is a function of the organic richness (or TOC) and thermal maturity of the shale.

Note that Eqn (12.9) is valid only for the case when the Langmuir model is applicable. In general, V_E in Eqn (12.9) can be replaced by a correlation of gas adsorption as a function of reservoir gas pressure, which

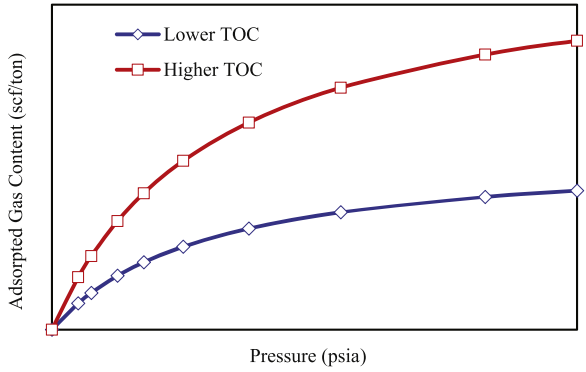

Figure 12.2 Marcellus shale adsorbed gas content *(Modified from EIA (2011))*.

may be defined by a table lookup or curves from laboratory studies for a given unconventional gas reservoir.

In the literature, the Langmuir model is nevertheless the most commonly used empirical model describing sorption onto organic carbon in shales (e.g., Gao et al., 1994). This adsorption model is based on the assumption that an instantaneous equilibrium exists between the adsorbed and the free gas; i.e., there is no transient-time lag between pressure changes and corresponding sorption/desorption responses. If the instantaneous equilibrium assumption cannot provide a good approximation in calculation of shale gas adsorption, a dynamic adsorption conceptual model has to be used. Several kinetic sorption models exist in the literature using diffusion approaches; however, the subject has not been fully investigated or thoroughly understood (Moridis et al., 2010).

12.2.4 Nonlinear Flow

Flow in unconventional reservoirs is subject to highly nonlinear behavior of multiphase fluid flow in extremely low-permeability rock, coupled by many coexisting physical processes, e.g., nonlinear and non-Darcy flow. A shale reservoir formation, for example, may consist of complicated pore geometry, e.g., four types of porous media: nonorganic matrix, organic matter, natural fractures, and hydraulic fractures (Wang et al., 2009). They have very different pore sizes, geometries, and flow properties. The flow through the four different porous media may be different and should be described differently using different flow equations, different parameters, or different correlations. In these very tight low-permeability unconventional reservoirs, hydrocarbon fluid-phase behavior and flow mechanisms are complicated and still not well understood (Alharthy et al., 2013). In addition, the nonlinear, nonlaminar, or non-Darcy-flow concept of high velocity may turn out to be an important flow mechanism in unconventional shale gas reservoirs (Blasingame, 2008; Moridis et al., 2010; Wu et al., 2014). These nonlinear or non-Darcy-flow behaviors of gas flow in different media of shale gas reservoirs may not be represented sufficiently by the REV-based Darcy's law alone, and some other flow equations, such as the *Forchheimer* equation or modified Darcy's law, should be resorted to for field-specific applications.

To describe flow through unconventional reservoirs, flow-governing equations should incorporate the key flow mechanisms, i.e., be able to handle: (1) extreme low permeability of nanodarcies; (2) complicated pore geometry and small pore size; (3) multiscale heterogeneity of nanopores

and microfractures; (4) nonlinear flow or non-Darcy-flow behavior; (5) geomechanical effects on fluid and rock properties; and (6) interactions among fluids and between fluids and rock solids, such as the Klinkenberg effect. In general, we propose a generic, generalized Darcy's law for multiphase flow in unconventional reservoirs as

$$F(\boldsymbol{v}_\beta, \nabla\Phi_\beta, S_\beta, P_\beta, \sigma'_{\mathrm{m}}, T_\beta, \ldots) = 0 \tag{12.10}$$

Equation (12.10) implicitly defines the Darcy or volumetric flow velocity vector, $\boldsymbol{v}_\beta$, (β = o for oil, g for gas, and w for water), as a function of flow potential gradient, $\nabla\Phi_\beta$, fluid saturation and pressure, mean stress, and reservoir temperature, etc.

It can be shown that the multiphase-flow Darcy's law, Eqn (2.1), the non-Darcy-flow model of the Forchheimer equation, Eqn (2.8), or the Barree and Conway model, Eqn (2.9), are all special cases of Eqn (12.10). However, for the generalized flow Eqn (12.10) to be useful in application, a specific form of Eqn (12.10) or the relationship among flow rate and controlling factors and parameters, must be determined in advance for a particular field or type of unconventional formation. More theoretical and experimental studies and analyses are needed for determination of flow mechanisms on various scales from molecular, nano, pore to continuum level.

12.3 FLOW-GOVERNING EQUATION

In this section, we discuss conceptual and mathematical formulation for multiphase flow in unconventional reservoirs. The multiphase-flow model couples multiphase fluid flow with the effect of geomechanics or rock deformation, adsorption and desorption processes, and the Klinkenberg effect. In numerical formulation, the integrated finite difference method (Pruess et al., 1999), as discussed in the previous chapters, will be used for space discretization of multidimensional multiphase fluid-flow equations in porous and fractured unconventional reservoirs using an unstructured grid. Time will be discretized fully implicitly using a first-order backward finite difference. Time and space discretization of mass balance equations results in a set of coupled nonlinear equations, to be solved fully implicitly using Newton iteration.

In many cases of oil or gas production from tight sand or shale gas reservoirs, a two-phase, gas–water, oil–gas, oil–water, or three-phase (oil–gas–water) flow model, i.e., a multiphase flow model, is considered

sufficient for most field simulation studies. This is because what we are concerned with in unconventional reservoir simulation is to model oil or gas flow from reservoir to well under different operational and geological conditions. There always exist multiphase fluids in conventional or unconventional reservoirs. In addition to an oil or gas phase, an aqueous brine is often coexisting with oil and/or gas and the water flow needs to be considered in the following cases: (1) there exists mobile *in situ* connate water; (2) there exist aqueous drilling or hydraulic fracturing fluids near wells, which are sucked into the formations surrounding wells during well drilling and completion or formation stimulation. Therefore, in this chapter we are interested in the two-phase and three-phase flow model and formulation and treat single-phase oil or gas flow or two-phase flow as a special case of the multiphase three-phase flow for simulation studies of unconventional oil or gas reservoirs.

A multiphase system of oil, gas, and water in a porous or fractured unconventional reservoir is assumed similar to what is described in a dead-oil model, composed of two phases: gaseous and aqueous phases, oil and aqueous phases, or three phases: oil, gaseous, and aqueous phases. For simplicity, the oil, gas, and water components are assumed present only in their own associated phases, and adsorbed gas is within the solid phase of the rock. Each fluid phase flows in response to pressure, gravitational, and capillary forces according to the multiphase extension of Darcy's law or extended Darcy or non-Darcy flow laws for incorporation of geo-mechanical, Klinkenberg, or other nonlinear effects. In an isothermal system containing three mass components, oil, gas, and water, subject to multiphase flow and gas adsorption, three mass-balance equations are needed to fully describe the system in an arbitrary flow region of a porous or fractured medium of an unconventional reservoir domain for flow of phase β,

$$\frac{\partial}{\partial t}\left(\phi\, S_\beta\, \rho_\beta + m_{\mathrm{g}}\right) = -\nabla\cdot\left(\rho_\beta \boldsymbol{v}_\beta\right) + q_\beta \tag{12.11}$$

in which the same notations and symbols are used as those in the other chapters, i.e., ϕ is the effective porosity of porous or fractured media; S_β is the saturation of fluid β; ρ_β is the density of fluid β; $\boldsymbol{v}_\beta$ is the volumetric velocity vector of fluid β, determined by Darcy's law, non-Darcy's flow models, or Eqn (12.10); t is time; m_{g} is the adsorption or desorption mass term only for gas component per unit volume of formation; and q_β is the sink/source term of phase (component) β per unit volume of formation.

12.4 NUMERICAL FORMULATION AND SOLUTION

As discussed previously, the Partial Differential Equation (PDE), Eqn (12.11), which governs oil, gas, and water flow in tight or shale petroleum reservoirs, is nonlinear. In addition, multiphase fluid flow in unconventional reservoirs is subject to many other nonlinear flow processes, such as rock deformation, adsorption, and the Klinkenberg effect. In general, the nonlinear flow-governing equation needs to be solved using a numerical approach. The following numerical formulation and solution follow the same methodology for reservoir simulation, as discussed and used in Chapters 4 and 9 to 11, i.e., using numerical approaches to simulate oil, gas, and water flow in the three steps: (1) spatial discretization of mass conservation equations; (2) time discretization; and (3) iterative approaches to solve the resulting nonlinear, discrete algebraic equations.

12.4.1 Discrete Equations

The three-phase or three-component mass-balance Eqn (12.11) is discretized in space using a control-volume or integrated finite difference concept (Pruess et al., 1999; Wu et al., 2014). Time discretization is carried out using a backward, first-order, fully implicit finite-difference scheme. The discrete nonlinear equations for components of oil, gas, and water at grid block or node i can be written in a general form:

$$\left\{\left[(\phi\rho S)+m_{\mathrm{g}}\right]_i^{\beta,n+1}-\left[(\phi\rho S)+m_{\mathrm{g}}\right]_i^{\beta,n}\right\}\frac{V_i}{\Delta t}=\sum_{j\in\eta_i} flow_{ij}^{\beta,n+1}+Q_i^{\beta,n+1}$$

$$(\beta=\mathrm{o},\mathrm{g}\ \text{ and }\ \mathrm{w})\ \text{ and }\ (i=1,2,3,\ldots,N) \tag{12.12}$$

in which superscript β serves also as an equation index for oil, gas, and water phase or components with $\beta = \mathrm{o}$ for oil, g for gas, and w for water; superscript n denotes the previous time level, with $n+1$ the current time level to be solved; subscript i refers to the index of grid block or node i, with N being the total number of nodes in the grid; Δt is time step size; V_i is the volume of node i; η_i contains the set of direct neighboring nodes (j) of node i; m_{g}, $flow_{ij}^{\beta}$, and Q_i^{β} are the absorption or desorption of gas, the phase/component mass "flow" term between nodes i and j, and sink/source term at node i for phase/component β, respectively.

The "flow" terms in Eqn (12.12) are mass fluxes by advective processes and are described by Darcy's law or non-Darcy flow equation as in Eqn (12.10),

When Darcy's law is applicable, by a discrete version of Darcy's law, i.e., the mass flux of fluid phase β along the connection is given by

$$flow_{ij}^{\beta} = \left(\rho_{\beta}\lambda_{\beta}\right)_{ij+1/2}^{n+1}\gamma_{ij}\left(\Phi_{\beta j}^{n+1} - \Phi_{\beta i}^{n+1}\right) \tag{12.13}$$

in which the notations and symbols are the same as in Section 4.2, i.e., $\lambda_{\beta,ij\,+\,1/2}$ is the mobility term to phase β, defined as

$$\lambda_{\beta,ij+1/2} = \left(\frac{k_{r\beta}}{\mu_{\beta}}\right)_{ij+1/2} \tag{12.14}$$

γ_{ij} is transmissivity, defined as in Eqn (4.9),

$$\gamma_{ij} = \frac{A_{ij}\ k_{ij+1/2}}{d_i + d_j} \tag{12.15}$$

12.4.2 Treatment of Coupled Physical Processes

Several key factors and processes, as discussed in Section 12.2, for multiphase fluid flow in unconventional reservoir porous media are incorporated into our numerical model formulation in this section. In addition, relative permeability is assumed as functions of fluid saturation, when multiphase flow Darcy's law or multiphase non-Darcy flow are concerned.

Geomechanical effect: There are several approaches commonly used for taking into account geomechanical or rock deformation effect on flow and transport in reservoirs. One is the fully coupled, rigorous method (e.g., Winterfeld and Wu, 2014), as discussed in Chapter 11, in which the stress balance equation is solved simultaneously with mass conservation equations. The other approach includes a simplified one, decoupled from solving the stress equation or stress field predetermined in advance. The applicability of this simple geomechanical coupling model in multiphase flow simulation for rock deformation effect requires that the initial distribution of effective stress or total stress field be predetermined as a function of spatial coordinates and pressure fields. In practice, the stress distribution may be estimated analytically, numerically, or from field measurements, because changes in effective stress are primarily caused by changes in reservoir pressure during production. This decoupled model may be applicable for coupling multiphase gas flow with rock deformation in stress-sensitive formations in numerical simulation. The favorite condition is when the *in situ* total stress in reservoirs remains almost constant or a function of spatial coordinates as well as fluid pressure

only. If the *in situ* total stress is controlled mainly by the weight of overlain rock mass, such as in a deep reservoir with relative thin production layers, this decoupled model will also provides a good approximation.

In this simple geomechanical model, effects of rock deformation on fluid flow can be evaluated using the coupling equations of effective porosity, absolute permeability, and capillary pressure in Section 12.2.1 with the effective mean stress concept. To include the effect of geomechanics or rock deformation in an unconventional reservoir, it is important to determine those correlations, in particular, for porosity and permeability, such as Eqns (12.3) and (12.4), as functions of mean effective stress from laboratory or field studies. The key procedure to incorporate the geomechanical effect in this simple coupling approach is as follows:

- Calculate effective stress or the changes at each Newton iteration as functions of fluid pressure according to Eqns (12.1) and (12.2),
- Calculate porosity, permeability, and capillary pressure using correlations, Eqns (12.3), (12.4), and (12.6), which are functions of the mean stress,
- Substitute the modified porosity, permeability, and capillary-pressure values in calculation of the accumulation term, flow potential, and flow or transmissivity terms in Eqns (12.12), (12.13), and (12.15).

Klinkenberg Effect: The Klinkenberg effect mainly influences gas flow by an enhanced gas permeability. To incorporate the Klinkenberg effect, which is mathematically expressed in Eqn (12.7), instead of varying the absolute transmissivity of Eqn (12.15), the mobility term to the gas phase in Eqn (12.14) is modified as

$$\lambda_{g,ij+1/2} = \left[\frac{k_{rg}}{\mu_g}\left(1 + \frac{b(P_g)}{p_g}\right)\right]_{ij+1/2} \tag{12.16}$$

The reason why the Klinkenberg effect is added in the mobility term instead of the transmissibility term is that the Klinkenberg effect is pressure dependent. Its value will change with the change of grid-block pressure during numerical calculation. In a numerical simulator, transmissibility terms for each connection are often calculated only once at the beginning and then these values are saved for the entire simulation. By contrast, the mobility term is changed with simulation at each Newtonian iteration step.

Note that for gas flow between two grid blocks: i and j, there are two permeability values calculated for the connection of $ij + 1/2$, one for each grid block. Therefore, a proper weighting of the two absolute permeabilities after the Klinkenberg correction is needed. In our simulation studies,

an upstream weighting method is applied to obtain the average of these two permeabilities.

Gas adsorption/desorption: Gas adsorption or desorption is treated as additional sink or source term to store with increase in pressure and release gas to the free gas in pores with decrease in pressure. As the pressure decreases with continuous gas production from the reservoir, adsorbed gases are released continuously and contribute to the gas production. Thus, the accumulation term in the gas-phase mass-balance Eqn (12.12) includes the adsorption or desorption term, which is evaluated at grid block i as

$$m_{g,i} = \left(\rho_R \rho_g V_L \frac{P_g}{P_g + P_L}\right)_i \tag{12.17}$$

in which m_g is absorbed gas mass per unit formation volume at grid block i.

Nonlinear and non-Darcy flow: Under the high-velocity, non-Darcy-flow condition in a medium, if the Forchheimer Equation is selected to describe the high-flow rates in the medium, the mass-flow term ($flow_{\beta,ij}$) in Eqn (12.13) along the connection (i,j), between grid blocks i and j, is replaced by Eqn (8.57) of Chapter 8. For the non-Darcy flow described by the Barree and Conway model, the mass-flow term of Eqn (12.13) is evaluated using Eqn (8.59). In general, if a particular form or expression of Eqn (12.10) is determined for a specific reservoir or type of porous media, this correlation should accordingly be used for modeling flow between the connected grid blocks of the porous medium.

Multiple types of porosity and fractures: Handling multiphase flow in multiple porosity and various-type fractures in shale and tight formations is critical in unconventional reservoir simulation, because oil and gas production from such low-permeability formations relies on the interporosity flow and the flow through variously scaled fractures, from microfractures, natural fractures, to hydraulic fractures, to provide flow channels for fluid flow into producing wells. Therefore, any unconventional simulation model must have the capability of handling fractures, fractured media, and multiporosity flow. The published modeling exercises in the literature have paid a lot of attention to modeling fractures in shale gas formations using different conceptual and modeling approaches (e.g., Cipolla et al., 2009, 2010; Moridis et al., 2010; Rubin, 2010; Freeman et al., 2011, 2013; Hinkley et al., 2013; Yao et al., 2013; Wu et al., 2014).

The multicontinuum modeling approach, as discussed in Chapter 9, includes many conceptual models of multiple porosity; multiple permeability; MINC, and explicit fracture as well as the single-porosity medium.

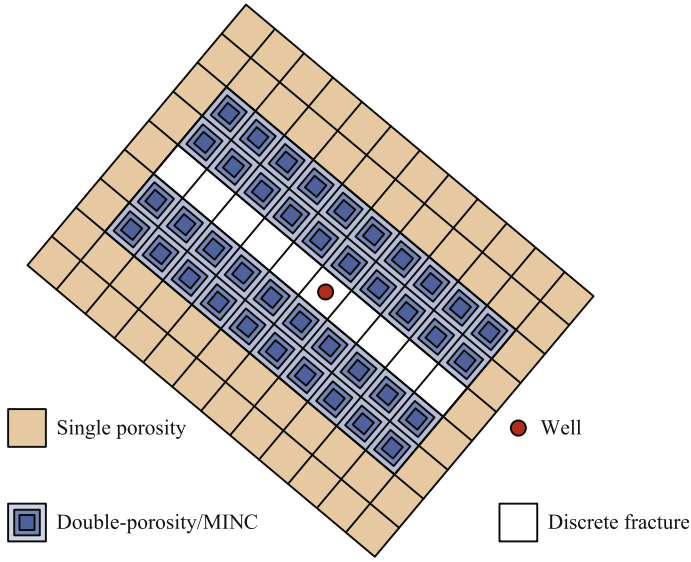

Figure 12.3 Schematic of a hybrid fracture model, coupling fluid flow and geomechanics for a hydraulically fractured reservoir system *(Modified from Wu and Fakcharoenphol (2011))*.

The multicontinuum model should apply for description of the flow between multiple porosities and various-scaled fractures in unconventional reservoirs. A hybrid-fracture modeling approach, defined as a combination of explicit-fracture (discrete-fracture model), MINC, and single-porosity modeling approaches (Wu and Fakcharoenphol, 2011), as shown in Figure 12.3, seems the best option for modeling a tight or shale reservoir with both hydraulic fractures and natural fractures. This is because hydraulic fractures, which have to be dealt with for unconventional oil and gas production, are better handled by the explicit fracture method. Note that hydraulic fractures cannot be modeled in general by a dual-continuum model, because of their sparse distribution in space. On the other hand, naturally fractured reservoirs are better modeled by a dual- or multicontinuum approach, such as MINC, for extremely low-permeability matrix in shale gas formations, which cannot be easily handled by an explicit-fracture model. In addition, if there exists heterogeneity in matrix blocks, as shown in Figure 12.3, these matrix blocks are then treated as multiporosity media with small fractures, vugs, organic and inorganic portions, or heterogeneous porous zones.

12.4.3 Numerical Solution

We use the fully implicit scheme and Newton iteration to solve the discrete nonlinear Eqn (12.12). Let us write the discrete nonlinear equation, Eqn (12.12), in a residual form as

$$R_i^{\beta,n+1} = \left\{ \left[(\phi\rho S) + m_g \right]_i^{\beta,n+1} - \left[(\phi\rho S) + m_g \right]_i^{\beta,n} \right\} \frac{V_i}{\Delta t} - \sum_{j\in\eta_i} flow_{ij}^{\beta,n+1} - Q_i^{\beta,n+1} = 0 \quad (\beta = \mathrm{o, g \ and \ w}) \ \text{and} \ (i = 1, 2, 3, \ldots, N) \tag{12.18}$$

Equation (12.18) defines a set of $3 \times N$ coupled nonlinear equations that need to be solved for every balance equation of mass components of oil, gas, and water, respectively. In general, three primary variables per node are needed to use the Newton iteration for the associated three equations per node. The primary variables selected are gas pressure and oil and gas saturation. The rest of the dependent variables, such as relative permeability, capillary pressures, mean stress, viscosity and densities, adsorption term, as well as nonselected pressure and saturation, are treated as secondary variables, which are calculated from selected primary variables.

In terms of the primary variables, the residual equation, Eqn (12.18), at a node i is regarded as a function of the primary variables at not only node i, but also at all its direct neighboring nodes *j*. The Newton iteration scheme gives rise to

$$\sum_m \frac{\partial R_i^{\beta,n+1}(x_{m,p})}{\partial x_m} (\delta x_{m,p+1}) = -R_i^{\beta,n+1}(x_{m,p}) \tag{12.19}$$

in which x_m is the primary variable m with $m = 1$, 2, and 3, respectively, at node i and all its direct neighbors; p is the iteration level; and $i = 1, 2, 3, \ldots, N$. The primary variables in Eqn (12.19) need to be updated after each iteration,

$$x_{m,p+1} = x_{m,p} + \delta x_{m,p+1} \tag{12.20}$$

The Newton iteration process continues until the residuals $R_i^{\beta,n+1}$ or changes in the primary variables $\delta x_{m,p+1}$ over iteration are reduced below preset convergence tolerances.

12.5 MODEL APPLICATION

In this section, we present one application example to demonstrate the application of the mathematical model and numerical formulation of this chapter for simulation of shale gas production (Wu et al., 2014). The example problem is conducting sensitivity analysis of key physical processes of shale gas production. In this model application example, we are concerned with gas flow toward one horizontal well with a 10-staged hydraulic fracture system in an extremely tight, uniformly porous and/or fractured reservoir (Figure 12.4). The reservoir contains liquid–gas, two phases; however, the liquid saturation is set at residual values as an immobile phase. This is actually a single-phase gas-flow problem and is modeled by the multiphase-flow model in which the liquid flow is controlled by liquid relative permeability curves as immobile.

To model gas production from a producer with 10-stage hydraulic fractures in a shale gas reservoir, we consider that there exists stress alteration induced by hydraulic fracturing, which may reactivate existing natural fractures, and therefore opens microflow channels in the drainage area of the stimulated well. Here, we present the simulation of a hydraulic fracturing problem as an example to illustrate the capability of the hybrid fracture model to capture such complex fracture network in unconventional reservoirs. Three different conceptual fracture models, as shown in Figure 12.5, are built and simulated, and their flow behavior is compared. The first fracture model (Figure 12.5(a)) considers that there is no natural fractured-active area surrounding the hydraulic fracture and the formation is single-porosity shale with low permeability. In the second model (Figure 12.5(b)), we assume that only the natural fractures within the SRV near the hydraulic fractures are active and the remaining natural fractures outside the SRV remain inactive. An increase in pore pressure around a

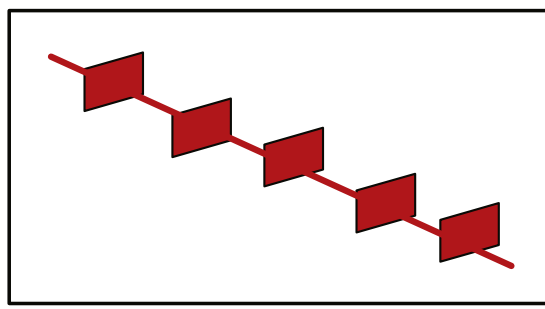

Figure 12.4 Horizontal and multistaged hydraulic fracture model.

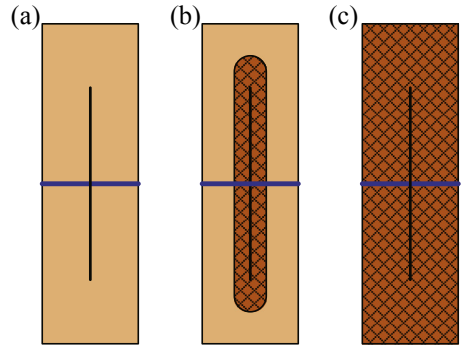

Figure 12.5 Three different conceptual fracture models; from left to right are (a) no natural fracture model, (b) Stimulated Reservoir Volume (SRV) model, and (c) all formation with natural fractures.

hydraulic fracture during the fracturing operation may cause a significant reduction in the effective stress, potentially opening or reactivating the existing healed natural fractures or creating new fractures. As a result, the permeability near hydraulic fractures may be improved. This effect would help increase the well productivity by enhancing flow into hydraulic fractures. The third fracture model (Figure 12.5(c)) is that the entire formation is naturally fractured.

In this example, the hybrid-fracture modeling approach is used, i.e., hydraulic fractures are represented by the discrete fracture model, an active naturally fractured reservoir area is described by the multicontinuum fracture model, whereas a nonactive natural fractured reservoir area is represented by the single-porosity porous medium. The basic parameter set for the simulation and discussion is summarized in Table 12.1, which is selected from representative field data. In analysis of modeling results, we first compare the gas production behavior for these three conceptual fracture models. Then, based on the second fracture model, i.e., reactivated natural fractures only in the SRV, we analyze the cumulative gas production curves with inclusion of Klinkenberg, geomechanical, and adsorption/desorption effects.

Figure 12.6 compares the performance of the fractured horizontal well for the three conceptual fracture models. The comparison indicates that fracture models make a large difference in well performance. The contribution from active natural fractures is evident and helps to yield higher cumulative production rates for a long period of time. Larger stimulated reservoir volume with reactivated natural fracture zones leads to higher gas

Table 12.1 Fluid and rock parameters and production data used for the example problem

Parameters, symbols, units	Value
Reservoir length, Δx, ft	5500
Reservoir width, Δy, ft	2000
Formation thickness, Δz, ft	250
Reservoir depth, h, ft	5800
Reservoir temperature, T, °F,	200
Initial reservoir pressure, P_i, psi	3800
Horizontal well length, L_h, ft	4800
Constant flowing bottomhole pressure, P_{wf}, psi	1000
Hydraulic fracture number	10
Distance between hydraulic fractures, $2y_e$, ft	500
Hydraulic fracture porosity, ϕ_{hf}	0.5
Hydraulic fracture total compressibility, c_{hf}, psi^{-1}	2.5×10^{-4}
Hydraulic fracture permeability, k_{hf}, md	1.0×10^{5}
Natural fracture porosity, ϕ_{nf}	0.001
Natural fracture total compressibility, c_{nf}, psi^{-1}	2.5×10^{-4}
Natural fracture permeability, k_{nf}, md	1600
Matrix total compressibility, c_{tm}, psi^{-1}	2.5×10^{-4}
Matrix permeability, k_m, md	3.2×10^{-5}
Matrix porosity, ϕ_m	0.05
Viscosity, μ, cP	0.0184
Langmuir's volume, V_L, scf/ton	77.56
Langmuir's pressure, P_L, psi	2285.7
Non-Darcy flow constant, β, m^{-1}	1.29×10^{6}
Hydraulic fracture half-length, X_f, ft	250

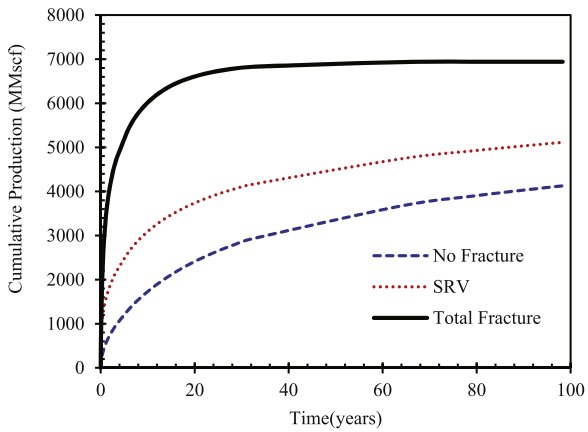

Figure 12.6 Simulated gas production performance for the three fracture models.

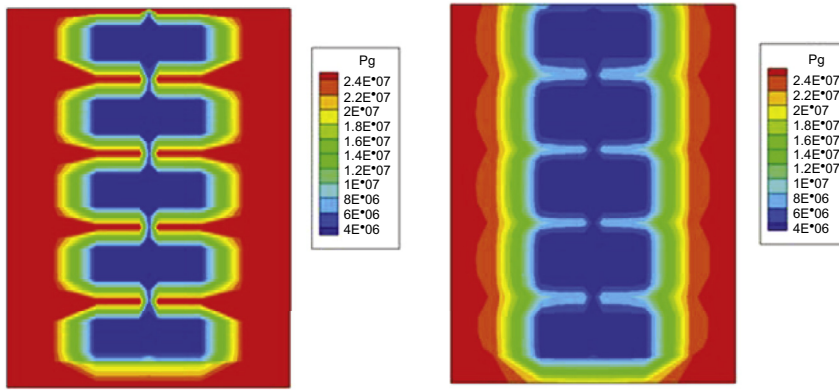

Figure 12.7 Pressure (Pa) distributions at one year (left) and 20 years (right) of fracture model #2.

production rates. For the second fracture model, pressure distribution at one year and 20 years are presented in Figure 12.7.

Figure 12.8 shows a comparison of the cumulative production between cases with and without the Klinkenberg effect. Here the Klinkenberg b-factor is not handled as a constant value, but changing with matrix permeability and gas pressure. As shown in Table 12.1, the input matrix permeability is 3.2×10^{-5} mD and the initial reservoir pressure is 3800 psi. With this permeability value and under higher pressure, the Klinkenberg

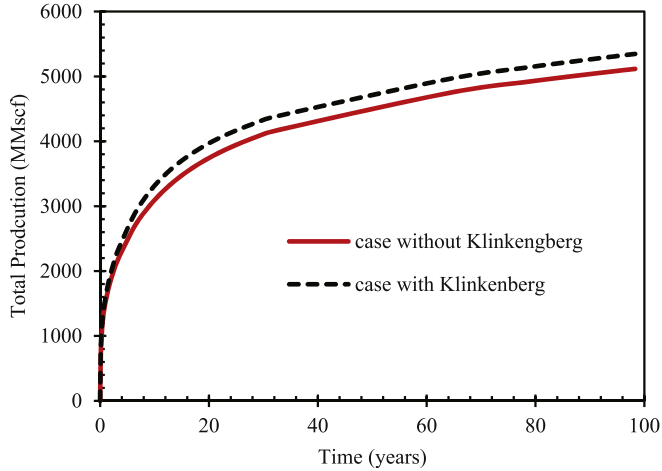

Figure 12.8 Gas cumulative production behavior with and without including the Klinkenberg effect.

effect will not be expected to have a large influence on the effective permeability for gas flow. However, the constant bottom-hole production pressure is set as 1000 psi, which is much smaller than the initial reservoir pressure. With the pressure of the area near the wellbore and hydraulic fracture decreasing quickly, the Klinkenberg effect becomes important for the flow in this pressure-lowering region. Our simulation results in Figure 12.8 also show the influence from the positive Klinkenberg effect, leading to about 10% increase to the total gas production.

The effect of non-Darcy flow on the gas production of a horizontal well plus multistage hydraulic fractures with natural fractures inside the SRV is shown in Figure 12.9, in which non-Darcy flow is simulated based on the Forchheimer equation. The difference is observed on the gas cumulative production between the case considering non-Darcy flow and that not considering it in the first six years. Not including the non-Darcy flow effect inside the hydraulic fractures could lead to an overestimation of about 5% of cumulative gas production in the first six years. After the first six years, the difference between the two cases diminishes and these two curves coincide at about 40 years, as shown in Figure 12.10.

Figure 12.11 shows the simulated well cumulative production versus time with and without including the geomechanical effects. The relationship used for describing effective stress and permeability of the unconventional reservoir is shown in Figure 11.1 of Chapter 11. As shown in Figure 12.11, geomechanical-flow coupling has a large impact on formation permeability,

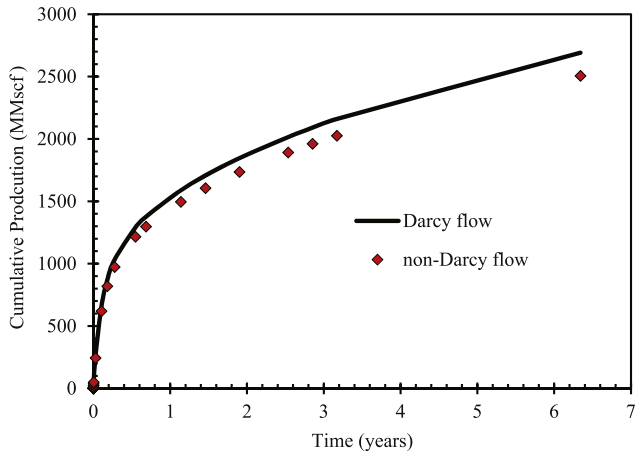

Figure 12.9 Gas cumulative production behavior with and without including the non-Darcy flow effect in the first six years.

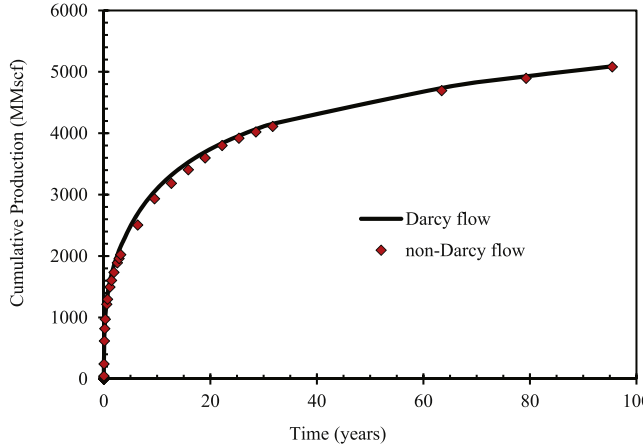

Figure 12.10 Gas cumulative production behavior with and without including the non-Darcy flow effect in 100 years.

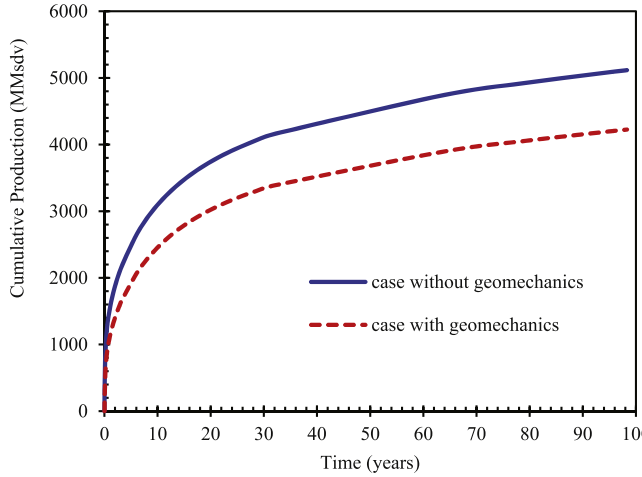

Figure 12.11 Gas cumulative production behaviors with and without including the geomechanical effects.

especially for the natural fracture system. Take the Muska Formation for example, when the effective stress increase from 1600 to 4800 psia, permeability decreases to one-twentieth of its original value. With the gas production, reservoir effective stress increases as pore pressure decreases, leading to the reduction in permeability as well as in cumulative gas production.

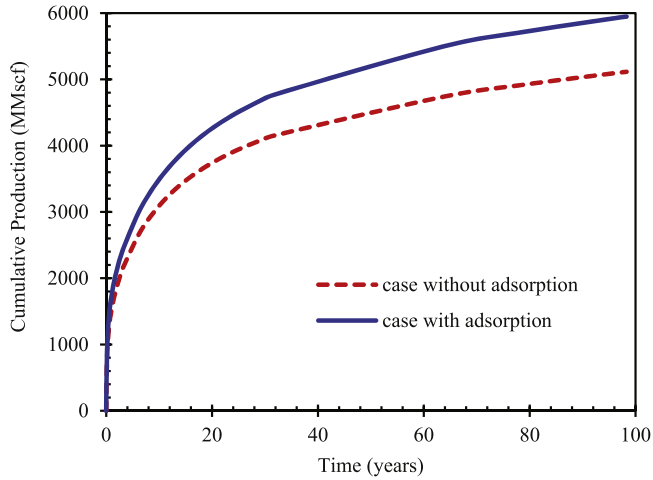

Figure 12.12 Gas cumulative production behaviors with and without considering adsorption.

Figure 12.12 presents the results for adsorption analysis using the numerical model. Based on the data in Table 12.1, we calculate the total gas mass consisting of free gas in the micropores and adsorbed gas at initial condition. The proportion of gas stored in the pore space as free gas is initially about 77%, whereas that stored as adsorption is 23%. Then we compare the cumulative gas production with and without considering adsorption. Simulation results (Figure 12.12) show the estimated gas production will increase with consideration of adsorption. This difference will become more and more evident with production time as pressure decreases.

12.6 SUMMARY AND CONCLUSIONS

This chapter discusses physical processes and mathematical modeling approaches for multiphase fluid flow in unconventional petroleum reservoirs. The mathematical model proposed is based on the current understanding and knowledge in this subject. Compared with flow in conventional reservoirs, multiphase flow in low-permeability unconventional reservoirs is a new topic under study. It is subject to more coupled, complicated physical processes, such as adsorption/desorption of hydrocarbon molecules on rock, nonlinear or non-Darcy flow, strong rock–fluid and fluid–fluid interaction, and effects of geomechanics within nanopores or micro- and natural fractures in rock and flow properties of unconventional formations.

The model formulation presented in this chapter incorporates many known nonlinear flow processes associated with oil and gas production from low-permeability unconventional reservoirs, including rock-deformation, Klinkenberg, non-Darcy flow, and nonlinear adsorption effects. The numerical model formulation and solution scheme are based on a generalized multiphase flow model using unstructured grids to handle heterogeneity and various scaled fractures. Specifically, a hybrid modeling approach is discussed by combining discrete fracture, multidomain, and multicontinuum concepts for handling hydraulic fractures in simulated reservoir volume (SRV), distributed natural fractures, microfractures, as well as heterogeneous porous matrix.

As an application example, we present modeling studies using three types of conceptual fracture models for gas production from a 10-stage hydraulically fractured, horizontal well, incorporating geomechanical, Klinkenberg effect, non-Darcy flow, and nonlinear adsorption effects. The model results show that there is a large impact of various fracture patterns on gas production rates as well as cumulative production.

There is a need for further development of fundamental and mechanistic understandings of hydrocarbon storage, flow, and transport in shale pores with multiple length scales and other tight rocks in unconventional reservoirs. This is because our current understandings are very limited. Without these in-depth understandings and related improved technologies, current production of unconventional fossil energy from shale or tight formations will not be sustainable for its potential as the main energy source to the world. This is because of low recovery rates, high cost, and significant environmental concerns with current approaches, i.e., massive horizontal drillings and extensive formation stimulations. The complexity of storage, flow, and transport in shale and tight formations requires more studies of multiple disciplinary research for understanding hydrocarbon storage, flow, and transport mechanisms to develop new technologies and efficient approaches for enhancing oil and gas recovery from such unconventional reservoirs.

REFERENCES

Akkutlu, I.Y., Fathi, E., 2012. Multiscale gas transport in shales with local kerogen heterogeneities. SPE Journal 17 (04), 1002–1011.

Alharthy, N.S., Nguyen, T., Kazemi, H., Teklu, T., Graves, R., 2013. Multiphase compositional modeling in small-scale pores of unconventional shale reservoirs. In: SPE Annual Technical Conference and Exhibition. Society of Petroleum Engineers, New Orleans, Louisiana, USA. http://dx.doi.org/10.2118/166306-MS.

Blasingame, T.A., 2008. The characteristic flow behavior of low-permeability reservoir systems. In: SPE Unconventional Reservoirs Conference. Keystone, Colorado, USA. http://dx.doi.org/10.2118/114168-MS.

Burns, C., Topham, A., Lakani, R., 2012. The challenges of shale gas exploration and appraisal in Europe and North Africa. In: SPE/EAGE European Unconventional Resources Conference and Exhibition, pp. 20–22. http://dx.doi.org/10.2118/151868-MS. Vienna, Austria.

Cipolla, C.L., Lolon, E., Erdle, J., Tathed, V.S., 2009. Modeling well performance in shale-gas reservoirs. In: SPE/EAGE Reservoir Characterization and Simulation Conference. Society of Petroleum Engineers, Abu Dhabi, UAE. http://dx.doi.org/10.2118/125532-MS.

Cipolla, C.L., Lolon, E.P., Erdle, J.C., Rubin, B., 2010. Reservoir modeling in shale-gas reservoirs. SPE Reservoir Evaluation & Engineering 13 (04), 638–653. http://dx.doi.org/10.2118/125530-PA.

EIA, U.S., 2011. International Energy Outlook 2011.

Ertekin, T., King, G.A., Schwerer, F.C., 1986. Dynamic gas slippage: a unique dual-mechanism approach to the flow of gas in tight formations. SPE Formation Evaluation 1 (01), 43–52.

Freeman, C.M., Moridis, G., Ilk, D., Blasingame, T.A., 2013. A numerical study of performance for tight gas and shale gas reservoir systems. Journal of Petroleum Science and Engineering 108, 22–39.

Freeman, C.M., Moridis, G.J., Blasingame, T.A., 2011. A numerical study of microscale flow behavior in tight gas and shale gas reservoir systems. Transport in Porous Media 90 (1), 253–268.

Gao, M., Peng, X., Shen, J., 1994. Polymer Langmuir-Blodgett film of organic-inorganic (Fe_2O_3) composite microgel. Thin Solid Films 248 (1), 106–109.

Hinkley, R.E., Wang, Q., Wang, K., Camilleri, D., Fleming, G., Watts, J.W., 2013. Flexible and efficient n-porosity, full-featured simulator design, and application. In: SPE Reservoir Simulation Symposium. Society of Petroleum Engineers, The Woodlands, Texas, USA. http://dx.doi.org/10.2118/163619-MS.

Holditch, S.A., 2006. Tight gas sands. Journal of Petroleum Technology 58 (6), 86–93.

Javadpour, F., 2009. Nanopores and apparent permeability of gas flow in mudrocks (shales and siltstone). Journal of Canadian Petroleum Technology 48 (08), 16–21.

Kelkar, M.G., Atiq, M., 2010. Upgridding method for tight gas reservoirs. In: SPE Annual Technical Conference and Exhibition. Society of Petroleum Engineers, Florence, Italy. http://dx.doi.org/10.2118/133301-MS.

Klinkenberg, L.J., 1941. The permeability of porous media to liquids and gases. In: Drilling and Production Practice. American Petroleum Institute.

Langmuir, I., 1918. The adsorption of gases on plane surfaces of glass, mica and platinum. Journal of the American Chemical Society 40 (9), 1361–1403.

Leverett, M.C., 1941. Capillary behavior in porous solids. Transactions of the AIME 142 (01), 152–169.

Mengal, S.A., Wattenbarger, R.A., 2011. Accounting for adsorbed gas in shale gas reservoirs. In: SPE Middle East Oil and Gas Show and Conference. Society of Petroleum Engineers, Manama, Bahrain. http://dx.doi.org/10.2118/141085-MS.

MIT, 2011. The Future of Natural Gas: An Interdisciplinary MIT Study. Massachusetts Institute of Technology, Cambridge, MA.

Moridis, G.J., Blasingame, T.A., Freeman, C.M., 2010. Analysis of mechanisms of flow in fractured tight-gas and shale-gas reservoirs. In: SPE Latin American and Caribbean Petroleum Engineering Conference. Society of Petroleum Engineers, Lima, Peru. http://dx.doi.org/10.2118/139250-MS.

Moridis, G.J., Freeman, C.M., 2014. The RealGas and RealGasH_2O options of the TOUGH+ code for the simulation of coupled fluid and heat flow in tight/shale gas systems. Computers & Geosciences 65, 56–71.

Pruess, K., Oldenburg, C.M., Moridis, G.J., 1999. TOUGH2 User's Guide Version 2.

Rubin, B., 2010. Accurate simulation of non Darcy flow in stimulated fractured shale reservoirs. In: SPE Western Regional Meeting. Society of Petroleum Engineers, Anaheim, California, USA. http://dx.doi.org/10.2118/132093-MS.

Silin, D., Kneafsey, T., 2012. Shale gas: nanometer-scale observations and well modelling. Journal of Canadian Petroleum Technology 51 (6), 464–475.

Sun, H., Chawathe, A., Hoteit, H., Shi, X., Li, L., 2015. Understanding shale gas flow behavior using numerical simulation. SPE Journal 20 (01), 142–154. http://dx.doi.org/10.2118/167753-PA.

Wang, F.P., Reed, R.M., Jackson, J.A., Jackson, K.G., 2009. Pore networks and fluid flow in gas shales. In: SPE Annual Technical Conference and Exhibition. New Orleans, Louisiana, USA. http://dx.doi.org/10.2118/124253-MS.

Winterfeld, P.H., Wu, Y.-S., 2014. Simulation of CO_2 sequestration in brine aquifers with geomechanical coupling. In: Al-Khoury, R., Bundschuh, J. (Eds.), Computational Models for CO_2 Geo-sequestration & Compressed Air Energy Storage. CRC Press, pp. 275–304.

Wu, Y.-S., Fakcharoenphol, P., 2011. A unified mathematical model for unconventional reservoir simulation. In: SPE EUROPEC/EAGE Annual Conference and Exhibition. Society of Petroleum Engineers, Vienna, Austria. http://dx.doi.org/10.2118/142884-MS.

Wu, Y.-S., Li, J., Ding, D., Wang, C., Di, Y., 2014. A generalized framework model for the simulation of gas production in unconventional gas reservoirs. SPE Journal 19 (05), 845–857.

Yao, J., Sun, H., Fan, D., Wang, C., Sun, Z., 2013. Numerical simulation of gas transport mechanisms in tight shale gas reservoirs. Petroleum Science 10 (4), 528–537.

Yu, W., Sepehrnoori, K., 2014. Simulation of gas desorption and geomechanical effects for unconventional gas reservoirs. Fuel 116, 455–464.

APPENDIX A

Program of Buckley-Leverett Solution in a One-dimensional Linear System

A.1 MATLAB CODE OF WELGE GRAPHIC METHOD

This Matlab code is a computational program realization of the Welge graphic method (Section 5.4.2) for Buckley–Leverett equation (Eqn (5.28) in Section 5.4.1).

```
%% Problem description
%  Analytical solution of Buckley-Leverett equation using Welge method
%  Brooks-Corey type relative permeability curves are used
close all; clear all; clc;

%% 1 Parameters initialization
% 1.1 rock properties
L       = 100.0;              % domain length [m]
A       = 1.0;                % area of cross-section [m^2]
phi     =  0.25;              % porosity
k       = 9.869e-12;          % absolute permeability [m^2]
theta   = pi*0.0;             % angle: x-direction vs horizontal[rad]

% 1.2 fluid properties
muo     = 5.0e-3;             % oil phase viscosity [Pa*s]
muw     = 1.0e-3;             % water phase viscosity [Pa*s]
rho_o   = 0.8e3;              % oil density [kg/m^3]
rho_w   = 1.0e3;              % water density [kg/m^3]
dlt_rho = rho_w-rho_o;        % density difference [kg/m^3]

% 1.3 relative permeability parameters
Sor     = 0.10;               % residual oil saturation
Swc     = 0.10;               % connate water saturation
no      = 1.00;               % exponent of oil phase
nw      = 2.00;               % exponent of water phase
kro_max = 0.80;               % maximum permeability of oil phase
krw_max = 0.80;               % maximum permeability of water phase
```

```
% 1.4 other initial parameters
dlt_Sw    = 1e-3;                          % constant saturation step
Sw        = [(Swc+eps):dlt_Sw:(1-Sor)]';   % water saturation vector
qt        = 1.0e-4;                        % constant water injection rate [m^3/s]
g         = 9.8067;                        % gravity acceleration constant [m/s^2]
time0     = 86400*0.1;                     % initial calculation time [s]
timef     = 86400*1.0;                     % final calculation time [s]
nts       = 4;                             % time steps for calculating
nsw       = size(Sw,1);                    % number of water saturation vector
format    = '%4.2e';                       % precision format for plotting legend

%% 2 Relative permeabilities, fractional flow function and its derivative
% 2.1 initialization of function handles
kr_w = @(S) krw_max.*((  S-Swc)/(1-Swc-Sor)).^nw;  % relative  permeability of water
kr_o = @(S) kro_max.*((1-S-Sor)/(1-Swc-Sor)).^no; % relative permeability of oil
mob  = @(S) (kr_o(S)./muo).*(muw./kr_w(S));          % mobility function
f_w  = @(S) 1./(1+mob(S))-A*k.*kr_o(S)./...          % fractional flow function fw
    (qt*muo)*dlt_rho*g*sin(theta)./(1+mob(S));
df_w = @(S) ((nw.*mob(S)./(S-Swc))+(no.*mob(S))...  % derivate of fw
     ./(1-S-Sor))./(1+mob(S)).^2+A*k.*kr_o(S)*no*dlt_rho*g*sin(theta)./...
     ((1-S-Sor)*qt*muo.*(1+mob(S)))+A*k.*kr_o(S)*dlt_rho*g*sin(theta)./...
     (qt*muo.*(1+mob(S)).^2).*(((nw.*mob(S)./(S-Swc))+(no.*mob(S))./...
     (1-S-Sor))./(1+mob(S)).^2);

% 2.2 relative permeability and fractional flow vectors
krw = kr_w(Sw);                          % relative permeability vector of water
kro = kr_o(Sw);                          % relative permeability vector of oil
fw  = f_w (Sw);                          % fractional flow vector
dfw = df_w(Sw);                          % fractional flow derivate vector

%% 3 Calculate advance frontal water saturation
% 3.1 Evaluate advance frontal water saturation Swf
[index, Swf, dfwf, bf] = calSatFront(Sw, fw, dfw);

% 3.2 Calculate the time when Swf reaches at production well
krw_swf = kr_w(Swf);
kro_swf = kr_o(Swf);
fw_swf  = f_w (Swf);
dfw_swf = df_w(Swf);
t_pw    = A*phi*L/(qt*dfw_swf);
%% 4 Calculate water saturation profile
t    = linspace(time0, timef, nts);
dfwt = dfw(end:-1:index);                % inverted sequence of dfw
Swt  =  Sw(end:-1:index);                % inverted sequence of Sw
for ti = 1:nts
    for i = 1:(nsw-index+1)
        Xsw(i,ti) = qt*t(ti)/(A*phi)*dfwt(i);
    end
end
```

```
%% 5 Plot results
% 5.1 Plot the relative permeability curves
h_fig1 = figure(1);
set(h_fig1, 'color', 'w', 'NumberTitle', 'off', 'Name', 'Relative Permeability
Curves: kr');
plot(Sw, krw, '-b', Sw, kro, '-r', 'LineWidth', 2.0);
axis([0.0 1.0 0.0 1.0]);
axis square;
set(gca, 'Fontname', 'Times New Roman','FontSize',10);
title('Relative permeability curves')
xlabel('{\it S}_w');
ylabel('{\it k}_{r {\it \beta}}');
set(gca, 'YTick', 0:0.2:1);
h_legend1 = legend('water phase', 'oil phase');
set(h_legend1,'Box', 'on', 'Location', 'best');

% 5.2 Plot the fractional flow function curve
h_fig2 = figure(2);
set(h_fig2, 'color', 'w', 'NumberTitle', 'off', 'Name', 'Fractional Flow Curve fw');
plot(Sw, fw, '-b', 'LineWidth', 2.0);
hold on;
plot(Sw, (dfwf.*Sw+bf), '-r', 'LineWidth', 2.0);
plot(Swc, 0, 'ro', 'Markersize', 8);
plot(Swf, fw(index), 'ro', 'Markersize', 8);
plot([Swf Swf], [0 fw(index)], '--r', 'LineWidth', 1.5);
plot([0 Swf], [fw(index) fw(index)], '--r', 'LineWidth', 1.5);
axis([0.0 1.0 0.0 1.0]);
axis square;
set(gca, 'Fontname', 'Times New Roman','FontSize',10);
title('fractional flow function curve')
xlabel('{\it S}_w');
ylabel('{\it f}_w');
set(gca, 'YTick', 0:0.2:1);

% 5.3 Plot the derivate curve of fractional flow function
h_fig3 = figure(3);
set(h_fig3, 'color', 'w', 'NumberTitle', 'off', 'Name', 'Derivatives of Fractional
Flow Curve dfw/dSw');
plot(Sw, dfw, '-b', 'LineWidth', 2.0);
set(gca, 'XLim', [0 1]);
set(gca, 'Fontname', 'Times New Roman','FontSize',10);
title('(c) derivatives of fractional flow function')
xlabel('{\it S}_w');
ylabel('d {\it f}_w / d {\it S}_w');
axis square;

% 5.4 Plot the water saturation profiles
h_fig4 = figure(4);
set(h_fig4, 'color', 'w', 'NumberTitle', 'off', 'Name', 'Water Saturation Profiles');
```

```
SwTime= [];
for ti = 1:nts
    plot(Xsw(:,ti), Swt, '-r', 'LineWidth', 2.0);
    hold on;
    plot([0 Xsw(1,ti)], [1-Sor 1-Sor], '-r', 'LineWidth', 2.0);
    SwTime = [ SwTime; ['Time = ' num2str(t(ti)/86400, format) ' day'] ];
    plot([Xsw(end,ti) Xsw(end,ti)], [Swf Swc], '-r', 'LineWidth', 2.0);
    plot([Xsw(end,ti) L], [Swc Swc], '-r', 'LineWidth', 2.0);
end
set(gca, 'YLim', [0 1], 'YTick', 0:0.2:1, 'XLim', [0 L]);
set(gca, 'Fontname', 'Times New Roman','FontSize',10);
title('(d) water saturation profiles')
xlabel('{\it x} (m)');
ylabel('{\it S}_w');
h_legend2 = legend(SwTime);
set(h_legend2,'Box', 'on', 'Location', 'best');
axis square;

%% end
```

A.2 MATLAB CODE OF INTEGRAL METHOD BASED ON MASS BALANCE PRINCIPLE

This Matlab code is a computational program realization of the integral method based on mass balance principle (Section 5.4.4) for Buckley–Leverett equation (Eqn (5.28) in Section 5.4.1). The calculation of pressure profile (Section 5.5.3) is also included in this code.

```
%% Problem description
% Analytical solution of Buckley-Leverett equation using integral method
% wetting phase fluid displacing non-wetting phase fluid
% Brooks-Corey relative permeability curve has been applied
close all; clear all; clc;

%% 1 Parameters initialization
% 1.1 rock properties
L       = 5.0;                          % domain length [m]
A       = 1.0;                          % area of cross-section [m^2]
phi     = 0.30;                         % porosity [-]
k       = 9.869e-12;                    % absolute permeability [m^2]
theta   = pi*0.0;                       % angle: x-direction vs horizontal [rad]

% 1.2 fluid properties
muo      = 5.0e-3;                      % oil phase viscosity [Pa*s]
muw      = 1.0e-3;                      % water phase viscosity [Pa*s]
rho_o    = 0.8e3;                       % oil density [kg/m^3]
rho_w    = 1.0e3;                       % water density [kg/m^3]
dlt_rho  = rho_w-rho_o;                 % density difference [kg/m^3]
```

```
% 1.3 relative permeability parameters
Sor     = 0.20;                          % residual oil saturation
Swc     = 0.20;                          % connate water saturation
no      = 2.00;                          % exponent of oil phase
nw      = 2.00;                          % exponent of water phase
kro_max = 0.75;                          % maximum permeability of oil
krw_max = 0.75;                          % maximum permeability of water

% 1.4 other initial parameters
dlt_Sw = 1e-3;                           % constant saturation step
Sw     = [(Swc+eps):dlt_Sw:(1-Sor)]';    % water saturation vector
qt     = 5.0e-4;                         % constant water injection rate [m^3/s]
g      = 9.8067;                         % gravity acceleration constant [m/s^2]
time0  = 3600*0.02;                      % initial calculation time [s]
timef  = 3600*0.20;                      % final calculation time [s]
nts    = 4;                              % time steps for calculating
nsw    = size(Sw,1);                     % number of wetting saturation vector
format = '%4.2e';                        % precision format for plotting legend

%% 2 Relative permeabilities, fractional flow function and its derivative
% 2.1 initialization of function handles
kr_w = @(S) krw_max.*((  S-Swc)/(1-Swc-Sor)).^nw;   % relative permeability of water
kr_o = @(S) kro_max.*((1-S-Sor)/(1-Swc-Sor)).^no;   % relative permeability of oil
mob  = @(S) (kr_o(S)./muo).*(muw./kr_w(S));         % mobility function
f_w  = @(S) 1./(1+mob(S))-A*k.*kr_o(S)./(qt*muo)*... % fractional flow function fw
    dlt_rho*g*sin(theta)./(1+mob(S));
df_w = @(S) ((nw.*mob(S)./(S-Swc))+(no.*mob(S))./(1-S-Sor))... % derivative of fw
   ./(1+mob(S)).^2+A*k.*kr_o(S)*no*dlt_rho*g*sin(theta)./...
   ((1-S-Sor)*qt*muo.*(1+mob(S)))+A*k.*kr_o(S)*dlt_rho*g*sin(theta)./...
   (qt*muo.*(1+mob(S)).^2).*...
   (((nw.*mob(S)./(S-Swc))+(no.*mob(S))./(1-S-Sor)).*(1+mob(S)).^2);

% 2.2 relative permeability and fractional flow vectors
krw  = kr_w(Sw);                         % relative permeability vector of water
kro  = kr_o(Sw);                         % relative permeability vector of oil
 fw  =  f_w(Sw);                         % fractional flow vector
dfw  = df_w(Sw);                         % fractional flow derivate vector

%% 3 Calculate advance frontal saturation and travelling distance
% 3.1 calculate travelling distance of every saturations
t  = linspace(time0, timef, nts);
dfwt = dfw(end:-1:1);                    % inverted sequence of dfw
fwt  =  fw(end:-1:1);                    % inverted sequence of fw
Swt  =  Sw(end:-1:1);                    % inverted sequence of Sw
for ti = 1:nts
    Wi(ti) = qt*t(ti);                   % injected wetting phase fluid volume
    for i = 1:nsw
       Xsw(i,ti) = qt*t(ti)/(A*phi)*dfwt(i); % calculate travelling distance
    end
```

```
    Xsw0 = [0; Xsw(1:end-1,ti)]; % the 2nd travelling distance vector
    dlt_Xsw = Xsw(:,ti) - Xsw0;    % dlt_Xsw = Xsw_j - Xsw_(j-1), x_0 = 0
    dlt_Swt = Swt - Swc;           % dlt_Swt = Swt,j - Swc
    for i = 1:nsw
        % calculate the injected fluid volume from 0 to Xswf
        Vi = A*phi*sum(dlt_Xsw(1:i).*dlt_Swt(1:i));
        if Vi >= Wi(ti)
            index(ti) = i;            % index of the Swf in Swt
            Swf(ti)   = Swt(i);       % advance front saturation: Swf
            Xswf(ti)  = Xsw(i,ti);    % the position of Swf
            break;
        end
    end
end
Xsw = Xsw(1:index(1),:);
Swt = Swt(1:index(1));

% 3.2 Calculate the time when Swf reaches at production well
krw_swf = kr_w(Swf(1));
kro_swf = kr_o(Swf(1));
 fw_swf =  f_w(Swf(1));
dfw_swf = df_w(Swf(1));
  t_pw   = A*phi*L/(qt*dfw_swf);

% 3.3 calculate pressure profiles
P_pw   = 1e5;
dlt_x  = L/1e2;
x      = [L:-dlt_x:0]';
P      = zeros(size(x,2),nts);
P(1,:)= P_pw;
for ti = 1:nts
    if Xswf(ti) <= L
        for i = 2:size(x,1)
        Swx = calObjFun(x(i), Swt, Xsw(:,ti));
        if Swx <= Swf(ti)
            fwx    = 0;
            krox   = kr_o(Swc);
            P(i,ti) = dlt_x*(qt*(1-fwx)*muo/(A*k*krox)-rho_o*g*sin(theta))+P(i-1,ti);
        else
            fwx    = calObjFun(Swx, fwt, Swt);
            krox   = kr_o(Swx);
            P(i,ti) = dlt_x*(qt*(1-fwx)*muo/(A*k*krox)-rho_o*g*sin(theta))+P(i-1,ti);
        end
     end
    else
     for i = 2:size(x,1)
         Swx        = calObjFun(x(i), Swt, Xsw(:,ti));
         fwx        = calObjFun(Swx, fwt, Swt);
```

```
            krox       = kr_o(Swx);
            P(i,ti)    = dlt_x*(qt*(1-fwx)*muo/(A*k*krox)-rho_o*g*sin(theta))+
            P(i-1,ti);
        end
    end
end

%% 4 Plot results
% 4.1 Plot the relative permeability curves
h_fig1 = figure(1);
set(h_fig1, 'color', 'w', 'NumberTitle', 'off', 'Name', 'Relative Permeability
Curves');
plot(Sw, krw, '-b', Sw, kro, '-r', 'LineWidth', 2.0);
axis([0.0  1.0  0.0  1.0]);
axis square;
set(gca, 'Fontname', 'Times New Roman','FontSize',10);
title('Brooks-Corey relative permeability curves')
xlabel('{\it S}_w');
ylabel('{\it k}_{r {\it \beta}}');
set(gca, 'YTick', 0:0.2:1);
h_legend1 = legend('water', 'oil');
set(h_legend1,'Box', 'on', 'Location', 'best');

% 4.2 Plot the fractional flow function curve
h_fig2 = figure(2);
set(h_fig2, 'color', 'w', 'NumberTitle', 'off', 'Name', 'Fractional Flow Curve fw');
plot(Sw, fw, '-b', 'LineWidth', 2.0);
hold on;
b = fw_swf-dfw_swf*Swf(1);
plot(Sw, (dfw_swf.*Sw+b), '-r', 'LineWidth', 2.0);
plot(Swc, 0, 'ro', 'Markersize', 8);
plot(Swf(1), fw_swf, 'ro', 'Markersize', 8);
plot([Swf(1) Swf(1)], [0 fwt(index(1))], '--r', 'LineWidth', 1.5);
plot([0 Swf(1)], [fwt(index(1)) fwt(index(1))], '--r', 'LineWidth', 1.5);
axis([0.0 1.0 0.0 1.0]);
axis square;
set(gca, 'Fontname', 'Times New Roman','FontSize',10);
title('fractional flow function curve')
xlabel('{\it S}_w');
ylabel('{\it f}_w');
set(gca, 'YTick', 0:0.2:1);

% 4.3 Plot the derivative curve of fractional flow function
h_fig3 = figure(3);
set(h_fig3, 'color', 'w', 'NumberTitle', 'off', 'Name', 'Derivatives of Fractional
Flow Curve dfw/dSw');
plot(Sw, dfw, '-b', 'LineWidth', 2.0);
set(gca, 'XLim', [0 1]);
set(gca, 'Fontname', 'Times New Roman','FontSize',10);
```

```
title('derivatives of fractional flow function')
xlabel('{\it S}_w');
ylabel('d {\it f}_w / d {\it S}_w');
axis square;

% 4.4 Plot the water saturation profiles
h_fig4 = figure(4);
set(h_fig4, 'color', 'w', 'NumberTitle', 'off', 'Name', 'water Saturation
Profiles: Sw(t)');
SwTime= [];
for ti = 1:nts
    plot(Xsw(:,ti), Swt, '-r', 'LineWidth', 2.0);
    hold on;
    plot([0 Xsw(1,ti)], [1-Sor 1-Sor], '-r', 'LineWidth', 2.0);
    SwTime = [ SwTime; ['Time = ' num2str(t(ti)/86400, format) ' day'] ];
    plot([Xsw(end,ti) Xsw(end,ti)], [Swf(ti) Swc], '-r', 'LineWidth', 2.0);
    plot([Xsw(end,ti) L], [Swc Swc], '-r', 'LineWidth', 2.0);
end
set(gca, 'YLim', [0 1], 'YTick', 0:0.2:1, 'XLim', [0 L]);
set(gca, 'Fontname', 'Times New Roman','FontSize',10);
title('water saturation profiles')
xlabel('{\it x} (m)');
ylabel('{\it S}_w');
h_legend4 = legend(SwTime);
set(h_legend4,'Box', 'on', 'Location', 'best');
axis square;

% 4.5 Plot the pressure profiles
h_fig5 = figure(5);
set(h_fig5, 'color', 'w', 'NumberTitle', 'off', 'Name', 'Pressure Profiles: P(t)');
SwTime= [];
for ti = 1:nts
    plot(x, P(:,ti)/1e6, '-r', 'LineWidth', 2.0);
    hold on;
    SwTime = [ SwTime; ['Time = ' num2str(t(ti)/86400, format) ' day'] ];
end
set(gca, 'XLim', [0 L]);
set(gca, 'Fontname', 'Times New Roman','FontSize',10);
title('Pressure profiles')
xlabel('{\it x} (m)');
ylabel('Pressure (MPa)');
h_legend5 = legend(SwTime);
set(h_legend5,'Box', 'on', 'Location', 'best');
axis square;

%% end
```

A.3 AUXILIARY FUNCTIONS

```
function [index, Swf, dfwf, bf] = calSatFront(Sw, fw, dfw)
%% calculate advance front  saturation using Welge graphic method
%          Sw ---- saturation vector of displacing wetting phase fluid
%          fw ---- fractional flow vector of displacing wetting phase fluid
%         dfw ---- fractional flow derivate vector of displacing wetting phase fluid
%       index ---- index of Swf in Sw
%         Swf ---- advance front saturation
%        dfwf ---- fractional flow derivative at Swf
%          bf ---- intercept value for tangent line
index  = 0;
ns     = size(Sw,1);
df     = 1/(Sw(ns)-Sw(1));
dlt_Sw = Sw(ns)-Sw(ns-1);
if nargin == 2
    % calculate derivate
    for i = 3:(ns-2)
        dfw(i) = (fw(i+1)-fw(i-1))/(2*dlt_Sw);
    end
    dfw(2)    = (-11*fw(2)+18*fw(3)-9*fw(4)+2*fw(5))/(6*dlt_Sw);
    dfw(1)    = abs(2*dfw(2)-dfw(3));
    dfw(ns-1) = -(-11*fw(nt-1)+18*fw(nt-2)-9*fw(nt-3)+2*fw(nt-4))/(6*dlt_Sw);
    dfw(ns)   = abs(2*dfw(nt-1)-dfw(nt-2));
    % calculate Swf and its index
    for i = 2:ns-1
        dfds = fw(i)/(Sw(i)-Sw(1));
        if (dfds < dfw(i-1)) &&  (dfds > dfw(i+1)) && (dfds >= df)
            index = i;
            Swf   = Sw(i);
            dfwf  = dfds;
            bf    = fw(i)-dfwf*Sw(i);
            break;
        end
    end
    if index == 0
        error('Can't find a tangent line through point (Swc,0). Decrease dlt_Sw!');
    end
elseif nargin == 3
    % calculate Swf and its index
    for i = 2:ns-1
        dfds = fw(i)/(Sw(i)-Sw(1));
        if (dfds < dfw(i-1)) &&  (dfds > dfw(i+1)) && (dfds >= df)
            index = i;
            Swf   = Sw(i);
```

```
            dfwf  = dfds;
            bf    = fw(i)-dfwf*Sw(i);
            break;
          end
       end
       if index == 0
          error('Can't find a tangent line through point (Swc,0). Decrease dlt_Sw!');
       end
  else
      error('the number of input arguments in function calSatFront is incorrect!');
  end
  end

%% end function calSatFront()

function obj_fun = calObjFun(obj_var, Fun, Var, index_var)
%% calculate obj_fun at obj_var using interpolation method
%        Fun --- basic function value vector
%        Var --- basic variable value vector
%    obj_var --- objective variable value vector
%    obj_fun --- objective function value vector
%      index --- optional for non-monotone Fun

ns      = size(obj_var,1);
obj_fun = zeros(ns,1);
if nargin == 3
     for i = 1:ns
         [~,index] = sort(abs(Var-obj_var(i)));
         obj_fun(i) = Fun(index(1));
     end
elseif nargin == 4
     for i = 1:ns
         [~,index] = sort(abs(Var-obj_var(i)));
         if index(1) >= index_var
              obj_fun(i) = Fun(index(1));
         else
            obj_fun(i) = Fun(index(2));
         end
     end
else
    error('Wrong input parameters in calObjFun function!');
end

end
%% end function calObjFun()
```

APPENDIX B

Program of Buckley–Leverett Solution in a Radial System and Linear and Radial Composite Systems

B.1 MATLAB CODE OF WELGE GRAPHIC METHOD IN A RADIAL SYSTEM

This Matlab code is a computational program realization of the Welge graphic method for Buckley–Leverett equation in a one-dimensional radial system (see Eqn (6.18) and Section 6.2.1).

```
%% Problem description
%  Analytical solution of Buckley-Leverett equation
%  in a radial system using Welge method
%  water phase fluid displacing oil phase fluid
%  Brooks-Corey type relative permeability curves are used
close all; clear all; clc;

%% 1 Parameters initialization
% 1.1 rock properties
R        = 10.00;                  % length of domain [m]
r        = 0.10;                   % radii of injection well [m]
h        = 1.0;                    % height of domain [m]
phi      = 0.25;                   % porosity
k        = 9.869e-14;              % absolute permeability [m^2]

% 1.2 fluid properties
muo      = 5.0e-3;                 % oil phase viscosity [Pa*s]
muw      = 1.0e-3;                 % water phase viscosity [Pa*s]
rho_o    = 0.8e3;                  % oil density [kg/m^3]
rho_w    = 1.0e3;                  % water density [kg/m^3]
dlt_rho  = rho_w - rho_o;          % density difference [kg/m^3]

% 1.3 relative permeability parameters
Sor      = 0.15;                   % residual oil saturation
Swc      = 0.15;                   % connate water saturation
no       = 2.00;                   % exponent of oil phase
nw       = 2.00;                   % exponent of water phase
```

```
kro_max = 0.75;                          % maximum permeability of oil
krw_max = 0.75;                          % maximum permeability of water

% 1.4 other initial parameters
dlt_Sw  = 1e-3;                          % constant saturation step
Sw      = [(Swc+eps):dlt_Sw:(1-Sor)]';   % water saturation vector
qt      = 1.0e-4;                        % constant water injection rate [m^3/s]
time0   = 86400*1.0;                     % initial calculation time [s]
timef   = 86400*2.2796;                  % final calculation time [s]
nts     = 4;                             % time steps for calculating
nsw     = size(Sw,1);                    % number of water saturation vector
format  = '%4.2e';                       % precision format for plotting legend

%% 2 Relative permeabilities, fractional flow function and its derivative
% 2.1 initialization of function handles
kr_w  = @(S) krw_max.*(( S-Swc)/(1-Swc-Sor)).^nw;  % relative permeability of water
kr_o  = @(S) kro_max.*((1-S-Sor)/(1-Swc-Sor)).^no; % relative permeability of oil
mob   = @(S) (kr_o(S)./muo).*(muw./kr_w(S));       % mobility function
f_w   = @(S) 1./(1+mob(S));                        % fractional flow function fw
df_w  = @(S) ((nw.*mob(S)./(S-Swc))+(no.*mob(S))./(1-S-Sor))...   % derivative of fw
   ./(1+mob(S)).^2;

% 2.2 relative permeability and fractional flow vectors
krw  = kr_w(Sw);                         % relative permeability vector of water
kro  = kr_o(Sw);                         % relative permeability vector of oil
fw   =  f_w(Sw);                         % fractional flow vector
dfw  = df_w(Sw);                         % fractional flow derivate vector

%% 3 Calculate advance frontal water saturation
% 3.1 Evaluate advance frontal water saturation Swf
[index, Swf, dfwf, bf] = calSatFront(Sw, fw, dfw);

% 3.2 Calculate the time when Swf reaches at production well
krw_swf = kr_w(Swf);
kro_swf = kr_o(Swf);
 fw_swf =  f_w(Swf);
dfw_swf = df_w(Swf);
t_pw    = pi*h*phi*(R^2-r^2)/(qt*dfw_swf);

%% 4 Calculate water saturation profile
t      = linspace(time0, timef, nts);
dfwt   = dfw(end:-1:index);              % inverted sequence of dfw
 Swt   =  Sw(end:-1:index);              % inverted sequence of Sw
for ti = 1:nts
    for i = 1:(nsw-index+1)
        Rsw(i,ti) = sqrt(r^2+qt*t(ti)/(pi*h*phi)*dfwt(i));
    end
end
```

```
%% 5 Plot results
% 5.2 Plot the relative permeability curves
h_fig1 = figure(1);
set(h_fig1, 'color', 'w', 'NumberTitle', 'off', 'Name', 'Relative
Permeability Curves: kr');
plot(Sw, krw, '-b', Sw, kro, '-r', 'LineWidth', 2.0);
axis([0.0 1.0 0.0 1.0]);
axis square;
set(gca, 'Fontname', 'Times New Roman','FontSize',10);
title('Brooks-Corey relative permeability curves')
xlabel('{\it S}_w');
ylabel('{\it k}_{r {\it \beta}}');
set(gca, 'YTick', 0:0.2:1);
h_legend1 = legend('water phase', 'oil phase');
set(h_legend1,'Box', 'on', 'Location', 'best');

% 5.2 Plot the fractional flow function curve
h_fig2 = figure(2);
set(h_fig2, 'color', 'w', 'NumberTitle', 'off', 'Name', 'Fractional Flow Curve fw');
plot(Sw, fw, '-b', 'LineWidth', 2.0);
hold on;
plot(Sw, (dfwf.*Sw+bf), '-r', 'LineWidth', 2.0);
plot(Swc, 0, 'ro', 'Markersize', 8);
plot(Swf, fw(index), 'ro', 'Markersize', 8);
plot([Swf Swf], [0 fw(index)], '--r', 'LineWidth', 1.5);
plot([0 Swf], [fw(index) fw(index)], '--r', 'LineWidth', 1.5);
axis([0.0 1.0  0.0 1.0]);
axis square;
set(gca, 'Fontname', 'Times New Roman','FontSize',10);
title('fractional flow function curve')
xlabel('{\it S}_w');
ylabel('{\it f}_w');
set(gca, 'YTick', 0:0.2:1);

% 5.3 Plot the derivative curve of fractional flow function
h_fig3 = figure(3);
set(h_fig3, 'color', 'w', 'NumberTitle', 'off', 'Name', 'Derivatives of Fractional
Flow Curve dfw/dSw');
plot(Sw, dfw, '-b', 'LineWidth', 2.0);
set(gca, 'XLim', [0 1]);
set(gca, 'Fontname', 'Times New Roman','FontSize',10);
title('derivatives of fractional flow function')
xlabel('{\it S}_w');
ylabel('d {\it f}_w / d {\it S}_w');
axis square;
```

```
% 5.4 Plot the water saturation profiles
h_fig4 = figure(4);
set(h_fig4, 'color', 'w', 'NumberTitle', 'off', 'Name', 'water Saturation
Profiles: Sw(t)');
SwTime= [];
for ti = 1:nts
    plot(Rsw(:,ti), Swt, '-r', 'LineWidth', 2.0);
    hold on;
    plot([0 Rsw(1,ti)], [1-Sor 1-Sor], '-r', 'LineWidth', 2.0);
    SwTime = [ SwTime; ['Time = ' num2str(t(1,ti)/86400, format) ' day'] ];
    plot([Rsw(end,ti) Rsw(end,ti)], [Swf Swc], '-r', 'LineWidth', 2.0);
    plot([Rsw(end,ti) R], [Swc Swc], '-r', 'LineWidth', 2.0);
end
set(gca, 'YLim', [0 1], 'YTick', 0:0.2:1, 'XLim', [0 R]);
set(gca, 'Fontname', 'Times New Roman','FontSize',10);
title('water saturation profiles')
xlabel('{\it x} (m)');
ylabel('{\it S}_w');
h_legend2 = legend(SwTime);
set(h_legend2,'Box', 'on', 'Location', 'best');
axis square;

%% end
```

B.2 MATLAB CODE OF INTEGRAL METHOD BASED ON MASS BALANCE PRINCIPLE IN A RADIAL SYSTEM

This Matlab code is a computational program realization of the integral method based on mass balance principle for Buckley–Leverett equation in a one-dimensional radial system (see Eqn (6.18) and Section 6.2.4).

```
%% Problem description
%   Analytical solution of Buckley-Leverett equation
%   in a radial system using integral method
%   wetting phase fluid displacing non-wetting phase fluid
%   Brooks-Corey type relative permeability curves are used
close all; clear all; clc;

%% 1 Parameters initialization
% 1.1 rock properties
R     = 100.0;                          % length of domain [m]
r     = 0.02;                           % radii of injection well [m]
h     = 1.0;                            % height of domain [m]
phi   = 0.25;                           % porosity
k     = 9.869e-13;                      % absolute permeability [m^2]
```

```
% 1.2 fluid properties
muo      = 5.0e-3;                          % oil phase viscosity [Pa*s]
muw      = 1.0e-3;                          % water phase viscosity [Pa*s]
rho_o    = 0.8e3;                           % oil density [kg/m^3]
rho_w    = 1.0e3;                           % water density [kg/m^3]
dlt_rho = rho_w - rho_o;                    % density difference [kg/m^3]

% 1.3 relative permeability parameters
Sor      = 0.15;                            % residual oil saturation
Swc      = 0.15;                            % connate water saturation
no       = 1.00;                            % exponent of oil phase
nw       = 2.00;                            % exponent of water phase
kro_max = 0.85;                             % maximum permeability of oil phase
krw_max = 0.85;                             % maximum permeability of water phase

% 1.4 other initial parameters
dlt_Sw  = 1e-3;                             % constant saturation step
Sw       = [(Swc+eps):dlt_Sw:(1-Sor)]';     % water saturation vector
qt       = 2.0e-3;                          % constant water injection rate [m^3/s]
time0   = 86400*1.0;                        % initial calculation time
timef   = 86400*9.0;                        % final calculation time
nts     = 4;                                % time steps for calculating
nsw     = size(Sw,1);                       % number of wetting-phase saturation
format  = '%3.2f';                          % precision format for plotting legend

%% 2 Relative permeabilities, fractional flow function and its derivative
% 2.1 initialization of function handles
kr_w  = @(S) krw_max.*((  S-Swc)/(1-Swc-Sor)).^nw;  % relative permeability of water
kr_o  = @(S) kro_max.*((1-S-Sor)/(1-Swc-Sor)).^no; % relative permeability of oil
mob   = @(S) (kr_o(S)./muo).*(muw./kr_w(S));        % mobility function
f_w   = @(S) 1./(1+mob(S));                         % fractional flow function fw
df_w  = @(S) ((nw.*mob(S)./(S-Swc))+(no.*mob(S))./(1-S-Sor))...  % derivative of fw
    ./(1+mob(S)).^2;

% 2.2 relative permeability and fractional flow vectors
krw  = kr_w(Sw);                            % relative permeability vector of water
kro  = kr_o(Sw);                            % relative permeability vector of oil
fw   =  f_w(Sw);                            % fractional flow vector
dfw  = df_w(Sw);                            % fractional flow derivate vector

%% 3 Calculate advance frontal saturation and travelling distance
% 3.1 calculate travelling distance of every saturations
t = linspace(time0, timef, nts);
dfwt  = dfw(end:-1:1);                      % inverted sequence of dfw
fwt   =  fw(end:-1:1);                      % inverted sequence of fw
Swt   =  Sw(end:-1:1);                      % inverted sequence of Sw
for ti = 1:nts
    Wi(ti) = qt*t(ti);                      % injected wetting phase fluid volume
    for i = 1:nsw
```

```
        Rsw(i,ti) = sqrt(r^2+qt*t(ti)/(pi*h*phi)*dfwt(i)); % the travelling distance
    end
    Rsw0  = [r; Rsw(1:end-1,ti)];           % the 2nd travelling distance vector
    dlt_Rsw = Rsw(:,ti).^2 - Rsw0.^2;       % dlt_Rsw=Rsw_j^2 - Rsw_(j-1)^2, r_0=r
    dlt_Swt = Swt - Swc;                    % dlt_Swt = Swt,j - Swc
    for i = 1:nsw
    % calculate the injected fluid volume from r to Rswf
        Vi = pi*phi*h*sum(dlt_Rsw(1:i).*dlt_Swt(1:i));
        if Vi >= Wi(ti)
            index(ti) = i;                  % index of the Swf in Swt
            Swf (ti) = Swt(i);              % advance front saturation: Swf
            Rswf (ti) = Rsw(i,ti);          % the position of Swf
            break;
        end
    end
end
Rsw = Rsw(1:index(1),:);
Swt = Swt(1:index(1));

% 3.2 Calculate the time when Swf reaches at production well
krw_swf  = kr_w(Swf(1));
kro_swf  = kr_o(Swf(1));
fw_swf   = f_w(Swf(1));
dfw_swf  = df_w(Swf(1));
t_pw     = pi*h*phi*(R^2-r^2)/(qt*dfw_swf);

%% 4 Plot results
% 4.1 Plot the relative permeability curves
h_fig1 = figure(1);
set(h_fig1, 'color', 'w', 'NumberTitle', 'off', 'Name', 'Relative Permeability
Curves: kr');
plot(Sw, krw, '-b', Sw, kro, '-r', 'LineWidth', 2.0);
axis([0.0  1.0  0.0  1.0]);
axis square;
set(gca, 'Fontname', 'Times New Roman','FontSize',10);
title('Brooks-Corey relative permeability curves')
xlabel('{\it S}_w');
ylabel('{\it k}_{r {\it \beta}}');
set(gca, 'YTick', 0:0.2:1);
h_legend1 = legend('water phase', 'oil phase');
set(h_legend1,'Box', 'on', 'Location', 'best');

% 4.2 Plot the fractional flow function curve
h_fig2 = figure(2);
set(h_fig2, 'color', 'w', 'NumberTitle', 'off', 'Name', 'Fractional Flow Curve fw');
plot(Sw, fw, '-b', 'LineWidth', 2.0);
hold on;
b = fw_swf-dfw_swf*Swf(1);
```

```
plot(Sw, (dfw_swf.*Sw+b), '-r', 'LineWidth', 2.0);
plot(Swc, 0, 'ro', 'Markersize', 8);
plot(Swf(1), fw_swf, 'ro', 'Markersize', 8);
plot([Swf(1) Swf(1)], [0 fwt(index(1))], '--r', 'LineWidth', 1.5);
plot([0 Swf(1)], [fwt(index(1)) fwt(index(1))], '--r', 'LineWidth', 1.5);
axis([0.0 1.0 0.0 1.0]);
axis square;
set(gca, 'Fontname', 'Times New Roman','FontSize',10);
title('fractional flow function curve')
xlabel('{\it S}_w');
ylabel('{\it f}_w');
set(gca, 'YTick', 0:0.2:1);

% 4.3 Plot the derivative curve of fractional flow function
h_fig3 = figure(3);
set(h_fig3, 'color', 'w', 'NumberTitle', 'off', 'Name', 'Derivatives of Fractional
Flow Curve dfw/dSw');
plot(Sw, dfw, '-b', 'LineWidth', 2.0);
set(gca, 'XLim', [0 1]);
set(gca, 'Fontname', 'Times New Roman','FontSize',10);
title('derivatives of fractional flow function')
xlabel('{\it S}_w');
ylabel('d {\it f}_w / d {\it S}_w');
axis square;

% 4.4 Plot the water saturation profiles
h_fig4 = figure(4);
set(h_fig4, 'color', 'w', 'NumberTitle', 'off', 'Name', 'water Saturation Profiles:
 Sw(t)');
SwTime= [];
for ti = 1:nts
    plot(Rsw(:,ti), Swt, '-r', 'LineWidth', 2.0);
    hold on;
    plot([r Rsw(1,ti)], [1-Sor 1-Sor], '-r', 'LineWidth', 2.0);
    SwTime = [ SwTime; ['Time = ' num2str(t(1,ti)/86400, format) ' day'] ];
    plot([Rsw(end,ti) Rsw(end,ti)], [Swf(ti) Swc], '-r', 'LineWidth', 2.0);
    plot([Rsw(end,ti) R], [Swc Swc], '-r', 'LineWidth', 2.0);
end
set(gca, 'Fontname', 'Times New Roman','FontSize',10);
set(gca, 'YLim', [0 1]);
title('water saturation profiles')
xlabel('{\it x} (m)');
ylabel('{\it S}_w');
h_legend4 = legend(SwTime);
set(h_legend4,'Box', 'on', 'Location', 'best');
axis square;

%% end
```

B.3 MATLAB CODE FOR BUCKLEY–LEVERETT SOLUTION IN A LINEAR COMPOSITE SYSTEM

This Matlab code is a computational program realization of the analytical solution of Buckley–Leverett equation (Eqn (6.32) in Section 6.3.1) in a linear composite system (see Section 6.3).

```
%% Problem description
%   Analytical solution of Buckley-Leverett equation using mass balance method
%   in one-dimensional composite porous medium system
%   Brooks-Corey type relative permeability curves are used
close all; clear all; clc;

%% 1 Parameters initialization for two domains
% 1.1 rock properties in domain 1
L1        = 6.00;           % length of domain 1 [m]
phi1      = 0.30;           % porosity of domain 1
k1        = 1.0e-14;        % permeability of domain 1 [m^2]
Sor1      = 0.20;           % residual oil saturation in domain 1
Swc1      = 0.20;           % connate water saturation in domain 1
no1       = 2.50;           % exponent of oil phase in domain 1
nw1       = 1.50;           % exponent of water phase in domain 1
kro1_max  = 0.80;           % maximum permeability of oil domain 1
krw1_max  = 0.80;           % maximum permeability of water domain 1
dlt_Sw1   = 1e-3;           % constant saturation step in domain 1
Sw1       = [(Swc1+eps):dlt_Sw1:(1-Sor1-eps)];     % water saturation vector for
domain 1

% 1.2 rock properties in domain 2
L2     = 6.00;              % length of domain 2 [m]
phi2   = 0.30;              % porosity of domain 2
k2        = 1.0e-14;        % permeability of domain 2 [m^2]
Sor2      = 0.20;           % residual oil saturation in domain 2
Swc2      = 0.20;           % connate water saturation in domain 2
no2       = 1.50;           % exponent of oil phase in domain 2
nw2       = 2.50;           % exponent of water phase in domain 2
kro2_max  = 0.75;           % maximum permeability of oil domain 2
krw2_max  = 0.75;           % maximum permeability of water domain 2
dlt_Sw2   = 1e-3;           % constant saturation step in domain 2
Sw2       = [(Swc2+eps):dlt_Sw2:(1-Sor2-eps)];    % water saturation vector
for domain 2

% 1.3 fluid properties for the composite system
muo       = 5.0e-3;         % oil phase viscosity [Pa*s]
muw       = 1.0e-3;         % water phase viscosity [Pa*s]
rho_o     = 0.8e3;          % oil density [kg/m^3]
rho_w     = 1.0e3;          % water density [kg/m^3]
dlt_rho   = rho_w - rho_o; % density difference [kg/m^3]
```

```
% 1.4 other parameters for calculation
A         = 1.0;            % area of cross-section [m^2]
qt        = 1.0e-5;         % constant water injection rate [m^3/s]
g         = 9.8067;         % gravity acceleration constant [m/s^2]
alpha     = pi*0.0;         % angle between x and horizontal [rad]
time0     = 86400*0.1;      % initial calculation time [s]
timef     = 86400*1.0;      % final calculation time [s]
nts1      = 5;              % time steps for domain 1
nts2      = 5;              % time steps for domain 2 [-]
nsw1      = size(Sw1,1);    % number of water saturation in domain 1
nsw2      = size(Sw2,1);    % number of water saturation in domain 2
format    = '%4.2e';        % precision format for plotting

%% 2 Calculate fractional flow function and plots
% 2.1 initialization of function handles in domain 1
kr_w1  = @(S) krw1_max.*(( S-Swc1)/(1-Swc1-Sor1)).^nw1;    % relative permeability krw1
kr_o1  = @(S) kro1_max.*((1-S-Sor1)/(1-Swc1-Sor1)).^no1;   % relative permeability kro1
mob1   = @(S) (kr_o1(S)./muo).*(muw./kr_w1(S));            % mobility function
f_w1   = @(S) 1./(1+mob1(S))-A*k1.*kr_o1(S)./(qt*muo)*...  % fractional flow fw1
   dlt_rho*g*sin(alpha)./(1+mob1(S));
df_w1  = @(S) ((nw1.*mob1(S)./(S-Swc1))+(no1.*mob1(S))./(1-S-Sor1))...  % derivate, fw1
   ./(1+mob1(S)).^2+A*k1.*kr_o1(S)*no1*dlt_rho*g*sin(alpha)./...
   ((1-S-Sor1)*qt*muo.*(1+mob1(S)))+A*k1.*kr_o1(S)*dlt_rho*g*sin(alpha)./...
   (qt*muo.*(1+mob1(S)).^2).*(((nw1.*mob1(S)./(S-Swc1))+(no1.*mob1(S))
   ./(1-S-Sor1))./(1+mob1(S)).^2);

% 2.1 initialization of function handles in domain 2
kr_w2  = @(S) krw2_max.*(( S-Swc2)/(1-Swc2-Sor2)).^nw2;    % relative permeability krw2
kr_o2  = @(S) kro2_max.*((1-S-Sor2)/(1-Swc2-Sor2)).^no2;   % relative permeability kro2
mob2  = @(S) (kr_o2(S)./muo).*(muw./kr_w2(S));             % mobility function
f_w2  = @(S) 1./(1+mob2(S))-A*k2.*kr_o2(S)./(qt*muo)*...   % fractional flow fw2
   dlt_rho*g*sin(alpha)./(1+mob2(S));
df_w2  = @(S) ((nw2.*mob2(S)./(S-Swc2))+(no2.*mob2(S))./(1-S-Sor2))... % derivate fw2
   ./(1+mob2(S)).^2+A*k2.*kr_o2(S)*no2*dlt_rho*g*sin(alpha)./...
   ((1-S-Sor2)*qt*muo.*(1+mob2(S)))+A*k2.*kr_o2(S)*dlt_rho*g*sin(alpha)./...
   (qt*muo.*(1+mob2(S)).^2).*(((nw2.*mob2(S)./(S-Swc2))+(no2.*mob2(S))
   ./(1-S-Sor2))./(1+mob2(S)).^2);

% 2.3 relative permeability and fractional flow vectors in domain 1
krw1  = kr_w1(Sw1);        % relative permeability vector of water
kro1  = kr_o1(Sw1);        % relative permeability vector of oil
 fw1   =  f_w1(Sw1);       % fractional flow vector
dfw1  = df_w1(Sw1);        % fractional flow derivate vector

% 2.4 relative permeability and fractional flow vectors in domain 2
krw2  = kr_w2(Sw2);        % relative permeability vector of water
kro2  = kr_o2(Sw2);        % relative permeability vector of oil
fw2   =  f_w2(Sw2);        % fractional flow vector
dfw2  = df_w2(Sw2);        % fractional flow derivate vector
```

```
% 2.5 plot relative permeability curves
h_fig1 = figure(1);
set(h_fig1, 'color', 'w', 'NumberTitle', 'off', ...
   'Name', 'Relative Permeability Curves: kr');
plot(Sw1, krw1, '-b', Sw1, kro1, '--b', 'LineWidth', 2.0);
hold on;
plot(Sw2, krw2, '-r', Sw2, kro2, '--r', 'LineWidth', 2.0);
axis([0.0 1.0 0.0 1.0]);
axis square;
set(gca, 'Fontname', 'Times New Roman','FontSize',10);
title('Brooks-Corey relative permeability curves')
xlabel('{\it S}_w');
ylabel('{\it k}_{r{\it \beta}}');
set(gca, 'YTick', 0:0.2:1);
h_legend1 = legend('domain 1: water', 'domain 1: oil', 'domain 2: water', 'domain 2: oil');
set(h_legend1,'Box', 'on', 'Location', 'best');

%% 3 Calculate advance frontal water saturation in domain 1 and plot
% 3.1 calculate sock front of water saturation
[index, Swf1, dfwf1, bf1] = calSatFront(Sw1, fw1, dfw1);

% 3.2 Plot the fractional flow function curves
h_fig2 = figure(2);
set(h_fig2, 'color', 'w', 'NumberTitle', 'off', ...
   'Name', 'Fractional Flow Curves: fw');
plot(Sw1, fw1, '-b', 'LineWidth', 2.0);
hold on;
plot(Sw2, fw2, '--b', 'LineWidth', 2.0);
plot(Sw1, (dfwf1.*Sw1+bf1), '-r', 'LineWidth', 2.0);
plot(Swc1, 0, 'ro');
plot(Swf1, fw1(index), 'ro');
plot([Swf1 Swf1], [0 fw1(index)], '--r', 'LineWidth', 2.0);
plot([0 Swf1], [fw1(index) fw1(index)], '--r', 'LineWidth', 2.0);
axis([0.0 1.0 0.0 1.0]);
set(gca, 'Fontname', 'Times New Roman','FontSize',10);
title('fractional flow function curves');
xlabel('{\it S}_w');
ylabel('{\it f}_w');
h_legend2 = legend('domain 1', 'domain 2');
set(gca, 'YTick', 0:0.2:1);
set(gca, 'Fontname', 'Times New Roman','FontSize',10);
set(h_legend2,'Box', 'on', 'Location', 'best');
axis square;

% 3.3 Plot the derivative curve of fractional flow function
h_fig3 = figure(3);
set(h_fig3, 'color', 'w', 'NumberTitle', 'off', ...
   'Name', 'Derivatives of Fractional Flow Curves: dfw/dSw');
```

```
plot(Sw1, dfw1, '-b', 'LineWidth', 2.0);
hold on;
plot(Sw2, dfw2, '--b', 'LineWidth', 2.0);
set(gca, 'XLim', [0 1]);
set(gca, 'Fontname', 'Times New Roman','FontSize',10);
title('derivatives of fractional flow function');
xlabel('{\it S}_w');
ylabel('d {\it f}_w / d {\it S}_w');
h_legend3 = legend('domain 1', 'domain 2');
set(h_legend3,'Box', 'on', 'Location', 'best');
axis square;

%% 4 Water saturation profiles in domain 1 before Swf1 reaches interface
% 4.1 the time when Swf reaches at the interface between domain1 and domain 2
krw1_swf  = kr_w1(Swf1);
kro1_swf  = kr_o1(Swf1);
fw1_swf   =  f_w1(Swf1);
dfw1_swf  = df_w1(Swf1);
t_inf     = A*phi1*L1/(qt*dfw1_swf);

% 4.2 calculate the travelling distance of specific water saturations Sw1
t1     = linspace(time0,t_inf,nts1);  % time vector for domain 1
dfwt1  = dfw1(end:-1:index);          % inverted sequence of dfw1
Swt1   =  Sw1(end:-1:index);          % inverted sequence of Sw1
for ti = 1:nts1                       % loop time vector
    for i = 1:(nsw1-index+1)
        Xsw1(i,ti) = qt*t1(ti)/(A*phi1)*dfwt1(i);
    end
end

% 4.3 figure 4: Plot the water saturation profiles in domain 1
h_fig4 = figure(4);
set(h_fig4, 'color', 'w', 'NumberTitle', 'off', 'Name', 'Water Saturation Profiles');
SwTime= [];
for ti = 1:nts1
    plot(Xsw1(:,ti), Swt1, '-r', 'LineWidth', 2.0);
    hold on;
    plot([0 Xsw1(1,ti)], [1-Sor1 1-Sor1], '-r', 'LineWidth', 2.0);
    SwTime = [ SwTime; ['Time = ' num2str(t1(ti)/86400, format) ' day'] ];
    plot([Xsw1(end,ti) Xsw1(end,ti)], [Swf1 Swc1], '-r', 'LineWidth', 2.0);
    plot([Xsw1(end,ti) L1], [Swc1 Swc1], '-r', 'LineWidth', 2.0);
end
set(gca, 'YLim', [0 1], 'YTick', 0:0.2:1, 'XLim', [0 L1]);
set(gca, 'Fontname', 'Times New Roman','FontSize',10);
title('water saturation profiles in domain 1');
xlabel('{\it x} (m)'); ylabel('{\it S}_w');
h_legend4 = legend(SwTime);
set(h_legend4,'Box', 'on', 'Location', 'best');
axis square;
```

```
%% 5 Calculate water saturation profile in domain 1 when time > t_inf
% 5.1 calculate the corresponding parameters at interface
if timef <= t_inf
    error('Please reset the timef due to timef <= t_inf!');
end
t2 = linspace(t_inf,timef,nts2)';
dfw1_inf  = A*phi1*L1/qt./t2;                  % dfw1 at the interface (upstream)
Sw1_inf   = calObjFun(dfw1_inf, Sw1, dfw1, index);   % Sw,1 at the interface
(upstream)
krw1_inf  = kr_w1(Sw1_inf);                    % relative permeability of water
kro1_inf  = kr_o1(Sw1_inf);                    % relative permeability of oil
fw1_inf   =  f_w1(Sw1_inf);                    % fractional flow function
Sw1_avg   = Sw1_inf+(1-fw1_inf)./dfw1_inf;   % average saturation of domain 1

% 5.2 % calculate the travelling distance of water saturations
dfwt1  = dfw1(end:-1:index);               % inverted sequence of dfw1
Swt1   =  Sw1(end:-1:index);               % inverted sequence of Sw1
for ti = 1:nts2                            % loop times vector
    for i = 1:(nsw1-index+1)
     Xsw1(i,ti+nts1) = qt*t2(ti)/(A*phi1)*dfwt1(i);
   end
end

%% 6 Calculate water saturation profile in domain 2 when time > t_inf
% 6.1 calculate water saturation at interface and injected fluid
fw2_inf  = fw1_inf;                        % fw,2 at the interface (downstream)
Sw2_inf  = calObjFun(fw2_inf,Sw2, fw2);    % Sw,2 at the interface (downstream)
Qt       = qt.*t2;                         % the injected water into domains
W1       = A*phi1*L1.*(Sw1_avg-Swc1);      % the injected water into domain 1
W2       = Qt - W1;                         % the injected water into domain 2
if (abs(W2(1)/Qt(1)) <= 1e-3); W2(1) = 0; end;   % enforce W2 == 0.0

% 6.1 calculate saturation profiles using mass balance principle
Sw2_k       = cell(nts2,1);                % water saturation Sw,2: initialization
Xsw2_k      = cell(nts2,1);                % initial travelling distance of Sw,2
Sw2_k{1,1}  = [Sw2_inf(1);Swc2];           % the saturation Sw,2 set at t_inf
Xsw2_k{1,1} = [L1; L1];                    % the distance Xsw,2 set at t_inf
for ti = 2:nts2
    % 6.1.1 select a set of saturation Sw,2
    % choose a set of saturation Sw,2: [Sw2,inf(1) Sw2,inf(ti)]
    Sw2_k1 = [(Sw2_inf(ti)-dlt_Sw2):(-dlt_Sw2):Sw2_inf(1)]';
    % choose a set of saturation Sw,2: [Swc2 Sw2,inf(1)])
   Sw2_k2 = [(Sw2_inf(1)-dlt_Sw2):(-dlt_Sw2):Swc2]';
   % the whole set of water saturation Sw,2
   Sw2_k{ti,1} = [Sw2_inf(ti); Sw2_k1; Sw2_k2];
```

```
    % 6.1.2 calculate saturation profiles for Sw2,inf(1) <= Sw,2 <= Sw2,inf(ti)
    krw2_k1  = kr_w2(Sw2_k1);              % relative permeability of water
    kro2_k1  = kr_o2(Sw2_k1);              % relative permeability of oil
    fw2_k1   = f_w2(Sw2_k1);               % fractional flow function
    dfw2_k1  = df_w2(Sw2_k1);              % derivate of fractional flow function
    fw1_k1   = fw2_k1;
    Sw1_k1   = calObjFun(fw1_k1,Sw1,fw1);  % Sw1 at interface in domain 1
    krw1_k1  = kr_w1(Sw1_k1);              % relative permeability of water
    kro1_k1  = kr_o1(Sw1_k1);              % relative permeability of oil
    fw1_k1   = f_w1(Sw1_k1);               % fractional flow function
    dfw1_k1  = df_w1(Sw1_k1);              % derivate of fractional flow function
    ts       = A*phi1*L1/qt./dfw1_k1;      % starting time for Sw2_k1 at x = L1
    Xsw2_k1 = L1 + qt/A/phi2.*dfw2_k1.*(t2(ti)-ts);   % travelling distance of Sw2_k1

    % 6.1.3 calculate saturation profiles for Swc2 <= Sw,2 <= Sw2,inf(1)
    krw2_k2  = kr_w2(Sw2_k2);              % relative permeability of water
    kro2_k2  = kr_o2(Sw2_k2);              % relative permeability of oil
    fw2_k2   = f_w2(Sw2_k2);               % fractional flow function
    dfw2_k2  = df_w2(Sw2_k2);              % derivate of fractional flow function
    Xsw2_k2 = L1 + qt/A/phi2.*dfw2_k2*(t2(ti)-t_inf); % travelling distance of Sw2_k2

    % 6.1.4 calculate the shock front saturation and its distance
    Xsw2_k{ti,1} = [L1; Xsw2_k1; Xsw2_k2];    % the travelling distance of Sw2_k
    % delta_Xsw2 = Xsw2_j - Xsw2_(j-1), x2_0 = L1
    dlt_xsw2 = Xsw2_k{ti,1}(2:end)-Xsw2_k{ti,1}(1:end-1);
    dlt_swk2 = Sw2_k{ti,1}(2:end)-Swc2;   % delta_Swk2 = Sw2,k - Swc2
    for i = 1:nsw2
    % calculate the injected fluid volume from L1 to Xswf
        V2 = A*phi2*sum(dlt_xsw2(1:i).*dlt_swk2(1:i));
        if V2 >= W2(ti)
            index2(ti) = i;
            Swf2(ti)  = Sw2_k{ti,1}(i);
            Xswf2(ti) = Xsw2_k{ti,1}(i);
            Sw2_k{ti,1}(i+1:end) = Swc2;
            break;
         end
       end
       Xsw2_k{ti,1} = Xsw2_k{ti,1}(1:index2(ti));
       Sw2_k{ti,1} = Sw2_k{ti,1}(1:index2(ti));
    end

% 6.2 figure 5-1: Plot the water saturation profiles in domain 1
h_fig5 = figure(5);
set(h_fig5, 'color', 'w', 'NumberTitle', 'off', 'Name', 'Water Saturation Profiles');
SwTime= [];
subplot(1,2,1);
for ti = 1:nts2
```

```
    plot(Xsw1(:,ti+nts1), Swt1, '-r', 'LineWidth', 2.0);
    hold on;
    plot([0 Xsw1(1,ti+nts1)], [1-Sor1 1-Sor1], '-r', 'LineWidth', 2.0);
    SwTime = [ SwTime; ['Time = ' num2str(t2(ti)/86400, format) ' day'] ];
end
plot([0 L1], [Sw2_inf(1) Sw2_inf(1)], '--k', 'LineWidth', 2.0);
set(gca, 'YLim', [0 1], 'YTick', 0:0.2:1, 'XLim', [0 L1]);
set(gca, 'Fontname', 'Times New Roman','FontSize',14);
title('domain 1');
xlabel('{\it x} (m)'); ylabel('{\it S}_w');
axis square;

% 6.3 figure 5-2: Plot the water saturation profiles in domain 2
subplot(1,2,2);
for ti = 1:nts2
    plot(Xsw2_k{ti,1}, Sw2_k{ti,1}, '-b', 'LineWidth', 2.0);
    hold on;
    plot([Xsw2_k{ti,1}(end) Xsw2_k{ti,1}(end)], [Sw2_k{ti,1}(end) Swc2], '-b',
    'LineWidth', 2.0);
     plot([Xsw2_k{ti,1}(end) L1+L2], [Swc2 Swc2], '-b', 'LineWidth', 2.0);
 end
plot([L1 L1+L2], [Sw2_inf(1) Sw2_inf(1)], '--k', 'LineWidth', 2.0);
plot(L1, Sw2_inf(1), 'ro', 'markersize', 8);
text(L1, Sw2_inf(1)-0.05, '{\it S}_{w2}^{*}', 'Color', 'k', 'Fontname',
'Times New Roman','FontSize',14);
set(gca, 'YLim', [0 1], 'YTick', 0:0.2:1, 'XLim', [L1 L1+L2]);
set(gca, 'Fontname', 'Times New Roman','FontSize',14);
set(gca, 'YAxisLocation', 'right');
title('domain 2');
xlabel('{\it x} (m)'); ylabel('{\it S}_w');
h_legend5 = legend(SwTime);
set(h_legend5,'Box', 'on', 'Location', 'best');
axis square;

%% end
```

B.4 MATLAB CODE FOR BUCKLEY–LEVERETT SOLUTION IN A RADIAL COMPOSITE SYSTEM

This Matlab code is a computational program realization of the analytical solution of Buckley–Leverett equation (Eqn (6.18) in Section 6.2.1) in a radial composite system (see Section 6.4).

```
%%  Problem description
%   Analytical solution of Buckley-Leverett equation using Welge's method
%   in a radial composite porous medium system
%   Brooks-Corey type relative permeability curves are used
close all; clear all; clc;
```

```
%% 1 Parameters initialization for two domains
% 1.1 rock properties in domain 1
R1        = 4.00;              % radius of domain 1 [m]
phi1      = 0.30;              % porosity of domain 1
k1        = 1.0e-13;           % permeability of domain 1 [m^2]
Sor1      = 0.20;              % residual oil saturation in domain 1
Swc1      = 0.20;              % connate water saturation in domain 1
no1       = 1.50;              % exponent of oil phase in domain
nw1       = 2.50;              % exponent of water phase in domain 1
kro1_max  = 0.75;              % maximum permeability of oil domain 1
krw1_max  = 0.75;              % maximum permeability of water domain 1
dlt_Sw1   = 1e-3;              % constant saturation step in domain 1
Sw1   = [(Swc1+eps):dlt_Sw1:(1-Sor1-eps)]';   % water saturation vector in domain 1

% 1.2 rock properties in domain 2
R2    = 8.00;                  % radius of domain 2 [m]
phi2  = 0.30;                  % porosity of domain 2
k2        = 1.0e-13;           % permeability of domain 2 [m^2]
Sor2      = 0.20;              % residual oil saturation in domain 2
Swc2      = 0.20;              % connate water saturation in domain 2
no2       = 2.50;              % exponent of oil phase in domain 2
nw2       = 1.50;              % exponent of water phase in domain 2
kro2_max  = 0.80;              % maximum permeability of oil domain 2
krw2_max  = 0.80;              % maximum permeability of water domain 2
dlt_Sw2   = 1e-3;              % constant saturation step in domain 2
Sw2       =
[(Swc2+eps):dlt_Sw2:(1-Sor2-eps)]';   % water saturation vector in domain 2

% 1.3 fluid properties for the composite system
muo     = 5.0e-3;              % oil phase viscosity [Pa*s]
muw     = 1.0e-3;              % water phase viscosity [Pa*s]
rho_o   = 0.8e3;               % oil density [kg/m^3]
rho_w   = 1.0e3;               % water density [kg/m^3]
dlt_rho = rho_w - rho_o;       % density difference [kg/m^3]

% 1.4 other parameters for calculation
rw      = 0.10;                % radius of injection well [m]
h       = 1.0;                 % reservoir thickness [m]
qt      = 2.5e-4;              % constant water injection rate [m^3/s]
g       = 9.8067;              % gravity acceleration constant [m/s^2]
time0   = 86400*0.1;           % initial calculation time [s]
timef   = 86400*0.463;         % final calculation time [s]
nts1    = 5;                   % time steps for domain 1
nts2    = 5;                   % time steps for domain 2
nsw1    = size(Sw1,1);         % number of water saturation in domain 1
nsw2    = size(Sw2,1);         % number of water saturation in domain 2
format  = '%4.3f';             % precision format for plotting
```

```
%% 2 Calculate fractional flow function and plots
% 2.1 initialization of function handles in domain 1
kr_w1  = @(S) krw1_max.*((  S-Swc1)/(1-Swc1-Sor1)).^nw1;       % relative permeability water
kr_o1  = @(S) kro1_max.*((1-S-Sor1)/(1-Swc1-Sor1)).^no1;       % relative permeability oil
mob1   = @(S) (kr_o1(S)./muo).*(muw./kr_w1(S));                % mobility function
f_w1   = @(S) 1./(1+mob1(S));                                  % fractional flow function
df_w1  = @(S) ((nw1.*mob1(S)./(S-Swc1))+(no1.*mob1(S))./(1-S-Sor1))...      % derivate
   ./(1+mob1(S)).^2;

% 2.2 initialization of function handles in domain 2
kr_w2  = @(S) krw2_max.*((  S-Swc2)/(1-Swc2-Sor2)).^nw2;       % relative permeability water
kr_o2  = @(S) kro2_max.*((1-S-Sor2)/(1-Swc2-Sor2)).^no2;       % relative permeability oil
mob2   = @(S) (kr_o2(S)./muo).*(muw./kr_w2(S));                % mobility function
f_w2   = @(S) 1./(1+mob2(S));                                  % fractional flow function
df_w2  = @(S) ((nw2.*mob2(S)./(S-Swc2))+(no2.*mob2(S))./(1-S-Sor2))...      % derivate
   ./(1+mob2(S)).^2;

% 2.3 relative permeability and fractional flow vectors in domain 1
krw1  = kr_w1(Sw1);   % relative permeability vector of water
kro1  = kr_o1(Sw1);   % relative permeability vector of oil
 fw1   =  f_w1(Sw1);    % fractional flow vector
dfw1  = df_w1(Sw1);   % fractional flow derivate vector

% 2.4 relative permeability and fractional flow vectors in domain 2
krw2  = kr_w2(Sw2);   % relative permeability vector of water
kro2  = kr_o2(Sw2);   % relative permeability vector of oil
 fw2   =  f_w2(Sw2);   % fractional flow vector
dfw2  = df_w2(Sw2);   % fractional flow derivate vector

% 2.5 plot relative permeability curves
h_fig1 = figure(1);
set(h_fig1, 'color', 'w', 'NumberTitle', 'off', ...
    'Name', 'Relative Permeability Curves: kr');
plot(Sw1, krw1, '-b', Sw1, kro1, '-r', 'LineWidth', 2.0);
hold on;
plot(Sw2, krw2, '--b', Sw2, kro2, '--r', 'LineWidth', 2.0);
axis([0.0  1.0  0.0  1.0]);
axis square;
set(gca, 'Fontname', 'Times New Roman','FontSize',10);
title('Brooks-Corey relative permeability curves')
xlabel('{\it S}_w');
ylabel('{\it k}_{r{\it \beta}}');
set(gca, 'YTick', 0:0.2:1);
h_legend1 = legend('domain 1: water', 'domain 1: oil', 'domain 2: water', 'domain 2:
oil');
set(h_legend1,'Box', 'on', 'Location', 'best');
```

```
%% 3 Calculate advance frontal water saturation in domain 1 and plot
% 3.1 calculate sock front of water saturation
[index, Swf1, dfwf1, bf1] = calSatFront(Sw1, fw1, dfw1);

% 3.2 Plot the fractional flow function curves
h_fig2 = figure(2);
set(h_fig2, 'color', 'w', 'NumberTitle', 'off', ...
    'Name', 'Fractional Flow Curves: fw');
plot(Sw1, fw1, '-b', 'LineWidth', 2.0);
hold on;
plot(Sw2, fw2, '--b', 'LineWidth', 2.0);
plot(Sw1, (dfwf1.*Sw1+bf1), '-r', 'LineWidth', 2.0);
plot(Swc1, 0, 'ro');
plot(Swf1, fw1(index), 'ro');
plot([Swf1 Swf1], [0 fw1(index)], '--r', 'LineWidth', 2.0);
plot([0 Swf1], [fw1(index) fw1(index)], '--r', 'LineWidth', 2.0);
axis([0.0  1.0  0.0  1.0]);
set(gca, 'Fontname', 'Times New Roman','FontSize',10);
title('fractional flow function curves');
xlabel('{\it S}_w');
ylabel('{\it f}_w');
h_legend2 = legend('domain 1', 'domain 2');
set(gca, 'YTick', 0:0.2:1);
set(gca, 'Fontname', 'Times New Roman','FontSize',10);
set(h_legend2,'Box', 'on', 'Location', 'best');
axis square;

% 3.3 Plot the derivative curve of fractional flow function
h_fig3 = figure(3);
set(h_fig3, 'color', 'w', 'NumberTitle', 'off', ...
   'Name', 'Derivatives of Fractional Flow Curves: dfw/dSw');
plot(Sw1, dfw1, '-b', 'LineWidth', 2.0);
hold on;
plot(Sw2, dfw2, '--b', 'LineWidth', 2.0);
set(gca, 'XLim', [0 1]);
set(gca, 'Fontname', 'Times New Roman','FontSize',10);
title('derivatives of fractional flow function');
xlabel('{\it S}_w');
ylabel('d {\it f}_w / d {\it S}_w');
h_legend3 = legend('domain 1', 'domain 2');
set(h_legend3,'Box', 'on', 'Location', 'best');
axis square;

%% 4 Water saturation profiles in domain 1 before Swf1 reaches interface
% 4.1 the time when Swf reaches at the interface between domain1 and domain 2
krw1_swf  = kr_w1(Swf1);
kro1_swf  = kr_o1(Swf1);
fw1_swf   =  f_w1(Swf1);
```

```
dfw1_swf  = df_w1(Swf1);
t_inf     = pi*h*phi1*(R1^2-rw^2)/(qt*dfw1_swf);

% 4.2 calculate the travelling distance of specific water saturations Sw1
t1     = linspace(time0,t_inf,nts1);          % time vector for domain 1
dfwt1  = dfw1(end:-1:index);                  % inverted sequence of dfw
Swt1   =  Sw1(end:-1:index);                  % inverted sequence of Sw
for ti = 1:nts1% loop times vector
    for i = 1:(nsw1-index+1)
        Rsw1(i,ti) = sqrt(rw^2+qt*t1(ti)/(pi*h*phi1)*dfwt1(i));
    end
end

% 4.3 figure 4: Plot the water saturation profiles in domain 1
h_fig4 = figure(4);
set(h_fig4, 'color', 'w', 'NumberTitle', 'off', 'Name', 'Water Saturation Profiles');
SwTime= [];
for ti = 1:nts1
    plot(Rsw1(:,ti), Swt1, '-r', 'LineWidth', 2.0);
    hold on;
    plot([rw Rsw1(1,ti)], [1-Sor1 1-Sor1], '-r', 'LineWidth', 2.0);
    SwTime = [ SwTime; ['Time = ' num2str(t1(ti)/86400, format) ' day'] ];
    plot([Rsw1(end,ti) Rsw1(end,ti)], [Swf1 Swc1], '-r', 'LineWidth', 2.0);
    plot([Rsw1(end,ti) R1], [Swc1 Swc1], '-r', 'LineWidth', 2.0);
end
set(gca, 'YLim', [0 1], 'YTick', 0:0.2:1, 'XLim', [0 R1]);
set(gca, 'Fontname', 'Times New Roman','FontSize',10);
title('water saturation profiles in domain 1');
xlabel('{\it x} (m)'); ylabel('{\it S}_w');
h_legend4 = legend(SwTime);
set(h_legend4,'Box', 'on', 'Location', 'best');
axis square;

%% 5 Calculate water saturation profile in domain 1 when time > t_inf
% 5.1 calculate the corresponding parameters at interface
if timef <= t_inf
    error('Please reset the timef due to timef <= t_inf!');
end
t2  = linspace(t_inf,timef,nts2)';
dfw1_inf  = pi*h*phi1*(R1^2-rw^2)/qt./t2;        % dfw,1 at the interface (upstream)
Sw1_inf  = calObjFun(dfw1_inf, Sw1, dfw1, index); % Sw,1 at the interface (upstream)
krw1_inf  = kr_w1(Sw1_inf);                       % relative water permeability
kro1_inf  = kr_o1(Sw1_inf);                       % relative permeability of oil
fw1_inf   =  f_w1(Sw1_inf);                      % fractional flow function for Sw1_inf
Sw1_avg   = Sw1_inf+(1-fw1_inf)./dfw1_inf;       % average saturation of domain 1

% 5.2 % calculate the travelling distance of water saturations
dfwt1  = dfw1(end:-1:index);           % inverted sequence of dfw
Swt1   =  Sw1(end:-1:index);           % inverted sequence of Sw
```

```
for ti = 1:nts2% loop times vector
    for i = 1:(nsw1-index+1)
        Rsw1(i,ti+nts1) = sqrt(rw^2+qt*t2(ti)/(pi*h*phi1)*dfwt1(i));
    end
end

%% 6 Calculate water saturation profile in domain 2 when time > t_inf
% 6.1 calculate water saturation at interface and injected fluid
fw2_inf  = fw1_inf;                                % fw,2 at the interface (downstream)
Sw2_inf  = calObjFun(fw2_inf,Sw2, fw2);            % Sw,2 at the interface (downstream)
Qt       = qt.*t2;                                 % the injected water into domains
W1   = pi*h*phi1*(R1^2-rw^2).*(Sw1_avg-Swc1);      % the injected water into domain 1
W2   = Qt - W1;                                    % the injected water into domain 2
if (abs(W2(1)/Qt(1)) <= 1e-3); W2(1) = 0; end;     % enforce W2 == 0.0

% 6.1 calculate saturation profiles using mass balance principle
Sw2_k        = cell(nts2,1);           % water saturation Sw,2: initialization
Rsw2_k       = cell(nts2,1);           % initial travelling distance of Sw,2
Sw2_k{1,1}   = [Sw2_inf(1);Swc2];      % the saturation Sw,2 set at t_inf
Rsw2_k{1,1} = [R1; R1];                % the distance Xsw,2 set at t_inf
for ti = 2:nts2
    % 6.1.1 select a set of saturation Sw,2
    % choose a set of saturation Sw,2: [Sw2,inf(1) Sw2,inf(ti)]
    Sw2_k1 = [(Sw2_inf(ti)-dlt_Sw2):(-dlt_Sw2):Sw2_inf(1)]';
    % choose a set of saturation Sw,2: [Swc2 Sw2,inf(1)])
    Sw2_k2 = [(Sw2_inf(1)-dlt_Sw2):(-dlt_Sw2):Swc2]';
    % the whole set of water saturation Sw,2
    Sw2_k{ti,1} = [Sw2_inf(ti); Sw2_k1; Sw2_k2];

    % 6.1.2 calculate saturation profiles for Sw2,inf(1) <= Sw,2 <= Sw2,inf(ti)
    krw2_k1  = kr_w2(Sw2_k1);                % relative permeability of water
    kro2_k1  = kr_o2(Sw2_k1);                % relative permeability of oil
    fw2_k1   =  f_w2(Sw2_k1);                % fractional flow function
    dfw2_k1  = df_w2(Sw2_k1);                % derivative of fractional flow function
    fw1_k1   = fw2_k1;
    Sw1_k1   = calObjFun(fw1_k1,Sw1,fw1);    % calculate the Sw1 at interface
    krw1_k1  = kr_w1(Sw1_k1);                % relative permeability of water
    kro1_k1  = kr_o1(Sw1_k1);                % relative permeability of oil
    fw1_k1   =  f_w1(Sw1_k1);                % fractional flow function
    dfw1_k1  = df_w1(Sw1_k1);                % derivative of fractional flow function
    ts       = pi*h*phi1*(R1^2-rw^2)/qt./dfw1_k1;  % starting time for Sw,2 at r = R1
    % calculate the travelling distance of Sw2_k1
    Rsw2_k1 = sqrt(R1^2+qt/(pi*h*phi2).*dfw2_k1.*(t2(ti)-ts));

    % 6.1.3 calculate saturation profiles for Swc2 <= Sw,2 <= Sw2,inf(1)
    krw2_k2 = kr_w2(Sw2_k2);                 % relative permeability of water
    kro2_k2 = kr_o2(Sw2_k2);                 % relative permeability of oil
```

```
    fw2_k2 = f_w2(Sw2_k2);                    % fractional flow function
    dfw2_k2 = df_w2(Sw2_k2);                  % derivative of fractional flow function
    % calculate the travelling distance of Sw2_k2
    Rsw2_k2 = sqrt(R1^2+qt/(pi*h*phi2).*dfw2_k2.*(t2(ti)-t_inf));

   % 6.1.4 calculate the shock front saturation and its distance
   % calculate the travelling distance of Sw2_k
   Rsw2_k{ti,1} = [R1; Rsw2_k1; Rsw2_k2];
   % delta_Rsw2 = Rsw2_j^2 - Rsw2_(j-1)^2, r2_0 = R1
   dlt_Rsw2 = Rsw2_k{ti,1}(2:end).^2-Rsw2_k{ti,1}(1:end-1).^2;
   % delta_Swk2 = Sw2,k - Swc2
  dlt_swk2 = Sw2_k{ti,1}(2:end)-Swc2;
  for i = 1:nsw2
  % calculate the injected fluid volume from R1 to Xswf
      V2 = pi*h*phi2*sum(dlt_Rsw2(1:i).*dlt_swk2(1:i));
      if V2 >= W2(ti)
        index2(ti) = i;
        Swf2(ti)  = Sw2_k{ti,1}(i);
        Rswf2(ti) = Rsw2_k{ti,1}(i);
        Sw2_k{ti,1}(i+1:end) = Swc2;
        break;
      end
    end
    Rsw2_k{ti,1} = Rsw2_k{ti,1}(1:index2(ti));
    Sw2_k{ti,1} = Sw2_k{ti,1}(1:index2(ti));
end

% 6.2 figure 5-1: Plot the water saturation profiles in domain 1
h_fig5 = figure(5);
set(h_fig5, 'color', 'w', 'NumberTitle', 'off', 'Name', 'Water Saturation Profiles');
SwTime= [];
subplot(1,2,1);
for ti = 1:nts2
    plot(Rsw1(:,ti+nts1), Swt1, '-r', 'LineWidth', 2.0);
    hold on;
    plot([rw Rsw1(1,ti+nts1)], [1-Sor1 1-Sor1], '-r', 'LineWidth', 2.0);
    SwTime = [ SwTime; ['Time = ' num2str(t2(ti)/86400, format) ' day'] ];
end
plot([rw R1], [Sw2_inf(1) Sw2_inf(1)], '--k', 'LineWidth', 2.0);
set(gca, 'YLim', [0 1], 'YTick', 0:0.2:1, 'XLim', [0 R1]);
set(gca, 'Fontname', 'Times New Roman','FontSize',14);
title('domain 1');
xlabel('{\it x} (m)'); ylabel('{\it S}_w');
axis square;

% 6.3 figure 5-2: Plot the water saturation profiles in domain 2
subplot(1,2,2);
for ti = 1:nts2
```

```
    plot(Rsw2_k{ti,1}, Sw2_k{ti,1}, '-b', 'LineWidth', 2.0);
    hold on;
    plot([Rsw2_k{ti,1}(end) Rsw2_k{ti,1}(end)], [Sw2_k{ti,1}(end) Swc2], '-b',
    'LineWidth', 2.0);
    plot([Rsw2_k{ti,1}(end) R1+R2], [Swc2 Swc2], '-b', 'LineWidth', 2.0);
end
plot([R1 R2], [Sw2_inf(1) Sw2_inf(1)], '-k', 'LineWidth', 2.0);
plot(R1, Sw2_inf(1), 'ro', 'markersize', 8);
text(R1, Sw2_inf(1)-0.05, '{\it S}_{w2}^{*}', 'Color', 'k', 'Fontname',
'Times New Roman','FontSize',14);
set(gca, 'YLim', [0 1], 'YTick', 0:0.2:1, 'XLim', [R1 R2]);
set(gca, 'Fontname', 'Times New Roman','FontSize',14);
set(gca, 'YAxisLocation', 'right');
title('domain 2');
xlabel('{\it x} (m)'); ylabel('{\it S}_w');
h_legend5 = legend(SwTime);
set(h_legend5,'Box', 'on', 'Location', 'best');
axis square;

%% end
```

B.5 AUXILIARY FUNCTIONS

```
function [index, Swf, dfwf, bf] = calSatFront(Sw, fw, dfw)
%% calculate advance front saturation using Welge graphic method
%     Sw    --- saturation vector of displacing wetting phase fluid
%     fw    --- fractional flow vector of displacing wetting phase fluid
%     dfw   --- fractional flow derivate vector of displacing wetting phase fluid
%     index --- index of Swf in Sw
%     Swf   --- advance front saturation
%     dfwf  --- fractional flow derivative at Swf
%     bf    --- intercept valuve for tangent line
index = 0;
ns    = size(Sw,1);
df    = 1/(Sw(ns)-Sw(1));
dlt_Sw = Sw(ns)-Sw(ns-1);
if nargin == 2
    % calculate derivate
    for i = 3:(ns-2)
        dfw(i) = (fw(i+1)-fw(i-1))/(2*dlt_Sw);
    end
    dfw(2)     = (-11*fw(2)+18*fw(3)-9*fw(4)+2*fw(5))/(6*dlt_Sw);
    dfw(1)     = abs(2*dfw(2)-dfw(3));
    dfw(ns-1)  = -(-11*fw(nt-1)+18*fw(nt-2)-9*fw(nt-3)+2*fw(nt-4))/(6*dlt_Sw);
    dfw(ns)    = abs(2*dfw(nt-1)-dfw(nt-2));
    % calculate Swf and its index
```

```
    for i = 2:ns-1
        dfds = fw(i)/(Sw(i)-Sw(1));
        if (dfds < dfw(i-1)) && (dfds > dfw(i+1)) && (dfds >= df)
            index = i;
            Swf = Sw(i);
            dfwf = dfds;
            bf = fw(i)-dfwf*Sw(i);
           break;
        end
    end
    if index == 0
        error('Can''t find a tagent line through point (Swc,0). Decrease dlt_Sw!');
    end
elseif nargin == 3
    % calculate Swf and its index
    for i = 2:ns-1
        dfds = fw(i)/(Sw(i)-Sw(1));
        if (dfds < dfw(i-1)) && (dfds > dfw(i+1)) && (dfds >= df)
            index = i;
            Swf = Sw(i);
            dfwf = dfds;
            bf = fw(i)-dfwf*Sw(i);
            break;
        end
    end
    if index == 0
        error('Can''t find a tagent line through point (Swc,0). Decrease dlt_Sw!');
    end
else
    error('the number of input arguments in function calSatFront is incorrect!');
end
end

%% end function calSatFront()

function obj_fun = calObjFun(obj_var, Fun, Var, index_var)
%% calculate obj_fun at obj_var using interpolation method
%      Fun     --- basic function value vector
%      Var     --- basic variable value vector
%      obj_var --- objective variable value vector
%      obj_fun --- objective function value vector
%      index   --- optional for non-monotone Fun

ns      = size(obj_var,1);
obj_fun = zeros(ns,1);
if nargin == 3
```

```
    for i = 1:ns
        [~,index] = sort(abs(Var-obj_var(i)));
        obj_fun(i) = Fun(index(1));
    end
elseif nargin == 4
     for i = 1:ns
         [~,index] = sort(abs(Var-obj_var(i)));
         if index(1) >= index_var
             obj_fun(i) = Fun(index(1));
         else
        obj_fun(i) = Fun(index(2));
      end
   end
else
   error('Wrong input parameters in calObjFun function!');
end

end
%% end function calObjFun()
```

APPENDIX C

Program of Buckley–Leverett Solution for Non-Newtonian Fluid Displacement

C.1 MATLAB CODE FOR BUCKLEY–LEVERETT SOLUTION: POWER-LAW NON-NEWTONIAN FLUID

This Matlab code is a computational program realization of the Welge graphic method for Buckley–Leverett equation in a one-dimensional linear system (see Eqn (7.27) and Section 7.4), in which a Newtonian fluid is displaced by a power-law non-Newtonian fluid (see Eqn 7.2).

```
%% Problem description
%  Analytical solution of Buckley-Leverett equation using Welge method
%  A Newtonian fluid displaced by a Power-law non-Newtonian fluid
%  Brooks-Corey relative permeability curve has been applied
close all; clear all; clc;

%% 1 Parameters initialization
% 1.1 rock properties
L         = 5.00;              % domain length [m]
phi       = 0.20;              % porosity
k         = 9.869e-13;         % absolute permeability [m^2]
A         = 1.0;               % area of cross-section [m^2]
alpha     = pi*0.0;            % angle between x and horizontal [rad]

% 1.2 fluid properties
mune      = 6.0e-3;           % Newtonian phase viscosity [Pa*s]
rho_ne    = 1.0e3;             % Newtonian phase density [kg/m^3]
rho_nn    = 0.8e3;             % non-Newtonian phase density [kg/m^3]
dlt_rho   = rho_nn - rho_ne;   % phase density difference [kg/m^3]
n         = 0.60;              % power-law index
H         = 0.010;             % power-law coefficient [Pa*s^n]

% 1.3 relative permeability parameters
Sner      = 0.15;              % residual Newtonian saturation
Snnr      = 0.15;              % residual non-Newtonian saturation
nn        = 3.00;              % exponent of non-Newtonian phase
ne        = 3.00;              % exponent of Newtonian phase
krnn_max = 0.85;               % maximum permeability of non-Newtonian
krne_max = 0.85;               % maximum permeability of Newtonian
```

```
% 1.4 other initial parameters
dlt_Snn    = 1e-3;                          % constant saturation step
eps        = 1e-5;                          % a very small number
Snn = [(Snnr+eps):dlt_Snn:(1-Sner-eps)]'; % wetting phase saturation vector
qt         = 1.0e-5;                        % injection rate [m^3/s]
px0        = -5.5e4;                        % initial pressure gradient, px [Pa/m]
g          = 9.80665;                       % gravity acceleration constant [m/s^2]
time0      = 3600*1.00;                     % initial calculation time [s]
timef      = 3600*10.0;                     % final calculation time [s]
nts        = 4;                             % time steps for calculating
nsn        = size(Snn,1);                   % size of Snn
format     = '%3.2e';                       % precision format for plotting

%% 2 Relative permeabilities, fractional flow function and its derivative
kr_nn = @(S) krnn_max.*(( S-Snnr)./(1-Snnr-Sner)).^nn;   % relative permeability
kr_ne = @(S) krne_max.*((1-S-Sner)./(1-Snnr-Sner)).^ne; % relative permeability
mu_ef = @(S) H/12*(9+3/n)^n*...                          % effective viscosity
(150*k.*kr_nn(S)*phi.*(S-Snnr)).^((1-n)/2);
mu_nn = @(S,p_x) ...                                     % apparent viscosity
   mu_ef(S).*( k.*kr_nn(S)./mu_ef(S).*abs(p_x)).^(1-1/n);
v_nn  = @(S,p_x) -k.*kr_nn(S)/mu_nn(S,p_x).*...          % velocity: nn
   (p_x+rho_nn*g*sin(alpha));
v_ne  = @(S,p_x) -k.*kr_ne(S)/mune.*(p_x+rho_ne*g*sin(alpha));  % velocity: ne
px   = zeros(nsn,1);                                     % initialization of dp/dx
for i = 1:nsn
    F = @(p_x) qt/A-v_nn(Snn(i),p_x)-v_ne(Snn(i),p_x);
    px(i) = fzero(F,px0);
    if isnan(px(i))
    error('Can not find the zero near x0! Reset parameters.');
    end
    px0= px(i);
end

krnn       = kr_nn(Snn);                  % relative permeability: non-Newtonian
krne       = kr_ne(Snn);                  % relative permeability: Newtonian fluid
muef       = mu_ef(Snn);                  % effective viscosity: non-Newtonian
munn       = mu_nn(Snn,px);               % non-Newtonian fluid viscosity
mob        = (krne./mune).*(munn./krnn); % mobility function
fnn        = 1./(1+mob)-...               % fractional flow function
     A*k.*krne./(qt*mune)*dlt_rho*g*sin(alpha)./(1+mob);
dfnn       = zeros(nsn,1);                % derivate of fractional flow function
for i      = 3:(nsn-2)
    dfnn(i) = (fnn(i+1)-fnn(i-1))/(2*dlt_Snn);
end
dfnn(2)    = (-11*fnn(2)+18*fnn(3)-9*fnn(4)+2*fnn(5))/(6*dlt_Snn);
dfnn(1)    = abs(2*dfnn(2)-dfnn(3));
```

```
dfnn(nsn-1)  = -(-11*fnn(nsn-1)+18*fnn(nsn-2)-9*fnn(nsn-3)+2*fnn(nsn-4))/
(6*dlt_Snn);
dfnn(nsn)    = abs(2*dfnn(nsn-1)-dfnn(nsn-2));

% figure 1: Plot the relative permeability curves
h_fig1 = figure(1);
set(h_fig1, 'color', 'w', 'NumberTitle', 'off', ...
    'Name', 'Relative Permeability Curves: kr');
plot(Snn, krnn, '-b', Snn, krne, '-r', 'LineWidth', 2.0);
hold on;
axis([0.0 1.0 0.0 1.0]);
axis square;
set(gca, 'Fontname', 'Times New Roman','FontSize',10);
title('Brooks-Corey relative permeability curves')
xlabel('{\it S}_{nn}');
ylabel('{\it k}_{r{\it \beta}}');
set(gca, 'YTick', 0:0.2:1);
h_legend1 = legend('non-Newtonian phase', 'Newtonian phase');
set(h_legend1, 'Box', 'on', 'Location', 'best');

% figure 2: Plot the dp/dx--Snn curves
h_fig2 = figure(2);
set(h_fig2, 'color', 'w', 'NumberTitle', 'off', ...
    'Name', 'Pressure gradient versus Snn');
plot(Snn, -px/1e5, '-b', 'LineWidth', 2.0);
set(gca, 'XLim', [0 1]);
set(gca, 'Fontname', 'Times New Roman','FontSize',10);
title('Pressure gradient (Bar/m)');
xlabel('{\it S}_{nn}');
ylabel('-d {\it p} / d {\it x}');
axis square;

% figure 2: Plot the fractional flow function curves
h_fig3 = figure(3);
set(h_fig3, 'color', 'w', 'NumberTitle', 'off', ...
    'Name', 'Fractional flow function curve');
plot(Snn, fnn, '-b', 'LineWidth', 2.0);
set(gca, 'XLim', [0 1]);
set(gca, 'Fontname', 'Times New Roman','FontSize',10);
title('Fractional flow function');
xlabel('{\it S}_{nn}');
ylabel('{\it f}_{nn}');
axis square;

%% 3 Calculate advance frontal saturation
% 3.1 Evaluate advance frontal non-Newtonian fluid saturation Snnf
[index, Snnf, dfnnf, bf] = calSatFront(Snn, fnn, dfnn);
```

```
    % 3.2 Evaluate the time of advance frontal saturation Snnf
    krnn_sf = kr_nn(Snnf);
    krne_sf = kr_ne(Snnf);
    munn_sf = calObjFun(Snnf, munn, Snn);
    mob_sf  = (munn_sf/krnn_sf)*(krne_sf/mune); % mobility function
    fnn_sf  = 1./(1+mob_sf)-...                 % fractional flow function
      A*k.*krne_sf./(qt*mune)*dlt_rho*g*sin(alpha)./(1+mob_sf);
    dfnn_sf = calObjFun(Snnf, dfnn, Snn);       % derivative of fractional flow function
    tpw     = A*phi*L/(qt*dfnn_sf);             % time: saturation front arrives at well

    %% 4 Calculate saturation profile and plots
    % 4.1 Calculate travelling distance of saturations
    t       = linspace(time0,timef,nts);
    dfnnt   = dfnn(end:-1:index);               % inverted sequence of dfnn
    Snnt    =  Snn(end:-1:index);               % inverted sequence of Snn
    for ti  = 1:nts
        for i = 1:(nsn-index+1)
         Xsf(i,ti) = qt*t(ti)/(A*phi)*dfnnt(i);
       end
    end

    % 4.2 Plot the derivative curve of fractional flow function
    h_fig4 = figure(4);
    set(h_fig4, 'color', 'w', 'NumberTitle', 'off', 'Name', 'Derivate of Fractional -
Flow Curves: dfw/dSw');
    plot(Snn, dfnn, '-b', 'LineWidth', 2.0);
    set(gca, 'XLim', [0 1]);
    set(gca, 'Fontname', 'Times New Roman','FontSize',10);
    title('derivate of fractional flow function')
    xlabel('{\it S}_{nn}');
    ylabel('d {\it f}_{nn} / d {\it S}_{nn}');
    axis square;

    % 4.3 Plot the non-Newtonian fluid saturation profiles
    h_fig5 = figure(5);
    set(h_fig5, 'color', 'w', 'NumberTitle', 'off', 'Name', 'non-Newtonian Saturation
    Profiles: Snn(t)');
    SwTime= [];
    for ti = 1:nts
        plot(Xsf(:,ti), Snnt, '-r', 'LineWidth', 2.0);
        hold on;
        plot([0 Xsf(1,ti)], [1-Sner 1-Sner], '-r', 'LineWidth', 2.0);
        SwTime = [ SwTime; ['Time = ' num2str(t(1,ti)/3600, format) ' hour'] ];
        plot([Xsf(end,ti) Xsf(end,ti)], [Snnf Snnr], '-r', 'LineWidth', 2.0);
        plot([Xsf(end,ti) L], [Snnr Snnr], '-r', 'LineWidth', 2.0);
    end
    set(gca, 'YLim', [0 1], 'YTick', 0:0.2:1, 'XLim', [0 L]);
    set(gca, 'Fontname', 'Times New Roman','FontSize',10);
```

```
title('non-Newtonian fluid saturation profiles')
xlabel('{\it x} (m)');
ylabel('{\it S}_{nn}');
h_legend5 = legend(SwTime);
set(h_legend5,'Box', 'on', 'Location', 'best');
axis square;

%% end
```

C.2 MATLAB CODE FOR BUCKLEY–LEVERETT SOLUTION: BINGHAM NON-NEWTONIAN FLUID

This Matlab code is a computational program realization of the integral method for Buckley–Leverett equation in a one-dimensional linear system (see Equation (7.27) and Section 7.6), in which a Bingham non-Newtonian fluid (see Equation (7.6)) is displaced by a Newtonian fluid.

```
%% Problem description
%  Analytical solution of Buckley -Lev erett equation using integral method
%  Immiscible displacement of a Bingham non-Newtonian fluid by a Newtonian
   fluid
%  Brooks-Corey relative permeability curve has been applied
close all; clear all; clc;

%% 1 Parameters initialization
% 1.1 rock properties
L          = 4.0;              % length of domain [m]
A          = 1.0;              % cross-sectional area [m^2]
phi        = 0.20;             % porosity of domain
k          = 9.869e-13;        % permeability of domain [m^2]
alpha      = pi*0.0;           % angle between x and horizontal [rad]

% 1.2 fluid properties
rho_ne     = 1.0e3;            % density of Newtonian fluid [kg/m^3]
rho_nn     = 0.9e3;            % density of Bingham fluid [kg/m^3]
dlt_rho    = rho_ne - rho_nn;  % density difference [kg/m^3]
mu_ne      = 1.0e-3;           % viscosity of Newtonian fluid [Pa*s]
mu_B       = 5.0e-3;           % Bingham plastic coefficient [Pa*s]
mu_inf     = 1.0e20;           % infinite viscosity [Pa*s]
G          = 5.0e3;            % threshold pressure gradient [Pa/m]

% 1.3 relative permeability parameters
Sner       = 0.00;             % irreducible Newtonian saturation
Snnr       = 0.20;             % initial non-Newtonian saturation
ne         = 2.00;             % exponent of Newtonian fluid
nn         = 2.00;             % exponent of non-Newtonian fluid
krne_max   = 0.75;             % maximum permeability of Newtonian
krnn_max   = 0.75;             % maximum permeability of Non-Newtonian
```

```
% 1.4 other initial parameters
dlt_Sne  = 1e-3;                          % constant saturation step [-]
Sne      = [(Sner+eps):dlt_Sne:(1-Snnr)]'; % Newtonian fluid saturation vector
g        = 9.8067;                        % gravitational acceleration [m/s^2]
qt       = 2e-6;                          % constant injection rate [m^3/s]
time0    = 86400*0.1;                     % initial calculation time [s]
timef    = 86400*1.0;                     % final calculation time [s]
nts      = 4;                             % the number of time steps
nsn      = size(Sne,1);                   % size of Sne vector
format   = '%4.2e';                       % precision format for plotting

%% 2 Relative permeabilities, fractional flow function and its derivative
% 2.1 function handles of relative permeability and potential gradient
kr_ne = @(S) krne_max.*((S-Sner)./(1-Sner-Snnr)).^ne; % relative permeability
kr_nn = @(S) krnn_max.*((1-S-Snnr)./(1-Sner-Snnr)).^nn; % relative
permeability
dpx  = @(S) -rho_nn*g*sin(alpha)+(qt/A/k+kr_nn(S)/mu_B*G+...% potential
gradient
   (kr_ne(S)/mu_ne*rho_ne+kr_nn(S)/mu_B*rho_nn)*g*sin(alpha))./(kr_ne(S)/
mu_ne+kr_nn(S)/mu_B);

% 2.2 calculate the non-Newtonian Bingham fluid viscosity
krne     = kr_ne(Sne);            % relative permeability Newtonian fluid
krnn     = kr_nn(Sne);            % relative permeability non-Newtonian
px       = dpx(Sne);              % minus potential gradient
mu_nn    = mu_inf*ones(nsn,1);    % initial Bingham fluid viscosity
for i    = 1:nsn                  % Bingham fluid viscosity
    if (abs(px(i))-G) >= 0.0
       mu_nn(i) = mu_B/(1-G/abs(px(i)));
    end
end

% 2.3 calculate fractional flow function
mob  = (kr_nn(Sne)./mu_nn).*(mu_ne./kr_ne(Sne));  % mobility function
fne  = 1./(1+mob)-(A*k.*kr_nn(Sne)./(qt.*mu_nn)*...% fractional flow function
     dlt_rho*g*sin(alpha)).*(1+mob);

% 2.4 Evaluate the max Newtonian fluid saturation
for i = 1:nsn
   if fne(i) == 1.0
      Sne_max  = Sne(i);
      fne_max  = 1.0;
      iSmax = i;
      break;
   end
end
```

```
% 2.5 reset the parameters and derivative of fractional flow function
Sne_B  = Sne(1:iSmax);
fne_B  = fne(1:iSmax);
nsb    = size(Sne_B,1);
dfne_B = ones(nsb,1);
for i  = 3:(nsb-2)
  dfne_B(i) = (fne_B(i+1)-fne_B(i-1))/(2*dlt_Sne);
end
dfne_B(2)      = (-11*fne_B(2)+18*fne_B(3)-9*fne_B(4)+2*fne_B(5))/(6*dlt_Sne);
dfne_B(1)      = abs(2*dfne_B(2)-dfne_B(3));
dfne_B(nsb-1)  = -(-11*fne_B(nsb-1)+18*fne_B(nsb-2)-9*fne_B(nsb-3)+
2*fne_B(nsb-4))/(6*dlt_Sne);
dfne_B(nsb)    = 2*dfne_B(nsb-1)-dfne_B(nsb-2);

%% 3 plot relative permeability, fractional flow and its derivative curves
% 3.1 figure 1: Plot the relative permeability curves
h_fig1 = figure(1);
set(h_fig1, 'color', 'w', 'NumberTitle', 'off', ...
    'Name', 'Relative Permeability Curves: kr');
plot(Sne, krne, '-b', Sne, krnn, '-r', 'LineWidth', 2.0);
hold on;
axis([0.0 1.0 0.0 1.0]);
axis square;
set(gca, 'Fontname', 'Times New Roman','FontSize',10);
title('Brooks-Corey relative permeability curves')
xlabel('{\it S}_{ne}');
ylabel('{\it k}_{r{\it \beta}}');
set(gca, 'YTick', 0:0.2:1);
h_legend1 = legend('Newtonian fluid', 'Bingham fluid');
set(h_legend1,'Box', 'on', 'Location', 'best');

% 3.2 figure 2: Plot the dp/dx-Sne curves
h_fig2 = figure(2);
set(h_fig2, 'color', 'w', 'NumberTitle', 'off', ...
    'Name', 'Relative Permeability Curves: kr');
plot(Sne, px/1e5, '-b';, 'LineWidth', 2.0);
set(gca, 'XLim', [0 1]);
set(gca, 'Fontname', 'Times New Roman','FontSize',10);
title('derivates of fractional flow function');
xlabel('{\it S}_{ne}');
ylabel('-d {\it p} / d {\it x}');
axis square;

% 3.3 figure 3: Plot the fractional flow function curve
h_fig3 = figure(3);
set(h_fig3, 'color', 'w', 'NumberTitle', 'off', ...
```

```
    'Name', 'Fractional flow function curve');
plot(Sne_B, fne_B, '-b', 'LineWidth', 2.0);
set(gca, 'XLim', [0 1], 'YLim', [0 1]);
set(gca, 'Fontname', 'Times New Roman','FontSize',10);
title('fractional flow function');
xlabel('{\it S}_{ne}');
ylabel('{\it f}_{ne}');
axis square;

% 3.4 Plot the derivate curve of fractional flow function
h_fig4 = figure(4);
set(h_fig4, 'color', 'w', 'NumberTitle', 'off', 'Name', 'Derivatives of Fractional
Flow Curves: dfw/dSw');
plot(Sne_B, dfne_B, '-b', 'LineWidth', 2.0);
set(gca, 'XLim', [0 1]);
set(gca, 'Fontname', 'Times New Roman','FontSize',10);
title('derivate of fractional flow function')
xlabel('{\it S}_{ne}');
ylabel('d {\it f}_{ne} / d {\it S}_{ne}');
axis square;

%% 4 Calculate advance frontal saturation and travelling distance
dfnet        = dfne_B(end:-1:1);              % inverted sequence of dfne
fnet         =  fne_B(end:-1:1);              % inverted sequence of fne
Snet         =  Sne_B(end:-1:1);              % inverted sequence of Sne

% 4.1 calculate travelling distance of every saturations
t            = linspace(time0, timef, nts);
Sne_t        = cell(nts,1);                   % saturation Sw,2: initial
Xsf_t        = cell(nts,1);                   % travelling distance of Sw,2: initial
for ti  = 1:nts
    Wi(ti) = qt*t(ti);                        % injected wetting phase fluid volume
    for i = 1:nsb
        Xsf(i,ti) = Wi(ti)/(A*phi)*dfnet(i);  % calculate travelling distance
    end
    Xsf0  = [0; Xsf(1:end-1,ti)]; % the 2nd travelling distance vector
    dlt_Xsf  = Xsf(:,ti) - Xsf0; % dlt_Xsf = Xsf_j - Xsf_(j-1), x_0 = 0
    dlt_Snet  = Snet - Sner; % dlt_Sne = Snet,j - Sner
    for j = 1:nsb
    % calculate the injected fluid volume from 0 to Xsf
        Vj = A*phi*sum(dlt_Xsf(1:j).*dlt_Snet(1:j));
        if Vj >= Wi(ti)
            index(ti)  = j;                   % index of the Snef in Snet
            Snef(ti)   = Snet(j);             % advance front saturation: Snef
            Xswf(ti)   = Xsf(j,ti);           % the position of Snef
            break;
        end
    end
```

```
    Xsf_t{ti,1} = Xsf(1:index(ti),ti);
    Sne_t{ti,1} = Snet(1:index(ti));
end

% 4.2 Evaluate the time of advance frontal saturation Snef
krne_sf  = kr_ne(Snef(1));
krnn_sf  = kr_nn(Snef(1));
munn_sf  = calObjFun(Snef(1), mu_nn, Sne_B);
mob_sf   = (krnn_sf/munn_sf)*(mu_ne/krne_sf); % mobility function
fne_sf   = 1./(1+mob_sf)-...                  % fractional flow function
    A*k.*krnn_sf./(qt*munn_sf)*dlt_rho*g*sin(alpha)./(1+mob_sf);
dfne_sf  = calObjFun(fne_sf, dfne_B, Sne_B);  % derivate of fractional flow function
tf       = A*phi*L/(qt*dfne_sf);

%% 5 Newtonian fluid saturation profile and plots
h_fig5  = figure(5);
set(h_fig5, 'color', 'w', 'NumberTitle', 'off', 'Name', 'Newtonian fluid
Saturation Profiles: Sne(t)');
SwTime= [];
for ti = 1:nts
    plot(Xsf_t{ti,1}, Sne_t{ti,1}, '-r', 'LineWidth', 2.0);
    hold on;
    plot([0 Xsf_t{ti,1}(1)], [Sne_max Sne_max], '-r', 'LineWidth', 2.0);
    SwTime = [ SwTime; ['Time = ' num2str(t(1,ti)/3600, format) '
    hours'] ];
    plot([Xsf_t{ti,1}(end) Xsf_t{ti,1}(end)], [Sne_t{ti,1}(end) Sner], '-r',
    'LineWidth', 2.0);
   plot([Xsf_t{ti,1}(end) L], [Sner Sner], '-r', 'LineWidth', 2.0);
end
set(gca, 'YLim', [0 1], 'YTick', 0:0.2:1, 'XLim', [0 L]);
set(gca, 'Fontname', 'Times New Roman','FontSize',10);
title('Newtonian fluid saturation profiles')
xlabel('{\it x} (m)');
ylabel('{\it S}_{ne}');
h_legend2 = legend(SwTime);
set(h_legend2,'Box', 'on', 'Location', 'best');
axis square;

%% end
```

C.3 AUXILIARY FUNCTIONS

```
function [index, Swf, dfwf, bf] = calSatFront(Sw, fw, dfw)
%% calculate advance front saturation using Welge graphic method
%       Sw --- saturation vector of displacing wetting phase fluid
%       fw --- fractional flow vector of displacing wetting phase fluid
%      dfw --- fractional flow derivate vector of displacing wetting phase fluid
%    index --- index of Swf in Sw
```

```
%      Swf --- advance front saturation
%     dfwf --- fractional flow derivative at Swf
%       bf --- intercept value for tangent line
index  = 0;
ns   = size(Sw,1);
df   = 1/(Sw(ns)-Sw(1));
dlt_Sw  = Sw(ns)-Sw(ns-1);
if nargin == 2
  % calculate derivate
  for i = 3:(ns-2)
      dfw(i) = (fw(i+1)-fw(i-1))/(2*dlt_Sw);
  end
  dfw(2)     = (-11*fw(2)+18*fw(3)-9*fw(4)+2*fw(5))/(6*dlt_Sw);
  dfw(1)     = abs(2*dfw(2)-dfw(3));
  dfw(ns-1) = -(-11*fw(nt-1)+18*fw(nt-2)-9*fw(nt-3)+2*fw(nt-4))/(6*dlt_Sw);
  dfw(ns)    = abs(2*dfw(nt-1)-dfw(nt-2));
  % calculate Swf and its index
  for i = 2:ns-1
      dfds = fw(i)/(Sw(i)-Sw(1));
      if (dfds < dfw(i-1)) && (dfds > dfw(i+1)) && (dfds >= df)
          index = i;
          Swf   = Sw(i);
          dfwf  = dfds;
          bf    = fw(i)-dfwf*Sw(i);
          break;
      end
  end
  if index == 0
      error('Can't find a tangent line through point (Swc,0). Decrease dlt_Sw!');
  end
elseif nargin == 3
  % calculate Swf and its index
  for i = 2:ns-1
      dfds = fw(i)/(Sw(i)-Sw(1));
      if (dfds < dfw(i-1)) && (dfds > dfw(i+1)) && (dfds >= df)
         index  = i;
          Swf    = Sw(i);
          dfwf   = dfds;
          bf     = fw(i)-dfwf*Sw(i);
          break;
      end
  end
  if index == 0
      error('Can't find a tangent line through point (Swc,0). Decrease dlt_Sw!');
  end
else
   error('the number of input arguments in function calSatFront is incorrect!');
end
end
```

```
%% end function calSatFront()

function obj_fun = calObjFun(obj_var, Fun, Var, index_var)
%% calculate obj_fun at obj_var using interpolation method
%         Fun --- basic function value vector
%         Var --- basic variable value vector
%    obj_var --- objective variable value vector
%    obj_fun --- objective function value vector
%      index --- optional for non-monotone Fun

ns    = size(obj_var,1);
obj_fun = zeros(ns,1);
if nargin == 3
    for i = 1:ns
        [~,index] = sort(abs(Var-obj_var(i)));
        obj_fun(i) = Fun(index(1));
    end
elseif nargin == 4
     for i = 1:ns
         [~,index] = sort(abs(Var-obj_var(i)));
         if index(1) >= index_var
             obj_fun(i) = Fun(index(1));
         else
             obj_fun(i) = Fun(index(2));
         end
     end
else
     error('Wrong input parameters in calObjFun function!');
end
end
%% end function calObjFun()
```

APPENDIX D

Program of Buckley–Leverett Solution for Non-Darcy Fluid Displacement

D.1 MATLAB CODE FOR BUCKLEY–LEVERETT SOLUTION: FORCHHEIMER EQUATION

This Matlab code is a computational program realization of the Buckley–Leverett solution for non-Darcy displacement according to *Forchheimer* equation (see Eqn (8.4)) by using the integral method based on mass balance principle (see Eqn (8.35) and Section 8.4).

```
%% Problem description
%  Analytical solution of Buckley-Leverett equation using integral method
%  non-Darcy flow: wetting phase fluid displacing non-wetting phase fluid
%  non-Darcy flow is described by Forchheimer equation
%  Brooks-Corey relative permeability curve has been applied
close all; clear all; clc;

%% 1 Parameters initialization
% 1.1 rock properties
L     = 5.00;              % domain length [m]
phi   = 0.30;              % porosity
k     = 9.869e-12;         % absolute permeability [m^2]
A     = 1.0;               % area of cross-section [m^2]
theta = pi*0.0;            % angle between x and horizontal [rad]

% 1.2 fluid properties
mun      = 5.0e-3;         % non-wetting phase viscosity [Pa*s]
muw      = 1.0e-3;         % wetting phase viscosity [Pa*s]
rho_n    = 0.8e3;          % non-wetting phase density [kg/m^3]
rho_w    = 1.0e3;          % wetting phase density [kg/m^3]
dlt_rho  = rho_w - rho_n;  % phase density difference [kg/m^3]

% 1.3 relative permeability parameters
Snr      = 0.20;           % residual saturation non-wetting phase
Swr      = 0.20;           % residual saturation wetting phase
nn       = 2.00;           % exponent of non-wetting phase
nw       = 2.00;           % exponent of wetting phase
```

```
krn_max   = 0.75;                              % maximum permeability of non-wetting
krw_max   = 0.75;                              % maximum permeability of wetting phase

% 1.4 other initial parameters
C_bw     = 3.20e-6;                            % non-Darcy flow constant [m^(3/2)]
C_bn     = 3.20e-6;                            % non-Darcy flow constant [m^(3/2)]
dlt_Sw   = 1e-3;                               % constant saturation step
Sw       = [(Swr+eps):dlt_Sw:(1-Snr-eps)]';    % wetting phase saturation vector
qt       = 5.0e-4;                             % injection rate [m^3/s]
px0      = -1e5;                               % initial test pressure gradient [Pa/m]
g        = 9.80665;                            % gravity acceleration constant [m/s^2]
time0    = 3600*0.02;                          % initial calculation time [s]
timef    = 3600*0.20;                          % final calculation time [s]
nts      = 4;                                  % time steps for calculating
nsw      = size(Sw,1);                         % size of Sw vector
format   = '%3.2e';                            % precision format for plotting

%% 2 Relative permeabilities, fractional flow function and its derivative
% 2.1 initialization of function handles
kr_w = @(S) krw_max.*((  S-Swr)/(1-Swr-Snr)).^nw;   % relative permeability function
kr_n = @(S) krn_max.*((1-S-Snr)/(1-Swr-Snr)).^nn;   % relative permeability function
b_w  = @(S) C_bw./(k.*kr_w(S)).^(5/4)./(phi.*(  S-Swr)).^(3/4);  % coefficient beta_w
b_n  = @(S) C_bn./(k.*kr_n(S)).^(5/4)./(phi.*(1-S-Snr)).^(3/4); % coefficient beta_n
v_w  = @(S,p_x) 1./(2*k*rho_w.*b_w(S)).*(-muw./kr_w(S)+...       % wetting phase
   sqrt((muw./kr_w(S)).^2-4*k^2*rho_w.*b_w(S).*(p_x+rho_w*g*sin(theta))));
v_n  = @(S,p_x) 1./(2*k*rho_n.*b_n(S)).*(-mun./kr_n(S)+...      % non-wetting phase
   sqrt((mun./kr_n(S)).^2-4*k^2*rho_n.*b_n(S).*(p_x+rho_n*g*sin(theta))))

% 2.2 calculate the pressure gradient at specific saturation
px  = zeros(nsw,1);                                % initialization of dp/dx
for i = 1:nsw
    F = @(p_x) qt/A - v_w(Sw(i),p_x)-v_n(Sw(i),p_x);
    px(i) = fzero(F,px0);
    if isnan(px(i))
       error('Can not find the zero near x0! Reset parameters.');
    end
    px0 = px(i);
end

% 2.3 calculate the velocity, fractional flow function and its derivate
krw   = kr_w(Sw);                              % relative permeability vector
krn   = kr_n(Sw);                              % relative permeability vector
bw    = b_w(Sw);                               % non-Darcy flow coefficient beta_w
bn    = b_n(Sw);                               % non-Darcy flow coefficient beta_n
vw    = v_w(Sw,px);                            % wetting phase velocity [m/s]
vn    = v_n(Sw,px);                            % non-wetting phase velocity [m/s]
fw    = vw./(vw+vn);                           % fractional flow function
dfw   = zeros(nsw,1);                          % derivate of fractional flow function
for i = 3:(nsw-2)
```

```
 dfw(i)    = (fw(i+1)-fw(i-1))/(2*dlt_Sw);
end
dfw(2)     = (-11*fw(2)+18*fw(3)-9*fw(4)+2*fw(5))/(6*dlt_Sw);
dfw(1)     = abs(2*dfw(2)-dfw(3));
dfw(nsw-1) = -(-11*fw(nsw-1)+18*fw(nsw-2)-9*fw(nsw-3)+2*fw(nsw-4))/(6*dlt_Sw);
dfw(nsw)   = abs(2*dfw(nsw-1)-dfw(nsw-2));

%% 3 Calculate advance frontal saturation and travelling distance
% 3.1 calculate travelling distance of every saturations
t    = linspace(time0, timef, nts);
dfwt = dfw(end:-1:1);                          % inverted sequence of dfw
fwt  = fw(end:-1:1);                           % inverted sequence of fw
Swt  = Sw(end:-1:1);                           % inverted sequence of Sw
for ti = 1:nts
    Wi(ti) = qt*t(ti);                         % injected wetting phase fluid volume
    for i = 1:nsw
        Xsw(i,ti) = qt*t(ti)/(A*phi)*dfwt(i);  % calculate travelling distance
    end
    Xsw0 = [0; Xsw(1:end-1,ti)];               % the 2nd travelling distance vector
    dlt_Xsw = Xsw(:,ti) - Xsw0;  % dlt_Xsw = Xsw_j - Xsw_(j-1), x_0 = 0
    dlt_Swt = Swt - Swr;                       % dlt_Swt = Swt,j - Swr
    for i = 1:nsw
    % calculate the injected fluid volume from 0 to Xswf
        Vi = A*phi*sum(dlt_Xsw(1:i).*dlt_Swt(1:i));
        if Vi >= Wi(ti)
            index(ti) = i;                     % index of the Swf in Swt
            Swf(ti) = Swt(i);                  % advance front saturation: Swf
            Xswf(ti) = Xsw(i,ti);              % the position of Swf
            break;
        end
    end
end
Xsw = Xsw(1:index(1),:);
Swt = Swt(1:index(1));

% 3.2 Calculate the time when Swf reaches at production well
krw_swf = kr_w(Swf(1));
krn_swf = kr_n(Swf(1));
fw_swf  = calObjFun(Swf(1), fw,Sw);
dfw_swf = calObjFun(Swf(1),dfw,Sw);
t_pw    = A*phi*L/(qt*dfw_swf);

%% 4 Plot results
% 4.1 Plot the relative permeability curves
h_fig1 = figure(1);
set(h_fig1, 'color', 'w', 'NumberTitle', 'off', 'Name', 'Relative Permeability
Curves: kr');
plot(Sw, krw, '-b', Sw, krn, '-r', 'LineWidth', 2.0);
```

```
axis([0.0 1.0 0.0 1.0]);
axis square;
set(gca, 'Fontname', 'Times New Roman','FontSize',10);
title('Brooks-Corey relative permeability curves')
xlabel('{\it S}_w');
ylabel('{\it k}_{r {\it l}}');
set(gca, 'YTick', 0:0.2:1);
h_legend1 = legend('wetting phase', 'non-wetting phase');
set(h_legend1,'Box', 'on', 'Location', 'best');

% 4.2 figure 2: Plot the dp/dx-Sne curves
px = -px/1e5;
h_fig2 = figure(2);
set(h_fig2, 'color', 'w', 'NumberTitle', 'off', ...
    'Name', 'Pressure gradient versus Sw');
plot(Sw, px, '-b', 'LineWidth', 2.0);
set(gca, 'XLim', [0 1]);
set(gca, 'Fontname', 'Times New Roman','FontSize',10);
title('pressure gradient');
xlabel('{\it S}_w');
ylabel('-d {\it p} / d {\it x}');
axis square;

% 4.3 Plot the non-Darcy flow coefficients curve
h_fig3 = figure(3);
set(h_fig3, 'color', 'w', 'NumberTitle', 'off', 'Name', 'non-Darcy coefficients');
semilogy(Sw, bw, '-b', Sw, bn, '-r','LineWidth', 2.0);
axis square;
axis([0.0 1.0 0.0 10^18]);
set(gca, 'Fontname', 'Times New Roman','FontSize',10);
title('non-Darcy flow coefficient')
xlabel('{\it S}_w');
ylabel('{\it \betal}_{l} (m^{-1})');
h_legend3 = legend('wetting phase', 'non-wetting phase');
set(h_legend3,'Box', 'on', 'Location', 'best');

% 4.4 Plot the fractional flow function curve
h_fig4 = figure(4);
set(h_fig4, 'color', 'w', 'NumberTitle', 'off', 'Name', 'Fractional Flow Curve fw');
plot(Sw, fw, '-b', 'LineWidth', 2.0);
axis([0.0 1.0 0.0 1.0]);
axis square;
set(gca, 'Fontname', 'Times New Roman','FontSize',10);
title('fractional flow function curve')
xlabel('{\it S}_w');
ylabel('{\it f}_w');
set(gca, 'YTick', 0:0.2:1);
```

```
% 4.5 Plot the derivative curve of fractional flow function
h_fig5 = figure(5);
set(h_fig5, 'color', 'w', 'NumberTitle', 'off', 'Name', 'Derivate of Fractional
Flow Curve dfw/dSw');
plot(Sw, dfw, '-b', 'LineWidth', 2.0);
set(gca, 'XLim', [0 1]);
set(gca, 'Fontname', 'Times New Roman','FontSize',10);
title('derivatives of fractional flow function')
xlabel('{\it S}_w');
ylabel('d {\it f}_w / d {\it S}_w');
axis square;

% 4.6 Plot the wetting phase saturation profiles
h_fig6 = figure(6);
set(h_fig6, 'color', 'w', 'NumberTitle', 'off', 'Name', 'Saturation Profiles: Sw(t)');
SwTime= [];
for ti = 1:nts
    plot(Xsw(:,ti), Swt, '-r', 'LineWidth', 2.0);
    hold on;
    plot([0 Xsw(1,ti)], [1-Snr 1-Snr], '-r', 'LineWidth', 2.0);
    SwTime = [ SwTime; ['Time = ' num2str(t(1,ti)/3600, format) ' hours'] ];
    plot([Xsw(end,ti) Xsw(end,ti)], [Swf(ti) Swr], '-r', 'LineWidth', 2.0);
    plot([Xsw(end,ti) L], [Swr Swr], '-r', 'LineWidth', 2.0);
end
set(gca, 'YLim', [0 1], 'YTick', 0:0.2:1, 'XLim', [0 L]);
set(gca, 'Fontname', 'Times New Roman','FontSize',10);
title('wetting phase saturation profiles')
xlabel('{\it x} (m)');
ylabel('{\it S}_w');
h_legend6 = legend(SwTime);
set(h_legend6,'Box', 'on', 'Location', 'best');
axis square;

%% end
```

D.2 MATLAB CODE FOR BUCKLEY–LEVERETT SOLUTION: BARREE AND CONWAY MODEL

This Matlab code is a computational program realization of the Buckley–Leverett solution for non-Darcy displacement according to the Barree–Conway model (see Eqn (8.16)) by using the integral method based on mass balance principle (see Eqn (8.35) and Section 8.5).

```
%% Problem description
%  Analytical solution of Buckley-Leverett equation using integral method
%  non-Darcy flow: wetting phase fluid displacing non-wetting phase fluid
%  non-Darcy flow is described by Barree-Conway model
```

```
% Brooks-Corey relative permeability curve has been applied
close all; clear all; clc;

%% 1 Parameters initialization
% 1.1 rock properties
L        = 5.00;                              % domain length [m]
phi      = 0.30;                              % porosity
kd       = 9.869e-13;                         % absolute permeability [m^2]
kmr      = 0.01;                              % minimum permeability ratio (fraction)
tau      = 5e2;                               % inverse of characteristic length [1/m]
A        = 1.0;                               % area of cross-section [m^2]
theta    = pi*0.0;                            % angle between x and horizontal [rad]

% 1.2 fluid properties
mun      = 5.0e-3;                            % non-wetting phase viscosity [Pa*s]
muw      = 1.0e-3;                            % wetting phase viscosity [Pa*s]
rho_n    = 0.8e3;                             % non-wetting phase density [kg/m^3]
rho_w    = 1.0e3;                             % wetting phase density [kg/m^3]
dlt_rho  = rho_w - rho_n;                     % phase density difference [kg/m^3]

% 1.3 relative permeability parameters
Snr      = 0.20;                              % residual saturation non-wetting phase
Swr      = 0.20;                              % residual saturation wetting phase
nn       = 2.00;                              % exponent of non-wetting phase
nw       = 2.00;                              % exponent of wetting phase
krn_max = 0.75;                               % maximum permeability non-wetting phase
krw_max = 0.75;                               % maximum permeability wetting phase

% 1.4 other initial parameters
dlt_Sw  = 1e-3;                               % constant saturation step
Sw       = [(Swr+eps):dlt_Sw:(1-Snr-eps)]';   % wetting phase saturation vector
px0      = -5e5;                              % find a zero of function near x_0
qt       = 1.0e-5;                            % injection rate [m^3/s]
g        = 9.80665;                           % gravity acceleration constant [m/s^2]
time0    = 3600*1.00;                         % initial calculation time [s]
timef    = 3600*10.0;                         % final calculation time [s]
nts      = 4;                                 % time steps for calculating
nsw      = size(Sw,1);                        % size of Sw vector
format  = '%3.2e';                            % precision format for plotting

%% 2 Relative permeabilities, fractional flow function and its derivative
% 2.1 initialization of function handles
kr_w = @(S) krw_max.*((  S-Swr)/(1-Swr-Snr)).^nw;  % relative permeability function
kr_n = @(S) krn_max.*((1-S-Snr)/(1-Swr-Snr)).^nn;  % relative permeability function
v_w  = @(S,p_x) -1./(2*muw*rho_w).*...             % non-Darcy flow velocity
    ( muw^2.*S*tau+(p_x+rho_w*g*sin(theta))*kd.*kr_w(S)*kmr*rho_w )
+1./(2*muw*rho_w).*...
    ( (muw^2.*S*tau+(p_x+rho_w*g*sin(theta))*kd.*kr_w(S)*kmr*rho_w).^2-...
    4*muw^2*rho_w*kd*tau.*S.*kr_w(S).*(p_x+rho_w*g*sin(theta)) ).^(1/2);
```

```
    v_n  = @(S,p_x) -1./(2*mun*rho_n).*...              % non-Darcy flow velocity
        ( mun^2.*(1-S)*tau+(p_x+rho_n*g*sin(theta))*kd.*kr_n(S)*kmr*rho_n )
+1./(2*mun*rho_n).*...
      ( (mun^2.*(1-S)*tau+(p_x+rho_n*g*sin(theta))*kd.*kr_n(S)*kmr*rho_n).^2-...
      4*mun^2*rho_n*kd*tau.*(1-S).*kr_n(S).*(p_x+rho_n*g*sin(theta)) ).^(1/2);

    % 2.2 calculate the pressure gradient at specific saturation
    px  = zeros(nsw,1);       % initialization of dp/dx
    for i = 1:nsw
        F = @(p_x) qt/A - v_w(Sw(i),p_x)-v_n(Sw(i),p_x);
        px(i) = fzero(F,px0);
        if isnan(px(i))
            error('Can not find the px near px0! Reset parameters.');
        end
        px0 = px(i);
    end

    % 2.3 calculate the velocity, fractional flow function and it's derivate
    krw   = kr_w(Sw);                          % relative permeability wetting phase
    krn   = kr_n(Sw);                          % relative permeability non-wetting phase
    vw    = v_w(Sw,px);                        % wetting phase velocity vector [m/s]
    vn    = v_n(Sw,px);                        % nonwetting phase velocity vector [m/s]
    fw    = vw./(vw+vn);                       % fractional flow function
    dfw   = zeros(nsw,1);                      % derivate of fractional flow function
    for i = 3:(nsw-2)
         dfw(i) = (fw(i+1)-fw(i-1))/(2*dlt_Sw);
    end
    dfw(2)       = (-11*fw(2)+18*fw(3)-9*fw(4)+2*fw(5))/(6*dlt_Sw);
    dfw(1)       = abs(2*dfw(2)-dfw(3));
    dfw(nsw-1)   = -(-11*fw(nsw-1)+18*fw(nsw-2)-9*fw(nsw-3)+2*fw(nsw-4))/(6*dlt_Sw);
    dfw(nsw)     = abs(2*dfw(nsw-1)-dfw(nsw-2));

    %% 3 Calculate advance frontal saturation and travelling distance
    % 3.1 calculate travelling distance of every saturations
    t     = linspace(time0, timef, nts);
    dfwt  = dfw(end:-1:1);                     % inverted sequence of dfw
    fwt   =  fw(end:-1:1);                     % inverted sequence of fw
    Swt   =  Sw(end:-1:1);                     % inverted sequence of Sw
    for ti = 1:nts
        Wi(ti) = qt*t(ti);                     % injected wetting phase fluid volume
        for i = 1:nsw
            Xsw(i,ti) = qt*t(ti)/(A*phi)*dfwt(i); % calculate travelling distance
        end
        Xsw0 = [0; Xsw(1:end-1,ti)];           % the 2nd travelling distance vector
        dlt_Xsw = Xsw(:,ti) - Xsw0;            % dlt_Xsw = Xsw_j - Xsw_(j-1), x_0 = 0
        dlt_Swt = Swt - Swr;                   % dlt_Swt = Swt,j - Swr
        for i = 1:nsw
```

```
    % calculate the injected fluid volume from 0 to Xswf
        Vi = A*phi*sum(dlt_Xsw(1:i).*dlt_Swt(1:i));
        if Vi >= Wi(ti)
            index(ti) = i;                  % index of the Swf in Swt
            Swf(ti)  = Swt(i);              % advance front saturation: Swf
            Xswf(ti) = Xsw(i,ti);           % the position of Swf
            break;
        end
    end
end
Xsw = Xsw(1:index(1),:);
Swt = Swt(1:index(1));

% 3.2 Calculate the time when Swf reaches at production well
krw_swf = kr_w(Swf(1));
krn_swf = kr_n(Swf(1));
fw_swf  = calObjFun(Swf(1), fw,Sw);
dfw_swf = calObjFun(Swf(1),dfw,Sw);
t_pw    = A*phi*L/(qt*dfw_swf);

%% 4 Plot results
% 4.1 Plot the relative permeability curves
h_fig1 = figure(1);
set(h_fig1, 'color', 'w', 'NumberTitle', 'off', 'Name', 'Relative Permeability
Curves: kr');
plot(Sw, krw, '-b', Sw, krn, '-r', 'LineWidth', 2.0);
axis([0.0 1.0 0.0 1.0]);
axis square;
set(gca, 'Fontname', 'Times New Roman','FontSize',10);
title('(Brooks-Corey relative permeability curves')
xlabel('{\it S}_w');
ylabel('{\it k}_{r {\it l}}');
set(gca, 'YTick', 0:0.2:1);
h_legend1 = legend('wetting phase', 'non-wetting phase');
set(h_legend1,'Box', 'on', 'Location', 'best');

% 4.2 figure 2: Plot the dp/dx--Sne curves
px = -px/1e5;
h_fig2 = figure(2);
set(h_fig2, 'color', 'w', 'NumberTitle', 'off', ...
    'Name', 'pressure gradient curve');
plot(Sw, px, '-b', 'LineWidth', 2.0);
set(gca, 'XLim', [0 1]);
set(gca, 'Fontname', 'Times New Roman','FontSize',10);
title('pressure gradient');
xlabel('{\it S}_{ne}');
ylabel('-d {\it p} / d {\it x}');
axis square;
```

```
% 4.3 Plot the fractional flow function curve
h_fig3 = figure(3);
set(h_fig3, 'color', 'w', 'NumberTitle', 'off', 'Name', 'Fractional Flow Curve fw');
plot(Sw, fw, '-b', 'LineWidth', 2.0);
axis([0.0  1.0  0.0  1.0]);
axis square;
set(gca, 'Fontname', 'Times New Roman','FontSize',10);
title('fractional flow function curve')
xlabel('{\it S}_w');
ylabel('{\it f}_w');
set(gca, 'YTick', 0:0.2:1);

% 4.4 Plot the derivative curve of fractional flow function
h_fig4 = figure(4);
set(h_fig4, 'color', 'w', 'NumberTitle', 'off', 'Name', 'Derivates of Fractional
Flow Curve dfw/dSw');
plot(Sw, dfw, '-b', 'LineWidth', 2.0);
set(gca, 'XLim', [0 1]);
set(gca, 'Fontname', 'Times New Roman','FontSize',10);
title('derivate of fractional flow function')
xlabel('{\it S}_w');
ylabel('d {\it f}_w / d {\it S}_w');
axis square;

% 4.5 Plot the water saturation profiles
h_fig5 = figure(5);
set(h_fig5, 'color', 'w', 'NumberTitle', 'off', 'Name', 'Saturation Profiles: Sw(t)');
SwTime= [];
for ti = 1:nts
    plot(Xsw(:,ti), Swt, '-r', 'LineWidth', 2.0);
    hold on;
    plot([0 Xsw(1,ti)], [1-Snr 1-Snr], '-r', 'LineWidth', 2.0);
    SwTime = [ SwTime; ['Time = ' num2str(t(1,ti)/3600, format) ' hours'] ];
    plot([Xsw(end,ti) Xsw(end,ti)], [Swf(ti) Swr], '-r', 'LineWidth', 2.0);
    plot([Xsw(end,ti) L], [Swr Swr], '-r', 'LineWidth', 2.0);
end
set(gca, 'YLim', [0 1], 'YTick', 0:0.2:1, 'XLim', [0 L]);
set(gca, 'Fontname', 'Times New Roman','FontSize',10);
title('wetting phase saturation profiles')
xlabel('{\it x} (m)');
ylabel('{\it S}_w');
h_legend5 = legend(SwTime);
set(h_legend5,'Box', 'on', 'Location', 'best');
axis square;
%% end
```

D.3 AUXILIARY FUNCTIONS

```
function [index, Swf, dfwf, bf] = calSatFront(Sw, fw, dfw)
%% calculate advance front saturation using Welge graphic method
%     Sw --- saturation vector of displacing wetting phase fluid
%     fw --- fractional flow vector of displacing wetting phase fluid
%    dfw --- fractional flow derivate vector of displacing wetting phase fluid
%  index --- index of Swf in Sw
%    Swf --- advance front saturation
%   dfwf --- fractional flow derivative at Swf
%     bf --- intercept value for tangent line
index  = 0;
ns     = size(Sw,1);
df     = 1/(Sw(ns)-Sw(1));
dlt_Sw = Sw(ns)-Sw(ns-1);
if nargin == 2
    % calculate derivate
    for i = 3:(ns-2)
        dfw(i) = (fw(i+1)-fw(i-1))/(2*dlt_Sw);
    end
    dfw(2) = (-11*fw(2)+18*fw(3)-9*fw(4)+2*fw(5))/(6*dlt_Sw);
    dfw(1) = abs(2*dfw(2)-dfw(3));
    dfw(ns-1) = -(-11*fw(nt-1)+18*fw(nt-2)-9*fw(nt-3)+2*fw(nt-4))/(6*dlt_Sw);
    dfw(ns) = abs(2*dfw(nt-1)-dfw(nt-2));
    % calculate Swf and its index
    for i = 2:ns-1
        dfds = fw(i)/(Sw(i)-Sw(1));
        if (dfds < dfw(i-1)) && (dfds > dfw(i+1)) && (dfds >= df)
            index = i;
            Swf = Sw(i);
            dfwf = dfds;
            bf = fw(i)-dfwf*Sw(i);
            break;
        end
    end
    if index == 0
        error('Can't find a tangent line through point (Swc,0). Decrease dlt_Sw!');
    end
elseif nargin == 3
    % calculate Swf and its index
    for i = 2:ns-1
        dfds = fw(i)/(Sw(i)-Sw(1));
        if (dfds < dfw(i-1)) && (dfds > dfw(i+1)) && (dfds >= df)
            index = i;
            Swf   = Sw(i);
```

```
            dfwf  = dfds;
            bf    = fw(i)-dfwf*Sw(i);
            break;
        end
    end
    if index == 0
        error('Can't find a tangent line through point (Swc,0). Decrease dlt_Sw!');
    end
else
    error('the number of input arguments in function calSatFront is incorrect!');
end
end

%% end function calSatFront()

function obj_fun = calObjFun(obj_var, Fun, Var, index_var)
%% calculate obj_fun at obj_var using interpolation method
%       Fun --- basic function value vector
%       Var --- basic variable value vector
%  obj_var --- objective variable value vector
%  obj_fun --- objective function value vector
%    index --- optional for non-monotone Fun

ns      = size(obj_var,1);
obj_fun = zeros(ns,1);
if nargin == 3
    for i = 1:ns
    [~,index] = sort(abs(Var-obj_var(i)));
    obj_fun(i) = Fun(index(1));
    end
elseif nargin == 4
    for i = 1:ns
        [~,index] = sort(abs(Var-obj_var(i)));
        if index(1) >= index_var
            obj_fun(i) = Fun(index(1));
        else
            obj_fun(i) = Fun(index(2));
        end
    end
else
    error('Wrong input parameters in calObjFun function!');
end

end
%% end function calObjFun()
```

APPENDIX E

Nomenclature

Symbols

A	Cross-sectional area	[m^2]
A_{ij}	Area between connected grid blocks i and j	[m^2]
A_i^k	The accumulation term at node i for component k	[kg/m^3]
A_i^β	The mass accumulation term of β fluid in grid block i	[kg/m^3]
A, B, C	Dimensions of matrix blocks along x, y, and z directions for a multi-continuum system	[m]
a, b, c	Fracture-spacings of small fractures along x, y, and z directions for a multi-continuum system	[m]
B_β	Formation volume factor for phase β	[-]
B_w^0	The formation volume factor of water at initial bubble point pressure	[-]
C_f	Compressibility of a fluid	[1/Pa]
C_k, C_p	Coefficients of relative permeability and capillary-pressure functions in Equations (9.11) and (9.12)	[-]
C_r	Rock compressibility	[1/Pa]
C_T	Thermal expansion coefficient of formation rock	[1/°C]
C_β	Non-Darcy flow constant in Forchheimer equation	[$m^{3/2}$]
D	A depth from a datum	[m]
$\boldsymbol{D}_\beta^k$	The hydrodynamic dispersion tensor, accounting for both molecular diffusion and mechanical dispersion for component k in phase β	[m^2/s]
d_i	The distance from the center of grid block i and the interface between grid blocks i and j	[m]
d_j	The distance from the center of grid block j and the interface between grid blocks i and j	[m]
d_m	Mean size of solid grains	[m]
d_β^k	The molecular diffusion coefficient of component k within fluid β	[m^2/s]
E	Constant in Barree–Conway model	[-]
$F_{A,ij}^k$	The net mass fluxes of component k by advection dispersion between grid blocks i and j	[$kg/(s \cdot m^2)$]
$F_{D,ij}^k$	The net mass fluxes of component k by hydrodynamic dispersion between grid blocks i and j	[$kg/(s \cdot m^2)$]
$\boldsymbol{F}_b$	The body force	[$kg \cdot m/s^2$]
$\boldsymbol{F}_\beta$	Mass flux vector for fluid β	[$kg/(s \cdot m^2)$]

Symbols

$\boldsymbol{F}_{\beta}^{k}$	The dispersive flux vector of component k within fluid β	[kg/(s·m^2)]
$\boldsymbol{F}^{\mathrm{T}}$	The combined heat flux vector, including both advective and conductive heat flow in a multiphase, multicomponent system	[W/m^2]
f	The fractional flow function	[-]
f_{β}	The fractional flow of a fluid phase β	[-]
$flow_{ij}^{k}$	The mass flux term between nodes i and j of component k	[kg/(s·m^2)]
$flow_{ij}^{\beta}$	The mass flux term between nodes i and j of phase β	[kg/(s·m^2)]
G	The minimum potential or threshold gradient of Bingham fluid flow or shear modulus	[Pa/m] [Pa]
$\boldsymbol{g}$	Gravitation acceleration vector	[m/s^2]
g	Gravitational acceleration constant (=9.80665)	[m/s^2]
H	The consistence parameter of power-law non-Newtonian fluids	[Pa·s^n]
h	The thickness of a reservoir	[m]
h_{β}	Specific enthalpies of fluid phase β	[J/kg]
h_{β}^{k}	Specific enthalpies of component k in fluid β	[J/kg]
$\boldsymbol{I}$	The identity matrix	[-]
K	The bulk modulus	[Pa]
K_{s}	The solid modulus	[Pa]
K_{T}	The overall thermal conductivity	[W/(m·°C)]
$K_{\alpha:\beta}^{k}$	The equilibrium partitioning coefficient of component k between phases α and β	[-]
K_{*}	The modulus of the porous medium without the fractures	[Pa]
$\boldsymbol{k}$	Absolute permeability tensor	[m^2]
k	Absolute permeability	[m^2]
k_{app}	Apparent permeability to describe non-Darcy (nonlinear) flow	[m^2]
k_{c}	Asymptotic values of permeability	[m^2]
k_{d}	Darcy permeability	[m^2]
$k_{\mathrm{g\_eff}}$	The effective permeability of gas phase	[m^2]
k_{min}	The minimum permeability plateau	[m^2]
k_{mr}	The ratio between k_{min} and k_{d}, i.e., $k_{\mathrm{min}}/k_{\mathrm{d}}$	[-]
k_{rne}	Relative permeability of Newtonian fluid	[-]
k_{rnn}	Relative permeability of non-Newtonian fluid	[-]
$k_{\mathrm{ro}}^{\mathrm{og}}$	Relative permeability to oil in the oil−gas two-phase system	[-]
$k_{\mathrm{ro}}^{\mathrm{ow}}$	Relative permeability to oil in the water−oil two-phase system	[-]

Symbols

$k_{\mathrm{ro}}^{*\mathrm{ow}}$	Relative permeability value to oil at residual water saturation in the water−oil two-phase system	[-]
$k_{\mathrm{r}\beta}$	Relative permeability of phase β	[-]
$k_{\mathrm{r}\beta,\max}$	The max relative permeability of phase β	[-]
L	Length of the formation	[m]
l_x, l_y, l_z	Lengths of small fractures from large fractures along x, y, and z directions for a multi-continuum system	[m]
N	The total number of grid blocks	[-]
N_{c}	The total number of mass components	[-]
N_{pd}	The oil recovery ratio	[-]
N_{Re}	The Reynolds number	[-]
$\boldsymbol{n}$	The unit vector, normal to surface s	[-]
n	The power-law index of power-law non-Newtonian fluids	[-]
n_β	Power-index of phase β in power-law relative permeability function	[-]
P	Fluid pressure	[Pa]
P_{b}	The bubble point (pressure) of the reservoir	[Pa]
P_{b}^0	Initial bubble point pressure	[Pa]
P_{c}	Capillary pressure	[Pa]
P_{d}	The entry pressure of the porous medium	[Pa]
P_{cgL}	The gas−Liquid capillary pressure	[Pa]
P_{cgo}	The gas−oil capillary pressure	[Pa]
P_{cgw}	The gas−water capillary pressure	[Pa]
$P_{\mathrm{cgo}}^{\mathrm{go}}$	Capillary pressure between gas and oil in a three-phase system	[Pa]
P_{cow}	The oil−water capillary pressure	[Pa]
$P_{\mathrm{cow}}^{\mathrm{ow}}$	Capillary pressure between oil and water in a three-phase system	[Pa]
P_{i}	The initial pore pressure	[Pa]
P_β	Fluid pressure of phase β	[Pa]
Q_i^k	The mass sink/source term at node i for component k	[kg/s/m^3]
Q_i^β	The mass sink/source term at node i for fluid β	[kg/s/m^3]
q_{inj}	Fluid injection rate	[m^3/s]
q_{t}	The total fluid flow flux	[m^3/s]
q_t	Fluid injection rate dependent time t	[m^3/s]
q_β	Mass source/sink term for fluid β	[kg/s/m^3]
R	The radius of a domain in a radial system	[m]
R_{s}	Solution gas−oil ratio	[-]
R_i^k	Residual term of mass balance of component k at grid block i	[kg/s]
R_i^β	Residual term of mass balance of phase β at grid block i	[kg/s]

Symbols

r	The radius at a radial system	[m]
r_e	The radius of the outside edge	[m]
r_{S_β}	The position or travelling distance of saturation S_β	[m]
r_w	The radius of the injection well	[m]
S	Saturation	[-]
S_L	Saturation of liquid phase	[-]
S_{Lr}	The irreducible liquid saturation	[-]
S_{or}	Residual oil saturation	[-]
S_{wc}	Connate water saturation (or residual water saturation)	[-]
S_{wf}	The water saturation shock front	[-]
S_{wp}	The water saturation in the producing well	[-]
S_w^k	The k-th saturation in a chosen set of water saturation	[-]
S_β	Saturation of phase β	[-]
$S_{\beta f}$	The saturation shock front of phase β	[-]
$\overline{S}_\beta$	Average saturation of phase β or normalized saturation of phase β	[-]
$\overline{S}_L$	Effective or normalized liquid (water or oil) saturation	[-]
s	Surface of a domain with volume V	[-]
T	Temperature	[°C]
t	Time	[s]
t_s	The starting time when the saturation arrives at the interface between domain 1 and 2 in a composite system	[s]
t^*	The time when the sharp front arrives at the interface between domain 1 and 2 in a composite system	[s]
Δt	Time step	[s]
U_β	The internal energies of fluid β	[J/kg]
U_s	The internal energies of rock solids	[J/kg]
u	Displacement	[m]
$\boldsymbol{u}$	Displacement vector	[m]
V	Volume of a grid block or a domain	[m^3]
V_s	Volume of the solid phase	[m^3]
v	Darcy's velocity	[m/s]
$\boldsymbol{v}_\beta$	Darcy's velocity vector or volumetric flow rate of phase β	[m/s]
v_{shock}	The velocity of the saturation shock	[m/s]
W_i	The cumulative water injected with q_{inj}	[m^3]
W_{id}	The dimensionless number of pore volumes (PV)	[-]
X_β^k	The mass fraction of component k in fluid β	[-]
x	x-Direction coordinate	[m]

Symbols

Δx	Distance step at x-direction	[m]
$x_{k,p}$	Primary variable, $k = 1$, 2, or 3 at the p-th Newton iteration level	[-] or [Pa]
x_s	Travelling distance of saturation in domain 2 in a composite system	[m]
x_{S_β}	The position or travelling distance of saturation S_β	[m]
y	y-Direction coordinate	[m]
z	z-Direction coordinate	[m]

Greek Symbols

α	Biot's coefficient	[-]
α_{go}	The parameter of van Genuchten function in three-phase system	[-]
α_{ow}	The parameter of van Genuchten function in three-phase system	[-]
α_{vG}	The parameter of van Genuchten function	[-]
α_T^β, α_L^β	Transverse and longitudinal dispersivities, respectively, in fluid β of porous media	[m]
α^*	Exponential coefficient of relative permeability function, Equation (9.11), and $\alpha^* = \beta^* + 1$	[-]
β	Effective non-Darcy flow coefficient or the parameter of the van Genuchten functions	$[m^{-1}]$ [-]
β^*	Exponential coefficient of capillary-pressure function, Equation (9.12), and $\alpha^* = \beta^* + 1$	[-]
β_T	Linear thermal expansion coefficient	[1/°C]
β_β	Effective non-Darcy flow coefficient of phase β	$[m^{-1}]$
δ_{ij}	The Kronecker delta function ($\delta_{ij} = 1$ for $i = j$, and $\delta_{ij} = 0$ for $i \neq j$) with i and j being coordinate indices	[-]
δ_1, δ_2	The two interpolation parameters in numerical simulation of power-law non-Newtonian fluid flow	[Pa/m]
ε, $\boldsymbol{\varepsilon}$	Strain, strain tensor	[-]
ε_A	The area strain	[-]
ε_d	The distance strain	[-]
ε_v	The volumetric strain	[-]
Φ	Flow potential	[Pa]
Φ_β	Flow potential of phase β	[Pa]
$\nabla\Phi_\beta$	Fluid flow potential gradient	[Pa/m]
$\nabla\Phi_e$	The effective potential gradient	[Pa/m]
ϕ	Porosity of a porous medium	[-]
ϕ_c	Asymptotic values of porosity	[-]
φ	The parameter of Brooks–Corey function	[-]
γ	The parameter of the van Genuchten functions	[-]

Greek Symbols

γ_{ij}	The transmissivity of flow terms between grid blocks i and j	[m^3]
λ	The pore size distribution (normal values of $0.3 \sim 3.0$) or the Lamé parameter in stress-strain relation equation	[-] or [Pa]
λ_β	The mobility of phase β	[1/(Pa·s)]
μ	Viscosity	[Pa·s]
μ_β	Fluid viscosity of phase β	[Pa·s]
θ	The angle between flow direction and horizontal plane	[rad]
ρ_β	Fluid density of phase β	[kg/m^3]
$\overline{\rho}_{\mathrm{dg}}$	Density of dissolved gas (dg) in oil phase at reservoir conditions	[kg/m^3]
$\overline{\rho}_{\mathrm{o}}$	Density of oil, excluding dissolved gas, at reservoir conditions	[kg/m^3]
σ, $\boldsymbol{\sigma}$	Stress, stress tensor	[Pa]
σ_{m}	The mean stress	[Pa]
σ_{go}	Interfacial tensions between gas and oil	[N/m]
σ_{ow}	Interfacial tensions between oil and water	[N/m]
σ'	The effective stress in porous media	[Pa]
τ	Inverse of the characteristic length or tortuosity of porous media of formation rock or shear stress	[1/m] [-] [Pa]
υ	Poisson's ratio	[-]
ω_l	The volume fraction of the l-th continuum system	[-]
$\omega_\alpha^k, \omega_\beta^k$	The mole fraction of component k in phase α and β	[-]

Subscript

0	A reference or initial (zero) conditions	[-]
1	Domain 1	[-]
2	Domain 2	[-]
B	Bingham	[-]
b	Bubble point	[-]
bt	Breakthrough	[-]
dg	Dissolved gas	[-]
eff	Effective	[-]
F	Large fractures	[-]
FM	Large fractures-matrix	[-]
FV	Large fractures-vug	[-]
f	Fluid or small fractures	[-]
fm	Fracture-matrix	[-]
id	Dimensionless injection	[-]
i	i-th node or grid block	[-]
j	j-th of node or grid block	[-]

Subscript

ij	Between the *i*-th and *j*-th nodes or grid blocks	[-]
ij+1/2	Proper averaging at the interface between grid blocks *i* and *j*	[-]
L	Liquid phase	[-]
l	*l*-th Continuum system	[-]
n	Non-wetting phase	[-]
Lr	Residual of Liquid phase	[-]
M	Matrix	[-]
VM	Vug-matrix	[-]
ne	Newtonian fluid	[-]
ne,ir	Irreducible saturation of the Newtonian phase	[-]
nn	Non-Newtonian fluid	[-]
nn,ir	Irreducible saturation of the non-Newtonian phase	[-]
p	Previous Newtonian–Raphson iterative level	[-]
p+1	Current Newtonian–Raphson iterative level	[-]
R	Rock	[-]
RC	Reservoir conditions	[-]
r	Reference elevation or condition	[-]
ref	Reference conditions	[-]
STC	Standard conditions (or storage tank conditions)	[-]
T	Temperature dependent	[-]
t	Time dependent	[-]
V	Vugs	[-]
w	Water or wetting phase	[-]
wp	Producing well	[-]
w,bt	Water breakthrough	[-]
o	Oil	[-]
g	Gas	[-]
β	Fluid phase, including oil (o), water (w), gas (g), and so on	[-]
+	Value ahead the shock front	[-]
−	Values behind the shock front	[-]

Superscript

0	Initial or reference conditions	[-]
E	External source/sink terms for energy	[-]
k	*k*-th Mass component	[-]
n	Previous time level	[-]
n+1	Current time level	[-]
T	Temperature dependent	[-]
β	Fluid phase, including oil (o), water (w), and gas (g)	[-]
+	Value ahead the interface between domain 1 and 2	[-]
−	Value behind the interface between domain 1 and 2	[-]

INDEX

Note: Page numbers followed by "f" and "t" indicates figures and tables respectively.

C

D

E

F

G

H

I

J

K

L

M

N

R

S

T

U

V

W

Y